

Theoretical and Mass Spectrometric Studies of Low-valent Heavier Tetrel and Transition Metal-Tetrel Compounds

Dissertation

zur

Erlangung des Doktorgrades (Dr. rer. nat.)

der

Mathematisch-Naturwissenschaftlichen Fakultät

der

Rheinischen Friedrich-Wilhelms-Universität Bonn

vorgelegt von

Leonard Ruben Maurer

aus

Kassel

Bonn, im April 2024

Angefertigt mit Genehmigung der Mathematisch-Naturwissenschaftlichen Fakultät der Rheinischen Friedrich-Wilhelms-Universität Bonn.

Gutachter/Betreuer: Prof. Dr. Alexander C. Filippou
Gutachter: Prof. Dr. Stefan Grimme

Datum der mündlichen Prüfung: 28.08.2024
Erscheinungsjahr: 2024

Ich versichere, dass ich die vorliegende Arbeit unter Einhaltung der Regeln guter wissenschaftlicher Praxis selbstständig verfasst, keine anderen als die angegebenen Quellen benutzt und die Zitate kenntlich gemacht habe.

Bonn, den 25.04.2024

Leonard R. Maurer

Acknowledgements

First I would like to thank my Ph.D. supervisor Professor Dr. Alexander C. Filippou for this great opportunity to carry out my dissertation in his group, his genuine interest in my work, for the inspiring discussions on the quite diverse topics studied herein and for the final amendments of my thesis.

I am grateful to PD Dr. Marianne Engeser for her support of my intention to combine mass spectrometry with low-valent organometallic chemistry as well as her huge efforts on the MS instruments to do so.

Also I would like to acknowledge Prof. Dr. Stefan Grimme, PD Dr. Marianne Engeser and Prof. Dr. Bernhard Ketzler for being part of my promotion committee.

The Fonds of the Chemical Industry (FCI) are highly appreciated for their financial support with a Kekulé Fellowship during the first three years of my doctorate.

This work would not have been possible without the great support of many colleagues and friends during the last years. All members of the group were always willing to answer my questions, especially regarding experimental topics. In particular, I want to thank

- Dr. Gregor Schnakenburg for this quantum-chemical (and culinary) guidance, his unhesitating IT-technical support regarding the server and cluster infrastructure, honest proof-reading of this work and, most importantly, his friendship over the last years.
- Charlotte Rödde as my office mate and for enduring my self-talk and curses. It was also nice to be a (thematically very distant) member of the X-ray department and very kind of her to often provide me early access to sc-XRD structures I wanted to use for my calculations.
- Dr. Jürgen Tirrée and Katrin Werthmann as good souls of this group for their eager support regarding technical questions and concerns of all kinds.
- my synthetically-working present and former colleagues Dr. Surendar Karwasara, Dr. Benjamin Peerless, Dr. Ujjal Das, Dr. Fabian Gstrein, Sandeep Kumar and Prasenjit Palui. Without their hard work I would have had far less interesting molecules to study.
- Christine Sondag and Karin Peters-Pflaumbaum from the Mass spectrometry department for their help with the LIFDI and APCI measurements.
- the whole Bonni-Dinner gang for many thrilling evenings. I wish that we continue this tradition, even if we are scattered to the four winds. Especially I want to thank Jens Rump (also for proof-reading of this thesis), Philipp Brehm, Tobias Deckstein, Marcel Krumpholz and Peer Depping (I haven't forgotten you, even though you now live beyond the great sea) for their inspiring and deep friendship.

- all my other friends here in Bonn, Kassel, Berlin and Düsseldorf which gave me a beautiful time during this work.

Special thanks must also go to my family, in particular my parents and my brother, for their never-doubting support of me and my path of life, and my girlfriend Anne for proof-reading of my thesis, her kind sympathy, patience and love.

WE MUST ALL SUFFER FROM ONE OF THE TWO PAINS:
THE PAIN OF DISCIPLINE OR THE PAIN OF REGRET.
THE DIFFERENCE IS DISCIPLINE WEIGHS OUNCES WHILE REGRET WEIGHS TONS.

— EMANUEL JAMES "JIM" ROHN

Contents

A. Computational Studies on Low-Valent Silicon and Germanium Compounds	1
1. Introduction to Computational Chemistry	3
1.1. Fundamental Concepts	4
1.2. Density Functional Theory	11
1.3. Analysis of the Wave Function	18
2. Computational Details	23
3. Iminosilylenylidenes	25
3.1. Introduction	26
3.2. NHC- and Isocyanide-stabilized Halosilyliumylidene and Ligand-Exchange Equilibrium	27
3.3. Iminosilylenylidene $A-1Ar^{Mes}$	31
3.4. Stereodynamics of Iminosilylenylidene $A-1Ar^{Mes}$	36
3.5. Si(NHC) Transfer to the NHC-stabilized Germasilyne $A-5$	37
4. Further Studies on Iminosilylenylidenes of the Type (carbene)SiCNR	41
4.1. Introduction	41
4.2. Analysis of Various Iminosilylenylidenes $A-1R$	43
4.3. Dimerization of Iminosilylenylidenes	47
4.4. Iminosilylenylidene Formation from (SIDippSi) ₂ and Isocyanides CNR	49
4.5. Iminosilylenylidene Formation by Substitution of $A-1Ar^{Mes}$ with Isocyanides CNR	53
5. Siladibene and Siladiimide Compounds	55
5.1. Introduction	55
5.2. Two Heteroleptic Siladibenes with N-heterocyclic Carbenes	59
5.3. Reactivity with Azides: Access to (NHC)-stabilized Siladiimides	79
6. CAAC-stabilized Heavier Ditetrelynes and Ditetrelenylenylidenes	85
6.1. Introduction	85
6.2. CAAC ^{Me} -stabilized Disilicon(I)-dihalide (CAAC ^{Me}) ₂ Si ₂ Br ₂ ($A-13Br$)	89

6.3.	Metathesis reaction to the CAAC ^{Me} -stabilized Germasilyne (CAAC ^{Me})Si(Br)GeTbb	90
6.4.	CAAC ^{Me} -stabilized disilavinylidene (A-17Si) and silagermenylidene (A-17Ge) . . .	97
6.5.	Calculations on the Reactivity of the CAAC ^{Me} -supported Bromogermasilyne A-14	109
6.6.	Calculations on the Reactivity of the CAAC ^{Me} -supported Disilavinylidene A-17Si .	116
B. Computational Studies on Heavier Tetrel Transition Metal Complexes		119
7.	Digermyne Cobalt Complexes	121
7.1.	Introduction	121
7.2.	Digermyne Cobalt Complexes [CoCp(CO)(RGeGeR)] (B-1R)	122
7.3.	Carbonyl-free <i>cis</i> -bent Digermyne Cobalt Complex [CoCp(TbbGeGeTbb)] (B-5) .	135
7.4.	Digerma-cobaltacyclopentatrienes [CoCp(TbbGe(RCCR)GeTbb)] (B-6 and B-7) .	140
7.5.	First insights into the reaction pathways involving complex B-6	146
8.	Group 10 Tetrylidyne Complexes	148
8.1.	Introduction	149
8.2.	Structural Results	150
8.3.	Molecular Orbital Analysis	152
8.4.	Bond Dissociation Energies and Natural Population Analysis	157
8.5.	ETS-NOCV and EDA Analyses	159
8.6.	Metallotetrylene Isomers	162
C. Mass Spectrometric Studies of Group 6 Germylidyne Complexes		165
9.	Fundamental Principles of Mass Spectrometry	167
10.	Mass Spectrometric Studies of Group 6 Germylidyne Complexes	170
10.1.	Introduction	171
10.2.	Results and Discussion	172
D. Summary and Outlook		179
11.	Summary and Outlook	181

E. Appendix	193
Bibliography	339

List of Figures

1.	Illustration of the main topics studied in this work.	XXV
1.1.	Illustrative overview of the main quantum chemical methods and their accuracy-to-cost regime.	5
1.2.	Jacob's ladder scheme for the hierarchical classification of DFAs.	14
3.1.	Lowest-lying singlet isomers A-I to A-VI of the [H,C,N,Si] potential energy hypersurface.	26
3.2.	Optimized gas phase structure of the silyliumylidene cation A-2 ⁺ and its HOMO.	28
3.3.	Natural Lewis structures of A-2 ⁺ and their NRT resonance weight.	29
3.4.	Optimized gas phase structure of the cation A-3 ⁺ with atom labelling.	30
3.5.	Silylsilylene regioisomers A-3 ⁺ to A-3c ⁺ ordered by increasing electronic energy in kJ·mol ⁻¹	31
3.6.	Optimized gas phase structures of A-1Ar ^{Mes} and its cyanosilylene isomer A-4Ar ^{Mes}	32
3.7.	Selected canonical MOs of A-1Ar ^{Mes} and their energy eigenvalues in eV.	33
3.8.	Proposed mechanism for the stereodynamics of A-1Ar ^{Mes}	37
3.9.	Selected canonical MOs of A-5 and their energy eigenvalues in eV.	39
4.1.	Optimized gas-phase structures of iminosilylenylidenes A-1R with various R.	44
4.2.	Selected canonical molecular orbitals of iminosilylenylidenes A-1Ar ^{Mes} (top), A-1Mes (second row), A-1pTol (third row) and A-1Me (bottom) and their energy eigenvalues.	46
4.3.	Optimized gas phase structures of the <i>hth</i> -dimerization products A-6R.	47
4.4.	Optimized gas phase structures of the disilirane-1,2-ylidene-3-imines A-7R.	51
4.5.	Calculated mechanistic pathway for the formation of the disilirane-1,2-ylidene-3-imine intermediate model system A-7X.	52
5.1.	Optimized gas phase structures of the siladicarbenes A-9S and A-9I.	59
5.2.	Stereoview of the siladicarbenes A-9S and A-9I along the C1–Si bond.	61
5.3.	Canonical molecular orbitals of the siladicarbene A-9S and their energy eigenvalues.	62
5.4.	Canonical molecular orbitals of the siladicarbene A-9I and their energy eigenvalues.	62
5.5.	Intrinsic bond orbitals (IBOs) of the siladicarbene A-9S and their atomic Löwdin orbital populations.	63

5.6.	Intrinsic bond orbitals (IBOs) of the siladiborane A-9I and their atomic Löwdin orbital populations.	64
5.7.	MO interaction diagram of A-9S between the structurally unrelaxed Si and (SIDipp+ IiPr_2Me_2) fragments in their singlet states.	65
5.8.	Optimized gas phase structures of the singly and doubly protonated siladiboranes.	69
5.9.	Newman-like projection of the siladiboranes A-9S and A-9I along the Si–C1 bond axis.	70
5.10.	Potential energy surface scan of the N2–C1–Si–C2 torsion angle for the siladiboranes A-9S and A-9I	72
5.11.	Optimized transition state A-9S-TS for the IiPr_2Me_2 carbene rotation.	73
5.12.	$\pi(\text{C1–Si–C2})$ IBOs of the coplanar conformers A-9S_c and A-9I_c and their Löwdin orbital populations.	74
5.13.	Optimized gas phase structures of all Lewis acid adducts of the siladiborane A-9S	77
5.14.	Selected canonical MOs of A-9S-Cu and their energetic eigenvalues.	78
5.15.	Selected canonical MOs of A-9S-Co and their energetic eigenvalues.	78
5.16.	Calculated gas phase structure of the IiPr_2Me_2 -stabilized siladiimide A-10	80
5.17.	Selected canonical MOs of the IiPr_2Me_2 -stabilized siladiimide A-10 and their energetic eigenvalues.	81
5.18.	Selected IBOs of the IiPr_2Me_2 stabilized siladiimide A-10 and their atomic Löwdin orbital populations.	83
6.1.	Relative energies in $\text{kJ}\cdot\text{mol}^{-1}$ for various isomers of the system HEEH (E = Si to Pb) by G. Frenking <i>et al.</i> at the BP86/QZ4P level of theory.	87
6.2.	Optimized gas phase structure of A-13Br and selected canonical orbitals with their energetic eigenvalues.	90
6.3.	Optimized gas phase structure of A-15 and selected canonical orbitals with their energetic eigenvalues.	92
6.4.	Optimized gas phase structures of the $\text{CAAC}^{\text{Me-}}$ - or SIDipp-stabilized germasilynes A-14 and A-14^{NHC}	94
6.5.	Canonical MOs of A-14 (top) and A-14^{NHC} (bottom) and atomic Löwdin orbital populations of the occupied orbitals.	95
6.6.	PES scans of the Si–Ge–C2–C _{ortho} torsion angle for A-14	97
6.7.	Calculated gas phase structures of the silyltetraylenes A-16Si and A-16Ge	99
6.8.	Selected canonical molecular orbitals of the silyltetraylenes A-16Si and A-16Ge and their energy eigenvalues.	100
6.9.	Optimized gas phase structures of the $\text{CAAC}^{\text{Me-}}$ -stabilized disilavinylidene A-17Si and silagermenylidene A-17Ge	101
6.10.	Selected canonical MOs of compounds A-17Si , A-17Ge and A-17Si^{NHC}	103
6.11.	PES scans of the E–Si'–C2–C _{ortho} torsion angle for A-17Si and A-17Ge	107

6.12.	PES scans of the N–C1–E–Si' torsion angle for the compounds A-17Si and A-17Ge.	108
6.13.	Optimized gas phase structure of compound A-18.	110
6.14.	Selected canonical molecular orbitals of the compound A-18 and their energy eigenvalues.	110
6.15.	Selected intrinsic bond orbitals (IBOs) of the CAAC ^{Me} -stabilized heavier acetylide salt A-18 and their atomic Loewdin orbital populations.	111
6.16.	Optimized gas phase structures of the compounds A-19 ⁺ , A-20 ⁺ and the transition state A-19 ⁺ -TS as well as their relative electronic energies.	113
6.17.	Selected canonical molecular orbitals of compound A-20 ⁺ and their energy eigenvalues.	114
6.18.	Optimized gas phase structure of the elusive intermediate A-22.	117
6.19.	Selected canonical molecular orbitals of compound A-22 and their energy eigenvalues.	117
7.1.	Optimized gas phase structures of the digermynes cobalt complexes B-1R with R = Tbb, H, Me and Ph.	123
7.2.	Two-dimensional energy hypersurface plot of the Ge1–Co and Ge2–Co bond lengths of the digermynes cobalt complex B-1Tbb.	125
7.3.	Selected canonical MOs of the digermynes cobalt complex B-1Tbb and their energy eigenvalues.	126
7.4.	Intrinsic bond orbitals (IBOs) of B-1Tbb, their ascribed bond type and atomic Loewdin orbital populations.	127
7.5.	Stack plot of the excerpts of VT- ¹ H-NMR spectra of B-1Tbb in d ₈ -thf in the temperature range of 233 to 313 K showing three chemical exchange processes.	128
7.6.	Optimized gas phase structure of the possible stereodynamics intermediate B-2.	130
7.7.	Optimized gas phase structure of the transition state B-3.	131
7.8.	Optimized gas phase structure of the transition state B-4.	132
7.9.	Optimized gas phase structures of the two intermediate germylene-germylidene complexes B-1Tbb-Z1 and B-1Tbb-E1 as well as their relative electronic energies.	133
7.10.	Selected canonical MOs of the germylene-germylidene complex B-1Tbb-Z1 and their energy eigenvalues.	134
7.11.	Optimized gas phase structure of the carbonyl-free digermynes cobalt complex B-5.	136
7.12.	Selected canonical molecular orbitals of the complex B-5 and their energy eigenvalues.	137
7.13.	Selected intrinsic bond orbitals (IBOs) of the complex B-5 and their atomic Loewdin orbital populations.	138
7.14.	NICS _{zz} (r) scan plots with variable distance r between the midpoint of the studied ring and the probe for B-5, the model complex B-5', and the cyclopropylium cation and benzene for comparison.	140

7.15. Optimized gas phase structures of the digermacobaltacyclopentatrienes B-6 and B-7 .	141
7.16. Selected canonical molecular orbitals of the complex B-6 and their energy eigenvalues.	143
7.17. Selected intrinsic bond orbitals (IBOs) of the complex B-6 and their atomic Loewdin orbital populations.	144
8.1. Selected canonical MOs of $\text{NiSiAr}^{\text{Mes}}$ and their respective orbital energies.	153
8.2. Selected canonical MOs of $\text{PtPbAr}^{\text{Mes}}$ and their respective orbital energies.	153
8.3. Pipek-Mezey-localized MOs of $\text{NiSiAr}^{\text{Mes}}$, their assigned orbital type and corresponding atomic Mulliken orbital populations.	154
8.4. Pipek-Mezey-localized MOs of $\text{PtPbAr}^{\text{Mes}}$, their assigned orbital type and corresponding atomic Mulliken orbital populations.	155
8.5. Illustration of the calculated NPA charges for the M and E atoms and the $[\text{ML}_3]$ and $[\text{ER}]$ units in the complex cations $[\text{L}_3\text{MEAr}^{\text{Mes}}]^+$	159
8.6. Isosurface plots of deformation densities $\Delta\rho_n$ in $\text{e}\cdot\text{Bohr}^{-3}$ of complementary NOCVs of NiSiTbb , $\text{NiGeAr}^{\text{Mes}}$ and $\text{PtPbAr}^{\text{Mes}}$	161
8.7. Optimized minimum gas phase structure of the even more bent isomer $\text{PtPbAr}^{\text{Mes}}\text{-2}$.	162
8.8. Pipek-Mezey LMOs and isosurface plots of deformation densities of complementary NOCVs of $\text{PtPbAr}^{\text{Mes}}\text{-2}$	163
9.1. Illustration of the key steps of a mass spectrometric measurement.	167
9.2. Schematical illustration of an APCI source.	169
9.3. Schematical illustration of the FD and LIFDI source setups.	169
10.1. LIFDI-MAT90 spectrum of the complex C-1Mo	172
10.2. LIFDI-MAT90 spectrum of C-1W	173
10.3. LIFDI-MAT90 spectrum of C-2Mo	173
10.4. LIFDI-MAT90 spectrum of C-2W	174
10.5. APCI-Orbitrap spectrum of C-1W	174
10.6. APCI-Orbitrap CID spectra for the fragmentation of C-1Mo	175
10.7. APCI-Orbitrap CID spectra for the fragmentation of C-1W	176
10.8. APCI-Orbitrap CID spectra for the fragmentation of complex C-2Mo	177
10.9. APCI-Orbitrap CID spectra for the fragmentation of complex C-2W	177
11.1. Selected canonical molecular orbitals of $(\text{SIDipp})\text{Si}(\text{CNAr}^{\text{Mes}})$ and their energy eigenvalues in eV.	182
11.2. Selected canonical molecular orbitals of $(\text{SIDipp})\text{Si}(\text{Cl})\text{GeAr}^{\text{Mes}}$ and their energy eigenvalues in eV.	183
11.3. Selected canonical molecular orbitals of $(\text{CAAC}^{\text{Me}})\text{Si}(\text{CNAr}^{\text{Mes}})$ and their energy eigenvalues in eV.	184

11.4. Selected canonical molecular orbitals of (SIDipp)Si(IiPr ₂ Me ₂) and their energy eigenvalues in eV.	185
11.5. Minimum gas phase structure and canonical MOs of the siladiimide Si(NAr ^{Mes}) ₂ .	187
11.6. Structures of the complexes [CoCp(CO)(TbbSiSiTbb)] and [CoCp(CO)(Ar ^{Dipp} SnSnAr ^{Dipp})].	190
11.7. Selected canonical molecular orbitals of the distannyne cobalt complex [CoCp(CO)(Ar ^{Dipp} SnSnAr ^{Dipp})].	190
11.8. Level of theory I-optimized gas phase structures of the isocyanides CNR with R = Ar ^{Mes} , Mes, <i>p</i> Tol and Me.	233
11.9. Level of theory I-optimized gas phase structures of N-heterocyclic carbenes.	236
11.10. Selected canonical molecular orbitals of the complex B-7 and their energy eigenvalues.	238
11.11. Selected intrinsic bond orbitals (IBOs) of the complex B-7 and their atomic Loewdin orbital populations.	239

List of Tables

3.1.	Selected bond parameters of the halosilyliumylidene cation $A-2^+$ and its experimental counterpart $A-2_{\text{exp}}^+$	28
3.2.	Results of the NBO and local NRT analysis of the cation $A-2^+$	29
3.3.	Selected bond parameters of the silylsilylene cation $A-3^+$ and its experimental counterpart $A-3_{\text{exp}}^+$	30
3.4.	Selected bond parameters of the calculated iminosilylenylidene $A-1Ar^{\text{Mes}}$ and its experimental counterpart $A-1Ar_{\text{exp}}^{\text{Mes}}$	33
3.5.	Selected results of the NBO and local NRT analyses of $A-1Ar^{\text{Mes}}$	34
3.6.	Calculated <i>BCEs</i> and <i>BDEs</i> for the SIDipp and $CNAr^{\text{Mes}}$ cleavages of $A-1Ar^{\text{Mes}}$	35
3.7.	Comparison of selected calculated and experimental sc-XRD structural parameters of the NHC-stabilized germasilynes $A-5$ and $A-5_{\text{exp}}$, and the NHC-stabilized germasilylenylidene $A-5V$	38
3.8.	Selected results of the NBO and local NRT analyses of the SIDipp-stabilized germasilyne $A-5$	39
3.9.	Calculated bond cleavage (<i>BCE</i>) and bond dissociation (<i>BDE</i>) energies for the SIDipp and Si–Ge cleavages of $A-5$	40
4.1.	Selected bond parameters of the calculated and experimental iminosilylenylidenes $A-1R$	45
4.2.	Selected bond parameters of the calculated and experimental iminosilylenylidene dimers $A-6R$	48
4.3.	Calculated thermochemical quantities for the iminosilylenylidene dimerization reactions to the 1,2-disiletan-bisylidenes $A-6R$	49
4.4.	Calculated thermochemical quantities for the formation of the iminosilylenylidenes $A-1R$ from $(\text{SIDippSi})_2$ and isocyanides CNR.	49
4.5.	Selected bond parameters of the calculated disilirane-1,2-ylidene-3-imines $A-7R$	52
4.6.	Calculated thermochemical quantities for the formation of the disilirane-1,2-ylidene-3-imines $A-7R$ from $(\text{SIDippSi})_2$ and isocyanides CNR.	53
4.7.	Calculated thermochemical quantities for the iminosilylenylidene formation by substitution of $A-1Ar^{\text{Mes}}$ with isocyanides CNR.	54
5.1.	Selected calculated and experimental sc-XRD analysis bonding parameters of the siladycarbenes $A-9S$ and $A-9I$	60

5.2.	Results of the NBO, local NRT and NPA analyses of the siladicalbenes A-9S and A-9I	66
5.3.	Calculated bond cleavage (<i>BCE</i>) and bond dissociation energies (<i>BDE</i>) for the homolytic and heterolytic $\text{Si}-\text{C}_{(\text{S})\text{IDipp}}$ cleavages.	67
5.4.	Calculated bond cleavage (<i>BCE</i>) and bond dissociation energies (<i>BDE</i>) for the heterolytic $\text{Si}-\text{C}_{\text{IPr}_2\text{Me}_2}$ cleavages.	67
5.5.	Structural parameters of the singly and doubly protonated siladicalbenes A-9S+H⁺ , A-9S+2H²⁺ , A-9I+H⁺ and A-9I+2H²⁺	69
5.6.	Selected bonding parameters of various calculated conformers of the siladicalbenes A-9S and A-9I	75
5.7.	Selected structural parameters of the calculated and experimental Lewis acid adducts A-9S-L	76
5.8.	Selected bond parameters of the calculated and experimental structures of NHC-stabilized siladiimides A-10 as well as of A-XVI	81
5.9.	Calculated bond cleavage (<i>BCE</i>) and bond dissociation energies (<i>BDE</i>) for the $\text{Si}-\text{C}_{\text{IPr}_2\text{Me}_2}$ and $\text{Si}-\text{N}$ cleavages.	84
6.1.	Selected structural parameters of calculated and experimental $\text{Si}(\text{I})$ bromide dimers.	89
6.2.	Selected bonding parameters of the calculated gas phase and experimental structures of A-15	93
6.3.	Selected bond parameters of the calculated and experimental CAAC^{Me} -stabilized germsilylenes A-14 and A-14_{exp} as well as the NHC-stabilized germsilylenes A-14^{NHC} and A-5	94
6.4.	Results of the NBO, local NRT and NPA analyses of the compound A-14	96
6.5.	Calculated bond cleavage (<i>BCE</i>) and bond dissociation (<i>BDE</i>) energies for the CAAC^{Me} and $\text{Si}-\text{Ge}$ cleavages of A-14	96
6.6.	Structural parameters of the calculated compounds A-16Si and A-16Ge and of the sc-XRD structures A-16Si_{exp} , A-16Ge_{exp} and $(\text{SIDipp})\text{Si}(\text{Br})\text{Si}(\text{Br})_2\text{Tbb}$ (A-16Si_{exp}^{NHC}).	99
6.7.	Selected bond parameters of the calculated and experimental CAAC^{Me} -stabilized heavier vinylidenes as well as the NHC-stabilized disilavinylidene A-17Si^{NHC}	101
6.8.	Results of the NBO, local NRT and NPA analyses of the compounds A-17Si , A-17Ge and A-17Si^{NHC}	105
6.9.	Calculated bond cleavage (<i>BCE</i>) and bond dissociation (<i>BDE</i>) energies for the carbene cleavages in the compounds A-17Si , A-17Ge and A-17Si^{NHC}	106
6.10.	Calculated bond cleavage (<i>BCE</i>) and bond dissociation (<i>BDE</i>) energies for the $\text{E}=\text{Si}'$ cleavages of the compounds A-17Si , A-17Ge and A-17Si^{NHC}	107
6.11.	Selected structural parameters of the calculated gas phase and experimental structures A-18 and A-18_{exp}	110

6.12.	Selected bond parameters of the calculated and experimental CAAC ^{Me} -stabilized silagermylenes A-20⁺ and A-20_{exp}⁺	113
6.13.	Results of the NBO, local NRT and NPA analyses of compound A-20⁺	115
6.14.	Selected structural parameters of the calculated heavier potassium acetylide A-22	117
7.1.	Selected bond parameters of the calculated and experimental digermine cobalt complexes B-1R	124
7.2.	Results of the NBO and NPA analysis of the digermine cobalt complex B-1Tbb	128
7.3.	Relative energies and selected structural parameters of the intermediate germylene-germylidene complexes B-1Tbb-Z1 and B-1Tbb-E1	134
7.4.	Selected bond parameters of the calculated and experimental carbonyl-free digermine complexes B-5 and B-5_{exp}	136
7.5.	Calculated atomic and group NPA charges of the complex B-5	139
7.6.	Selected bond parameters of the calculated and experimental digermacobaltacyclopentatrienes B-6 , B-6_{exp} , B-7 and B-7_{exp}	142
7.7.	Results of the NBO, local NRT and NPA analyses of complex B-6	145
8.1.	Selected structural parameters of the calculated and experimentally obtained group 10 tetrylidyne complex cations MER	151
8.2.	Calculated <i>BCEs</i> and <i>BDEs</i> of the M–E bonds of the MER complexes.	157
8.3.	Calculated NPA charges in the MER complexes.	158
11.1.	Selected structural parameters of the calculated isocyanides CNR	233
11.2.	Selected structural parameters of the calculated free NHCs SIDipp , IDipp and IiPr₂Me₂	236
11.3.	Calculated thermochemical values of the reaction pathways proposed in Scheme 11.2.	240

List of Schemes

3.1.	Unselective formation of the targeted iminosilyliidene A-1Ar^{Mes}	26
3.2.	Conversion of (SIDipp)SiBr ₂ to the silyliumylidene salts A-2[B(Ar^F)₄] and A-3[B(Ar^F)₄] , and ligand exchange equilibrium between A-2[B(Ar^F)₄] and A-3[B(Ar^F)₄]	27
3.3.	Two-electron reduction of the Si ^{II} halosilyliumylidene salt A-2[B(Ar^F)₄] to the Si ⁰ iminosilyliidene A-1Ar^{Mes}	31
3.4.	Natural Lewis structures of A-1Ar^{Mes} and their NRT resonance weight.	34
3.5.	Synthesis of the NHC-stabilized germasilyne (SIDipp)Si(Cl)GeAr ^{Mes} (A-5).	38
3.6.	Natural Lewis structures of A-5 and their NRT resonance weight.	40
4.1.	Synthesis of the mesityl-substituted iminosilyliidene derivative A-1Mes	41
4.2.	Experimental reaction outcomes of (SIDippSi) ₂ with various isocyanides CNR.	42
4.3.	Experimental reaction outcomes of the substitution reaction of A-1Ar^{Mes} with different isocyanides CNR.	43
4.4.	Formation of the presumed disilirane-1,2-ylidene-3-imine intermediate A-7R and further reaction to the iminosilyliidenes A-1R	50
5.1.	Various resonance formulas A-VIII-a to A-VIII-d and donor-acceptor arrow notation A-VIII-e for carbodiphosphanes.	55
5.2.	Lewis structures of the first isolated carbodicarbenes.	57
5.3.	The first tristannaallene and trisilaallene by N. Wiberg <i>et al.</i> and M. Kira <i>et al.</i>	57
5.4.	The first homoleptic and heteroleptic siladicarbenes.	58
5.5.	Synthesis of the first heteroleptic siladicarbenes SiLL', where L, L' = NHC.	59
5.6.	Decomposition of the NRT resonance hybrid into the major bond motifs for A-9S and A-9I	64
5.7.	Lewis structures of various calculated conformers of the siladicarbenes A-9S and A-9I and their relative energies.	73
5.8.	Reaction sequence from the siladicarbene A-9S to the hypothetical NHC-free siladiimide A-12 via the experimentally accessible NHC-stabilized siladiimide A-10 and bis(amido)silylene A-11	79
5.9.	Most dominant Lewis structures of the NHC-stabilized siladiimide A-10	82
6.1.	The first literature-reported heavier ditetrelenes with an E=E double bond.	85
6.2.	The first literature-reported heavier ditetrelynes REER.	86

6.3.	Reported isolated mixed ditetrelynes with and without stabilization of the tetrel centre with a Lewis base.	86
6.4.	Literature-known isolated heavier vinylidenes.	88
6.5.	Synthesis of the CAAC ^{Me} -stabilized disilicon(I)-dihalide A-13Br by F. Gstrein. . .	89
6.6.	Synthesis of the CAAC ^{Me} -stabilized germasilyne A-14 via main group metathesis reaction by P. Palui.	91
6.7.	Proposed radical pathway of the metathesis reaction and calculated reaction energies ΔE for each reaction step.	92
6.8.	Step-wise synthesis of the CAAC ^{Me} -stabilized germasilyne A-14 via the adduct A-15 . . .	92
6.9.	Most dominant resonance contributions of A-14 and their NRT resonance weight. . .	95
6.10.	Attempted disilicon(I)-disilyne cross metathesis, which was not successful.	97
6.11.	Reaction between (CAAC ^{Me})EBr ₂ and the disilene TbbSiBrSiBrTbb to the silyltetrylenes A-16E (E = Si, Ge).	98
6.12.	Conceivable resonance formulas for the pyramidal tetrelene class of compounds. . .	99
6.13.	Reduction of the silyltetrylenes A-16E to the first CAAC ^{Me} -supported disilavinylidene A-17Si and silagermylidene A-17Ge	100
6.14.	Suggested partial rotation of the CAAC ^{Me} ligand via a C _S -symmetric conformer. . .	108
6.15.	Synthesis of (CAAC ^{Me})Si(K)GeTbb (A-18) as reported by P. Palui.	109
6.16.	Most dominant resonance contributions of A-18 and their NRT resonance weights. . .	112
6.17.	Synthesis of the CAAC ^{Me} -stabilized heavier acetylium cation [(CAAC ^{Me})Si(Tbb)Ge] ⁺ A-20⁺ via the presumed intermediate A-19⁺	112
6.18.	Most dominant resonance contributions of A-20⁺ and their NRT resonance weights. . .	114
6.19.	Reaction scheme for the bromide addition to A-20⁺ yielding compound A-21 and subsequent isomerization to the CAAC ^{Me} -supported silagermylidene A-17Ge . . .	115
6.20.	Reduction of the disilavinylidene A-17Si via the putative heavier potassium acetylide A-22 to the C–H-bond activation product A-23	116
7.1.	Various heavier ditetrelene transition metal complexes studied by theory and experiment.	122
7.2.	Synthesis of the digermene cobalt complex B-1Tbb by P. Palui.	123
7.3.	Two possible resonance formulas for complex B-1Tbb	126
7.4.	Visualization of the conceivable topomerization and enantiomerization process in the complex B-1Tbb	131
7.5.	Formation of germylene-germylidene complexes as outcome of the [CoCp(CO)] torsional PES scans.	132
7.6.	Access to the enantiomerization and topomerization products of B-1Tbb starting from the germylene-germylidene complex B-1Tbb-Z2	135
7.7.	Alternative synthetic route to the carbonyl-free digermene complex B-5	135
7.8.	Synthesis of the digermacobaltacyclopentatrienes B-6 and B-7	141

7.9.	Selected examples for literature-known silametallacyclobutadiene complexes. . . .	141
7.10.	Most contributing NRT resonance structures of complex B-6 and their resonance weight.	144
7.11.	Observed reaction of complex B-5 with 2-butyne, leading to the digermacobaltacyclopentatriene complex B-6 and the digermacyclobutadiene cobalt complex B-8	146
7.12.	Experimental thermally induced isomerization of complex B-8 to complex B-6 . . .	146
7.13.	Conceivable mechanisms for the reaction of the digermyne cobalt complex B-1Tbb to the digermacobaltacyclopentatriene B-6	147
8.1.	Schematic representation of the dominant orbital interactions in tetrylidyne complexes.	149
8.2.	Two-step synthesis of the group 10 metal tetrylidyne complexes $[(\text{PMe}_3)_3\text{MER}]$. . .	150
8.3.	Qualitative MO interaction diagram depicting the bonding situations of a) the tetrylidyne complex and b) the metallotetrylene case.	156
8.4.	Classification of the studied group 10 tetrylidyne complexes.	156
8.5.	Representation of the bonding situations found in the studied MER complexes. . .	160
10.1.	Lewis formulae of the complexes C-1M and C-2M ($M = \text{Mo}, \text{W}$).	171
11.1.	Suggested dominating resonance formulas for the digermyne cobalt complex $[\text{CoCp}(\text{CO})(\text{TbbGeGeTbb})]$	188
11.2.	Conceivable mechanisms for the reaction of the digermyne cobalt complex B-1Tbb to the digermacobaltacyclopentatriene B-6	240

Overview

This thesis is written to provide an overview on various topics I worked on extensively during my doctoral studies and it comprises different areas of theoretical and experimental inorganic molecular chemistry. The thesis is split into three main parts, which are illustrated by Figure 1:

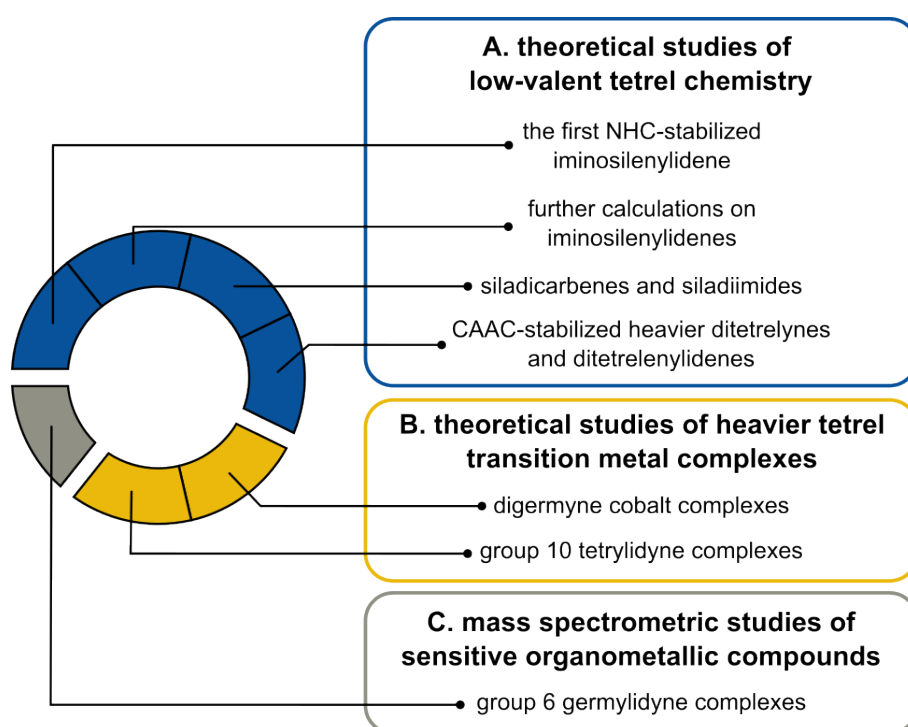


Figure 1: Illustration of the main topics studied in this work.

Part A deals with theoretical studies carried out on low-valent silicon and germanium main group compounds. Innovative achievements by synthetically-working colleagues in our group were comprehensively studied by computational methods. Their structural features and experimental properties but mainly the electronic structure were investigated and rationalized. Herein, special attention is provided to the influence of N-heterocyclic carbene (NHC) and cyclic alkyl amino carbene (CAAC) ligands on the electronic structure.

Part B features a similarly straightforward computational analysis of heavier tetrel transition metal compounds. Herein, the peculiar properties of the heavier tetrel atoms Si to Pb contribute to an unprecedented reactivity of the resulting complexes, which differs from that of similar carbon analogues.

Standing on its own, Part C is meant to cover efforts in mass spectrometry applied on transition metal germylidyne complexes. After a brief introduction into mass spectrometry, the process leading to an inert measurement without significant sample decomposition is summarized.

In the end, Part D is providing a summary of the herein presented results and outlines further work that goes beyond the scope of this thesis.

Some chapters of this work have already been published in scientific journals. According to the guidelines of the doctoral regulations of the Mathematisch-Naturwissenschaftlichen Fakultät Bonn the contents of the respective publications are summarized, my own contributions are highlighted and the full manuscript and the relevant parts of the supporting information are provided in the appendix in part E.

Part A.

Computational Studies on Low-Valent Silicon and Germanium Compounds

1. Introduction to Computational Chemistry

Computational chemistry or quantum chemistry is a branch of theoretical chemistry, in which properties of atoms or molecules are calculated using mathematical expressions. In its beginnings in the first half of the 20th century, quantum chemistry was usually confined to atoms or molecules with only a few atoms. However, the tremendous progress in computer sciences led to a close interweaving with quantum chemistry and greatly contributes to the accuracy and atom number range of modern computational methods.

Nowadays, calculations are possible for every state of matter and there is a plethora of different quantum chemical methods available to calculate desired properties, each coming with its own accuracy-to-cost ratio, where computational cost usually refers to the most valuable resource we have – time.

On the one hand, quantum chemical calculations can support experimental results. They can underline experimentally obtained molecular properties and rationalize what cannot or hardly be accessed by the experiment, such as transition states, short-lived intermediates or higher-energy isomers. On the other hand, the great predictive power enables the exploration of the chemical space and can guide the experimental chemist to unprecedented molecules.

In the following, a brief overview over the most prevalent concepts of quantum chemistry is given to guide the reader into the computational domain. The basic equations derived from the fundamental laws of physics will be presented, however, a detailed mathematical derivation will be omitted here, as this is readily available in established text books.^[1, 2]

1.1. Fundamental Concepts

The Schrödinger Equation

The key task of quantum chemistry is to solve the Schrödinger equation of the system, derived by E. Schrödinger in 1926, not considering relativistic effects,^[3]

$$\hat{H}(r, t)\Psi(r, t) = \frac{i\partial\Psi(r, t)}{\partial t} \quad (1.1)$$

with the time-dependent Hamilton operator $\hat{H}(r, t)$ and wave function $\Psi(r, t)$ of the system. For time-independent problems, however, the equation is simplified to its time-independent form,

$$\hat{H}(r)\Psi(r) = E(r)\Psi(r) \quad (1.2)$$

with $E(r)$ being the energy of the system dependent on the spatial position of the considered particles. The Hamilton operator can be divided into the kinetic (\hat{T}) and potential (\hat{V}) contributions of the electrons e and the nuclei N:

$$\hat{H}_{\text{tot}} = \hat{H}_e + \hat{T}_N \quad (1.3)$$

$$\hat{H}_e = \hat{T}_e + \hat{V}_{\text{Ne}} + \hat{V}_{\text{ee}} + \hat{V}_{\text{NN}} \quad (1.4)$$

Here, \hat{T}_e corresponds to the kinetic energy operator of the electrons, \hat{V}_{Ne} to the attractive nucleus-electron potential, \hat{V}_{ee} to the electron-electron potential, and \hat{V}_{NN} to the repulsion between the nuclei N. Unfortunately, being a many-body-problem, where the particles influence each other's movements, no analytical solution exists for a system with more than two particles. It is thus necessary to introduce approximations that allow to calculate the multiple-particle system without compromising the accuracy too much.

One of those is the *Born-Oppenheimer approximation*,^[4] where nuclei of atoms are assumed to be infinitely heavier than the electrons, which is reasonable to do as the masses of the protons and electrons differ by three orders of magnitude ($m_p/m_e \approx 1800$). This allows to separate the movement of the electrons from the movement of the nuclei which are considered to stand still ($\hat{T}_N \approx 0$, $\hat{V}_{\text{NN}} \approx \text{const.}$). The total Schrödinger equation can now be separated into an equation for the nuclei and for the electrons, where the latter is only *parametrically* dependent on the nuclear coordinates. The resulting electronic Schrödinger equation is given as

$$\hat{H}_e\Psi_e = E_e\Psi_e \quad (1.5)$$

with the electronic Hamilton operator \hat{H}_e :

$$\hat{H}_e = \hat{T}_e + \hat{V}_{\text{Ne}} + \hat{V}_{\text{ee}} = \hat{h}_e + \hat{V}_{\text{ee}} \quad (1.6)$$

where the kinetic energy and its Coulomb attraction to the nuclei can be combined into the one-electron operator \hat{h}_e . The respective operators are hereby given as

$$\hat{T}_e = - \sum_i^N \frac{1}{2} \nabla_i^2 \quad (1.7)$$

$$\hat{V}_{Ne} = - \sum_A^M \sum_i^N \frac{Z_A}{|R_A - r_i|} \quad (1.8)$$

$$\hat{V}_{ee} = \sum_i^N \sum_{j>i}^N \frac{1}{|r_i - r_j|} \quad (1.9)$$

where Z , R and r are the nuclear charge, and positions of the nuclei and electrons, respectively. At this point, different computational methods exist that include various approximations in order to derive the electronic energy E_e of a given system (Figure 1.1). Each level of approximation reduces the general accuracy of the method and their generality, but increases the possible system size and lowers the computational cost.

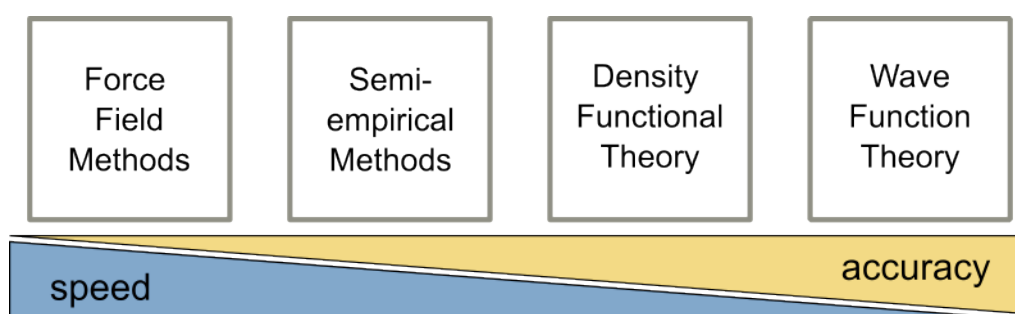


Figure 1.1: Illustrative overview of the main quantum chemical methods and their accuracy-to-cost regime.

Force-field methods, for example, treat whole atoms as classical particles and bypass the Schrödinger equation, as the electronic energy is written as a parametric function of the nuclear coordinates. The hereby necessary parameters are derived by fitting to experimental results or from high-level theoretical data. This level of empiricism limits the methods to those systems that are suitable for the employed fitting parameters, but allows to calculate large molecular structures like proteins at a reasonable amount of time.

Semi-empirical methods aim to solve the Schrödinger equation, but simplify the system (e.g. by considering only valence electrons) or mathematical terms (e.g. by neglecting unimportant integrals) to decrease the computational time. These approximations can be caught by careful parameter fitting and thus semi-empirical methods provide a reasonable accuracy/cost ratio for larger systems.

At the verge of empirical and *ab-initio* methods, density functional theory (DFT) employs functionals to access the electronic energy via the electron density ρ . These functionals can contain

fitting parameters, but do not necessarily have to. Their efficient accuracy/cost ratio made them prevalent for electronic structure calculations in the recent decades and they are applicable for a wide range of molecular properties.

Finally, wave function theory (WFT) uses the complete Schrödinger equation by determining the wave function Ψ of the system. As it typically does not employ empirical parameters, WFT methods offer a high generality. Also, WFT is systematically improvable leading to an exact solution in principle within the Born-Oppenheimer formalism, but this also comes with a large computational cost and thus a heavily limited system size.

Hartree-Fock Theory

The electronic energy E can be obtained as expectation value of the electronic Hamilton operator over the normalized wave function (the index e is omitted from now on as only the electronic parts are considered):

$$E = \frac{\langle \Psi | \hat{H} | \Psi \rangle}{\langle \Psi | \Psi \rangle} \quad (1.10)$$

Two conditions for the wave function have to be fulfilled: The Pauli principle^[5] demands that two electrons must not coincide in their quantum numbers, and the antisymmetry of the wave function must lead to a sign change when two electrons are interchanged. It was found that building the wave function from normalized *Slater determinants* Φ (SD) consisting of N single electron wave functions called *molecular orbitals* (MOs) ϕ fulfils these requirements.^[6] Within Hartree-Fock theory it is assumed that the total (exact) wave function can be described using only one ground state Slater determinant Φ_0 :

$$\Psi \approx \Psi_{\text{HF}} = \Phi_0 = \frac{1}{\sqrt{N!}} \begin{vmatrix} \phi_1(1) & \phi_2(1) & \cdots & \phi_N(1) \\ \phi_1(2) & \phi_2(2) & \cdots & \phi_N(2) \\ \vdots & \vdots & \ddots & \vdots \\ \phi_1(N) & \phi_2(N) & \cdots & \phi_N(N) \end{vmatrix} \quad (1.11)$$

These molecular orbitals are orthonormal and it holds:

$$\langle \phi_i | \phi_j \rangle = \begin{cases} 0 & \text{for } i \neq j \\ 1 & \text{for } i = j \end{cases} \quad (1.12)$$

As the exact wave function is not known, an approximate one, Ψ' has to be constructed. For this, the *variational principle* states that the corresponding energy E' must be above or equal to the exact energy E obtained with the exact wave function Ψ :

$$\langle \Psi' | \hat{H} | \Psi' \rangle = E' \geq E = \langle \Psi | \hat{H} | \Psi \rangle \quad (1.13)$$

This allows a procedure where the trial wave function (or its molecular orbitals ϕ_i) are optimized iteratively to approach the exact result. Lagrange multipliers λ are used to also ensure the condition of the orthonormality of the MOs and lead to the set of *Hartree-Fock equations*:

$$\hat{f}_i \phi_i = \sum_j^N \lambda_{ij} \phi_j, \quad (1.14)$$

wherein the *Fock operator* \hat{f}_i is an effective one-electron operator that includes the kinetic electron energy and the attraction to all nuclei (within \hat{h}_i), and the repulsion to all other electrons:

$$\hat{f}_i = \hat{h}_i + \sum_j^N (\hat{J}_{ij} - \hat{K}_{ij}) \quad (1.15)$$

The Coulomb operator \hat{J}_{ij} corresponds to the classical repulsion between two electrons, regardless of their spin, whereas the exchange term \hat{K}_{ij} is a non-classical, energy-lowering contribution to the electron-electron repulsion only between electrons with the same spin.

By employing a unitary transformation of the MOs to the special set of *canonical* molecular orbitals, which is a process that does not change the total wave function, the Lagrange multipliers can be converted into a diagonal form, i.e. $\lambda_{ij} = 0$ for $i \neq j$ and $\lambda_{ii} = \varepsilon_i$.

$$\hat{f}_i \phi_i = \sum_j^N \varepsilon_{ij} \phi_j \quad (1.16)$$

It was found that the ε_i can be interpreted in terms of molecular orbital energies, being the expectation value of the Fock operator over the MO space:

$$\langle \phi_i | \hat{f}_i | \phi_i \rangle = \varepsilon_i \langle \phi_i | \phi_i \rangle = \varepsilon_i \quad (1.17)$$

Summed up over all MOs ϕ_i , the Hartree-Fock equations form a set of pseudo-eigenvalue equations (*pseudo* because the one-electron Fock operator \hat{f}_i depends on all the other orbitals j via the Coulomb and exchange operators \hat{J}_{ij} and \hat{K}_{ij}), and iterative methods are necessary to obtain the so-called *self-consistent field (SCF) orbitals*.

It is important to note that the total energy of the system is not just the sum of all occupied MO orbital energies, as this would count the electron-electron repulsion twice and needs to be corrected:

$$E = \sum_i^N \varepsilon_i - \frac{1}{2} \sum_{ij}^N (J_{ij} - K_{ij}) + V_{nn}; \quad E \neq \sum_i^N \varepsilon_i \quad (1.18)$$

The canonical MOs ϕ_i of the wave function are unknown, but can be expanded in a set of known functions in terms of a linear combination:^[7, 8]

$$\phi_i = \sum_{\alpha}^{basis} c_{\alpha i} \chi_{\alpha} \quad (1.19)$$

The basis functions χ are conveniently called *atomic orbitals*, although it should be kept in mind that they do not represent the solutions to the atomic HF equations. For a complete set of basis functions χ , a *complete basis set* is reached and the linear combination of atomic orbitals (LCAO) ansatz becomes exact.

If equation 1.19 is now applied to the Hartree-Fock equations from equation 1.16, this leads to

$$\hat{f}_i \sum_{\alpha}^{basis} c_{\alpha i} \chi_{\alpha} = \varepsilon_i \sum_{\alpha}^{basis} c_{\alpha i} \chi_{\alpha}, \quad (1.20)$$

or, in matrix notation,

$$\mathbf{FC} = \mathbf{SC}\boldsymbol{\varepsilon} \quad (1.21)$$

where \mathbf{F} , \mathbf{C} and \mathbf{S} correspond to the Fock matrix, the LCAO coefficient matrix and the overlap matrix, respectively. In these so-called *Roothaan-Hall equations*,^[9, 10] the eigenvalues of the Fock matrix are calculated. However, due to the pseudo-eigenvalue nature of the Fock matrix, the coefficients \mathbf{C} are guessed in the first place and then optimized self-consistently in an iterative way. Due to the two electron integrals that involve integration over four basis functions, the formal scaling of HF methods is $O(basis)^4$ (O is a prefactor).

Following the *Aufbau principle*, which states that electrons occupy the lowest-lying molecular orbitals for a ground state system, a set of $\frac{1}{2}N$ occupied and $basis - \frac{1}{2}N$ virtual MOs are obtained. The latter are orthogonal to the occupied MOs but have no direct physical meaning.

Basis Sets

Equation 1.19 demands a complete basis set in order to provide an exact transformation of atomic orbitals χ to molecular orbitals ϕ . However, such a complete basis is computationally demanding and the basis set is often truncated, thus the quality of the approximation correlates to the size of the basis set.

Generally, a basis set consists of several basis functions, that are a specific type of mathematical functions suitable to describe the electron distribution of an atom. Two types of basis functions are nowadays well-established: Slater-type orbitals (STOs) and Gaussian-type orbitals (GTOs).

Slater-type orbitals are defined by the quantum numbers n , l and m as

$$\chi_{\zeta, n, l, m}^{STO}(r, \theta, \varphi) = N Y_{l, m}(\theta, \varphi) r^{n-1} e^{-\zeta r} \quad (1.22)$$

in a polar coordinate system. The $Y_{l,m}$ are the spherical harmonic functions, normalized by the normalization constant N , whereas the exponential part is described by the orbital coefficient ζ . STOs are physically more accurate as the radial decay fits to the analytically derived orbitals for hydrogen-like atoms, ensuring a rapid convergence with only a few basis functions used. However, the cusp at the nuclear position prohibits an analytic solution of three- and four-center two-electron integrals, making STOs computationally demanding. The nowadays wider employed alternative is the use of GTOs of the form

$$\chi_{\zeta,n,l,m}^{GTO}(r, \theta, \varphi) = NY_{l,m}(\theta, \varphi)r^{2n-2-l}e^{-\zeta r^2} \quad (1.23)$$

These functions are generally worse in describing the near-nucleus behaviour. Therefore, more so-called *primitive* GTOs, combined to *contracted* GTOs by linear combination, are necessary to obtain a slope similar to STOs. However, GTOs have the decisive advantage that their integrals are easy to calculate.

Over the years, various basis sets were developed and each provides its own accuracy and may be optimized for a specific property.^[11, 12] Seminal contributions include the minimal basis sets of the STO- n G type (with n being the number of primitive GTOs used for fitting to represent a STO),^[13-15] the Pople-style k - lm G^[16-19] or k - lmn G^[20] basis sets, the correlation consistent basis sets by T. H. Dunning that are suitable for high-end wave function methods,^[21] and the Karlsruhe basis sets by the group of R. Ahlrichs.^[22-24] The second generation of the latter^[25] are almost exclusively used in this thesis and belong to the class of split-valence basis sets, meaning that the chemically relevant valence orbital region is treated by the double (def2-SVP, *split-valence*), triple (def2-TZVP, *triple- ζ*) or quadruple (def2-QZVP, *quadruple- ζ*) amount of basis functions. The basis sets are further enhanced by polarization functions ("P") and can additionally be combined with diffuse ("D") functions, leading, for example, to the large quadruple- ζ def2-QZVPPD basis set. Herein, polarization functions are higher-angular momentum functions that are used to treat a directionally polarized electron distribution, whereas the diffuse functions improve the long-range behaviour of the basis set, which becomes important for anions or generally systems with loosely bound electrons (e.g. excited states).

Apart from the *basis set incompleteness error* (BSIE), that occurs when an incomplete basis is used, another basis set related problem can be the *basis set superposition error* (BSSE). Herein, basis functions centered on one atom or molecule compensate the incomplete basis at another part of the system, which leads to an artificial lowering of the energy, and it is especially problematic when weak non-covalent interactions are described. The BSSE can in principle be decreased when the basis set is enlarged, however, this is often not computationally feasible, and thus correction schemes can be employed to estimate the error as an alternative.^[26]

A further feature related to basis sets are *effective core potentials* (ECPs).^[27-29] The lower half of the periodic table comprises elements with many core electrons, that cannot be neglected, as well as an increasing influence of relativistic effects. In order to avoid computationally demanding rela-

tivistic full-electron calculations, the core electrons are instead modelled by a fitted function, thus only valence electrons are treated explicitly. By this, the computational time can often be decreased without a considerable loss of accuracy.^[30]

Treatment of Electron Correlation

Even with a complete basis set, the Hartree-Fock energy E_{HF} does not correspond to the exact energy obtained by the non-relativistic Schrödinger equation, because the electron-electron interaction is only treated in an average fashion (mean field approximation). Thus, the correlated electron movement is not described correctly, and the missing electron correlation energy E_{corr} is defined as

$$E_{\text{corr}} = E_{\text{exact}} - E_{\text{HF}} \quad (1.24)$$

In order to correct the electron correlation, it is necessary that the overall wave function Ψ contains more than one Slater determinant:

$$\Psi = a_0 \Phi_{\text{HF}} + \sum_{i=1} a_i \Phi_i \quad (1.25)$$

These additional Slater determinants Φ_i can be generated by exciting electrons from the ground state Hartree-Fock determinant Φ_{HF} . If all possible determinants are included, the Schrödinger equation can be solved exactly (within the framework of the Born-Oppenheimer approximation and the neglect of relativistic effects), given that an infinite basis set is provided. Established methods that use the Hartree-Fock SD to generate more Slater determinants are the Configuration Interaction (CI)^[6, 31–33] and Coupled-Cluster (CC)^[34, 35] approaches. Here, the truncation of possible electron excitations determines the accuracy but also the computational cost. Especially the CCSD(T) method with single, double and perturbative triple excitations^[36] is nowadays referred to as the *gold standard* of computational chemistry, as it is found to achieve an error of only 4 kJ·mol⁻¹ compared to the exact energy.^[35, 37–40] However, this is accompanied with a high $O(\text{basis})^7$ scaling, making it only affordable for small systems, and current research focuses on introducing well-balanced approximations to reduce the scaling drastically, for example seen by the domain-based local pair natural orbital coupled cluster (DLPNO-CCSD(T)) method.^[41]

Alternatively, the electron correlation can be assessed by perturbational theory methods. A widely-used term for correcting the Hartree-Fock energy is obtained by second-order Møller-Plesset (MP2) theory.^[42, 43]

$$E_{\text{MP2}} = \sum_{i < j}^{\text{occ}} \sum_{a < b}^{\text{vir}} \frac{(\langle \phi_i \phi_j | \phi_a \phi_b \rangle - \langle \phi_i \phi_j | \phi_b \phi_a \rangle)^2}{\varepsilon_i + \varepsilon_j - \varepsilon_a - \varepsilon_b} \quad (1.26)$$

The MP2 correction scales with $O(\text{basis})^5$, however, because it does not involve an SCF procedure its actual computational effort is similar to a HF calculation. As it is able to recover 80 to 90 % of

the electron correlation energy, the MP2 scheme is an efficient way to improve the basic Hartree-Fock result, being faster but less accurate compared to advanced CI or CC corrections. However, it should be kept in mind that the MP2 energy is added to the HF reference wave function, thus its performance also depends on the latter, and poor HF solutions are insufficiently corrected by MP2. Furthermore, as visible from equation 1.26, the MP2 term (incorrectly) converges to infinity for systems with close-lying occupied and virtual orbital energies.

1.2. Density Functional Theory

In the year 1964, P. Hohenberg and W. Kohn were able to prove that the ground state electronic energy of a system is completely determined by its electron density ρ in the form of the functional $E[\rho]$.^[44] The great advantage of this discovery is that the electron density is shown to be independent of the number of electrons N , in contrast to wave function theory where $4N$ coordinates have to be considered (three spatial and one for the electron spin). However, until today the exact functional $E[\rho]$ connecting the electron density and the energy of the system is not known and the resulting density functional approximations (DFAs) cannot be systematically improved as it is possible for wave function theory.^[45, 46]

Similar to HF theory, the total energy functional can be separated into functional contributions from the kinetic energy $T[\rho]$, the nucleus-electron attraction $E_{\text{Ne}}[\rho]$ and the electron-electron repulsion $E_{\text{ee}}[\rho]$, whereas the latter can further be divided into Coulomb $J[\rho]$ and exchange $K[\rho]$ parts. The nucleus-electron potential and the Coulomb term can simply be given as

$$E_{\text{Ne}}[\rho] = - \sum_A^M \int \frac{Z_A \rho(r)}{|R_A - r|} dr \quad (1.27)$$

and

$$J[\rho] = \frac{1}{2} \int \int \frac{\rho(r)\rho(r')}{|r - r'|} dr dr' \quad (1.28)$$

However, the expressions for the kinetic and exchange functionals are less straightforward. Assuming a uniform electron gas, L. Thomas and E. Fermi could derive a first expression for the kinetic energy,^[47-49]

$$T_{\text{TF}}[\rho] = \frac{3}{10} (3\pi^2)^{\frac{2}{3}} \int \rho^{\frac{5}{3}}(r) dr \quad (1.29)$$

leading to a term for the total energy functional $E_{\text{TF}}[\rho]$ within the Thomas-Fermi theory:

$$E_{\text{TF}}[\rho] = T_{\text{TF}}[\rho] + E_{\text{Ne}}[\rho] + J[\rho] \quad (1.30)$$

The neglect of the exchange part leads to very poor results, and F. Bloch derived an expression for the exchange part $K_D[\rho]$ in 1929,^[50] which was later adopted by P. Dirac in 1930,^[51] resulting in an improved energy functional expression (Thomas-Fermi-Dirac theory):

$$K_D[\rho] = -\frac{3}{4} \left(\frac{3}{\pi} \right)^{\frac{1}{3}} \int \rho^{\frac{4}{3}}(r) dr \quad (1.31)$$

$$E_{\text{TFD}}[\rho] = T_{\text{TF}}[\rho] + E_{\text{Ne}}[\rho] + J[\rho] + K_D[\rho] \quad (1.32)$$

The Thomas-Fermi-Dirac energy functional $E_{\text{TFD}}[\rho]$ yields acceptable results for metallic systems, but works poorly for atoms and molecules. Assuming a non-uniform electron gas, where derivatives of the electron density are included, improves the model but the overall accuracy is still below the wave function method level.

An alternative approach was developed by W. Kohn and L. J. Sham with the idea to split the kinetic energy functional $T[\rho]$ into two parts:^[52] The first, $T_S[\rho]$, corresponds to non-interacting electrons and represents the dominant contribution to $T[\rho]$. It can be exactly calculated similarly to the HF approach (c.f. Equation 1.7), but has the disadvantage that orbitals need to be re-introduced, increasing the complexity again to a $4N$ problem:

$$T[\rho] \approx T_S[\rho] = \sum_{i=1}^N \langle \phi_i | -\frac{1}{2} \nabla^2 | \phi_i \rangle \quad (1.33)$$

The second part $T[\rho] - T_S[\rho]$ corresponds to the remaining kinetic correlation energy and is assumed to be small ($\approx 1\%$). It is combined with the missing exchange term into the *exchange-correlation* functional $E_{\text{xc}}[\rho]$, and the general DFT energy $E_{\text{DFT}}[\rho]$ expression is given by

$$E_{\text{DFT}}[\rho] = T_S[\rho] + E_{\text{Ne}}[\rho] + J[\rho] + E_{\text{xc}}[\rho] \quad (1.34)$$

where $E_{\text{xc}}[\rho]$ is defined as

$$E_{\text{xc}}[\rho] = \underbrace{(T[\rho] - T_S[\rho])}_{\text{kinetic correlation energy}} + \underbrace{(E_{\text{ee}}[\rho] - J[\rho])}_{\text{correlation \& exchange energy}} \quad (1.35)$$

The great advantage of Kohn-Sham density functional theory (KS-DFT) is that the energy can be calculated much more accurately than that in the orbital-free Thomas-Fermi-Dirac model, as the approximate exchange-correlation functionals have a much smaller impact than approximations in the kinetic energy functional, because both corresponding energies differ by an order of magnitude. Analogous to HF theory, a set of Kohn-Sham equations is obtained that involves the Kohn-Sham orbitals ϕ_i :

$$\hat{f}_i^{\text{KS}} \phi_i = \varepsilon_i \phi_i \quad (1.36)$$

where the one-electron Kohn-Sham operator \hat{f}_i^{KS} is defined similar as in equation 1.15 but uses the exchange-correlation potential $V_{xc}[\rho]$:

$$\hat{f}_i^{KS} = \hat{h}_i[\rho] + \sum_j^N (\hat{J}_{ij}[\rho] - V_{xc}[\rho]) \quad (1.37)$$

By expanding the Kohn-Sham orbitals ϕ_i in an atomic basis set

$$\phi_i = \sum_{\alpha}^{basis} c_{\alpha i} \chi_{\alpha} \quad (1.38)$$

the Kohn-Sham equations in matrix notation are obtained:

$$\mathbf{F}^{KS} \mathbf{C} = \mathbf{S} \mathbf{C} \boldsymbol{\varepsilon} \quad (1.39)$$

However, a notable difference in DFT is that the integrals involving the $V_{xc}[\rho]$ potential cannot be solved analytically as $V_{xc}[\rho]$ depends implicitly on the integration variables, which is why a numerical grid is typically introduced for DFT to evaluate these integrals.

As mentioned before, density functional theory comprises the crucial disadvantage that the unknown exchange-correlation functional is not systematically improvable. Accordingly, a large number of DFAs are available nowadays that were either designed by requiring them to fulfil (known) criteria of the exact density functional, or by adding fitting parameters to experimental data.^[46, 53, 54] J. P. Perdew and K. Schmitz suggested a *Jacob's ladder* scheme in 2001,^[55] where the DFAs are grouped according to the complexity of how $V_{xc}[\rho]$ is treated (Figure 1.2). It ranges from the *Hartree hell* and leads over several rungs to the *heaven of chemical accuracy*. Each rung, briefly discussed in the following, is typically associated with an overall increase of both the accuracy and the computational cost, but there is no inherent guarantee that higher-rung DFAs generally perform better than lower-rung ones.

Local (Spin) Density Approximation

For the simplest DFAs, it is assumed that the electron density can locally be treated as a uniform electron gas. The exchange term E_x^{LDA} is then given by the Dirac term of equation 1.31, whereas the correlation term can be deduced analytically from the uniform electron gas. If the electron spin is considered and the spin densities ρ_{α} and ρ_{β} are treated differently, the local (spin) density approximation (L(S)DA) method is obtained.

It is worthwhile to note that L(S)DA methods are exact for systems that exhibit a uniform electron gas, which makes these methods applicable in solid state physics. However, as this is not the case for molecular systems, LSDA DFAs show high errors for these and lead to artificially overestimated bond strengths and overstabilized higher spin states.

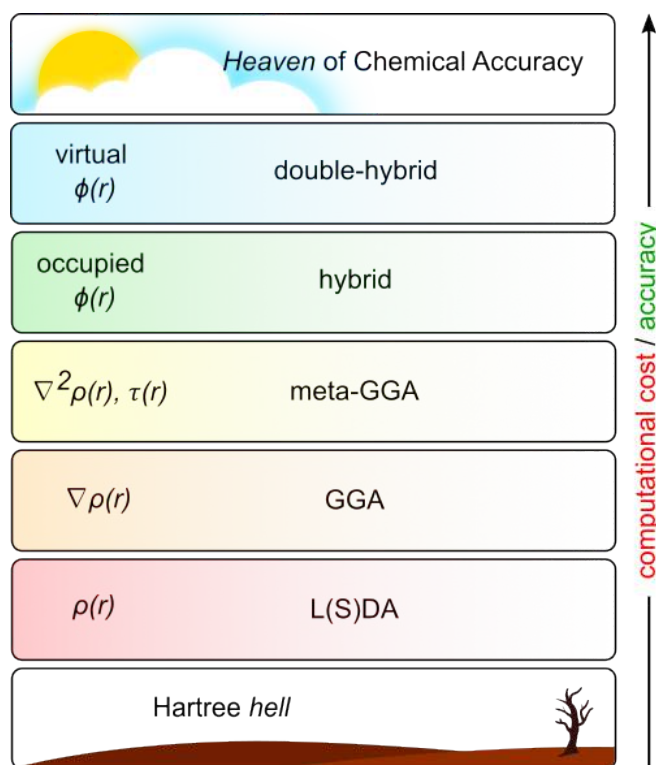


Figure 1.2: Jacob's ladder scheme for the hierarchical classification of density functional approximations. The higher-rung methods include additional information about the electron density ρ , which is typically (but not necessarily) associated with an increase of both accuracy and computational cost. The illustration is adapted from references [56] and [57].

Generalized Gradient Approximation

An improvement of L(S)DA methods is directly obtained if the electron density is considered as non-uniform, i.e. the derivative of the electron density ρ is used. This can be done by correcting the LDA exchange-correlation term by an *enhancement factor* $F^{\text{GGA}}(\nabla\rho)$ that depends on the gradient of the electron density:

$$E_{\text{xc}}^{\text{GGA}} = E_{\text{xc}}^{\text{LDA}} F^{\text{GGA}}(\nabla\rho) \quad (1.40)$$

Hereby, the electron density is treated in a semi-local fashion. The resulting semi-local GGA DFAs have a substantially smaller error for molecular systems compared to L(S)DA methods.

Meta-Generalized Gradient Approximation

The next rung of the Jacob's ladder scheme is held by meta-GGA methods which include higher-order derivatives of the electron density, for example by using the laplacian $\nabla^2\rho$ of the electron density. However, as this was proven to be numerically unstable, the orbital kinetic energy density τ is employed instead:^[58, 59]

$$\tau(r) = \frac{1}{2} \sum_i^{occ} |\nabla\phi_i(r)|^2 \quad (1.41)$$

The exchange-correlation term is then dependent on τ .

Hybrid DFT Methods

The exchange-correlation energy E_{xc} can be exactly described with the *adiabatic connection formula* by a potential V_{xc} that acts on the wave function of the system:^[60]

$$E_{xc} = \int_0^1 \langle \Psi_\lambda | V_{xc}(\lambda) | \Psi_\lambda \rangle d\lambda, \quad (1.42)$$

where the integration variable λ corresponds to the degree of electron-electron correlation. Equation 1.42 can be approximated by assuming a linear progression of λ and using an average of end-point values:

$$E_{xc} \approx \frac{1}{2} \left(\underbrace{\langle \Psi_0 | V_{xc}(0) | \Psi_0 \rangle}_{\substack{\text{no electron} \\ \text{correlation,} \\ \cong \text{HF}}} + \underbrace{\langle \Psi_1 | V_{xc}(1) | \Psi_1 \rangle}_{\substack{\text{full electron} \\ \text{correlation,} \\ \text{unknown}}} \right) \quad (1.43)$$

Whereas the second term is still unknown, now the first summand corresponds to non-interacting electrons and has no contribution of the correlation energy, which is by definition equal to the result given by Hartree-Fock theory (equation 1.24). Thus, this leads to the *Half-and-Half* method,^[61] where one half of the exchange-correlation energy is given by exact Fock exchange E_x^{HF} and the other half is approximated by L(S)DA results:

$$E_{xc}^{\text{H+H}} = \frac{1}{2} E_x^{\text{HF}} + \frac{1}{2} (E_x^{\text{L(S)DA}} + E_c^{\text{L(S)DA}}) \quad (1.44)$$

This method can be further improved if the amount of Fock exchange is variable and the uniform electron gas of the L(S)DA term is corrected by GGA or meta-GGA terms. Thus, a more general formula for hybrid DFT methods is given with equation 1.45, where the parameter a is usually obtained by fitting to experimental data:

$$E_{xc}^{\text{hybrid}} = a E_x^{\text{HF}} + (1 - a) E_x^{(\text{meta-})\text{GGA}} + E_c^{(\text{meta-})\text{GGA}} \quad (1.45)$$

Hybrid DFAs often improve the calculated results, which is attributed to a reduction of the self-interaction error that is inherent in (meta-)GGA methods. However, there is no universal optimal amount of Fock exchange to be included and various methods are available with different fractions of exact exchange.

An alternative way to implement Fock exchange is used for *range-separated* DFAs: Generally, density functional theory tends to overdelocalize the electron density, which results in an artificial energy-lowering of delocalized systems and an incorrect long-range behaviour of the exchange-correlation potential. The latter can be encountered by separating the electron-electron operator $\frac{1}{r_{12}}$ into a short-range part, that is typically treated by pure DFT methods, and a long-range part that uses the Fock exchange:^[62] Hereby, the transition between both parts is administered by the control parameter ω and an error function *erf*.

$$\frac{1}{r_{12}} = \frac{1 - \text{erf}(\omega r_{12})}{r_{12}} + \frac{\text{erf}(\omega r_{12})}{r_{12}} \quad (1.46)$$

Double-Hybrid DFT Methods

Finally, the highest rung in the Jacob's ladder scheme is assigned to double-hybrid DFT methods. Whereas hybrid DFT methods contain information about occupied HF orbitals to correct the exchange part of the exchange-correlation functional, for double-hybrid methods information about virtual orbitals is employed to improve the correlation energy. This is typically done by adding MP2 electron correlation (equation 1.26) using the KS orbitals and orbital energies, and the general formula for the exchange-correlation energy is given as:^[63]

$$E_{xc}^{\text{double-hybrid}} = aE_x^{\text{HF}} + (1 - a)E_x^{(\text{meta-})\text{GGA}} + bE_c^{\text{MP2}} + (1 - b)E_c^{(\text{meta-})\text{GGA}} \quad (1.47)$$

The inclusion of WFT electron correlation is seen to further improve the accuracy. However, double-hybrid DFT methods suffer from the same problems as MP2, that is the high computational cost of $O(\text{basis})^5$, the slower basis set convergence compared to HF and DFT methods and the instability for energetically close-lying occupied and virtual orbitals.

Corrections for the London Dispersion Interactions

A serious disadvantage of standard DFT is its incapability to describe London dispersion forces. These mid-to-long-range electron correlation effects result from the attractive interaction between instantaneously induced dipoles caused by electronic fluctuations in both polar and non-polar atoms and molecules.^[64, 65] Together with the repulsive Pauli force they form the non-covalent van-der-Waals interactions. Although a single interatomic contribution is small, London dispersion forces become more important for larger systems with high polarizabilities, and DFAs need to be corrected in order to approach chemical accuracy.^[66]

The most direct approach would be to include a functional into the exchange-correlation part that

explicitly accounts for the dispersion energy. In these non-local van-der-Waals functionals^[67] the dispersion energy is given by

$$E_{disp}^{NL} = \frac{1}{2} \int \rho(r) \Phi(r, r') \rho(r') dr dr' \quad (1.48)$$

where $\Phi(r, r')$ is a non-local correlation kernel that explicitly considers the interaction of long-range electron density fluctuations.

Alternatively, apart from modifying the exchange-correlation functional, additive schemes can be used that post-correct the calculated SCF energy. A well-established example are the semi-classical DFT-D x ($x = 1, 2, 3, 4$) dispersion corrections by the group of S. Grimme:^[68–71] Herein, the dispersion energy E_{disp}^{DFT-D} is calculated by an atom pair-wise scheme based on averaged isotropic n -th order atomic dispersion coefficients C_n^{AB} :

$$E_{disp}^{DFT-D} = - \sum_{A,B} \sum_{n=6,8,10,\dots} s_n \frac{C_n^{AB}}{r_{AB}^n} f_{damp}(r_{AB}) \quad (1.49)$$

where f_{damp} is a damping function. The s_n correspond to global DFA-dependent scaling factors, as every DFA is differently repulsive in its long-range behaviour and need to be individually adjusted. In the DFT-D3 revision, the reference dispersion coefficients are calculated by time-dependent DFT (TD-DFT) using a modified Casimir-Polder formula:

$$C_{6,ref}^{AB}(CN^A, CN^B) = \frac{3}{\pi} \int_0^\infty \frac{1}{m} [\alpha^{A_m H_n}(i\omega) - \frac{n}{2} \alpha^{H_2}(i\omega)] \frac{1}{k} [\alpha^{B_k H_l}(i\omega) - \frac{l}{2} \alpha^{H_2}(i\omega)] d\omega \quad (1.50)$$

$A_m H_n$ and $B_k H_l$ are reference compounds of atoms A and B and α the molecular polarizabilities, as it was shown that the calculation of only atomic polarizabilities α^A and α^B leads to an instability of the method. Additionally, the dispersion coefficients are dependent on the coordination of atoms A and B, which is accounted for by fractional coordination numbers (CNs). The series is terminated after $n = 8$ to prevent numerical instability, and the higher-order dispersion coefficients C_8^{AB} are obtained by recursion from the atomic multipole-type expectation values $\langle r_A^4 \rangle$, $\langle r_A^2 \rangle$ and the atomic element number Z_A :

$$C_8^{AB} = 3C_6^{AB} \sqrt{\sqrt{Z_A} \frac{\langle r_A^4 \rangle}{\langle r_A^2 \rangle}} \sqrt{\sqrt{Z_B} \frac{\langle r_B^4 \rangle}{\langle r_B^2 \rangle}} \quad (1.51)$$

As DFAs treat some electron-correlation effects via the exchange-correlation part in the short-range region, it is essential to dampen the contribution of the dispersion correction for the short-range part. The damping function $f_{damp}(r_{AB})$ (Equation 1.49) is recommended to be of the type by

A. D. Becke and E. R. Johnson (BJ)^[72] and approaches a finite value at short interatomic distances with two functional-specific parameters a_1 and a_2 :

$$f_{\text{damp,BJ}}^n(r_{AB}) = \frac{r_{AB}^n}{r_{AB}^n + (a_1 r_0 + a_2)^n} \quad (1.52)$$

and the radius r_0 is given as

$$r_0 = \sqrt{C_8^{AB}/C_6^{AB}} \quad (1.53)$$

Finally, it is recommended to include a three-body correction $E_{\text{disp}}^{(3)}$ to the pair-wise terms $E^{(2)}$, which typically amounts to approx. 5 % of the total dispersion energy.^[66] For the D3 and D4 methods this correction is given in terms of third-order perturbation theory derived by B. M. Axilrod, E. Teller and Y. Muto (ATM):^[73, 74]

$$E^{ABC} = \frac{C_9^{ABC}(3\cos(\theta_a)\cos(\theta_b)\cos(\theta_c) + 1)}{(r_{AB}r_{BC}r_{AC})^3} \quad (1.54)$$

where θ_a , θ_b and θ_c are the angles spanned by the atoms A, B and C. The tripole-tripole dispersion constants C_9^{ABC} can also be derived by employing the Casimir-Polder equation, but, as this is computationally demanding, they are usually approximated:

$$C_9^{ABC} = \frac{3}{\pi} \int_0^\infty \alpha^A(i\omega)\alpha^B(i\omega)\alpha^C(i\omega)d\omega \approx -\sqrt{C_6^{AB}C_6^{BC}C_6^{AC}} \quad (1.55)$$

Despite being a semi-classical post-SCF correction scheme, the DFT-D3 and DFT-D4 methods provide an excellent accuracy-to-cost ratio and benchmark studies show that they can well compete with other dispersion correction methods that consider the actual electron density of the system.^[66, 75]

1.3. Analysis of the Wave Function

Calculating the wave function of a system and its total energy is the first step in analyzing the electronic structure. To gain more insight, however, it is necessary to analyze the wave function by various quantum chemical tools. In the following, a brief overview over the main methods employed in this thesis will be given:

Orbital Localization

The most direct approach to investigate the bonding situation in a molecule is to have a look at the canonical orbitals, where the frontier molecular orbitals (highest occupied molecular orbital, HOMO, and lowest unoccupied molecular orbital, LUMO) reveal the energetically highest and thus most reactive parts of a molecule (for orbital-controlled reactions). However, a major drawback is the delocalized nature of canonical orbitals that exacerbate the assignment of meaningful chemical

bonding types. If substituents or ligands with large aromatic backbones are present, this effect is even more pronounced.

In the year 1950, J. E. Lennard-Jones and J. A. Pople introduced the concept of localized orthonormal molecular orbitals (LMOs):^[76] As the orbitals from the HF equations are just one of many solutions of the Schrödinger equation,^[77] other MO bases can be employed that help analyzing ground-state properties of molecules or compact the virtual space for post-SCF electron correlation methods.^[78] If these MO bases are obtained by a unitary transformation of the canonical MO basis, the overall wave function is not changed. This is due to a single-determinant, many-electron wave function being invariant with respect to unitary transformations of its orbitals.^[79]

$$|\phi'_i\rangle = \sum_j^{N_{\text{orb}}} U_{ij} |\phi_j\rangle; \quad UU^\dagger = 1 \quad (1.56)$$

Thus, orbital localization methods try to find a unity transformed orbital set $|\phi'_i\rangle$ with chemically intuitive 2-center orbitals with small spatial volume that allow to interpret the bonding in molecules.

Various localization algorithms are available with different localization criteria in order to obtain the LMOs, such as a maximum self-repulsion energy in the method by C. Edmiston and K. Ruedenberg,^[77, 80] a maximized charge-density overlap function in the method by W. van Niessen^[81] or a minimized spatial extent of the MOs by J. M. Foster and S. F. Boys.^[82] The latter method gained popularity due to its low basis function scaling, however it does not support σ - π separation and yields banana bonds for double bonds that are $\sigma + \pi$ and $\sigma - \pi$ linear combinations.

In contrast, the localization scheme by J. Pipek and P. G. Mezey separates σ and π orbitals while also maintaining the low scaling of the Foster-Boys scheme.^[83] Therein, a localization quantity d_i can be defined as

$$d_i = \frac{1}{\sum_{A=1}^n (Q_A^i)^2} \quad (1.57)$$

with the number of atoms n and the gross atomic Mulliken population^[84, 85] Q_A^i of the orbital ϕ_i . d_i lies in the range of $0 < d_i \leq n$ and corresponds to the number of atoms where the orbital ϕ_i is localized on. By averaging over all orbitals, the mean delocalization D is obtained:

$$\frac{1}{D} = \frac{1}{N \sum_i^N d_i} \quad (1.58)$$

Accordingly, Pipek-Mezey localization schemes rely on population localization, and the mean delocalization D is minimized iteratively until a predetermined tolerance parameter is satisfied. The converged localized orbitals can then be visualized. Hereby, the orbital polarization can further be assessed by orbital decomposition analysis to obtain the atom coefficients. A disadvantage, though, is the usage of the Mulliken population analysis as it is known to have no converging basis set limit, possibly leading to arbitrary results.^[86-90] A study of S. Lehtola *et al.* in the year 2014 shows that

qualitatively similar Pipek-Mezey LMOs can be obtained when various population schemes with very different atomic partial charges are employed.^[90] Besides more reliable population schemes such as the Voronoi partition^[87, 91] or Hirshfeld atomic charges,^[92] atomic orbital populations can also be obtained by projection.^[88, 93] One recent example by G. Knizia is the combination of intrinsic atomic orbitals (IAOs) and the Pipek-Mezey localization scheme:^[94] For a given molecular SCF wave function Θ , defined by its occupied MOs ϕ_i that are expanded in a set of atomic orbitals χ (see Equation 1.19), a new set of polarized AOs ρ can be constructed by employing Equation 1.59 and exactly express the occupied MOs ϕ_i of Θ .

$$|\rho\rangle = (O\tilde{O} + (1 - O)(1 - \tilde{O}))P_{12}|\tilde{\rho}\rangle \quad (1.59)$$

where O and \tilde{O} correspond to the polarized and depolarized occupied spaces

$$O = \sum_i |\phi_i\rangle\langle\phi_i|, \quad \tilde{O} = \sum_i |\tilde{\phi}_i\rangle\langle\tilde{\phi}_i| \quad (1.60)$$

and P_{12} and $\tilde{\rho}$ to the projector operator on the basis of χ and a tabulated free-atom basis, respectively. After orthogonalization of ρ , the orthonormal minimal IAO basis is obtained that can be used to obtain intrinsic bond orbitals (IBOs) by employing the above-discussed Pipek-Mezey localization scheme.

Natural Bond Orbital Theory

As a different approach to the problem of wave function analysis, the Natural Bond Orbital (NBO) theory was developed by F. Weinhold *et al.*^[86, 95-97] and is based on the Natural Orbital (NO) theory by P.-O. Löwdin,^[98] that suggests to use the one-electron reduced density matrix Γ ,

$$\Gamma(r_1, r'_1) = N \int \Psi^*(r'_1, r_2, \dots, r_N) \times \Psi(r_1, r_2, \dots, r_N) dr_2 \cdots dr_N \quad (1.61)$$

which can be directly calculated from the wave function. After diagonalization the hereby obtained eigenvectors and eigenvalues are the *Natural Orbitals* and *Occupation Numbers*.

In the NBO framework, the wave function (in form of the density matrix) is projected into a single Lewis structure that best describes the electronic structure of the molecule. For this, the density matrix in the AO basis is rearranged in such a way that the atomic basis functions on each atom A, B, C, ... are written in a block-wise form:

$$D = \begin{pmatrix} D^{AA} & D^{AB} & D^{AC} & \dots \\ D^{BA} & D^{BB} & D^{BC} & \dots \\ D^{CA} & D^{CB} & D^{CC} & \dots \\ \vdots & \vdots & \vdots & \ddots \end{pmatrix} \quad (1.62)$$

However, this matrix is not yet orthogonalized, and orthogonalization and diagonalization of the AO set is achieved by a multi-step (in general non-unitary) transformation process to finally yield a set of *Natural Atomic Orbitals* (NAOs). The individual NAOs on each atom are then obtained analogously to the NO formalism as eigenvectors of the one-center subblocks of \mathbf{D} with the eigenvalues indicating the occupation. They can further be divided into a strongly-occupied *natural minimal basis* (NMB) and a weakly-occupied *Rydberg basis* (RB), where the latter contains the remaining electron density that cannot be described by the NMB orbitals. The NAO set is identical to the NO set of P.-O. Löwdin for isolated atoms, however it retains the atom-localized shape for a molecular system, in contrast to NOs that are delocalized for a molecule. As with other atomic population schemes, the NAOs can also be used to obtain atomic natural partial charges in the NAO basis (Natural Population Analysis, NPA). These NPA charges are found to be in good agreement with density integration method charges and show a smooth convergence as they are intrinsic to the wave function.^[86]

In a one-center atomic block, core-orbitals can be identified by occupation numbers very close to 2. After removing the contribution of the core-orbitals by subtraction, the remaining occupied NAOs with large occupation numbers are attributed to lone pair (LP) natural hybrid orbitals (NHOs), which are subsequently also removed from \mathbf{D} . Two-center and three-center natural bonds can be obtained by diagonalization of two-by-two or three-by-three interatomic subblocks of the density matrix, respectively. The eigenfunction, a natural bond orbital (NBO), can then be decomposed to its atomic NHO contributions h_i :

$$\text{NBO}(A - B) = c_A h_A + c_B h_B; \quad \text{NBO}(A - B - C) = c_A h_A + c_B h_B + c_C h_C \quad (1.63)$$

If the sum of the occupation numbers ρ_{Lewis} of the found core, lone pair and bond orbitals does not match the total electron number N , the threshold for identifying an NBO is lowered and the density matrix is examined again. After convergence, the combined lone pair and bond orbitals yield the final Natural Lewis structure (NLS) of the molecule, and its accuracy can be directly assessed by the amount of *non-Lewis electrons* $\rho_{\text{NL}} = N - \rho_{\text{Lewis}}$. Accordingly, when different Lewis structures are calculated by the NBO method (e.g. by user-controlled input) they can be ranked by their remaining non-Lewis electron density that should be as low as possible.

The NBO set can be considered similar to a LMO set discussed above as it contains localized core, lone pair and bond orbitals for the occupied space and antibonding, lone valence (LV) and Rydberg orbitals for the virtual space. By weakly delocalizing the NBO set a natural localized molecular orbital (NLMO) set is obtained and its delocalization tails can be examined by going through its NBO components. The NLMOs are found to be very similar to the LMOs of Edmiston and Ruedenberg, but preserve σ - π separation, similar to Pipek-Mezey LMOs. Optionally, by diagonalizing

the Fock matrix in the NLMO basis, a connection between canonical MOs and NLMOs can be made. Overall, this leads to the following order of transformations for NBO theory:

$$\text{AOs} \rightarrow \text{NAOs} \rightarrow \text{NHOs} \rightarrow \text{NBOs} \rightarrow \text{NLMOs} \rightarrow \text{MOs} \quad (1.64)$$

A further extension to the NBO framework was made by F. Weinhold and co-workers in 1998 with the Natural Resonance Theory (NRT) suite^[99-101] based on the resonance theory by Pauling and Wheland,^[102] which in turn traces back to the seminal work of F. A. Kekulé.^[99] The basic idea of NRT is to use not only one NLS to represent the underlying wave function, but a linear combination of multiple NLS. In detail, it is assumed that the first-order density matrix Γ of the overall system can be expressed by a convex weighted combination of density matrices Γ_α for localized natural Lewis structures α :^[99]

$$\Gamma = \sum_{\alpha} w_{\alpha} \Gamma_{\alpha}, \quad (1.65)$$

with the convex weighting scheme given in Equation 1.66, whose admissibility was recently discussed in the literature.^[103-105]

$$w_{\alpha} \geq 0; \quad \sum_{\alpha} w_{\alpha} = 1 \quad (1.66)$$

By minimizing the difference between the density matrix and the sum of density matrices for the resonance structures,

$$\min \left\| \Gamma - \sum_{\alpha} w_{\alpha} \Gamma_{\alpha} \right\| \quad (1.67)$$

the unknown weighting factors w_{α} can be derived in a variational manner. These weighting factors allow the formulation of weighted NRT bond orders b_{AB} between atoms A and B,^[100]

$$b_{AB} = \sum_{\alpha} w_{\alpha} b_{AB}^{(\alpha)} \quad (1.68)$$

which are chemically easily comprehensible as they are derived from a set of (natural) Lewis structures.

2. Computational Details

Most calculations of this work were carried out with the ORCA program package versions 4.1.1 or 5.0.3. The GGA density functional approximation B97-D3^[69] was selected as method, which shows a generally good performance according to various benchmark studies.^[54, 69, 106] It offers a beneficial accuracy to cost ratio and proved to be robust for both main group and transition metal chemistry. Its coherent inclusion of London dispersion forces via S. Grimme's D3 method and Becke-Johnson damping for the short-ranged interatomic distances^[70, 72] is complemented with the additive three-body correction of B. M. Axilrod, E. Teller and Y. Muto.^[73, 74]

As basis set, the triple- ζ def2-TZVP basis by the group of R. Ahlrichs was chosen,^[25] resulting in the level of theory B97-D3(BJ)-ATM/def2-TZVP (denoted as I).

If higher accuracy was necessary (e.g. for accurate thermochemistry or transition state barriers), the double-hybrid DFA PWPB95^[107] with D3(BJ)-ATM dispersion correction and def2-QZVPP basis set^[25] was used, which offers a convincing performance.^[54, 107-109] As structure optimizations are computationally not feasible for all but small molecules, only electronic energies were evaluated with the double-hybrid method and the preceding structure optimization was carried out on level of theory I, resulting in the total level of theory PWPB95-D3(BJ)-ATM/def2-QZVPP//B97-D3(BJ)-ATM/def2-TZVP (denoted as II).

For both levels of theory I and II, Stuttgart/Dresden effective core potentials were employed for the elements Rb to Rn.^[30, 110]

The grid settings for numerical integration of the DFT methods were set to *GRID3* for the SCF iterations and *FINALGRID5* for the final energy evaluation after SCF convergence for ORCA 4.1.1, and *defGrid2* for ORCA 5.0.3.

The Coulomb part of the DFAs B97-D3 and PWPB95 was approximated with the RI-J method^[111] utilizing the def2/J auxiliary basis sets.^[112] Furthermore, for the DFA PWPB95, the calculation of the exchange and MP2 correlation parts was accelerated by the RI-JK method^[113] with the matching def2/JK basis set^[114] and the RI method with the def2-QZVPP/C auxiliary basis set,^[115] respectively.

Structure optimizations were carried out starting from experimental single-crystal X-ray structures, if available. Derivatives and compounds without an obtainable starting structure were modelled by hand using Avogadro^[116] or GaussView.^[117]

The minimum character of computed structures was checked with subsequent numerical (harmonic two-sided differentiation of the analytical gradients) or analytical frequency calculations. Imaginary vibrations with frequencies $< 20i \text{ cm}^{-1}$, that have no share at the molecular core, were

considered insignificant and were neglected. The calculated electronic energies E are given without the zero-point vibrational energy. A temperature of 298.15 K and a pressure of 1.00 atm were used for the thermochemical quantities U , H , S and G . The quasi rigid rotor harmonic oscillator (QRRHO) model was used for the vibrational entropy.^[118]

NBO, NPA and NRT analyses were carried out with the commercially available NBO 6.0.18a^[119] and NBO 7.0.10^[120] program packages using the molecular structure and wave function generated with level of theory I as input. Wiberg bond indices were calculated in the NAO basis as done by the NBO program package. Note that the total NRT bond orders can differ from the sum of their covalent and ionic contributions due to rounding. The same is true for the sum of the NBO polarisations.

Cube files of canonical and localized molecular orbitals were generated with the powerful Multi-WFN program (versions 3.6 and 3.8)^[121] from the wave function obtained on the level of theory I. Molecular structures and orbitals were visualized with the program UCSF Chimera version 1.13.1.^[122] If not stated otherwise, hydrogen atoms are omitted in the structure and MO plots. The isosurface value for MO plots is set to $0.04 e^{1/2} \cdot \text{Bohr}^{-3/2}$.

Transition state searches were carried out using the growing string (GSM) method,^[123] the Nudge Elastic Band (NEB) method as implemented in ORCA^[124] or chemically reasonable trial structures for the transition state optimization input.

For the bond cleavage energies (BCEs), the fragments were calculated in all conceivable spin states and the lowest energy difference between the fragments in the same spin state and the supermolecule is calculated. The bond dissociation energies (BDEs) and bond dissociation free Gibbs energies (BDGs) include the structural relaxation of the fragments and the spin ground states of the fragments. Constitutional isomerizations during the structure optimizations of the fragments were avoided to only obtain information about the bond meant to be broken. Structural rearrangements such as bond activations or isomerizations are indicated in the respective section, if found.

The chemical schemes in this work were created with ChemDraw Prime 16.0. The data was managed utilizing Microsoft Excel within Microsoft Office Standard 2019.

In addition to the programs listed above several small scripts were created using the bash or Python scripting languages to manage and facilitate the evaluation of the thermodynamic, NBO and NRT data, or to accelerate the generation of calculation inputs.

3. Iminosilylenes

The results presented in the following chapter were already published and the content is reprinted (adapted) with permission from

S. Karwasara, L. R. Maurer, B. Peerless, G. Schnakenburg, U. Das, A. C. Filippou, *(NHC)Si=C=N-R: A Two-Coordinated Si⁰-Isocyanide Compound as Si(NHC) Transfer Reagent*, *J. Am. Chem. Soc.* **2021**, *143*, 14780-14794; doi 10.1021/jacs.1c06628. Copyright 2023 American Chemical Society.

My own manuscript contributions comprise

- Performing the calculations
- Interpretation of the theoretical results
- Co-writing the manuscript (mainly the theoretical part) and proofreading

The following chapter provides an overview of the topic's main results and conclusions. In addition to my own contributions (see above), which are in the focus of this chapter, experimental results will be presented that were obtained by the co-authors listed above. The complete publication can be found in the appendix.

3.1. Introduction

The potential energy hypersurface of the system [H,C,N,Si], as calculated in a theoretical study by J. R. Flores *et al.*,^[125] shows several constitutional isomers A-I to A-VI (Figure 3.1), with the cyanosilylene HSiCN (A-I) being the energetically lowest. Among these isomers, only some could be observed so far in the experiment, e.g. the cyanosilylene A-I and isocyanosilylene A-II by fluorescence spectroscopy,^[126, 127] or 3-H-2-aza-1-silacyclopropenylidene A-III, silaisocyanocarbene A-IV and also A-I by infra-red spectroscopy in an argon matrix.^[128]

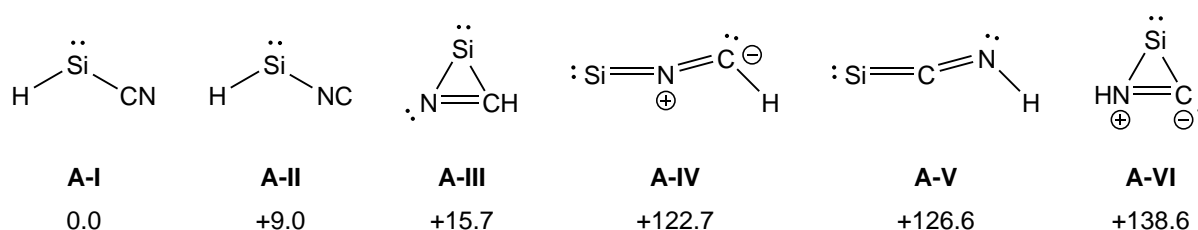


Figure 3.1: Lowest-lying singlet isomers A-I to A-VI of the [H,C,N,Si] potential energy hypersurface and their relative corrected electronic energies in $\text{kJ}\cdot\text{mol}^{-1}$ at the RHF-UCCSD(∞)/CBS//B3LYP/6-311G** level of theory according to J. R. Flores *et al.*^[125]

Although the energetically high-lying iminosilylenylidene A-V is still elusive so far, great effort in the past years allowed the isolation of related compounds, for example isocyanide-silylene adducts with the general formula $\text{R}_2\text{Si}(\text{CNR})$ ^[129–133] or the lithium silaketeniminide $[\text{CH}_2\text{N}(\text{R}')_2\text{BSi}(\text{Li})\text{CNR}]$ by C. Cui *et al.* ($\text{R}' = \text{B}[\text{N}(\text{Dipp})\text{CH}]_2$, $\text{Dipp} = 2,6\text{-iPr}_2\text{-C}_6\text{H}_3$, $\text{R}'' = 1\text{-adamantyl}$).^[134] Their electronic structures could be rationalized by experimental and quantum chemical studies to lie between the allenic ($\text{Si}=\text{C}=\text{N}$) and zwitterionic ($^-\text{Si}-\text{C}\equiv\text{N}^+$) resonance formulas, and thus the different reactivity compared to silenes and 1-silaallenes is comprehensible.^[135–137]

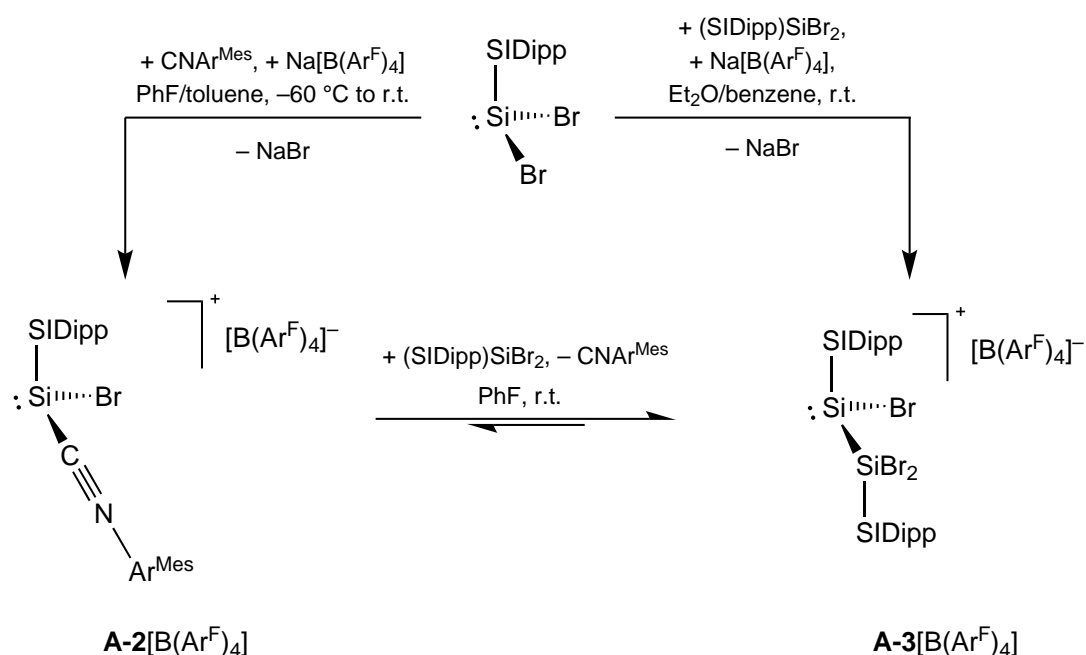
In an attempt to obtain an N-heterocyclic carbene (NHC)-stabilized neutral iminosilylenylidene, the NHC-supported Si(II)dibromide $(\text{SIDipp})\text{SiBr}_2$ ^[138] was reduced with potassium graphite in the presence of the bulky isocyanide CNAr^{Mes} to afford directly the targeted iminosilylenylidene $(\text{SIDipp})\text{SiCNAr}^{\text{Mes}}$ (**A-1Ar^{Mes}**). However, the reaction proceeds unselectively with a yield of only 16 % for **A-1Ar^{Mes}** among other reduction products as evidenced by $^1\text{H-NMR}$ spectroscopy (scheme 3.1).



Scheme 3.1: Unselective formation of the targeted iminosilylenylidene **A-1Ar^{Mes}** by co-reduction as evidenced by $^1\text{H-NMR}$ spectroscopy.

3.2. NHC- and Isocyanide-stabilized Halosilyliumylidene and Ligand-Exchange Equilibrium

Seeking a more selective approach to target $A-1Ar^{Mes}$, the isocyanide ligand was preinstalled by treating $(SIDipp)SiBr_2$ with $Na[B(Ar^F)_4]$ in the presence of $CNAr^{Mes}$, and the NHC- and isocyanide-stabilized halosilyliumylidene salt $[(SIDipp)SiBrCNAr^{Mes}] (A-2[B(Ar^F)_4])$ was obtained selectively (Scheme 3.2).



Scheme 3.2: Conversion of the starting material $(SIDipp)SiBr_2$ to the silyliumylidene salts $A-2[B(Ar^F)_4]$ and $A-3[B(Ar^F)_4]$, and ligand exchange equilibrium between $A-2[B(Ar^F)_4]$ and $A-3[B(Ar^F)_4]$.

The optimized gas phase structure of cation $A-2^+$ (Figure 3.2 left) fits well to the experimental single-crystal X-ray diffraction (sc-XRD) solid state structure and features a tri-coordinated, strongly pyramidalized silicon atom ($\Sigma\angle(Si) = 291.9^\circ$, Table 3.1). It further suggests the presence of a stereoactive electron lone pair at the silicon atom, which can be found in the HOMO (Figure 3.2 right). The silicon isocyanide bond $Si-C_{CNR}$ is slightly shorter with 193.5 pm than the $Si-C_{NHC}$ bond (197.6 pm), whereas both lie in the range of typical $Si-C$ donor-acceptor σ -bonds.

Table 3.1: Selected bond parameters of the halosilyliumylidene cation $A-2^+$ and its experimental counterpart $A-2^+_{\text{exp}}$ by sc-XRD analysis. Bond lengths and angles are given in pm and degrees, respectively.

	Si–C _{NHC}	Si–Br	Si–C _{CNR}	C _{CNR} –N	N–C _R
$A-2^+$	197.6	231.6	193.5	117.1	137.4
$A-2^+_{\text{exp}}$	197.7(4)	226.1(3)	195.2(5)	115.0(5)	140.0(6)
	C _{NHC} –Si–C _{CNR}	Si–C _{CNR} –N	C _{CNR} –N–C _R	N _{NHC} –C _{NHC} –Si–C _{CNR}	$\Sigma\angle(\text{Si})$
$A-2^+$	100.1	149.7	178.4	–8.2	291.9
$A-2^+_{\text{exp}}$	100.3(2)	148.8(4)	171.9(5)	–25.3(4)	286.7(5)

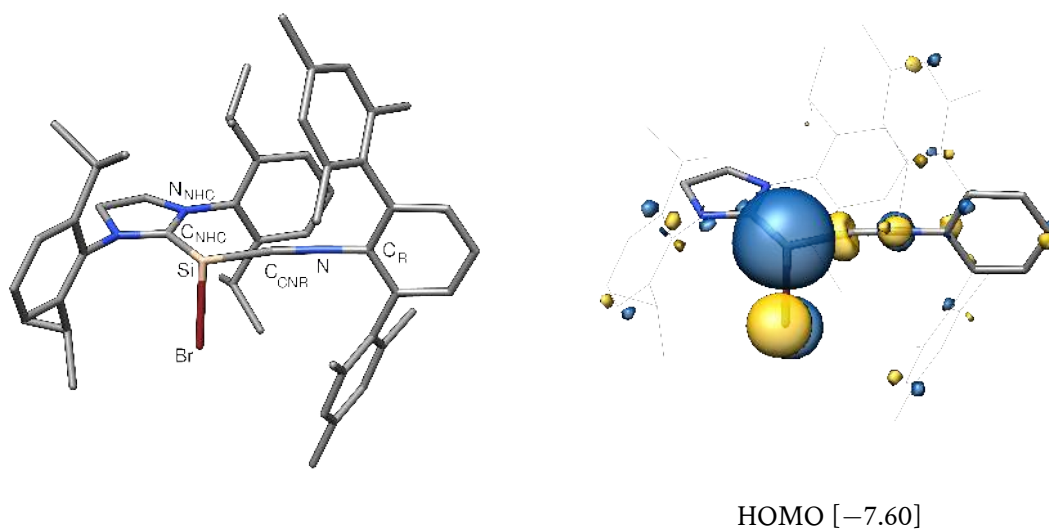


Figure 3.2: Left: Optimized gas phase structure of the silyliumylidene cation $A-2^+$ with atom labelling. Right: HOMO of $A-2^+$ with its energy eigenvalue in eV.

A subsequent bond analysis with the NBO6 program package confirms this bond situation and yields a resonance hybrid, which is dominated by the bond motif $A-2^+ \text{-a}$ (78 % contribution, see Figure 3.3) with Si–C_{NHC}, Si–Br and Si–C_{CNR} single bonds and a C–N triple bond. Other resonance structures, such as the zwitterionic formula $A-2^+ \text{-b}$ (5 %), the silaketimine ($A-2^+ \text{-c}$, 3 %) or silene motif ($A-2^+ \text{-d}$, 2 %), are found to be negligible, which is also reflected in the overall NRT bond orders for the Si–C_{NHC} (1.0) and Si–C_{CNR} (1.0) bonds, respectively (Table 3.2).

A closer inspection of NLS $A-2^+ \text{-a}$ reveals localized $\sigma(\text{Si}-\text{C}_{\text{NHC}})$, $\sigma(\text{Si}-\text{C}_{\text{CNR}})$, $\sigma(\text{Si}-\text{Br})$, $\sigma(\text{C}_{\text{CNR}}-\text{N})$ and $\pi(\text{C}_{\text{CNR}}-\text{N})$ NBOs with high occupations $> 1.9 e^-$ as well as an electron lone pair at the silicon atom ($1.76 e^-$) with expected high *s*-character of 71 % (Table 3.2).

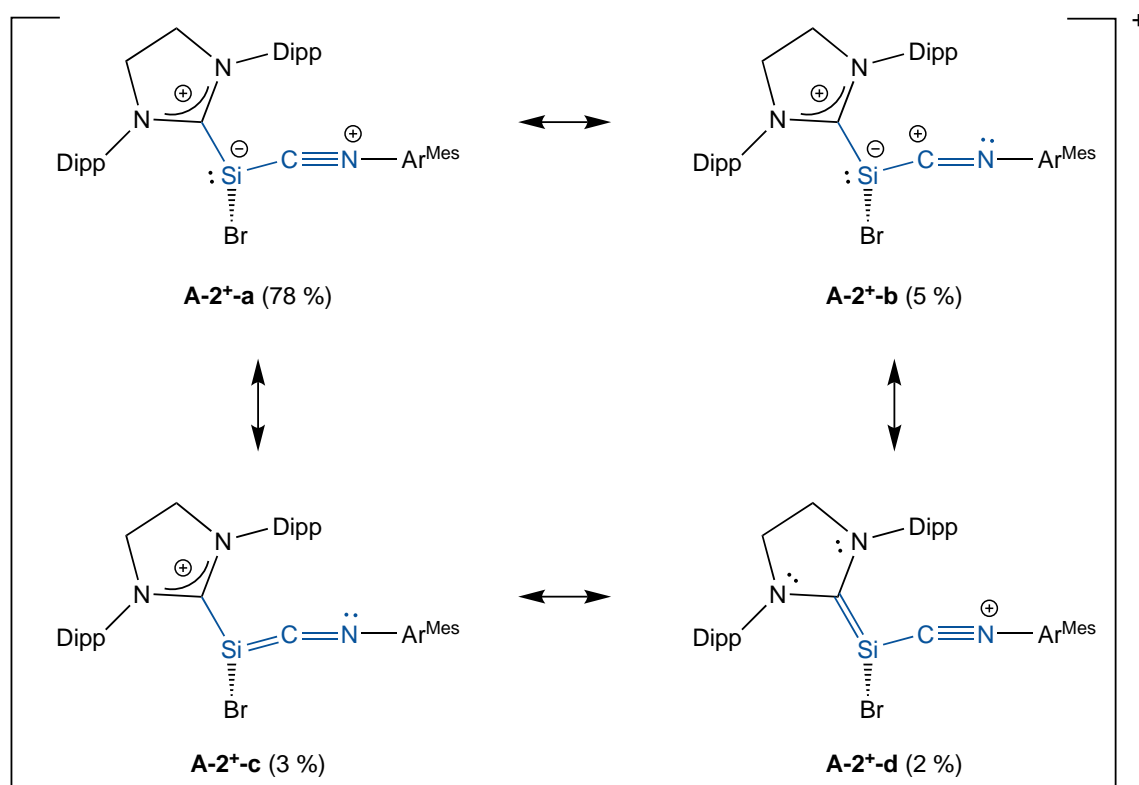


Figure 3.3: Natural Lewis structures of $A-2^+$ and their NRT resonance weight. The resonance structures from a local NRT analysis (with the N_{NHC} , C_{NHC} , Br, Si, C_{CNR} , N and C atoms of the central phenyl ring of Ar^{Mes}) were collected according to their bond motif (marked in blue).

Table 3.2: Results of the NBO and local NRT analysis of the cation $A-2^+$ (with the N_{NHC} , C_{NHC} , Br, Si, C_{CNR} , N and C atoms of the central phenyl ring of Ar^{Mes}).

NBO A–B	Occ./ e^-	NHO (A,B) pol./% (hybr.)	WBI	NRT-BO tot/cov/ion	NPA/e
LP(Si)	1.76	($sp^{0.4}$)			Si +0.69
$\sigma(\text{Si}-C_{\text{NHC}})$	1.92	23 ($sp^{8.5}$), 77 ($sp^{1.5}$)	0.7	1.0/0.5/0.5	C_{CNR} +0.18
$\sigma(\text{Si}-C_{\text{CNR}})$	1.96	23 ($sp^{10.5}$), 77 ($sp^{0.6}$)	0.9	1.0/0.5/0.6	N -0.33
$\sigma(C_{\text{CNR}}-N)$	1.99	34 ($sp^{1.6}$), 66 ($sp^{0.9}$)	2.3	2.8/1.9/0.9	Br -0.30
$\pi_1(C_{\text{CNR}}-N)$	1.98	33 (p), 67 (p)			[CNR] +0.19
$\pi_2(C_{\text{CNR}}-N)$	1.95	35 (p), 65 (p)			[NHC] +0.42

When an excess of $(\text{SIDipp})\text{SiBr}_2$ is present during the formation of compound $A-2[\text{B}(\text{Ar}^{\text{F}})_4]$, it replaces the isocyanide ligand and the silylsilylene salt $[(\text{SIDipp})\text{Si}(\text{Br})\text{SiBr}_2(\text{SIDipp})][\text{B}(\text{Ar}^{\text{F}})_4]$ ($A-3[\text{B}(\text{Ar}^{\text{F}})_4]$) is obtained (Scheme 3.2). ^1H - and ^{29}Si -NMR spectroscopic studies reveals an equilibrium reaction that is slightly shifted to the side of the silylsilylene salt $A-3[\text{B}(\text{Ar}^{\text{F}})_4]$ with a $\Delta G_{\text{exp}}^\circ$ (298 K) value of $-5.9(\pm 0.4) \text{ kJ}\cdot\text{mol}^{-1}$.

The gas phase structure of cation $A-3^+$, depicted in Figure 3.4, was calculated using the sc-XRD structure $A-3_{\text{exp}}^+$ and reproduces its features well (Table 3.3). Among these are a tricoordinated

Si1 center with a high degree of pyramidalization ($\Sigma\angle(\text{Si1}) = 286.4^\circ$), bonded to a tetrahedrally coordinated Si2 atom with a Si1–Si2 bond length of 237.0 pm that is close to that of α -silicon (235.2 pm).^[139] Both Si–C_{NHC} bond lengths (Si1–C1: 198.1 pm, Si2–C28: 198.5 pm) are similar to that of A-2⁺ and suggest strong Si–C_{NHC} σ -bonds without considerable multiple-bond character. Furthermore, the shift of the equilibrium between A-2⁺ and A-3⁺ as mentioned above could be reproduced to lie on the site of A-3⁺ with $\Delta G = -22.1 \text{ kJ}\cdot\text{mol}^{-1}$.

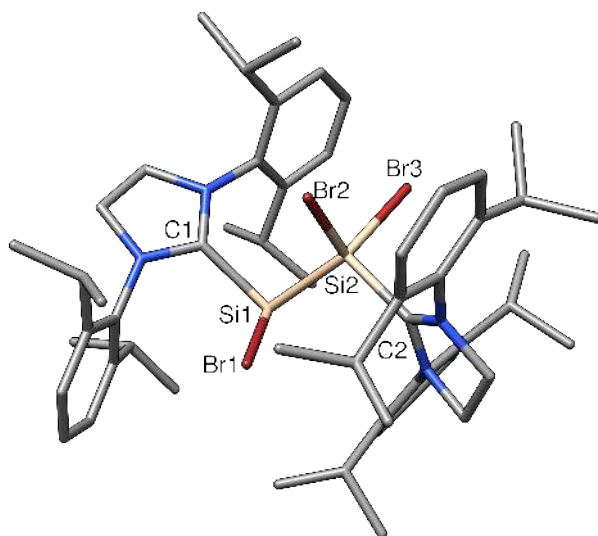


Figure 3.4: Optimized gas phase structure of the cation A-3⁺ with atom labelling.

Table 3.3: Selected bond parameters of the silylsilylene cation A-3⁺ and its experimental counterpart A-3⁺_{exp} by sc-XRD analysis. Bond lengths and angles are given in pm and deg, respectively.

	Si1–C1	Si2–C2	Si1–Si2	Si1–Br1
A-3 ⁺	198.1	198.5	237.0	239.1
A-3 ⁺ _{exp}	197.3(5)	197.0(5)	235.3(2)	231.6(1)
	Si2–Br2	Si2–Br3	C1–Si1–Si2–C2	$\Sigma\angle(\text{Si1})$
A-3 ⁺	226.2	225.0	163.0	286.4
A-3 ⁺ _{exp}	223.4(1)	219.7(1)	155.7(2)	284.3(4)

Additionally, the potential energy hypersurface of cation A-3⁺ was checked for energetically close-lying constitutional isomers. The cations A-3a⁺, A-3b⁺ and A-3c⁺ (Figure 3.5) were found, which feature a different arrangement of the SIDipp and bromine substituents at the silicon centers. However, both the bridging bromine structure A-3a⁺ (+81.5 kJ·mol⁻¹) and A-3b⁺ (+159.7 kJ·mol⁻¹) as well as the isomer A-3c⁺ (+203.6 kJ·mol⁻¹) with two SIDipp substituents at one silicon atom are significantly unfavoured and leave A-3⁺ as ground-state isomer. This is in line with the experimen-

tal observation of two distinct silicon atoms in solution without the occurrence of topomerization of the NHC ligands.

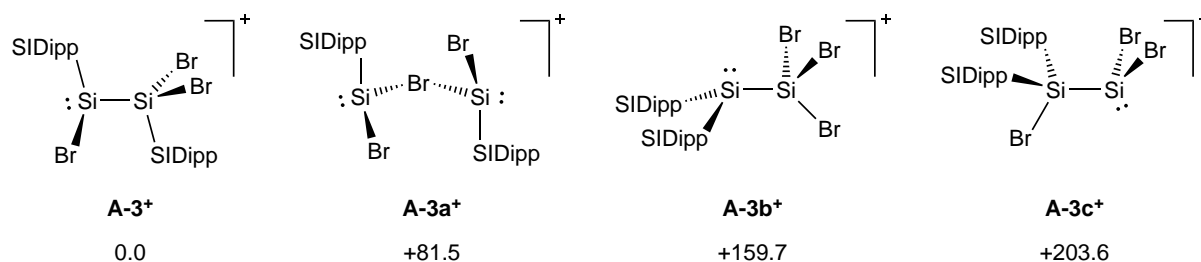
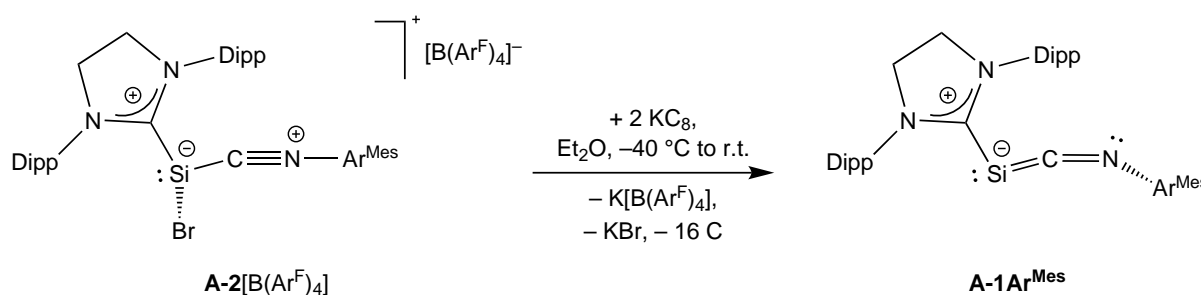


Figure 3.5: Silylsilylene regioisomers A-3⁺ to A-3c⁺ ordered by increasing electronic energy in kJ·mol⁻¹.

3.3. Iminosilylenylidene A-1Ar^{Mes}

With the halosilyliumylidene salt A-2[B(ArF)₄] as precursor in hand, the two-electron reduction with potassium graphite straightforwardly afforded the iminosilylenylidene (SIDipp)SiCNAr^{Mes} (A-1Ar^{Mes}, Scheme 3.3) that could be isolated and fully characterized, being the first reported neutral Si⁰ isocyanide compound.



Scheme 3.3: Two-electron reduction of the Si^{II} halosilyliumylidene salt A-2[B(Ar^F)₄] to the Si⁰ iminosilylenylidene A-1Ar^{Mes}.

As stated above, the NHC-free iminosilylenylidene A-V is found to be energetically unfavoured by 126.6 kJ·mol⁻¹ compared to its cyanosilylene isomer A-I (Figure 3.1). Notably, also the iminosilylenylidene A-1Ar^{Mes} is revealed to be not the global minimum on the PES, but at level of theory II 33.0 kJ·mol⁻¹ less stable than its NHC-stabilized cyanosilylene isomer (A-4Ar^{Mes}, see Figure 3.6). Additional calculations were carried out on the model systems (SIME)SiCNMe and (SIME)Si(CN)Me, featuring the sterically less demanding N-heterocyclic carbene SIME = C[N(Me)CH₂]₂ and methyl substituents on the nitrogen atoms. These show an even higher energy difference of 161.3 kJ·mol⁻¹, favouring the cyanosilylene. This suggests a considerable kinetic stabilization in the iminosilylenylidene A-1Ar^{Mes} as it is not found experimentally to isomerize to A-4Ar^{Mes} (see the appendix for

more information about $\mathbf{A-4Ar}^{\text{Mes}}$, $(\text{SiMe})\text{SiCNMe}$ and $(\text{SiMe})\text{Si}(\text{CN})\text{Me}$.

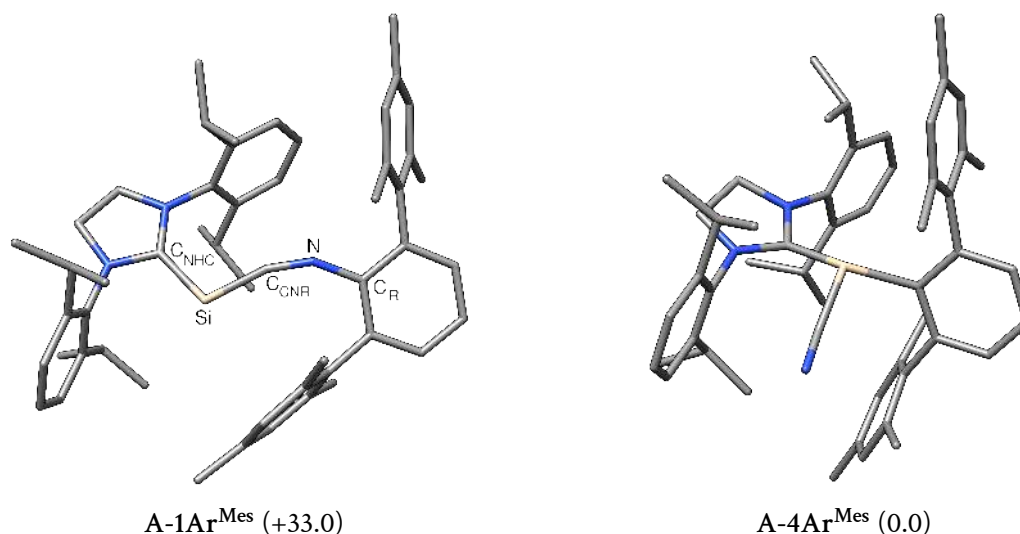


Figure 3.6: Optimized gas phase structures of $\mathbf{A-1Ar}^{\text{Mes}}$ and its cyanosilylene isomer $\mathbf{A-4Ar}^{\text{Mes}}$. Relative energies are given in $\text{kJ}\cdot\text{mol}^{-1}$ and obtained on level of theory II.

The optimized gas phase structure of $\mathbf{A-1Ar}^{\text{Mes}}$ was successfully obtained starting from the experimental sc-XRD solid state structure $\mathbf{A-1Ar}^{\text{Mes}}_{\text{exp}}$ and reveals a cumulene-type $\text{Si}=\text{C}=\text{N}$ skeleton, which is slightly bent ($\angle(\text{Si}-\text{C}_{\text{CNR}}-\text{N}) = 156.6^\circ$, Table 3.4) with a two-coordinated, highly bent silicon atom ($\angle(\text{C}_{\text{NHC}}-\text{Si}-\text{C}_{\text{CNR}}) = 101.5^\circ$), suggesting the presence of a stereochemically active electron lone pair. The NHC substituent is oriented coplanar to the $\text{Si}=\text{C}=\text{N}$ skeleton, as indicated by the interplanar twist angle of 2.7° between the central SiDipp ring plane and the $(\text{C}_{\text{NHC}}\text{SiC}_{\text{CNR}}\text{N})$ plane. This allows the conjugation of the out-of-plane $\pi_{\text{oop}}(\text{Si}-\text{C}_{\text{CNR}})$ bond to the NHC, which is confirmed by the electronic structure analysis (*vide infra*). Accordingly, compared to the $\text{Si}-\text{C}_{\text{NHC}}$ bonds in $\mathbf{A-2}^+$ (197.6 pm) and $\mathbf{A-3}^+$ (198.1 and 198.5 pm), that bond is significantly shortened to 187.5 pm in $\mathbf{A-1Ar}^{\text{Mes}}$.

A delocalization over the $\text{Si}-\text{C}_{\text{NHC}}$ bond would weaken the $\text{Si}-\text{C}_{\text{CNR}}$ bond and increase its bond distance. This, in fact, is found for $\mathbf{A-1Ar}^{\text{Mes}}$ as the $\text{Si}-\text{C}_{\text{CNR}}$ bond distance of 180.3 pm is shorter than typical $\text{Si}-\text{C}$ single bonds (187 to 191 pm),^[140] but longer than the $\text{Si}=\text{C}$ double bonds in silenes (169 to 176 pm),^[136] and fits well with the experimental $\text{Si}-\text{C}_{\text{CNR}}$ bond lengths of the dialkylsilaketanimines $[\text{CH}_2\text{C}(\text{TMS})]_2\text{SiCNR}$ by T. Iwamoto *et al.* (R = 1-adamantyl: 178.2(2) pm, R = Dipp: 179.4(3) pm).^[130]

In contrast to the short $\text{C}_{\text{CNR}}-\text{N}$ triple bond length of 117.1 pm in $\mathbf{A-2}^+$, the $\text{C}_{\text{CNR}}-\text{N}$ distance is found to be longer in $\mathbf{A-1Ar}^{\text{Mes}}$ with 121.3 pm, being considerably elongated than that of free calculated (117.8 pm) or experimental (115.8(3) pm) isocyanide CNAr^{Mes} ,^[141] and suggests a $\text{C}-\text{N}$ bond order smaller than three. The canonical orbitals of $\mathbf{A-1Ar}^{\text{Mes}}$ underline the trends observed from the molecular structure: The HOMO-1 is of lone pair character at the silicon atom with high s-orbital contribution and the HOMO shows a bonding interaction between the C_{NHC} , Si and C_{CNR}

Table 3.4: Selected bond parameters of the calculated iminosilylenylidene A-1Ar^{Mes} and its experimental counterpart A-1Ar^{Mes}_{exp} from sc-XRD analysis. Bond lengths and angles are given in pm and deg, respectively.

	Si–C _{NHC}	Si–C _{CNR}	C _{CNR} –N	N–C _R
A-1Ar ^{Mes}	187.5	180.3	121.3	137.3
A-1Ar ^{Mes} _{exp}	189.4(2)	178.4(2)	122.4(2)	141.1(2)
	C _{NHC} –Si–C _{CNR}	Si–C _{CNR} –N	C _{CNR} –N–C _R	C _{NHC} –Si–C _{CNR} –N
A-1Ar ^{Mes}	101.5	156.6	148.3	167.8
A-1Ar ^{Mes} _{exp}	100.4(1)	158.8(1)	133.0(1)	173.8(2)

atoms. This $3c-2e^- - \pi_{\text{oop}}(\text{C}_{\text{NHC}}-\text{Si}-\text{C}_{\text{CNR}})$ orbital is rationalized by delocalization of the second Si⁰ electron lone pair orbital with high p-character into the antibonding $\pi_{\text{oop}}^*(\text{N}_{\text{NHC}}-\text{C}_{\text{NHC}}-\text{N}_{\text{NHC}})$ and $\pi_{\text{oop}}^*(\text{C}_{\text{CNR}}-\text{N})$ orbitals. The LUMO can be viewed as the non-binding combination of these three orbitals, being mainly of $\pi_{\text{oop}}^*(\text{C}_{\text{CNR}}-\text{N})$ character.

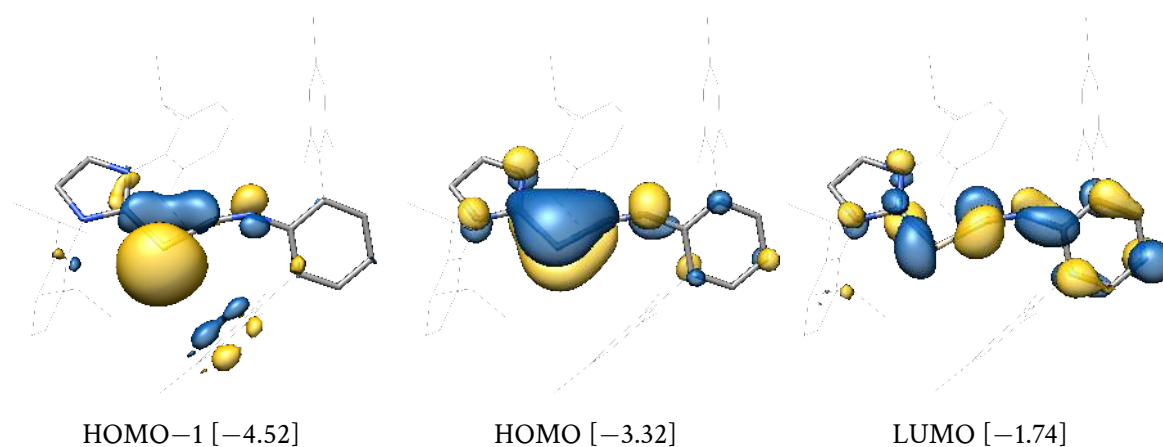


Figure 3.7: Selected canonical MOs of A-1Ar^{Mes} and their energy eigenvalues in eV.

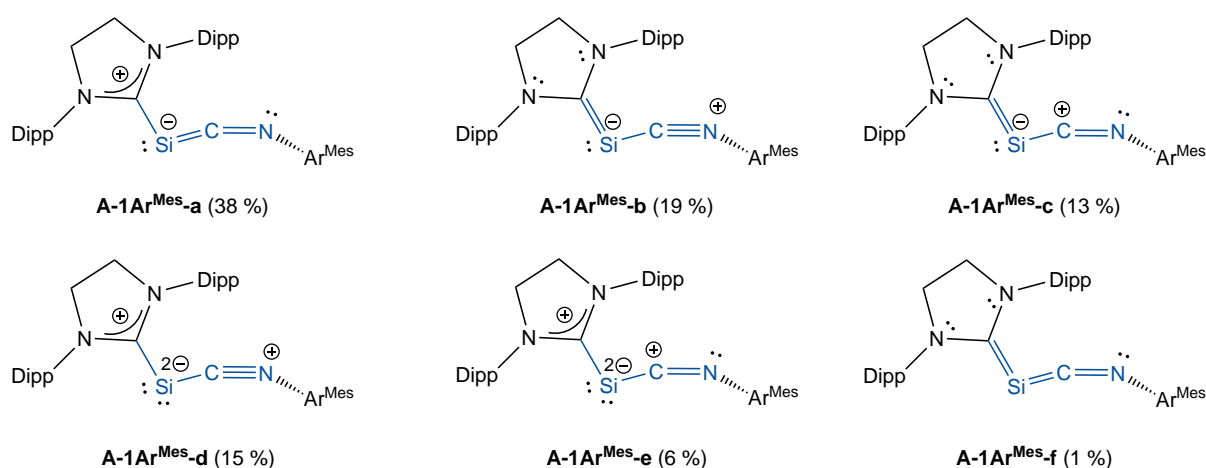
This bond picture is further confirmed by a successive NBO analysis (Table 3.5): Both the Si–C_{NHC} and Si–C_{CNR} bonds show total NRT bond orders of 1.3 and 1.5, respectively, whereas the formal isocyanide C≡N triple bond is reduced to a bond order of 2.3. An investigation of the NRT resonance hybrid of A-1Ar^{Mes} reveals several Lewis structures that can be collected according to their bond motif (Scheme 3.4). They comprise structures with a Si=C_{CNR} double bond (A-1Ar^{Mes}-a, 38 %) or Si=C_{NHC} double bond (A-1Ar^{Mes}-b, 19 %; A-1Ar^{Mes}-c, 13 %) with similar weight. The existence of silylone-type resonance formulas with two electron lone pairs located at the Si atom (A-1Ar^{Mes}-d, 15 %, and A-1Ar^{Mes}-e, 6 %) is not surprising, as the compound A-1Ar^{Mes} can also strikingly be viewed as an LSi⁰L' system in analogy to typical silylone compounds (L = neutral donor ligand).^[142–144] Finally, a 2-silaallenic contribution (A-1Ar^{Mes}-f, 1 %) was found to be negligible.

The NBO results of Table 3.5 further reveal $\sigma(\text{Si}-\text{C}_{\text{NHC}})$, $\sigma(\text{Si}-\text{C}_{\text{CNR}})$, $\sigma(\text{C}_{\text{CNR}}-\text{N})$ and $\pi(\text{C}_{\text{CNR}}-\text{N})$ bond orbitals with high electron occupations above $1.90 e^-$ and NHO polarizations that follow the trends of atom electronegativities. As expected, the resonating $\pi(\text{Si}-\text{C}_{\text{CNR}})$ bond and the electron lone pair at N exhibit low occupations of only 1.57 and $1.55 e^-$. Whereas the lone pair at the silicon atom resides in an NHO with high s -character ($sp^{0.4}$), the isocyanide nitrogen lone pair has high p -character ($sp^{7.3}$), presumably due to its resonance with the second $\pi(\text{C}_{\text{CNR}}-\text{N})$ bond (c.f. resonance structures **A-1Ar^{Mes}-b** and **A-1Ar^{Mes}-c**).

The calculated NPA charges summarized in Table 3.5 feature a positively charged silicon atom ($+0.40 e$) and an almost electroneutral C_{CNR} atom ($-0.04 e$) as well as a neutral group charge for the NHC fragment ($-0.01 e$), that illustrates the charge-flow via the $\pi_{\text{oop}}(\text{C}_{\text{NHC}}-\text{Si}-\text{C}_{\text{CNR}})$ bond from the silicon atom back to both NHC and isocyanide despite their strong σ -donating capabilities.

Table 3.5: Selected results of the NBO and local NRT (with N_{NHC} , C_{NHC} , Si, C_{CNR} , N and C atoms of the central phenyl ring of Ar^{Mes}) analyses of the iminosilylenylidene **A-1Ar^{Mes}**.

NBO A-B	Occ./ e^-	NHO (A,B) pol./% (hyb.)	WBI	NRT-BO tot/cov/ion	NPA / e	
$\sigma(\text{Si}-\text{C}_{\text{NHC}})$	1.92	23 ($sp^{6.5}$), 77 ($sp^{1.3}$)	1.0	1.3/0.7/0.6	Si	+0.40
$\sigma(\text{Si}-\text{C}_{\text{CNR}})$	1.96	24 ($sp^{6.4}$), 76 ($sp^{0.6}$)	1.3	1.5/0.9/0.6	C_{CNR}	-0.04
$\pi(\text{Si}-\text{C}_{\text{CNR}})$	1.57	47 (p), 53 (p)			N	-0.45
$\sigma(\text{C}_{\text{CNR}}-\text{N})$	1.91	35 ($sp^{1.7}$), 65 ($sp^{0.9}$)	1.9	2.3/1.5/0.8	[CNAr^{Mes}]	-0.39
$\pi(\text{C}_{\text{CNR}}-\text{N})$	1.91	34 (p), 66 (p)			[SIDipp]	-0.01
LP(Si)	1.75	($sp^{0.4}$)				
LP(N)	1.55	($sp^{7.3}$)				



Scheme 3.4: Natural Lewis structures of **A-1Ar^{Mes}** and their NRT resonance weight. The resonance structures from a local NRT analysis (with the N_{NHC} , C_{NHC} , Br, Si, C_{CNR} , N and C atoms of the central phenyl ring of Ar^{Mes}) were collected according to their bond motif (marked in blue).

The Si–C_{CNR} bond was also studied with the Extended Transition State method^[145] combined with natural orbitals of chemical valence (ETS-NOCV)^[146, 147] and yields two main interactions between the (SIDipp)Si and CNAr^{Mes} fragments in their singlet states. The first corresponds to a donation of 0.74 e[−] from the carbon lone pair in CNAr^{Mes} into the vacant σ -centered orbital at silicon ($\Delta E_{\text{orb}(1)} = -136.2 \text{ kJ}\cdot\text{mol}^{-1}$), whereas the second involves an even stronger back-donation of 0.93 e[−] from the $\pi(\text{Si}-\text{C}_{\text{NHC}})$ orbital into the antibonding $\pi_{\text{oop}}^*(\text{C}-\text{NAr}^{\text{Mes}})$ orbital (see chapter B.7 for more general information on the ETS-NOCV analysis).

Finally, the *BCEs* and *BDEs* were calculated for the Si–C_{NHC} and Si–C_{CNR} bond dissociations (Table 3.6). Both the free Si(CNAr^{Mes}) and (SIDipp)Si fragments are found to have triplet ground states with $\Delta E_{s \rightarrow t} = -37.1$ and $-19.4 \text{ kJ}\cdot\text{mol}^{-1}$, respectively, whereas the NHC and the isocyanide are clearly singlet ground state molecules with 295.7 and 296.3 $\text{kJ}\cdot\text{mol}^{-1}$. Due to the large singlet-triplet splittings of the latter, in both cases the singlet *BCEs* are preferred by a factor of two over the triplet *BCEs* and amount to 334.3 and 273.3 $\text{kJ}\cdot\text{mol}^{-1}$. A higher energy is also obtained for the Si–SIDipp dissociation after structural relaxation of the fragments in terms of the *BDE* (252.6 $\text{kJ}\cdot\text{mol}^{-1}$, 216.9 $\text{kJ}\cdot\text{mol}^{-1}$ for the Si–C_{CNR} *BDE*), and the entropic contribution considerably decreases the necessary energy to split the bonds, as *BDGs* of only 160.7 and 120.5 $\text{kJ}\cdot\text{mol}^{-1}$ are calculated. Especially the low free Gibbs energy of the latter is interesting, as it suggests a participation in ligand exchange reactions at the silicon atom, which could be confirmed experimentally (*vide infra*).

Table 3.6: Level of theory I-calculated *BCEs* and *BDEs* for the SIDipp and CNAr^{Mes} cleavages of A-1Ar^{Mes} in $\text{kJ}\cdot\text{mol}^{-1}$, entropies in $\text{J}\cdot\text{K}^{-1}\cdot\text{mol}^{-1}$. s = singlet, t = triplet multiplicity.

	ΔE	mult.	ΔE	ΔU	ΔH	ΔS	ΔG
SIDipp cleavage	<i>BCE</i>		<i>BDE</i> (parent \rightarrow SIDipp + SiCNR)				
A-1Ar ^{Mes}	334.3 (s) 616.2 (t)	(s \rightarrow s, t)	252.6	240.4	242.8	275.5	160.7
CNR cleavage	<i>BCE</i>		<i>BDE</i> (parent \rightarrow (SIDipp)Si + CNR)				
A-1Ar ^{Mes}	273.3 (s) 583.9 (t)	(s \rightarrow t, s)	216.9	207.8	210.3	301.0	120.5

3.4. Stereodynamics of Iminosilylenylidene **A-1Ar^{Mes}**

The NMR spectroscopic analysis of **A-1Ar^{Mes}** reveals a fluxional structure in solution, showing only two singlet signals for the methyl CH_3 protons of the Ar^{Mes} substituent, and only two doublet signals for the methyl CH_3 protons, one septet signal for the methine CH protons and one singlet signal for the methylene CH_2 protons of the NHC ligand. However, this stereodynamic process could not be resolved by variable-temperature (VT) 1H -NMR spectroscopy in the temperature range of 183 to 298 K in toluene- d_8 , suggesting low energetic barriers.

In order to elucidate the dynamic process, several potential energy surface scans were carried out for **A-1Ar^{Mes}** that show that the compound is, in fact, considerably flexible. Varying the $N_2-C_{NHC}-Si-C_{CNR}$ torsion angle (β) afforded the transition state (**R_a**)-**TS_{rot}** (Figure 3.8) with a single imaginary frequency of $43i\text{ cm}^{-1}$, that connects the topomers (**R_a**) and (**R_a**)* with an energy barrier of only $41.0\text{ kJ}\cdot\text{mol}^{-1}$. As the rotation of the NHC ligand is not sufficient to interconvert the enantiomers (**R_a**) and (**S_a**), another process must take place, that requires a C_S -symmetric transition state with the symmetry plane passing through the $C_{NHC}-Si-C_{CNR}-N$ skeletal plane. PES scans of the $Si-N-C_R-C_2$ torsion angle showed that the Ar^{Mes} substituent easily rotates around the $N-C_R$ bond, with a maximal energy of only $12.7\text{ kJ}\cdot\text{mol}^{-1}$. Notably, this motion is associated with an increase of the $C_{CNR}-N-C_R$ angle (γ) towards linearity ($\gamma = 170.9^\circ$) and a change of the $C_{NHC}-Si-N-C_R$ skeletal torsion angle α towards an antiperiplanar conformation ($\alpha = -177^\circ$). Accordingly, studying the linearization of the $C_{CNR}-N-C_R$ moiety revealed the presence of the local minimum structure **linN** with $\gamma = 180^\circ$ that lies only $16.4\text{ kJ}\cdot\text{mol}^{-1}$ higher in energy than **R_a** and allows an almost barrierless rotation of the Ar^{Mes} substituent, interconverting the enantiomers (**R_a**)* and (**S_a**)*.

In contrast to this stepwise process, the hypersurface of **A-1Ar^{Mes}** was also scanned for a pathway of a concerted topomerization (via NHC rotation) and enantiomerization. Employing a structure optimization with constrained C_S -symmetry¹, the structure **SP** was identified as second-order saddle point with an relative energy of $+64.5\text{ kJ}\cdot\text{mol}^{-1}$ and two imaginary frequencies at $101i$ and $88i\text{ cm}^{-1}$ (Figure 3.8), being energetically inferior compared to the stepwise stereodynamical process described before.

¹The employed ORCA version does not allow to use molecular symmetry for structure optimizations. Thus, only the energies and gradients were calculated with ORCA and then fed into the symmetry-supporting optimization algorithm of the Gaussian03 program package.^[148]

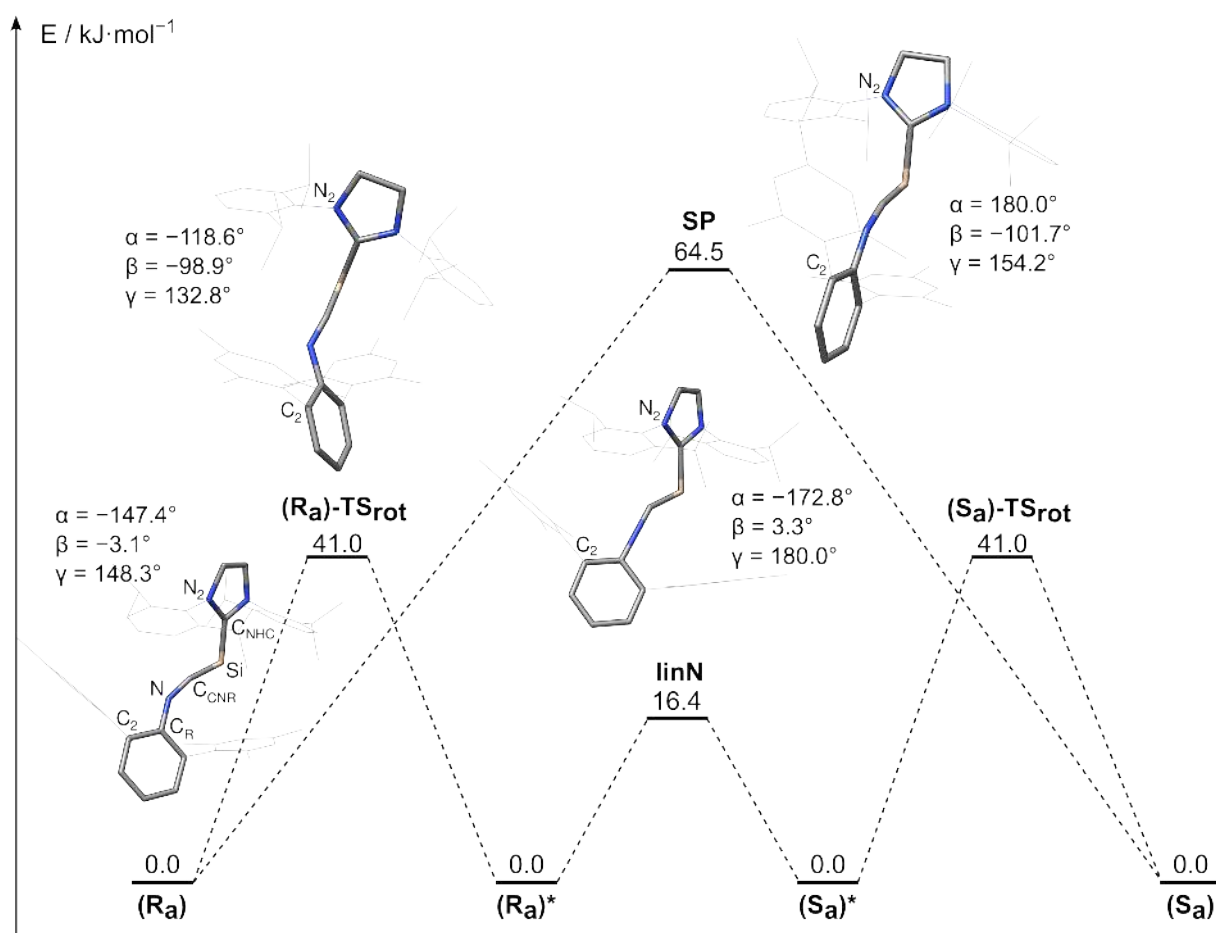
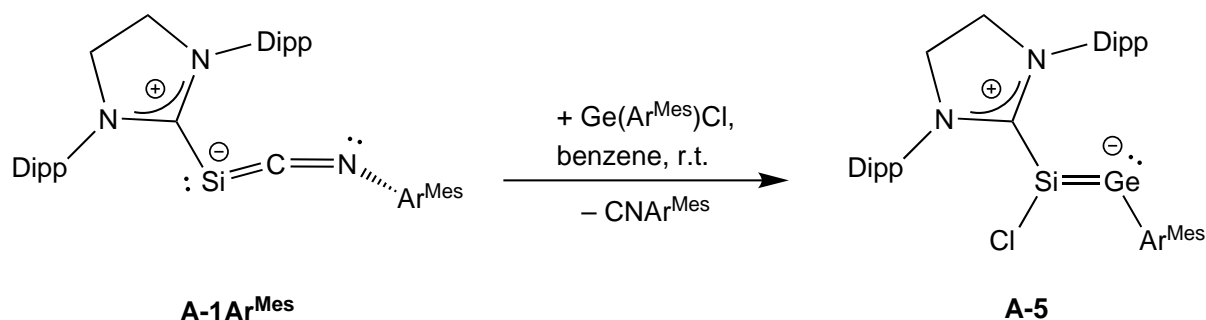


Figure 3.8: Proposed mechanism for the stereodynamics of **A-1Ar^{Mes}**. α : skeletal torsion angle $\text{C}_{\text{NHC}}-\text{Si}-\text{N}-\text{C}_{\text{R}}$, β : NHC torsion angle $\text{N}_2-\text{C}_{\text{NHC}}-\text{Si}-\text{C}_{\text{CNR}}$, γ : isocyanide nitrogen angle $\text{C}_{\text{CNR}}-\text{N}-\text{C}_{\text{R}}$.

3.5. Si(NHC) Transfer to the NHC-stabilized Germasilyne A-5

As discussed above, the low $\text{Si}-\text{C}_{\text{CNR}}$ *BDEs* indicate the synthetic potential of **A-1Ar^{Mes}** as a $\text{Si}^0(\text{NHC})$ transfer agent, which was probed accordingly by its reaction with the chlorogermylene $\text{Ge}(\text{Ar}^{\text{Mes}})\text{Cl}$ (Scheme 3.5). This led to the formation of the first reported NHC-stabilized germasilyne $(\text{SIDipp})\text{Si}(\text{Cl})\text{GeAr}^{\text{Mes}}$ (**A-5**), presumably after formation of a Lewis base-acid adduct $(\text{SIDipp})\text{Si}(\text{CNAr}^{\text{Mes}})\text{Ge}(\text{Cl})\text{Ar}^{\text{Mes}}$, subsequent chloride migration from Ge to Si and elimination of the isocyanide. Compound **A-5** could be isolated and fully characterized experimentally.

Compared to this, the theoretical investigation of the PES of **A-5** afforded the NHC-stabilized germasilynylidene $(Z)-(\text{SIDipp})\text{SiGe}(\text{Cl})\text{Ar}^{\text{Mes}}$ (**A-5V**), which could also be obtained as minimum structure, although lying at a higher energy compared to **A-5** (+41 $\text{kJ}\cdot\text{mol}^{-1}$). Interestingly, the opposite relative stability was found for the NHC-stabilized disilavinylidene $(Z)-(\text{NHC})\text{SiSi}(\text{Br})\text{R}$ ($\text{NHC} = \text{C}[\text{N}(\text{C}_6\text{H}_3-2,6-\text{Me}_2)\text{CH}_2]_2$, $\text{R} = \text{C}_6\text{H}_3-2,6-[\text{CH}(\text{SiH}_3)_2]_2$), that was calculated to be



Scheme 3.5: Synthesis of the NHC-stabilized germasilyne (SIDipp)Si(Cl)GeAr^{Mes} (A-5).

more stable by 33 kJ·mol⁻¹ than its NHC-stabilized bromodisilyne isomer (Z)-(NHC)Si(Br)SiR at the similar B97-D3/TZVP level of theory.^[149]

Selected structural parameters of A-5 and A-5V are given in Table 3.7 together with those of the experimentally obtained sc-XRD structure A-5_{exp}. Both the short Si–C_{NHC} bond of 187.0 pm, which is very similar to that of A-1Ar^{Mes} (187.5 pm), and the co-planarity of the central NHC imidazoline ring and the [C_{NHC}SiClGeC_R] molecular core, as evidenced by an interplanar twist angle τ of 4.9°, indicate again a significant amount of $\pi(\text{Si} \rightarrow \text{C}_{\text{NHC}})$ back donation. This is confirmed by the 3c-2e⁻-interaction found in the HOMO of A-5 (Figure 3.9). Accordingly, the silicon atom adopts a trigonal-planar orientation with a sum of angles $\Sigma\angle(\text{Si})$ of 359.8°. The analysis of the frontier orbitals of A-5 further reveals the presence of an electron lone pair at Ge (HOMO–1), as expected from the narrow Si–Ge–C_R angle of 97.6°.

The NRT analysis of compound A-5 yields a slightly delocalized structure, where the formal p-type electron pair at the silicon atom is delocalized to the germanium atom (A-5-a) and to the SIDipp

Table 3.7: Comparison of selected calculated and experimental sc-XRD structural parameters of the NHC-stabilized germasilynes A-5 and A-5_{exp}, and the NHC-stabilized germasilylenylidene A-5V. Bond lengths are given in pm, angles in deg. τ is defined as interplanar twist angle between the mean central NHC ring plane and that composed of the C_{NHC}, Si, Ge, Cl and C_R atoms. For A-5_{exp} the structural parameters of two independent molecules in the unit cell are given.

	Si–C _{NHC}	Si–Ge	Ge–Cl	Ge–C _R	C _{NHC} –Si–Cl
A-5	187.0	231.1	212.0	204.6	108.5
A-5 _{exp}	187.7(2)	228.4(1)	210.3(1)	202.4(2)	107.1(1)
A-5V	191.0	227.5	224.2	200.3	–
	Si–Ge–Cl	C _{NHC} –Si–Ge	Si–Ge–C _R	$\Sigma\angle(\text{Si})$	τ
A-5	–	121.2	97.6	359.8	4.9
A-5 _{exp}	–	122.0(1)	100.9(1)	359.9(2)	2.19(5)
A-5V	144.5	110.5	113.5	–	4.6

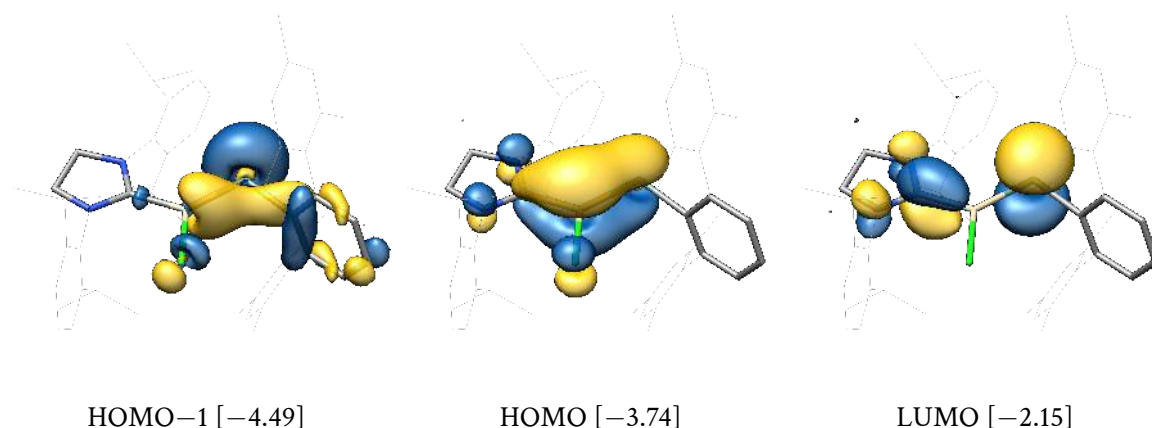


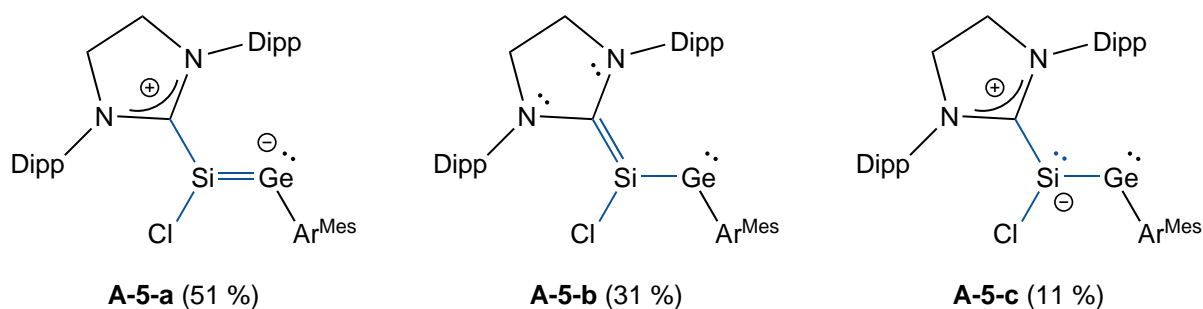
Figure 3.9: Selected canonical MOs of A-5 and their energy eigenvalues in eV.

ligand (A-5-b) by 51 and 31 %, respectively (see Scheme 3.6). Similar to A-1Ar^{Mes}, there is also a contribution where the lone pair is located at the silicon atom (A-5-c, 11 %).

As the resonance structure A-5-a is a combination of two equivalent resonance structures with 9.41 non-Lewis electrons (nLe⁻) according to NBO, where each NHC nitrogen atom delocalizes its lone pair, the best single natural Lewis structure is represented by A-5-b with 9.38 nLe⁻. An NBO analysis on the latter reveals highly localized $\sigma(\text{Si}-\text{C}_{\text{NHC}})$, $\sigma(\text{Si}-\text{Ge})$ and $\sigma(\text{Si}-\text{Cl})$ NBOs with occupations above 1.90 e⁻ as well as a lone pair orbital at Ge with high occupation (1.89 e⁻) and s-character (sp^{0.2}). As expected from the structure, MO and NRT analyses, the found $\pi(\text{Si}-\text{C}_{\text{NHC}})$ has a low occupation of only 1.59 e⁻ and is slightly polarized towards the silicon atom (57 %). The total NRT bond orders show a considerable multiple bond character for the Si-C_{NHC} (1.3) and Si-Ge bonds (1.5) but none for the Si-Cl bond (1.0).

Table 3.8: Selected results of the NBO and local NRT (with N_{NHC}, C_{NHC}, Si, Cl, Ge and C atoms of the central phenyl ring of Ar^{Mes}) analyses of the SIDipp-stabilized germasilyne A-5.

NBO A-B	Occ./e ⁻	NHO (A,B) pol./% (hyb.)	WBI	NRT-BO tot/cov/ion	NPA / e	
$\sigma(\text{Si}-\text{C}_{\text{NHC}})$	1.95	25 (sp ^{2.8}), 75 (sp ^{1.5})	1.0	1.3/0.7/0.6	Si	+0.53
$\pi(\text{Si}-\text{C}_{\text{NHC}})$	1.59	57 (p), 43 (p)			Ge	+0.29
$\sigma(\text{Si}-\text{Ge})$	1.93	63 (sp ^{0.8}), 37 (sp ^{9.8})	1.4	1.5/1.0/0.5	Cl	-0.40
$\sigma(\text{Si}-\text{Cl})$	1.98	24 (sp ^{4.3}), 76 (sp ^{3.0})	0.8	1.0/0.5/0.5	[NHC]	+0.06
LP(Ge)	1.89	(sp ^{0.2})			[ArMes]	-0.48



Scheme 3.6: Natural Lewis structures of **A-5** and their NRT resonance weight. The resonance structures from a local NRT analysis (with the N_{NHC} , C_{NHC} , Cl, Si, Ge and C atoms of the central phenyl ring of Ar^{Mes}) were collected according to their bond motif (marked in blue).

Finally, the Si– C_{NHC} and Si–Ge bond dissociations were calculated (Table 3.9). Regarding the Si– C_{SIDipp} dissociation, both the *BCE* and *BDE* are found to be similar with 392.5 and 272.1 $\text{kJ}\cdot\text{mol}^{-1}$ to those of **A-1Ar^{Mes}** (334.3 and 252.6 $\text{kJ}\cdot\text{mol}^{-1}$, see Table 3.6), as expected from the similar bond situation regarding the NHC–Si–Ge unit. This is also the case for the calculated energies of the Si–Ge bond dissociation with 269.4 and 233.5 $\text{kJ}\cdot\text{mol}^{-1}$ (273.3 and 216.9 $\text{kJ}\cdot\text{mol}^{-1}$ for **A-1Ar^{Mes}**). Notably, the Si–Ge bond dissociation of **A-5** proceeds via the two neutral doublet-state fragments SIDippSiCl and GeAr^{Mes} , as the singlet splitting leads to charged fragments, which are highly unfavoured in the gas phase (singlet *BCE*: 750.1 $\text{kJ}\cdot\text{mol}^{-1}$).

Table 3.9: Level of theory I-calculated bond cleavage (*BCE*) and bond dissociation (*BDE*) energies for the SIDipp and Si–Ge cleavages of **A-5** in $\text{kJ}\cdot\text{mol}^{-1}$, entropies in $\text{J}\cdot\text{K}^{-1}\cdot\text{mol}^{-1}$. s = singlet, d = doublet multiplicity.

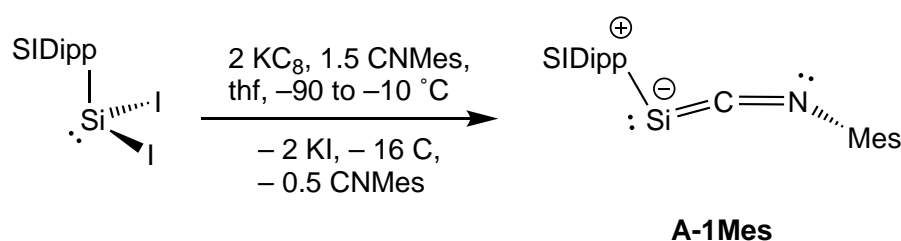
	ΔE	mult.	ΔE	ΔU	ΔH	ΔS	ΔG
SIDipp cleavage	<i>BCE</i>	<i>BDE</i> (parent \rightarrow $\text{SIDipp} + \text{ClSiGeAr}^{\text{Mes}}$)					
A-5	392.5 (s)	(s \rightarrow s, s)	272.1	260.2	262.7	234.6	192.8
Si–Ge cleavage	<i>BCEs</i>	<i>BDE</i> (parent \rightarrow $(\text{SIDipp})\text{SiBr} + \text{GeAr}^{\text{Mes}}$)					
A-5	269.4	(s \rightarrow d, d)	233.5	223.0	225.5	253.6	149.8

4. Further Studies on Iminosilylenylidenes of the Type (carbene)SiCNR

4.1. Introduction

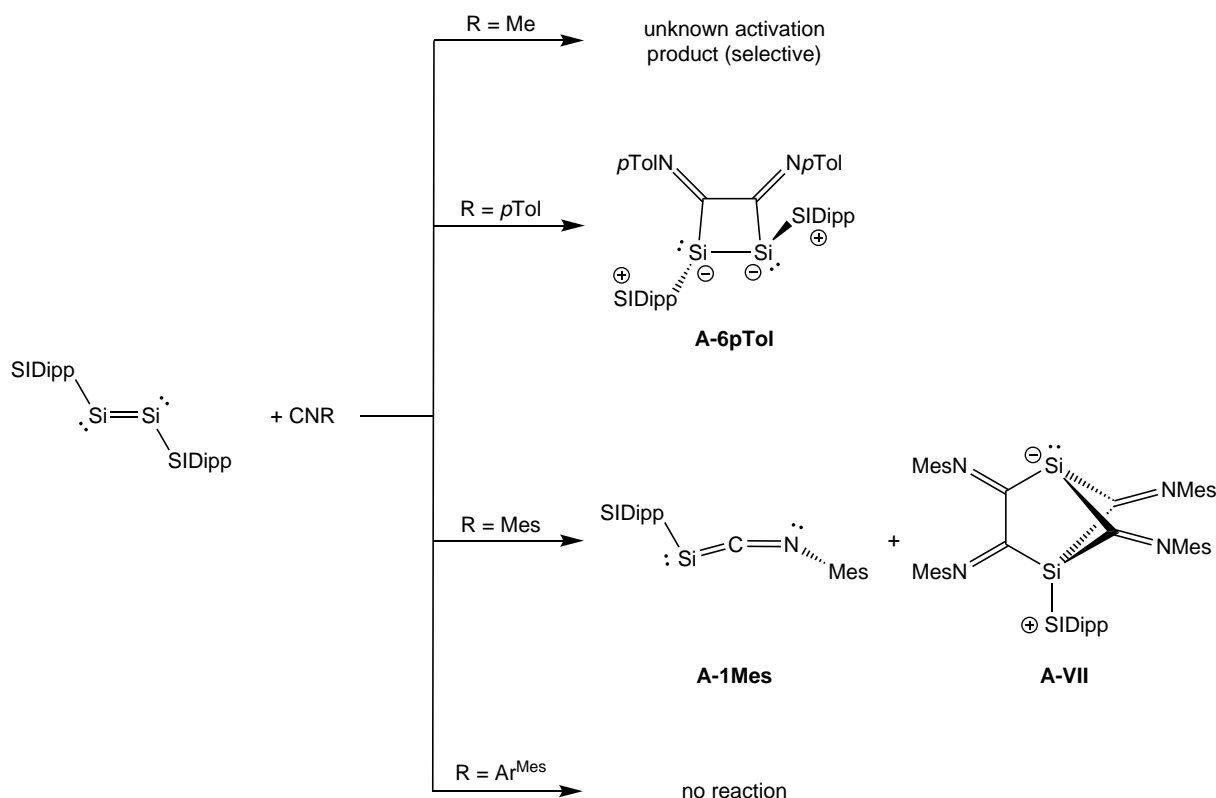
In the preceding chapter, the iminosilylenylidene (SIDipp)Si(CNAr^{Mes}) (**A-1Ar^{Mes}**) was introduced as a potent (NHC)Si⁰ transfer reagent, which bears a great synthetic potential as the attached isocyanide CNAr^{Mes} can be displaced. One successful example for this is the already discussed reaction to the first NHC-stabilized germasilyne **A-5**.

Kinetic protection of the molecular core plays a major role for the reactivity of a compound, and the iminosilylenylidene **A-1Ar^{Mes}** features both a large N-heterocyclic carbene with Dipp groups as well as an isocyanide ligand with a sterically demanding Ar^{Mes} substituent. In this regard, S. Kumar from our group put a tremendous effort into not only exploring the reactivity of compound **A-1Ar^{Mes}**, but also into synthesizing more reactive derivatives.^[150] For example, he was successful in isolating the mesityl-substituted iminosilylenylidene (SIDipp)Si(CNMe₃) (**A-1Mes**) via a similar co-reduction pathway as for **A-1Ar^{Mes}**:



Scheme 4.1: Synthesis of the mesityl-substituted iminosilylenylidene derivative **A-1Mes** via a co-reduction pathway.^[150]

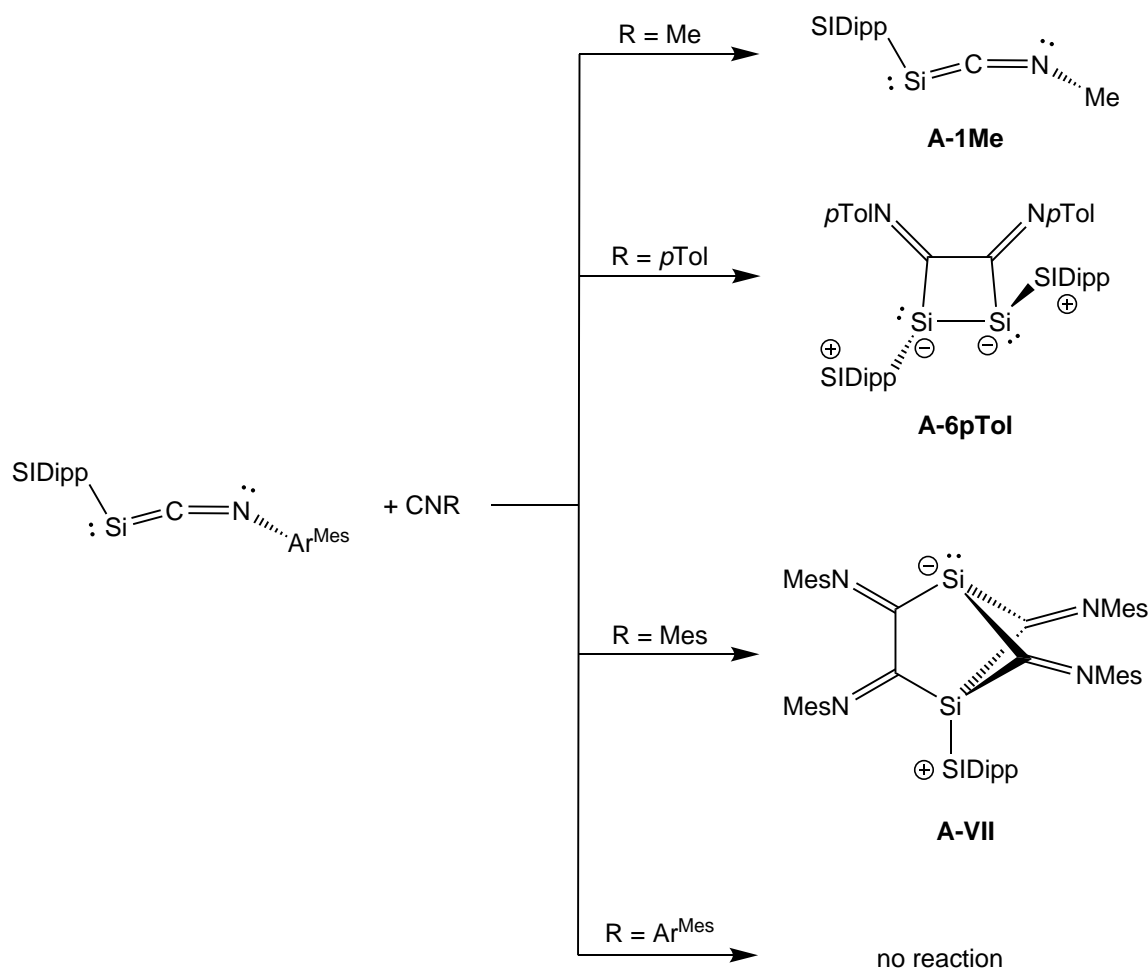
The iminosilylenylidene **A-1Mes** could also be prepared directly from the NHC-stabilized disilicon(0) compound (SIDippSi)₂^[151] in a reaction with mesityl isocyanide. This reaction, depicted in Scheme 4.2, also affords a SIDipp-supported disila-bicyclo[2.1.1]hexanylidene (**A-VII**) with imino groups on each of the bridgehead carbon atoms. Notably, such a reaction does not take place when the CNAr^{Mes} isocyanide is used.



Scheme 4.2: Experimental reaction outcomes of $(\text{SIDippSi})_2$ with various isocyanides CNR.

Another alternative route to the iminosilylidene **A-1Mes** originates from the discussed ability of **A-1Ar^{Mes}** to transfer the (SIDipp)Si unit: When **A-1Ar^{Mes}** is reacted with free mesityl isocyanide, the intermediate formation of **A-1Mes** can be observed via substitution of the isocyanide ligands, which then reacts further to the bicyclo[2.1.1] compound **A-VII** (Scheme 4.3). This reaction was also tried with *para*-tolyl isocyanide CN*p*Tol, which gives neither the monomeric iminosilylidene **A-1pTol** nor the corresponding bicyclo[2.1.1] compound, but instead the *head-to-head* (*hth*) dimerization product $[(\text{SIDippSi}(\text{CN}_{p\text{Tol}}))]_2$ (**A-6pTol**). Presumably, the reaction proceeds via the *p*Tol-substituted iminosilylidene **A-1pTol** as an intermediate before dimerization, because in the reaction between **A-1Ar^{Mes}** and 3,4-dimethylphenylisocyanide, the corresponding monomeric iminosilylidene could be observed but not isolated before the reaction ends in the *hth*-dimer. The *hth*-dimer **A-6pTol** is also obtained selectively in the reaction of $(\text{SIDippSi})_2$ with the isocyanide CN*p*Tol.

Most surprising, however, is the substitution reaction of **A-1Ar^{Mes}** with the small methylisocyanide CNMe, that selectively yields the monomeric methyl-substituted iminosilylidene $(\text{SIDippSi}(\text{CNMe}))$ (**A-1Me**, Scheme 4.3), and neither the formation of the bicyclo[2.2.1] compound nor the 1,2-disiletane-1,2-ylidene-3,4-imine dimerization product $[(\text{SIDippSi}(\text{CNMe}))]_2$ (**A-6Me**) is observed.



Scheme 4.3: Experimental reaction outcomes of the substitution reaction of $\text{A-1Ar}^{\text{Mes}}$ with different isocyanides CNR .

The following chapter provides a comparative theoretical study on differently substituted iminosilylenes **A-1R**, calculated thermochemical quantities for their formation starting from $(\text{SIDippSi})_2$ or substitution from $\text{A-1Ar}^{\text{Mes}}$ and first insight into possible mechanistic pathways of their formation.

4.2. Analysis of Various Iminosilylenes A-1R

The first iminosilylene $\text{A-1Ar}^{\text{Mes}}$ features the sterically demanding Ar^{Mes} substituent at the isocyanide nitrogen atom. As more iminosilylenes could be isolated or observed as intermediates, the question arises which impact the isocyanide substituent has on the electronic structure of the molecular core.

Therefore, the gas phase structures of the iminosilylenes $(\text{SIDipp})\text{SiCNR}$ ($\text{R} = \text{Ar}^{\text{Mes}}$ (**A-1Ar**^{Mes}), Mes (**A-1Mes**), Me (**A-1Me**)) were obtained by structure optimizations with the ORCA 5.0.3 program version starting from the experimentally available sc-XRD results (Figure 4.1). In favor of

consistency with the other compounds, the structure of $A-1Ar^{Mes}$ was reoptimized on the newer ORCA version and shows only negligible differences to the structure obtained with the ORCA version 4.1.1 that was already discussed in chapter A.3. Furthermore, the experimentally elusive compound *p*Tolyl-substituted iminosilylenide (SIDipp)SiCN*p*Tol $A-1pTol$ was also calculated.

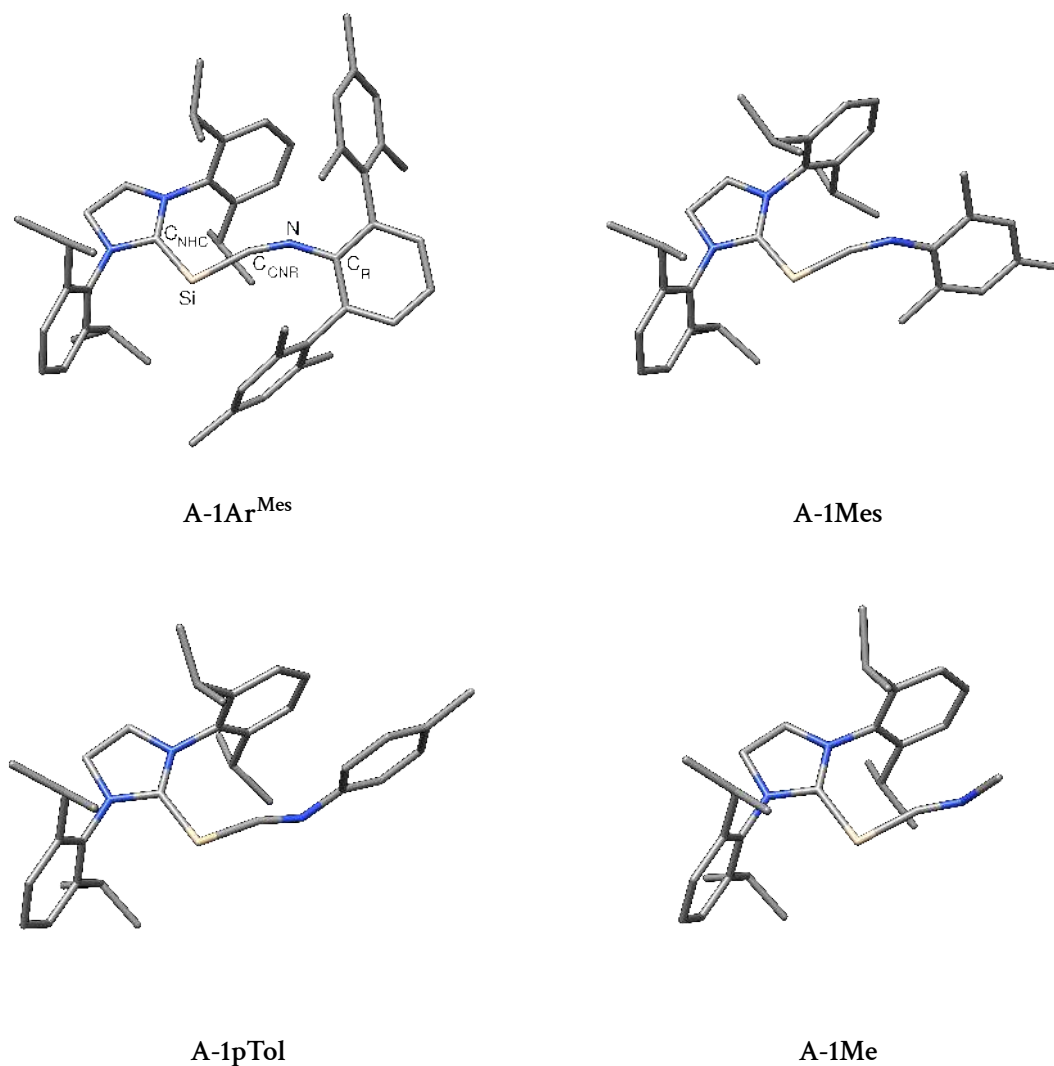


Figure 4.1: Optimized gas-phase structures of iminosilylenes $A-1R$ with various isocyanide substituents R . The atom labelling of $A-1Ar^{Mes}$ is also used for the other compounds.

Selected bonding parameters of all compounds are summarized in Table 4.1. Generally, the calculated gas phase structures are in good agreement with the experimental solid state structures, despite the flexible $Si-C_{CNR}-N-C_R$ core. One notable deviation concerns compound $A-1Mes$, where the $N-C_R$ bond length is found considerably longer in the solid state structure (146.0(7) pm) than in the gas phase (138.6 pm). However, a deeper analysis of the sc-XRD solution reveals the presence of a crystallographic split layer with 48 % occupation, where the $N-C_R$ bond length amounts to 141.4(9) pm, which is closer to the calculated structure and underlines the flexibility of these molecules.

Table 4.1: Selected bond parameters of the calculated and experimental iminosilylenes A-1R. Bond lengths are given in pm and angles in degrees.

	Si–C _{NHC}	Si–C _{CNR}	C _{CNR} –N	N–C _R
A-1Ar ^{Mes}	187.2	180.5	120.9	136.9
A-1Ar ^{Mes} _{exp}	189.4(2)	178.4(2)	122.43(2)	141.1(2)
A-1Mes	188.0	179.7	121.5	138.6
A-1Mes _{exp}	187.6(3)	179.1(4)	119.9(4)	146.0(7)
A-1pTol	190.3	178.1	122.5	140.1
A-1Me	189.8	179.6	121.5	145.0
A-1Me _{exp}	191.4(3)	176.2(3)	123.3(4)	147.5(4)
	192.7(3)	176.0(4)	122.2(5)	146.1(5)
	C _{NHC} –Si–C _{CNR}	Si–C _{CNR} –N	C _{CNR} –N–C _R	C _{NHC} –Si–C _{CNR} –N
A-1Ar ^{Mes}	101.2	157.2	151.0	167.0
A-1Ar ^{Mes} _{exp}	100.4(1)	158.8(1)	133.0(1)	173.8(2)
A-1Mes	96.9	161.4	143.3	170.6
A-1Mes _{exp}	98.0(2)	163.8(3)	142.0(4)	–174.2(11)
A-1pTol	96.0	164.1	131.7	–156.3
A-1Me	97.1	163.0	131.8	–169.5
A-1Me _{exp}	98.2(2)	164.0(2)	122.8(3)	–167.4(9)
	97.3(2)	164.6(5)	126.3(4)	–164.9(18)

The isocyanide substituent has only a minor impact on the bonding parameters of the iminosilylene core: The Si–C_{NHC} bond lengths range from 187.2 to 190.3 pm, with the longest bond found for A-1pTol. In contrast, compound A-1pTol has the shortest Si–C_{CNR} bond (178.1 pm), which indicates a slight decrease of the $\pi(\text{Si}-\text{SiDipp})$ back-bonding. Furthermore, the elusive compound also features the longest C_{CNR}–N bond (122.5 pm) compared to A-1Me (121.5 pm), A-1Mes (121.5 pm) and A-1Ar^{Mes} (120.9 pm), which is understandable as the $\pi(\text{Si}-\text{C}_{\text{CNR}})$ back-bonding should be slightly enhanced. The N–C_R bond lengths increase in the order A-1Ar^{Mes} (136.9 pm) < A-1Mes (138.6 pm) < A-1pTol (140.1 pm) < A-1Me (145.0 pm), where the longer bond for A-1Me can be easily understood by the hybridization change at the carbon atom from approximately sp² to sp³. Following Bent's rule,^[152] this translates to a bond elongation as observed. Compared to A-1Ar^{Mes}, the C_{NHC}–Si–C_{CNR} angle is lowered by ca. 5° in the other iminosilylenes, which is caused presumably due to sterics, similar to the decrease of the C_{CNR}–N–C_R angle by 8° for A-1Mes and 20° for A-1pTol and A-1Me compared to A-1Ar^{Mes} (151.0°).

Given these small but observable trends regarding the isocyanide substitution pattern, it is expected that the molecular orbitals look very similar for all compounds A-1R. Indeed, the selected canonical MOs of Figure 4.2 for the compounds A-1Mes, A-1pTol and A-1Me look almost identical to those of A-1Ar^{Mes} (see also Figure 3.7 in chapter A3), and show the lone pair at the silicon atom (HOMO–1), the 3-center-2-electron- $\pi(\text{C}_{\text{NHC}}-\text{Si}-\text{C}_{\text{CNR}})$ bond (HOMO) and its non-bonding combination in the LUMO.

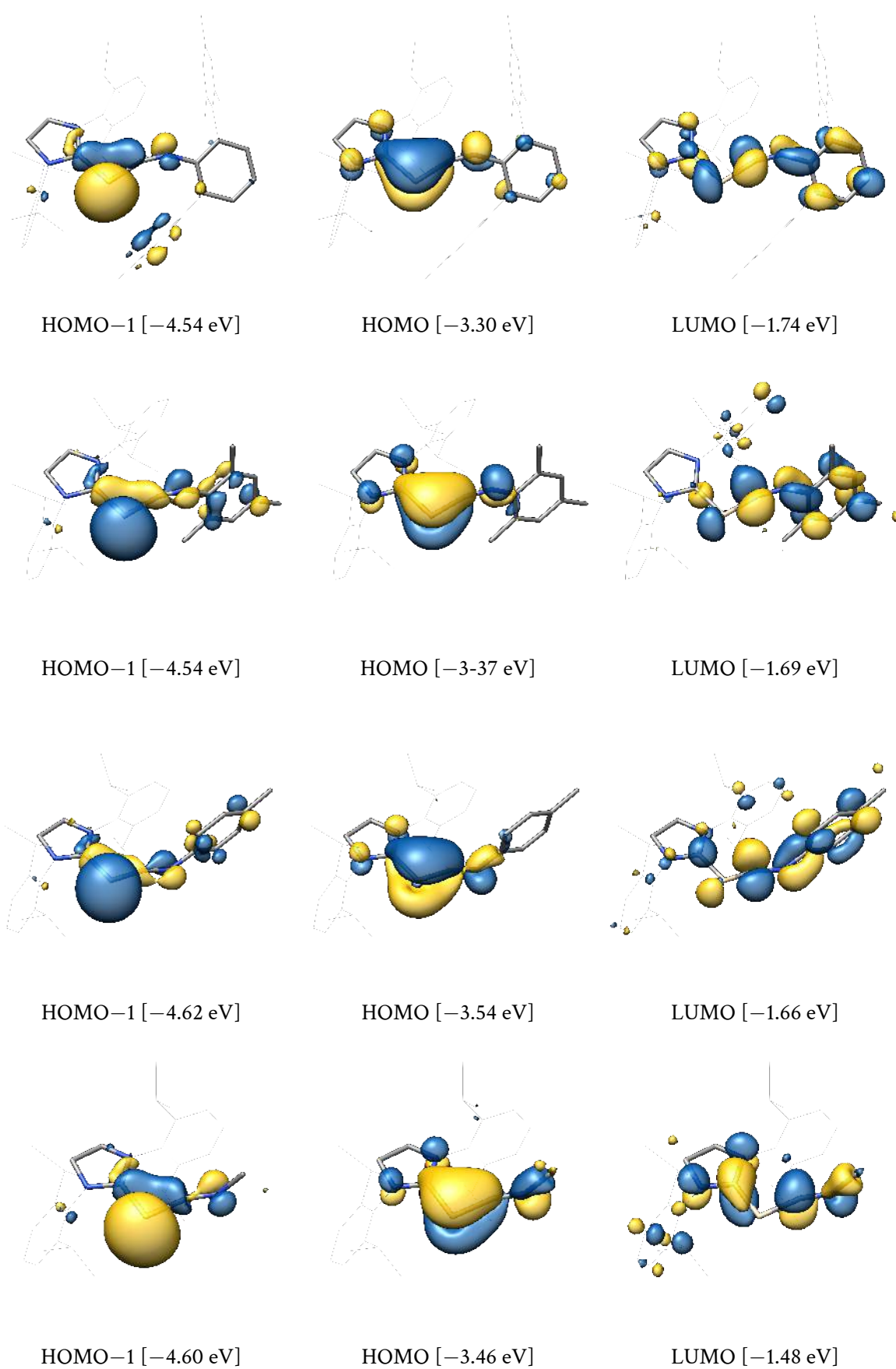


Figure 4.2: Selected canonical molecular orbitals of iminosilylenes A-1Ar^{Mes} (top), A-1Mes (second row), A-1pTol (third row) and A-1Me (bottom) and their energy eigenvalues.

4.3. Dimerization of Iminosilylenes

The reactions of schemes 4.2 and 4.3 show that the presumed iminosilylidene intermediate A-1pTol directly dimerizes to the *hth* dimer $[(\text{SIDipp})\text{Si}(\text{CNR})]_2$ with $\text{R} = p\text{Tol}$ (A-6pTol). The gas phase structure of A-6pTol was obtained starting from the available sc-XRD structure, and also the compounds with $\text{R} = \text{Mes}$ (A-6Mes) and Me (A-6Me) could be calculated (Figure 4.3). The structure optimization to afford compound A-6Ar^{Mes} was not successful despite several attempts and only resulted in distorted higher-energy conformers, presumably due to the huge sterical effects in this compound.

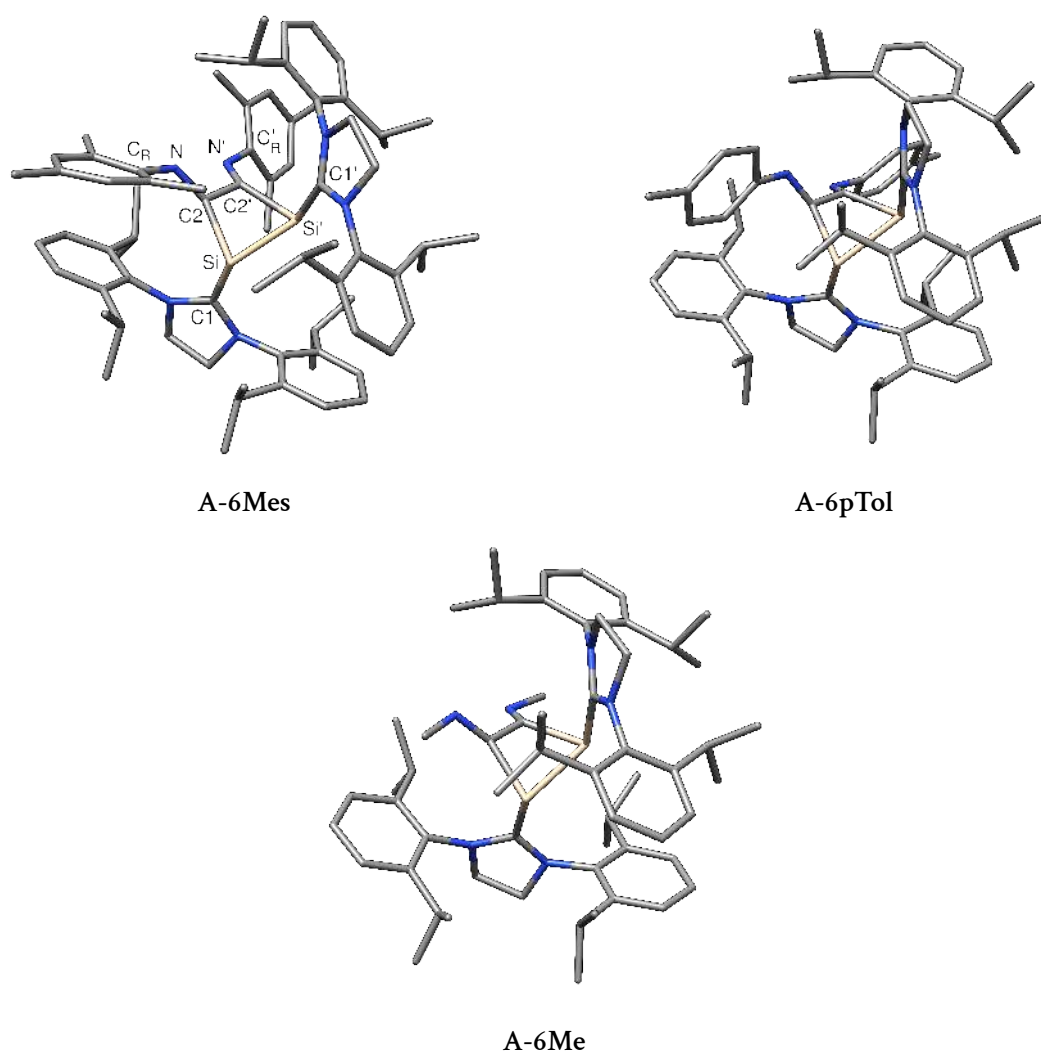


Figure 4.3: Optimized gas phase structures of the *hth*-dimerization products A-6R of the iminosilylenes A-1R.

The structural parameters of A-6pTol are in good agreement with those of the solid state structure and also similar to the other dimer structures, which suggests a low influence of the isocyanide substituents.

The folded four-membered ring structures with C2–Si–Si'–C2' torsion angles between -15 and -22° feature two three-coordinated silicon atom. They are stabilized by the SIDipp ligands in a highly trigonal-pyramidal fashion ($\Sigma\angle(\text{Si}) = 266.7$ to 278.1°) due to the expected electron lone pairs at the Si atoms. The silicon-carbene Si–C1 bond lengths in the range of 191.1 to 193.1 pm are slightly longer than in the iminosilylenylidene monomers, however, the Si–C2 bonds are considerably elongated to 199.2 to 200.9 pm and indicate no multiple bond character. Similarly, the Si–Si' bond lengths of 244.6 to 249.4 pm are even longer than in the silylsilylene A-3⁺ (237.0 pm) and in α -silicon (235.2 pm).^[139] The other bond lengths, such as C2–N (127.9 to 128.8 pm), N–C_R (138.7 to 144.7 pm) and C2–C2' (148.5 to 149.3 pm), are ordinary and fulfil the expectations of their drawn Lewis formulae (Scheme 4.2).

Compound A-6pTol_{exp} is the first isolated representative for this class of compounds and thus a reasonable comparison to the literature is difficult. One notable molecule that is related to A-6, *hth*-[(*t*Bu)₂Si(CNDipp)]₂, was reported by M. Weidenbruch *et al.* in the year 1991 and also features a SiSiCC four-membered ring with two imine groups, however, also two alkyl substituents on the silicon atoms instead of an electron lone pair and an NHC substituent.^[153] Nevertheless, its mean sc-XRD structural parameters agree well with those calculated for the A-6R compounds (e.g. Si–Si': 241.6(3) pm; Si–C2: 196.3(6) pm; C2–C2': 152.7(8) pm; C2–N: 127.9(7) pm).

Table 4.2: Selected bond parameters of the calculated and experimental iminosilylenylidene dimers A-6R. Mean bond lengths and angles are given in pm and degrees, respectively.

	Si–C1	Si–C2	Si–Si'	C2–N	N–C _R
A-6Mes	193.0	200.9	244.6	128.1	138.7
A-6pTol	193.1	199.2	249.4	128.8	139.3
A-6pTol _{exp}	193.0(3)	196.8(3)	245.6(2)	128.9(4)	141.8(4)
A-6Me	191.3	200.0	245.8	127.9	144.7
	Si···C2'	C2–C2'	C2–Si–Si'	C2–N–C _R	$\Sigma\angle(\text{Si})$
A-6Mes	273.3	149.3	75.0	129.7	278.1
A-6pTol	268.2	148.5	72.5	124.4	266.7
A-6pTol _{exp}	266.2(3)	149.3(4)	73.0(1)	121.9(2)	267.9(4)
A-6Me	271.5	149.1	74.2	119.1	269.3

The calculated dimerization energies ($2 \text{ A-1R} \rightarrow \text{A-6R}$), provided in Table 4.3, reveal that this reaction is favoured not only energetically ($\Delta E = -208.7$ to $-148.5 \text{ kJ}\cdot\text{mol}^{-1}$), but also in terms of the free Gibbs enthalpy ($\Delta G = -106.1$ to $-30.1 \text{ kJ}\cdot\text{mol}^{-1}$), although the large exotropic contributions ΔS of -359.7 to $-308.2 \text{ J}\cdot\text{K}^{-1}\cdot\text{mol}^{-1}$ dampen the exergonicity of the dimerizations considerably. The lowest ΔE and ΔG values are obtained for R = *p*Tol, whereas it is assumed that the increased steric hindrance of the mesityl substituents lead to the significantly higher thermochemical values for A-6Mes.

As all ΔG values are negative, a dimerization is expected to occur for all compounds. This is the case for A-6pTol, but not for A-6Mes and A-6Me. Especially the dimerization of the latter is

favoured similarly to A-6pTol, but does not happen according to experimental studies. It is therefore assumed that the dimerization of the iminosilylenylidene A-6Me is prohibited by a high kinetic barrier. A thorough investigation of this issue was not successful so far and is subject to further work on this topic.

Table 4.3: Calculated thermochemical quantities for the iminosilylenylidene dimerization reactions to the 1,2-disilylenylidene bisylidenes A-6R. Energies and enthalpies are given in $\text{kJ}\cdot\text{mol}^{-1}$ and entropies in $\text{J}\cdot\text{K}^{-1}\cdot\text{mol}^{-1}$.

	ΔE	ΔU	ΔH	ΔS	ΔG
A-6Mes	-148.5	-134.9	-137.3	-359.7	-30.1
A-6pTol	-208.7	-195.5	-198.0	-308.2	-106.1
A-6Me	-186.6	-174.6	-177.1	-320.9	-81.4

4.4. Iminosilylenylidene Formation from (SIDippSi)₂ and Isocyanides CNR

Experimental results indicate that the formation of the iminosilylenylidenes is also achievable starting from (SIDippSi)₂ and isocyanides CNR (without $\text{R} = \text{Ar}^{\text{Mes}}$, see Scheme 4.2). However, although being selective, the presumably formed iminosilylenylidene intermediates A-1R react further by activation ($\text{R} = \text{Me}$), dimerization ($\text{R} = p\text{Tol}$, 3,4-dimethylphenyl) or bicyclization ($\text{R} = \text{Mes}$).

Table 4.4: Calculated thermochemical quantities for the formation of the iminosilylenylidenes A-1R from (SIDippSi)₂ and isocyanides CNR (c.f. Scheme 4.2). Energies and enthalpies are given in $\text{kJ}\cdot\text{mol}^{-1}$ and entropies in $\text{J}\cdot\text{K}^{-1}\cdot\text{mol}^{-1}$. For the ΔE^{nodisp} values, the contribution of the D3(BJ)-ATM dispersion correction scheme for the final single point energy evaluation was removed.

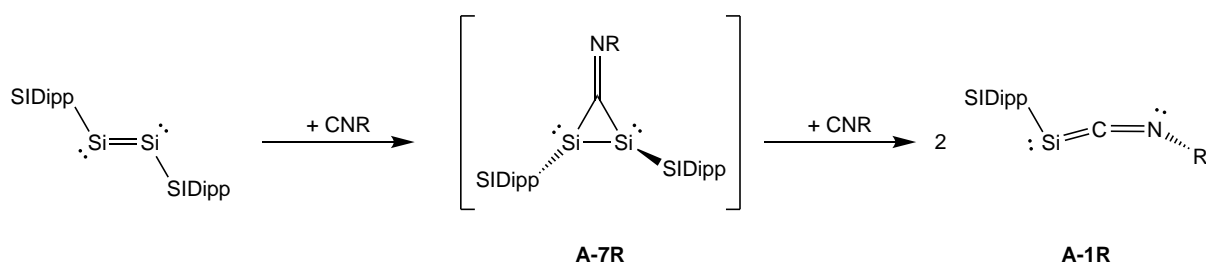
	ΔE	ΔE^{nodisp}	ΔU	ΔH	ΔS	ΔG
$\text{R} = \text{Ar}^{\text{Mes}}$	-150.9	-14.9	-142.3	-144.8	-275.5	-62.7
$\text{R} = \text{Mes}$	-80.3	-108.9	-73.5	-76.0	-168.6	-25.7
$\text{R} = p\text{Tol}$	-142.3	-164.7	-122.8	-125.3	-121.8	-89.0
$\text{R} = \text{Me}$	-66.8	-140.0	-60.1	-62.6	-96.9	-33.7

The calculated thermochemical quantities for the iminosilylenylidene formation reveal that all reactions are energetically favoured and exergonic (Table 4.4, the calculated structures of the isocyanides and (SIDippSi)₂ are provided in the appendix). The reaction is energetically most preferred for $\text{R} = \text{Ar}^{\text{Mes}}$ ($-150.9 \text{ kJ}\cdot\text{mol}^{-1}$), directly followed by $\text{R} = p\text{Tol}$ ($-142.3 \text{ kJ}\cdot\text{mol}^{-1}$), but considerably less for the methyl and mesityl isocyanides with ΔE values of -66.8 and $-80.3 \text{ kJ}\cdot\text{mol}^{-1}$, respectively. However, two questions arise from these values: Why is the reaction energy similar for $\text{R} = p\text{Tol}$ and Ar^{Mes} , but not for the mesityl substituent? Also, why is the value for $\text{R} = \text{Me}$

similar to that of mesityl, but not to $R = p\text{Tol}$? To answer these questions, the energies were recalculated without the D3(BJ)-ATM correction for London dispersion forces, yielding the electronic energies ΔE^{nodisp} (Table 4.4). Whereas the dispersion-uncorrected relative energies for $R = p\text{Tol}$ and Mes decrease only slightly to -164.7 and $-108.9 \text{ kJ}\cdot\text{mol}^{-1}$, the reaction of $(\text{SIDippSi})_2$ with CNMe becomes considerably more favoured ($-140.0 \text{ kJ}\cdot\text{mol}^{-1}$), but drastically less favoured for the Ar^{Mes} substituent ($-14.9 \text{ kJ}\cdot\text{mol}^{-1}$). A more detailed evaluation of the reactants' energies reveals that the decisive factor is the dispersion stabilization of the iminosilylenide versus that of the reagent $(\text{SIDippSi})_2$. The latter is comparably large due to the four Dipp groups in the molecule, and for $R = \text{Me}$ it outweighs that of **A-1Me**, favouring the reactants. This effect is only weak for the $p\text{Tolyl}$ and mesityl substituents, leading to similar relative energies with and without dispersion correction. However, the non-covalent contacts between the Dipp groups and the Ar^{Mes} substituent in **A-1Ar^{Mes}** decrease the energy of the products considerably and favour the formation of the iminosilylenide. Additionally, when the dispersion-uncorrected relative energies are considered, it becomes evident that the methyl and $p\text{Tolyl}$ systems are similarly favoured as originally expected, and that the increase of the sterical hindrance of the substituents over Mes to Ar^{Mes} unfavours the iminosilylenide formation.

The calculated relative free Gibbs energies ΔG are generally higher than the electronic energies, as expected from the exothermic reactions, but still negative for all reactions with a range of -25.7 to $-89.0 \text{ kJ}\cdot\text{mol}^{-1}$.

Experimental NMR-spectroscopic studies by S. Kumar suggest that these reactions proceed via a 3-membered ring intermediate, $[(\text{SIDippSi})_2(\text{CNR})]$ (**A-7R**),¹ where the incoming isocyanide occupies a bridging position between both silicon atoms (Scheme 4.4).



Scheme 4.4: Formation of the presumed disilirane-1,2-ylidene-3-imine intermediate **A-7R** and further reaction to the iminosilylenes **A-1R**.

The disilirane-1,2-ylidene-3-imine compounds could be successfully calculated for the substituents $R = \text{Ar}^{\text{Mes}}$ (**A-7Ar^{Mes}**, Figure 4.4), Mes (**A-7Mes**), $p\text{Tol}$ (**A-7pTol**) and Me (**A-7Me**) and feature a SiSiC-three-membered ring with strongly pyramidalized silicon atoms ($\sum\angle(\text{Si}) = 242.2$ to 280.2°) and trigonal-planar carbon atoms ($\sum\angle(\text{C1}) = 356.4$ to 360.0°). The exception is here the compound

¹To be precise, this observation of the three-membered ring intermediate was made for the analogous CAAC^{Me} compounds $(\text{CAAC}^{\text{Me}}\text{Si})_2$ and $(\text{CAAC}^{\text{Me}}\text{Si})\text{CNR}$. Their theoretical analyses revealed a very similar electronic and spatial structure (not included in this thesis), which is why the same reaction pathway is assumed.

A-7pTol, where the carbon atom appears to be significantly pyramidalized ($\Sigma\angle(C1) = 335.5^\circ$). The Si–C_{NHC} bond lengths of 192.2 to 195.2 pm are slightly longer than in the precursor molecule (SIDippSi)₂ (192.1 pm), whereas the Si–Si bonds are clearly elongated (236.7 to 245.5 pm) compared to (SIDippSi)₂ (224.6 pm), indicating the loss of the multiple bond character between the silicon atoms. However, the antiperiplanar orientation of the carbenes as found in (SIDippSi)₂ ($C_{NHC}-Si-Si'-C_{NHC}' = 180.0^\circ$) is retained in the compounds **A-7R**, except for **A-7Ar^{Mes}** where steric hindrance of the large substituents causes the angle to change (-155.6°). Notably, in **A-7Ar^{Mes}** and **A-7Mes** the SiSiC rings are not isosceles as indicated by their differing Si–C2 bonds (**A-7Ar^{Mes}**: 193.6 and 199.7 pm; **A-7Mes**: 187.6 and 203.6 pm). This asymmetry is presumably caused by the large Ar^{Mes} and mesityl substituents, as the rings of **A-7pTol** (193.5 and 192.8 pm) and **A-7Me** (195.9 and 193.5 pm) are more isosceles.

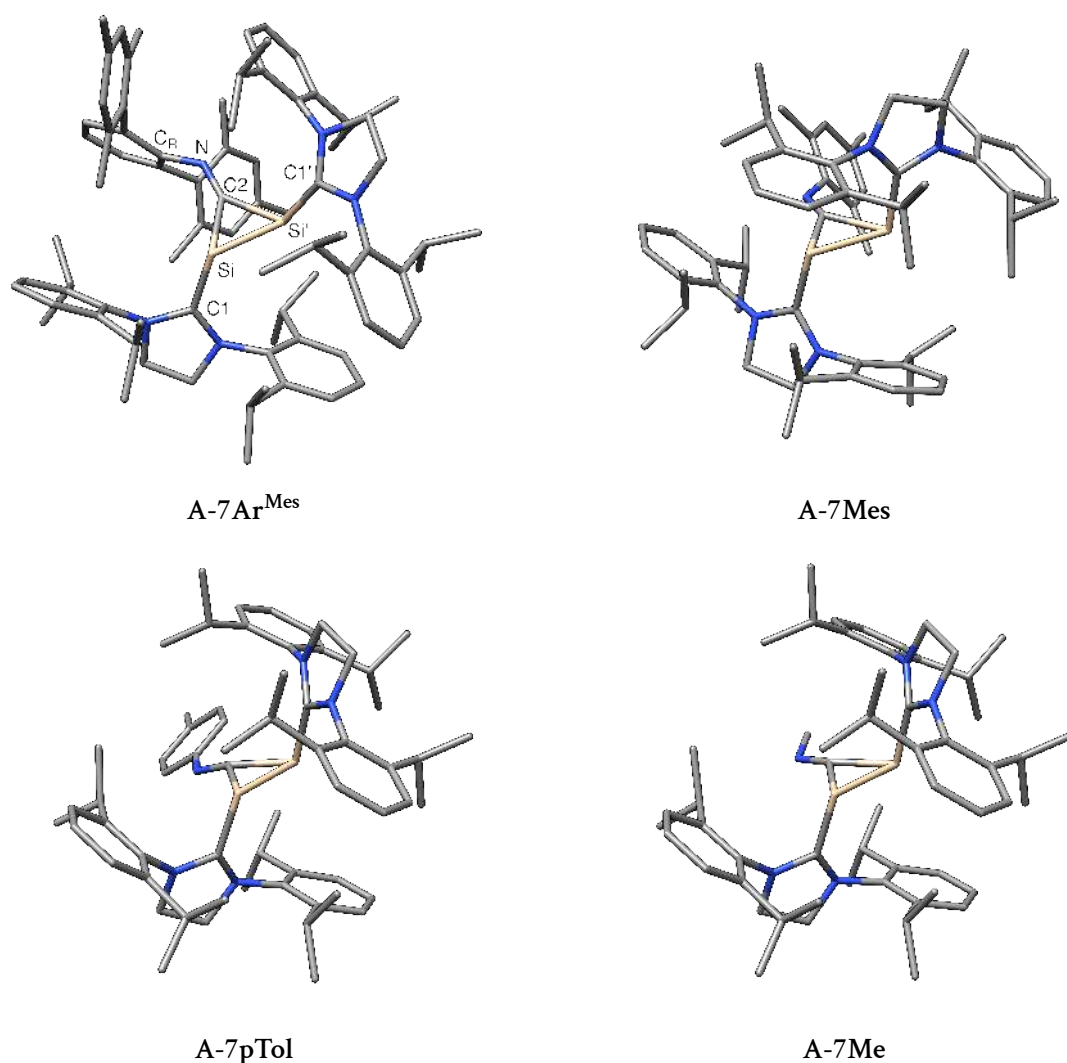


Figure 4.4: Optimized gas phase structures of the disilirane-1,2-ylidene-3-imines **A-7R**.

The relative thermodynamic quantities of the reaction towards the disilirane-1,2-ylidene-3-imines **A-7R** according to Scheme 4.4 were calculated and are given in Table 4.6. Regarding the electronic

Table 4.5: Selected bond parameters of the calculated disilirane-1,2-ylidene-3-imines **A-7R**. Bond lengths and angles are given in pm and degrees, respectively.

	Si–C1	Si–Si'	Si–C2	C2–N	N–C _R	C2–Si–Si'	C1–Si–Si'–C1'	$\Sigma\angle(\text{Si})$	$\Sigma\angle(\text{C2})$
A-7Ar^{Mes}	192.6	236.7	193.6	126.4	138.4	54.2	–155.6	277.4	360.0
	194.6		199.7			51.8		280.2	
A-7Mes	192.2	245.5	187.6	126.4	139.1	54.1	179.9	255.2	358.5
	193.9		203.6			48.3		242.2	
A-7pTol	195.2	242.4	193.5	128.5	139.8	51.0	–176.5	247.9	335.5
	192.5		192.8			51.3		247.1	
A-7Me	194.7	241.2	195.9	126.9	145.6	51.3	–178.2	246.2	356.4
	191.7		193.5			52.2		250.5	

energies, the reaction is most favoured for the *p*Tol substituent ($-120.2 \text{ kJ}\cdot\text{mol}^{-1}$) and less for the other substituents (-74.5 to $-46.8 \text{ kJ}\cdot\text{mol}^{-1}$). As the reactions are associated with a large decrease of entropy (-317.2 to $-194.1 \text{ J}\cdot\text{K}^{-1}\cdot\text{mol}^{-1}$), the relative free Gibbs energies are only negative for $\text{R} = \text{Me}$ ($-12.2 \text{ kJ}\cdot\text{mol}^{-1}$) and *p*Tol ($-48.0 \text{ kJ}\cdot\text{mol}^{-1}$), whereas for $\text{R} = \text{Mes}$ ($7.4 \text{ kJ}\cdot\text{mol}^{-1}$) and Ar^{Mes} ($54.6 \text{ kJ}\cdot\text{mol}^{-1}$), the reactions are found to proceed endergonically at 298 K.

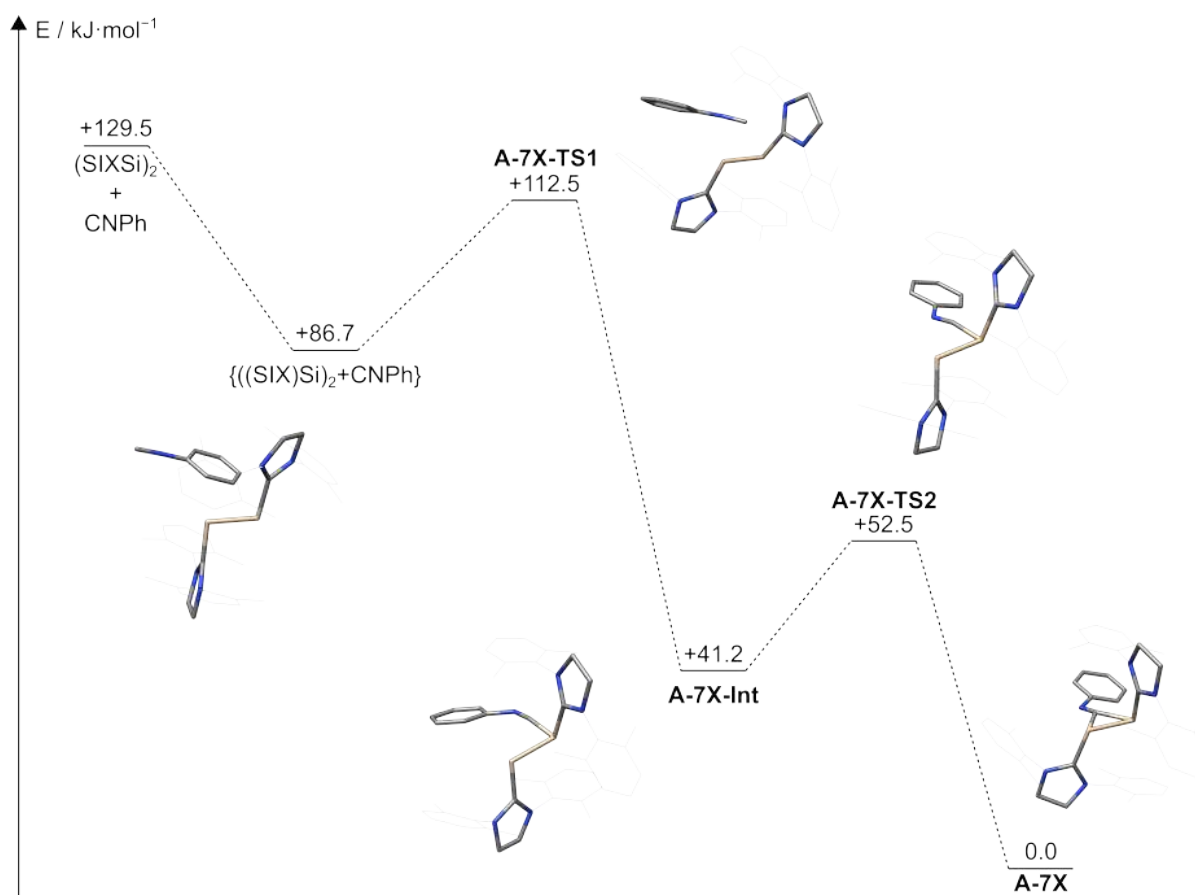
**Figure 4.5:** Calculated mechanistic pathway for the formation of the disilirane-1,2-ylidene-3-imine intermediate model system **A-7X**. More information on the optimized structures can be found in the appendix.

Table 4.6: Calculated thermochemical quantities for the formation of the disilirane-1,2-ylidene-3-imines A-7R from (SIDippSi)₂ and isocyanides CNR. Energies and enthalpies are given in kJ·mol⁻¹ and entropies in J·K⁻¹·mol⁻¹.

	ΔE	ΔU	ΔH	ΔS	ΔG
R = Ar ^{Mes}	-46.8	-37.5	-40.0	-317.2	54.6
R = Mes	-71.4	-63.6	-66.0	-246.4	7.4
R = <i>p</i> Tol	-120.2	-106.4	-108.9	-204.2	-48.0
R = Me	-74.5	-67.6	-70.0	-194.1	-12.2

The mechanism of the disilirane-1,2-ylidene-3-imine formation was further studied in more detail. For this, the smaller model system ((SIX)Si)₂CNPh (A-7X) was used, where the Dipp groups of the carbene are reduced to 2,6-dimethylphenyl groups (*meta*-xylene) and the isocyanide substituent to a phenyl group. A thorough transition state search combined with the Nudged Elastic Band method^[124] finally yielded the reaction path depicted in Figure 4.5. First, the reactants ((SIX)Si)₂ and CNPh form the loose contact pair {((SIX)Si)₂+CNPh}, lowering the relative energy from +129.5 to +86.7 kJ·mol⁻¹. Then the intermediate A-7X-Int is formed via the transition state A-7X-TS1 at +112.5 kJ·mol⁻¹ ($\nu_{\text{TS}} = 77i \text{ cm}^{-1}$). Compound A-7X-Int lies at +41.2 kJ·mol⁻¹ compared to A-7X and features an asymmetric coordination of the isocyanide carbon atom to one silicon atom of ((SIX)Si)₂ with a short Si–C_{CNR} bond of 180.8 pm. The product formation is then possible via the energetically slightly higher-lying transition state A-7X-TS2 (+52.5 kJ·mol⁻¹, $\nu_{\text{TS}} = 40i \text{ cm}^{-1}$).

4.5. Iminosilylenylidene Formation by Substitution of A-1Ar^{Mes} with Isocyanides CNR

As mentioned before, the reaction of A-1Ar^{Mes} with other isocyanides CNR leads to other iminosilylenylidenes A-1R which could, however, be only successfully isolated for R = Me. The calculated reaction energies, enthalpies and entropies of the substitution are given in Table 4.7 and show a generally unfavoured reaction for CNMe ($\Delta E = 42.1 \text{ kJ}\cdot\text{mol}^{-1}$, $\Delta G = 14.5$) and Mes ($\Delta E = 35.3 \text{ kJ}\cdot\text{mol}^{-1}$, $\Delta G = 18.5 \text{ kJ}\cdot\text{mol}^{-1}$), whereas the reaction with CN*p*Tol proceeds almost isoenergetically ($\Delta E = 4.3 \text{ kJ}\cdot\text{mol}^{-1}$) and is slightly exergonic ($\Delta G = -13.2 \text{ kJ}\cdot\text{mol}^{-1}$).

As the experiment shows that the substitution reaction of A-1Ar^{Mes} with CNMe to A-1Me and free Ar^{Mes} actually proceeds in solution at room temperature, the effect of a higher-rung density functional approximation and solvation treatment were briefly investigated: Compared to the ΔG value of +14.5 kJ·mol⁻¹ for level of theory I, the level of theory II yields an only marginally lower value of +10.2 kJ·mol⁻¹. However, the modelling of solution effects of benzene with the implicit solvation model density (SMD) method^[154] decreases the energy to -5.7 kJ·mol⁻¹ with the B97-D3 DFA (B97-D3(BJ)-ATM-SMD(benzene)/def2-TZVP) and to -11.0 kJ·mol⁻¹ using the double-

hybrid DFA level of theory RI-PWPB95-D3(BJ)-ATM-SMD(benzene)/def2-QZVPP//B97-D3(BJ)-ATM-SMD(benzene)/def2-TZVP. The solvation-corrected thermodynamical values for the other reactions and the elucidation of the substitution reaction mechanism is subject to further calculations.

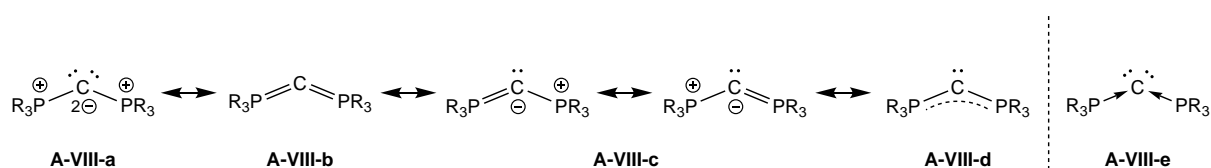
Table 4.7: Calculated thermochemical quantities for the iminosilylidene formation by substitution of $\mathbf{A-1Ar}^{\text{Mes}}$ with isocyanides CNR. Energies and enthalpies at level of theory I are given in $\text{kJ}\cdot\text{mol}^{-1}$ and entropies in $\text{J}\cdot\text{K}^{-1}\cdot\text{mol}^{-1}$.

	ΔE	ΔU	ΔH	ΔS	ΔG
R = Mes	35.3	34.4	34.4	53.5	18.5
R = <i>p</i> Tol	4.3	9.8	9.8	76.9	-13.2
R = Me	42.1	41.1	41.1	89.3	14.5

5. Siladibene and Siladiimide Compounds

5.1. Introduction

In the year 1961, F. Ramirez *et al.* reported the synthesis of the first carbodiphosphorane $C(PPh_3)_2$,^[155] a class of compounds with a dicoordinated carbon atom and a bent and flexible P–C–P core (130 to 144°).^[156] In their study, the authors suggested a resonance hybrid between carbon-diylide (A-VIII-a) and heteroallene (A-VIII-b) for its electronic structure (Scheme 5.1).^[155] In the following years, the group of H. Schmidbaur not only increased the number of isolable phosphorane and arsorane derivatives,^[157–159] but also postulated two more important resonance structures A-VIII-c based on experimental structure data and theoretical MO considerations, which are of ylidene type, where one electron lone pair resides at the carbon atom and one $\pi(C-P)$ is formed. Using the short form A-VIII-d to combine both ylidene resonance formulas, H. Schmidbaur concluded that A-VIII-d is best suited to describe the structural and electronic properties of carbodiphosphoranes.^[156] In a later study, Schmidbaur *et al.* reported that carbodiphosphoranes can also be rationalized as donor-acceptor phosphine complexes of elemental carbon, presented with arrows in Lewis formula A-VIII-e (Scheme 5.1).^[158]



Scheme 5.1: Various resonance formulas A-VIII-a to A-VIII-d and donor-acceptor arrow notation A-VIII-e for carbodiphosphoranes.

Half a century after F. Ramirez' discovery of the carbodiphosphoranes, G. Frenking *et al.* reinvestigated this class of compounds with modern quantum chemical methods and affirmed the donor-acceptor character of the P–C bonds (Lewis formula A-VIII-e), yielding a divalent carbon atom in the formal oxidation state zero with two free electron lone pairs on the carbon atom, stabilized by two phosphane ligands.^[160] Due to the supposedly dominant Lewis structure A-VIII-a or A-VIII-e, respectively, G. Frenking *et al.* suggested later on to name the general class of divalent carbon(0) compounds CL_2 *carbones*, as a distinction to the prominent carbene field of chemistry with carbon in the formal oxidation state +II.^[161]

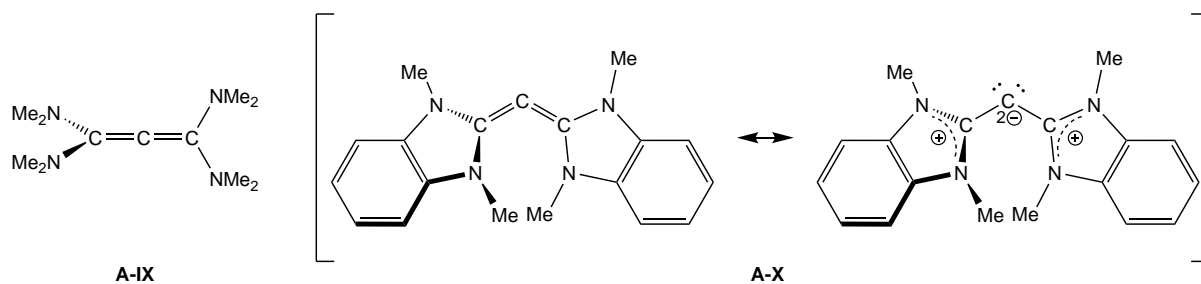
Further theoretical studies by G. Frenking *et al.* on carbodiphosphoranes followed,^[161–166] and were expanded to include the promising class of carbodicarbenes $C(CR_2)_2$.^[161–163, 165, 167] The main features of these compounds are:

- a two-coordinated carbon atom in the formal oxidation state zero, in contrast to carbenes with a carbon atom in the oxidation state +II.
- a non-linear arrangement of the L–C–L moiety with bond angles of approx. 130°.
- carbon-ligand C–L bonds that are in the upper range between typical C–L single and C=L double bonds, due to the $\sigma(C\leftarrow L)$ donation and $\pi(C\rightarrow L)$ back donation.
- in the HOMO a p-type lone pair at the carbon atom that is delocalized towards suitable orbitals of similar symmetry of the ligands L. Their extent of delocalization, and thus the ylidone (A-VIII-a) vs ylidene (A-VIII-d) character, heavily depends on the π -accepting abilities of the ligands L.
- in the HOMO–1 an s-type lone pair at the carbon atom lying in the L–C–L plane.
- a highly negative charge accumulation on the central carbon atom leading to a strongly nucleophilic centre.
- very large first and second proton affinities, which is in contrast to carbon(II) compounds, and the capability to form doubly-bonded Lewis acid (LA) adducts $L_2C(LA)_2$.

Meanwhile, the groups of A. Fürstner and G. Bertrand independently succeeded to isolate the first carbodicarbenes $(Me_2N)_2CCC(NMe_2)_2$ (A-IX, Scheme 5.2) and bis(*N*-methylbenzimidazol-2-yl)carbon (A-X).^[168, 169] Whereas the tetraaminoallenes like A-IX display a quasi-linear structure with only hidden carbene character according to calculations by G. Frenking *et al.*^[162, 163, 167, 170] and other groups,^[171, 172] compound A-X features a non-linear C–C–C core (134.8°), short C=C bonds (134.3 pm) and twisted carbene planes with an (N1,C1,N2),(N3,C2,N4) interplanar twist angle of 69°. Other examples for carbon(0) complexes followed over the years,^[173–177] and a discussion about their classification as *bent allenes* in contrast to *normal allenes* emerged.^[165, 171, 172, 178–181] On the one hand, this discrimination can be made experimentally via the CCC bending angle, the twist angle between the CR_2 substituents or the reactivity towards electrophiles (the central carbon atom is the most nucleophilic point in carbon(0) complexes).

On the other hand, theory contributed significantly to this issue, and the carbene character in such compounds can be well estimated by calculating the first and second proton affinities or studying the frontier molecular orbitals. For the latter, a high carbene character is usually visible by the non-degenerate HOMO ($\pi(C-C-C)$) and HOMO–1 ($LP_s(C)$) in contrast to the two degenerate, orthogonal $\pi(C-C)$ bond orbitals in allenes.

The group of G. Frenking also investigated the analogous heavier tetrel compounds $E(L)_2$, where $E = Si$,^[166, 182, 183] Ge ,^[166, 183] Sn ,^[166, 183] Pb ^[166, 184] and $L = PR_3, CR_2$, and could also confirm the main

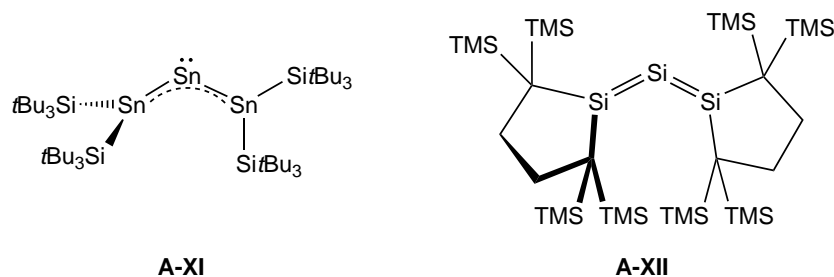


Scheme 5.2: Lewis structures of the first isolated carbidicarbene.

characteristics of the carbon compounds to its heavier homologues. However, notable differences include

- less negatively charged tetrel centres due to the lower electronegativity of the heavier tetrels compared to carbon,
- generally lower first and second proton affinities. However, the second proton affinity is still considerably higher than in typical tetrel(II) compounds.
- a larger energetic separation between the $\pi(L-E-L)$ orbital (typically the HOMO) and the s -type lone pair at the tetrel (mostly HOMO-1, sometimes lower). As a consequence, electrophiles prefer to coordinate to the π -type orbital in an out-of-plane fashion, resulting in a strongly pyramidalized tetrel atom. In contrast, in carbon(0) complexes the adduct formation proceeds within the $L-C-L$ plane and leads to a trigonal-planar central carbon atom.

Prior to these theoretical considerations for heavier $E(L)_2$ compounds, the groups of N. Wiberg and M. Kira succeeded already in 1999 and 2003 with the isolation of the first stable tristannaallene, $Sn(Sn(Si^tBu_3)_2)_2$ (A-XI, Scheme 5.3),^[185] and trisilaallene, $Si(CDASi)_2$ (A-XII, CDASi = cyclic dialkylsilylene, $Si(C(TMS)_2CH_2)_2$),^[186] respectively, where the latter can be seen as result of exploring the synthetic potential of the first isolable dialkylsilylene CDASi reported in the year 1999 by the same group.^[187]



Scheme 5.3: The first tristannaallene and trisilaallene by N. Wiberg *et al.* and M. Kira *et al.*

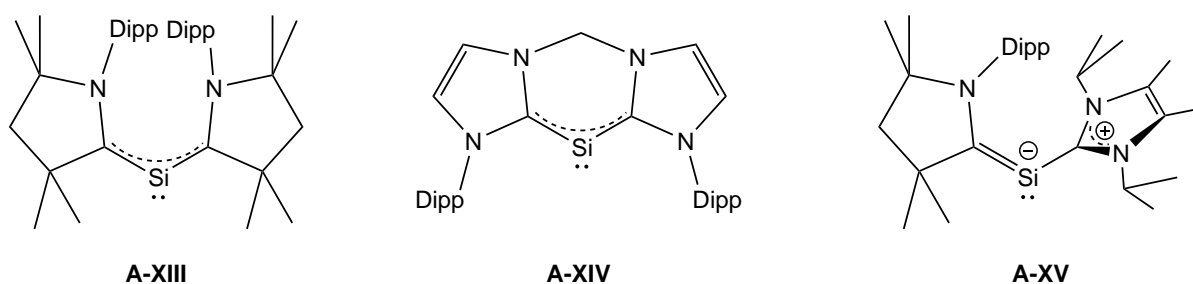
Both compounds feature a considerably bent $E-E-E$ core (A-XI: 155.9° , A-XII: 136.5°), short $E-E$ distances in the range of typical $E=E$ double bonds and perpendicular orientations of the two R_2E groups to each other. Whereas the electronic structure of A-XI was rationalized by the ylidic

structure, compound A-XII and other related derivatives $R_2EE'ER_2$ ($E = Si, Ge; E' = Si, Ge$) were classified as bent allenes by experimental and theoretical studies.^[188–196] In contrast, G. Frenking *et al.* concluded in a study on various dicoordinated silicon(0) compounds that A-XII is better described as a siladisilylene with $CDASi \rightarrow Si$ donor-acceptor bonds and high silylone character.^[182] Genuine siladibenes $Si(carbene)_2$ were not isolated before the year 2013, when H. W. Roesky *et al.* reported the synthesis of $Si(CAAC^{Me})_2$ (A-XIII, Scheme 5.4, $CAAC^{Me} =$ cyclic alkylaminocarbenes, $C[N(Dipp)CMe_2CH_2CMe_2]$),^[197, 198] motivated by the seminal work of G. H. Robinson *et al.* on the disilicon(0) complex $(IDipp)_2Si_2$ in the year 2008.^[199] The reduction of the precursor $(CAAC^{Me})_2SiCl_2$ leads to A-XIII, the first example of a single silicon atom coordinated by two carbenes. The sc-XRD structure analysis revealed a bent C–Si–C core ($117.18(8)^\circ$) and short Si–C bonds (184.11(18) and 184.17(17) pm) due to $\pi(C \leftarrow Si \rightarrow C)$ back-donation as evidenced by the HOMO (an NBO calculation yields a 30:40:30 distribution for the $3c-2e^- - \pi(C-Si-C)$ interaction). Interestingly, the π -acceptor ability of the CAAC ligand is strong enough that A-XIII shows small, but considerable biradical character.

In the same year, M. Driess *et al.* were able to isolate the cyclic siladibene $Si(bNHC)$ (A-XIV) using a chelating bis(N-heterocyclic carbene) ligand (Scheme 5.4).^[200] Due to the forced six-membered ring environment, the C–Si–C angle is considerably narrower with 88.7° , but otherwise the compound features the typical characteristics of siladibenes (*vide supra*).^[200, 201]

Since then, various siladibenes^[202, 203], siladisilylenes^[204–207], siladigermylenes^[208] and even heavier congeners like germaditetrylenes^[209–212], stannaditetrylenes^[213] and plumbaditetrylenes^[214] could be synthesized.

Within those, the first heteroleptic siladibene $Si(CAAC^{Me})(iPr_2Me_2)$ (A-XV, Scheme 5.4) reported by the group of C.-W. So in the year 2016 is particularly noteworthy,^[202] as the heteroleptic environment causes an asymmetric structure, where the silicon atom is doubly bonded towards the $CAAC^{Me}$ ligand and the iPr_2Me_2 ligand is oriented perpendicular to the C–Si–C plane ($iPr_2Me_2 = C[N(iPr)C(CH_3)]_2$).



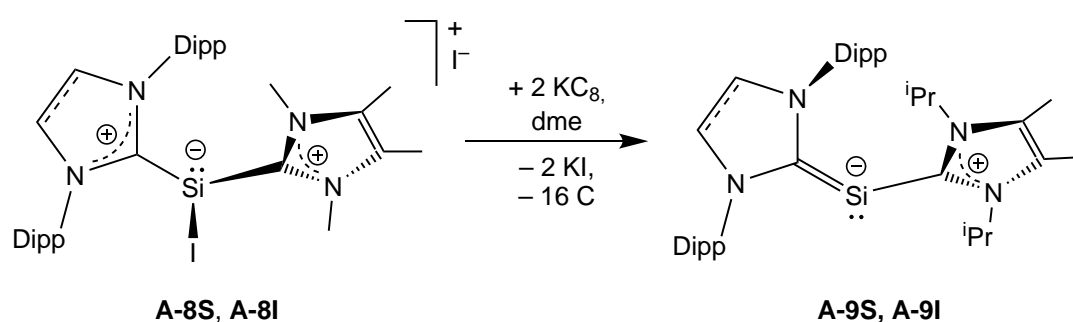
Scheme 5.4: The first homoleptic and heteroleptic siladibenes.

With the homoleptic $(CAAC)_2Si$ and $(NHC)_2Si$ as well as the heteroleptic $(CAAC)Si(NHC)$ compounds known, the elusive puzzle piece remains to be a heteroleptic siladibene with N-heterocyclic carbenes only. As NHCs are less π -acidic than CAAC ligands, it would be interesting to see if there is a considerable change in the electronic structure compared to A-XV.

5.2. Two Heteroleptic Siladivcarbenes with N-heterocyclic Carbenes

Access to the targeted compound was provided by the IiPr_2Me_2 -stabilized iodosilyliumylidene $[(\text{IDipp})\text{Si}(\text{IiPr}_2\text{Me}_2)]\text{I}$ (A-8I), reported in 2013 by our group.^[215] The analogous SIDipp-substituted iodosilyliumylidene $[(\text{SIDipp})\text{Si}(\text{IiPr}_2\text{Me}_2)]\text{I}$ (A-8S) could also be obtained by S. Kumar via a similar route.^[150]

Reductive dehalogenation of the precursors A-8S and A-8I with potassium graphite selectively afforded the heteroleptic siladivcarbenes A-9S and A-9I as red and black-brown solids, respectively (Scheme 5.5).



Scheme 5.5: Synthesis of the first heteroleptic siladivcarbenes SiLL' , where $\text{L}, \text{L}' = \text{NHC}$, by S. Kumar.^[150] dme = dimethoxyethane.

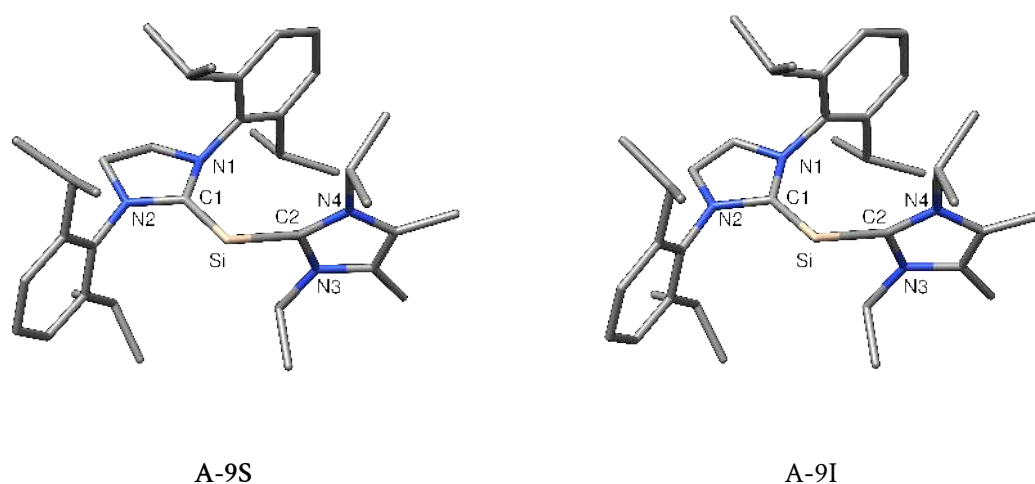


Figure 5.1: Optimized gas phase structures of the siladivcarbenes A-9S and A-9I.

The optimized gas phase structures of A-9S and A-9I (Figure 5.1) are in good agreement with the experimentally determined sc-XRD structures A-9S_{exp} and A-9I_{exp} , and the analysis of the structural parameters, summarized in Table 5.1, reveal:

Table 5.1: Selected calculated and experimental sc-XRD analysis bonding parameters of the siladibcarbenes **A-9S** and **A-9I**. Bond lengths are given in pm and angles in degrees. τ is defined as the interplanar twist angle between the NHC ring planes.

	Si–C1	Si–C2	C1–N1	C1–N2	C2–N3
A-9S	182.2	195.9	141.2	140.1	137.0
A-9S_{exp}	182.5(6)	195.1(7)	141.7(8)	140.2(8)	136.8(9)
	181.8(7)	195.9(7)	142.1(8)	140.0(9)	135.1(9)
A-9I	183.8	194.3	142.1	141.4	138.1
A-9I_{exp}	182.1(2)	195.3(3)	141.7(3)	141.3(3)	136.0(2)
	C2–N4	C1–Si–C2	$\Sigma\angle(N1)$	$\Sigma\angle(N2)$	τ
A-9S	137.5	98.9	351.7	359.7	94.6
A-9S_{exp}	138.0(9)	101.2(3)	357.3(15)	349.8(15)	84.9(3)
	136.4(9)	101.3(3)	357.8(15)	350.3(15)	100.1(3)
A-9I	137.3	99.1	352.1	359.4	87.1
A-9I_{exp}	136.7(3)	102.0(1)	352.2(6)	358.6(6)	81.6(1)

- a dicoordinated silicon atom in a V-shaped C1–Si–C2 environment (**A-9S**: 98.9°, **A-9I**: 99.1°). The degree of bending is smaller than in the cyclic siladibcarbene **A-XIV** (89.1(1)°), similar to that of **A-XV** (102.8(2)°) but larger than in **A-XIII** (117.7(1)°).
- an asymmetric coordination of the NHC ligands: The Si–C1 bond distances of 182.2 pm (**A-9S**) and 183.8 pm (**A-9I**) are considerably shorter than the Si–C2 bonds (**A-9S**: 195.9 pm, **A-9I**: 194.3 pm). Although the Si–C1 bonds are slightly larger than the Si–C_{CAAC} in **A-XV** (179.2(4) pm), they indicate considerable double-bond character for the Si–C1 bond in contrast to the Si–C2 bond.
- significantly elongated C1–N1 and C1–N2 bond lengths of 141.2 and 140.1 pm (**A-9S**) and 142.1 and 140.1 pm (**A-9I**) compared to the free carbene ligands SIDipp (134.8 pm) and IDipp (137.4 pm), respectively (see the appendix for the calculated structures of the free carbenes). This lengthening can be understood as competitive donation from the π -type orbital coming from silicon (*vide infra*) into the empty p-orbital of the carbene carbon atom, or more precisely, into the anti-bonding $\pi^*(N1-C1-N2)$ MO of the NHC. The lengthening of the C–N bonds within the IiPr₂Me₂ ligand is found to be much smaller (**A-9S**: 137.0 pm, 137.5 pm; **A-9I**: 137.3 pm, 138.1 pm; free IiPr₂Me₂: 136.8 pm).
- an orthogonal arrangement of the central five-membered NHC rings with interplanar twist angles of 94.6° and 87.1° for **A-9S** and **A-9I**, respectively, suggesting the absence of a 3c-2e[−]- $\pi(C1-Si-C2)$ conjugation as found for carbodiphosphoranes and siladibcarbenes with approximately co-planar carbene substituents.
- non-planar N1 carbene nitrogen atoms with sums of angles $\Sigma\angle(N1)$ of 351.7° and 352.1° for **A-9S** and **A-9I**, respectively. In contrast, the sum of angles at the N2 nitrogen atoms of

the (S)IDipp ligands is close to planarity (A-9S: 359.7°, A-9I: 359.4°). This slight nitrogen pyramidalization causes the up-bent Dipp groups at the N1 atom in A-9S and A-9I, which leave the mean N1–C1–N2–Si plane, as seen in the calculated structures (Figure 5.1). As the IiPr_2Me_2 carbene is also bent off the N1–C1–N2–Si plane, but in the opposite direction (Figure 5.2), this orientation can be explained as consequence of steric repulsion between the Dipp group of the (S)IDipp and the IiPr_2Me_2 carbene. Interestingly, this also gives rise to axial chirality in these compounds, which will be further discussed below. Another effect contributing to the Dipp group bending is the $\pi(\text{Si}-\text{C}1)$ backbonding as confirmed by the MO analysis (*vide infra*) that competes against the $\pi(\text{N}-\text{C}-\text{N})$ delocalization of the carbene. As a consequence, the nitrogen lone pair character is enhanced compared to the free carbene.

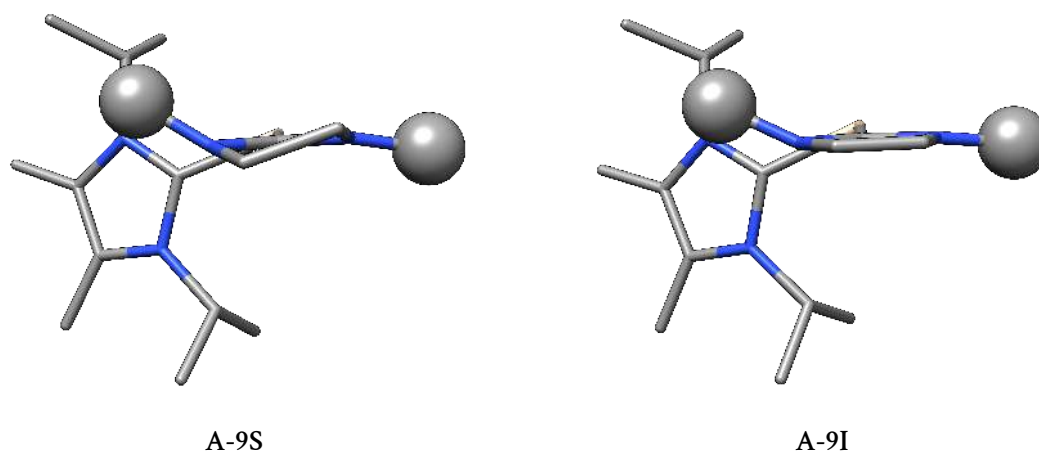


Figure 5.2: Stereoview of the siladicalbenes A-9S and A-9I along the C1–Si bond. The Dipp groups are simplified by large spheres giving the position of the C_{ipso} atoms.

Selected frontier molecular orbitals of the siladicalbenes A-9S and A-9I are presented in Figures 5.3 and 5.4 and appear similar. Both HOMO–1 show the electron lone pair at the silicon atom, lying in the C1–Si–C2 plane. The HOMO is of $\pi(\text{Si}-\text{C}1)$ character without significant delocalization to the IiPr_2Me_2 carbene and resembles the $\pi(\text{Si}-\text{CAAC}^{\text{Me}})$ orbital of A-XV. Due to the oppositely phased orbital lobes on the N1 and N2 atoms, this interaction can be rationalized as $\text{LP}_{\pi}(\text{Si}) \rightarrow \pi^*(\text{N}-\text{C}-\text{N})$ back-donation of the out-of-plane silicon lone pair into the (S)IDipp carbene and explains the found short Si–C1 bond distances. As no back-donation towards the perpendicular oriented IiPr_2Me_2 carbene is visible, the Si–C2 bond is obtained longer, and the LUMO only contains the $\pi^*(\text{N}-\text{C}-\text{N})$ of the IiPr_2Me_2 carbene besides some aryl orbital density without any contribution of the silicon atom.

Localized intrinsic bond orbitals (IBOs) for the $\sigma(\text{Si}-\text{C}1)$, $\pi(\text{Si}-\text{C}1)$, $\sigma(\text{Si}-\text{C}2)$ bonds and the $\text{LP}(\text{Si})$ could be obtained for A-9S and A-9I and underline the observations from the canonical MOs (Figures 5.5 and 5.6). The respective atomic Löwdin populations confirm the localized character of the $\pi(\text{Si}-\text{C}1)$ orbitals (A-9S: 45.3 % (Si), 35.8 % (C1); A-9I: 46.9 % (Si), 33.6 % (C1)), with only

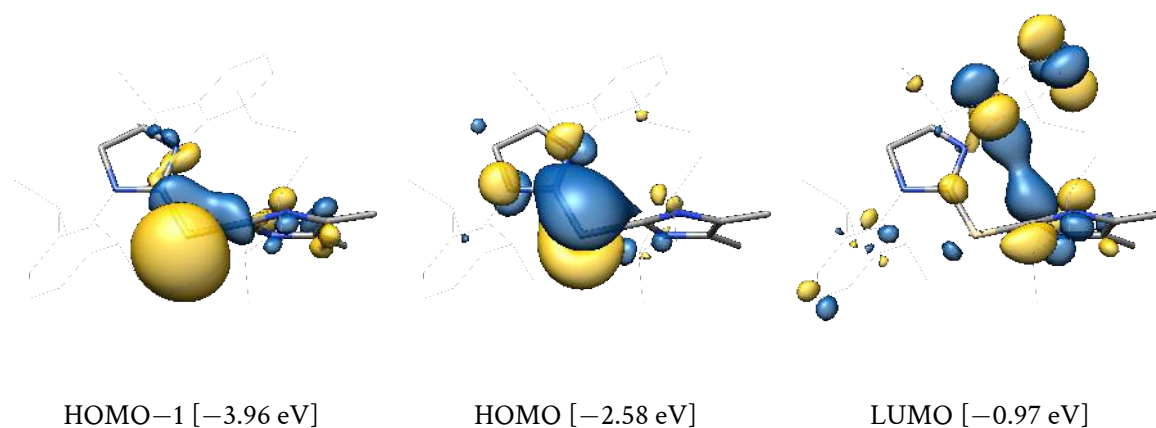


Figure 5.3: Canonical molecular orbitals of the siladibene A-9S and their energy eigenvalues.

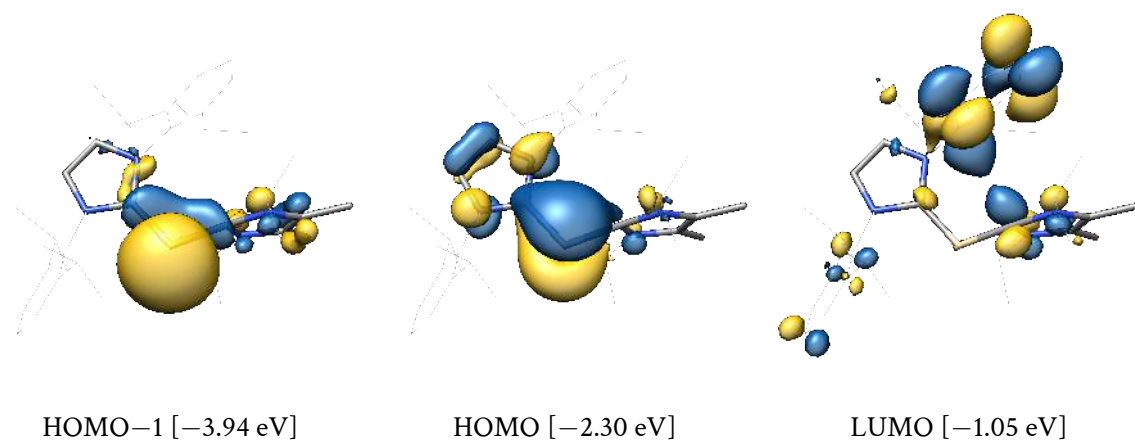


Figure 5.4: Canonical molecular orbitals of the siladibene A-9I and their energy eigenvalues.

a very low participation of the C2 carbene atom (3.9 and 5.4 % for A-9S and A-9I, respectively). Furthermore, as the in-plane electron lone pair at the silicon atom has only small contributions of the C1 and C2 atoms with 4.6 %, 6.6 %, 4.8 % and 6.8 % for A-9S and A-9I, respectively, the compounds show no considerable bent allene character according to the MO analysis.

The bond interactions between the silicon atom and both carbenes were further investigated by MO diagrams considering the structurally unrelaxed fragment MO (FMO) interactions for A-9S (Figure 5.7, the MO interaction diagram for A-9I is obtained similarly). After excitation of the triplet ground state of the silicon atom to the singlet state ($\Delta E_{s \rightarrow t} = -107.0 \text{ kJ}\cdot\text{mol}^{-1}$), it can interact with the (SIDipp+IiPr₂Me₂) fragment, also in its singlet state ($\Delta E_{s \rightarrow t} = +176.6 \text{ kJ}\cdot\text{mol}^{-1}$). As a consequence of unfavoured spin-pairing in the silicon atom singlet state, its doubly-occupied 3p_z orbital lies energetically higher than the unoccupied degenerate 3p_x and 3p_y orbitals.

Three main interactions can be found in the diagram: First, the silicon 3s² lone pair can interact with the constructive combination of the NHC carbenic lone pairs (HOFMO-2) to form a 3-center-2-electron $\sigma(\text{C1}-\text{Si}-\text{C2})$ bond, that is found in the HOMO-50 of A-9S. The destructive combination of the NHC lone pairs can be found in the HOFMO and interacts with a p-orbital at the silicon atom, again resulting in a 3-center-2-electron $\sigma(\text{C1}-\text{Si}-\text{C2})$ bond (HOMO-12). By

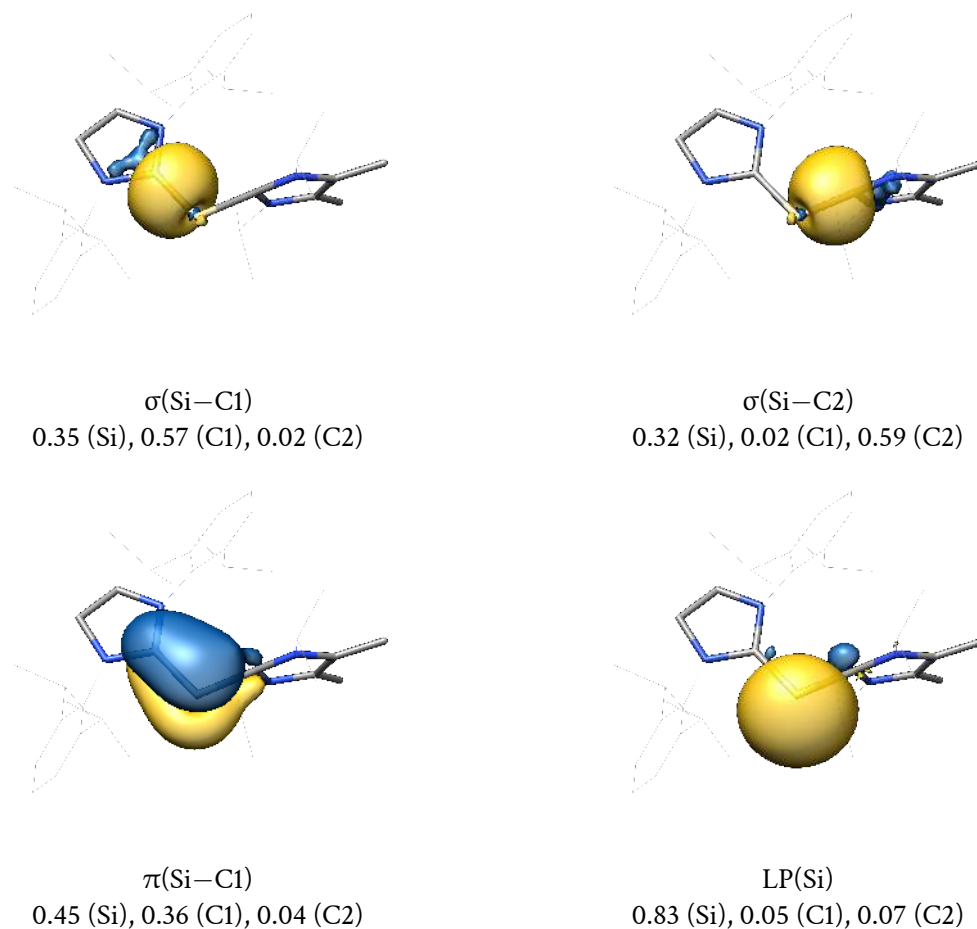


Figure 5.5: Intrinsic bond orbitals (IBOs) of the siladicalcarbene **A-9S** and their atomic Loewdin orbital populations.

s- and *p*-orbital mixing also a lone pair at the silicon atom is retained, located in the HOMO–1 of **A-9S**, as discussed above. Finally, the occupied p_z orbital at the silicon atom can interact with the $\pi^*(\text{N1}-\text{C1}-\text{N2})$ orbital of the SIDipp substituent (LUFMO), which is properly aligned, in contrast to the $\pi^*(\text{N3}-\text{C2}-\text{N4})$ orbital of the IiPr_2Me_2 substituent (LUFMO+7). This donation from silicon is then responsible for the $\pi(\text{Si}-\text{C1})$ bond found in the HOMO of **A-9S**, with its anti-bonding combination in the LUMO+6. The non-interacting $\pi^*(\text{N3}-\text{C2}-\text{N4})$ orbital of the IiPr_2Me_2 carbene can then be found in the LUMO of **A-9S**.

Overall, by these interactions two σ bonds between the silicon atom and both carbenes, one π bond between the silicon atom and the SIDipp substituent, and one residual electron lone pair at the silicon atom are obtained, which fits to the previous considerations by discussion of the structural parameters and MOs.

Additional insight into the electronic structures of **A-9S** and **A-9I** was provided by the NBO7 method. Local NRT analyses yield the resonance hybrid contributions depicted in Scheme 5.6 and suggest the ylidene-type structure **A-9-a** to be major for **A-9S** (42 %), followed by the silylionic formula **A-9-d** (28 %) with two lone pairs at the silicon atom and two Si–carbene single bonds. No significant contributions are obtained for the $\text{Si}=\text{IiPr}_2\text{Me}_2$ ylidene (**A-9-b**, 4 %) and

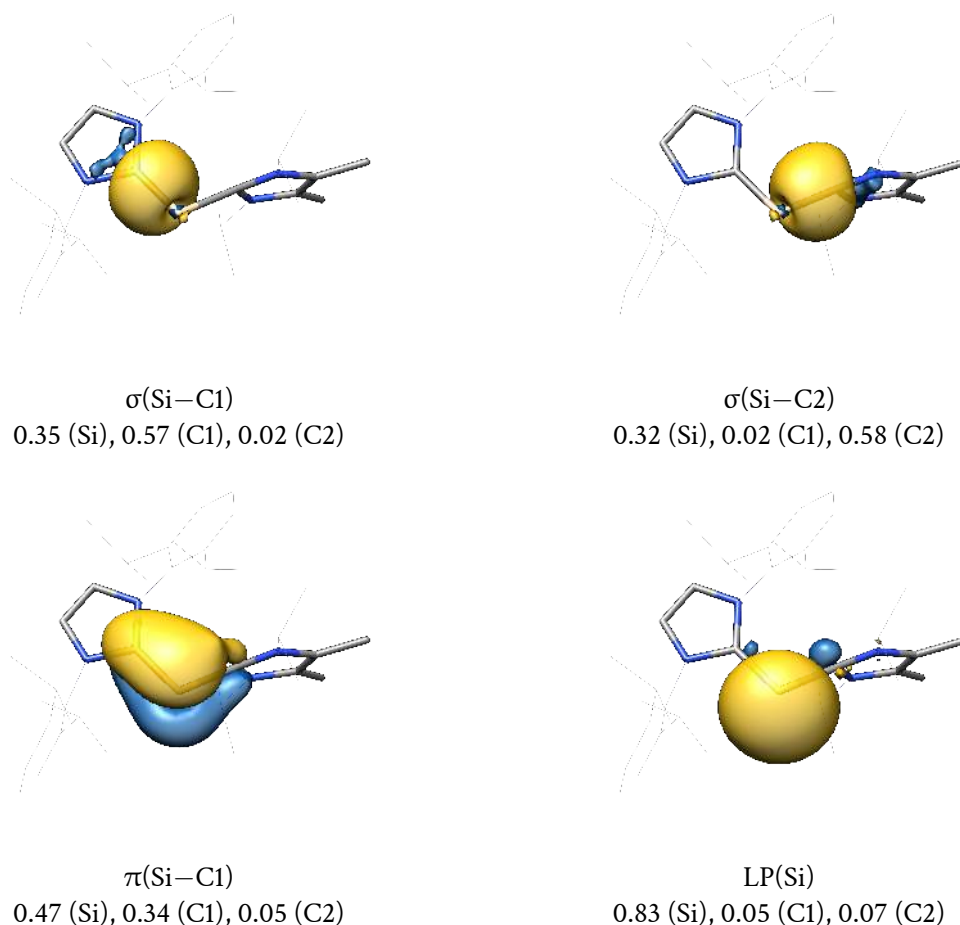
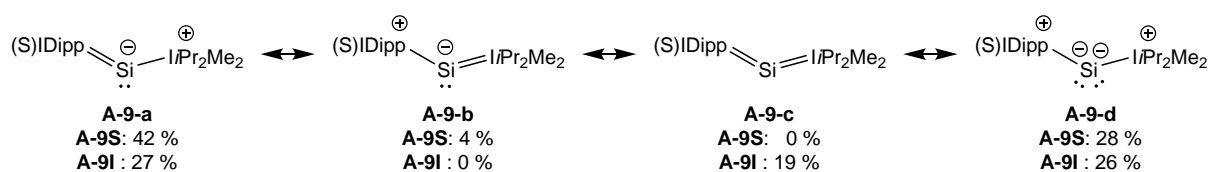


Figure 5.6: Intrinsic bond orbitals (IBOs) of the siladibene **A-9I** and their atomic Löwdin orbital populations.

allenic resonance structures (**A-9-c**, 0 %) for compound **A-9S**. The NRT analysis reveals a similar share for the silylionic resonance structure for compound **A-9I** of 26 %, however, the contribution of **A-9-a** is lowered. Instead, the weight of the allenic resonance formula **A-9-c** amounts to 19 %. Such a considerable delocalization of the second silicon lone pair to the $i\text{Pr}_2\text{Me}_2$ carbene was not observed by the MO analysis above and might be an NRT artifact. It would, however, be consistent with the Energy Decomposition Analysis (EDA) results of the similar compound **A-XV** that gives a share of 14.5 % for a $\text{Si} \rightarrow \pi^*(\text{N}-\text{C}-\text{N})$ donation for the total covalent interaction of the $\text{Si}-i\text{Pr}_2\text{Me}_2$ bond.^[202]



Scheme 5.6: Decomposition of the NRT resonance hybrid into the major bond motifs for **A-9S** and **A-9I**. The local NRT analyses comprise the Si and imidazole/imidazolene ring atoms of the carbene ligands.

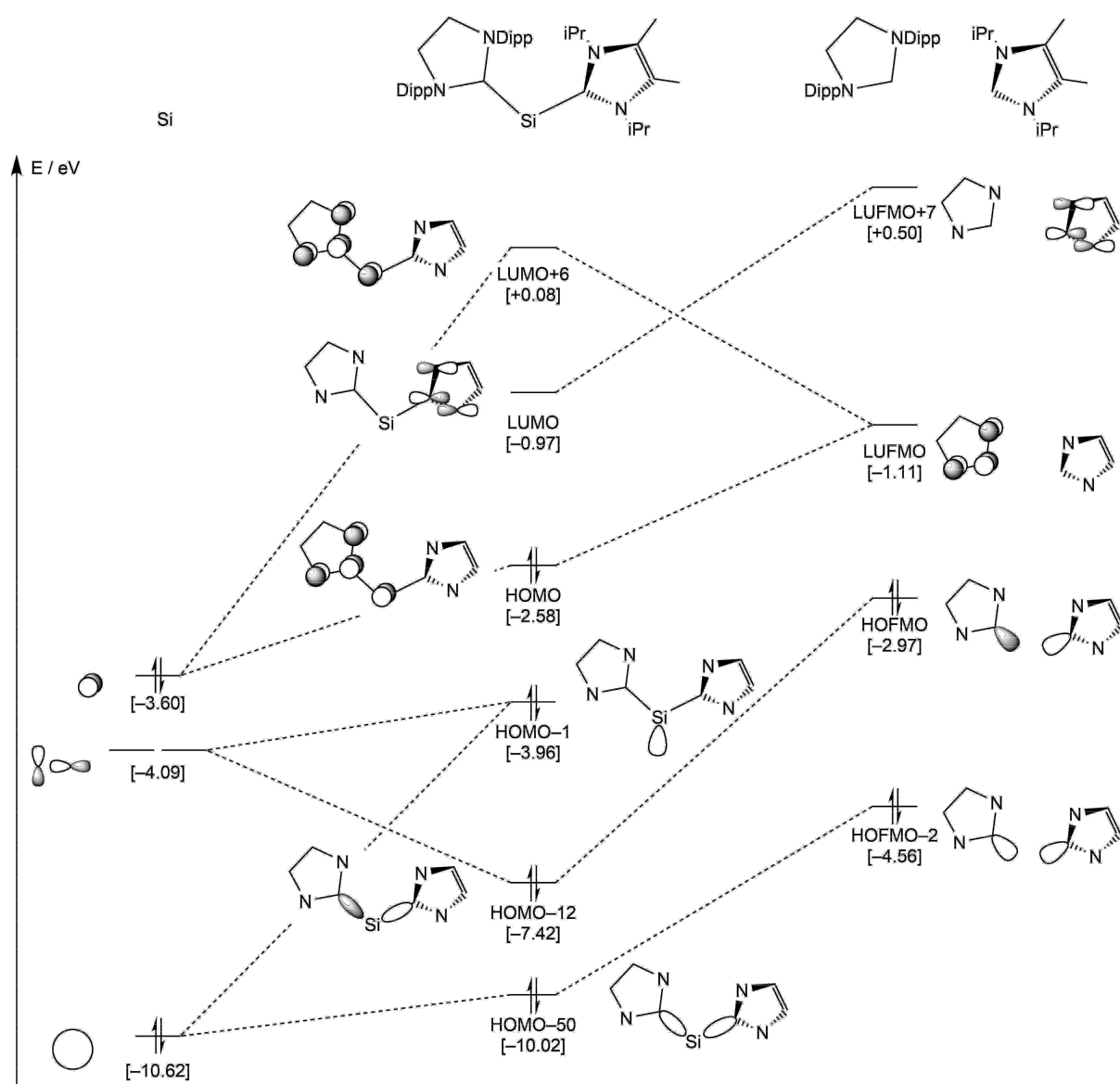


Figure 5.7: MO interaction diagram of A-9S between the structurally unrelaxed Si and (SIDipp+IiPr₂Me₂) fragments in their singlet states. Orbital energies of selected MOs are given in eV in square brackets. HOFMO = highest occupied fragment MO, LUFMO = lowest unoccupied fragment MO. Only the cores of the NHCs are depicted for clarity. The MO interaction diagram for A-9I is obtained similarly.

The results of the NBO analyses on the dominant Lewis structure A-9-a are summarized in Table 5.2 and appear similar for both compounds A-9S and A-9I. The silicon lone pair NBO has a high occupancy and is, as expected, of rather large s-character ($1.84 e^-$, $sp^{0.4}$ (A-9S); $1.83 e^-$, $sp^{0.4}$ (A-9I)). Two NBOs are found for the Si–C1 bond in each compound with occupancies larger than $1.80 e^-$. The first is of σ -type and polarized towards the more electronegative carbon atom (76 % for both siladivcarbenes). In contrast, the second Si–C1 NBO shows π -character with only p-type NAOs involved for both atoms, and it is almost unpolarized (55 % C1 A-9S, 53 % C1 (A-9I)). Their WBIs of 1.3 and 1.2 as well as the total NRT bond orders of 1.6 and 1.7 are greater than 1.0 and confirm the multiple bond character of the Si–C1 bond. In contrast, the WBIs of the Si–IiPr₂Me₂ bonds

are smaller with 0.8 and 0.9 for A-9S and A-9I, respectively. The total NRT-BO of 1.0 for A-9S indicates no multiple bond character, whereas for A-9I, it is slightly increased (1.2) due to the NRT contribution of the allenic resonance structure A-9-c. However, the respective $\sigma(\text{Si}-\text{C}2)$ NBOs are very similar for both siladibenes with occupancies of $1.94 e^-$ and bond polarizations of 78 and 77 % towards carbon. Furthermore, the stabilization by $\text{LP}(\text{Si}) \rightarrow \text{p}(\text{C}2)$ delocalization is found to be similar, as the corresponding Second-Order Perturbation Theory (SOPT) contributions amount to 83.0 and 91.3 $\text{kJ}\cdot\text{mol}^{-1}$ for A-9S and A-9I, respectively. The only slightly higher value for the latter compound can thus not be used as an explanation for the found low allenic character and the NRT Si-C2 bond order of 1.2.

The calculated NPA charges reveal slightly positive silicon atoms ($+0.23 e$, $+0.16 e$), but, as a result of the $\pi(\text{Si} \rightarrow \text{C}1)$ back donation, a considerable charge flow to the (S)IDipp carbenes with -0.45 (A-9S) and $-0.34 e$ (A-9I). This is in contrast to the only σ -donating but not receiving IiPr_2Me_2 carbene that is positively charged ($+0.22$ and $+0.17 e$). These NPA charges fit well to those calculated by C.-W. So *et al.* for A-XV: There the CAAC^{Me} carbene receives more electron density from the silicon atom ($+0.32 e$) and is thus even more negatively charged with $-0.54 e$, whereas the IiPr_2Me_2 carbene bears virtually the same charge ($+0.21 e$) as in A-9S and A-9I.

Finally, considerable SOPT contributions of 460 and 558 $\text{kJ}\cdot\text{mol}^{-1}$ were found for the $\pi(\text{Si}-\text{C}1) \rightarrow \pi^*(\text{Si}-\text{C}1)$ intra-bond interaction in order to account for the silylonic resonance formula A-9-d.

Table 5.2: Results of the NBO, local NRT (with the Si and imidazoline/imidazolene ring atoms included) and NPA analyses of the siladibenes A-9S and A-9I.

NBO A-B	Occ./ e^-	NHO (A,B) pol./% (hyb.)	WBI	NRT-BO tot/cov/ion	NPA / e	
A-9S						
LP(Si)	1.84	($\text{sp}^{0.4}$)			Si	+0.23
$\sigma(\text{Si}-\text{C}1)$	1.93	24 ($\text{sp}^{4.7}$), 76 ($\text{sp}^{1.2}$)	1.3	1.6/1.0/0.5	[SIDipp]	-0.45
$\pi(\text{Si}-\text{C}1)$	1.81	45 (p), 55 (p)			[IiPr ₂ Me ₂]	+0.22
$\sigma(\text{Si}-\text{C}2)$	1.94	22 ($\text{sp}^{8.3}$), 78 ($\text{sp}^{1.3}$)	0.8	1.0/0.4/0.6		
A-9I						
LP(Si)	1.83	($\text{sp}^{0.4}$)			Si	+0.16
$\sigma(\text{Si}-\text{C}1)$	1.94	24 ($\text{sp}^{5.1}$), 76 ($\text{sp}^{1.1}$)	1.2	1.7/1.2/0.5	[IDipp]	-0.34
$\pi(\text{Si}-\text{C}1)$	1.81	47 (p), 53 (p)			[IiPr ₂ Me ₂]	+0.17
$\sigma(\text{Si}-\text{C}2)$	1.94	23 ($\text{sp}^{7.7}$), 77 ($\text{sp}^{1.3}$)	0.9	1.2/0.7/0.5		

Bond cleavage and bond dissociation energies were calculated for both the $\text{Si}-\text{C}_{(\text{S})\text{IDipp}}$ and $\text{Si}-\text{C}_{\text{IiPr}_2\text{Me}_2}$ bonds, summarized in Tables 5.3 and 5.4. The thermochemical calculations for A-9S and A-9I reveal that for the $\text{Si}-\text{C}_{(\text{S})\text{IDipp}}$ bond a cleavage into two singlet fragments is clearly favoured (352.3 and 307.9 $\text{kJ}\cdot\text{mol}^{-1}$) over the cleavage into triplet fragments (584.1 and 602.3 $\text{kJ}\cdot\text{mol}^{-1}$). However, as the $\text{Si}(\text{IiPr}_2\text{Me}_2)$ fragment has a triplet ground state by 43.5 $\text{kJ}\cdot\text{mol}^{-1}$, the bond dissociation including structural relaxation and free choice of multiplicity for the fragments is of overall (s \rightarrow s, t) type with similar BDEs of 225.1 and 201.3 $\text{kJ}\cdot\text{mol}^{-1}$ for A-9S and

A-9I, respectively. In comparison, the calculated *BDE* in the compound A-XV is higher with $340 \text{ kJ}\cdot\text{mol}^{-1}$,^[202] as expected from the generally stronger-binding CAAC substituents in contrast to NHCs.^[216–218] Interestingly, the Si–C_{(S)IDipp} *BDEs* of A-9S and A-9I are also significantly smaller than those calculated for the iminosilylidene (SIDipp)SiCNAr^{Mes} (A-1Ar^{Mes}, $252.6 \text{ kJ}\cdot\text{mol}^{-1}$, see chapter A.3) despite the lower Si–NHC multiple bond character in the latter.

Table 5.3: Level of theory II-calculated bond cleavage (*BCE*) and bond dissociation energies (*BDE*) for the homolytic (hom.) and heterolytic (het.) Si–C_{(S)IDipp} cleavages. Energies in $\text{kJ}\cdot\text{mol}^{-1}$, entropies in $\text{J}\cdot\text{K}^{-1}\cdot\text{mol}^{-1}$, s = singlet, t = triplet multiplicity. The calculated values for A-XV at the BP86/TZVP//BP86/def2-SVP level of theory are taken from ref. [202].

(S)IDipp cleavage	<i>BCE</i> ΔE	<i>BDE</i> (parent \rightarrow (S)IDipp + Si(IiPr ₂ Me ₂))					
		mult.	ΔE	ΔU	ΔH	ΔS	ΔG
A-9S (het.)	352.3 (s)	(s \rightarrow s, t)	225.1	213.4	215.8	257.2	139.2
A-9S (hom.)	584.1 (t)						
A-9I (het.)	307.9 (s)	(s \rightarrow s, t)	201.3	189.3	191.8	232	122.6
A-9I (hom.)	602.3 (t)						
A-XV ^a (het)	353 (s)		340				
A-XV ^a (hom)	454 (t)						

a) CAAC^{Me} cleavage instead of (S)IDipp cleavage

Table 5.4: Level of theory II-calculated bond cleavage (*BCE*) and bond dissociation energies (*BDE*) for the heterolytic (het.) Si–C_{IiPr₂Me₂} cleavages. Energies in $\text{kJ}\cdot\text{mol}^{-1}$, entropies in $\text{J}\cdot\text{K}^{-1}\cdot\text{mol}^{-1}$, s = singlet, t = triplet multiplicity. The calculated values for A-XV at the BP86/TZVP//BP86/def2-SVP level of theory are taken from ref. [202].

IiPr ₂ Me ₂ cleavage	<i>BCE</i> ΔE	<i>BDE</i> (parent \rightarrow (S)IDippSi + IiPr ₂ Me ₂)					
		mult.	ΔE	ΔU	ΔH	ΔS	ΔG
A-9S (het.)	257.9 (s)	(s \rightarrow s, s)	218.4	206.6	209.1	250.2	134.5
A-9S (het.)	679.3 (t)						
A-9I (het.)	256.6 (s)	(s \rightarrow t, s)	202.8	192	194.5	254.6	118.6
A-9I (het.)	641.6 (t)						
A-XV ^a (het.)	173 (s)		148				
A-XV ^a (hom.)	868 (t)						

a) IiPr₂Me₂ cleavage into the fragments CAAC^{Me}Si and IiPr₂Me₂

For the Si–C_{IiPr₂Me₂} bond, a cleavage is possible into the two triplet (679.3 and $641.6 \text{ kJ}\cdot\text{mol}^{-1}$), or singlet state (257.9 and $256.6 \text{ kJ}\cdot\text{mol}^{-1}$) fragments ((S)IDipp)Si and IiPr₂Me₂, of which the latter is favoured by far. Noteworthy, the (SIDipp)Si fragment was found to barely have a singlet ground state on level of theory II with a $\Delta E_{s\rightarrow t}$ of $+7.4 \text{ kJ}\cdot\text{mol}^{-1}$, but $-19.2 \text{ kJ}\cdot\text{mol}^{-1}$ for level of theory I, favouring the triplet spin state. However, the triplet spin state is preferred for the (IDipp)Si fragment at both levels of theory II and I with $\Delta E_{s\rightarrow t}$ of -20.6 and $-42.6 \text{ kJ}\cdot\text{mol}^{-1}$. Thus, following the trends of level of theory II, the *BDE* of the Si–SIDipp bond is of (s \rightarrow s, s) type, whereas the

Si–IDipp bond dissociation in **A-9I** is best described as ($s \rightarrow t$, s) type. Independent of their classification, the obtained *BDEs* for **A-9S** and **A-9I** are very similar with 218.4 and 202.8 $\text{kJ}\cdot\text{mol}^{-1}$. Interestingly, the values are considerably higher than the calculated Si– IiPr_2Me_2 bond dissociation energy in **A-XV** of 148 $\text{kJ}\cdot\text{mol}^{-1}$. A reason for this could be the different level of theory (M06/def2-TZVPP//BP86/def2-TZVPP) in the calculations of So *et al.*, resulting in an artificially weaker bond in the parent molecule.

In conclusion, the *BCEs* of the Si– $\text{C}_{(\text{S})\text{IDipp}}$ bonds are found to be significantly higher than those of the Si– IiPr_2Me_2 bond, which is in agreement with the shorter Si–C1 bond distances and higher Si–C1 bond orders as discussed above. However, because the *BDEs* include the structural relaxation of the ((S)IDipp)Si and (IiPr_2Me_2)Si fragments, they become essentially identical with 225.1 and 218.4 $\text{kJ}\cdot\text{mol}^{-1}$ for **A-9S** and 201.3 and 202.8 $\text{kJ}\cdot\text{mol}^{-1}$ for **A-9I**.

First and Second Proton Affinities

A method to assess the silylone character is to calculate the first and second proton affinities, as mentioned in the introduction to this chapter, and thus, the structures of the singly and doubly protonated siladibene cations $[\text{((S)IDipp)Si(H)(IiPr}_2\text{Me}_2)]^+$ (**A-9S+H⁺**, **A-9I+H⁺**) and $[\text{((S)IDipp)Si(H)}_2\text{(IiPr}_2\text{Me}_2)]^{2+}$ (**A-9S+2H²⁺**, **A-9I+2H²⁺**) were calculated (Figure 5.8). Their structural parameters, summarized in Table 5.5, confirm for the monocations a coordination of the proton at the $\pi(\text{Si}-\text{C}1)$ bond as evidenced by nearly orthogonal (HSi),(C1SiC2) bond-to-plane angles of 100.9° (**A-9S+H⁺**) and 99.1° (**A-9I+H⁺**) between the H–Si bond and the (C1SiC2) plane, as seen in previous protonation calculations.^[182] As a consequence, the $\pi(\text{Si}-\text{C})$ bond is lost, causing the Si–C1 bond to elongate to 191.8 and 193.0 pm for **A-9S+H⁺** and **A-9I+H⁺**, respectively, whereas the Si–C2 bond is rather unaffected (195.7 and 196.8 pm). Overall, the silicon atom is strongly pyramidalized with sum of angles of 297.2 and 293.3°, respectively.

The second protonation to the dications proceeds via the formation of a four-coordinated, tetrahedral silicon atom. Interestingly, the dications **A-9S+2H²⁺** and **A-9I+2H²⁺** show significantly shortened Si–C2 bond lengths of 188.5 and 188.8 pm compared to the neutral siladibenes (**A-9S**: 195.9 pm, **A-9I**: 194.3 pm) as well as a widening of the C1–Si–C2 bond angle from 99° to approximately 114° for both compounds. This effect is also observed for the Si–C1 bond of **A-9I+2H²⁺** which shortens to 189.0 pm upon the second protonation and can be rationalized by the loss of the mainly *s*-hybridized silicon electron lone pair in the dications and, after rehybridization, a higher *s*-character in the silicon-carbene bonds. As a result, the bonds shorten and the angle increases, in accordance with Bent's rule.^[152, 219]

Finally, the calculated first and second proton affinities provide further support for high silylone character in the here-studied siladibenes: The first PAs are close for both compounds with 1242.5 and 1262.5 $\text{kJ}\cdot\text{mol}^{-1}$ and agree well with the value of 1154.9 $\text{kJ}\cdot\text{mol}^{-1}$ calculated by G. Frenking *et al.* for the model siladibene $\text{Si}(\text{C}(\text{N}(\text{H})\text{CH})_2)_2$.^[182] The second PAs of 860.0 and 876.7 $\text{kJ}\cdot\text{mol}^{-1}$ are considerably higher than those calculated by Frenking *et al.* (697.8 $\text{kJ}\cdot\text{mol}^{-1}$)

in the same study and illustrate the high remaining nucleophilicity of the compounds even after a first protonation.

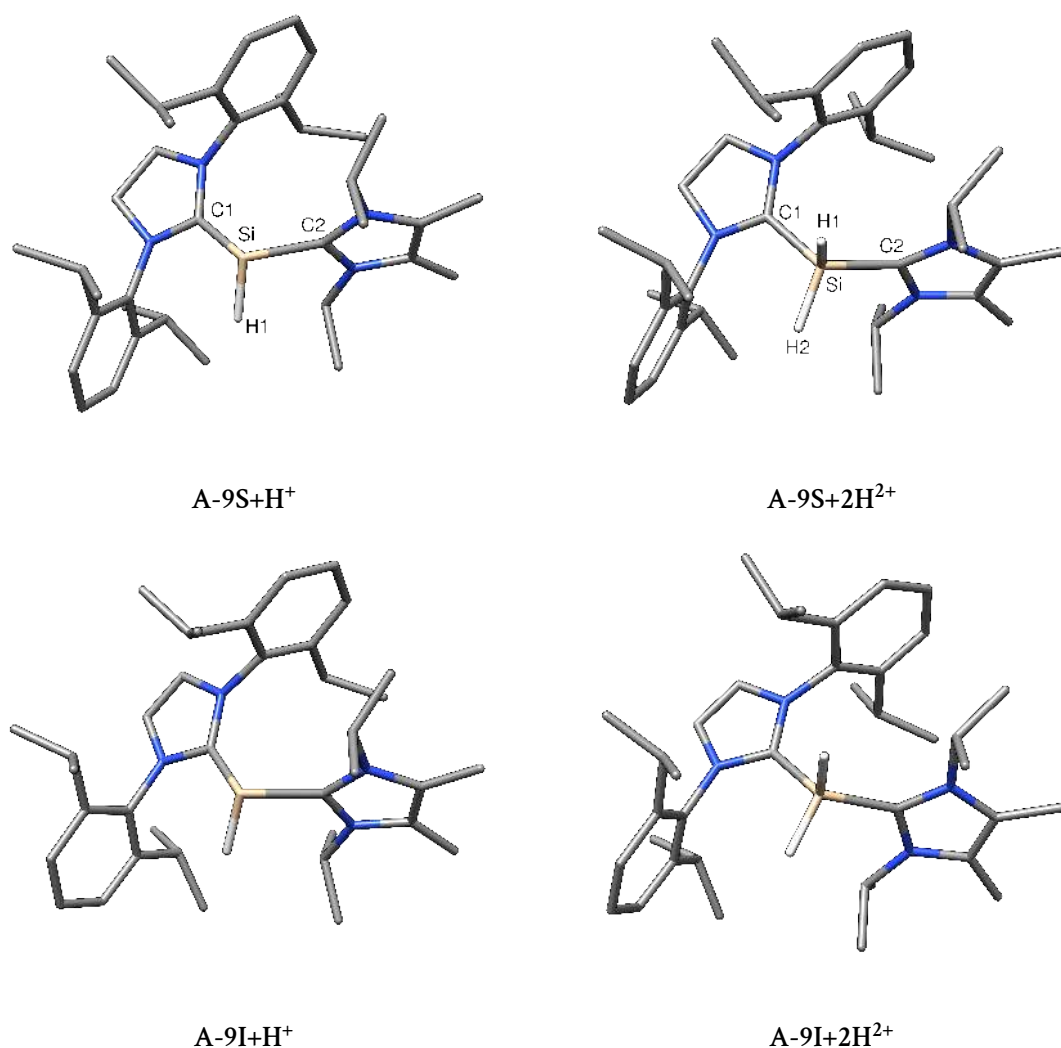


Figure 5.8: Optimized gas phase structures of the singly and doubly protonated siladiboranes.

Table 5.5: Structural parameters of the singly and doubly protonated siladiboranes A-9S+H⁺, A-9S+2H²⁺, A-9I+H⁺ and A-9I+2H²⁺. Bond lengths and angles are given in pm and degrees, respectively, and θ corresponds to the bending angle between the Si–H bond and the (C1SiC2) plane.

	Si–C1	Si–C2	Si–H	C1–Si–C2	$\Sigma\angle(\text{Si})$	θ
A-9S+H ⁺	191.8	195.7	150.7	103.8	297.2	100.9
A-9S+2H ²⁺	191.8	188.5	147.1	114.4	–	–
A-9I+H ⁺	193.0	196.8	151.0	102.0	293.3	99.1
A-9I+2H ²⁺	189.0	188.8	147.2	113.5	–	–

Stereodynamic Processes of the Siladibenes A-9S and A-9I

As mentioned above, one of the flanking Dipp groups of the (S)IDipp ligand and the iPr_2Me_2 carbene avoid each other by bending up and down off the (SiC1N1N2) plane, respectively, which results in axial chirality for the compounds A-9S and A-9I. If the view is aligned along the Si–C1 bond, a Newman projection can be applied to determine the absolute configuration (Figure 5.9). Other conceivable diastereomers were attempted to be calculated by bringing the Dipp group and the iPr_2Me_2 carbene on the same side, or by inverting the backbone in A-9S. However, none of those were observed to be stationary points on the PES, and their structure optimization directly led to one of the enantiomers.

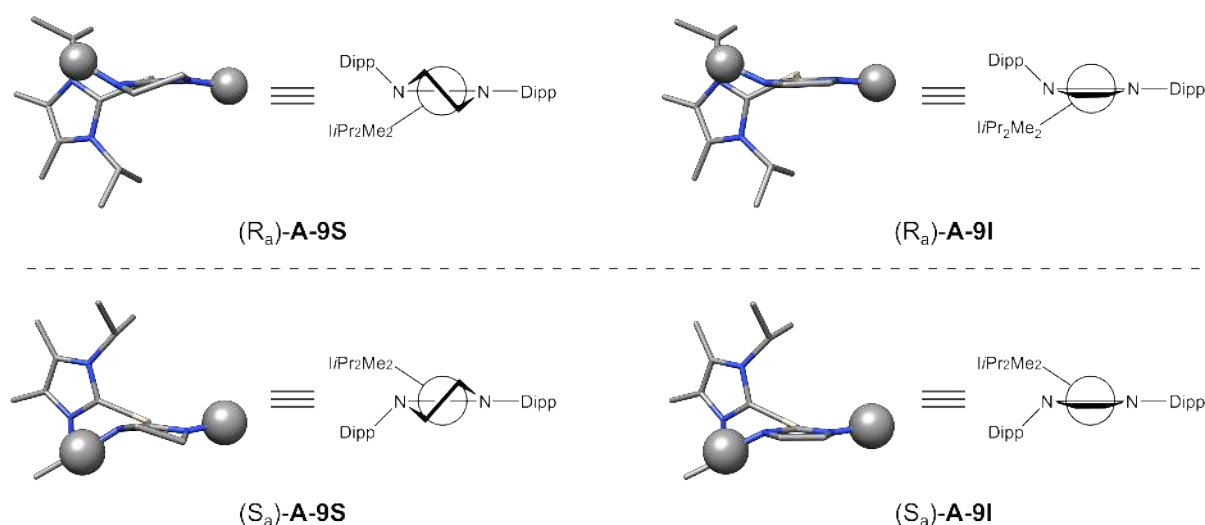


Figure 5.9: Newman-like projection of the siladibenes A-9S and A-9I along the Si–C1 bond axis to determine the absolute configuration of the axial isomers.

According to experimental VT-NMR spectroscopy, siladibenes A-9S and A-9I display stereodynamics in solution, showing three different processes:

- **Symmetrization:** At 203 K, the 1H -NMR spectrum of A-9S shows four septet signals for the isopropyl groups of the Dipp substituents, as well as two septet and four doublet signals for the isopropyl methine and methyl protons of the iPr_2Me_2 ligand, respectively. At the coalescence temperature of 243 K, these signals merge to two septet signals for the Dipp groups, and one septet and two doublet signals for the iPr_2Me_2 carbene. This cannot be explained by an individual process for each carbene (e.g. Si–C_{carbene} bond rotation), but rather a local time-averaged C_5 -symmetric structure is suggested above 243 K with an experimentally derived barrier of $\Delta G_{exp}^\ddagger = > 47.0(\pm 2.1) \text{ kJ}\cdot\text{mol}^{-1}$. For A-9I, this process is observed even at 203 K and could not be resolved, suggesting a lower barrier than in A-9S. It is conceivable that the interconversion of the axial enantiomers (R_a)-A-9I and (S_a)-A-9I may proceed via a C_5 -symmetric structure, in which both the Dipp group at the pyrami-

dalized nitrogen atom and the IiPr_2Me_2 ligand come into the (Si,C1,N1,N2) plane. This assumption is supported by an NEB calculation which affords a nearly C_S -symmetric maximum structure with a relative electronic energy of $53.3 \text{ kJ}\cdot\text{mol}^{-1}$, but three imaginary frequencies of $60i$, $47i$ and $29i \text{ cm}^{-1}$. The presence of three imaginary frequencies indicates three separate vibrations and thus no concerted symmetrization process due to a higher-order transition state. However, a closer analysis of the vibration modes reveals that all their corresponding trajectories describe similarly the desymmetrization of the molecule by bending the Dipp group at the N1 atom or the IiPr_2Me_2 carbene ring out of the symmetry plane. Despite several attempts, the separation of the imaginary frequencies via transition state optimizations was not successful, and a well-defined transition state for the symmetrization process could not be obtained. Similarly, only an estimate by the NEB method could be obtained for the symmetrization of compound A-9S with approx. $60 \text{ kJ}\cdot\text{mol}^{-1}$. The slightly higher energy compared to A-9I presumably results from the additional flip of the imidazolidine ring of the SIDipp ligand that is necessary to interconvert the axial enantiomers (R_a)-A-9S and (S_a)-A-9S (c.f. Figure 5.9).

- **Si–(S)IDipp bond rotation:** A rotation around the Si–(S)IDipp bond would be evident from NMR spectroscopy by a merging of the remaining two septet signals for the Dipp groups to only one signal. Such a process, however, was only observed for A-9I at a coalescence temperature of 313 K, but not for the Si– C_{SIDipp} bond in A-9S up to 373 K, and only a lowest-limit free Gibbs energy $\Delta G_{\text{exp}}^\ddagger$ of $> 78 \text{ kJ}\cdot\text{mol}^{-1}$ could be estimated. In contrast, the value for A-9I was obtained as $\Delta G_{\text{exp}}^\ddagger = 64.0(\pm 3.6) \text{ kJ}\cdot\text{mol}^{-1}$. To assess those values theoretically, PES scans of the N2–C1–Si–C2 torsion angle from 0° to 180° with an increment of 10° were carried out for both siladicalbenes (Figure 5.10). Almost symmetrical progressions are obtained with expected maxima at torsion angles of 90° and relative energies of 99.4 and $77.6 \text{ kJ}\cdot\text{mol}^{-1}$ for A-9S and A-9I, respectively. Subsequent frequency calculations yield no imaginary frequencies, thus showing that the found maxima points are intermediate points. Further calculations to find transition states near the intermediate maximum points were not successful. However, the calculated gas phase free Gibbs energies ΔG at level of theory II of 105.7 and $81.3 \text{ kJ}\cdot\text{mol}^{-1}$ for the intermediate points fit already reasonably well to the experimentally obtained rotation barriers $\Delta G_{\text{exp}}^\ddagger$, and more importantly, they show that the barrier for A-9S lies at higher energies than for A-9I.
- **Si– IiPr_2Me_2 bond rotation:** The third dynamic process was found to be the rotation of the IiPr_2Me_2 carbene around the Si–C2 bond, setting in at temperatures above 323 K according to NMR spectroscopy. The corresponding line shape analysis was carried out using VT- ^{13}C -NMR spectra due to a poor resolution of the region in question in the ^1H -NMR spectrum and yields an experimental $\Delta G_{\text{exp}}^\ddagger$ value of $80.8(\pm 6) \text{ kJ}\cdot\text{mol}^{-1}$ for compound A-9S. A respective experimental barrier for the IiPr_2Me_2 rotation in the siladicalbene A-9I was not obtained.

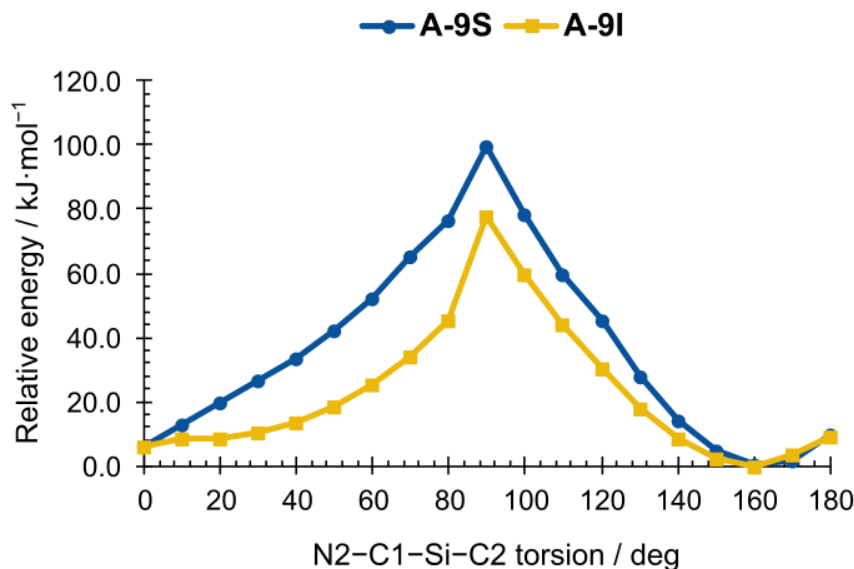


Figure 5.10: Potential energy surface scan of the N2–C1–Si–C2 torsion angle for the siladibenes A-9S and A-9I.

Unfortunately, the rotation could not be studied by PES scans of the C1–Si–C2–N3 torsional angle as this leads only to an artificial distortion of the molecule for both A-9S and A-9I. Instead, the rotation trajectory was modelled by the NEB method.

For A-9S, the NEB calculations successfully afforded one clear maximum point, which could subsequently be optimized to obtain the transition state A-9S-TS (Figure 5.11). It features a coplanar orientation of both carbene rings and has only one imaginary frequency at $36i\text{ cm}^{-1}$ whose vibrational trajectory correctly describes the rotation of the IiPr_2Me_2 carbene out of the C1–Si–C2 plane. The calculated relative energy at the level of theory I lies at $84.0\text{ kJ}\cdot\text{mol}^{-1}$ ($90.7\text{ kJ}\cdot\text{mol}^{-1}$ at the level of theory II), and the relative Gibbs free energy in the gas phase $\Delta G = 78.1\text{ kJ}\cdot\text{mol}^{-1}$ ($84.9\text{ kJ}\cdot\text{mol}^{-1}$ at the level of theory II) is nearly identical to the experimental barrier of $80.8(\pm 6)\text{ kJ}\cdot\text{mol}^{-1}$ in solution.

In contrast, the NEB calculations for A-9I proved to be less insightful and no optimized transition state could be obtained. From an NEB calculation at the level of theory I, the energetic barrier for the IiPr_2Me_2 carbene rotation is crudely estimated to be $100\text{ kJ}\cdot\text{mol}^{-1}$. This value is slightly higher than the calculated barrier of rotation for compound A-9S, which is due to its unoptimized character and the presumed slightly higher multiple bond character in the Si–C2 bond in A-9I as discussed above.

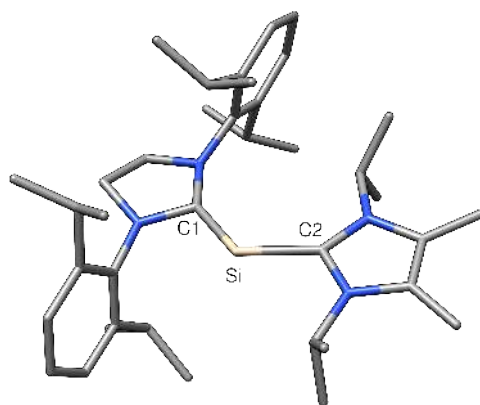
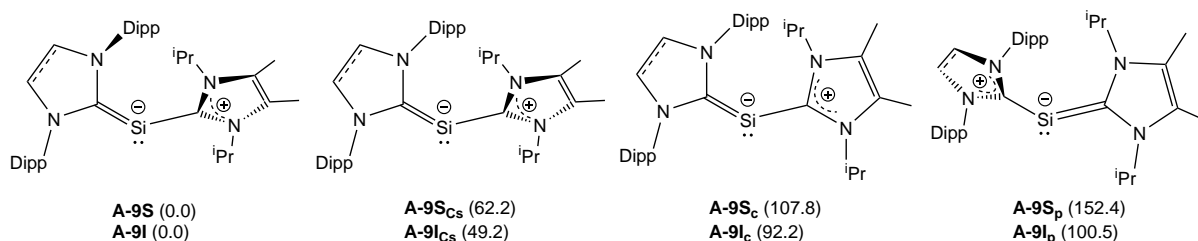


Figure 5.11: Optimized gas phase structure of the transition state **A-9S-TS** describing the IiPr_2Me_2 carbene rotation. Selected structural parameters: $\text{Si1}-\text{C1}$: 186.9 pm, $\text{Si}-\text{C2}$: 194.3 pm, $\text{C1}-\text{Si}-\text{C2}$: 121.3° , NHC interplanar twist angle τ : 6.3° .

Conceivable Conformers of Siladicalbenes **A-9S** and **A-9I**

The heteroleptic siladicalbenes **A-9S** and **A-9I** feature a distinct structure with C_1 -symmetry with one co-planar and one orthogonal NHC ligand relative to the $\text{C1}-\text{Si}-\text{C2}$ plane, as discussed above, and a slightly pyramidal N1 nitrogen atom. The rigidity of this conformer was further studied by calculating other conceivable conformers of the minimum structures, depicted in Scheme 5.7. None of the higher-energy conformers appeared to be minimum structures, hence Gaussian03^[148]-ORCA4-coupled structure optimizations with fixed molecular C_S -symmetry were carried out.



Scheme 5.7: Lewis structures of various calculated conformers of the siladicalbenes **A-9S** and **A-9I** and their relative energies in $\text{kJ}\cdot\text{mol}^{-1}$ at the level of theory II.

The symmetrization of the C_1 -symmetric minimum structures to molecular C_S -symmetry yields the conformers **A-9S_{C_S}** and **A-9I_{C_S}**, which are 62.2 and 49.2 $\text{kJ}\cdot\text{mol}^{-1}$ higher in energy than the minimum structures (at level of theory II). The analysis of their structural parameters, summarized in Table 5.6, shows a slight increase in the $\text{Si}-\text{C1}$ and $\text{Si}-\text{C2}$ bond lengths to 184.3 and 197.9 pm (**A-9S_{C_S}**) and 184.4 and 197.7 pm (**A-9I_{C_S}**) as well as for the $\text{C1}-\text{Si}-\text{C2}$ bond angles to 112.2 and 111.8° . These changes are attributed to the increased steric repulsion between the now closer-aligned IiPr_2Me_2 carbene and the flanking Dipp group of the (S)IDipp ligand. The slight energy differences between **A-9S_{C_S}** and **A-9I_{C_S}** can be explained by the additional energy that is necessary to planarize the SIDipp imidazoline backbone in **A-9S_{C_S}**.

Of particular interest are the structures **A-9S_c** and **A-9I_c**, where both carbenes are forced to become perfectly coplanar, as evidenced by their interplanar twist angles of 0°. This also leads to a considerable increase of the Si–C1 bond length and the C1–Si–C2 bond angle (**A-9S_c**: 188.6 pm, 125.7°; **A-9I_c**: 189.6 pm, 124.6°), whereas the Si–C2 bond length is marginally decreased by less than 1 pm.

The IBO analysis of the coplanar structures now yields three-centered $\pi(\text{C1-Si-C2})$ orbitals with significantly increased orbital coefficients on the C2 atom of 0.15 and 0.17 compared to 0.04 and 0.05 in the ground-state structures (Figure 5.12). This is accompanied by a decrease of the C1 coefficient to 0.26 and 0.25, respectively, which weakens the Si–C1 bond and explains the bond elongation together with the increased steric repulsion between the carbenes. However, as the (S)IDipp carbene is a better π -acceptor than the *i*Pr₂Me₂ carbene, the higher coefficient is still found on the C1 atom. Also, the increased sterical repulsion between the carbenes is counteracted by the C1–Si–C2 bond angle widening of ca. 25° (see Table 5.6), which is unfavoured as this decreases the desired high *s*-character in the lone pair orbital at the silicon atom according to Bent's rule. As a result, the coplanar conformers **A-9S_c** and **A-9I_c** are energetically highly unfavoured with +107.8 and +92.2 kJ·mol⁻¹ compared to their minimum structures.

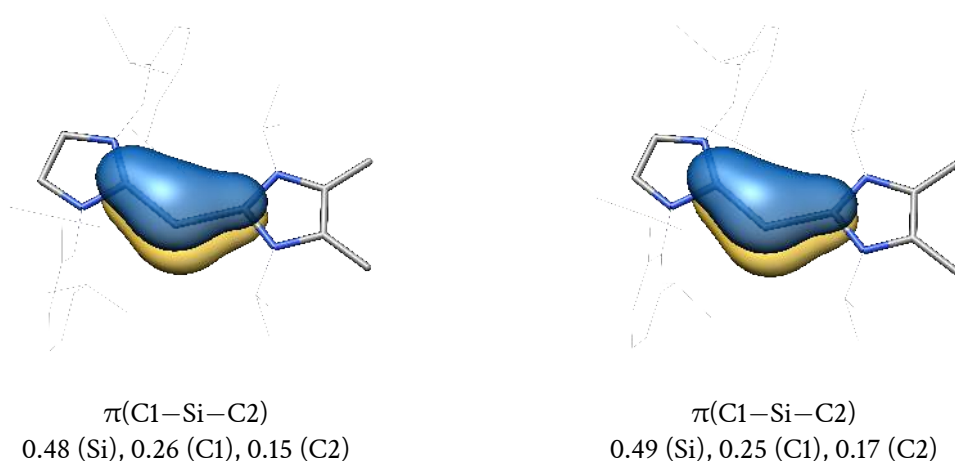


Figure 5.12: $\pi(\text{C1-Si-C2})$ IBOs of the coplanar conformers **A-9S_c** (left) and **A-9I_c** (right) and their Loewdin orbital populations.

The difference in the π -acceptor capabilities between the *i*Pr₂Me₂ and (S)IDipp carbenes can further be assessed by calculating the inverse-planar structures **A-9S_p** and **A-9I_p**, where the *i*Pr₂Me₂ ligand is coplanar to the C1–Si–C2 plane and the (S)IDipp ligand orthogonal. This arrangement interchanges the observed Si–C1 and Si–C2 bond lengths (**A-9S_p**: 193.6 pm, 184.4 pm; **A-9I_p**: 194.1 pm, 185.2 pm) and leads to a widening of the C1–Si–C2 bond angle to 115.7 and 116.4°, respectively, but is associated with a large increase of energy (152.4 and 100.5 kJ·mol⁻¹).

Table 5.6: Selected bond lengths and angles in pm and degrees, respectively, of various calculated conformers of the siladicarbenes **A-9S** and **A-9I**. τ corresponds to the interplanar twist angle between the two NHC central ring planes.

	Si–C1	Si–C2	C1–Si–C2	τ
A-9S	182.2	195.9	98.9	94.6
A-9S_{Cs}	184.3	197.9	112.2	90.0
A-9S_c	188.6	195.7	125.7	0.0
A-9S_p	193.6	184.4	115.7	90.0
A-9I	183.8	194.3	99.1	87.1
A-9I_{Cs}	184.4	196.7	111.8	90.0
A-9I_c	189.6	193.7	124.6	0.0
A-9I_p	194.1	185.2	116.4	90.0

Reactivity of the Siladicarbene **A-9S** towards Lewis Acids

The nucleophilicity of the compound **A-9S** was assessed by its reaction with several main-group and transition metal Lewis acids, and the monoadducts (SIDipp)Si(L)(iPr₂Me₂) could be characterized experimentally, where L = AlMe₃ (**A-9S-AlMe₃**), AlMes₂Br (**A-9S-AlMes₂Br**), GeCl₂ (**A-9S-Ge**), Fe(CO)₄ (**A-9S-Fe**), CpCo(C₂H₄) (**A-9S-Co**) and CuCl (**A-9S-Cu**).^[150] These were calculated as well as the gas phase structures of two more adducts (L = BH₃ (**A-9S-BH₃**) and AlH₃ (**A-9S-AlH₃**)) without their experimental structure available.

The structural parameters of the Lewis acid-adducts, provided in Table 5.7, show a good agreement between the calculated and experimental sc-XRD structures, however, with larger differences of several pm for the Si–C1 bond in **A-9S-Fe**, **A-9S-Co** and **A-9S-Ge**, and the Si–L bond for all complexes. In all cases except for **A-9S-Fe**, a shorter Si–L bond in the solid-state structures is observed. The elongation of donor-acceptor bonds in the gas phase is an effect which was already discussed in a comparative solid state versus gas phase study of other Lewis acid-base adducts by G. Frenking *et al.* in the year 1994.^[220]

Overall, the following structural trends are observed for the herein calculated adducts:

- The smaller Lewis acids coordinate the silicon atom out of the (C1SiC2) plane, as evidenced by (L–Si),(C1SiC2) bending angles of 44.2° (**A-9S-AlH₃**), 46.8° (**A-9S-BH₃**), 55.0° (**A-9S-Cu**) or 56.3° (**A-9S-Ge**), whereas larger adducts adopt an approximately trigonal-planar structure around the silicon atom with (L–Si)(C1SiC2) bending angles below 32°. In the former case, the silicon atom is considerably pyramidalized ($\Sigma\angle(\text{Si}) = 321$ to 334°), indicating the presence of an electron lone pair at the silicon atom with high s-character. On the other hand, larger Lewis acids result in an approximately trigonal-planar environment around the silicon atom ($\Sigma\angle(\text{Si}) = 348$ to 360°), which is counterintuitive as the HOMO of **A-9S** contains the $\pi(\text{Si}-\text{C1})$ bond and favours the out-of-plane coordination in heavier

tetreladibcarbenes.^[182–184] The adduct of **A-9S** with the smallest Lewis acid possible, a naked proton (**A-9S+H⁺**, *vide supra*), features precisely such an orthogonal placement of the proton on the (C1SiC2) plane and a highly pyramidalized silicon atom ($\Sigma\angle(\text{Si}) = 297.2^\circ$). This further underlines the sterical hindrance of the Lewis acid as determining factor of the position. In fact, only one other example of a planar tetreladitetrylene Lewis acid-base complex is known, which is the sterically crowded 9-borabicyclo[3.3.1]nonane (9-BBN) adduct of a germa-disilylene reported by M. Driess *et al.* in 2019.^[212]

- The Si–C1 bond lengths are quite similar for most adduct complexes compared to the parent siladibcarbene **A-9S** (182.2 pm), e.g. in **A-9S-BH₃** (183.9 pm) or **A-9S-Fe** (183.1 pm). Interestingly, the bond shortens in the cobalt adduct **A-9S-Co** to 179.1 pm (sc-XRD: 176.8(5) pm) and is found to be the shortest Si–C_{NHC} bond to date according to a Cambridge Crystallographic Data Centre (CCDC) search.
- The C1–Si–C2 angle widens slightly for all adducts from 98.9° to 101.5 – 108.4°, presumably to account for the increased sterical repulsion due to a third substituent at silicon.
- The calculated energies and free Gibbs energies of adduct formation ΔE and ΔG reveal a generally favoured reaction for all studied siladibcarbene Lewis acid base pairs. The energies range from $-117.6 \text{ kJ}\cdot\text{mol}^{-1}$ (**A-9S-AlMe₃**) to $-289 \text{ kJ}\cdot\text{mol}^{-1}$ (**A-9S-Cu**) for ΔE and from $-49.3 \text{ kJ}\cdot\text{mol}^{-1}$ (**A-9S-AlMe₃**) to $-233.8 \text{ kJ}\cdot\text{mol}^{-1}$ (**A-9S-Cu**).

Table 5.7: Selected structural parameters of the calculated and experimental Lewis acid adducts **A-9S-L** of the siladibcarbene **A-9S** as well as calculated energies ΔE and free Gibbs energies ΔG of adduct formation. The atom labelling follows that of the siladibcarbene **A-9S**, *L* is defined as the coordinating atom of the Lewis acid. Bond lengths and angles are given in pm and degrees, respectively, and energies in $\text{kJ}\cdot\text{mol}^{-1}$. θ corresponds to the bending angle between the Si–L bond and the (C1SiC2) plane.

	Si–C1	Si–C2	Si–L	C1–Si–C2	$\Sigma\angle(\text{Si})$	θ	ΔE	ΔG
A-9S-BH₃	183.9	195.2	206.6	102.4	331.9	46.8	–161.3	–106.8
A-9S-AlH₃	183.6	193.9	255.2	102.9	334.0	44.2	–152.7	–95.9
A-9S-AlMe₃	181.1	193.0	260.5	103.9	355.8	16.2	–117.6	–49.3
A-9S-AlMe₃exp	180.6(3)	192.8(3)	255.61(12)	104.64(12)	356.5	15.1		
A-9S-AlMe₂Br	181.8	192.1	260.8	102.8	356.2	15.1	–155.4	–65.6
A-9S-AlMe₂Br_{exp}	180.0(5)	192.7(5)	256.8(2)	103.4(2)	357.3	12.9		
A-9S-Ge	185.8	194.4	260.8	101.5	321.0	56.3	–193.6	–128.2
A-9S-Ge_{exp}	189.2(4)	194.6(4)	252.08(12)	99.50(17)	309.8	65.4		
A-9S-Fe	183.1	194.6	237.3	108.4	347.9	31.1	–280.0	–195.8
A-9S-Fe_{exp}	179.4(3)	192.8(3)	233.00(9)	106.23(12)	352.6	23.6		
A-9S-Co	179.1	194.1	218.0	103.6	360.0	1.7	–173.4	–93.5
A-9S-Co_{exp}	176.8(5)	193.3(6)	220.08(18)	105.9(2)	359.4	6.5		
A-9S-Cu	184.6	195.3	224.0	102.7	324.6	55.0	–289.4	–233.8
A-9S-Cu_{exp}	183.8(3)	193.1(3)	222.39(8)	102.50(12)	330.4	49.6		

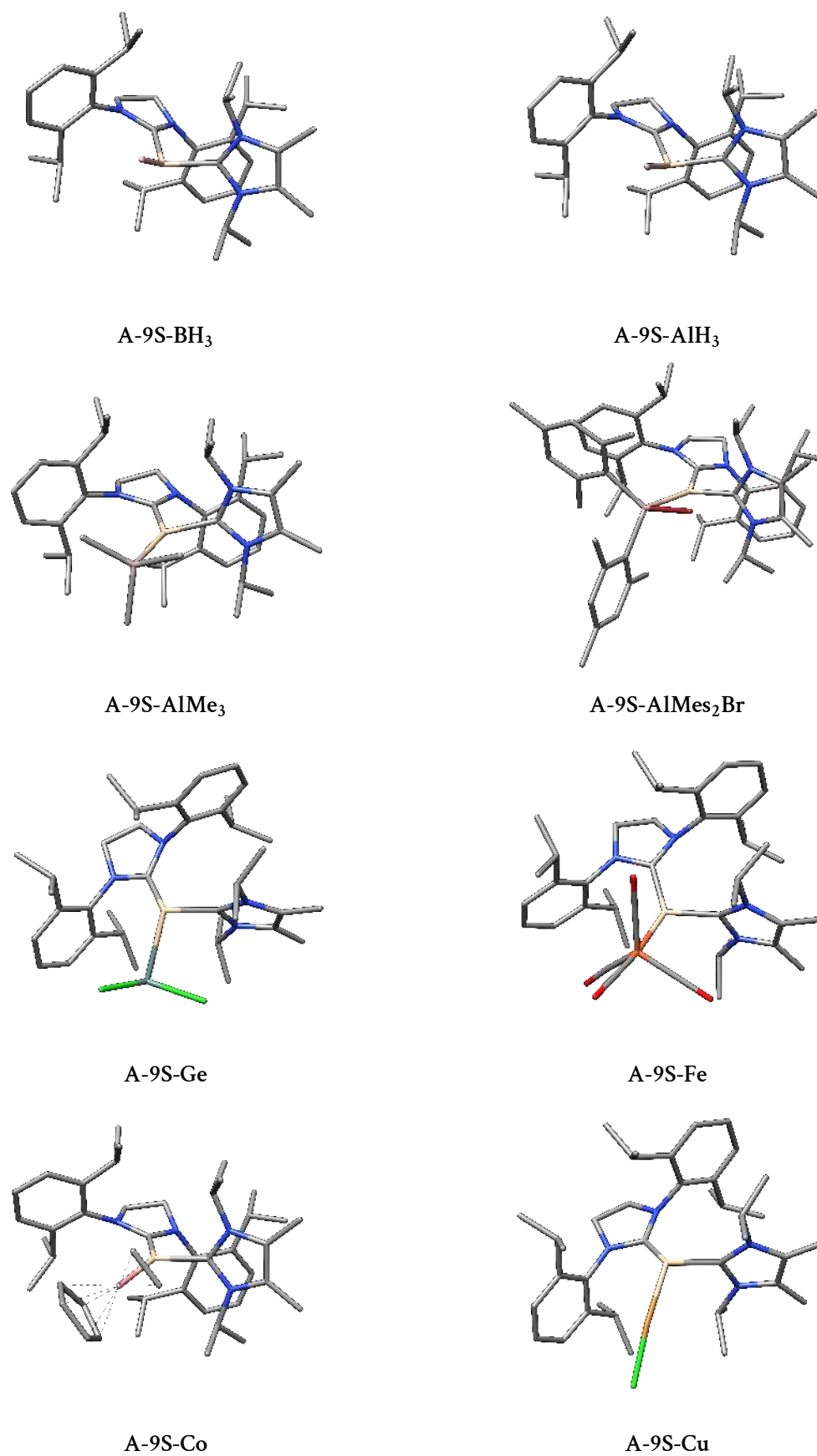


Figure 5.13: Optimized gas phase structures of all Lewis acid adducts of the siladiborane A-9S.

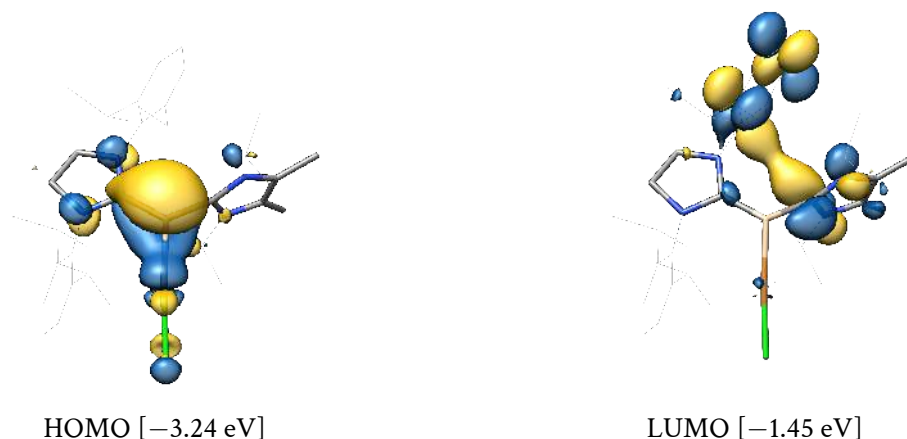


Figure 5.14: Selected canonical MOs of A-9S-Cu and their energetic eigenvalues.

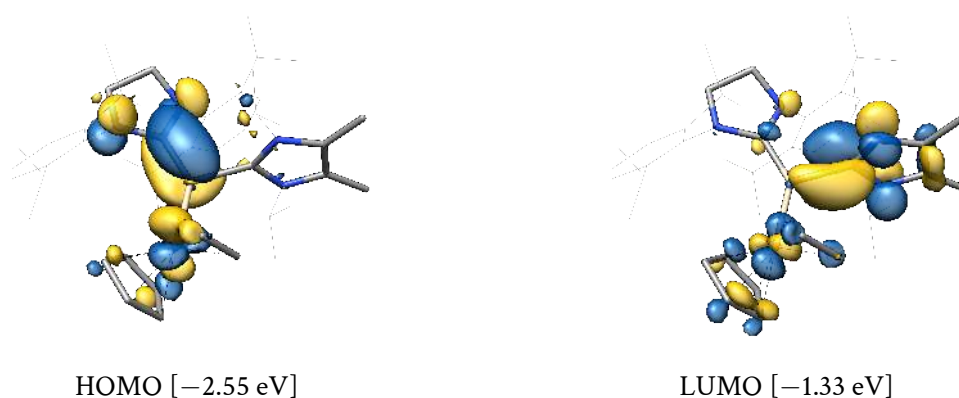


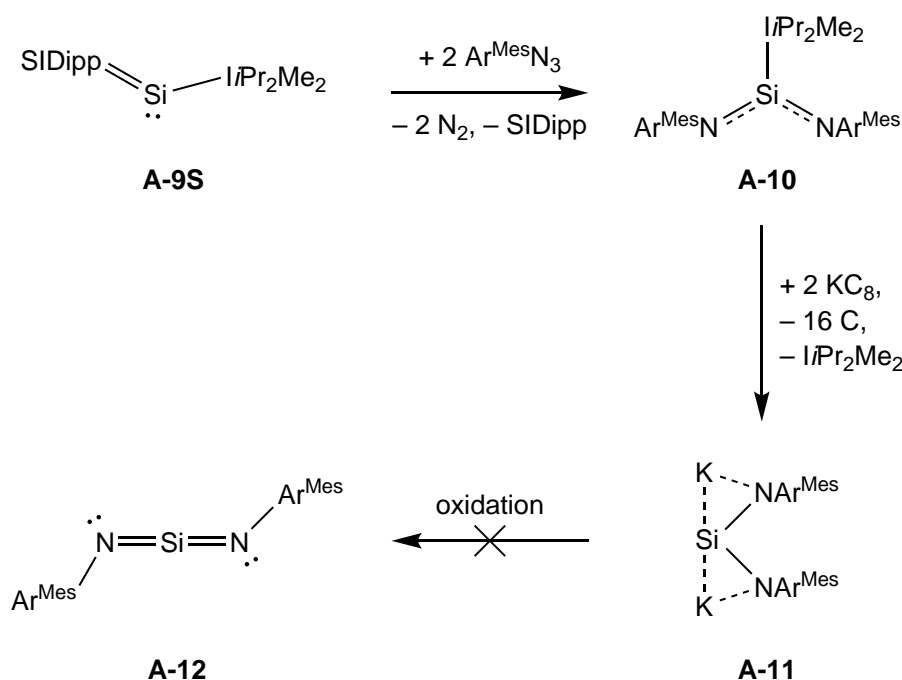
Figure 5.15: Selected canonical MOs of A-9S-Co and their energetic eigenvalues.

The compounds A-9S-Cu and A-9S-Co were studied in more detail, and Figures 5.14 and 5.15 depict their selected canonical MOs. The HOMO of the adduct A-9S-Cu prominently displays a remaining electron lone pair at the silicon atom (41 %), which is slightly π -delocalized into the C1 (11 %) atom according to a Löwdin population analysis. The LUMO is not silicon-centered but shows the unoccupied $\pi^*(\text{N3}-\text{C2}-\text{N4})$ orbital of the IiPr_2Me_2 carbene besides some Dipp aryl orbital density.

The frontier orbitals of A-9S-Co display a pronounced $\pi(\text{Si}-\text{C1})$ interaction in the HOMO, which is responsible for the drastic bending of the SIDipp Dipp groups, and IiPr_2Me_2 orbital density in the LUMO.

5.3. Reactivity with Azides: Access to (NHC)-stabilized Siladiimides

Experimentally, compound **A-9S** reacts with two equivalents of the azide $\text{Ar}^{\text{Mes}}\text{N}_3$ under loss of the larger carbene SIDipp and dinitrogen to the NHC-stabilized siladiimide $(\text{I}i\text{Pr}_2\text{Me}_2)\text{Si}(\text{NAr}^{\text{Mes}})_2$ (**A-10**, Scheme 5.8), which can further be reduced under NHC cleavage to the bis(amido)silylene $\text{K}_2[\text{Si}(\text{NAr}^{\text{Mes}})_2]$ (**A-11**). However, the final oxidation of the dianion salt **A-11** to the neutral, NHC-free siladiimide $\text{Si}(\text{NAr}^{\text{Mes}})_2$ (**A-12**) was not successful so far and only resulted in an unselective mixture according to *in-situ* $^1\text{H-NMR}$ spectroscopy.^[150]



Scheme 5.8: Reaction sequence from the siladycarbene **A-9S** to the hypothetical NHC-free siladiimide **A-12** via the experimentally accessible NHC-stabilized siladiimide **A-10** and bis(amido)silylene **A-11**.

The literature search reveals that siladiimides are a less known class of compounds. C. Thomson and C. Glidewell calculated in 1983 the relative stabilities of the isomers of CH_2N_2 and SiH_2N_2 .^[221] Their calculations of HNSiNH at the HF/3-21G level of theory afforded a linear $\text{N}=\text{Si}=\text{N}$ moiety, which is planar and has a *trans*-arrangement of the NH group (C_{2h} symmetry). When they recalculated the structure with the semi-empirical MNDO method, a C_{2v} -symmetric structure with an $\text{N}-\text{Si}-\text{N}$ angle of only 117° was obtained. In the year 1987, the group of R. West could confirm the existence of free $\text{Si}(\text{NSiMe}_3)_2$ by UV/vis spectroscopy and trapping experiments in a low-temperature matrix.^[222] Shortly after, M. S. Gordon *et al.* reported the molecular and electronic structure of siladiimides and other allenic $\text{X}=\text{Y}=\text{X}$ compounds and also obtained a C_{2h} -symmetric structure at the HF/6-31G(d) level of theory. However, when electron correlation treatment via the MP2 method is included, a C_s -symmetric structure with a non-linear $\text{N}=\text{Si}=\text{N}$

moiety (156.9°) and non-coplanar hydrogen atoms (HNNH torsion angle = -89°) was obtained, lying ca. $8 \text{ kJ}\cdot\text{mol}^{-1}$ lower in energy than the C_{2h} -symmetric conformer.^[223] A combined matrix-spectroscopic and DFT study of the $[\text{H}_2\text{SiN}_2]$ system by G. Maier *et al.* in the year 2006 found the siladiimide approximately $52 \text{ kJ}\cdot\text{mol}^{-1}$ higher in energy than the silylene-nitrogen complex $[\text{H}_2\text{Si}\cdot\text{N}_2]$.^[224] Advanced CCSD(T)/aug-cc-pV(T+d)Z calculations by D. A. Dixon *et al.* yield a C_2 -symmetric structure with a non-linear N–Si–N unit (the exact value was not specified) and a HNNH torsion angle of -83° .^[225] Several cyclic siladiimides $\text{Si}(\text{N}(\text{CH}_2)_n\text{N})$ ($n = 2$ to 9) were studied by R. Damrauer in the year 2015, with the focus lying on the transition state search between torsional conformers.^[226] Finally, the group of C.-W. So achieved the isolation of the room-temperature stable, NHC-stabilized siladiimide (IDipp)Si(NDipp)₂ (A-XVI) in the year 2016,^[227] being very similar to compound A-10.

The calculated structure of A-10 is very close to that obtained by sc-XRD analysis and features a trigonal planar silicon atom ($\Sigma \angle(\text{Si}) = 360^\circ$) and a IiPr_2Me_2 ligand that is tilted with respect to the $(\text{NSiC}_{\text{NHC}}\text{N})$ plane as evidenced by the $(\text{IiPr}_2\text{Me}_2),(\text{N1SiC}_{\text{NHC}}\text{N2})$ interplanar twist angle of 31.5° . Compared to the calculated structure of compound A-XVI (60.3°), the smaller IiPr_2Me_2 ligand is significantly more coplanarly oriented in the present compound A-10, which suggests some degree of multiple bond character for the Si–C_{NHC} bond. This is further underlined by the shortened Si–C_{IiPr₂Me₂} bond (191.9 pm) compared to the siladibenes A-9S and A-9I with 195.9 and 194.3 pm, which is, however, identical to that of compound A-XVI (192.0 pm). The NHC-stabilized siladiimide A-10 shows a bent N–Si–N core, revealed by both theory (132.1°) and sc-XRD experiment ($129.7(1)^\circ$), which is slightly narrower than in A-XVI (148.4°) that employs the larger Dipp groups at the carbene and imide substituents. The short Si–N bond lengths of 159.7 pm lie in between the sum of Pyykkö double (167 pm) and triple (156 pm) bond radii^[228] and suggest multiple bond character within the siladiimide unit, which could be confirmed by a subsequent MO analysis (*vide infra*). Noteworthy, compound A-10 adopts an anticlinal C1–N1–N2–C2 conformation (-149.0°) of the imide groups in contrast to A-XVI (-17.1°).

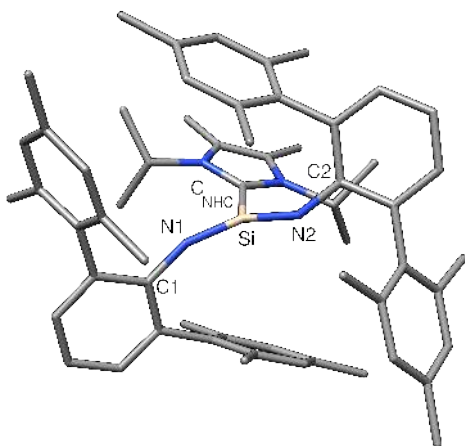


Figure 5.16: Calculated gas phase structure of the IiPr_2Me_2 -stabilized siladiimide A-10.

Table 5.8: Selected bond parameters of the calculated and experimental sc-XRD structures of NHC-stabilized siladiimides A-10 as well as of A-XVI from ref. [227]. Mean bond lengths and angles are given in pm and degrees, respectively, and τ corresponds to the (NHC),(N1SiC_{NHC}N2) interplanar twist angle between the central NHC ring and (N1SiC_{NHC}N2) planes.

	Si–C _{NHC}	Si–N	N–C	N1–Si–N2	C1–N1–N2–C2	$\Sigma\angle(\text{Si})$	τ
A-10	191.8	159.7	135.5	132.1	–149.0	360.0	31.5
A-10 _{exp}	191.3(2)	159.1(2)	136.5(2)	129.7(1)	–157.6(3)	360.0(1)	32.3(1)
A-XVI ^{a)}	192.0	160.6	137.9	148.4	–17.1	359.8	60.3
A-XVI _{exp}	188.9(6)	159.3(1)	138.2(7)	147.6(2)	25.9(6)	360.0(2)	58.8(2)

a) at the B3PW91/6-31G* level of theory.

The inspection of the molecular orbitals of A-10 (Figure 5.17) reveals a weak $\pi_{\text{oop}}(\text{Si}-\text{C}_{\text{NHC}})$ bond interaction (HOMO–14) with only small orbital lobes at silicon, a $\pi_{\text{oop}}(\text{N}-\text{Si}-\text{N})$ bond (HOMO–13) and several MOs with lone pair density at the imide nitrogen atoms (HOMO–2, HOMO–1, HOMO).

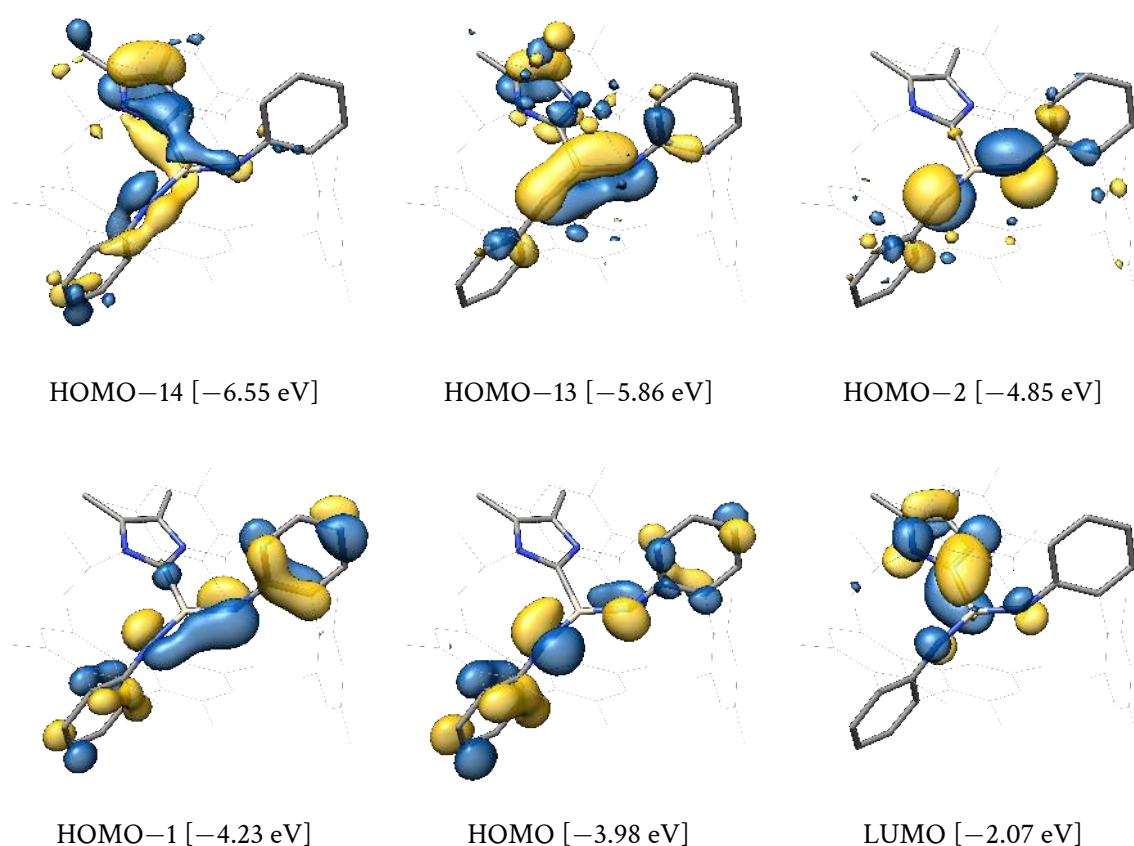
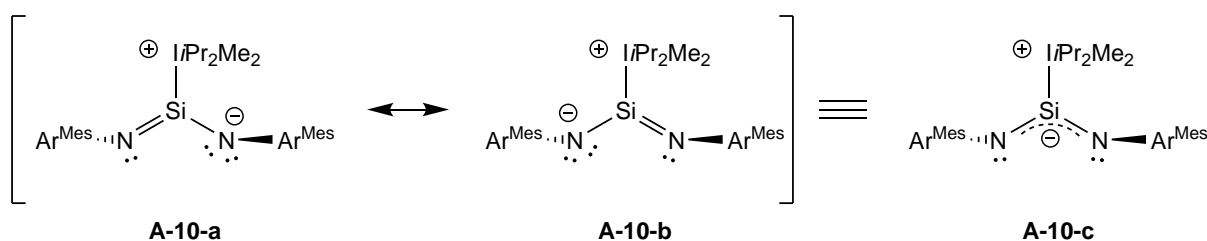


Figure 5.17: Selected canonical MOs of the IiPr₂Me₂-stabilized siladiimide A-10 and their energetic eigenvalues.

Further insight into the electronic structure of compound A-10 is provided by an IBO analysis that reveals three σ -type IBOs and four nitrogen lone pair orbitals for the core unit (Figure 5.18). The $\sigma(\text{Si}-\text{C}_{\text{NHC}})$, $\sigma(\text{Si}-\text{N1})$ and $\sigma(\text{Si}-\text{N2})$ IBOs are polarized towards the more electronegative car-

bon (58 %) and nitrogen atoms (58 %), respectively, with Loewdin orbital populations at the silicon atom of ca. 35 %. The two electron lone pairs on each nitrogen atom are found to be delocalized towards the silicon atom (16 to 19 %), establishing weak $\pi(\text{Si}-\text{N})$ bonding interactions. Notably, no $\pi(\text{Si}-\text{C}_{\text{NHC}})$ -type interaction was found in the IBOs, underlining that the Si–C interaction of HOMO–14 is rather weak.

As a conclusion, it is suggested that the bond situation in **A-10** can be described by the two resonance formulas **A-10-a** and **A-10-b** (Scheme 5.9), that were also proposed by C.-W. So *et al.* in their study of compound **A-XVI**,^[227] and can be summarized by the general Lewis formula **A-10-c** with a 3-center-4-electron hyperbond. A more quantitative consideration of the resonance hybrid in terms of a NRT calculation was attempted, however both a full NRT calculation and one with a local NRT atom subset failed due to technical problems.



Scheme 5.9: Most dominant Lewis structures of the NHC-stabilized siladiimide **A-10**.

The bond dissociation energy of the IiPr_2Me_2 carbene in **A-10** was calculated to cost $250 \text{ kJ}\cdot\text{mol}^{-1}$, and, when considering the entropic contribution, the bond dissociation free Gibbs energy amounts only to $158 \text{ kJ}\cdot\text{mol}^{-1}$ and is thus only slightly higher than in the siladibenes (**A-9S**: $134.5 \text{ kJ}\cdot\text{mol}^{-1}$, **A-9I**: $118.6 \text{ kJ}\cdot\text{mol}^{-1}$). Both the carbene and the siladiimide fragments have a singlet ground state with large singlet-triplet gap energies $\Delta E_{s\rightarrow t} = 365.1$ and $103.9 \text{ kJ}\cdot\text{mol}^{-1}$, respectively, but different structural relaxation energies (SRE) of only $-15 \text{ kJ}\cdot\text{mol}^{-1}$ for IiPr_2Me_2 and $-99.7 \text{ kJ}\cdot\text{mol}^{-1}$ for the $\text{Si}(\text{NAr}^{\text{Mes}})_2$ fragment. The large value of the latter indicates that the structure of the free siladiimide differs significantly from that of the NHC-stabilized compound **A-10**.

The bond dissociation of one NAr^{Mes} group (one Si–N bond) lies much higher in energy ($BDE = 422.7 \text{ kJ}\cdot\text{mol}^{-1}$, $BDG = 306.8 \text{ kJ}\cdot\text{mol}^{-1}$) and yields the $(\text{IiPr}_2\text{Me}_2)\text{Si}(\text{NAr}^{\text{Mes}})$ and NAr^{Mes} fragments in their singlet and triplet ground state, respectively. Although the structure optimization of the latter in the singlet state shows an activation of the adjacent C_{ortho} atom of the central Ar^{Mes} phenyl ring by the nitrogen atom to an azirine, by which the singlet state is artificially lowered in energy, the triplet state is still favoured by $21.7 \text{ kJ}\cdot\text{mol}^{-1}$ over the singlet state of the bond-activated fragment.

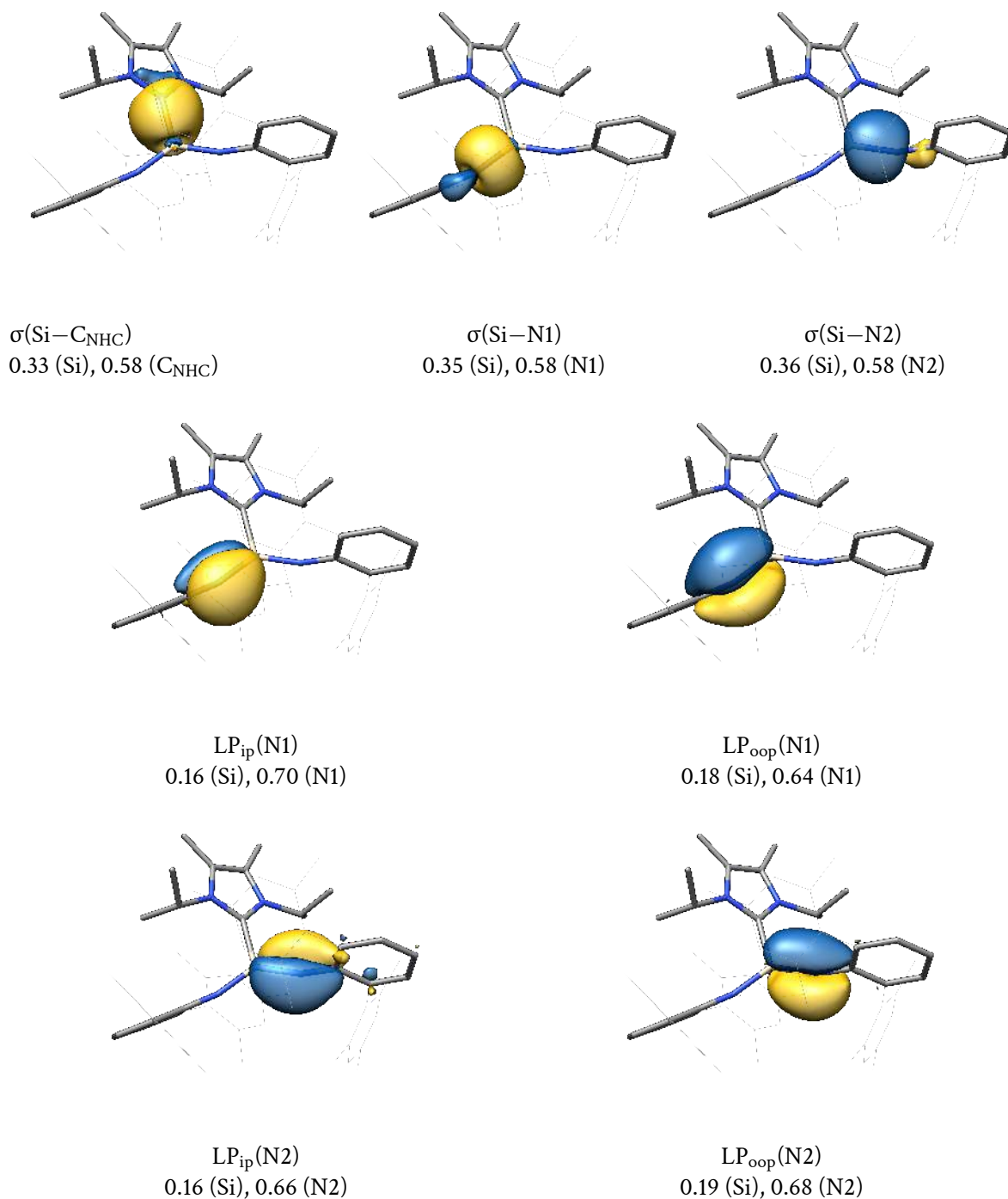


Figure 5.18: Selected IBOs of the iPr_2Me_2 stabilized siladiimide A-10 and their atomic Löwdin orbital populations.

Table 5.9: Level of theory II-calculated bond cleavage (*BCE*) and bond dissociation energies (*BDE*) for the Si–C_{IiPr₂Me₂} and Si–N cleavages. Energies in kJ·mol⁻¹, entropies in J·K⁻¹·mol⁻¹, s = singlet, t = triplet multiplicity.

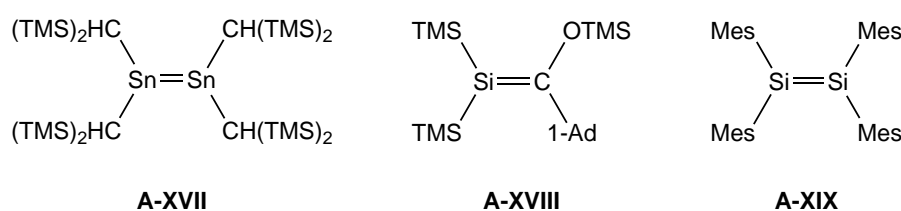
	<i>BCE</i>		<i>BDE</i> (parent → IiPr ₂ Me ₂ + Si(NAr ^{Mes}) ₂)				
	ΔE	mult	ΔE	ΔU	ΔH	ΔS	ΔG
IiPr ₂ Me ₂ cleavage	365.6 (s)	(s → s, s)	250.5	229.1	231.6	246.7	158.0
			<i>BDE</i> (parent → (IiPr ₂ Me ₂)Si(NAr ^{Mes}) + NAr ^{Mes})				
NAr ^{Mes} cleavage	635.5 (s)	(s → s, t)	422.7	400.1	402.5	321.1	306.8
	620.2 (t)						

6. CAAC-stabilized Heavier Ditetrelynes and Ditetrelenylenes

6.1. Introduction

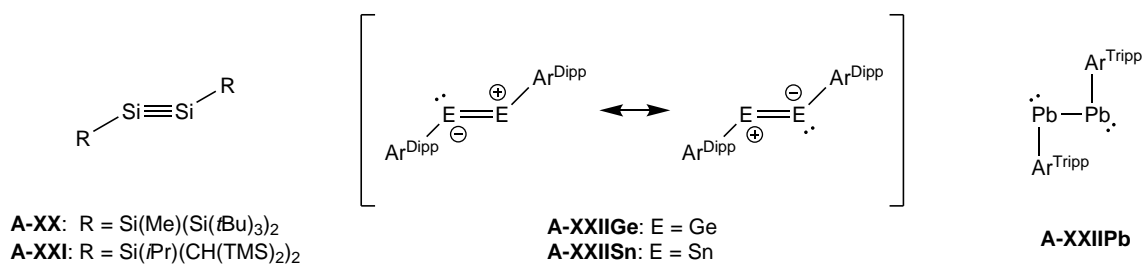
The empirically found *double bond rule*^[229–232] was valid until about the year 1980 and stated the inability of elements of the third and higher periods to form multiple bonds. In low-valent group 14 tetrel chemistry, famous *rule breakers* comprise the isolable distannene $(\text{TMS}_2\text{CH})_2\text{Sn}=\text{Sn}(\text{CHTMS}_2)_2$ (A-XVII) by M. F. Lappert *et al.* in 1973^[233] (the proof for the dimeric solid state structure followed in 1976),^[234] the silene $(\text{TMS})_2\text{Si}=\text{C}(\text{OTMS})$ (1-Ad) (A-XVIII)^[235] by A. G. Brook *et al.* and the disilene $(\text{Mes})_2\text{Si}=\text{Si}(\text{Mes})_2$ (A-XIX) by R. West *et al.* in the year 1981 (Scheme 6.1).^[236, 237] These compounds feature a E=E double bond (E being a tetrel atom) and are followed by myriads of derivatives and analogues, also for group 13 and group 16 elements.^[238]

Noteworthy, M. F. Lappert *et al.* also succeeded in the isolation of the first heavier tetrel transition metal double bond in form of the chromium stannylidene complex $[\text{Cr}(\text{CO})_5\text{Sn}(\text{CH}(\text{TMS})_2)_2]$ already in 1974,^[239] which also violates the *double bond rule*.



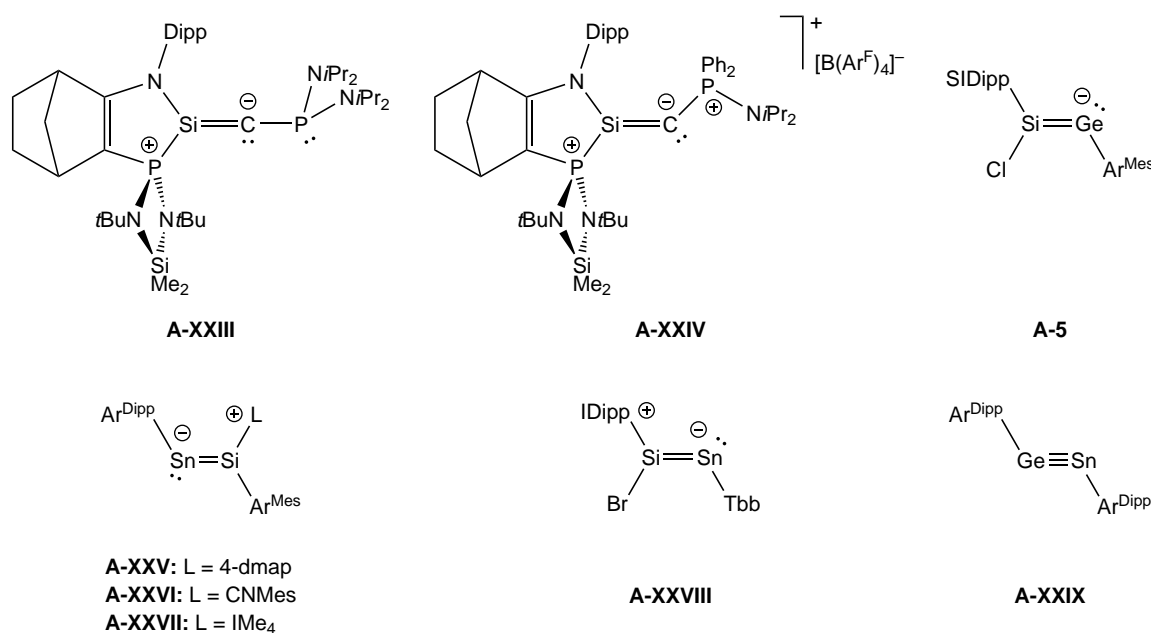
Scheme 6.1: The first literature-reported heavier ditetrelenes with an E=E double bond. TMS = Si(CH₃)₃; 1-Ad = 1-adamantyl; Mes = mesityl = 1,3,5-trimethylphenyl.

The progress in the development of new, sterically highly demanding substituents even facilitated the isolation of heavier homologues of alkynes with the general formula REER, and the first representatives of disilynes (A-XX and A-XXI),^[240–242] digermynes (A-XXIIGe),^[243] distannynes (A-XXIISn)^[244] and diplumbynes (A-XXIIPb)^[245] were reported in the last 25 years. In contrast to the linear, triply bonded carbon congener, the heavier alkynes feature a *trans*-bent R–E–E–R arrangement and bond orders lower than three,^[246] as the lone pair character on the tetrel increases with increasing size of the tetrel atom (Scheme 6.2).



Scheme 6.2: The first literature-reported heavier ditetrelynes REER. Note that the multiple bond character decreases from Si to Pb whereas the lone pair character increases. Ar^{Dipp} = 2,6-(Dipp)₂-phenyl; Dipp = 2,6-diisopropylphenyl; Ar^{Tripp} = 2,6-(Tripp)₂-phenyl; Tripp = 2,4,6-triisopropylphenyl.

Up to the present day, several examples of isolable ditetrelynes followed^[238] and found application in bond activation and catalysis.^[247] However, mixed heavier alkynes REE'R are still scarce. Due to their strong tendency to dimerize and isomerize,^[248] only a few mixed ditetrelynes could be isolated by stabilizing the tetrel atoms with an additional donor ligand. These are reported by the group of T. Kato (A-XXIII and A-XXIV, Scheme 6.3),^[249, 250] or by our group with the SIDipp-supported chlorogermasilyne (SIDipp)Si(Cl)GeAr^{Mes} (A-5) already discussed in this thesis (see chapter A.3). Furthermore, three examples by A. Singh (Ar^{Dipp}SnSi(L)Ar^{Mes}) with L = 4-dmap (A-XXV), IMe₄ (A-XXVI) and CNMes (A-XXVII)^[251], and one by S. Kumar (A-XXVIII)^[150] from our group have been synthesized recently (Scheme 6.3, IMe₄ = C[N(Me)C(Me)]₂). Notable is also a report of a base-free stannagermyne, Ar^{Dipp}Sn≡GeAr^{Dipp} (A-XXIX), by D. Hoffmann from our group,^[252] which was fully characterized. However, the same Ar^{Dipp} substituents at each tetrel lead to a 50/50 exchange of the atom sites in the X-ray diffraction solution and impede the interpretation.



Scheme 6.3: Reported isolated mixed ditetrelynes with and without stabilization of the tetrel centre with a Lewis base. 4-dmap = 4-dimethylaminopyridine; IMe₄ = C[N(Me)C(Me)]₂.

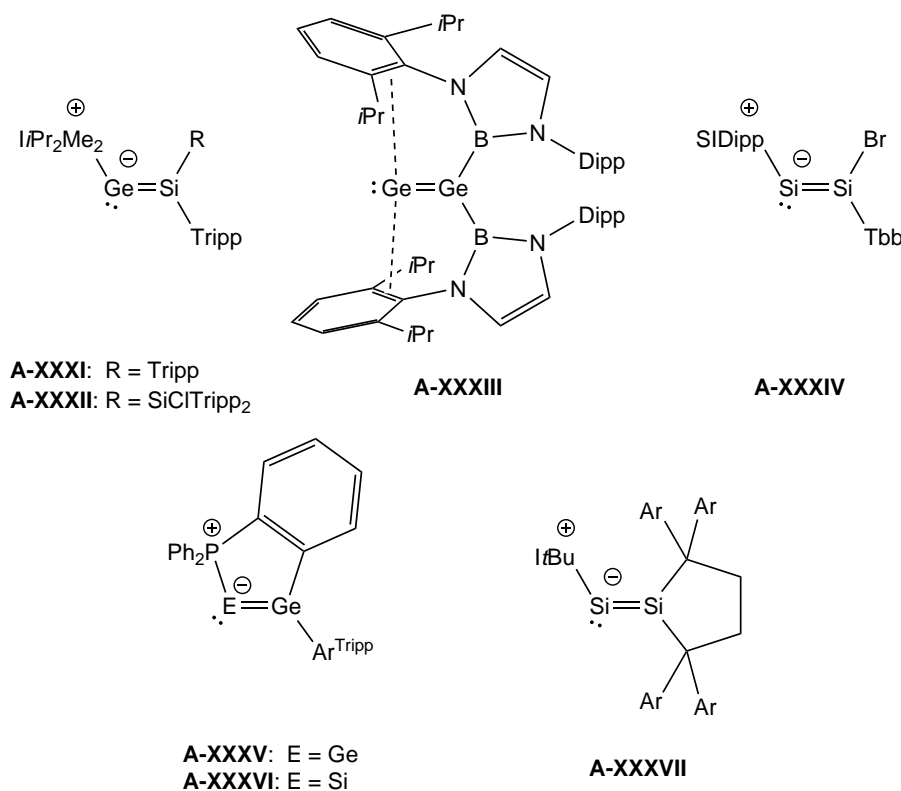
One of the challenging isomerization reactions of the heavier ditetrelynes REER is their intramolecular rearrangement to heavier vinylidenes EER_2 . High-level *ab-initio* calculations on the hypersurface of the parent carbon vinylidene $H_2C=C$ reveal that the rearrangement to the linear alkyne $HC\equiv CH$ is strongly favoured by ca. $180\text{ kJ}\cdot\text{mol}^{-1}$ with a barrier of only $19\text{ kJ}\cdot\text{mol}^{-1}$.^[253, 254] In contrast, the most favoured isomer of the heavier E_2H_2 systems ($E = \text{Si to Pb}$) is the hydrogen-dibridged structure A-XXX-a, with the heavier vinylidenes A-XXX-c lying 64 (Si) to 113 (Pb) $\text{kJ}\cdot\text{mol}^{-1}$ higher in energy (Figure 6.1). If the size of the substituents at the heavier tetrel centre is increased, the doubly-bridged isomers A-XXX-a are omitted and the heavier vinylidenes A-XXX-c become the ground state isomers. This is present for example in the case of Si_2Me_2 , where the disilavinylidene $\text{Si}=\text{SiMe}_2$ is favoured over the *trans*-bent dimethyldisilyne $\text{MeSi}\equiv\text{SiMe}$ by $51\text{ kJ}\cdot\text{mol}^{-1}$ according to calculations by H. F. Schaefer III *et al.*^[255, 256] S. Nagase *et al.* concluded in their theoretical study in the year 1997 that large silyl substituents like $\text{Si}(t\text{Bu})_3$ or $\text{Si}(2,6\text{-Et}_2\text{C}_6\text{H}_3)_3$ in fact yield the disilyne as ground state structure, favoured over the disilavinylidene isomer by 41 and 50 $\text{kJ}\cdot\text{mol}^{-1}$, respectively.^[257]

	A-XXX-a	A-XXX-b	A-XXX-c	A-XXX-d	A-XXX-e
E = Si	0	41.4	64.0	83.3	173.7
E = Ge	0	45.6	69.1	93.3	233.1
E = Sn	0	56.9	80.8	105.9	270.4
E = Pb	0	71.2	113.4	129.8	387.2

Figure 6.1: Relative energies in $\text{kJ}\cdot\text{mol}^{-1}$ for various isomers of the system HEEH ($E = \text{Si to Pb}$) by G. Frenking *et al.* at the BP86/QZ4P level of theory.^[258] The lines between the atoms only represent the connectivity and not $2c-2e^-$ bonds. Similar results are obtained by other studies.^[259–262]

With these considerations in mind, both suitable substituents and a proper synthetic route are key for the isolation of heavier vinylidenes, which was first realized by the group of D. Scheschkewitz in the year 2013 with the IiPr_2Me_2 -stabilized silagermenylidene $(\text{Tripp})_2\text{SiGe}(\text{IiPr}_2\text{Me}_2)$ (A-XXXI, Scheme 6.4),^[263] followed by another silyl-substituted derivative, $(\text{Tripp})_2\text{ClSi}(\text{Tripp})\text{SiGe}(\text{IiPr}_2\text{Me}_2)$ (A-XXXII), one year later.^[264] Remarkably, in the year 2016 the group of S. Aldridge reported the first *naked* digermavinylidene A-XXXIII, where the terminal germanium atom is only stabilized by weak arene-Ge π interactions.^[265] One year before, the group of A. C. Filippou succeeded in the isolation of the first NHC-supported disilavinyl-

dene (*Z*)-(SIDipp)SiSi(Br)Tbb (A-XXXIV), and its fruitful reactivity has since been thoroughly investigated.^[266–268] Another NHC-stabilized disilavinylidene was reported by the group of T. Iwamoto in 2021 (A-XXXVII),^[269] and the phosphine-stabilized digermavinylidene A-XXXV and germasilylenidene A-XXXVI were obtained by L. Wesemann *et al.* in the years 2019 and 2021, respectively.^[270, 271]

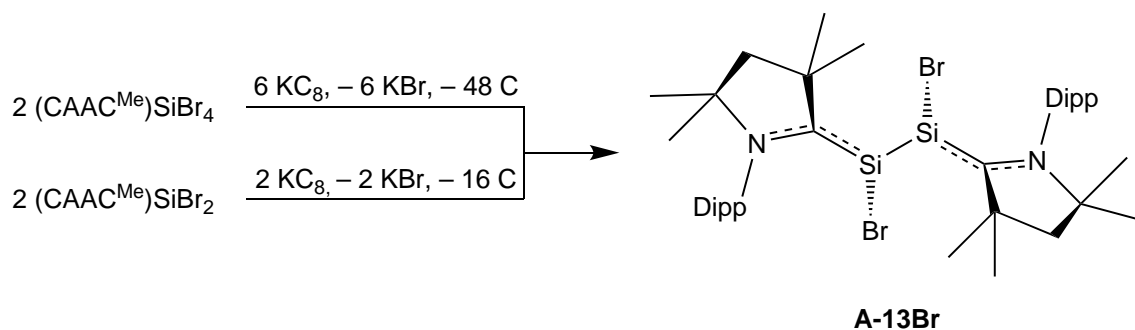


Scheme 6.4: Literature-known isolated heavier vinylidenes. ItBu = C[N(*t*Bu)CH]₂, Ar = 3,5-(*t*Bu)₂-4-OMe-C₆H₂.

The common feature of these heavier vinylidenes (except for A-XXXIII) is the stabilization of the terminal, one-coordinated tetrel atom by either phosphanes or N-heterocyclic carbenes. However, there are no reports of the use of cyclic alkyl amino carbenes (CAACs) to support heavier vinylidenes. This class of ligands was introduced by the group of G. Bertrand in the year 2005.^[272] By replacing one of the amino groups of an NHC by an electron-pushing alkyl group, the carbene carbon atom becomes even more electron rich and the energy of the HOMO increases. In contrast, the energy of the LUMO decreases due to the absence of the second π -donating amino group. Thus, the overall HOMO-LUMO gap decreases, transforming the NHC into an even stronger σ -donating and π -accepting ligand.^[273] To date, CAAC ligands could be successfully employed for the activation of small molecules like CO, H₂, NH₃, and P₄,^[218, 273–275] for the stabilization of highly reactive main-group and transition metal species,^[218, 274, 275] and for the activation of enthalpically strong bonds like B–H, C–H and Si–H.^[275] This general applicability and the electronic properties of CAACs illustrate the potential of this class of ligands for the stabilisation of heavier vinylidenes and tailoring of their electronic structure compared to similar NHC analogues.

6.2. CAAC^{Me}-stabilized Disilicon(I)-dihalide (CAAC^{Me})₂Si₂Br₂ (A-13Br)

Experimental work by F. Gstrein from the group of A. C. Filippou reveals that the 3e⁻ reduction of (CAAC^{Me})SiBr₄ or the 1e⁻ reduction of (CAAC^{Me})SiBr₂, respectively, leads to the CAAC^{Me}-stabilized disilicon(I)-dibromide (CAAC^{Me})₂Si₂Br₂ (A-13Br, see Scheme 6.5, CAAC^{Me} = C[N(Dipp)C(Me)₂CH₂C(Me)₂]).



Scheme 6.5: Synthesis of the CAAC^{Me}-stabilized disilicon(I)-dihalide A-13Br by F. Gstrein.^[276]

The calculated structure depicted in Figure 6.2 agrees well with the sc-XRD structure (A-13Br_{exp}) and features two trigonal-pyramidally coordinated silicon atoms ($\Sigma\angle(\text{Si}) = 327.4^\circ$, Table 6.1), indicating the presence of a stereoactive free electron lone pair at each Si atom, as also evidenced by the HOMO-1 and HOMO (Figure 6.2). The CAAC^{Me} substituents are *trans*-oriented to each other ($\text{C1-Si-Si'-C1}' = 170.6^\circ$) and *gauche*-oriented with respect to the C1-Si-Si'-C1' plane (interplanar (CAAC), (C1SiSi'C1') angle $\tau = 52.0^\circ$). The Si-Si' bond length of 236.0 pm is close to that of α -silicon (235.2 pm)^[139] and in the range of typical Si-Si single bonds. The Si-C1 bond of 185.6 pm is comparably short for a Si-C_{carbene} bond and indicates partial multiple bond character (which can also be seen in the HOMO of A-13Br). This is in contrast to the NHC-stabilized analogue (IDipp)₂Si₂Br₂ (A-13Br^{NHC}) reported in the year 2015 by our group with 193.8 pm and 304.4° for the Si-C1 bond and the sum of angles at the silicon atom, respectively.^[277] Furthermore, compound A-13Br fits in well with other dimeric CAAC^{Me}-stabilized disilicon(I) derivatives (CAAC^{Me})₂Si₂R₂ that were previously reported by other groups (R = Cl,^[278] I,^[202] H,^[279] Me,^[280] Ph^[281]).

Table 6.1: Selected structural parameters of calculated and experimental Si(I)bromide dimers. Bond lengths are given in pm, angles in degrees. τ corresponds to the interplanar twist angle between the azolidine ring of the CAAC^{Me} ligand and the (C1SiSi'C1') plane.

	Si-Si'	Si-C1	Si-Br	C1-Si-Si'	C1-Si-Si'-C1'	$\Sigma\angle(\text{Si})$	τ
A-13Br	236.0	185.6	233.6	105.7	170.6	327.4	52.0
A-13Br_{exp}	234.1(2)	184.4(4)	229.5(2)	106.7(2)	169.5(2)	326.9(4)	51.3(3)
A-13Br^{NHC}	241.3	193.8	240.6	97.6	160.9	304.4	56.8

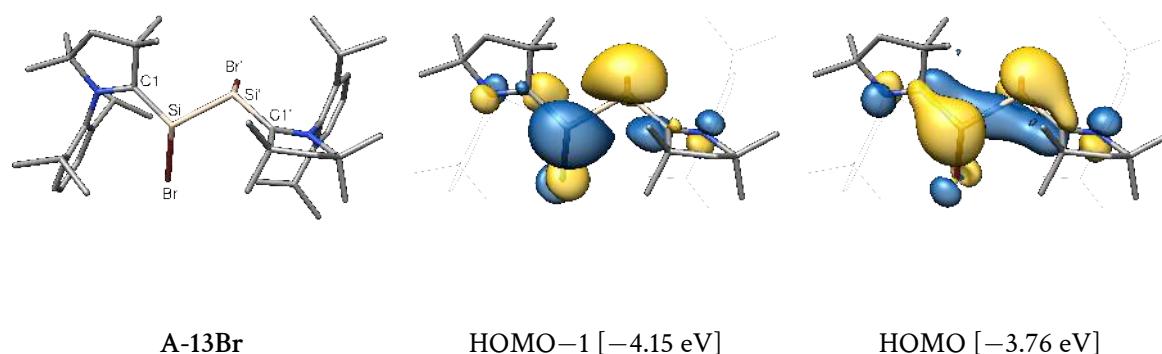
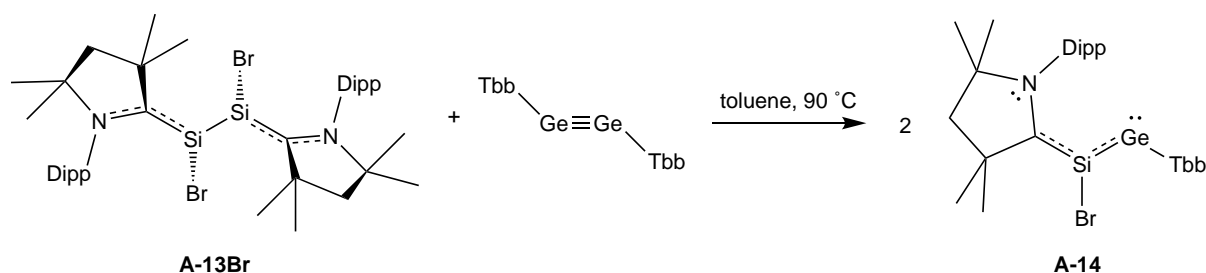


Figure 6.2: Optimized gas phase structure of **A-13Br** and selected canonical orbitals with their energetic eigenvalues.

Noteworthy though, experimental $^1\text{H-NMR}$ spectra of compound **A-13Br** reveal an averaged C_S -symmetry in solution, which can be frozen out at 223 K. The stereodynamic process was studied theoretically by R. Fleischer in the context of a bachelor thesis and rationalized as a fast enantiomerization of the two silicon centres via two narcissistic enantiomeric reaction pathways.^[282] The therein calculated barrier for the inversion of one silicon centre of $39.7 \text{ kJ}\cdot\text{mol}^{-1}$ fits well to the experimentally determined value of $55.3(\pm 3.4) \text{ kJ}\cdot\text{mol}^{-1}$ of a full line shape analysis of recorded VT- $^1\text{H-NMR}$ spectra. For a more detailed discussion, see ref [276].

6.3. Metathesis reaction to the CAAC^{Me} -stabilized Germasilyne $(\text{CAAC}^{\text{Me}})\text{Si}(\text{Br})\text{GeTbb}$

Experimental work by P. Palui from the group of A. C. Filippou shows that compound **A-13Br** reacts with the digermynes TbbGeGeTbb at 90°C , affording directly the CAAC^{Me} -stabilized germasilyne $(\text{CAAC}^{\text{Me}})\text{Si}(\text{Br})\text{GeTbb}$ (**A-14**, Scheme 6.6, $\text{Tbb} = 2,6\text{-}[\text{CH}(\text{SiMe}_3)_2]\text{-4-}t\text{Bu-C}_6\text{H}_2$). This represents the first example of a metathesis reaction between a heavier ditetrelene and a low-valent silicon compound, which is intriguing, as the selective cleavage of the $\text{E}\equiv\text{E}$ triple bond of heavier ditetrelynes could only be achieved so far by reaction with dihydrogen, alkenes, alkynes or transition metal complexes.^[283, 284] The CAAC^{Me} ligand is essential here, as the analogous reactions of the NHC-derivatives $\text{A-13X}^{\text{NHC}}$ with TbbSiSiTbb and TbbGeGeTbb were unsuccessful due to thermal decomposition of $\text{A-13X}^{\text{NHC}}$. Notably, the value of the CAAC^{Me} carbene was already underlined before by the remarkable ene-yne cross metathesis reaction of the compound $(\text{CAAC}^{\text{Me}})\text{B}(\text{X})\text{B}(\text{X})(\text{CAAC}^{\text{Me}})$ with acetylene ($\text{X} = \text{H}, \text{CN}$), reported by H. Braunschweig *et al.* recently in 2021.^[285]



Scheme 6.6: Synthesis of the CAAC^{Me}-stabilized germasilyne A-14 via main group metathesis reaction by P. Palui.^[286]

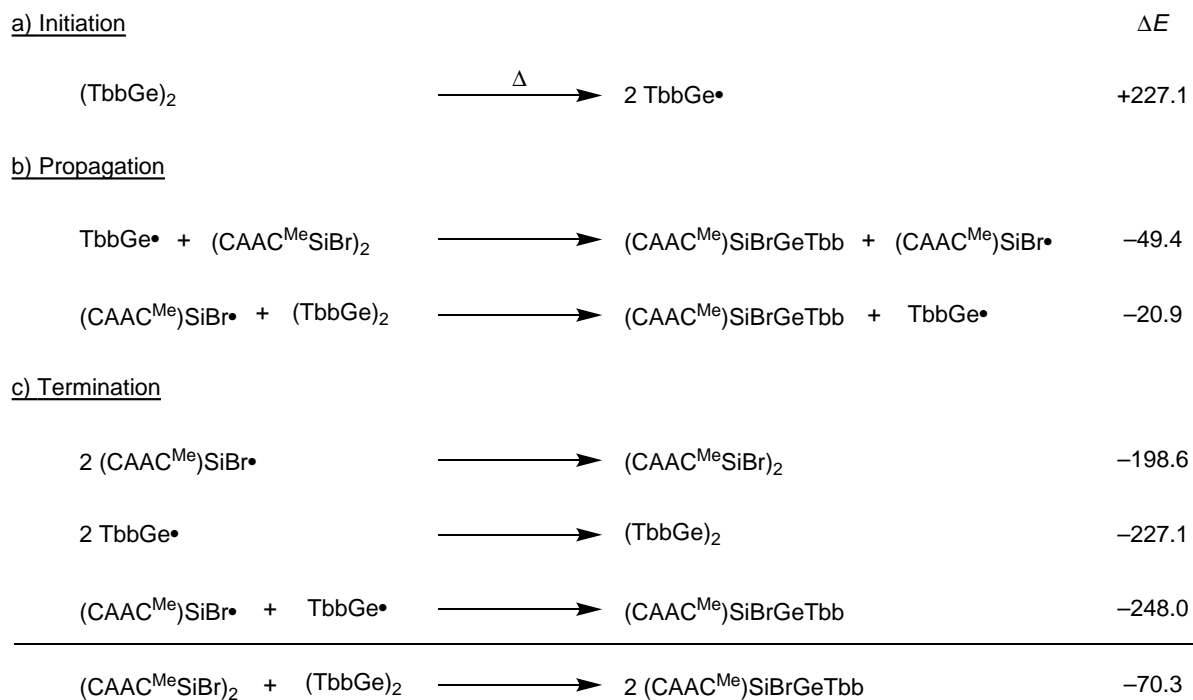
First insight into the reaction mechanism leading to compound A-14 is obtained by experimental kinetic studies.¹ They reveal a reaction of pseudo first order regarding A-13Br (experimentally determined reaction order: 0.99 ± 0.21) and a reaction of fractional order for the digermene TbbGeGeTbb (0.43 ± 0.03), suggesting a radical pathway via a thermally induced dissociation of the digermene into TbbGe· radicals (Scheme 6.7). As expected, such an initiation step is calculated to be highly energetically unfavoured ($\Delta E = +227.1 \text{ kJ}\cdot\text{mol}^{-1}$), but is compensated by the propagation and termination steps. The chain propagation can proceed via the activation of the dimer (CAAC^{Me}SiBr)₂ by a germylydyne fragment TbbGe· ($-49.4 \text{ kJ}\cdot\text{mol}^{-1}$), or via the activation of the digermene (TbbGe)₂ by a previously generated (CAAC^{Me})SiBr· radical ($-20.9 \text{ kJ}\cdot\text{mol}^{-1}$). In contrast to the slightly negative reaction energies for the propagation, all termination steps, i.e. the recombination of the *in situ* formed radical species, are highly preferred with ΔE values between -248.0 and $-198.6 \text{ kJ}\cdot\text{mol}^{-1}$. Overall, the reaction of Scheme 6.6 is calculated to be thermodynamically favoured with $-70.3 \text{ kJ}\cdot\text{mol}^{-1}$.

Notably, the cleavage of the digermene is also observed with the Si(II) precursor (CAAC^{Me})SiBr₂ and leads to the formation of the germasilyne A-14 and half an equivalent of the digermene TbbGe(Br)Ge(Br)Tbb. A more atom-economic approach was found by the step-wise process given in Scheme 6.8: The reaction between (CAAC^{Me})SiBr₂ and the digermene TbbGe(Br)Ge(Br)Tbb affords the silicon-germanium adduct (CAAC^{Me})SiBr₂GeBrTbb A-15, which can then be reduced with potassium graphite to obtain again compound A-14.

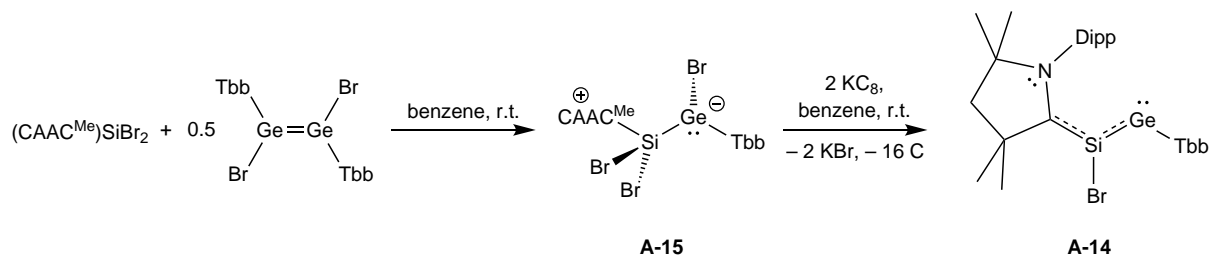
The calculated structure of A-15 (Figure 6.3 left) can reproduce the sc-XRD structure A-15_{exp} well and features a long Si–C1 single bond (198.3 pm) at the distorted tetrahedral silicon atom. The structural parameters given in Table 6.2 also reveal a pyramidalized germanium centre with a sum of angles of 318.2° that indicates an electron lone pair, which can be found in the HOMO. The LUMO has mainly antibonding $\pi^*(\text{C1}-\text{N})$ character.

After the report of the first NHC-stabilized germasilyne (SIDipp)Si(Cl)GeAr^{Mes} (A-5) by our group in 2021 (see chapter A.3), compound A-14 represents the first CAAC-supported analogue. Its gas phase structure, depicted in Figure 6.4 left, was calculated starting from the sc-XRD structure A-14_{exp} and selected bonding parameters are summarized in Table 6.3, together with those

¹F. Gstrein, *personal communication*.



Scheme 6.7: Proposed radical pathway of the metathesis reaction and calculated reaction energies ΔE for each reaction step.



Scheme 6.8: Step-wise synthesis of the CAAC^{Me} -stabilized germasilyne A-14 via the adduct A-15.

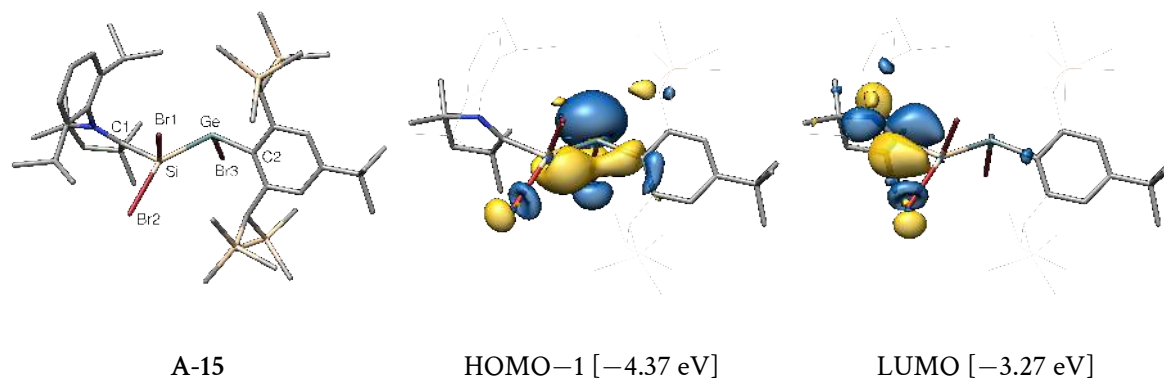


Figure 6.3: Optimized gas phase structure of A-15 and selected canonical orbitals with their energetic eigenvalues.

Table 6.2: Selected bonding parameters of the calculated gas phase and experimental sc-XRD structures of **A-15**. Bond lengths are given in pm, angles in degrees. τ corresponds to the interplanar twist angle between the azolidine ring of the CAAC^{Me}-ligand and the (C1SiGe'C1') plane.

	Si–C1	Si–Ge	Ge–Br	Ge–C2	C1–Si–Ge	$\Sigma\angle(\text{Ge})$	τ
A-15	198.3	247.6	247.9	203.4	110.1	318.2	67.8
A-15_{exp}	197.2(8)	247.4(2)	244.47(12)	201.0(7)	111.8(2)	314.3(5)	67.7(3)

of the calculated NHC-supported germasilynes (SIDipp)Si(Br)GeTbb (Figure 6.4 right) and **A-5** for comparison. The structure of **A-14**, which agrees well with that of **A-14_{exp}**, features a nearly trigonal-planar silicon atom ($\Sigma\angle = 358.6^\circ$) and a bent, two-coordinate germanium atom. For the latter, the Si–Ge–C2 angle of 102.4° indicates the presence of a stereoactive electron lone pair at Ge, which is located in the HOMO–1 (Figure 6.5) and was already seen for **A-5**. In fact, the NHC analogues **A-14^{NHC}** and **A-5** show similar structures to **A-14** with comparable sums of angles at the silicon atom of 359.7 and 359.8° , respectively. Furthermore, the ligating carbenes are coplanar to the reactive core of the molecules, as indicated by (CAAC^{Me}),(C1SiXGeC2) interplanar twist angles close to zero (**A-14**: 16.9° , **A-14^{NHC}**: 9.6° , **A-5**: 5.7°). This orientation allows the delocalization of the $\pi(\text{Si–Ge})$ orbital into the antibonding $\pi^*(\text{C–N})$ orbital ($\pi^*(\text{N–C–N}')$ for **A-14^{NHC}** and **A-5**) and can be found in the HOMO of **A-14**. As CAAC ligands are better π -acceptors than NHCs, the $\pi(\text{Si–C1})$ character is expected to be stronger, which is reflected in the shorter Si–C1 bond of 184.3 pm in contrast to 188.2 and 187.0 pm for **A-14^{NHC}** and **A-5**, respectively. As a consequence, the $\pi(\text{Si–Ge})$ character decreases and thus the Si–Ge bond length increases (235.0 pm for **A-14**, but only 231.6 and 231.1 pm for **A-14^{NHC}** and **A-5**, respectively). This further agrees well with the Loewdin orbital populations of the HOMO, which has a slightly higher share on the C1 atom for **A-14** (0.11) in contrast to **A-14^{NHC}** (0.07). The coefficients on Si (0.37, 0.42) and Ge (0.16, 0.21) are similar.

A local NRT analysis of compound **A-14** affords the Si=Ge doubly-bonded resonance structure **A-14-a** to be the most dominant one (46 %, Scheme 6.9). However, the resonance structure **A-14-b** with a Si=C double bond has a similar NRT weight of 39 %, which underlines the high π -accepting capabilities of the CAAC^{Me} ligand. In contrast, the corresponding resonance structures **A-5-a** (51 %) and **A-5-b** (31 %) of the SIDipp-supported germasilyne **A-5** show a larger difference and a smaller absolute value of the latter Lewis structure (cf. 3.6). Accordingly, the calculated total NRT bond orders for the Si–C1 and Si–Ge bonds of 1.4 and 1.5, respectively, reflect the very similar multiple-bond character in these bonds (Table 6.4). Additionally, the Wiberg bond indices for the Si–C1 and Si–Ge bonds of 1.1 and 1.3 are significantly higher than those of the Si–Br (0.8) and Ge–C2 (0.8) bonds, which are expected to be typical single bonds.

The detailed NBO analysis on the most dominant resonance structure **A-14-a** reveals high occupations above $1.85 e^-$ for all NBOs expect for the $\pi(\text{Si–Ge})$ bond ($1.39 e^-$). This underlines the presence of the resonance structure **A-14-b**, just like the considerable occupation of $0.63 e^-$ of the

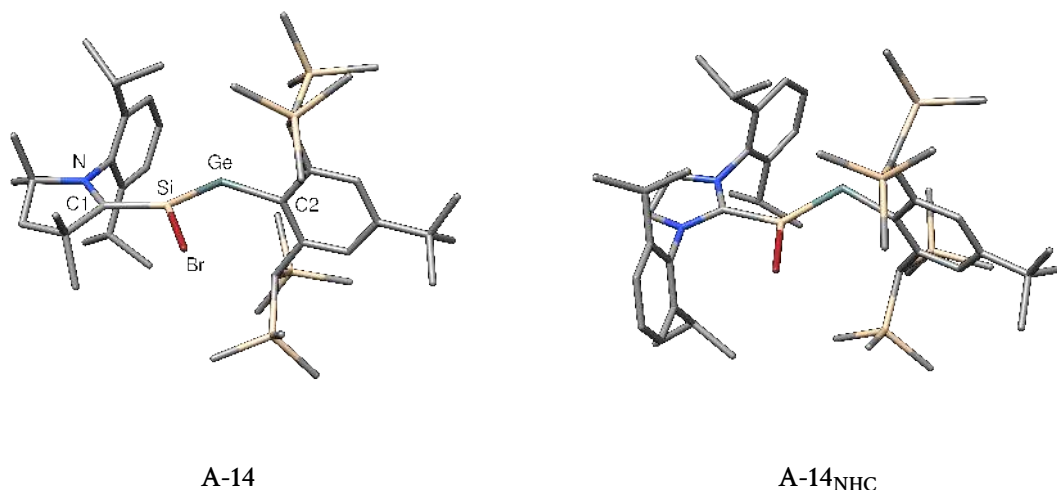


Figure 6.4: Optimized gas phase structures of the CAAC^{Me}- or SIDipp-stabilized germasilynes A-14 and A-14^{NHC}.

Table 6.3: Selected bond parameters of the calculated and experimental CAAC^{Me}-stabilized germasilynes A-14 and A-14_{exp} as well as the NHC-stabilized germasilynes A-14^{NHC} and A-5. Bond lengths are given in pm and angles in degrees. τ and ϕ describe the interplanar twist angles between the CAAC^{Me} azolidine or SIDipp-imidazoline rings and the (C1SiGeC2) plane, and between the central Tbb phenyl ring and the (C1SiGeC2) plane, respectively.

	Si–C1	Si–Ge	Ge–C2	Si–X	Si–Ge–C2
A-14	184.3	235.0	203.4	231.1	102.4
A-14 _{exp}	182.9(4)	232.7(2)	200.8(4)	227.5(2)	100.6(2)
A-14 ^{NHC}	188.2	231.6	203.9	229.7	101.4
A-5	187.0	231.1	204.6	212.0	97.6
	C1–Si–Ge–C2	$\Sigma\angle(E)$	τ	ϕ	
A-14	–169.0	358.6	16.9	86.4	
A-14 _{exp}		–175.2(2)	359.9(4)	11.9(2)	82.8(2)
A-14 ^{NHC}		–176.3	359.7	2.9	82.3
A-5		–177.1	359.8	5.7	88.5

$\pi^*(C1-N)$ NBO, caused by the $\pi(Si-Ge) \rightarrow \pi^*(C1-N)$ delocalization. Typical bond polarizations are found for the Si–Br (27 % Si), Si–C1 (25 % Si) and Ge–C2 (28 % NBOs according to electronegativity trends. Notably, both the $\sigma(Si-Ge)$ and $\pi(Si-Ge)$ bonds are polarized towards the silicon atom with 63 and 72 %.

The silicon and germanium atoms bear positive NPA charges of +0.53 and +0.36 e, whereas the electronegative bromine atom has a negative partial charge of –0.35 e. In contrast to the slightly positive group charge of +0.06 e of the SIDipp ligand in A-5, that of the CAAC^{Me} carbene is negative with –0.12 e, which again underlines the back-donation of electron density from the silicon atom as suggested by the MO and NRT results. The most negative NPA charge is found for the Tbb group attached to the germanium atom (–0.42 e).

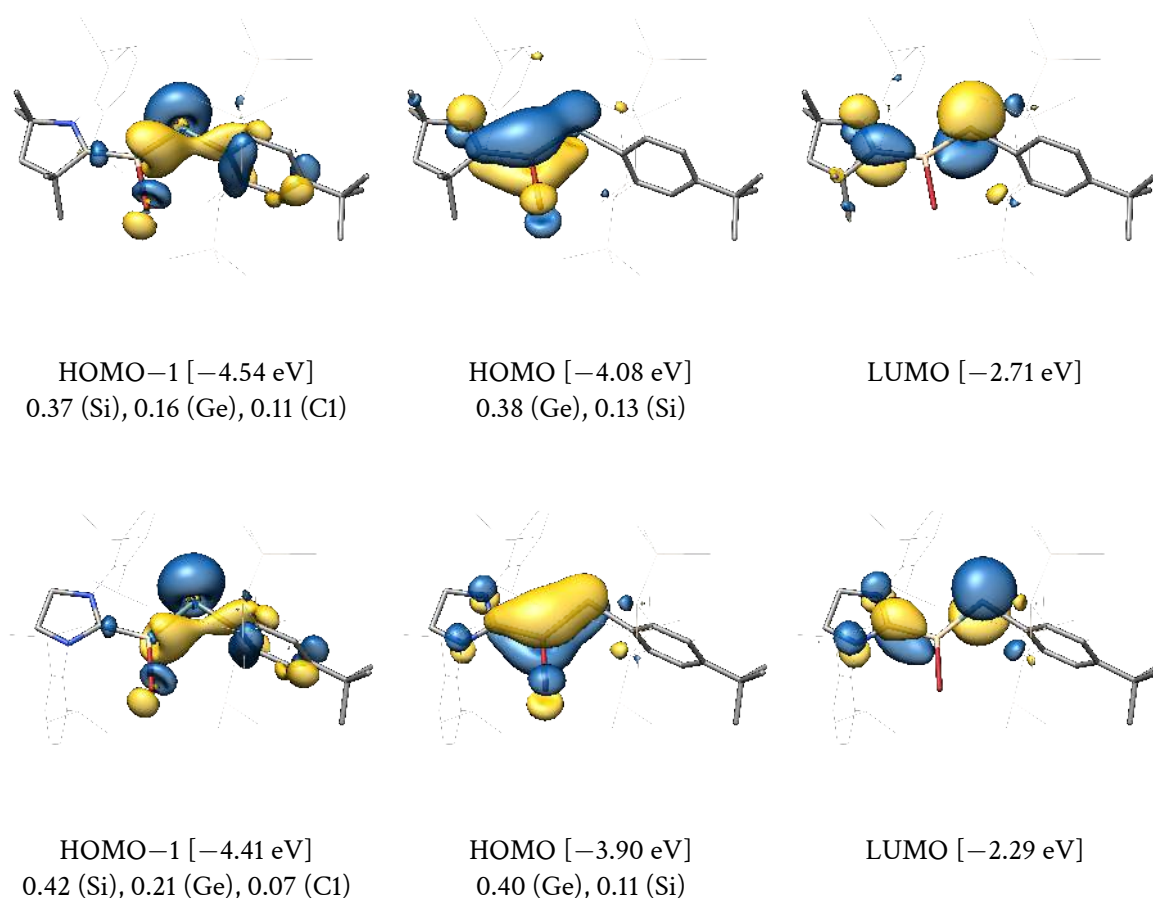
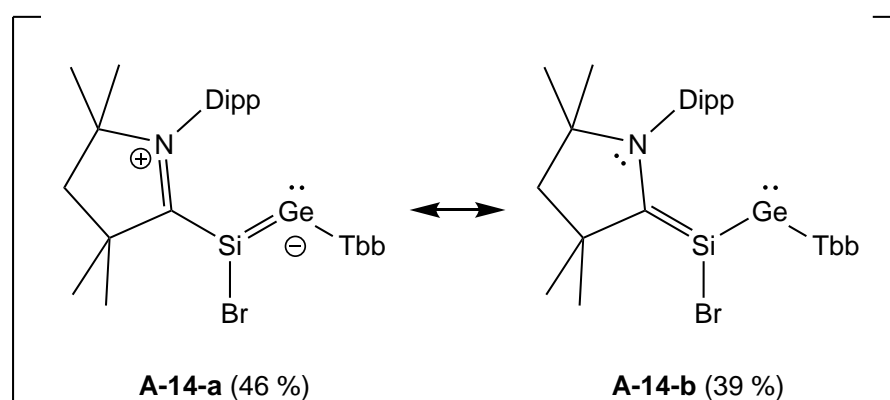


Figure 6.5: Canonical MOs of A-14 (top) and A-14^{NHC} (bottom) and atomic Loewdin orbital populations of the occupied orbitals.



Scheme 6.9: Most dominant resonance contributions of A-14 and their resonance weight from a local NRT analysis comprising the N, C1, Si, Br, Ge and C2 atoms.

The results of further bond cleavage and bond dissociation analyses of compound A-14 are summarized in Table 6.5, which were carried out for the Si–C_{CAAC^{Me}} and Si–Ge bonds. The cleavage of the carbene is favoured to proceed via singlet fragments (413.9 kJ·mol⁻¹) over triplet fragments (551.1 kJ·mol⁻¹). Thus, compared to the SIDipp cleavage in A-5 (392.5 kJ·mol⁻¹), singlet frag-

Table 6.4: Results of the NBO, local NRT (with the N, C1, Si, Br, Ge and C2 atoms) and NPA analyses of the compound A-14.

NBO A-B	Occ./ e ⁻	NHO (A,B) pol./% (hyb.)	WBI	NRT-BO tot/cov/ion	NPA / e	
LP(Ge)	1.88	(sp ^{0.2})			Si	+0.53
σ(Si-C1)	1.95	25 (sp ^{2.4}), 75 (sp ^{1.6})	1.1	1.4/0.9/0.5	Ge	+0.36
σ(Si-Ge)	1.93	63 (sp ^{0.9}), 37 (p)	1.3	1.5/1.0/0.5	Br	-0.35
π(Si-Ge)	1.39	72 (p), 28 (p)			[CAAC ^{Me}]	-0.12
σ(Si-Br)	1.97	27 (sp ^{4.7}), 74 (sp ^{4.2})	0.8	0.9/0.5/0.4	[Tbb]	-0.42
σ(Ge-C2)	1.93	28 (sp ^{8.9}), 72 (sp ^{2.6})	0.8	0.9/0.5/0.4		
π*(C1-N)	0.63	27 (p), 73 (p)	1.3	1.5/1.0/0.5		

ments; see Table 3.9), the cleavage of the Si-C_{CAAC^{Me}} bond costs slightly more energy. Upon structural relaxation of the germsilyne fragment BrSiGeTbb, a direct isomerization into the silagermenylidene GeSiBrTbb takes place, which is not observed during the structure optimization of the ClSiGeAr^{Mes} fragment in the case of A-5. As a consequence, the BDE of A-14 is artificially lowered to 257.1 kJ·mol⁻¹ (177 kJ·mol⁻¹ for the BDG) and is smaller than that of A-5 (BDE: 272.1 kJ·mol⁻¹, BDG: 192.8 kJ·mol⁻¹).

Finally, the Si-Ge bond cleavage is found to be nearly identical for A-14 and A-5: The bond splitting into the two neutral doublet state fragments (carbene)SiBr and GeR shows BCEs of 274.4 and 269.4 kJ·mol⁻¹, respectively, and, upon structural relaxation, BDEs of 237.3 and 233.5 kJ·mol⁻¹. Notably, the BCEs for the Si-Ge cleavage are approximately 150 kJ·mol⁻¹ lower than those for the Si-carbene bonds, which illustrates the strong donor-acceptor bonds of cyclic alkyl amino carbenes and N-heterocyclic carbenes as mentioned in the introduction.

Table 6.5: Level of theory I-calculated bond cleavage (BCE) and bond dissociation (BDE) energies for the CAAC^{Me} and Si-Ge cleavages of A-14 in kJ·mol⁻¹, entropies in J·K⁻¹·mol⁻¹. s = singlet, d = doublet, t = triplet multiplicity.

	ΔE	mult.	ΔE	ΔU	ΔH	ΔS	ΔG
CAAC ^{Me} cleavage	BCE	BDE (parent → CAAC ^{Me} + BrSiGeTbb)					
A-14	413.9 (s) 551.1 (t)	(s → s, s)	257.1	247.9	250.4	246.1	177.0
Si-Ge cleavage	BCE	BDE (parent → (CAAC ^{Me})SiBr + GeTbb)					
A-14	274.4 (d)	(s → d, d)	237.3	226.8	229.3	265.7	150.1

The approximately C_s-symmetric structure of A-14, that was found in the solid state by sc-XRD and in the gas phase by calculations, is also observable in solution as detected by NMR-spectroscopy. However, VT-NMR studies reveal a splitting of the TMS singlet signal from one to two signals below 243 K, which corresponds to a hindered rotation of the Tbb substituent around the Ge-C2 bond. The lineshape analysis of the recorded spectra affords an experimental free Gibbs energy ΔG[‡] of 53.0(±1.9) kJ·mol⁻¹ for the rotation barrier at 298 K. To confirm this theoretically, a po-

tential energy surface scan was carried out for the Si–Ge–C2–C_{ortho} torsion angle that describes the rotation of the Tbb substituent (Figure 6.6). Its highest point is located at -15° with an relative energy of $\Delta E = 54.7 \text{ kJ}\cdot\text{mol}^{-1}$, which is close to the experimental free Gibbs energy in solution. To check for side minima, the PES scan was repeated in backwards direction and yields a similar progression with its highest point at -25° ($48.7 \text{ kJ}\cdot\text{mol}^{-1}$).

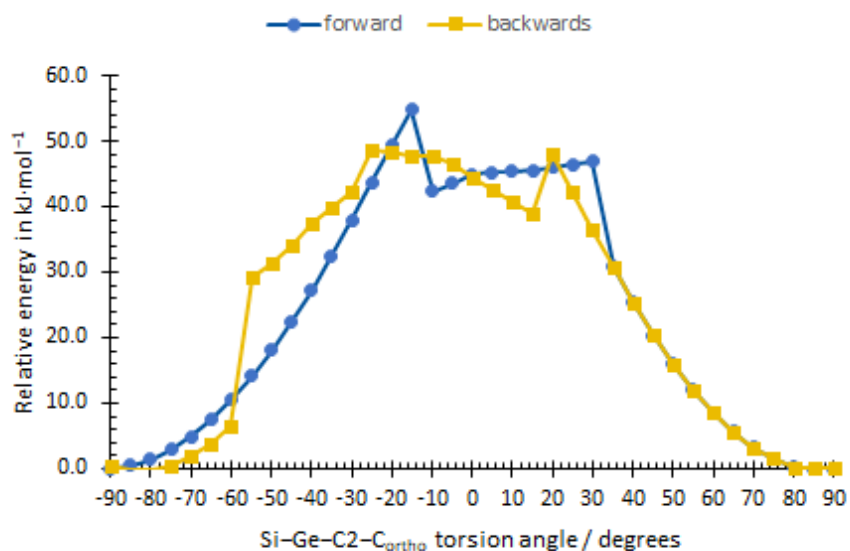
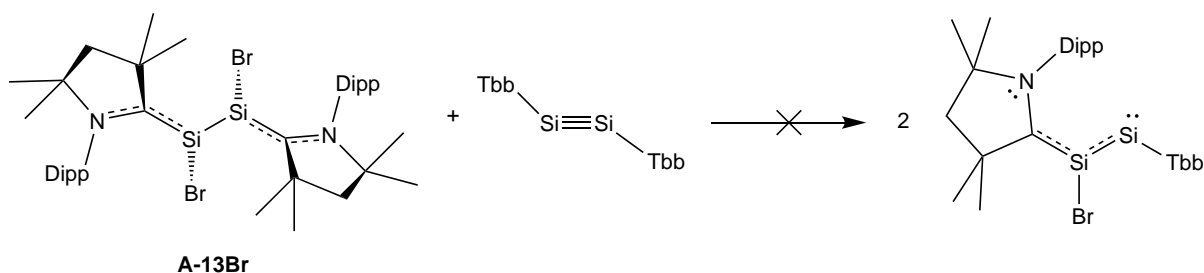


Figure 6.6: PES scans of the Si–Ge–C2–C_{ortho} torsion angle for A-14 in forward (-90° to $+90^\circ$) and backward direction ($+90^\circ$ to -90°) with a step size of 5° .

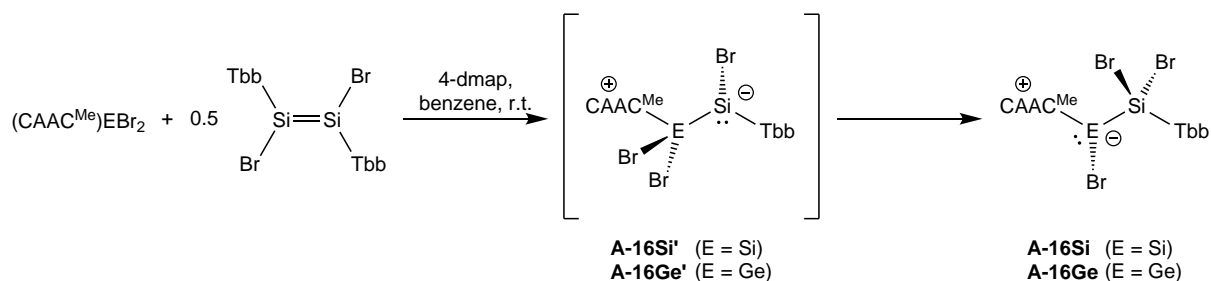
6.4. CAAC^{Me}-stabilized disilavinylidene (A-17Si) and silagermenylidene (A-17Ge)

The metathesis reaction between the Si(I) dimer A-13Br and the digermene TbbGeGeTbb afforded the unprecedented CAAC^{Me}-supported germsilyne A-14. In a similar manner, F. Gstrein tried to initiate a reaction between compound A-13Br and the more reactive disilyne TbbSiSiTbb to the CAAC^{Me}-stabilized disilyne (CAAC^{Me})SiBrSiTbb, which, however, failed and only led to the unselective decomposition of the disilyne without a reaction of A-13Br (Scheme 6.10).



Scheme 6.10: Attempted disilicon(I)-disilyne cross metathesis, which was not successful.

Access to the targeted compound via the alternative 2-step process that already worked for **A-14** (Scheme 6.8) was unsuccessful. Here, the reaction between $(\text{CAAC}^{\text{Me}})\text{EBr}_2$ ($\text{E} = \text{Si}, \text{Ge}$) and the disilene $\text{TbbSi}(\text{Br})\text{Si}(\text{Br})\text{Tbb}$ affords the CAAC^{Me} -supported bromosilyltetrylenes $(\text{CAAC}^{\text{Me}})\text{E}(\text{Br})\text{Si}(\text{Br})_2\text{Tbb}$ (**A-16E**) and not simply the targeted adducts $(\text{CAAC}^{\text{Me}})\text{E}(\text{Br})_2\text{Si}(\text{Br})\text{Tbb}$ (**A-16E'**), as depicted in Scheme 6.11.



Scheme 6.11: Reaction between $(\text{CAAC}^{\text{Me}})\text{EBr}_2$ and the disilene TbbSiBrSiBrTbb to the silyltetrylenes **A-16E** ($\text{E} = \text{Si}, \text{Ge}$). The simple adducts **A-16E'** could not be detected in the experiment due to the favoured 1,2-migration of the bromine atom. 4-dmap = 4-dimethylaminopyridine.

The reaction mechanism can be rationalized as follows: After the disilene is activated by the Lewis base 4-dimethylaminopyridine (4-dmap), the *in situ*-generated 4-dmap-stabilized bromosilylene $(4\text{-dmap})\text{SiBrTbb}$ and the dibromosilene $(\text{CAAC}^{\text{Me}})\text{SiBr}_2$ form the adduct **A-16E'** under displacement of 4-dmap, which in the final step isomerizes to **A-16E** by a bromine rearrangement. Calculations reveal in this context that the isomerization from **A-16E'** to **A-16E** is highly favoured by -81.9 and $-102.7 \text{ kJ}\cdot\text{mol}^{-1}$ for $\text{E} = \text{Si}$ and Ge , respectively. The key structural features of **A-16E'** are the elongated Si–Si bond of 241.4 pm for **A-16Si'** and, in the case of **A-16Ge'**, the dissociation into the $(\text{CAAC}^{\text{Me}})\text{GeBr}_2$ and SiBrTbb fragments as evidenced by the long $\text{Ge}\cdots\text{Si}$ distance of 298.4 pm (see the Appendix for more structural information on compounds **A-16E'**).

The calculated gas phase structures of the bromosilyltetrylenes **A-16E** are shown in Figure 6.7 and feature a strongly pyramidal orientation of the substituents around the three-coordinated tetrel atoms ($\Sigma\angle(\text{Si}) = 316.7^\circ$; $\Sigma\angle(\text{Ge}) = 292.1^\circ$, see Table 6.6), where the sum of angles for the germanium compound **A-16Ge** is similar to that of the reported NHC-stabilized bromosilylsilylene analogue $(\text{SIDipp})\text{SiBrSiBr}_2\text{Tbb}$ (**A-16Si_{exp}^{NHC}**, $\Sigma\angle(\text{Si}) = 287.4^\circ$).^[266] As a consequence, the more planarized silicon atom in compound **A-16Si** allows for a better $\pi(\text{Si1}-\text{C1})$ back-bonding, which is reflected by the shape of the HOMO (Figure 6.8 top) and in the shorter Si–C1 bond length of 187.2 pm compared to 197.8(3) pm in **A-16Si_{exp}^{NHC}**. In contrast, the azolidine ring of the CAAC^{Me} ligand in **A-16Ge** is oriented perpendicular to the stereoactive lone pair and prevents a π -back-bonding interaction. This can also be seen in its HOMO (and the $\pi^*(\text{C1}-\text{N})$ orbital density without an antibonding germanium contribution in the LUMO, Figure 6.8 bottom), and leads to a rather long Ge–C1 bond of 210.8 pm. As the compound **A-16Si** shows a high degree of silene character due to the strong π -accepting capability of the CAAC^{Me} ligand, it was recently suggested to term this class of compounds *pyramidal tetrylenes*.^[276] Accordingly, among the possible resonance structures **A-16-a**

(ylidic form, see Scheme 6.12) and A-16-b (tetrelene form), the first is more dominant for A-16Ge, whereas the latter is more pronounced for the silicon compound A-16Si.

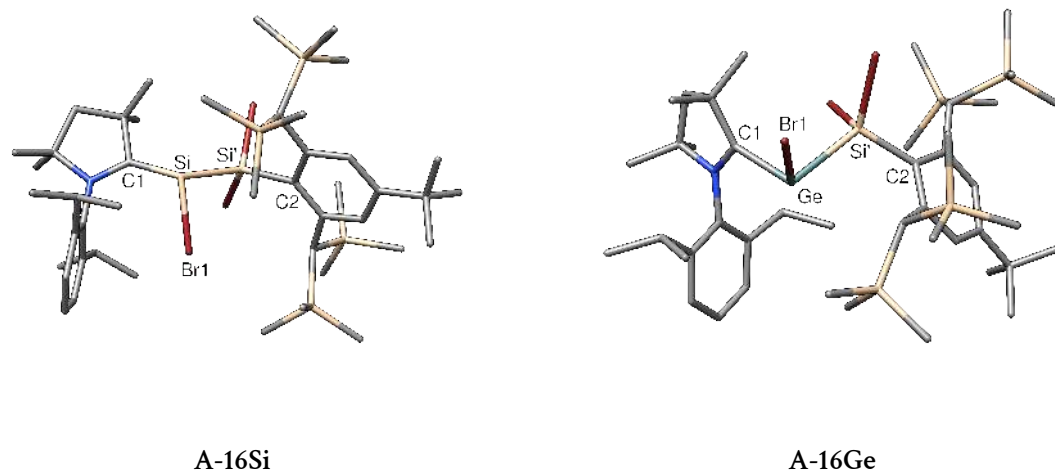
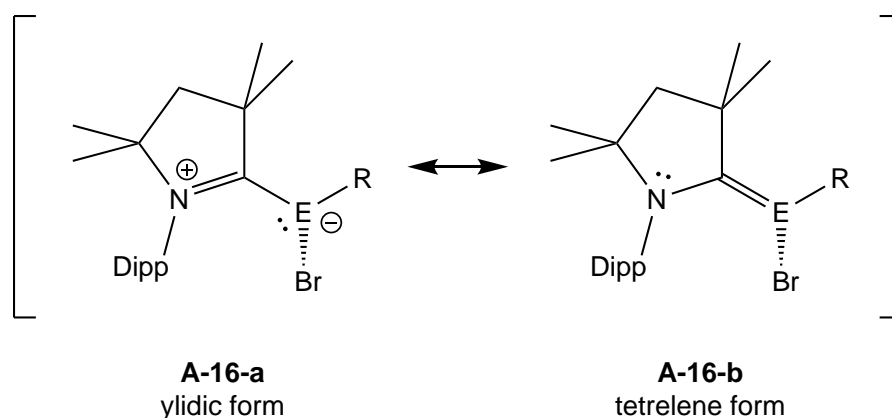


Figure 6.7: Calculated gas phase structures of the silyltetrelenes A-16Si and A-16Ge.

Table 6.6: Selected structural parameters of the calculated compounds A-16Si and A-16Ge as well as of the sc-XRD structures of A-16Si_{exp}, A-16Ge_{exp} and (SIDipp)Si(Br)Si(Br)₂Tbb (A-16Si_{exp}^{NHC}), taken from ref. [266]. Bond lengths and angles are given in pm and degrees, respectively. τ is defined as the interplanar twist angle between the carbene and (C1ESi'C2) planes.

	E–C1	E–Si'	E–Br	Si'–C2	C1–E–Si'	$\Sigma\angle(\text{E})$	τ
A-16Si	187.2	238.7	233.0	191.0	113.6	316.7	58.5
A-16Si _{exp}	187.9(8)	236.9(3)	230.3(2)	190.3(8)	112.7(3)	313.6(7)	58.0(3)
A-16Si _{exp} ^{NHC}	197.8(3)	239.1(1)	234.2(1)	192.1(3)	102.1(1)	287.3(3)	72.8(2)
A-16Ge	210.8	254.9	248.8	189.9	96.6	292.1	63.2
A-16Ge _{exp}	208.6(9)	251.0(3)	246.1(2)	187.8(9)	97.9(2)	291.1(5)	61.1(4)



Scheme 6.12: Conceivable resonance formulas for the pyramidal tetrelene class of compounds.

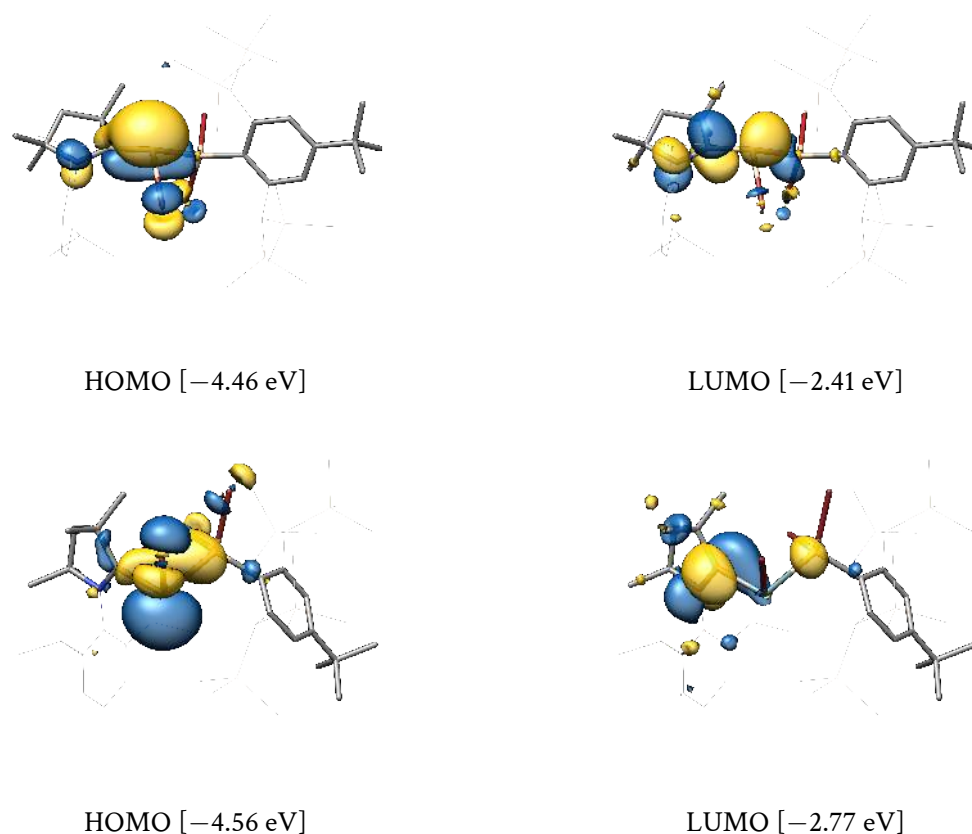
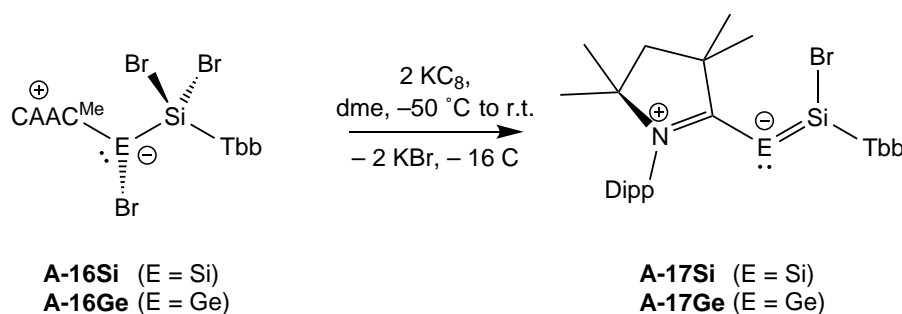


Figure 6.8: Selected canonical molecular orbitals of the silyltetrelenes A-16Si (top) and A-16Ge (bottom) and their energy eigenvalues.

Scheme 6.13 illustrates that the straightforward reductions of A-16Si and A-16Ge with two equivalents of potassium graphite yield the CAAC^{Me}-supported disilavinylidene (CAAC^{Me})SiSi(Br)Tbb (A-17Si) and silagermenylidene (CAAC^{Me})GeSi(Br)Tbb (A-17Ge), which are the first examples of CAAC^{Me}-stabilized ditetrelidenes. Notably, both compounds still feature a E–Br bond which allow for further functionalization (*vide infra*), similar to their NHC-stabilized analogue (SIDipp)SiSi(Br)Tbb (A-XXXIV). The latter compound will also be synonymously abbreviated as A-17Si^{NHC} in the following discussion for comparison reasons.



Scheme 6.13: Reduction of the silyltetrelenes A-16E to the first CAAC^{Me}-supported disilavinylidene A-17Si and silagermenylidene A-17Ge.

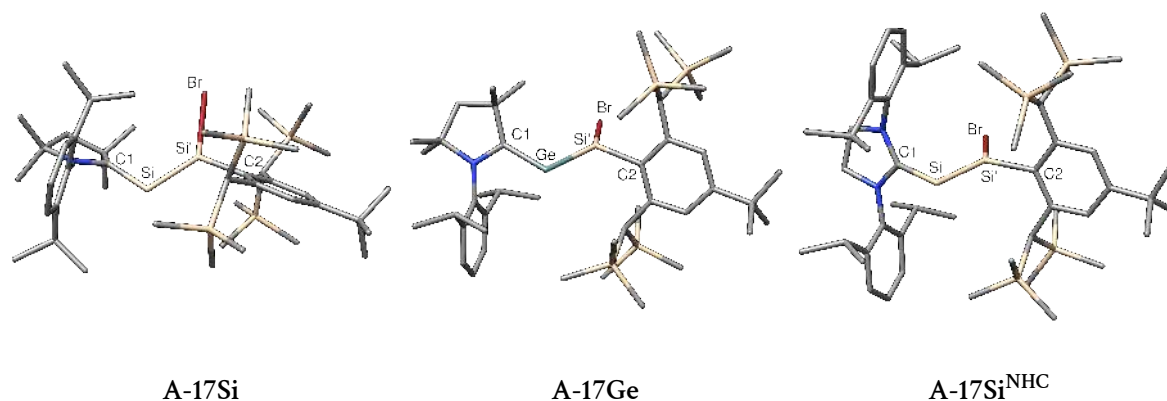


Figure 6.9: Optimized gas phase structures of the CAAC^{Me}-stabilized disilavinylidene A-17Si and silagermenylidene A-17Ge. The depicted structure of the NHC-stabilized disilavinylidene A-17Si^{NHC} at the level of theory I is very similar to that of ref. [266] at the B97-D3/TZVP level of theory.

The calculated gas phase structures of the compounds A-17Si and A-17Ge are depicted in Figure 6.9, and Table 6.7 provides an overview of selected structural parameters of the calculated compounds A-17Si, A-17Ge, their well-agreeing experimental sc-XRD counterparts A-17E_{exp} and the calculated structure of A-17Si^{NHC}. The latter was structurally reoptimized at the level of theory I for consistency and in close agreement with the experimental and calculated structure of reference [266]. Some particularly notable trends are:

Table 6.7: Selected bond parameters of the calculated and experimental CAAC^{Me}-stabilized heavier vinylidenes as well as the NHC-stabilized disilavinylidene A-17Si^{NHC}. Bond lengths are given in pm and angles in degrees. τ and ϕ describe the interplanar twist angles between the CAAC^{Me} azolidine or SIDipp-imidazoline rings and the (C1ESi'C2) plane and the central Tbb phenyl ring and the (C1ESi'C2) plane, respectively.

	E–C1	E–Si'	Si'–C2	Si'–Br	C1–E–Si'
A-17Si	186.7	220.7	188.9	231.2	107.7
A-17Si _{exp}	187.8(5)	219.4(2)	187.4(5)	227.8(2)	106.8(2)
	186.8(6)	218.1(2)	187.9(5)	227.3(2)	105.6(2)
A-17Si ^{NHC}	192.3	217.8	189.2	230.7	99.0
A-17Ge	197.7	227.8	189.3	231.4	106.7
A-17Ge _{exp}	198.7(2)	224.9(1)	189.0(2)	228.1(1)	105.5(1)
	C1–E–Si'–C2	$\Sigma\angle(\text{Si}')$	τ	ϕ	
A-17Si	–179.3	353.7	44.8	56.4	
A-17Si _{exp}	178.2(3)	354.1(4)	58.1(2)	53.8(2)	
	176.9(2)	354.8(4)	46.3(3)	64.4(2)	
A-17Si ^{NHC}	–176.7	358.1	70.4	78.3	
A-17Ge	–178.4	353.8	43.7	57.1	
A-17Ge _{exp}	180.0(2)	354.8(2)	49.5(1)	81.4(1)	

- In all compounds, the disubstituted tetrel atom adopts a V-shaped coordination with obtuse C1–E–Si' angles of 107.7° (A-17Si), 106.7° (A-17Ge) and 99.0° (A-17Si^{NHC}), which indicate the expected presence of a stereoactive lone pair of electrons that are clearly visible in the HOMO–1 for each compound (Figure 6.10).
- The SIDipp ligand in A-17Si^{NHC} adopts an approximately orthogonal orientation with respect to the (C1SiSi'C2) plane, as evidenced by the interplanar twist angle τ of 70.4°, which is even more pronounced in the solid state (85.2(1)°, c.f. ref. [266]) and leads to molecular C₃-symmetry. In contrast, the CAAC^{Me} ligands in A-17Si and A-17Ge adopt a *gauche*-orientation with 44.8 and 43.7°, respectively, resulting only in molecular C₁-symmetry. However, this orientation allows for π (E–C1) back-bonding via a π (E–Si') → π^* (C1–N) donation that can further be observed in the HOMO of A-17Si and A-17Ge, but not for A-17Si^{NHC} (Figure 6.10). In the case of the CAAC^{Me}-stabilized ditetrelidenes, the LUMO corresponds to the non-bonding combination (π^* (C1–N) + p(Si')), and for A-17Si^{NHC} only to the π^* (N–C1–N') orbital of the SIDipp ligand.
- As a consequence from the π (E–C1) back-bonding, it is expected that the E–C1 bond shortens and the E–Si' bond elongates. In fact, the Si–C1 bond distance in A-17Si of 186.7 pm is considerably smaller than that of A-17Si^{NHC} (192.3 pm), similar to that of the pyramidal silene A-16Si (187.2 pm) and slightly longer than in the CAAC^{Me}-stabilized bromogermasilyne A-14 (184.3 pm). Accordingly, the Si=Si' bond length in A-17Si of 220.7 pm is somewhat larger than in A-17Si^{NHC} (217.8 pm). The Ge–C1 bond length of 197.7 pm is also shortened, for example compared to the CAAC^{Me}-stabilized dibromogermylene (CAAC^{Me})GeBr₂ (212.8(3) pm).^[276]
- The molecular C1–E–Si'–C2 skeleton has an antiperiplanar conformation as evidenced by the C1–E–Si'–C2 torsion angles of –179.3° (E = Si) and –178.4° (E = Ge), which are almost identical to that of A-17Si^{NHC} (–176.7°).
- The Si'–C2 bond distance seems to be independent from the choice of the tetrel (A-17Si: 188.9 pm; A-17Ge: 189.3 pm) and carbene (A-17Si^{NHC}: 189.2 pm). The Tbb substituent is aligned almost orthogonally to the C1–E–Si'–C2 skeleton in A-17Si^{NHC} with an interplanar twist angle ϕ of 78.3°, whereas it is oriented more towards the plane in the case of A-17Si (56.4°) and A-17Ge (57.1°).

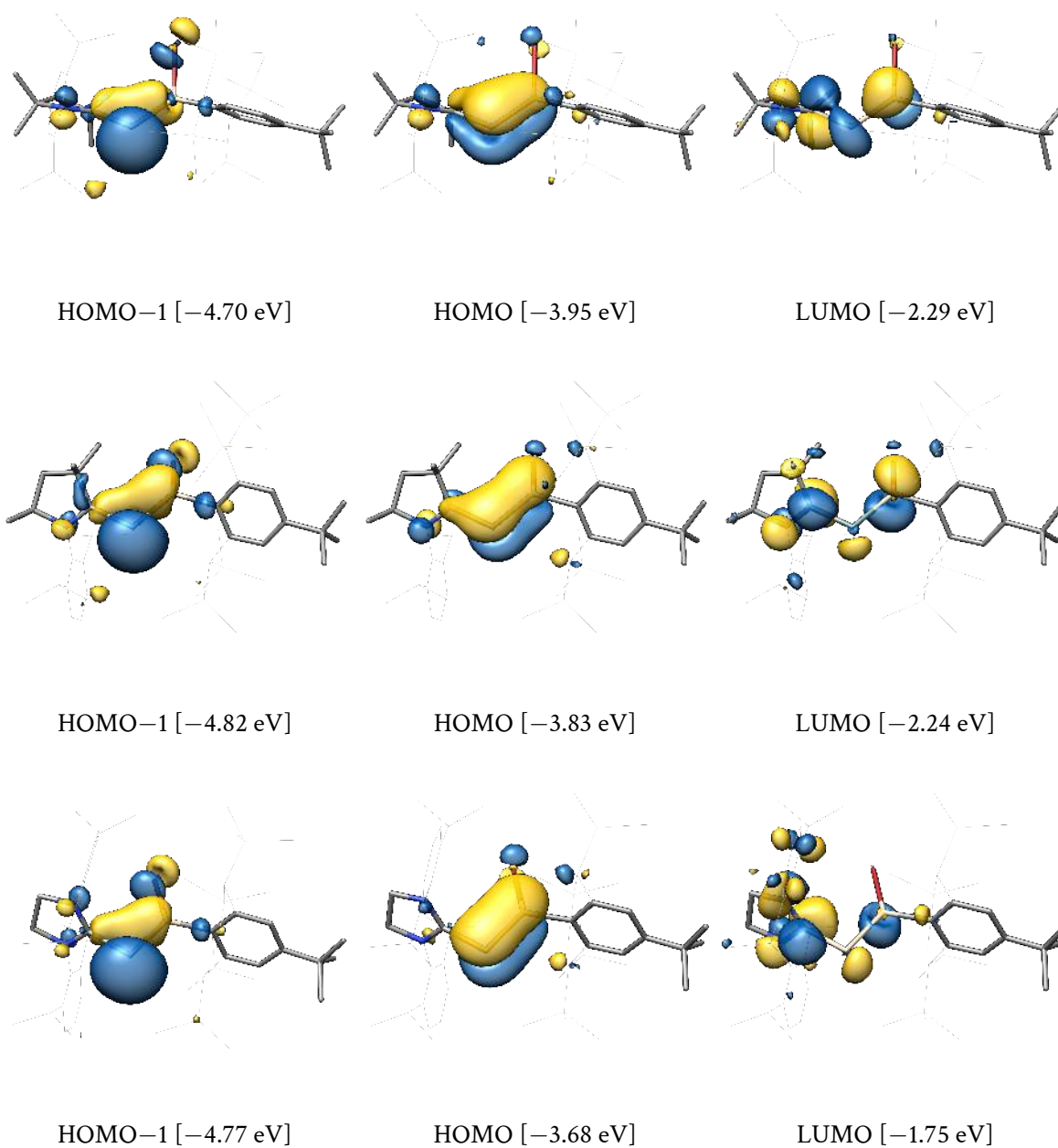


Figure 6.10: Selected canonical MOs of compounds A-17Si, A-17Ge and A-17Si^{NHC}. The MOs of the latter are obtained very similarly as already depicted in reference [266].

The electronic structures of **A-17Si**, **A-17Ge** and **A-17Si^{NHC}** were further analyzed by NRT calculations with the NBO7 program package. NBO, NRT and NPA results for **A-17Si^{NHC}** with the NBO6 program package were already published in ref. [266], and the herein presented values obtained with the NBO7 version for consistency are highly comparable to those presented before.

The calculated NRT bond orders of 1.1 and 1.9 for the Si–C1 and Si–Si' bonds provided in Table 6.8 confirm that the electronic structure of the NHC-stabilized disilavinylidene **A-17Si^{NHC}** is considerably localized and close to the given Lewis structure depicted in Scheme 6.4, which was already concluded in reference [266]. In contrast, the multiple bond character shifts in case of **A-17Ge** with 1.3 (Ge–C1) and 1.8 (Ge–Si'), and is even more pronounced for the compound **A-17Si** where the bond orders converge (1.5 and 1.7). Whereas the covalent and ionic shares are similar for the E–C1, Si'–Br and Si'–C2 bonds, the E–Si' bond is almost exclusively of covalent character with > 80 % covalency. The delocalized electronic structure can alternatively be deduced from the progressing depopulations of the $\pi(\text{E}-\text{Si}')$ NBO (1.83, 1.64 and 1.63 e^-) for **A-17Si^{NHC}**, **A-17Ge** and **A-17Si**, respectively.

The $\sigma(\text{E}-\text{C1})$, $\sigma(\text{E}-\text{Si}')$, $\sigma(\text{Si}'-\text{Br})$ and $\sigma(\text{Si}'-\text{C2})$ NBOs all show large occupations > 1.90 e^- with the expected bond polarizations towards the more electronegative atom. Likewise, the electron lone pairs on the dicoordinate tetrel atoms display lone-pair-typical occupation of ca. 1.75 e^- and high s-character (ca. $sp^{0.3}$ hybridization).

Finally, the calculated NPA charges support an increased charge-backflow from the tetrel to the CAAC^{Me} ligand, as the NPA charges of the dicoordinated tetrel atom increase slightly to +0.14 (**A-17Si**) and +0.06 e (**A-17Ge**) in contrast to the neutral silicon atom (0.00 e) in **A-17Si^{NHC}**. The corresponding NPA charges of the carbenes decrease accordingly slightly from +0.01 e (**A-17Si^{NHC}**) to –0.04 e (**A-17Si**).

The strength of the E–C_{carbene} and E–Si' bonds was assessed by *BCE* and *BDE* calculations. For comparison, they were also computed for **A-17Si^{NHC}** as they were not reported before.

Regarding the E–C1 bond, its cleavage into the carbene and ESi'BrTbb singlet state fragments is energetically favoured by more than 200 $\text{kJ}\cdot\text{mol}^{-1}$ than into two triplet fragments (Table 6.9). This preference is dominated by the large $\Delta E_{s\rightarrow t}$ splittings of the CAAC^{Me} (ca. 200 $\text{kJ}\cdot\text{mol}^{-1}$) and SIDipp (ca. 315 $\text{kJ}\cdot\text{mol}^{-1}$) carbene ligands. The largest singlet *BCEs* are obtained for the compounds **A-17Si** and **A-17Si^{NHC}** with 353.5 and 338.6 $\text{kJ}\cdot\text{mol}^{-1}$, respectively, whereas that of **A-17Ge** is slightly lower (314.5 $\text{kJ}\cdot\text{mol}^{-1}$). All singlet E–C_{carbene} *BCEs* are thus smaller than that of the CAAC^{Me}-stabilized germasilyne **A-14** (413.9 $\text{kJ}\cdot\text{mol}^{-1}$). After structural relaxation, it was found that the singlet and triplet spin states of the ESi(Br)Tbb fragments are isoenergetic ($\Delta E_{s\rightarrow t} = -1.1, -1.7$ and $+0.9$ $\text{kJ}\cdot\text{mol}^{-1}$ for **A-17Si**, **A-17Si^{NHC}** and **A-17Ge**, respectively).² Separate calculations on the model disilavinylidene system SiSi(Br)Ph afforded a singlet-triplet spin state gap $\Delta E_{s\rightarrow t}$ of

²After cleaving off the carbenes CAAC^{Me} and SIDipp from the compounds **A-17Si** and **A-17Si^{NHC}**, both resulting fragments are technically the same, namely SiSi(Br)Tbb. However, as the starting point for the structure optimizations is based on the parent molecule, there may be small conformation changes that lead to (minor) differences in the energies between the optimized fragments, as seen here for the singlet-triplet state splittings.

Table 6.8: Results of the NBO, local NRT (N, C1, E, Si', Br, C2) and NPA analyses of the compounds A-17Si, A-17Ge and A-17Si^{NHC}.

NBO A-B	Occ./ e ⁻	NHO (A,B) pol./% (hyb.)	WBI	NRT-BO tot/cov/ion	NPA / e	
A-17Si						
LP(Si)	1.69	(sp ^{0.4})			Si	+0.14
σ(Si-C1)	1.94	23 (sp ^{5.8}), 77 (sp ^{1.4})	1.0	1.5/0.9/0.6	Si'	+0.67
σ(Si-Si')	1.92	39 (sp ^{8.9}), 62 (sp ^{0.9})	1.6	1.7/1.5/0.2	Br	-0.36
π(Si-Si')	1.63	52 (p), 48 (p)			[CAAC ^{Me}]	-0.04
σ(Si'-Br)	1.97	25 (sp ^{5.0}), 75 (sp ^{3.9})	0.8	1.1/0.5/0.6	[Tbb]	-0.41
σ(Si'-C2)	1.94	28 (sp ^{2.4}), 72 (sp ^{2.5})	0.8	0.9/0.5/0.4		
π*(C1-N)	0.50	27 (p), 73 (p)	1.3	1.5/0.9/0.5		
A-17Ge						
LP(Ge)	1.76	(sp ^{0.2})			Ge	+0.06
σ(Ge-C1)	1.93	24 (sp ^{8.1}), 76 (sp ^{1.5})	1.0	1.3/0.8/0.5	Si'	+0.67
σ(Ge-Si')	1.91	38 (p), 62 (sp ^{0.9})	1.6	1.8/1.5/0.3	Br	-0.36
π(Ge-Si')	1.64	52 (p), 48 (p)			[CAAC ^{Me}]	+0.05
σ(Si'-Br)	1.97	25 (sp ^{4.8}), 75 (sp ^{3.9})	0.8	1.0/0.4/0.6	[Tbb]	-0.42
σ(Si'-C2)	1.94	28 (sp ^{2.4}), 72 (sp ^{2.5})	0.8	0.9/0.5/0.4		
π*(C1-N)	0.45	26 (p), 74 (p)	1.3	1.7/1.0/0.6		
A-17Si^{NHC}						
LP(Si)	1.77	(sp ^{0.3})			Si	0.00
σ(Si-C1)	1.93	22 (sp ^{7.7}), 78 (sp ^{1.3})	0.8	1.1/0.6/0.5	Si'	+0.61
σ(Si-Si')	1.91	41 (sp ^{8.7}), 59 (sp ^{1.2})	1.8	1.9/1.7/0.2	Br	-0.36
π(Si-Si')	1.83	50 (p), 50 (p)			[SIDipp]	+0.01
σ(Si'-Br)	1.97	26 (sp ^{4.8}), 74 (sp ^{3.9})	0.8	0.8/0.4/0.4	[Tbb]	-0.26
σ(Si'-C2)	1.94	28 (sp ^{2.3}), 72 (sp ^{2.5})	0.8	1.0/0.6/0.4		
π*(C1-N)	0.53	78 (p), 22 (p)	1.2	1.4/0.9/0.5		

-14.4 kJ·mol⁻¹, which is in contrast to the clear singlet ground state of the parent disilavinylidene, SiSiH₂, with $\Delta E_{s \rightarrow t} = +43$ kJ·mol⁻¹ according to high-level *ab-initio* calculations by J. F. Stanton *et al.*^[287] However, M. Z. Kassaei *et al.* reported in 2019 calculations of a series of differently substituted disilavinylidenes SiSiR₂ which comprise $\Delta E_{s \rightarrow t}$ gaps ranging from 3.8 to -11.2 kJ·mol⁻¹.^[288] These fit well to the present observations for the disilavinylidene fragment SiSi(Br)Tbb. The hereby resulting *BDEs* are formally of (s→s,t) type for A-17Si and A-17Si^{NHC} and of (s→s,s) type for A-17Ge and comparable to A-17Si (307.5 kJ·mol⁻¹) and A-17Si^{NHC} (292.0 kJ·mol⁻¹). The calculated *BDE* of A-17Ge is slightly smaller with 272.1 kJ·mol⁻¹, which follows the observed trend of the *BCEs*. As expected due to the entropic term, the resulting *BDGs* are lowered compared to the *BDEs* and lie in the range of 187 to 222 kJ·mol⁻¹.

A similar spin state uncertainty was observed for the (carbene)E fragments within the calculation of the E-Si' dissociation energies (Table 6.10). When cleaving the bond in two fragments of the same spin, singlet state fragments are clearly favoured in all cases with similar *BCEs* for A-17Si (272.5 kJ·mol⁻¹) and A-17Ge (264.6 kJ·mol⁻¹), but a significantly higher *BCE* for A-17Si^{NHC}

Table 6.9: Level of theory I-calculated bond cleavage (BCE) and bond dissociation (BDE) energies for the carbene cleavages in the compounds A-17Si, A-17Ge and A-17Si^{NHC} in $\text{kJ}\cdot\text{mol}^{-1}$, entropies in $\text{J}\cdot\text{K}^{-1}\cdot\text{mol}^{-1}$. s = singlet, t = triplet multiplicity.

carbene cleavage	BCE	BDE (parent \rightarrow carbene + ESi'(Br)Tbb)					
	ΔE	mult.	ΔE	ΔU	ΔH	ΔS	ΔG
A-17Si	353.3 (s)	(s \rightarrow s, t)	307.5	294.8	297.3	252.5	222.0
	548.4 (t)						
A-17Ge	314.5 (s)	(s \rightarrow s, s)	272.1	258.4	260.9	248.3	186.9
	513.9 (t)						
A-17Si ^{NHC}	338.6 (s)	(s \rightarrow s, t)	292.0	276.6	279.1	268.8	198.9
	647.3 (t)						

(336.9 $\text{kJ}\cdot\text{mol}^{-1}$). The lower singlet state BCEs in the CAAC^{Me}-supported ditetrelenylenes can be rationalized by the competitive $\pi(\text{Si}-\text{C}1)$ back-bonding as discussed above. The triplet BCEs are ca. 100 $\text{kJ}\cdot\text{mol}^{-1}$ higher in energy, ranging from 387.9 to 429.2 $\text{kJ}\cdot\text{mol}^{-1}$. Upon structural relaxation, the silylene fragment Si'BrTbb displays in every case a clear singlet ground state ($\Delta E_{s\rightarrow t} \approx +128 \text{ kJ}\cdot\text{mol}^{-1}$). However, the (CAAC^{Me})E fragment has virtually isoenergetic singlet and triplet spin states with $\Delta E_{s\rightarrow t}$ values of +8.4 and +2.4 $\text{kJ}\cdot\text{mol}^{-1}$ for E = Si and Ge, respectively, whereas the triplet state of the (SIDipp)Si fragment is preferred ($\Delta E_{s\rightarrow t} = -19.4 \text{ kJ}\cdot\text{mol}^{-1}$). For comparison, several theoretical studies show that the parent system, 1-silynylidene SiCH₂, unequivocally has a singlet ground state with calculated $\Delta E_{s\rightarrow t}$ spin state gaps in the range of +127 to +149 $\text{kJ}\cdot\text{mol}^{-1}$.^[289-291] Notably, the analogous carbon vinylidene H₂CC features a singlet ground state, whereas it was recently shown by M. M. Hansmann *et al.* via quantum chemical calculations and EPR experiments that carbene-derived vinylidenes (carbene)C possess a triplet ground spin state.^[292] It is therefore assumed that the triplet state stabilizing effect of carbene ligands is also present for the heavier tetrelenylenes ECR₂ and thus responsible for the observed spin-degeneracy of the (carbene)E fragment.

Overall, the E-Si' BDEs are similar with 234.6 to 266.6 $\text{kJ}\cdot\text{mol}^{-1}$ and comparable to that of A-14 (237.3 $\text{kJ}\cdot\text{mol}^{-1}$). Interestingly, the obtained free Gibbs bond dissociation energies of 158.9, 146.3 and 172.1 $\text{kJ}\cdot\text{mol}^{-1}$ for A-17Si, A-17Ge and A-17Si^{NHC}, respectively, are slightly smaller than the above-discussed E-C_{carb} dissociation energies by approx. 30 to 60 $\text{kJ}\cdot\text{mol}^{-1}$, which again corroborates the ligand properties of the NHC and CAAC^{Me} substituents.

The experimental ¹H-, ¹³C{¹H}- and ²⁹Si{¹H}-NMR spectra of the compounds A-17Si and A-17Ge reveal an averaged C_s-symmetric structure in solution, in contrast to the C₁-symmetric structure found in the solid state by sc-XRD analysis and in the gas phase by DFT calculations. This can be rationalized by a rapid rotation of the CAAC^{Me} and Tbb substituents about their respective E-C and Si-C bonds.^[276] With VT-NMR spectroscopy below 253 K a splitting of the signal of the TMS groups was found, corresponding to the hindered rotation of the Tbb substituent. Subsequent line-shape analyses of recorded VT-¹H-NMR spectra afforded free Gibbs energies of activation $\Delta G_{\text{exp}}^{\ddagger}$ of 53.3(\pm 1.7) $\text{kJ}\cdot\text{mol}^{-1}$ and 51.6(\pm 3.8) $\text{kJ}\cdot\text{mol}^{-1}$ at 298 K for A-17Si and A-17Ge, respectively. In

Table 6.10: Level of theory I-calculated bond cleavage (*BCE*) and bond dissociation (*BDE*) energies for the E=Si' cleavages of the compounds A-17Si, A-17Ge and A-17Si^{NHC} in kJ·mol⁻¹, entropies in J·K⁻¹·mol⁻¹. s = singlet, t = triplet multiplicity.

E=Si' cleavage	<i>BCE</i> ΔE	<i>BDE</i> (parent \rightarrow (carbene)E + Si'(Br)Tbb) mult.	<i>BDE</i>				
			ΔE	ΔU	ΔH	ΔS	ΔG
A-17Si	272.5 (s)	(s \rightarrow s, s)	242.6	229.9	232.4	246.5	158.9
	402.3 (t)						
A-17Ge	264.6 (s)	(s \rightarrow s, s)	234.6	221.0	223.5	258.7	146.3
	387.9 (t)						
A-17Si ^{NHC}	336.9 (s)	(s \rightarrow t, s)	266.6	251.0	253.5	273.0	172.1
	429.2 (t)						

contrast, the rotation of the CAAC^{Me} ligand could not be frozen out, even at 193 K.

The Si'–C2 bond rotation was assessed by PES scans of the torsion angle E–Si'–C2–C_{ortho} from –60 to 120° in A-17Si and A-17Ge, yielding the Tbb rotation profile depicted in Figure 6.11. The curve progressions appear similarly with a slight shift of ca. 15°, and one maximum is clearly found for both compounds, with their relative energies of +52.8 (A-17Si) and +65.4 kJ·mol⁻¹ (A-17Ge) fitting well to the observed experimental barriers.

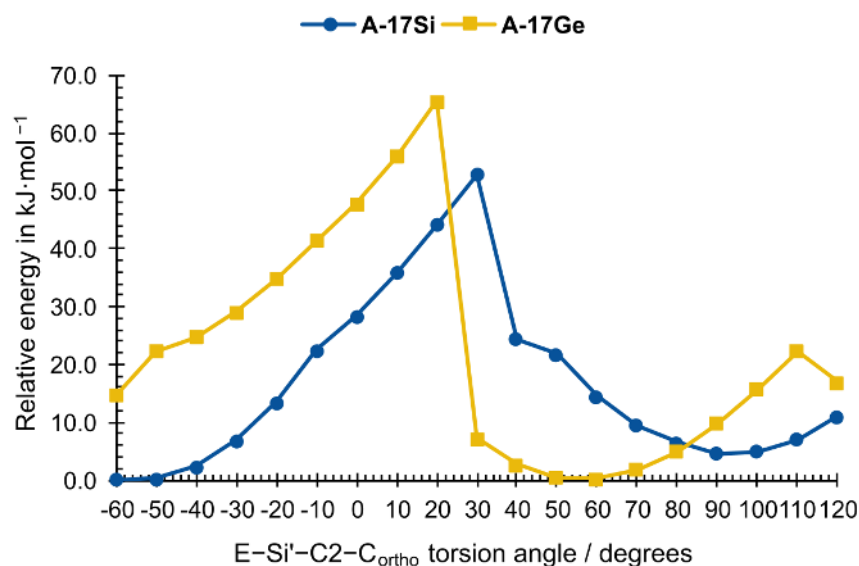


Figure 6.11: PES scans of the E–Si'–C2–C_{ortho} torsion angle for the compounds A-17Si and A-17Ge to study the rotation of the Tbb substituent.

Complementary, the rotation profile of the Si–C1 bond (CAAC^{Me} rotation) was studied by PES scans of the N–C1–E–Si' torsion angle from –180 to 170° (180° $\hat{=}$ –180°) that are given in Figure 6.12. The diagram is again similar for both compounds and reveals that a full rotation has to proceed via the maxima at ca. –60 and +60°. However, their relative energies of ca. 40 (A-17Si) and 30 kJ·mol⁻¹ (A-17Ge) are too high to be not observable by the experiment. Instead, a partial rotation of the CAAC^{Me} ligand is suggested from –140° to +140° via a (–)180° conformation with

C_5 -symmetry (assuming an orthogonally oriented Tbb substituent) that is lying only 14.2 (A-17Si) and 8.3 $\text{kJ}\cdot\text{mol}^{-1}$ (A-17Ge) higher in energy (Scheme 6.14).

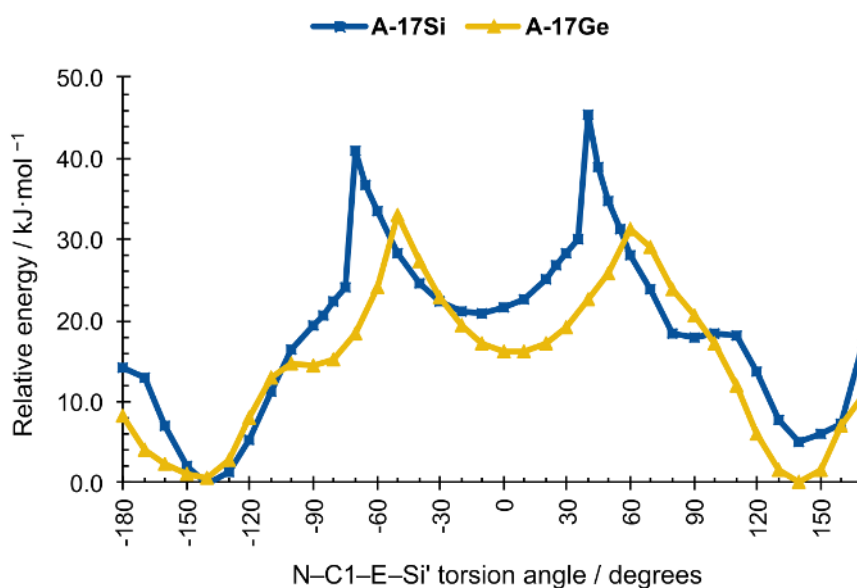
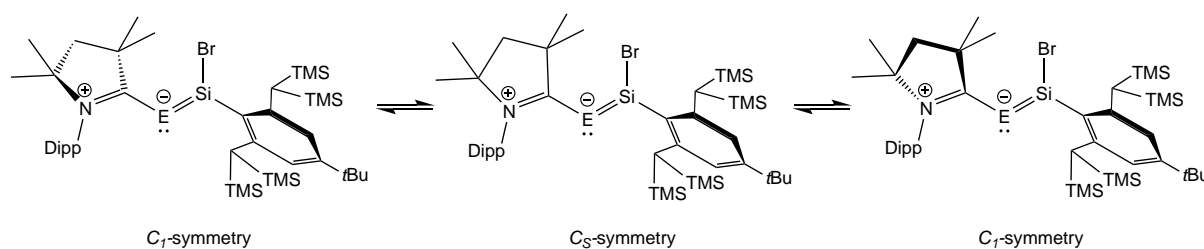


Figure 6.12: PES scans of the N–C1–E–Si' torsion angle for the compounds A-17Si and A-17Ge to study the rotation of the CAAC^{Me} ligand.

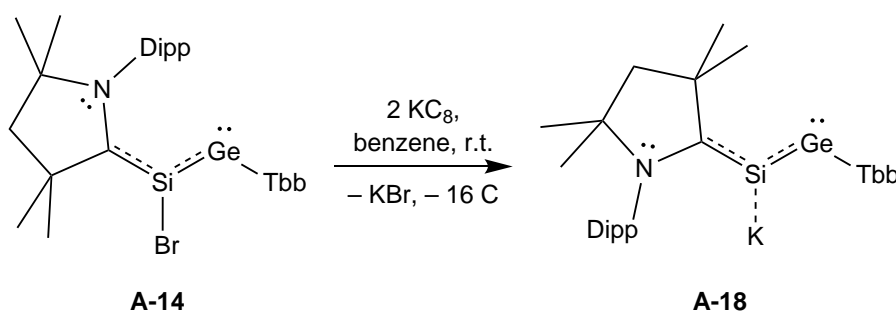


Scheme 6.14: Suggested partial rotation of the CAAC^{Me} ligand via a C_5 -symmetric conformer.

6.5. Calculations on the Reactivity of the CAAC^{Me}-supported Bromogermasilyne A-14

All three compounds A-14, A-17Si and A-17Ge feature a reactive Si–Br bond, which can be used for further functionalization. In this section, accompanying theoretical results to the experimental reactivity studies of compound A-14 by P. Palui^[286] will be presented. The next section will then cover the insight into the reactivity of A-17Si.

The reduction of the compound A-14 with two equivalents of potassium graphite directly leads to (CAAC^{Me})Si(K)GeTbb (A-18), which can be viewed as the first example of a potassium salt of a CAAC^{Me}-stabilized heavier analogue of an acetylide ion [HCC][−].



Scheme 6.15: Synthesis of (CAAC^{Me})Si(K)GeTbb (A-18) as reported by P. Palui.^[286]

The gas phase structure optimization was carried out for the neutral (CAAC^{Me})Si(K)GeTbb molecule, including the potassium cation. The structure is depicted in Figure 6.13 and agrees well with the experimental solid state structure, as the comparison of selected structure parameters from Table 6.11 shows. The only large difference concerns the calculated Si–K bond distance of 326.8 pm, which is longer than their sum of the Pyykkö single bond radii (312 pm),^[228] but still considerably shorter than in the solid state structure (344.2(3) pm). As single molecule gas phase structures tend to minimize charge accumulations, a shortening of the Si–K distance compared to the solid state result seems plausible. Furthermore, a closer inspection of the solid state structure revealed a chain-like arrangement of [(CAAC^{Me})SiGeTbb][−] anions, which are connected via Si···K···Ge bridges that further contribute to the Si–K bond lengthening, as the potassium atoms are effectively two-coordinated.

The compound A-18 is structurally close to its precursor A-14: It features an antiperiplanar C1–Si–Ge–C2 core (172.5°) with a V-shaped dicoordinated germanium atom as evidenced by the Si–Ge–C2 angle of 99.1° (102.4° in A-14). This again suggests the presence of an electron lone pair at the germanium atom which can indeed be found in the HOMO of A-18 (Figure 6.14). The Tbb substituent is approximately orthogonally oriented ($\phi = 75.4^\circ$), whereas the inclination of the CAAC^{Me} ligand of 32.9° is more pronounced than in A-14 (16.9°). This leads to a weakening of the $\pi(\text{Si}-\text{C}1)$ back-donation found in the HOMO–1 (with its non-bonding and anti-bonding combinations in the LUMO and LUMO+4, respectively) and is reflected in the slight increase of the

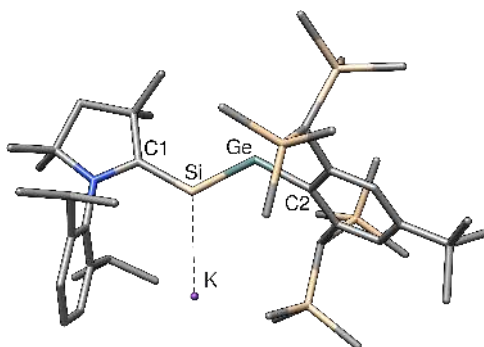


Figure 6.13: Optimized gas phase structure of compound A-18.

Si–C1 bond from 184.3 pm in A-14 to 186.1 pm in A-18. The calculated Si–Ge and Ge–C2 bond lengths of 236.9 pm and 205.4 pm are also similar to those of A-14 (235.0 pm and 203.4 pm).

Table 6.11: Selected structural parameters of the calculated gas phase and experimental sc-XRD structures A-18 and A-18_{exp}. Bond lengths are given in pm and angles in degrees. τ and ϕ describe the interplanar twist angle between the CAAC^{Me} azolidine ring or Tbb ring planes and the (C1SiGeC2) plane, respectively.

	Si–C1	Si–Ge	Si–K	Ge–C2	C1–Si–Ge
A-18	186.1	236.9	326.8	205.4	105.7
A-18 _{exp}	186.5(2)	234.6(3)	344.2(3)	202.5(1)	104.8(3)
	Si–Ge–C2	C1–Si–Ge–C2	τ	ϕ	
A-18	99.1	172.5	32.9	75.4	
A-18 _{exp}	103.4(2)	171.9(4)	33.3(4)	78.9(3)	

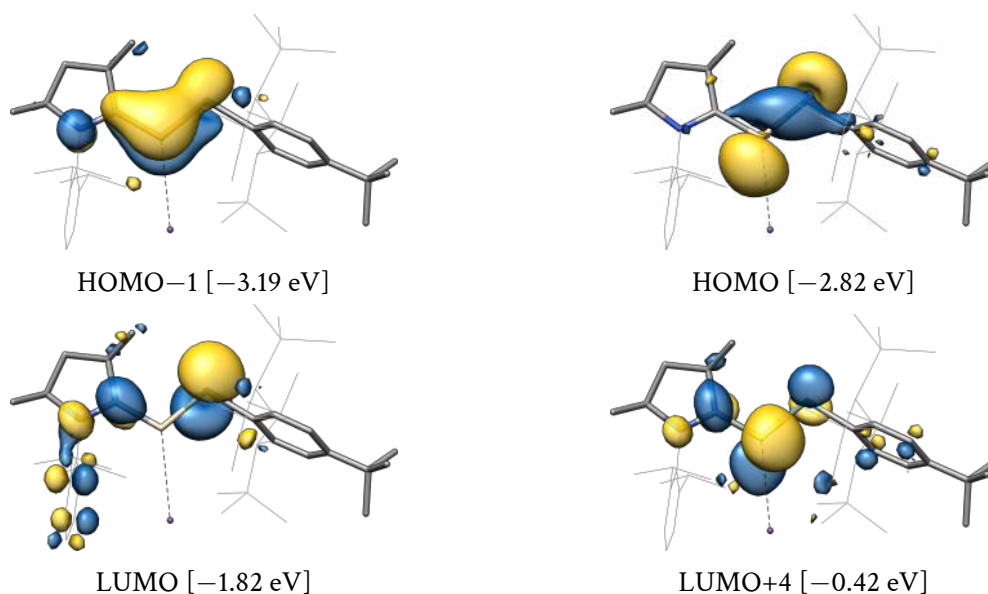


Figure 6.14: Selected canonical molecular orbitals of the compound A-18 and their energy eigenvalues.

The HOMO of compound **A-18** displays lone pair density at both tetrel atoms with the same phase and corresponds to an average of one electron per tetrel. It is expected that another MO showing heavier tetrel lone pair density with different orbital phases should be present in the canonical MOs, however, an unambiguous example for this was not found. As each heavier tetrel atom should bear a lone pair consisting of two electrons, which could not be identified due to the delocalized nature of the canonical set of molecular orbitals, the wave function was further analyzed by the IBO localization and NBO methods.

In fact, the set of localized IBOs comprises a 2-electron lone pair orbital for each heavier tetrel atom (Figure 6.15). The Loewdin orbital populations reveal a slightly lower localization of the Si lone pair at Si (0.71) than for germanium (0.87), which can be explained by the contribution of the potassium atom at the Si lone pair (0.14) and indicates some Si–K orbital interaction. Beside the expected $\sigma(\text{Si}-\text{C}1)$, $\sigma(\text{Si}-\text{Ge})$ and $\sigma(\text{Ge}-\text{C}2)$ bond orbitals, The IBO method can also reproduce the $\pi_{\text{oop}}(\text{C}1-\text{Si}-\text{Ge})$ 3c-2e⁻ bond well.

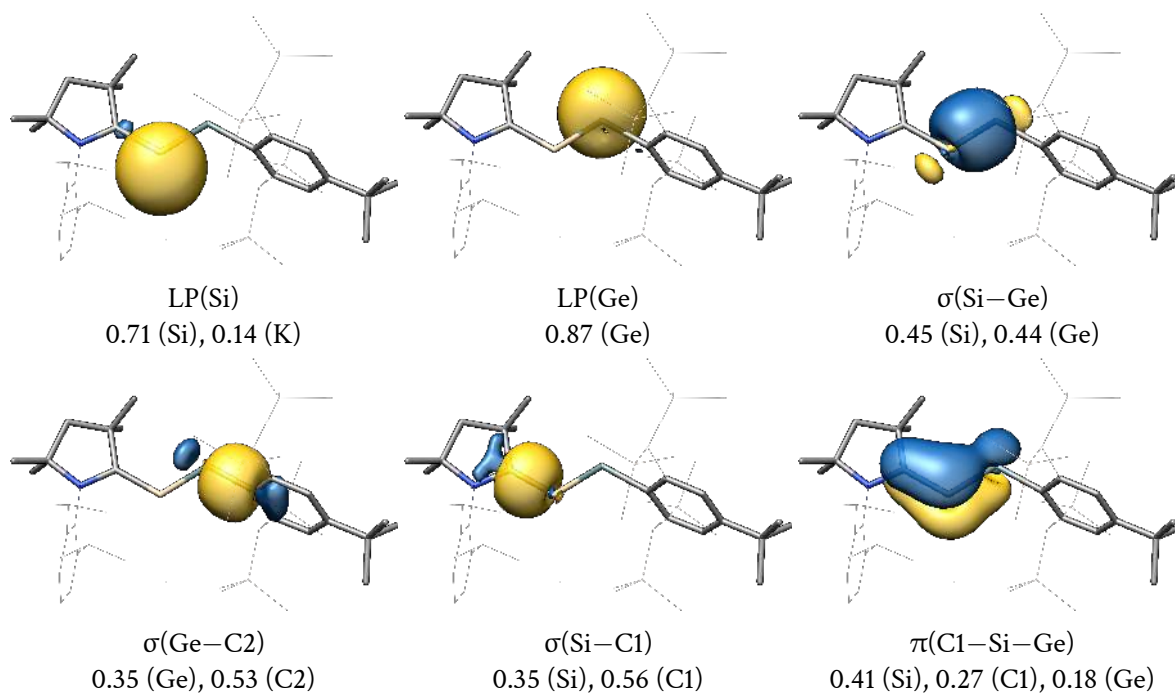
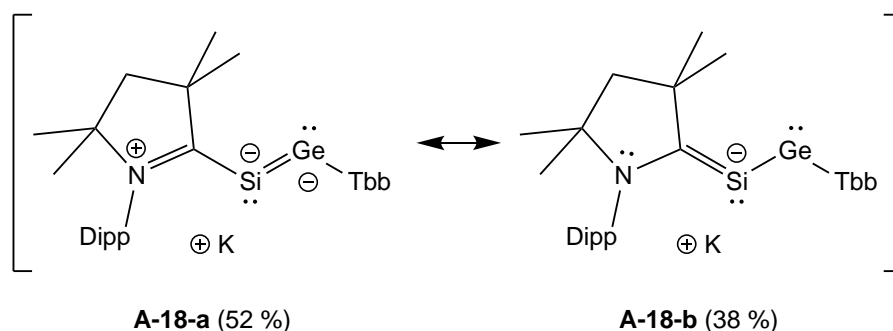


Figure 6.15: Selected intrinsic bond orbitals (IBOs) of the CAAC^{Me}-stabilized heavier acetylide salt **A-18** and their atomic Loewdin orbital populations.

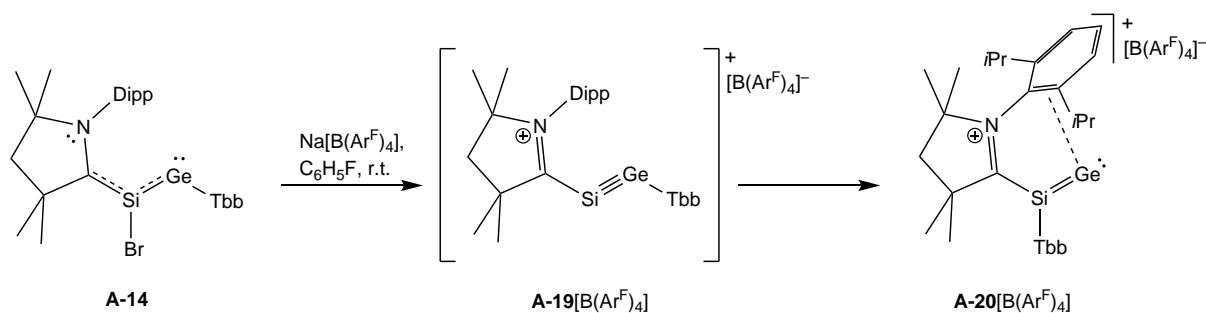
Further support comes from the NBO results: The most dominant contributions to the NRT resonance hybrid are **A-18-a** (52 %) and **A-18-b** (38 %) that feature electron lone pairs on each heavier tetrel atom, no Si–K bond and differ only in the position of the double bond, underlining the presence of the aforementioned $\pi_{\text{oop}}(\text{C}1-\text{Si}-\text{Ge})$ 3c-2e⁻ bond (Scheme 6.16).

Alternatively, the bromine substituent can be abstracted by a halide scavenger instead of reduction. In this regard, the reaction of **A-14** with Na[B(Ar^F)₄] would afford the cation [(CAAC^{Me})SiGeTbb]⁺ (**A-19**⁺), however, only the constitutional isomer [(CAAC^{Me})Si(Tbb)Ge]⁺ (**A-20**⁺) is observed (Scheme 6.17). Its formation can be rationalized by the abstraction of the bromide ion to the cation



Scheme 6.16: Most dominant resonance contributions of **A-18** and their resonance weights from a local NRT analysis comprising the N, C1, Si, K, Ge and C2 atoms.

A-19⁺, followed by the immediate migration of the Tbb substituent to the silicon atom, leaving behind a bare germanium atom. The last step from **A-19⁺** to **A-20⁺** was calculated to be favoured in terms of energy ($\Delta E = -64.3 \text{ kJ}\cdot\text{mol}^{-1}$) and free Gibbs energy ($\Delta G = -57.3 \text{ kJ}\cdot\text{mol}^{-1}$). The reaction path was then modelled by the double-ended growing string method (GSM)^[123] at the level of theory I that yields the transition state **A-19⁺-TS** (Figure 6.16). Herein, the Tbb substituent lies between the silicon and germanium atom (Si–C2: 241.8 pm, Ge–C2: 228.4 pm), reminiscent of a Wheland complex via an arenium ion. A subsequent frequency calculation confirms that the cation **A-19⁺-TS** has an imaginary frequency of 114i cm^{-1} that describes the motion of the Tbb group well. However, it also contains a second frequency at 72i cm^{-1} which shows the vibration of several methyl groups within the molecule. Unfortunately, all attempts to remove the second negative vibration have been unsuccessful so far. **A-19⁺-TS** lies 60.3 $\text{kJ}\cdot\text{mol}^{-1}$ higher in electronic energy than **A-19⁺** ($\Delta G = 66.0 \text{ kJ}\cdot\text{mol}^{-1}$), but is expected to decrease further in energy if a proper transition state optimization is successful.



Scheme 6.17: Synthesis of the CAAC^{Me}-stabilized heavier acetylium cation [(CAAC^{Me})Si(Tbb)Ge]⁺ **A-20⁺** via the presumed intermediate **A-19⁺**.

Compound **A-20⁺** represents the first example of a CAAC^{Me}-stabilized heavier analogue of the acetylium ion [HC≡C]⁺, but can also be viewed as silagermenylenium cation. Its calculated gas phase structure, depicted in Figure 6.16, compares generally well with the experimental sc-XRD structure **A-20⁺_{exp}**, although the Si–C1 bond length of 184.4 pm was found slightly longer than in the solid state (179.3(2) pm, see Table 6.12), but identical to that of compound **A-14** (184.3 pm). The silicon atom adopts a trigonal-pyramidal orientation with a sum of angles $\Sigma\angle(\text{Si}) = 359.9^\circ$,

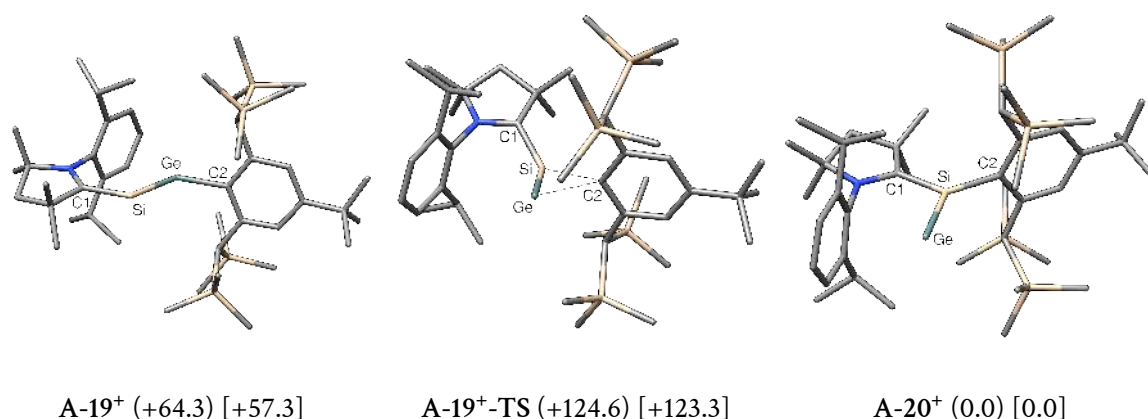


Figure 6.16: Optimized gas phase structures of the compounds A-19⁺, A-20⁺ and the transition state A-19⁺-TS as well as their relative electronic energies in kJ·mol⁻¹ (ΔG in square brackets). Selected structural parameters of A-19⁺: Si–C1: 185.9 pm, Si–Ge: 224.2 pm, Ge–C2: 193.4 pm, C1–Si–Ge: 119.0°, Si–Ge–C2: 128.3°, C1–Si–Ge–C2: –173.0°. Selected structural parameters for A-19⁺-TS: Si–C1: 185.4 pm, Si–Ge: 226.7 pm, Si–C2: 241.8 pm, Ge–C2: 228.4 pm, C1–Si–Ge: 129.2°.

forming bonds with the terminal germanium atom (Si–Ge: 232.1 pm) and the Tbb substituent (Si–C2: 188.5 pm). The (CAAC^{Me}), (C1SiGeC2) interplanar twist angle τ of 1.4° indicates an almost perfect coplanarity of the azolidine ring with the (C1SiGeC2) core, whereas the Tbb substituent adopts an almost perfect orthogonal orientation (88.6°). The coplanarity once again enables a π (Si–C1) back-bonding by delocalization of the π_{oop} (Si–Ge) bond into the π_{oop}^* (C1–N) orbital of the CAAC^{Me} ligand, which can be identified in the HOMO, and its non-bonding combination in the LUMO (Figure 6.17). The HOMO–3 (and HOMO–2, albeit less pronounced) correspond to a residual electron lone pair at the germanium atom and the σ (Si–Ge) bond. Further stabilization of the germanium atom stems from the π -system of the Dipp substituent of the CAAC^{Me} ligand, as the rather close Ge–C_{ipso} contact of 276.7 pm enables a π (C–C) \rightarrow p(Ge) interaction. This is supported by the HOMO–14 and, more impressively, by the anti-bonding combination visible in the LUMO+1, which is mostly the empty p orbital at the Ge atom.

Table 6.12: Selected bond parameters of the calculated and experimental sc-XRD CAAC^{Me}-stabilized silagermenylidenes A-20⁺ and A-20⁺_{exp}. Bond lengths are given in pm and angles in degrees. τ and ϕ describe the interplanar twist angle between the CAAC^{Me} azolidine ring or Tbb ring planes and the (C1SiGeC2) plane, respectively.

	Si–C1	Si–C2	Si–Ge	C1–Si–C2	$\Sigma\angle(\text{Si})$	τ	ϕ
A-20 ⁺	184.4	188.5	232.1	122.4	359.9	1.4	88.6
A-20 ⁺ _{exp}	179.3(2)	190.8(2)	230.6(1)	121.6(1)	359.9(2)	5.9(1)	87.1(1)

The two most dominant contributions to the NRT resonance hybrid of A-20⁺ are depicted in Scheme 6.18. The Si–Ge doubly-bonded Lewis structure A-20⁺-a has the highest share of 55 %, followed by A-20⁺-b, where the double bond is shifted to the Si–C1 bond (35 %).

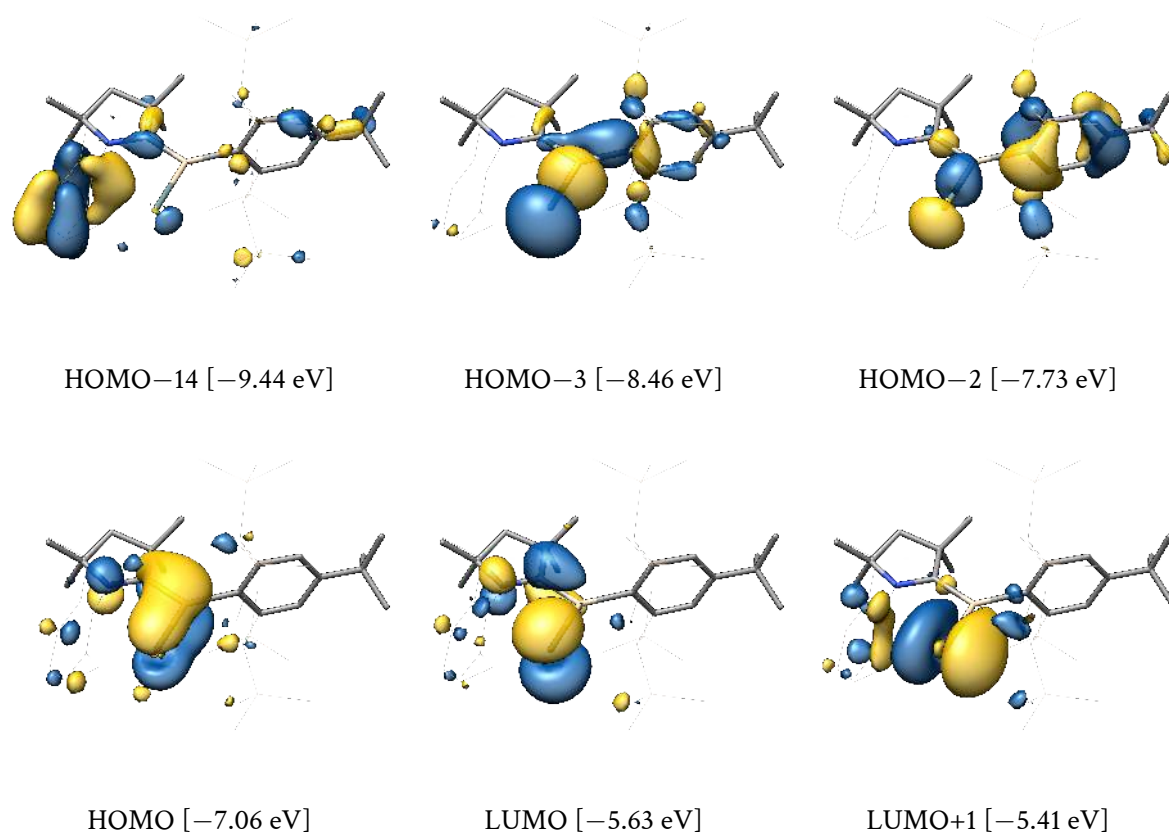
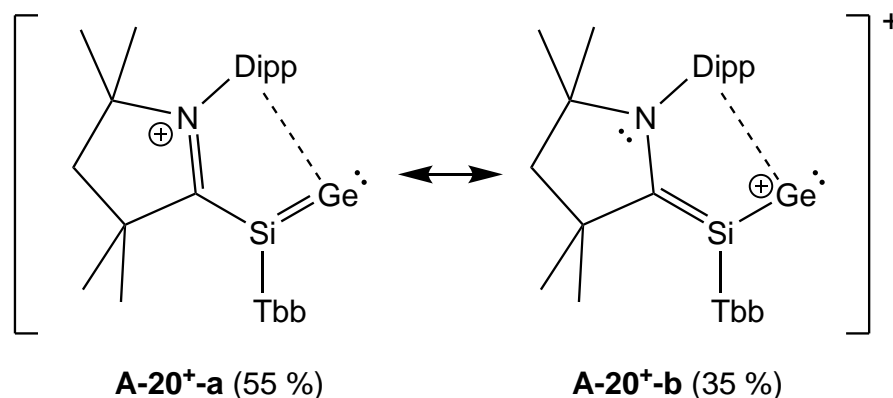


Figure 6.17: Selected canonical molecular orbitals of compound A-20⁺ and their energy eigenvalues.



Scheme 6.18: Most dominant resonance contributions of A-20⁺ and their resonance weights from a local NRT analysis comprising the N, C1, Si, Ge and C2 atoms.

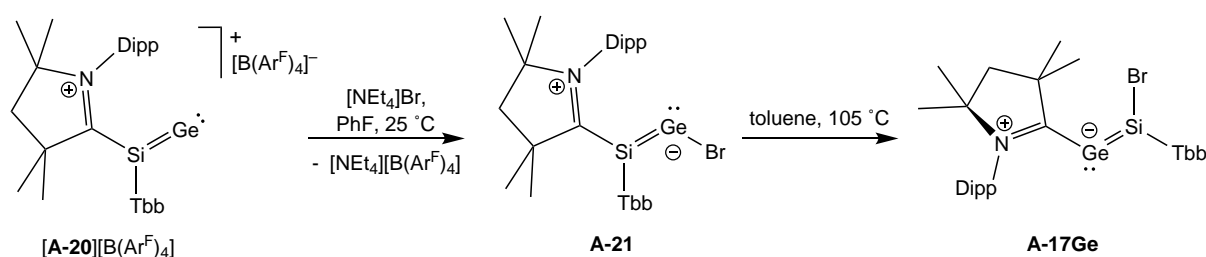
Thus, the total NRT bond orders of 1.6 and 1.4 for the Si–Ge and Si–C1 bonds are similar and mostly of covalent character (0.9, 1.3). The NBOs of the $\sigma(\text{Si}-\text{C}1)$, $\sigma(\text{Si}-\text{C}2)$ and $\sigma(\text{Si}-\text{Ge})$ bonds as well of the lone pair at the germanium atom have large occupations $> 1.93 e^-$ (Table 6.13), whereas it is considerably lower for the delocalized $\pi(\text{Si}-\text{Ge})$ NBO ($1.47 e^-$). The NPA analysis of the cationic compound reveals large charge accumulations on the silicon (+0.72 e) and germanium

Table 6.13: Results of the NBO, local NRT (Si,Ge,C1,N,C2 atoms) and NPA analyses of compound A-20⁺.

NBO A-B	Occ./ e ⁻	NHO (A,B) pol./% (hyb.)	WBI	NRT-BO tot/cov/ion	NPA / e	
LP(Ge)	1.96	(sp ^{0.13})			Si	+0.72
σ(Si-C1)	1.95	25 (sp ^{2.8}), 75 (sp ^{1.5})	1.0	1.4/0.9/0.5	Ge	+0.43
σ(Si-C2)	1.95	31 (sp ^{1.8}), 69 (sp ^{2.6})	0.8	0.9/0.6/0.4	[CAAC ^{Me}]	+0.11
σ(Si-Ge)	1.93	59 (sp ^{1.6}), 41 (sp ^{7.6})	1.4	1.6/1.3/0.3	[Tbb]	-0.26
π(Si-Ge)	1.47	62 (p), 38 (p)				
LV(Ge)	0.17	(p)				
π*(C1-N)	0.54	27 (p), 73 (p)	1.3	1.6/1.0/0.6		

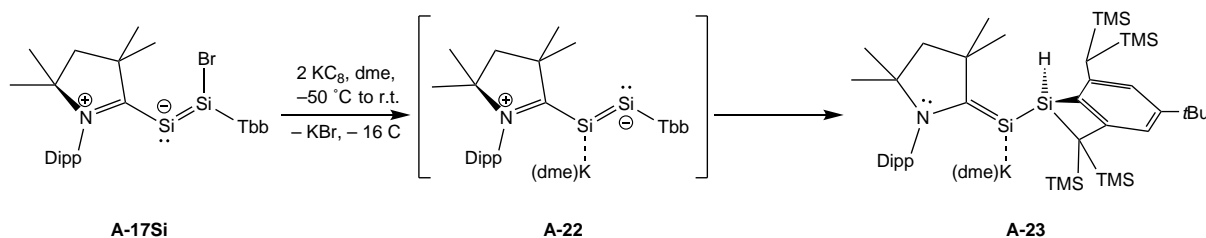
atoms (+0.43 e), whereas the CAAC^{Me} ligand bears only a low positive charge of +0.11 e. The Tbb substituent is found to even contain a negative group charge of -0.26 e.

Interestingly, a re-addition of a bromide ion to the cation A-20⁺ results in the formation of the neutral CAAC^{Me}-supported bromogermasilyne A-21, which is a constitutional isomer of the CAAC^{Me}-supported bromogermasilyne A-14 and differs in the positions of the bromine and Tbb substituents (see the appendix for its calculated structure). Relative to A-14, it lies -10.1 kJ·mol⁻¹ lower in energy, but +3.3 kJ·mol⁻¹ higher in terms of the free Gibbs energy Δ*G*. However, heating of compound A-21 does not yield the CAAC^{Me}-supported germasilyne A-14, but instead its other constitutional isomer, the CAAC^{Me}-supported heavier silagermenylidene (CAAC^{Me})GeSi(Br)Tbb (A-17Ge), is obtained (Scheme 6.19). Calculations reveal that such a reaction is indeed slightly favoured thermodynamically, as the computed reaction energy Δ*E* and free Gibbs energy Δ*G* amount to -5.2 and -14.4 kJ·mol⁻¹. However, the detailed mechanism of the isomerization reaction could not be studied yet.

**Scheme 6.19:** Reaction scheme for the bromide addition to A-20⁺ yielding compound A-21 and subsequent thermally-induced isomerization to the CAAC^{Me}-supported silagermenylidene A-17Ge.

6.6. Calculations on the Reactivity of the CAAC^{Me}-supported Disilavinylidene A-17Si

The CAAC^{Me}-supported disilavinylidene A-17Si features a reactive Si–Br bond that can be used for further functionalization, just as with compound A-14. F. Gstrein carried out the reduction of the compound A-17Si with two equivalents of potassium graphite in dimethoxyethane (dme) in order to obtain the heavier potassium acetylide (CAAC^{Me})Si(K)SiTbb (A-22),^[276] which would be the lighter homologue to compound A-18. However, only the selective formation of the C–H bond activated potassium silenide salt (CAAC^{Me})Si(K(dme))SiTbb (A-23) is observed (Scheme 6.20). In this compound, the Tbb-bonded silicon atom has activated the C–H bond of one of the bisyl (CH(SiMe₃)₂) groups of the Tbb substituent.



Scheme 6.20: Reduction of the disilavinylidene A-17Si via the putative heavier potassium acetylide A-22 to the C–H-bond activation product A-23.

The structure of the elusive molecule A-22 was optimized as neutral compound in the gas phase with the dme-coordinated potassium atom (Figure 6.18, Table 6.14). The obtained Si–Si' bond length of 228.9 pm is longer than that in the disilavinylidene A-17Si (220.7 pm), but shorter than in the Si(I) dimer A-13 (236.0 pm), lying in between typical Si–Si single (234 pm) and Si=Si double bonds (214 pm).^[140] The Si–C1 bond length of 185.9 pm is still quite short and indicates some multiple-bond character, which is supported by the HOMO–1 depicted in Figure 6.19. Therein, the $\pi(\text{Si}–\text{Si}')$ orbital is slightly delocalized into the $\pi^*(\text{C1}–\text{N})$ as discussed before for other compounds. In the LUMO and LUMO+4 the corresponding non- and anti-bonding orbital combinations can be observed. Similar to compound A-18, each silicon atom of the molecular core is expected to bear one electron lone pair. In fact, the out-of-phase and in-phase combinations of those can be found in the HOMO–2 and HOMO, respectively. Overall, this mainly results in the electronic structure depicted in the Lewis formula of Scheme 6.20 for A-22.

Finally, the reaction energy for the activation of A-22 to A-23 was also calculated and amounts to $-56.6 \text{ kJ}\cdot\text{mol}^{-1}$ ($-55.4 \text{ kJ}\cdot\text{mol}^{-1}$ for ΔG), which renders the observed reaction thermodynamically reasonable. More information on the calculated structure of the activation product A-23 is deposited in the appendix.

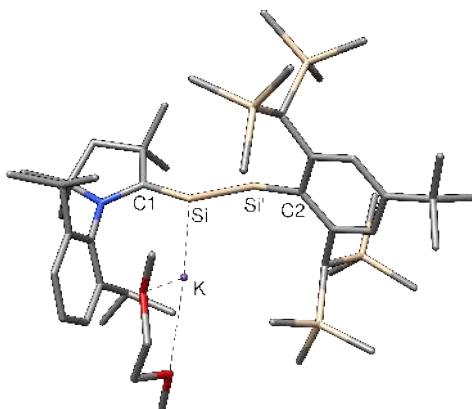


Figure 6.18: Optimized gas phase structure of the elusive intermediate A-22.

Table 6.14: Selected structural parameters of the calculated heavier potassium acetylide A-22. Bond lengths and angles are given in pm and degrees, respectively. τ and ϕ describe the interplanar twist angle between the CAAC^{Me} azolidine ring or Tbb ring planes and the (C1SiGSi'C2) plane, respectively.

	Si-C1	Si-Si'	Si-K	Si'-C2	C1-Si-Si'	τ	ϕ
A-22	185.9	228.9	331.5	194.1	105.7	37.4	73.2

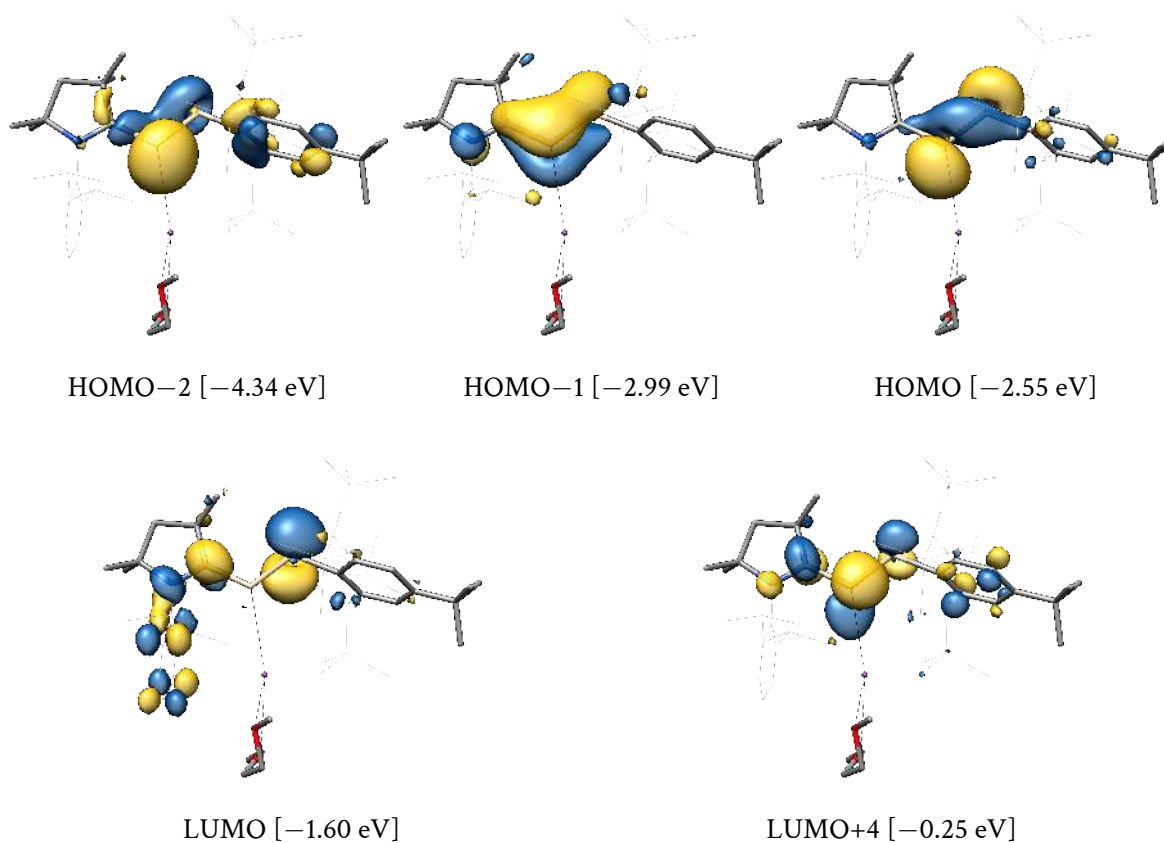


Figure 6.19: Selected canonical molecular orbitals of compound A-22 and their energy eigenvalues.

Part B.

Computational Studies on Heavier Tetrel Transition Metal Complexes

7. Digermyne Cobalt Complexes

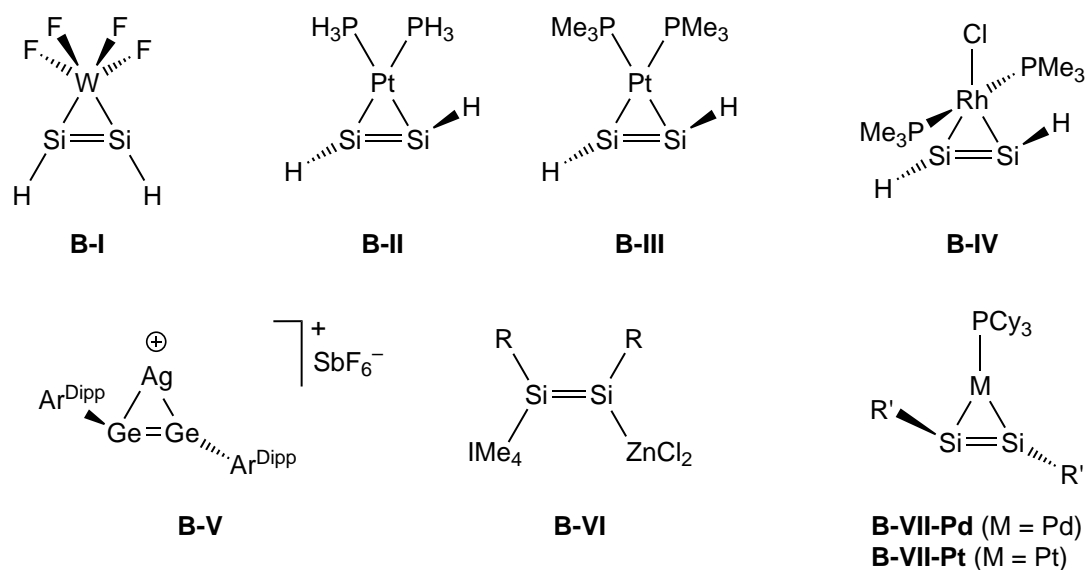
7.1. Introduction

Since their discovery almost 25 years ago, the heavier ditetrelynes REER (E = Si to Pb) prove to be fascinating compounds and their potential in main group catalysis and the activation of small molecules is subject of eager investigation.^[232, 246, 247] In contrast, the coordination chemistry of heavier ditetrelynes to transition metals is still underdeveloped and only a few theoretical and experimental studies on the unique ligand properties of this class of compounds exist. Already in the year 1995, R. Stegmann and G. Frenking reported calculations that show that the energetical order of the Si₂H₂ isomers (see Scheme 6.1 in chapter A6) is completely changed when coordinated to a [WF₄] metal fragment.^[293] In fact, the lowest-lying isomer for the disilyne tungsten complex [WF₄(Si₂H₂)] (B-I, Scheme 7.1) was found to display a *cis-bent* arrangement of the disilyne fragment and metallacyclopropene character. Another early theoretical report by S. Sakaki *et al.* from the year 2005 addressed the coordination and energetics of the Si₂H₂ isomers in the platinum complexes [Pt(PH₃)₂(Si₂H₂)] (B-II) and [Pt(PMe₃)₂(Si₂H₂)] (B-III) as well as of the rhodium complex [RhCl(PMe₃)₂(Si₂H₂)] (B-IV).^[294] Therein, the most favoured coordination mode of the disilyne Si₂H₂ was calculated to be its disilavinylidene or hydrogen-dibridged isomers, with the η^2 -disilyne coordinated complex lying 20 to 40 kJ·mol⁻¹ higher in energy.

The first experimental evidence of a heavier ditetrellyne acting as a Lewis base towards a transition metal comes from the group of P. P. Power from the year 2010.^[295] The digermine Ar^{Dipp}GeGeAr^{Dipp} was reacted with the silver salt Ag[SbF₆] to afford the digermine-silver complex [Ag(Ar^{Dipp}GeGeAr^{Dipp})[SbF₆] (B-V) in which the digermine acts as a η^2 -donor towards the silver cation. By subsequent DFT calculations on a model system, the authors concluded that B-V is best described by both the π -complex and σ -metallacyclopropene Lewis structures.

In the same year, A. Sekiguchi *et al.* reported the push-pull complex (*E*)-[RSi(IME₄)Si(ZnCl₂)R] (B-VI, R = Si(*i*Pr)(CH(TMS)₂)), where the disilyne was first coordinated by the small NHC IME₄ and then, in the second step, reacted with ZnCl₂.^[296] A disilyne was also used by T. Iwamoto *et al.* as ligand in the monophosphane palladium and platinum complexes [M(PCy₃)(R'SiSiR')] (M = Pd (B-VII-Pd), Pt (B-VII-Pt); R' = C(TMS)₂(CH₂*t*Bu)), which feature an almost symmetrical η^2 -disilyne coordination with *trans-bent* and slightly bent-back substituents R' as well as dominant metallacycle character according to quantum chemical calculations.^[297]

Finally, the heavier ditetrellyne π -complexes [M(CO)₅(Ar^{Dipp}EEAr^{Dipp})] of group 6 transition metals (M = Cr, Mo, W; E = Ge, Sn) were presumed to be intermediates in the reactions between the



Scheme 7.1: Various heavier ditetrelene transition metal complexes studied by theory and experiment. $\text{Ar}^{\text{Dipp}} = 2,6\text{-}(\text{C}_6\text{H}_3\text{-}2,6\text{-iPr}_2)_2\text{-C}_6\text{H}_3$, $\text{IMe}_4 = 1,3,4,5\text{-tetramethylimidazol-}2\text{-ylidene}$, $\text{R} = \text{Si}(\text{iPr})(\text{CH}(\text{TMS})_2)$, $\text{R}' = \text{C}(\text{TMS})_2(\text{CH}_2\text{tBu})$.

ditetrelenes $\text{Ar}^{\text{Dipp}}\text{EAr}^{\text{Dipp}}$ and the metal carbonyl complexes $[\text{M}(\text{CO})_6]$, although they could not be observed.^[298]

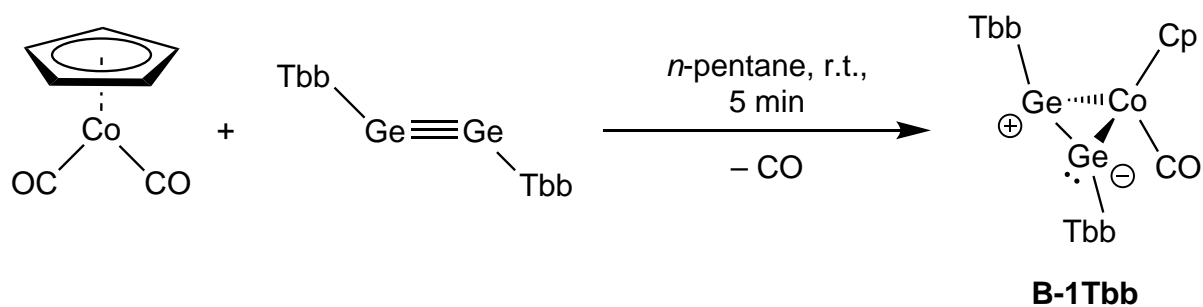
However, no reports of heavier ditetrelenes as ligands are known for cobalt. This is in stark contrast to the well-known alkyne chemistry, where cobalt is part of important organometallic reactions such as the alkyne cyclotrimerization^[299–301] or the Pauson-Khand reaction.^[302–304] The absence of studies on heavier ditetrelene complexes of cobalt makes these complexes a valuable target, and, due to their *trans*-bent character, an alkyne-unlike reactivity is expected for this compound class.

7.2. Digermyne Cobalt Complexes

[CoCp(CO)(RGeGeR)] (B-1R)

In this context, P. Palui from our group succeeded with the reaction of $[\text{CoCp}(\text{CO})_2]$ with one equivalent of the digermene TbbGeGeTbb , affording the first cobalt digermene complex $[\text{CoCp}(\text{CO})(\text{TbbGeGeTbb})]$ (**B-1Tbb**, see Scheme 7.2).^[286] This outcome is remarkable as there are only two examples known for carbon where an alkyne substitutes a carbonyl ligand of $[\text{CoCp}(\text{CO})_2]$ and forms a alkyne cobalt complex.^[305, 306]

The structure of **B-1Tbb** was calculated using the ORCA 4.1.1 program package on level of theory I starting from the available sc-XRD structure **B-1Tbb_{exp}**, and selected structural parameters are summarized in Table 7.1.



Scheme 7.2: Synthesis of the digermine cobalt complex B-1Tbb by P. Palui.^[286]

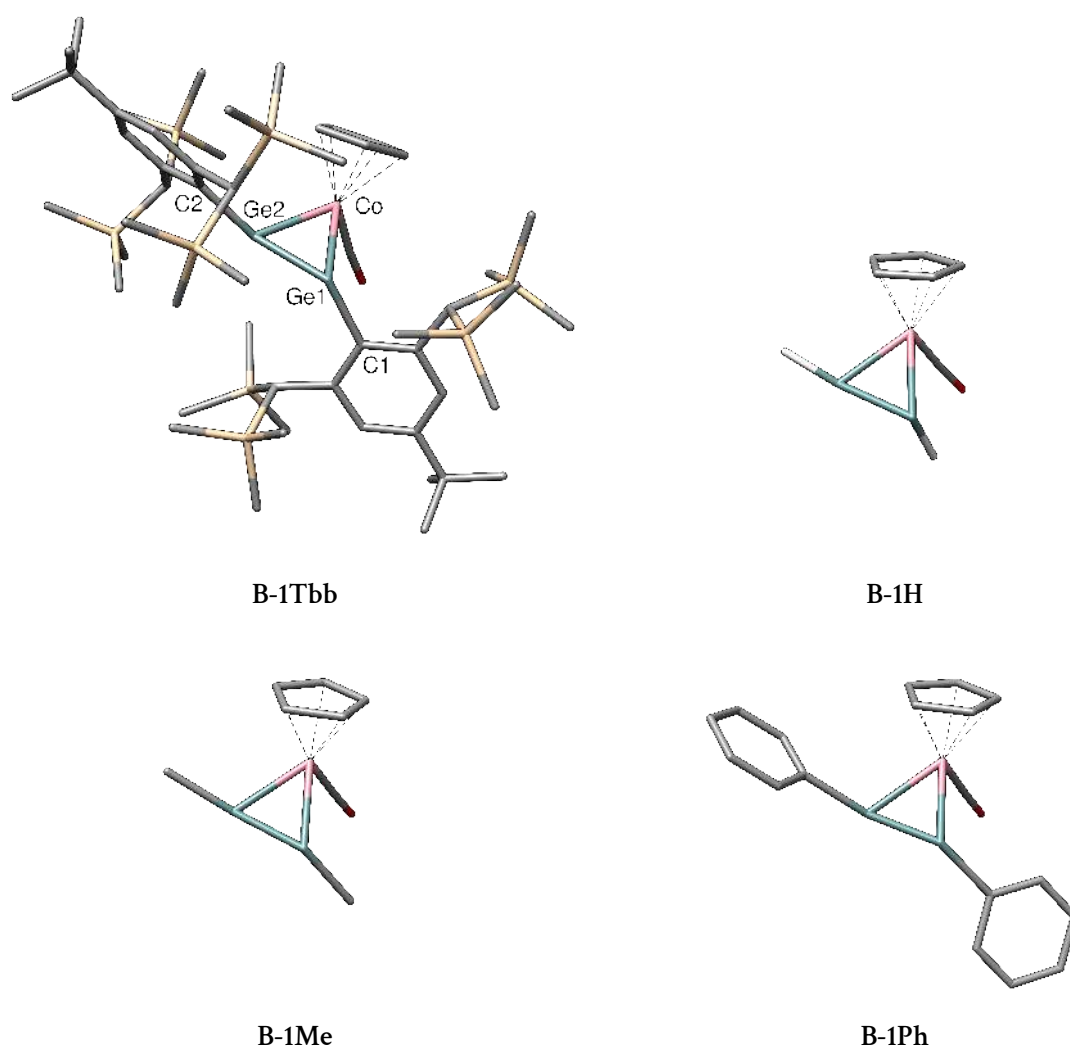


Figure 7.1: Optimized gas phase structures of the digermine cobalt complexes B-1R with R = Tbb, H, Me and Ph. All hydrogen atoms are omitted for clarity except in B-1H.

As visible from Figure 7.1, the digermine ligand in B-1Tbb coordinates in a η^2 -fashion, as already seen in the complexes B-V and B-VII-M, and retains its *trans*-bent orientation (C1–Ge1–Ge2–C2: 159.7°). However, the different Ge1–Co and Ge2–Co bond lengths of 257.0 and 236.2 pm reveal a pronounced asymmetric coordination with $\Delta d = |d(E1-M) - d(E2-M)| = 20.8$ pm of the digermine, which was not described in the case of B-V ($\Delta d = 0$ pm) and only slightly for B-VII-M

Table 7.1: Selected bond parameters of the calculated and experimental diggermyne cobalt complexes **B-1R**. Bond lengths are given in pm and angles in degrees.

	Ge1–Ge2	Ge1–Co	Ge2–Co3	Ge1–C1	Ge2–C2
B-1Tbb	238.9	257.0	236.2	200.0	200.4
B-1Tbb_{exp}	234.5(1)	250.1(1)	236.8(1)	198.0(2)	197.3(2)
B-1H	242.1	258.0	228.7	159.4 ^{a)}	158.3 ^{a)}
B-1Me	241.3	250.7	235.0	202.3	201.4
B-1Ph	241.5	246.1	238.0	198.7	199.1
	Ge1–Co–Ge2	C1–Ge1–Ge2–C2	$\Sigma\angle(\text{Ge1})$	$\Sigma\angle(\text{Ge2})$	
B-1Tbb	57.8	159.7	290.3	315.5	
B-1Tbb_{exp}	57.5(1)	155.9(2)	306.6(2)	316.9(2)	
B-1H	59.3	165.8 ^{b)}	250.4	321.3	
B-1Me	59.5	164.4	284.1	310.5	
B-1Ph	59.8	165.6	289.9	298.0	

a) Ge–H distance; b) H1–Ge1–Ge2–H2 torsion angle.

($\Delta d = 2$ pm). Whereas the Ge2–Co bond lengths in the calculated structure **B-1Tbb** (236.2 pm) and the experimental structure **B-1Tbb_{exp}** (236.8(1) pm) are nearly identical, a considerable deviation is found for the Ge1–Co bond (**B-1Tbb**: 257.0 pm, **B-1Tbb_{exp}**: 250.1(1) pm), which is indicating a rather flat energy hypersurface with respect to the Ge1–Co bond. In fact, a two-dimensional PES scan shows only a negligible change of energy below 10 kJ·mol⁻¹ when both Ge–Co bond lengths are varied in a wide range from 230 to 260 pm (Figure 7.2), and a symmetric coordination can be easily obtained below 5 kJ·mol⁻¹.

The large Δd values are also rather independent of the substituent at the diggermyne, as calculations on the model complexes [CoCp(CO)(RGeGeR)] reveal similarly asymmetrically coordinated diggermyne ligands for R = H ($\Delta d = 29.3$ pm), Me (15.7 pm) and Ph (8.1 pm, see Figure 7.1 and Table 7.1 for their calculated structures and bond parameters).

The Ge1–Ge2 bond length in **B-1Tbb** of 238.9 pm lies in the upper range of typical Ge=Ge double bonds,^[307] whereas the Tbb groups are bonded to the germanium atoms via classical Ge–C single bonds (Ge1–C1: 200.0 pm, Ge2–C2: 200.4 pm). Due to the intact *trans*-bent character of the diggermyne moiety in complex **B-1Tbb**, both three-coordinated germanium atoms are considerably pyramidalized ($\Sigma\angle(\text{Ge1})$: 290.3°, $\Sigma\angle(\text{Ge2})$: 315.5°), with a smaller sum of angles found for the Ge1 atom.

The electronic structure of complex **B-1Tbb** was first assessed by the analysis of their canonical MOs, depicted in Figure 7.3, which, however, appear strongly delocalized and hard to interpret. Evidence for $\sigma(\text{Ge–Co})$ bonding can be found in the HOMO–8 and HOMO–7, which also contain huge contributions of the Tbb substituents. The HOMO–1 shows the $\pi(\text{Ge–Ge})$ orbital, which is slightly delocalized towards the cobalt center (with its anti-bonding combination in the LUMO+1), whereas the HOMO indicates electron lone pair density at the Ge1 and Ge2 atoms, which is slightly larger at the Ge1 atom as a consequence of the longer Ge1–Co bond distance.

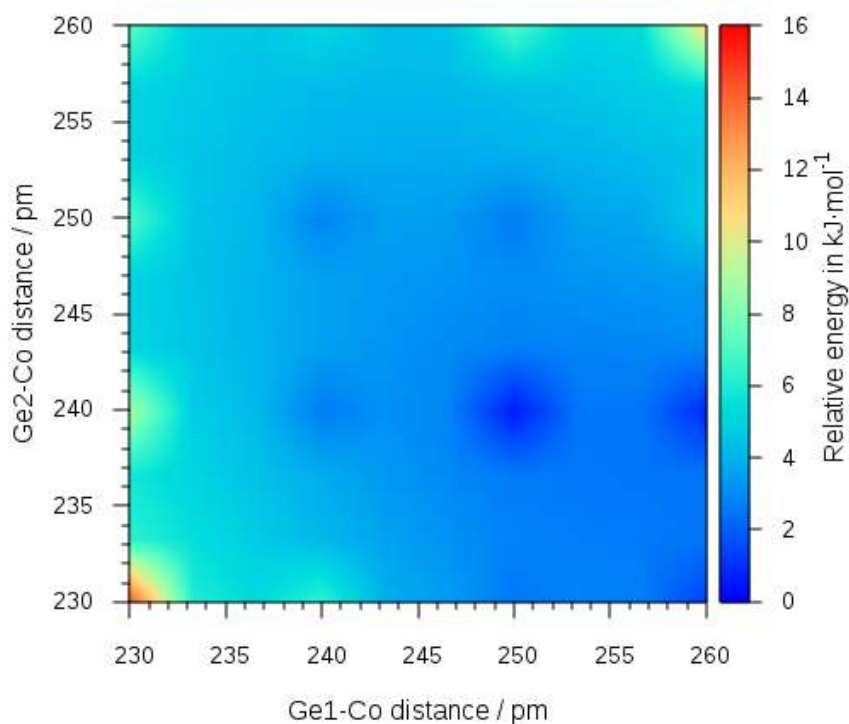


Figure 7.2: Two-dimensional energy hypersurface plot of the Ge1–Co and Ge2–Co bond lengths of the digermine cobalt complex **B-1Tbb**.

The analysis of the localized MOs via the intrinsic bond orbital (IBO) method underlines that the digermine ligand acts as a $2e^-$ -donor and $2e^-$ acceptor in **B-1Tbb**: Along with the expected $\sigma(\text{Ge1}-\text{C1})$ and $\sigma(\text{Ge2}-\text{C2})$ orbitals, depicted in Figure 7.4, two different IBOs are found for the Ge-Co bonding that resemble the respective canonical MOs HOMO–8, HOMO–7 and HOMO–1. Two strongly polarized IBOs are also present for the Ge–Ge bonding that can be described as complimentary $\text{LP}(\text{Ge}) \rightarrow \text{p}(\text{Ge})$ donor-acceptor bonds with remaining lone pair character on the germanium atoms, which is slightly higher on the Ge1 atom according to the Loewdin population analysis.

Overall, the analysis of the canonical and localized molecular orbitals indicates that two resonance structures are possible to describe the complex **B-1Tbb** (Scheme 7.3): a zwitterionic Lewis structure **B-1Tbb-a** with two Ge–Co bonds, a Ge1–Ge2 bond as well as a lone pair at the Ge1 atom, and **B-1Tbb-b** with two Ge–Co bonds and a Ge1=Ge2 double bond. NBO calculations were carried out on both Lewis structures with the NBO6 program and show that **B-1Tbb-a** fits better to describe the complex **B-1Tbb** as it has a lesser amount of non-Lewis electrons (9.26 nLe^-) than **B-1Tbb-b** (10.74 nLe^-).

Accordingly, the results of the NBO and NPA analysis on Lewis structure **B-1Tbb-a** are provided in Table 7.2. The lone pair NBO at the Ge1 atom has a lowered occupation of $1.65 e^-$ and is almost exclusively of s-character ($sp^{0.2}$). Accordingly, the Ge1–Ge2 bond is polarized towards the Ge2 atom

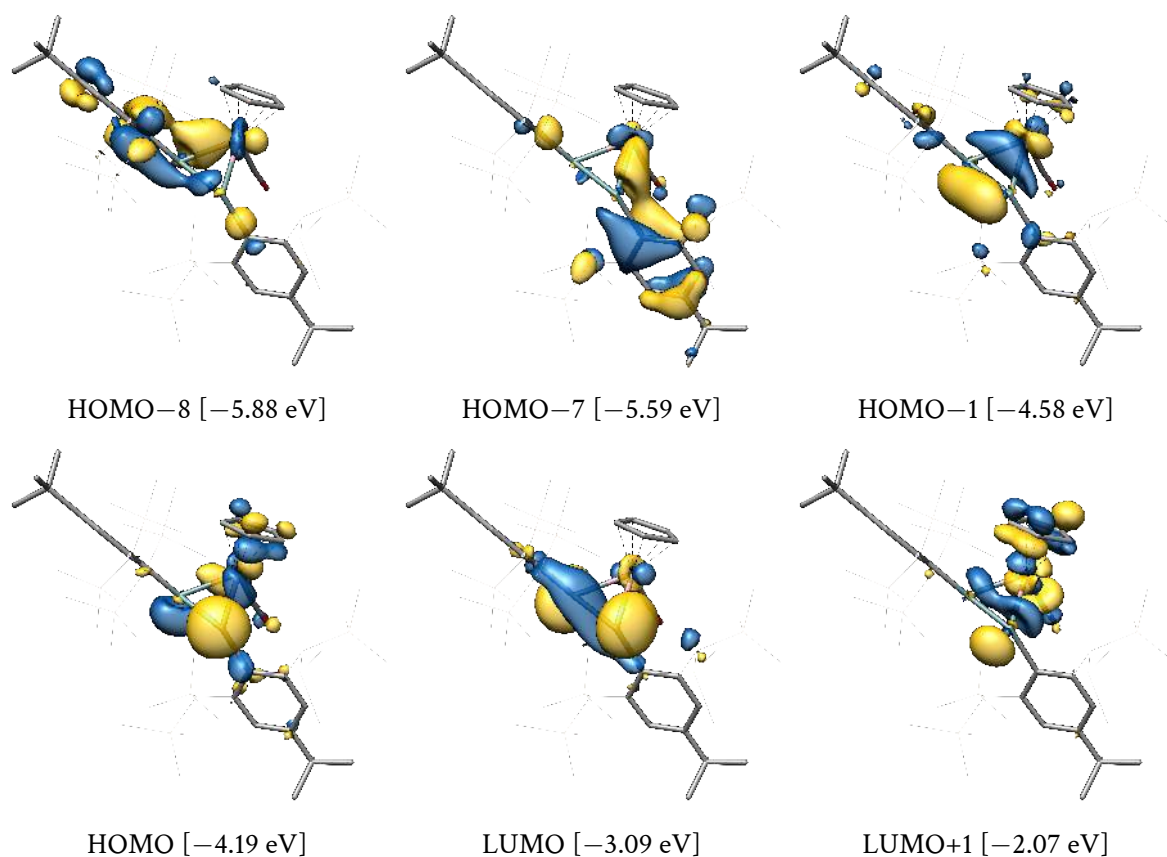
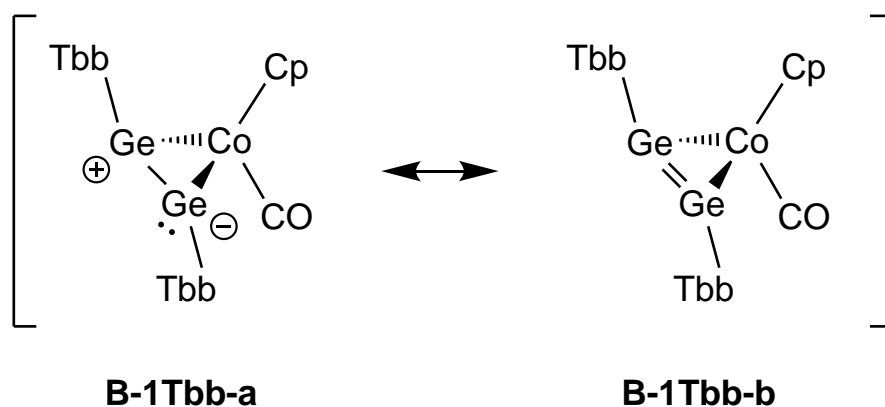


Figure 7.3: Selected canonical MOs of the digermine cobalt complex B-1Tbb and their energy eigenvalues.



Scheme 7.3: Two possible resonance formulas for complex B-1Tbb.

(71 %) and employs a pure p orbital at Ge1 and a $sp^{1.1}$ hybrid orbital at the Ge2 atom, as expected from the $LP(Ge2) \rightarrow p(Ge1)$ donor-acceptor interaction as mentioned above. The Ge1–Co and Ge2–Co bonds both display lowered occupations of 1.62 and 1.71 e^- , respectively, and are polarized towards the Co atom (73 %, 64 %). Whereas the Ge1 atom uses an almost pure p-orbital for the bond ($sp^{22.6}$, the s-character is almost exclusively located in the $LP(Ge1)$ NBO), the s-character is larger for the Ge2 atom ($sp^{4.1}$), which directly corresponds to the found shorter Ge2–Co bond distance according to Bent's rule.^[152] The presumed contribution of the double-bond resonance structure B-1Tbb-b

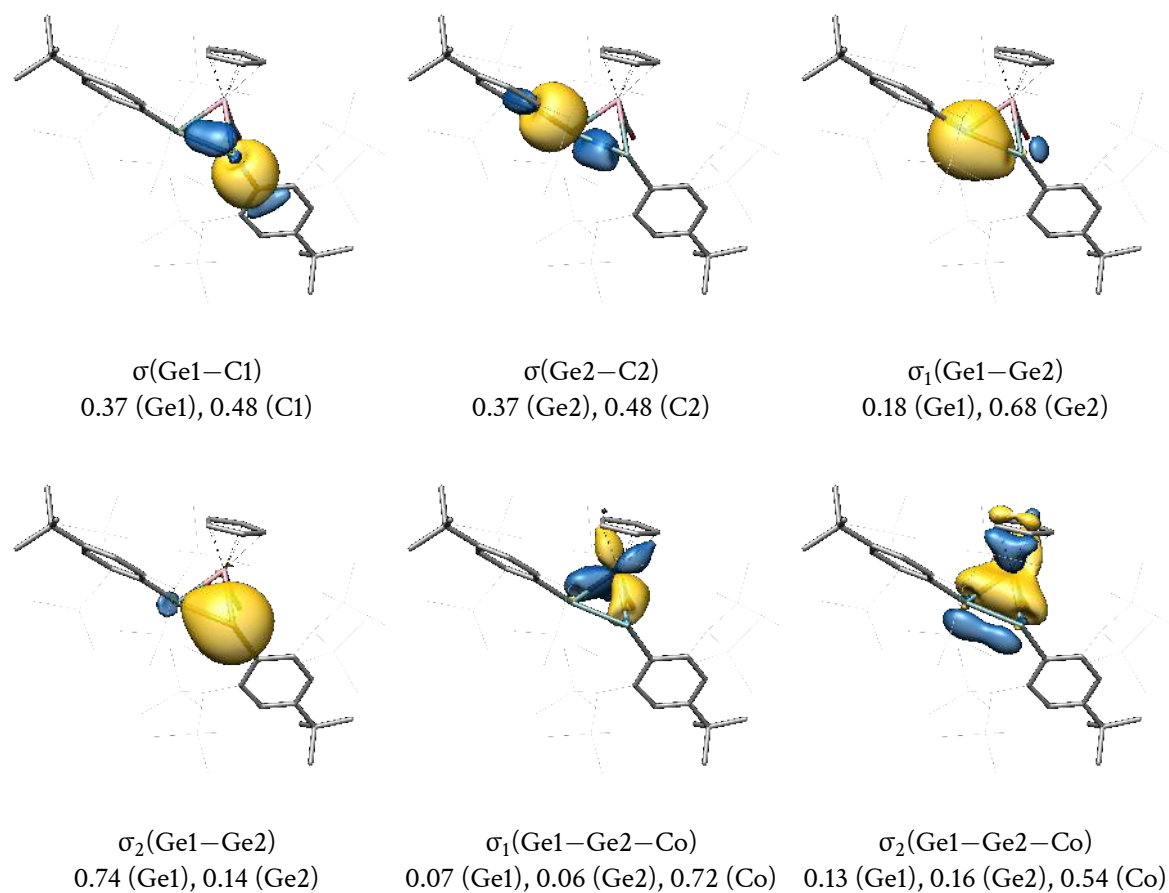


Figure 7.4: Intrinsic bond orbitals (IBOs) of **B-1Tbb**, their ascribed bond type and atomic Loewdin orbital populations.

can also be seen in the considerable occupation of $0.53 e^-$ of the lone valence (LV) orbital at the Ge2 atom with pure p-character, that serves as the acceptor orbital for the $\text{LP}(\text{Ge1}) \rightarrow \text{p}(\text{Ge2})$ interaction.

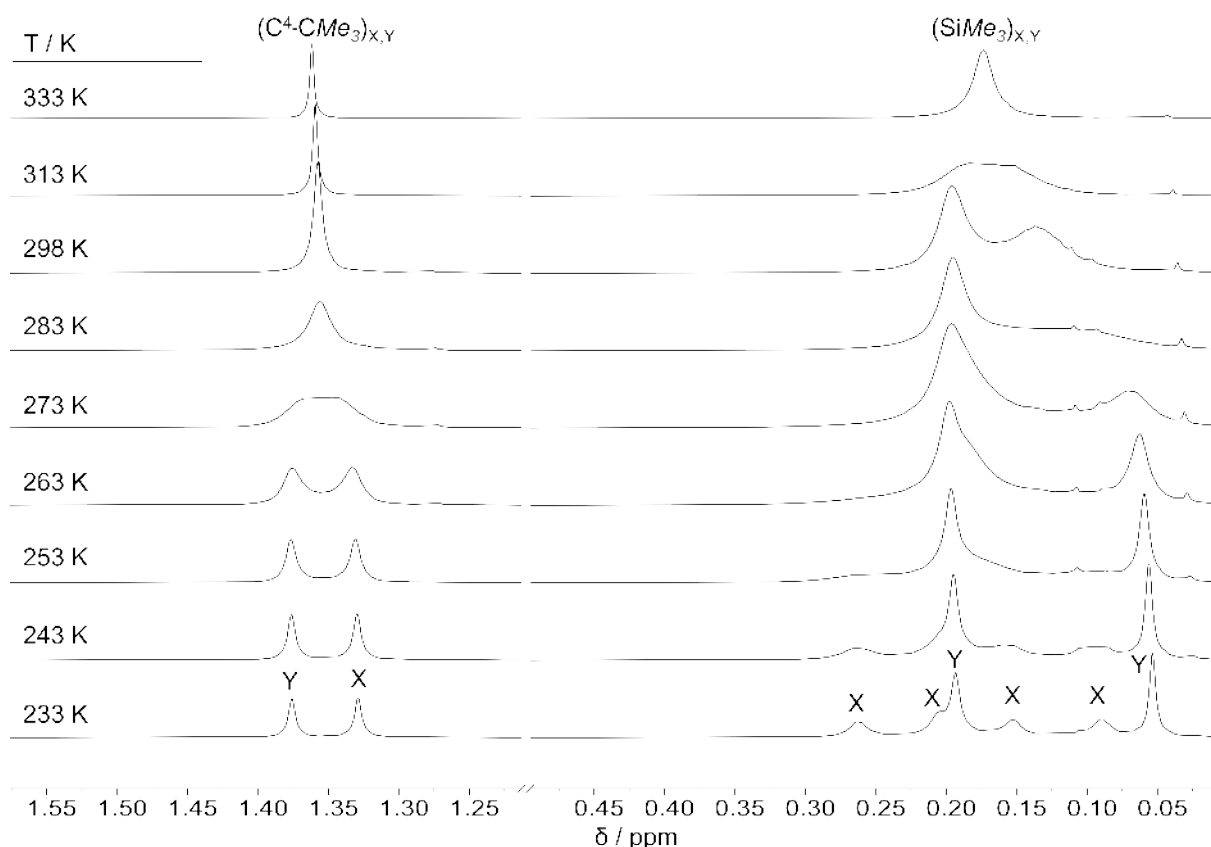
The calculated NPA charges for the complex **B-1Tbb** yield two positively charged germanium atoms (Ge1: $+0.42 e$, Ge2: $+0.51 e$) and an almost electroneutral cobalt atom ($-0.02 e$). The group charge of the digermine [**TbbGeGeTbb**] is positive with $+0.23 e$, revealing that its charge donation towards the [CoCp(CO)] fragment outweighs the back-donation.

Stereodynamics of **B-1Tbb**

The *trans*-bent structure of the digermine ligand in **B-1Tbb** generates two prochiral faces, (*Re*) and (*Si*), and thus the position of the [CoCp(CO)] fragment determines which enantiomer is formed, (*R,R*)-**B-1Tbb** or (*S,S*)-**B-1Tbb**. The (*R,R*)-**B-1Tbb** enantiomer was used for the analysis of the electronic structure discussed above, whereas the reaction outcome in solution and by sc-XRD analysis in the solid state affords a racemic mixture of both stereoisomers.

Table 7.2: Results of the NBO and NPA analysis of the digermyne cobalt complex **B-1Tbb**.

NBO A–B	Occ. / e ⁻	NHO (A,B) pol. / % (hyb.)	NPA / e	
LP(Ge1)	1.65	(sp ^{0.16})	Ge1	+0.42
σ(Ge1–Ge2)	1.86	29 (p), 71 (sp ^{1.1})	Ge2	+0.51
σ(Ge1–Co)	1.62	27 (sp ^{2.6}), 73 (sd ^{3.1})	Co	-0.02
σ(Ge2–Co)	1.71	36 (sp ^{4.1}), 64 (sd ^{2.3})	[Ge ₂ Tbb ₂]	+0.23
σ(Ge1–C1)	1.88	28 (sp ^{10.6}) 72 (sp ^{2.6})	[CoCp(CO)]	-0.23
σ(Ge2–C2)	1.92	31 (sp ^{2.2}) 69 (sp ^{3.0})		
LV(Ge2)	0.53	(p)		

**Figure 7.5:** Stack plot of the excerpts of VT-¹H-NMR spectra of **B-1Tbb** in *d*₈-thf in the temperature range of 233 to 313 K showing three chemical exchange processes. The spectrum is adapted from reference [286].

A VT-¹H-NMR spectroscopic study was carried out between 233 and 333 K and an excerpt of the resulting stack plot is shown in Figure 7.5.^[286] At the lowest temperature, two singlet signals for the *t*Bu groups of the diastereopic Tbb substituents (arbitrarily labelled as Tbb_X and Tbb_Y) are obtained as well as 6 TMS signals (4x Tbb_X, 2x Tbb_Y). The latter set of signals is rationalized by a rotation of the Tbb substituent around the Ge–C bond, which is frozen out at 233 K for Tbb_X but not for Tbb_Y. At higher temperatures, the *t*Bu proton signals merge to one singlet signal at the coalescence temperature $T_c = 273$ K, which shows that the *t*Bu groups exchange. Also, the

4 Tbb_x TMS signals are found to merge to a very broad signal between 233 and 273 K, which again coalescence with the 2 Tbb_y TMS signals to only one signal for all eight TMS groups of the complex B-1Tbb. In addition, in the fast exchange limit spectrum at 333 K a time-averaged local C_{2v}-symmetry is observed.

The experimental barriers for the three conceivable processes (Tbb rotation, *t*Bu exchange, TMS signal equilibration) were estimated using the Gutowsky-Holm and Eyring-Polanyi formulae and found to be similar with $\Delta G_{1,GH}^\ddagger = 54 \text{ kJ}\cdot\text{mol}^{-1}$, $\Delta G_{2,GH}^\ddagger = 59 \text{ kJ}\cdot\text{mol}^{-1}$ and $\Delta G_{3,GH}^\ddagger = 64.5 \text{ kJ}\cdot\text{mol}^{-1}$. The first and second processes could further be analyzed via full line shape analysis resulting in $\Delta G_{1,LS}^\ddagger = 55.6(\pm 4.1) \text{ kJ}\cdot\text{mol}^{-1}$ and $\Delta G_{2,LS}^\ddagger = 58.2(\pm 2.5) \text{ kJ}\cdot\text{mol}^{-1}$, whereas it was unsuccessful for the third stereodynamic process.

The first process is rationalized to occur due to the rotation of the Tbb substituents, however, the *t*Bu group exchange and the coalescence of the TMS groups to a single singlet signal can be rationalized by several mechanisms, which is why computational theory was employed to search for the most favoured stereodynamic pathways. The results will be summarized in the following:

Dissociation of the digermyne ligand

The simplest process to explain the observed stereodynamics in solution would be the complete dissociation and re-coordination of the digermyne ligand from and to the [CoCp(CO)] fragment. In the free digermyne TbbGeGeTbb the Tbb groups are homotopic and thus only one signal is observed for each of the *t*Bu and TMS protons in the ¹H-NMR spectrum.^[308] However, the calculated bond dissociation energy and free Gibbs energy for the digermyne dissociation (breaking both Ge–Co bonds) amount to 244.6 and 143.9 kJ·mol⁻¹, respectively, when cleaving the compound B-1Tbb into the triplet [CoCp(CO)] and singlet TbbGeGeTbb spin ground state fragments. This is far off the experimentally estimated values of ca. 60 kJ·mol⁻¹, and accordingly such a process is not likely to occur at room temperature. Additionally, the re-coordination would require the spin state change of the [CoCp(CO)] triplet state fragment back to the energetically higher-lying singlet state ($\Delta E_{s \rightarrow \uparrow} = -51.4 \text{ kJ}\cdot\text{mol}^{-1}$ at level of theory I), which is expected to be unlikely to fit to the present stereodynamics.

CO-bridged structure [CoCp(TbbGeC(O)GeTbb)] (B-2)

The NMR-spectroscopic results can also be explained by a C_{2v}-symmetric intermediate that is formed in solution. This molecular symmetry is realized by migration of the carbonyl ligand to a bridging position between the germanium atoms after Ge–Ge bond cleavage, leading to the complex [CoCp(TbbGeC(O)GeTbb)] (B-2, see Figure 7.6).

The complex B-2 is lying 85.2 kJ·mol⁻¹ higher in energy than the minimum structure B-1Tbb with a relative Gibbs energy of 64.6 kJ·mol⁻¹. The latter is quite close to the experimental values, but B-2 was found to be a minimum structure, thus the transition state connecting the molecules B-1Tbb

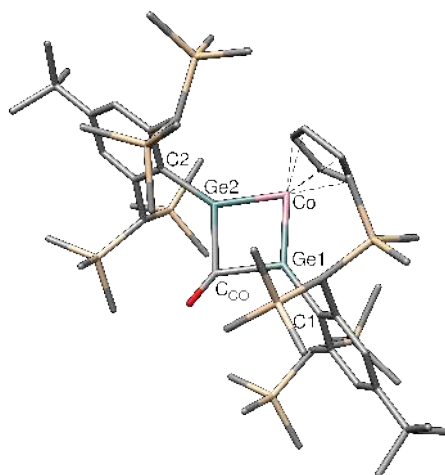


Figure 7.6: Optimized gas phase structure of the possible stereodynamics intermediate B-2. Selected structural parameters: Ge \cdots Ge: 282.6 pm, Ge1–Co3: 223.0 pm, Ge2–Co3: 222.7 pm, Ge1–C_{CO}: 209.0 pm, Ge2–C_{CO}: 210.4 pm, Ge1–C1: 198.1 pm, Ge2–C2: 198.4 pm, Ge1–Co–Ge2: 78.7°, $\Sigma\angle(\text{Ge1})$: 359.7°, $\Sigma\angle(\text{Ge2})$: 359.9°, $\Sigma\angle(\text{C}_{\text{CO}})$: 359.4°.

and B-2 is expected to lie clearly higher in energy, as a larger reorientation of the molecule and a Ge–Ge bond breaking is involved in the rearrangement. This is underlined by a NEB calculation at the B97-D3(BJ)-ATM/def2-SVP level of theory that yields a preliminary reaction barrier of +248 kJ·mol⁻¹ compared to B-1Tbb. However, a proper transition state connecting the complexes B-1Tbb and B-2 could not be obtained so far.

Cis-bent structure B-3 by synchronous C1–Ge1–Ge2–C2 torsion

Another conceivable stereodynamic process, albeit without bond breaking, is represented by the synchronous C1–Ge1–Ge2–C2 torsion, leading to the *cis*-bent digermine complex B-3 (Figure 7.7). This structural motif is typical for alkyne complexes,^[309] and it was also calculated in the theoretical studies of G. Frenking *et al.*^[293] and S. Sakaki *et al.*^[294] The gas phase structure optimization of the complex B-3 only converges back into the complex B-1Tbb. Instead, a constrained optimization with a fixed C1–Ge1–Ge2–C2 torsion angle of 0.0° and subsequent transition state optimization yields a first-order saddle point (transition state) with one imaginary frequency at 141.4i cm⁻¹, and relative ΔE and ΔG values of +75.2 and +66.7 kJ·mol⁻¹, respectively.

The energy of the transition state B-3 matches well with the experimentally estimated barrier, however its *C_s*-symmetry combined with the assumed Tbb rotation can not explain the observed NMR spectrum, as the mirror plane, going through the Co and carbonyl atoms and the midpoints of the Cp ligand and Ge–Ge bond, makes the opposing Tbb groups equal, but not the TMS groups of the bisyl unit within one Tbb substituent, thus only leading to two TMS proton signals.

To obtain only one TMS proton signal, an additional rotation of the [CoCp(CO)] fragment is necessary. This was investigated by calculating a *C_s*-symmetric structure, where the [CoCp(CO)] fragment is rotated by 90° around the Co-digermyne axis and the resulting mirror plane passes through the atoms Ge1, Ge2, Co, C_{CO} and O. However, despite several attempts a structurally

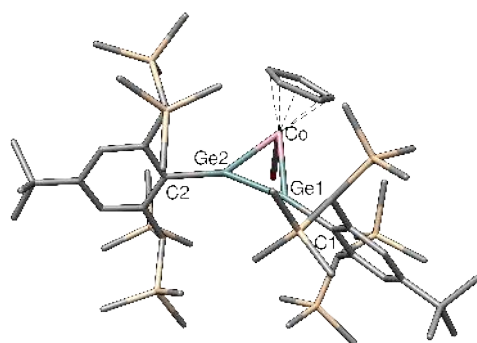
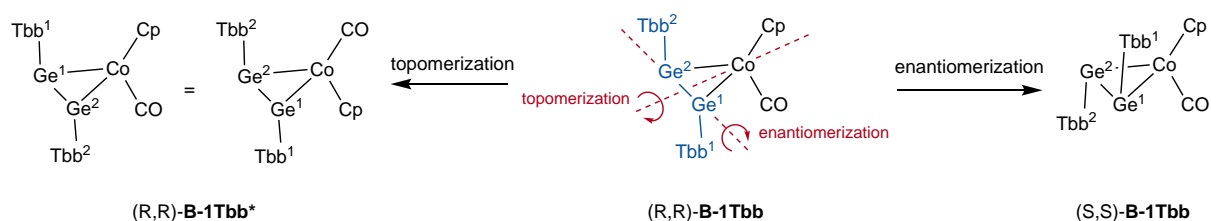


Figure 7.7: Optimized gas phase structure of the conceivable stereodynamics transition state B-3. Selected structural parameters: Ge1–Ge2: 221.1 pm, Ge1–Co: 249.9 pm, Ge2–Co: 241.9 pm, Ge1–C1: 197.5 pm, Ge2–C2: 198.1 pm, Ge1–Co–Ge2: 53.4°, C1–Ge1–Ge2–C2: 7.6°, $\Sigma\angle(\text{Ge1})$: 360.0°, $\Sigma\angle(\text{Ge2})$: 359.5°.

optimized structure could not be obtained which indicates that such a rotation is not favoured and only results in an artificial higher-energy structure.

Combined topomerization and enantiomerization via germylidene complexes

Finally, the equilibrated NMR signals can also be explained by a combination of topomerization and enantiomerization that occur simultaneously. Their mechanisms are schematically depicted in Scheme 7.4. Herein, a topomerization to the complex B-1Tbb* is achieved by the rotation of the [CoCp(CO)] fragment around the Co–*m*(GeGe) axis where *m*(GeGe) denotes the midpoint of the GeGe bond. This does not change the stereoconfiguration of the complex but exchanges the germanium atoms and Tbb groups, and is often observed in transition metal alkyne complexes.^[310–312] For an enantiomerization, either the [CoCp(CO)] fragment needs to move to the other prochiral face of the digermine or the digermine ligand needs to rotate around the Ge–Ge bond axis.



Scheme 7.4: Visualization of the conceivable topomerization and enantiomerization process in the complex B-1Tbb. Electron lone pairs and formal charges are omitted for simplicity.

At first the topomerization was studied by calculating the structure B-4 where the [CoCp(CO)] fragment is rotated by 90° (Figure 7.8). Additionally, the Ge2–Ge1–Co–C_{CO} torsion angle was confined to 180.0° to prevent the optimization from converging back to the minimum conformer.

The hereby obtained structure **B-4** has several imaginary frequencies and lies $+68.0 \text{ kJ}\cdot\text{mol}^{-1}$ higher in energy than **B-1Tbb**.

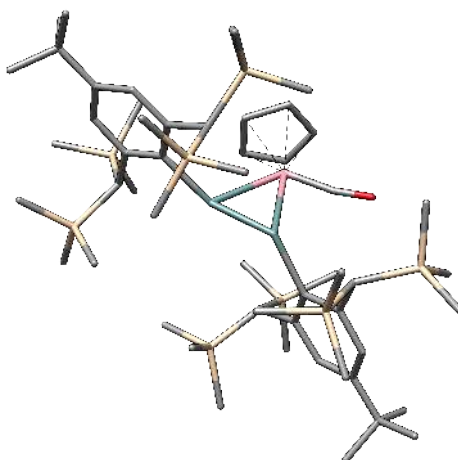
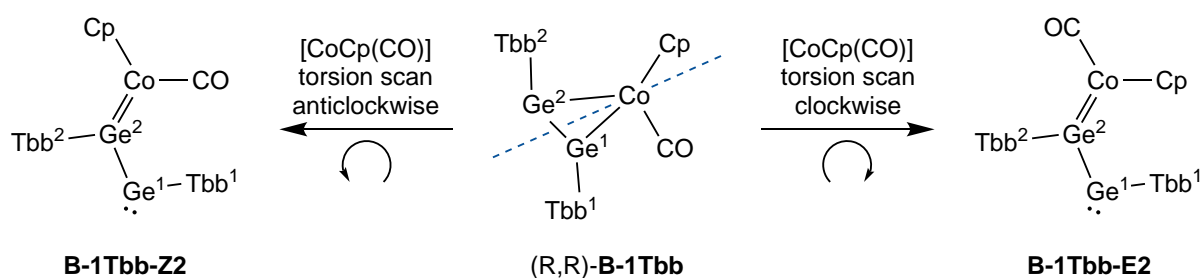


Figure 7.8: Optimized gas phase structure of the conceivable stereodynamics higher-order transition state **B-4**. Selected structural parameters: Ge1–Ge2: 234.0 pm, Ge1–Co: 271.3 pm, Ge2–Co: 254.7 pm, Ge1–C1: 202.7 pm, Ge2–C2: 200.2 pm, Ge1–Co–Ge2: 52.7° , C1–Ge1–Ge2–C2: 158.3° , $\Sigma\angle(\text{Ge1})$: 300.7° , $\Sigma\angle(\text{Ge2})$: 318.9° .

The rotation is further studied by a PES scan of the Ge1–Ge2–Co–C_{CO} torsion angle from 80° to 180° in a clockwise direction (looking towards the [CoCp(CO)] fragment from the digermine). There it was observed that the long Ge1–Co bond is cleaved and the [CoCp(CO)] fragment moves to the in-plane position of the digermine ligand. By this $\eta^2 \rightarrow \kappa$ -Ge slippage, the germylene-germylidene complex (*E*)-[CoCp(CO)Ge(Tbb)GeTbb] (**B-1Tbb-E2**) is formed (see Scheme 7.5). In contrast, the anticlockwise PES scan of the torsion angle from 80° to 0° yields the diastereomer, (*Z*)-[CoCp(CO)Ge(Tbb)GeTbb] (**B-1Tbb-Z2**).



Scheme 7.5: Formation of germylene-germylidene complexes as outcome of the [CoCp(CO)] torsional PES scans.

Similarly, PES scans of the Ge–Ge–Co bond angles from 60° to 120° also reveal the formation of germylene-germylidene complexes where the cobalt fragment sits at the Ge1 (**B-1Tbb-E1**) or Ge2 atoms (**B-1Tbb-Z2**) (see Figure 7.9). Notably, the C1–Ge1–Ge2–C2 torsion angle stays roughly constant for all scan steps in both the [CoCp(CO)] torsion and Ge–Ge–Co bond angle PES scans, and thus no mixing of the digermine slippage and torsional stereodynamics is expected. The formation of the remaining (*Z*)-configured germylene-germylidene complex with the cobalt fragment

residing at the Ge1 atom (**B-1Tbb-Z1**) is considered to be likewise accessible, due to the very shallow stretching potential of the Ge–Co bonds in complex **B-1Tbb** (c.f. Figure 7.2). However, this was not directly observed in the above-mentioned PES scans.

The structures of the two diastereomeric germylene-germylidene complexes **B-1Tbb-Z1** and **B-1Tbb-E1** could be calculated (see Figure 7.9) and the subsequent frequency calculations confirm them to be minimum structures, with only a negligible imaginary frequency of $8.7i \text{ cm}^{-1}$ found for the isomer **B-1Tbb-E1**. The other diastereomeric pair of complexes, **B-1Tbb-Z2** and **B-1Tbb-E2** are topomers of **B-1Tbb-Z1** and **B-1Tbb-E1**, respectively, and thus *must* have the same energy by symmetry considerations. The calculated relative electronic energies show that the germylene-germylidene complexes are easily accessible intermediates with $+29.5 \text{ kJ}\cdot\text{mol}^{-1}$ (**B-1Tbb-Z1**) and $+33.9 \text{ kJ}\cdot\text{mol}^{-1}$ (**B-1Tbb-E1**).

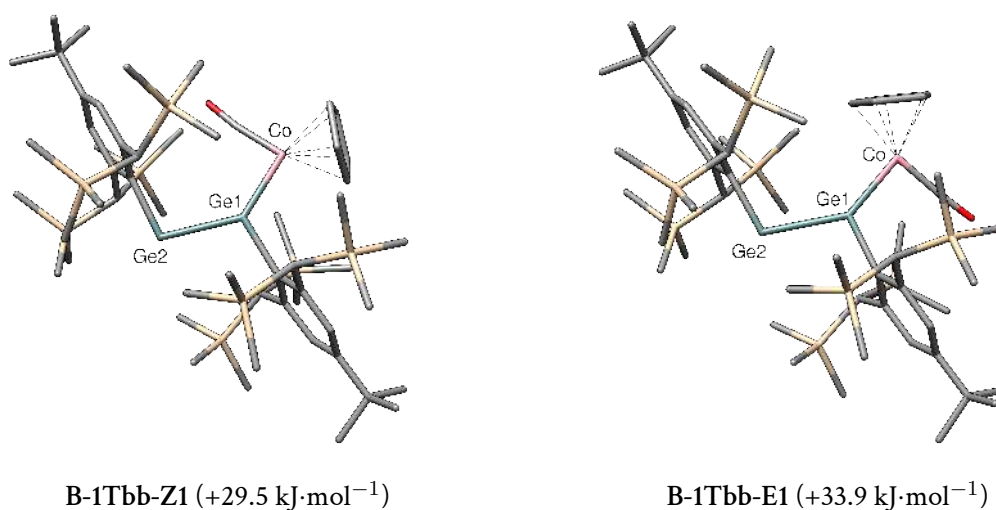


Figure 7.9: Optimized gas phase structures of the two intermediate germylene-germylidene complexes **B-1Tbb-Z1** and **B-1Tbb-E1** as well as their electronic energies relative to complex **B-1Tbb**.

Selected structural parameters of the germylene-germylidene intermediates **B-1Tbb-Z1** and **B-1Tbb-E1** are summarized in Table 7.3. The V-shaped arrangement of the substituents at the two-coordinated germanium atom $\text{Ge}^{2\text{C}}$ with narrow $\text{Ge}^{3\text{C}}-\text{Ge}^{2\text{C}}-\text{C}$ bond angles of 103.4 and 108.0° indicates the presence of an electron lone pair, which can be found in the HOMO (Figure 7.10). The three-coordinate $\text{Ge}^{3\text{C}}$ atom displays an almost trigonal planar arrangement of the substituents ($\sum\angle(\text{Ge}^{3\text{C}}) = 357.0^\circ, 359.4^\circ$) as expected. The $\text{Ge}^{3\text{C}}-\text{Co}$ bonds of 222.9 and 223.1 pm are considerably shorter than in the digermene complex **B-1Tbb** ($238.9 \text{ pm}, 257.0 \text{ pm}$), which is rationalized by the presence of a $\pi(\text{Ge}-\text{Co})$ orbital that can be found in the HOMO–1.

The C_s -symmetric germylene-germylidene complexes feature a mirror plane that lies in the Ge1–Ge2–Co plane and are hence achiral. Using complex **B-1Tbb-Z2** as example, Scheme 7.6 illustrates that four isomers are conceivable for each intermediate: the *original* enantiomer (R,R), its topomer, its (S,S)-enantiomer and the topo-enantiomer. Their formation depends on the out-of-plane rotation of the [CoCp(CO)] fragment (clockwise or anticlockwise) and if the [CoCp(CO)]

Table 7.3: Electronic and free Gibbs energies in $\text{kJ}\cdot\text{mol}^{-1}$ relative to the minimum structure **B-1Tbb** and selected structural parameters of the intermediate germylene-germylidene complexes **B-1Tbb-Z1** and **B-1Tbb-E1**. $\text{Ge}^{2\text{C}}$ and $\text{Ge}^{3\text{C}}$ refer to the two- and three-coordinated germanium atoms in the complexes, respectively. Bond lengths are given in pm and angles in degrees. The structures of the topomers **B-1Tbb-Z2** and **B-1Tbb-E2** have to be identical to those of **B-1Tbb-Z1** and **B-1Tbb-E2** due to symmetry.

	ΔE	ΔG	$\text{Ge}^{3\text{C}}-\text{Co}$	$\text{Ge}^{2\text{C}}-\text{Ge}^{3\text{C}}$	$\text{Ge}^{3\text{C}}-\text{Ge}^{2\text{C}}-\text{C}$	$\text{C}-\text{Ge}^{2\text{C}}-\text{Ge}^{3\text{C}}-\text{C}'$	$\Sigma\angle(\text{Ge}^{3\text{C}})$
B-1Tbb-Z1	29.5	22.9	222.9	256.4	103.4	176.8	357.0
B-1Tbb-E1	33.9	28.6	223.1	261.4	108.0	173.4	359.4

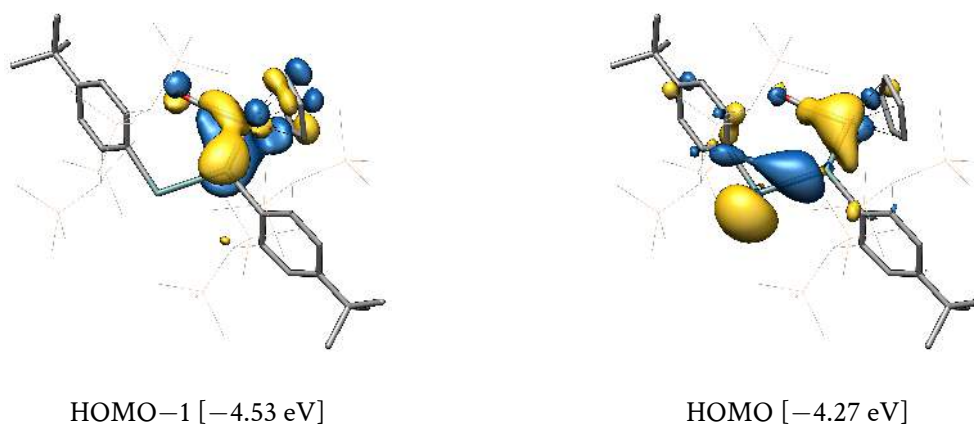
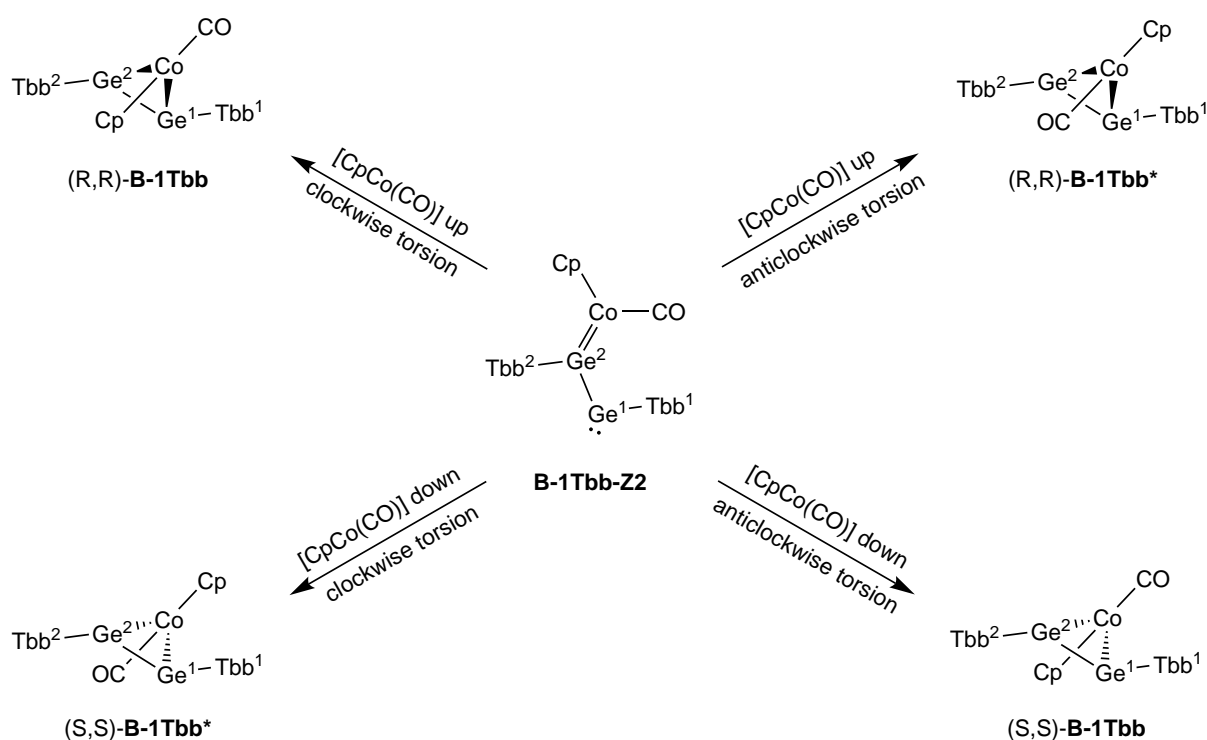


Figure 7.10: Selected canonical MOs of the germylene-germylidene complex **B-1Tbb-Z1** and their energy eigenvalues. The MOs of the other isomers **B-1Tbb-E1**, **B-1Tbb-Z2** and **B-1Tbb-E2** appear very similarly.

fragment moves below or above the symmetry plane. Due to the mentioned C_5 -symmetry and the stereochemic relationship of the four resulting digermine complexes, each pathway *must* have the same barrier and thus an equal population of all isomers. Overall, this leads to 4 germylene-germylidene complexes \times 4 isomers = 16 isomerization pathways. Combined with the assumed Tbb rotation (the exchange of the Tbb substituents and TMS groups), only one signal for the *t*Bu groups and also only one signal for the TMS protons is expected, which rationalizes well the observed results from the experimental NMR spectra.

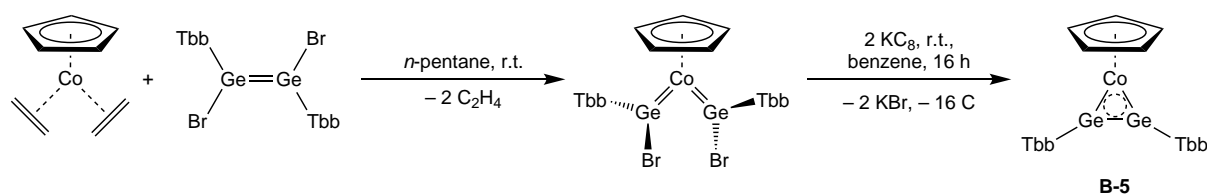
Despite all efforts, optimized transition states connecting the digermine complex **B-1Tbb** and the germylene-germylidene complexes could not be located due to the flat PES of the $\text{Ge}1-\text{Ge}2-\text{Co}$ moiety. However, as the barriers are expected to lie only slightly above the relative energy of the germylene-germylidene complexes of approx. $30 \text{ kJ}\cdot\text{mol}^{-1}$, the $\eta^2 \rightarrow \kappa$ -Ge slippage is found to be the energetically lowest and thus most favoured stereodynamic process studied here and is therefore very likely to be responsible for the observed stereodynamics in solution.



Scheme 7.6: Access to the enantiomerization and topomerization products of **B-1Tbb** starting from the germylene-germylidene complex **B-1Tbb-Z2**. *up* and *down* refer to a motion of the [CoCp(CO)] fragment above or below the digermene plane, respectively.

7.3. Carbonyl-free *cis*-bent Digermyne Cobalt Complex [CoCp(TbbGeGeTbb)] (B-5)

The digermene ligand in **B-1Tbb** acts as a two electron-donor towards the 16 valence electron cobalt fragment [CoCp(CO)]. In *cis*-bent alkyne ligands both $\pi(\text{C}-\text{C})$ bonds are available for the coordination to the metal, allowing to donate overall four electrons. Thus, it was tried experimentally to remove the carbonyl ligand to generate a 14 valence electron [CoCp] fragment which can thus receive four electrons by donation from the digermene. However, the attempts to decarbonylate the complex **B-1Tbb** thermolytically and photolytically failed.^[286] An alternative synthetic route comprises the reduction of the carbonyl-free bisgermylidene precursor complex [CoCp(GeBrTbb)₂] which in turn was obtained via the reaction between the digermene (TbbGeBr)₂ and the ethylene cobalt complex [CoCp(C₂H₄)₂] (Scheme 7.7). Thereby the carbonyl-free digermene cobalt complex [CoCp(TbbGeGeTbb)] (**B-5**) was obtained selectively and could be fully characterized.^[286]



Scheme 7.7: Alternative synthetic route to the carbonyl-free digermene complex **B-5**.

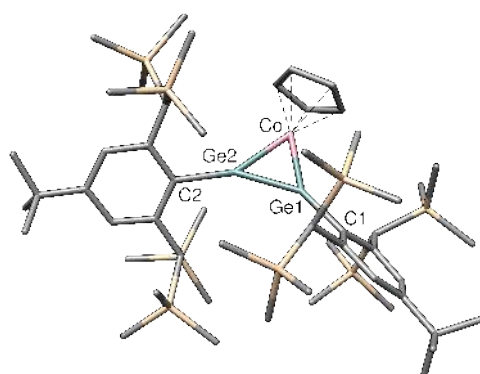


Figure 7.11: Optimized gas phase structure of the carbonyl-free digermine cobalt complex **B-5**.

The calculated gas phase structure of the complex **B-5** (Figure 7.11) agrees well with that obtained by sc-XRD analysis (**B-5_{exp}**) and features an approximately C_{2v} -symmetric digermacobaltirene heterocycle. The structural parameters, summarized in Table 7.4, reveal in fact a *cis*-bent arrangement of the digermine (C1–Ge1–Ge2–C2: 29.8°) with considerable bending angles C–Ge–Ge' of 152.9° and 146.8° at the trigonal planar Ge1 ($\Sigma\angle(\text{Ge1}) = 358.7^\circ$) and Ge2 ($\Sigma\angle(\text{Ge2}) = 357.9^\circ$) atoms, respectively. Noteworthy, the only larger difference between the structures **B-5** and **B-5_{exp}** is the difference in the C1–Ge1–Ge2–C2 torsion angle, which was found to be smaller with 4.3(2)° in the solid state structure.

The Ge1–Ge2 bond distance of 232.2 pm is considerably longer than in the free digermine Tb-bGeGeTbb (calculated structure: 223.0 pm; sc-XRD structure:^[308] 223.2(1) pm), but shorter than in the complex **B-1Tbb** (238.9 pm), indicating some Ge–Ge multiple bond character. The Ge1–Co and Ge2–Co bonds in **B-5** of 223.8 and 222.8 pm are also much shorter than in complex **B-1Tbb** (257.0 pm, 236.2 pm, c.f. Table 7.1) and point towards a stronger, now symmetric digermine-cobalt bonding.

Table 7.4: Selected bond parameters of the calculated and experimental carbonyl-free digermine complexes **B-5** and **B-5_{exp}**. Bond lengths are given in pm and angles in degrees.

	Ge1–Ge2	Ge1–Co	Ge2–Co	Ge1–C1	Ge2–C2
B-5	232.2	223.8	222.8	197.2	196.4
B-5_{exp}	231.4(1)	222.7(1)	222.2(1)	195.3(2)	195.5(2)
	Ge1–Co–Ge2	C1–Ge1–Ge2–C2	$\Sigma\angle(\text{Ge1})$	$\Sigma\angle(\text{Ge2})$	
B-5	62.6	29.8	358.7	357.9	
B-5_{exp}	62.7(1)	4.3(2)	360.0(2)	359.6(2)	

These considerations are reflected in the canonical MOs and localized IBOs that were calculated for complex **B-5**: Two $\sigma(\text{Ge–Co})$ bonding orbitals can be identified in the HOMO–7 and HOMO–2 (Figure 7.12). Whereas the first can be seen as back-donation of a cobalt-centered d_{xz} lone pair into the anti-bonding $\pi^*_{ip}(\text{Ge–Ge})$ orbital, the higher-lying HOMO–2 constitutes the weakly over-

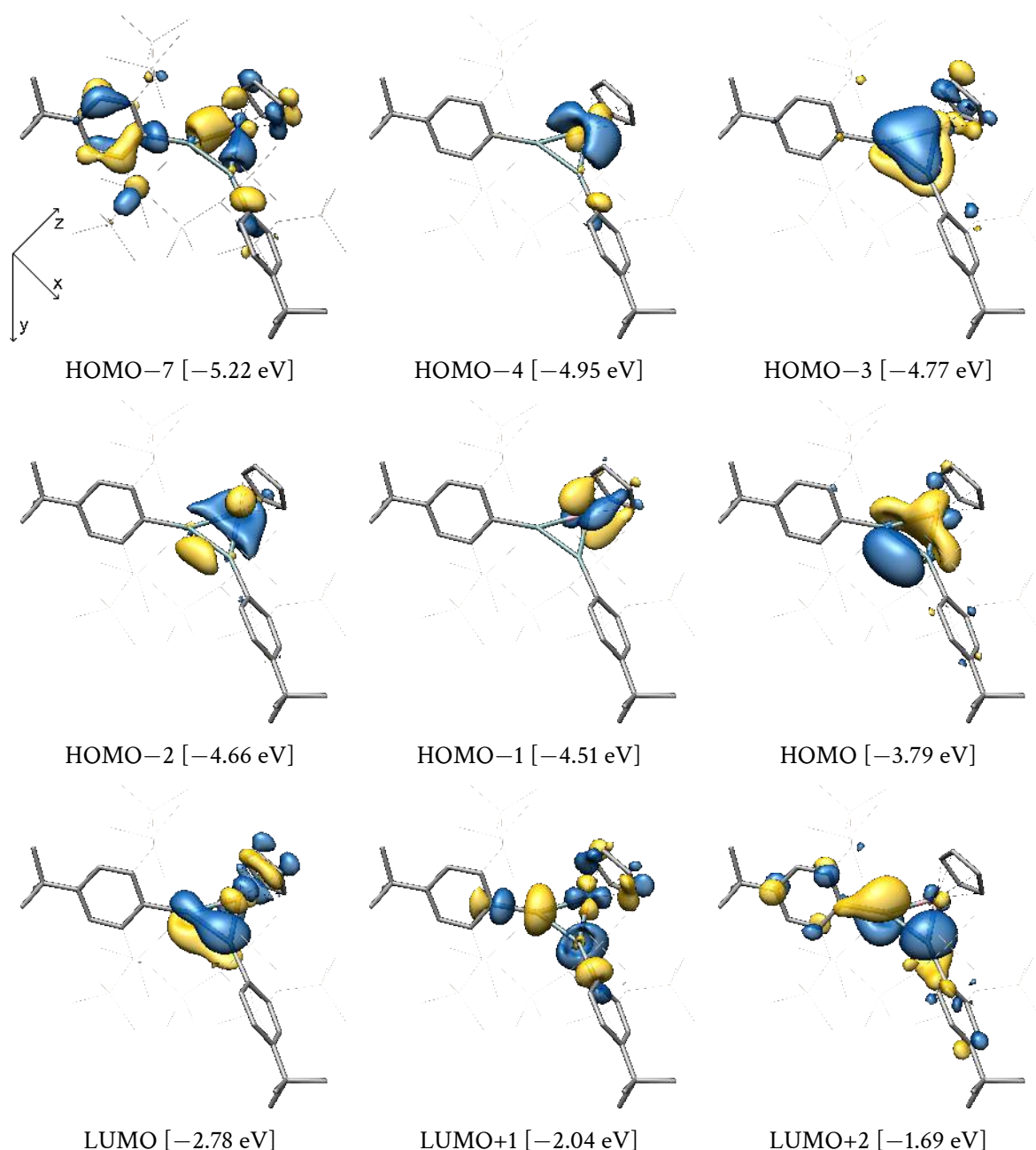


Figure 7.12: Selected canonical molecular orbitals of the complex B-5 and their energy eigenvalues.

lapping combination of the $\pi_{ip}(\text{Ge}-\text{Ge})$ orbital with a d_{y^2} -type orbital at cobalt. A remarkably clear $\pi_{oop}(\text{Ge}-\text{Ge}-\text{Co})$ 3-center-2-electron bond is identified in the HOMO-3 and two cobalt-centered electron lone pairs are located in the HOMO-4 and HOMO-1 of complex B-5. In principle, the latter orbital has the correct symmetry to form a δ -type bond with the digermine fragment via a $d_{xy} \rightarrow \pi_{oop}^*(\text{Ge}-\text{Ge})$ donation, which is however not observed in this complex, as no orbital contribution is present on the germanium atoms.¹

Particular attention should be paid to the HOMO of complex B-5: At first glance, the orbital shape

¹A note regarding the proof of the symmetrical consideration: When the isosurface value for the HOMO-1 is decreased to unreasonably low values, the δ -type bond indeed appears. The δ bond in the complex B-5 is accordingly so weak that it is effectively just the cobalt electron lone pair.

may tempt one to classify this interaction to be of bonding $\pi_{ip}(\text{Ge}-\text{Ge}) \rightarrow d(\text{Co})$ type, similar to that one found in the HOMO-2. However, a deeper analysis of the underlying orbitals reveals the presence of a $d_{x^2-y^2}$ -type orbital at the cobalt, and the resulting interaction between this orbital and the $\pi_{ip}(\text{Ge}-\text{Ge})$ bond of the digermine has to be non-bonding. Thus, the HOMO should rather be seen as a parallel presence of $\pi(\text{Ge}-\text{Ge})$ bond character and a $d_{x^2-y^2}$ -type electron lone pair at cobalt. The unoccupied LUMO, LUMO+1 and LUMO+2 represent the antibonding $\pi_{oop}^*(\text{Ge}-\text{Ge}-\text{Co})$, $\pi_{ip}^*(\text{Ge}-\text{Ge}-\text{Co})$ and $\pi_{oop}^*(\text{Ge1}-\text{Ge2})$ orbital interaction, respectively.

Further support stems from the localized IBOs, depicted in Figure 7.13. Aside from the expected $\sigma(\text{Ge1}-\text{Ge2})$ bond orbital, the presence of two $\sigma(\text{Ge}-\text{Co})$ bond orbitals as well as the $3c-2e^-$ - $\pi_{oop}(\text{Ge1}-\text{Ge2}-\text{Co})$ interaction can be confirmed. Notably, also in the IBO that is showing the cobalt-centered d_{xy} orbital, there is no significant overlap with fitting germanium-centered orbitals visible, effectively ruling out δ -type bonding in complex B-5.

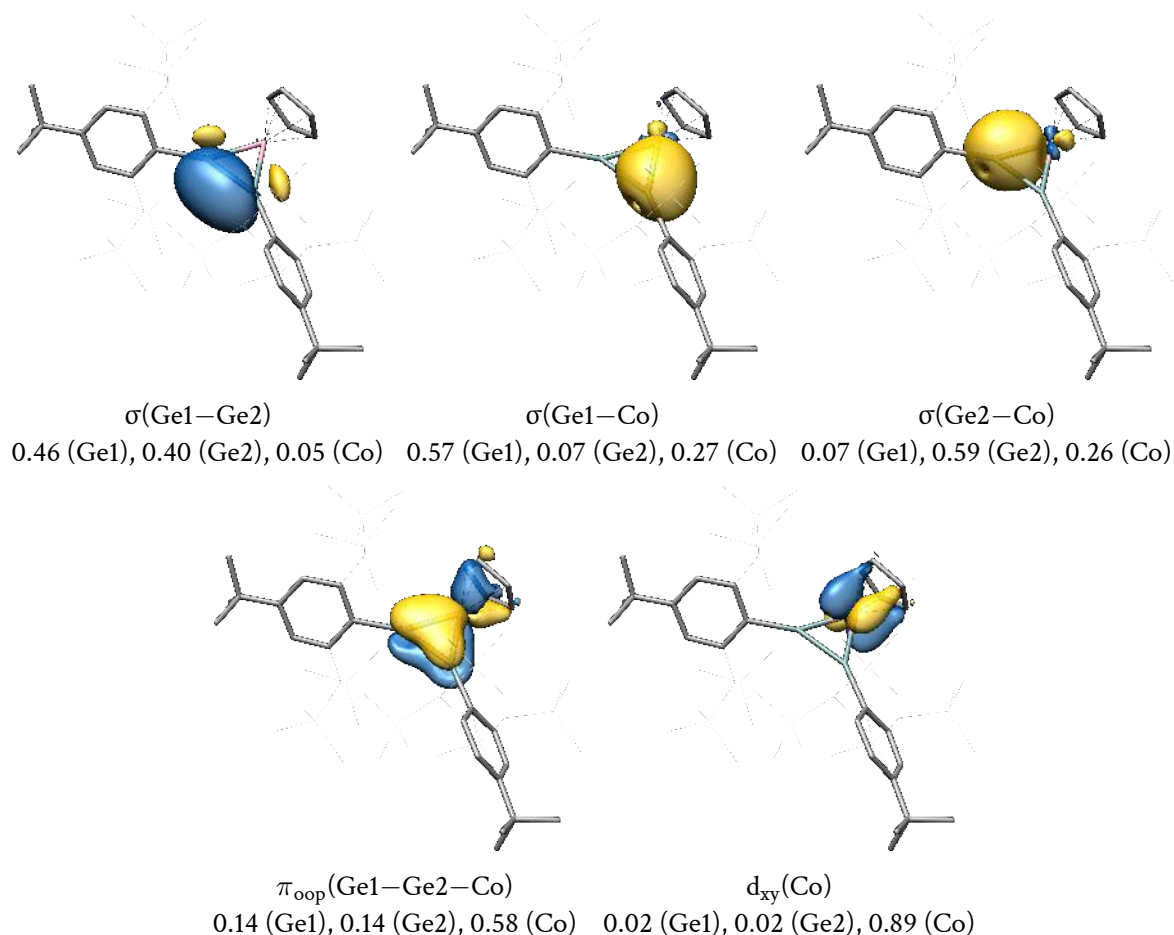


Figure 7.13: Selected intrinsic bond orbitals (IBOs) of the complex B-5 and their atomic Löwdin orbital populations.

Finally, the calculated NPA charges in complex B-5, given in Table 7.5, are in accordance with the molecular orbital analysis. They reveal that the donation of electron density from the *cis*-bent digermine ligand outweighs the received back donation from the cobalt fragment, as the NPA group charge of the digermine fragment [TbbGeGeTbb] is positive (+0.22 e). Both germanium atoms

are found to be quite positively charged with +0.41 and +0.43 e, respectively, whereas the cobalt atom is electroneutral (+0.02 e). The cyclopentadienyl ligand (−0.24 e) and the Tbb substituents (both −0.31 e) are center of negative charge accumulation.

Table 7.5: Calculated atomic and group NPA charges of the complex B-5 in fractions of the elementary charge e.

Ge1	Ge2	Co	[Tbb@Ge1]	[Tbb@Ge2]	[Cp]	[TbbGeGeTbb]	[CoCp]
+0.41	+0.43	+0.02	−0.31	−0.31	−0.24	+0.22	−0.22

Calculation of the nucleus-independent chemical shift (NICS)

As discussed above, the HOMO−3 of complex B-5 corresponds to a $3c-2e^- - \pi_{oop}(\text{Ge1}-\text{Ge2}-\text{Co})$ bond, which is found to be the only contribution to delocalized electron density out of the digermacobaltirene plane. Thus, this raises the question if an aromatic ring current is present in the three-membered ring, as Hückel's rule suggests aromaticity with $4^*n + 2 = 2 \pi$ -electrons for $n = 0$, which is valid here. To study this further, the popular nucleus-independent chemical shift (NICS) method was used.^[313]

First introduced by P. v. R. Schleyer *et al.* in 1996, the NICS method uses calculated negative absolute magnetic shieldings at selected points in the space around the cyclic compound in question as a criterion for aromaticity or anti-aromaticity.^[314] Over the years, the NICS method was subject to steady improvement by the group of Schleyer and other researchers,^[313, 315–318] for example by varying the position of the probe from the geometrical center of the ring (denoted as NICS(0)) to 1.0 Å above the ring plane (NICS(1)), or splitting the isotropic shielding tensors in their directional contributions (i.e. using NICS_{zz} instead of NICS_{iso}). Particularly the work of A. Stanger should be mentioned, who suggests to use one-dimensional NICS scans, where the NICS values are calculated at varying positions on a vector orthonormal to the ring plane. Then the resulting curve is analyzed instead of just one single value.^[316] This procedure can also be expanded to multidimensional scans to get a full NICS-based density map.^[319, 320]

The aromaticity of complex B-5 was studied by calculating NICS_{zz}(r) values between $r = 0.0$ and 5.0 Å using gauge including atomic orbitals (GIAOs)^[321] as implemented in ORCA 4.1.1. For comparison, the same was carried out for the classical aromatic compounds benzene and the cyclopropenium cation $[\text{C}_3\text{H}_3]^+$. Their NICS_{zz}(r) curves in Figure 7.14 show a smooth asymptotic convergence with the distance in the region of negative NICS values, which corresponds to an aromatic ring current in these compounds. Note that the NICS values between 0.0 and 1.0 Å are given here for completeness, but should not be interpreted, as they are biased by off-center and σ -type effects.^[320] This effect is expected to be even more pronounced for heterocycles involving heavier atoms, which is why the values for complex B-5 are inconclusive as no clear asymptotic progression is visible as observed for benzene and the cyclopropenium cation.

A detailed inspection of the molecular structure shows that the space above and below the digerma-cobaltirene plane is occupied by the Tbb substituents and thus a severe bias due to them is expected. To overcome this problem, the $\text{CH}(\text{TMS})_2$ and *t*Bu groups of the Tbb substituents were replaced by hydrogen atoms and only their positions relaxed. The NICS scan of this model compound B-5' has a completely different progression than that of B-5, as now a smooth convergence is observed, however from positive NICS_{zz}(*r*) values to zero. In conclusion, the Tbb-unbiased, weakly positive NICS_{zz}(*r*) values between 2 and 5 Å do not support an aromatic ring current in complex B-5, but rather a nonaromatic (or even weakly anti-aromatic) electron delocalization.

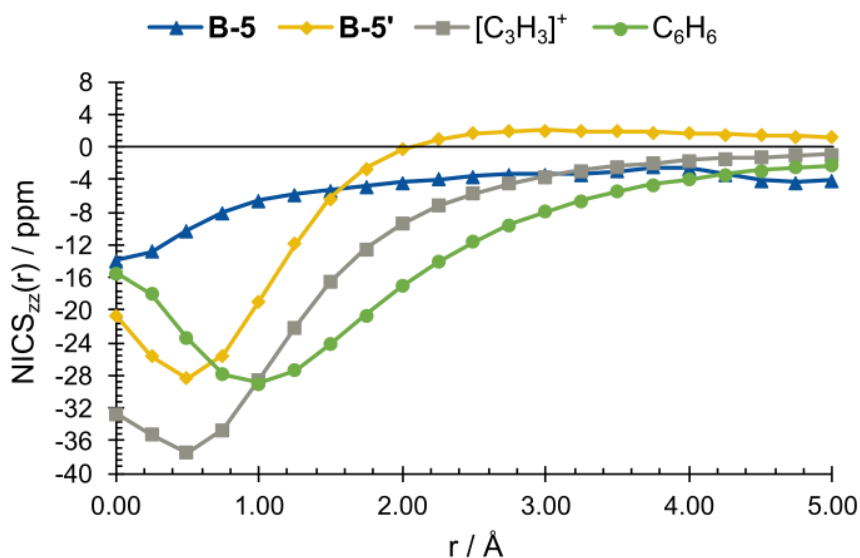


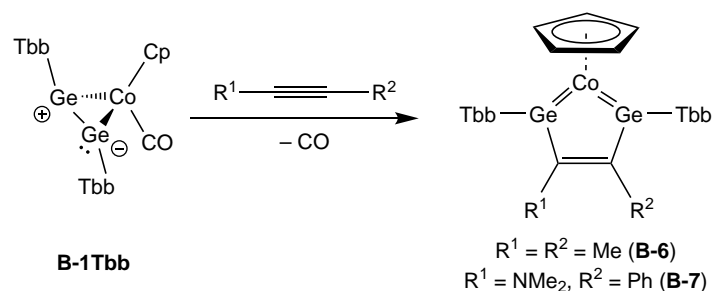
Figure 7.14: NICS_{zz}(*r*) scan plots with variable distance *r* between the midpoint of the studied ring and the probe for B-5, the model complex B-5', and the cyclopropylium cation and benzene for comparison.

7.4. Digerma-cobaltacyclopentatrienes

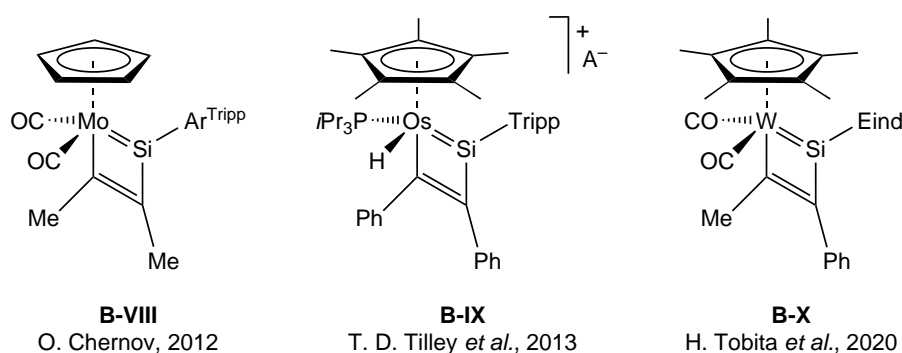
[CoCp(TbbGe(RCCR)GeTbb)] (B-6 and B-7)

So far, the experimental and theoretical studies suggest a germanium-centered reactivity for the digermyne cobalt complex B-1Tbb. In fact, its reactions with several homo- and heterosubstituted alkynes happen at the germanium atoms and lead to the formation of carbonyl-free 2,5-digermacobaltacyclopentatrienes [CoCp(TbbGe(RCCR)GeTbb)] (Scheme 7.8).^[286]

This compound class of heavier tetrel metallacyclopolyenes is rather rare and there are no examples for five- and six-membered rings. However, several silametallacyclobutadienes are known, for example compounds B-VIII to B-X (Scheme 7.9), that are all obtained as [2+2] cycloaddition products from the reaction of silyldiyne complexes with alkynes.^[151, 322–325] Thus, the now-synthesized germanium compounds are the first examples of heavier *ditetrel*metallacyclopolyenes.



Scheme 7.8: Synthesis of the digermacobaltacyclopentatrienes **B-6** and **B-7**. Further reaction conditions: *n*-hexane, 60 °C (**B-6**); toluene, 95 °C (**B-7**).



Scheme 7.9: Selected examples for silametallacyclobutadiene complexes from O. Chernov,^[151] T. D. Tilley *et al.*^[322] and H. Tobita *et al.*^[324] More complexes can be found in the references [151, 323–325]. Ar^{Tripp} = 2,6-(Tripp)₂-C₆H₂; Tripp = 2,4,6-(*i*Pr)₃-C₆H₂; Eind = 1,1,3,3,5,5,7,7-octaethyl-*s*-hydrindacene-4-yl; A⁻ = [HB(C₆F₅)₃]⁻.

Two of the experimentally accessible compounds, the symmetrically and asymmetrically substituted complexes [CoCp(Ge(Tbb)C(Me)C(Me)Ge(Tbb))] (**B-6**) and [CoCp(Ge(Tbb)C(NMe₂)C(Ph)Ge(Tbb))] (**B-7**),^[286] were calculated in good agreement starting from the sc-XRD structures **B-6_{exp}** and **B-7_{exp}**, respectively, and are depicted in Figure 7.15.

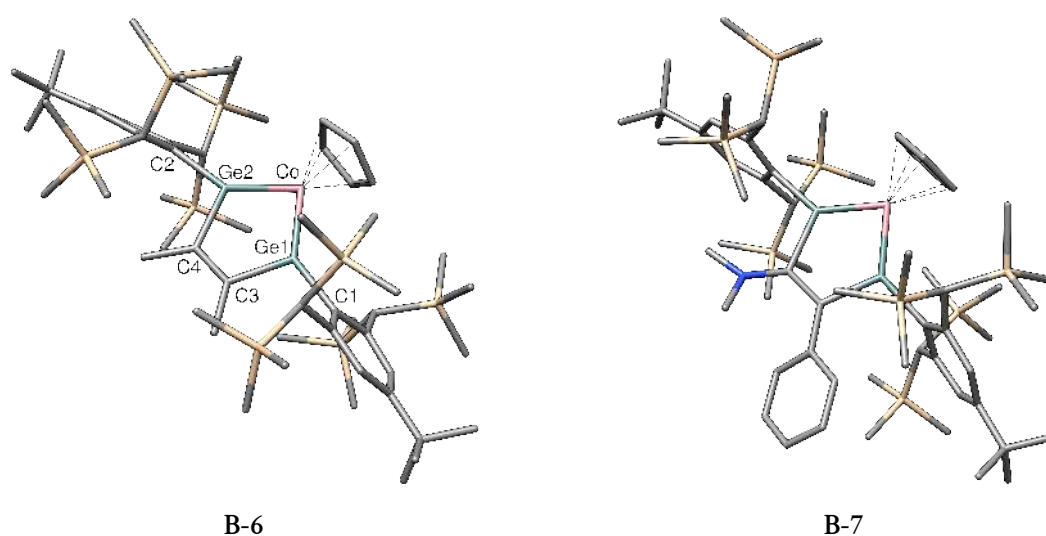


Figure 7.15: Optimized gas phase structures of the digermacobaltacyclopentatrienes **B-6** and **B-7**.

The triene-character in the five-membered ring of both complexes is supported by short Ge1–Co and Ge2–Co bond distances of 218.9 and 219.7 pm (**B-6**, see Table 7.6), and 219.7 and 216.4 pm (**B-7**), which are even shorter than in the complex **B-5** (223.8 and 222.8 pm, see Table 7.4). Furthermore, the C3–C4 bond distances of 134.8 and 138.4 pm are in the range of typical C=C double bonds. The Ge–C bonds are found to be similar in length with a range of 199.2 to 202.1 pm except for the Ge–C4 bond in the complex **B-7** (207.1 pm), which also appears longer than in the sc-XRD structure (200.5(7) pm). The rather long Ge–C distances suggest no multiple bond character, but instead localized Ge1–Co, Ge2–Co and C3–C4 double bonds.

Table 7.6: Selected bond parameters of the calculated and experimental digermacobaltcyclopentatrienes **B-6**, **B-6_{exp}**, **B-7** and **B-7_{exp}**. Bond lengths are given in pm and angles in degrees.

	Ge1–Co	Ge2–Co	Ge1–C1	Ge2–C2	Ge1–C3
B-6	218.9	219.7	199.2	199.5	200.9
B-6_{exp}	217.9(1)	218.5(1)	196.5(2)	197.4(2)	197.4(2)
B-7	219.7	216.4	198.8	198.8	199.0
B-7_{exp}	218.0(1)	216.7(2)	196.7(5)	197.8(5)	197.9(7)
	Ge2–C4	Ge1···Ge2	C3–C4	$\Sigma\angle(\text{Ge1})$	$\Sigma\angle(\text{Ge2})$
B-6	202.1	292.3	134.8	360.0	359.4
B-6_{exp}	199.2(2)	289.5(1)	132.5(2)	360.0(2)	359.4(2)
B-7	207.1	286.6	138.4	359.9	360.0
B-7_{exp}	200.5(7)	284.4(1)	136.6(8)	360.0(7)	360.0(7)

This consideration is reflected in the canonical MOs, exemplarily depicted in Figure 7.16 for the 2-butyne adduct complex **B-6**: Whereas the HOMO–12 and HOMO–4 describe the combined orbitals of the $\sigma(\text{Ge–Co})$ bonds (in-phase and out-of-phase combinations), out-of-plane π -electrons can clearly be identified in the HOMO–10 ($\pi_{\text{oop}}(\text{C3–C4})$) and HOMO ($\pi_{\text{oop}}(\text{Ge1–Co–Ge2})$). The remaining two electrons are suspected to be part of a weak δ -type interaction between the germanium and cobalt atoms (HOMO–2). Although this orbital interaction looks similar to that of the HOMO–1 of complex **B-5**, here the orbital coefficients on the germanium atoms are slightly higher.² The HOMO–3 and HOMO–1 show electron lone pairs centered at the cobalt atom. The calculated IBOs (Figure 7.17) not only comprise the presence of the expected $\sigma(\text{Ge1–Co})$, $\sigma(\text{Ge2–Co})$, $\sigma(\text{Ge1–C3})$, $\sigma(\text{Ge2–C4})$ and $\sigma(\text{C3–C4})$ orbitals, but also the $\pi_{\text{oop}}(\text{C3–C4})$, $\pi_{\text{oop}}(\text{Ge1–Co–Ge2})$ and $\delta(\text{Ge1–Co–Ge2})$ -type interactions. The latter is again strongly polarized towards the cobalt atom with atomic Löwdin populations of 0.05, 0.05 and 0.83 for the Ge1, Ge2 and Co atoms, thus this interaction should rather be seen as between a weak δ bond and an electron lone pair at the Co atom. The canonical and localized MOs of the complex **B-7** are obtained similarly as for **B-6**, although they are more polarized due to the asymmetric substitution and can be found in the appendix.

²In analogy to complex **B-5**, if the isosurface value for the HOMO–2 is lowered, the suspected $\delta(\text{Ge1–Co–Ge2})$ interaction is clearly observed.

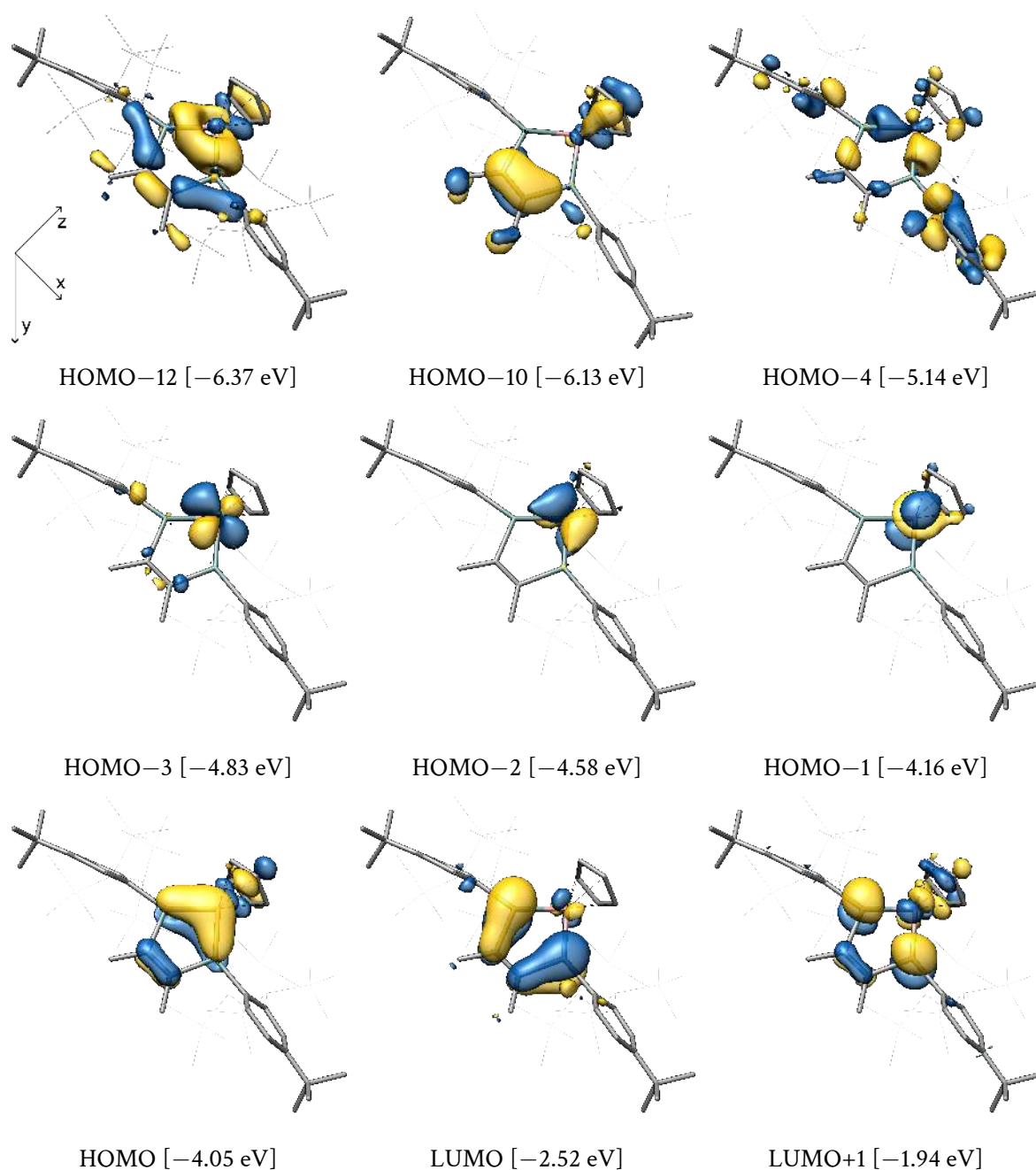


Figure 7.16: Selected canonical molecular orbitals of the complex **B-6** and their energy eigenvalues.

The complex **B-6** was also studied using the NBO7 program to obtain further insight in its electronic nature. A local NRT analysis reveals the dominant Lewis structure for the ring to be **B-6-a** with 52 % (Scheme 7.10), where two Ge=Co double bonds, two Ge-C single bonds and a C=C double bond are present, which reflects the results of the MO/IBO analysis. However, the remaining NRT resonance hybrid consists of various individual structures, each with low contributions that cannot be reasonably summarized. Those with the highest weight are also depicted in Scheme 7.10.

The results of the NBO analysis of Lewis structure **B-6-a** are summarized in Table 7.7. Two NBOs each are found for the $\sigma(\text{Ge}-\text{Co})$ and $\pi(\text{Ge}-\text{Co})$ bonds, where the first are rather polarized to-

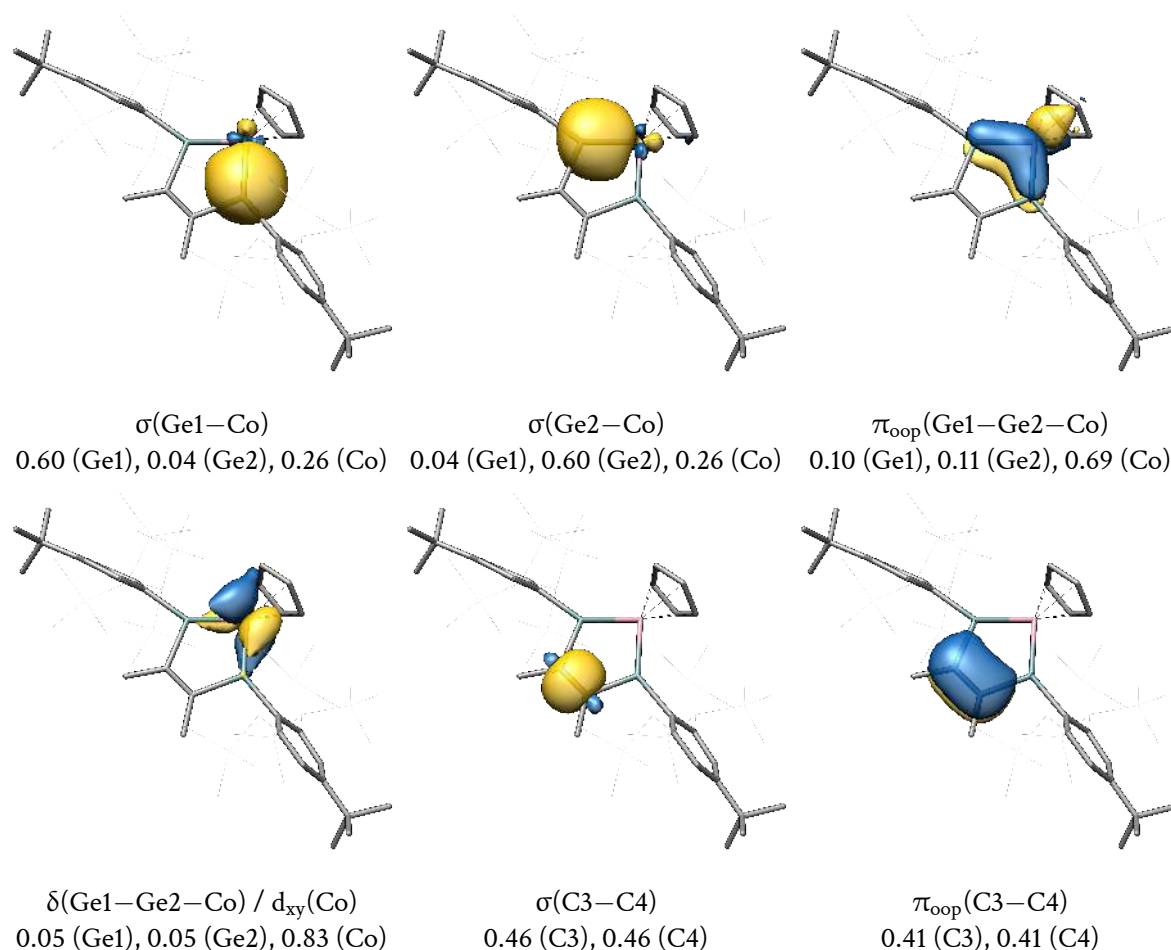
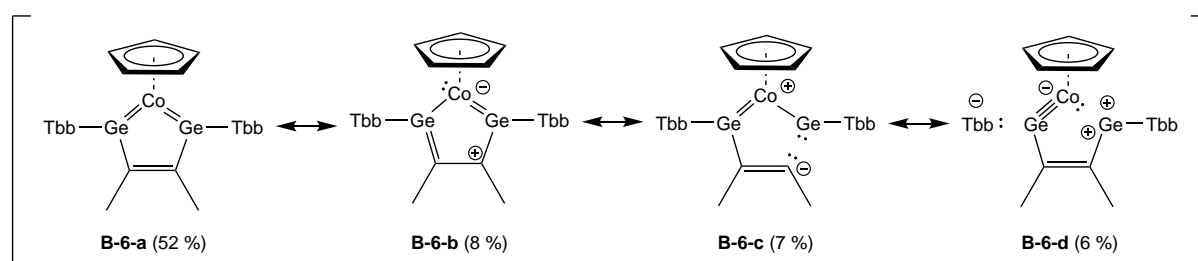


Figure 7.17: Selected intrinsic bond orbitals (IBOs) of the complex **B-6** and their atomic Löwdin orbital populations.



Scheme 7.10: Most contributing NRT resonance structures of complex **B-6** and their resonance weight. The local NRT subset comprises the Ge1, Ge2, Co, C3, C4 and the phenylic carbon atoms of the Tbb substituents.

wards the germanium atoms (62 %, 64 %). The π -type NBOs are strongly polarized towards the cobalt atom (88 %, 88 %) and describe localized 2-center-2-electron bonds in contrast to the 3-center-2-electron- π -type MOs and IBOs. Their large polarization towards the cobalt atom and the non-negligible occupation of the corresponding anti-bonding NBOs ($0.27 e^-$) again indicates a borderline case between a bond and a free electron lone pair on the cobalt atom. Accordingly, the calculated total NRT bond orders for the Ge1–Co (1.6) and Ge2–Co (1.8) bonds are smaller

than 2 in the case of an ideal metallacyclopentatriene structure. Although the C3–C4 bond also has a total NRT bond order slightly smaller than 2 (1.8), an identical Wiberg bond index is calculated. In contrast, the WBIs of the Ge–Co bonds are considerably smaller with 0.8.

The total NRT orders of 0.8 to 1.0 and similar WBIs also confirm the presence of typical Ge–C single bonds for the Ge–C^{Tbb} and Ge–C^{alkyne} pairs and show typical NBO occupations and polarization of approx. 1.9 e[−] and 70 % towards the more electronegative carbon atom, respectively. Thus, a considerable electron delocalization within the five-membered ring is not observed.

Table 7.7: Results of the NBO, local NRT and NPA analyses of complex B-6.

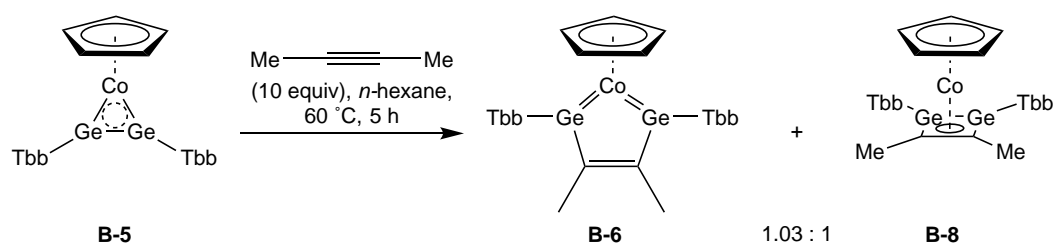
NBO A–B	Occ. / e [−]	NHO (A,B) pol. / % (hyb.)	WBI	NRT-BO tot/cov/ion	NPA / e	
σ(Ge1–Co)	1.77	62 (sp ^{1.2}), 38 (sd ^{1.1})	0.8	1.6/0.9/0.7	Ge1	+1.02
π(Ge1–Co)	1.89	12 (p), 88 (d)			Ge2	+0.99
σ(Ge2–Co)	1.77	64 (sp ^{1.1}), 36 (sd ^{1.0})	0.8	1.8/1.0/0.7	Co	−0.13
π(Ge2–Co)	1.90	12 (p), 88 (d)			C3	−0.38
σ(Ge1–C1)	1.92	29 (sp ^{2.6}), 71 (sp ^{2.8})	0.7	0.9/0.5/0.4	C4	−0.37
σ(Ge2–C2)	1.92	29 (sp ^{2.7}), 71 (sp ^{2.9})	0.7	0.8/0.5/0.3	[Cp]	−0.33
σ(Ge1–C3)	1.91	28 (sp ^{2.8}), 72 (sp ^{2.9})	0.7	0.9/0.5/0.4	[Tbb@Ge1]	−0.38
σ(Ge2–C4)	1.91	28 (sp ^{2.9}), 72 (sp ^{2.7})	0.7	1.0/0.5/0.5	[Tbb@Ge2]	−0.38
σ(C3–C4)	1.98	50 (sp ^{1.5}), 50 (sp ^{1.5})	1.8	1.8/1.8/0.0	[MeCCMe]	−0.79
π(C3–C4)	1.86	50 (p), 50 (p)				

The calculated atom and group NPA charges reveal the expected negative charge accumulations on the Tbb (both −0.38 e) and Cp (−0.33 e) substituents, but more positively-charged germanium atoms with +1.02 and +0.99 e than in the complexes B-1Tbb (+0.42, +0.51 e) and B-5 (+0.41, +0.43 e). This is caused by the alkyne fragment, which bears a rather large negative group charge of −0.79 e. The NPA charge on the cobalt atom (−0.13 e) is slightly more negative than that of complex B-5 (+0.02 e) and suggests a similar charge transfer between the cobalt and germanium atoms.

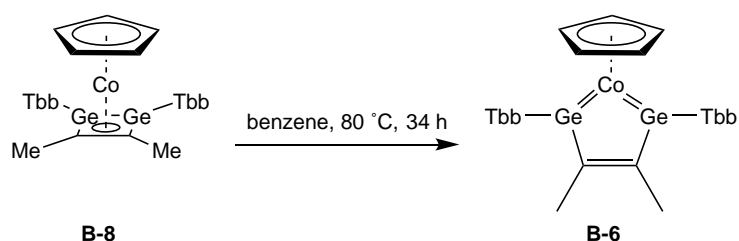
Finally, the question should be addressed, if there is a transannular interaction present between the germanium atoms in the complex B-6. Whereas the bond motif of a σ(Ge–Ge) single bond is only observed with 4 % in the overall resonance hybrid (leading to a very low total NRT bond order of 0.04), the calculated WBI amounts to 0.3, which is only slightly less than half of the WBIs for the Ge–C bonds and would indicate a weak Ge···Ge interaction. Considering the large Ge···Ge distance of 292.3 pm, which is far above the sum of the Pyykkoe single bond radii for Ge (242 pm),^[228] an effective binding transannular interaction between the germanium atoms is ruled out further. Additionally, an Atoms In Molecules (AIM)^[326] analysis with the AIM2000 program^[327] does not find a bond-critical point between the germanium atoms, but only the expected ring-critical point for the digerma-cobaltacyclopentatriene and bond-critical points between the adjacent ring atoms.

7.5. First insights into the reaction pathways involving complex B-6

The reaction of the digermine cobalt complex **B-1Tbb** with 2-butyne affords the digermacobaltacyclopentatriene **B-6** (Scheme 7.8), but not its conceivable constitutional isomer, the η^4 -digermacyclobutadiene complex [CoCp- η^4 -(Ge(Tbb)C(Me)C(Me)Ge(Tbb))] (**B-8**). Instead, compound **B-8** is observed as side product in the reaction of **B-5** with 2-butyne (Scheme 7.11), and can be interconverted quantitatively to **B-6** by a thermally induced isomerization at 80 °C (Scheme 7.12).^[286]



Scheme 7.11: Observed reaction of complex **B-5** with 2-butyne, leading to the digermacobaltacyclopentatriene complex **B-6** and the digermacyclobutadiene cobalt complex **B-8**.

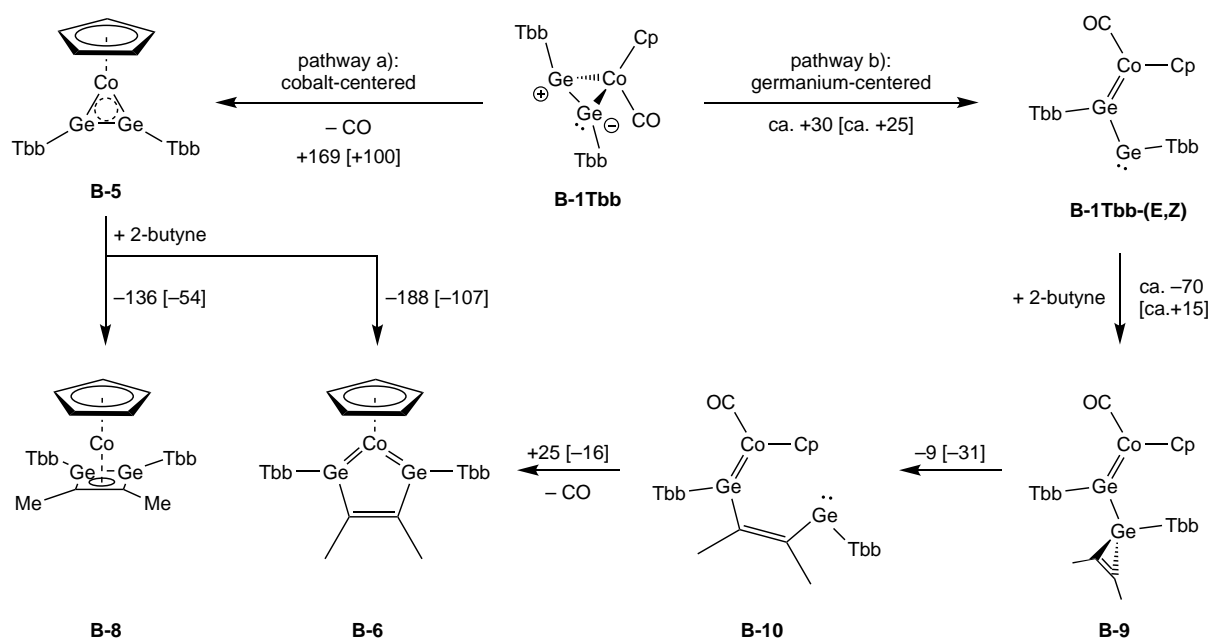


Scheme 7.12: Experimental thermally induced isomerization of complex **B-8** to complex **B-6**.

The digermacyclobutadiene cobalt complex **B-8** was calculated starting from the available sc-XRD structure and can be found in the appendix. The calculated thermodynamic parameters for the reaction of Scheme 7.12 indeed support the experimental finding, as the reaction is found to be favoured by -52.0 and -52.8 $\text{kJ}\cdot\text{mol}^{-1}$ in terms of the electronic energy ΔE and Gibbs energy ΔG .

In contrast, the reaction of the complex **B-1Tbb** with 2-butyne proceeds very selectively to **B-6**, and in Scheme 7.13 two major conceivable mechanistic pathways for its formation are provided. In the following discussion, the calculated free Gibbs energies (all calculated at 298 K) are given in square brackets after the respective electronic energies. The full table with more thermodynamic reaction parameters (ΔU , ΔH , ΔS) for each step can be found in the appendix.

The first pathway a) is cobalt-centered and starts with the dissociation of the carbonyl ligand, forming the digermacobaltarene complex **B-5**, which then reacts with 2-butyne to the digermacobaltacyclopentatriene **B-6**. However, the separate reaction of the carbonyl-free compound **B-5** with



Scheme 7.13: Conceivable mechanisms for the reaction of the digermine cobalt complex **B-1Tbb** to the digermacobaltacyclopentatriene **B-6**. The germylene-germylidene complex **B-1Tbb-ZZ** is used here as representative. The numbers without and within square brackets give the reaction electronic and free Gibbs energies, respectively.

2-butyne, as seen before in Scheme 7.11, yields a traceable amount of the digermacyclobutadiene complex **B-8**, which is not observed in the reaction between **B-1Tbb** and 2-butyne. A direct *in-situ* isomerization from **B-8** to **B-6** is also unlikely to happen at 60 °C, as this reaction could not be observed below 80 °C (see Scheme 7.12).

Instead, the germanium-centered pathway b) via the above-discussed germylene-germylidene complexes **B-1Tbb-(E,Z)** is proposed, which are easily accessible at 60 °C as they are lying only up to 30 kJ·mol⁻¹ higher in electronic and Gibbs energy (*vide supra*). Therein, the germylene center can add the alkyne via a [2+1]-cycloaddition (**B-9**), which is favoured in terms of energy ($\Delta E \approx -70$ kJ·mol⁻¹) and easily accessible in terms of the free Gibbs energy $\Delta G (\approx +15$ kJ·mol⁻¹), and was already observed before at other germylene centers known in the literature.^[283, 328-333] The alkyne fragment then inserts into the Ge–Ge bond (-9.2 [-30.8] kJ·mol⁻¹), forming again a germylene-germylidene complex (**B-10**). As the final step in the formation of **B-6**, the carbonyl ligand leaves the cobalt atom. This dissociation reaction is, in contrast to the first step of pathway a), much more favoured with electronic and free Gibbs reaction energies of +24.5 and even -16.4 kJ·mol⁻¹. Overall, the full reaction **B-1Tbb** + 2-butyne \rightarrow **B-6** + CO as depicted in Scheme 7.8 is calculated to be only slightly favoured ($\Delta E = -18.7$ kJ·mol⁻¹) and exergonic ($\Delta G = -6.9$ kJ·mol⁻¹) at 298 K.

Transition states for the proposed mechanism shown in Scheme 7.13, that would elucidate the kinetic regime, could not be obtained so far, but are subject to further investigations on this topic in the future.

8. Group 10 Tetrylidyne Complexes

The work presented in the this chapter was already published and is reprinted (adapted) with permission of the other authors from

L. R. Maurer, J. Rump, A. C. Filippou, *The Electronic Nature of Cationic Group 10 Ylidyne Complexes*, *Inorganics* **2023**, *11*, 129; DOI 10.3390/inorganics11030129.

My own manuscript contributions comprise

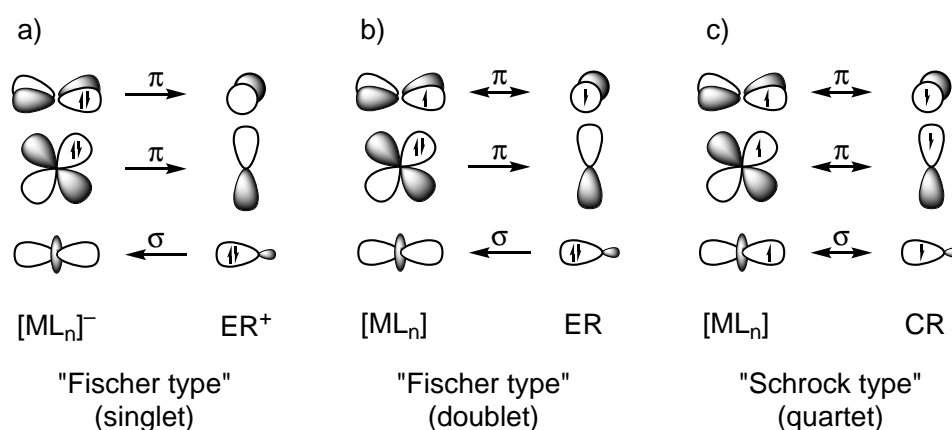
- Interpretation of the results regarding the canonical, fragment and localized MOs
- Performing the calculations regarding the compounds by T. Hadlington *et al.* and interpretation of the results
- Co-writing the manuscript (especially chapters 1, 2.1, 2.2, 2.5, 3 and 4) and proof-reading

The following chapter is supposed to provide an overview of the main results and conclusions of the topic, and thus, the complete publication is summarized. Apart from my own contribution listed above, which are in the focus, this also includes contributions of the other authors, mainly by Jens Rump. The complete publication can be found in the appendix.

8.1. Introduction

Transition metal complexes of the general formula $[L_nM\equiv E-R]$ ($E = \text{Si to Pb}$, $R = \text{singly-bonded substituent}$, $L_n = \text{ligand sphere}$) represent the heavier homologues of Fischer-type carbyne complexes,^[334–338] featuring a triple bond between the transition metal M and the tetrel E . After the first report of a germylydine complex by P. P. Power *et al.* in 1996,^[339, 340] the group of A. C. Filippou succeeded in isolating the first tetrylydine complex representatives for tin,^[341, 342] lead,^[343–345] and even silicon.^[346] Herein, the $M\equiv E$ functionality needs to be carefully protected by electronic or steric stabilization to circumvent head-to-tail dimerizations^[347] or intra- and intermolecular σ -bond activation, similarly to the electrophilic low-valent tetrel centers also discussed in part A of this thesis.

Quantum chemical studies of the heavier tetrylydine complexes reveal that they are electronically similar to Fischer-type carbyne complexes,^[337, 342–344, 348–354] having a $\sigma(M-E)$ bond polarized towards the tetrel and two $\pi(M-E)$ bonds polarized towards the metal atom. Using the Dewar-Chatt-Duncanson model,^[355, 356] the $M\equiv E$ bonding can be well rationalized by a combination of one $\sigma(ER^+ \rightarrow ML_n^-)$ donation and two $\pi(ML_n^- \rightarrow ER^+)$ back donations (Scheme 8.1 a). Alternatively, the bond situation in tetrylydine complexes can be described by b) the interaction of two neutral fragments $[ML_n]$ and ER in their electronic doublet state, or c) in their quartet electronic state.^[350] The latter is typically found in Schrock-type alkylidyne complexes and results in two rather unpolar $\pi(M-E)$ bonds.^[357, 358]

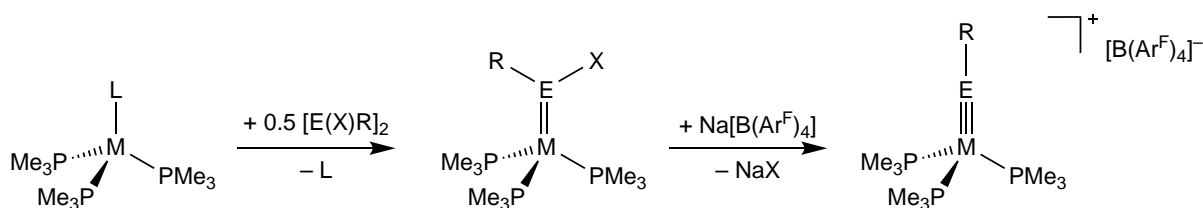


Scheme 8.1: Schematic representation of the dominant orbital interactions in the heavier group 10 tetrylydine complexes and Fischer-type carbyne complexes using a) charged, closed-shell fragments or b) neutral fragments in the doublet state; c) dominant orbital interactions in the Schrock-type alkylidyne complexes using neutral, open-shell fragments in their quartet spin states.

Whereas the initial development of heavier tetrylydine complexes is focussed on group 6 transition metals, today examples exist for the groups 4 to 10 where a heavier tetrel could be successfully incorporated into triple bonding with a metal atom.^[359–366]

Particular of interest are group 10 tetrylydine complexes, as only a few representatives exist and

even for the lightest homologue, a group 10 carbyne complex, only one compound is known for 40 years by E. O. Fischer *et al.*^[367] The first heavier group 10 tetrylidyne complex cations $[(\text{PMe}_3)_3\text{M}\equiv\text{ER}]^+$ could be isolated by I. Papazoglou during his doctoral studies for $\text{M} = \text{Ni}$ ($\text{E} = \text{Si}$ ($\text{NiSiTbb}_{\text{exp}}$), Ge ($\text{NiGeAr}^{\text{Mes}}_{\text{exp}}$), Sn ($\text{NiSnAr}^{\text{Mes}}_{\text{exp}}$)) and Pt ($\text{E} = \text{Si}$ ($\text{PtSiTbb}_{\text{exp}}$), Ge ($\text{PtGeAr}^{\text{Mes}}_{\text{exp}}$)).^[368] Scheme 8.2 illustrates the two-step synthetical route via the corresponding tetrylidene complexes $[(\text{PMe}_3)_3\text{M}=\text{E}(\text{X})(\text{R})]$, which are then transformed into the targeted tetrylidyne complexes after abstraction of the halide X with $\text{Na}[\text{B}(\text{Ar}^{\text{F}})_4]$. The same route was also employed very recently by T. J. Hadlington *et al.* for the analogues triphenylphosphane nickel complex cations $[(\text{PPh}_3)_3\text{Ni}\equiv\text{EN}(\text{Si}(i\text{Pr})_3)(\text{Dipp})]^+$ ($\text{E} = \text{Ge}$ ($\text{B-XI-Ge}_{\text{exp}}$), Sn ($\text{B-XI-Sn}_{\text{exp}}$)).^[369]



Scheme 8.2: [

$\text{B}(\text{Ar}^{\text{F}})_4]$ developed by I. Papazoglou.] Two-step synthesis of the group 10 metal tetrylidyne complexes $[(\text{PMe}_3)_3\text{MER}][\text{B}(\text{Ar}^{\text{F}})_4]$ developed by I. Papazoglou.^[368] $\text{M} = \text{Ni}, \text{Pt}$; $\text{L} = \text{PMe}_3$, $\text{Ga}(\text{C}_5(\text{CH}_3)_5)$; $\text{E} = \text{Si}, \text{Ge}, \text{Sn}$; $\text{X} = \text{Cl}, \text{Br}$; $\text{R} = \text{Tbb}, \text{Ar}^{\text{Mes}}$; $\text{Ar}^{\text{F}} = 3,5\text{-(CF}_3)_2\text{-C}_6\text{H}_3$.

A basic rationalization of the bond description in the complexes by I. Papazoglou and T. J. Hadlington *et al.* is given in their respective references. However, no extensive theoretical study about the whole series of the group 10 tetrylidyne complex cations $[(\text{PMe}_3)_3\text{MER}]^+$ (MER : $\text{M} = \text{Ni}, \text{Pd}, \text{Pt}$; $\text{E} = \text{C}, \text{Si}, \text{Ge}, \text{Sn}, \text{Pb}$; $\text{R} = \text{Ar}^{\text{Mes}}, \text{Tbb}$ (only for Si)), that outlines the electronic structure of the hitherto unknown complexes and puts them into context with each other and the known ones, was available before this work, and will be presented in the following.

8.2. Structural Results

The experimentally available tetrylidyne complex cations by I. Papazoglou were chosen as anchor points of this study and were complemented by the experimentally missing MER combinations with $\text{M} = \text{Ni}, \text{Pd}, \text{Pt}$; $\text{E} = \text{C}, \text{Si}, \text{Ge}, \text{Sn}, \text{Pb}$; $\text{R} = \text{Ar}^{\text{Mes}}$, resulting in a total of 15 compounds. Additionally, the Tbb substituent was used for the silicon complexes to compare them with the experimentally known systems $\text{NiSiTbb}_{\text{exp}}$ and $\text{PtSiTbb}_{\text{exp}}$. The structures of all MER complexes and the compounds by T. J. Hadlington *et al.* ($\text{B-XI-Ge}_{\text{exp}}$, $\text{B-XI-Sn}_{\text{exp}}$) were calculated with the ORCA 5.0.3 program package at level of theory I and confirmed as minima by successive numerical or analytical frequency calculations. Whereas the most important results of the MER complexes are summarized in the following, the discussion of the results regarding the complexes B-XI-E is omitted here, but can be found in the full publication text included in the appendix.

Table 8.1: Selected structural parameters of the calculated and experimentally obtained group 10 tetrylidyne complex cations **MER**. Experimental sc-XRD bonding parameters of the MER_{exp} complexes are obtained from reference [368]. For the compounds $\text{NiGeAr}^{\text{Mes}}_{\text{exp}}$ and $\text{PtGeAr}^{\text{Mes}}_{\text{exp}}$, the bonding parameters of two independent complex cations found in the unit cell are listed. Bond lengths and angles are given in pm and degrees, respectively.

	M–E	E–C1	M–E–C1
$\text{NiCAr}^{\text{Mes}}$	169.1	141.3	168.4
NiSiTbb	204.5	184	167.2
$\text{NiSiTbb}_{\text{exp}}$	203.11(7)	183.8(2)	172.40(8)
$\text{NiSiAr}^{\text{Mes}}$	204.2	186.6	163.8
$\text{NiGeAr}^{\text{Mes}}$	213.3	197.1	165.3
$\text{NiGeAr}^{\text{Mes}}_{\text{exp}}$	210.40(6)	194.6(4)	164.9(1)
	210.20(6)	195.0(4)	166.5(1)
$\text{NiSnAr}^{\text{Mes}}$	235.1	219.4	150.9
$\text{NiSnAr}^{\text{Mes}}_{\text{exp}}$	228.08(9)	214.0(5)	165.1(2)
$\text{NiPbAr}^{\text{Mes}}$	244.9	229.7	142.7
$\text{PdCAr}^{\text{Mes}}$	182	140.9	168.4
PdSiTbb	215.1	184	163.1
$\text{PdSiAr}^{\text{Mes}}$	216.1	187.6	150.7
$\text{PdGeAr}^{\text{Mes}}$	227.9	199.5	144.9
$\text{PdSnAr}^{\text{Mes}}$	251.6	222.9	134.4
$\text{PdPbAr}^{\text{Mes}}$	263.1	232.4	129.6
$\text{PtCAr}^{\text{Mes}}$	179.9	141.2	175.1
PtSiTbb	215.8	183.8	168.1
$\text{PtSiTbb}_{\text{exp}}$	213.43(7)	184.2(3)	173.83(9)
$\text{PtSiAr}^{\text{Mes}}$	215.7	186.3	166.1
$\text{PtGeAr}^{\text{Mes}}$	228.4	198.9	149.7
$\text{PtGeAr}^{\text{Mes}}_{\text{exp}}$	222.42(7)	194.7(7)	161.8(2)
	222.69(8)	195.2(7)	163.3(2)
$\text{PtSnAr}^{\text{Mes}}$	255.1	223.9	132.1
$\text{PtPbAr}^{\text{Mes}}$	267.7	233.1	127.3

The evaluation of selected structural parameters, summarized in Table 8.1, indicates several trends, which are briefly discussed in the following:

- The calculated structures generally agree well with the experimental solid-state structures, however the deviation for the M–E bond lengths is found to increase slightly with an increasing atomic number of the tetrel and transition metal and ranges between 1.4 and 7.0 pm. The same is true for the E–C1 bond lengths with differences ranging from 2.3 to 5.4 pm. Also for the M–E–C1 bond angles significant deviations are observed for the heavier complexes. This is attributed to the inherent contrast of experimental solid state structures obtained by single-crystal X-ray diffraction at 100 to 123 K and single molecule gas phase calculations at 0 K, but also due to the very flat hypersurface of the M–E–R moiety as found

by PES scans. (see the full publication for more information). The influence of the level of theory and relativistic effects was also checked but did not yield any salient effects.

- The calculated (and experimental) M–E bond distances are considerably shorter than observed in the preceding tetrylidene complexes presented by I. Papazoglou^[368] and indicate the presence of M≡E triple bonds. As expected, complexes with heavier metals and tetrrels feature longer M–E bond lengths, although this trend is weakened for the transition from palladium to platinum due to the lanthanide contraction effect.
- Interestingly, the calculated M–E–C1 angles show a high degree of variability with values ranging from 175.1° (PtCAr^{Mes}) down to 127.3° (PtPbAr^{Mes}). All carbyne and silylidyne complexes show rather large angles around 170° in the range of typical heavier tetrylidyne complexes (156 to 179°).^[362, 370] This is also observed for NiGeAr^{Mes} (165.3°), but for M = Pd, Pt and E = Ge, Sn, Pb the calculated M–E–C1 angles are considerably smaller, decreasing in the order Ge > Sn > Pb, which suggests a different electronic structure in these complexes.

8.3. Molecular Orbital Analysis

Selected canonical MOs of the complexes NiSiAr^{Mes} and PtPbAr^{Mes} are depicted in the Figures 8.1 and 8.2, respectively, being the anticipated extremes regarding the bonding situation. For NiSiAr^{Mes}, the energetically low-lying delocalized HOMO–11 corresponds to a $\sigma(\text{Ni–Si})$ bond with accompanying $\sigma(\text{Si–C1})$ bond character in this MO. Two metal-centered $\pi(\text{Ni–Si})$ bonds could be identified in the HOMO–7 and HOMO–8, with their anti-bonding combinations present in the LUMO and LUMO+1, resulting in an overall Ni≡Si triple bonding.

In the complex PtPbAr^{Mes}, also an energetically low-lying $\sigma(\text{M–E})$ interaction is found (HOMO–11). However, in contrast to the complex NiSiAr^{Mes} no clear $\pi(\text{Pt–Pb})$ orbitals can be identified, but rather metal-centered d_{xz} and d_{yz} orbitals in the HOMO–10 and HOMO–9, respectively, without significant orbital contribution from the lead atom. Accordingly, the LUMO and LUMO+1 mainly correspond to the empty p_x and p_y orbitals at the tetrel atom, with only a small participation of the metal. A lead atom triply-bonded to the metal is thus not observed here, but instead the absence of $\pi(\text{M–E})$ orbitals and the strongly bent Pt–Pb–C1 moiety (127.3°) suggest the presence of metallotetrylene character with a platinum-lead single bond and an electron lone pair on the Pb atom. However, a convincing MO for the latter could not be found, presumably due to the large relativistic stabilization, which causes a downward energetic shift.

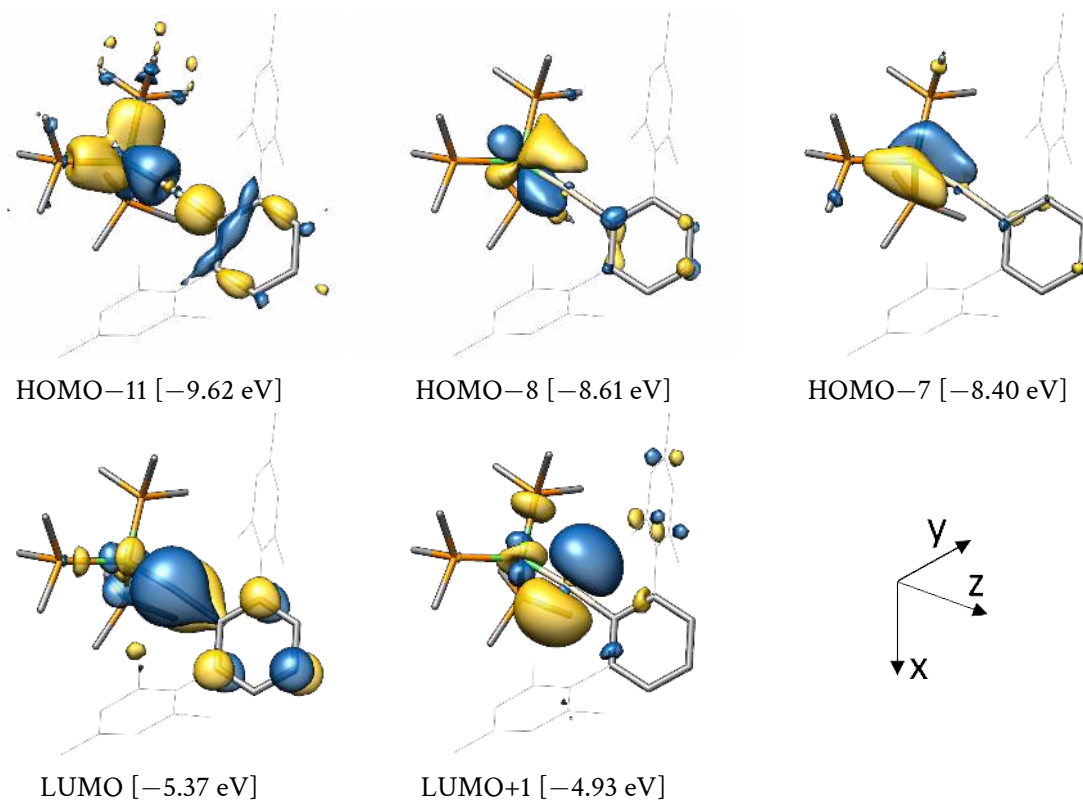


Figure 8.1: Selected canonical MOs of NiSiAr^{Mes} and their respective orbital energies.

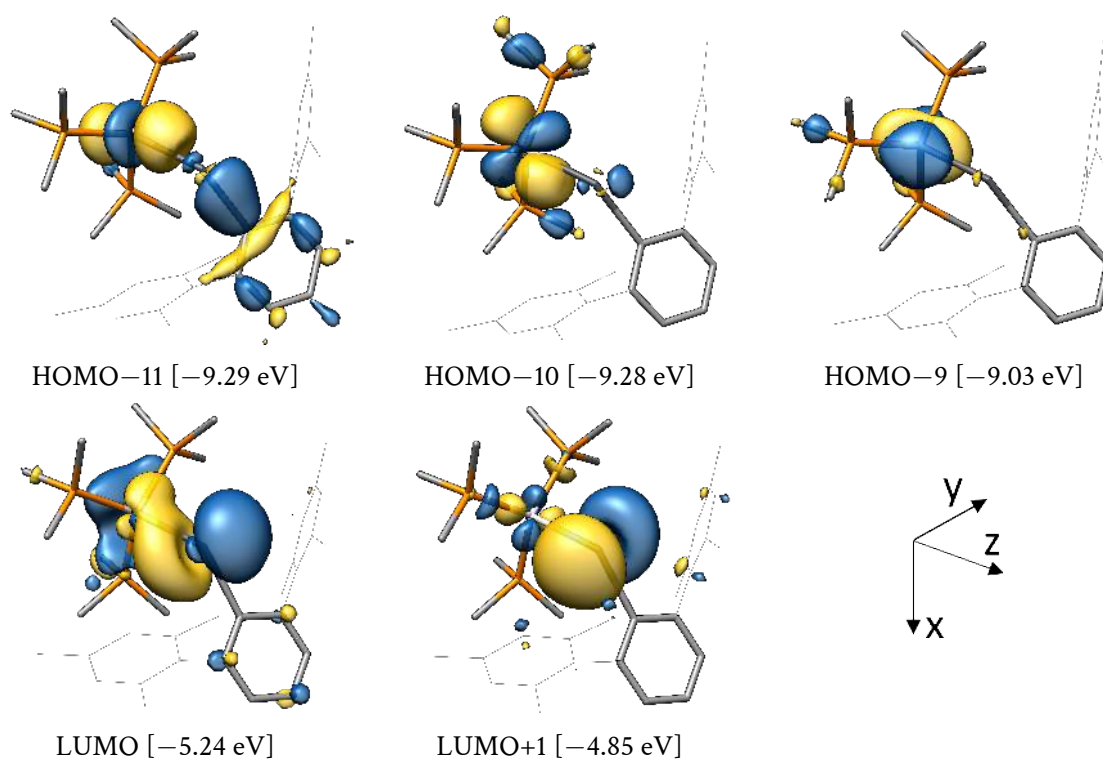


Figure 8.2: Selected canonical MOs of PtPbAr^{Mes} and their respective orbital energies.

Further support for these different bonding descriptions is derived from the analysis of the localized Pipek-Mezey MOs. Localized MOs for the $\sigma(\text{M}-\text{E})$, $\pi_{xz}(\text{M}-\text{E})$ and $\pi_{yz}(\text{M}-\text{E})$ bonds are found for the complex $\text{NiSiAr}^{\text{Mes}}$ (Figure 8.3) in accordance with the canonical MO analysis. The corresponding atomic Mulliken orbital populations reveal a strong polarization of the σ -bond towards the silicon atom (0.81) and strongly Ni-centered π bonds (0.80 for both π_{xz} and π_{yz}), reminiscent to the Fischer-type carbyne complexes (*vide supra*). The remaining filled d-orbitals of the d^{10} -configured nickel atom are also observed in the LMOs and have no significant orbital contribution at the silicon atom (< 0.04).

In contrast, for $\text{PtPbAr}^{\text{Mes}}$ no $\pi(\text{Pt}-\text{Pb})$ binding LMOs are found in agreement with the canonical MO analysis, but instead almost pure filled d_{xz} and d_{yz} orbitals at the platinum atom (Figure 8.4). The assumed metallotetrylene situation is further confirmed by the presence of a $\sigma(\text{Pt}-\text{Pb})$ LMO polarized towards the Pt atom (0.82) and an electron lone pair, which is completely localized at the lead atom without visible Pt–Pb overlap.

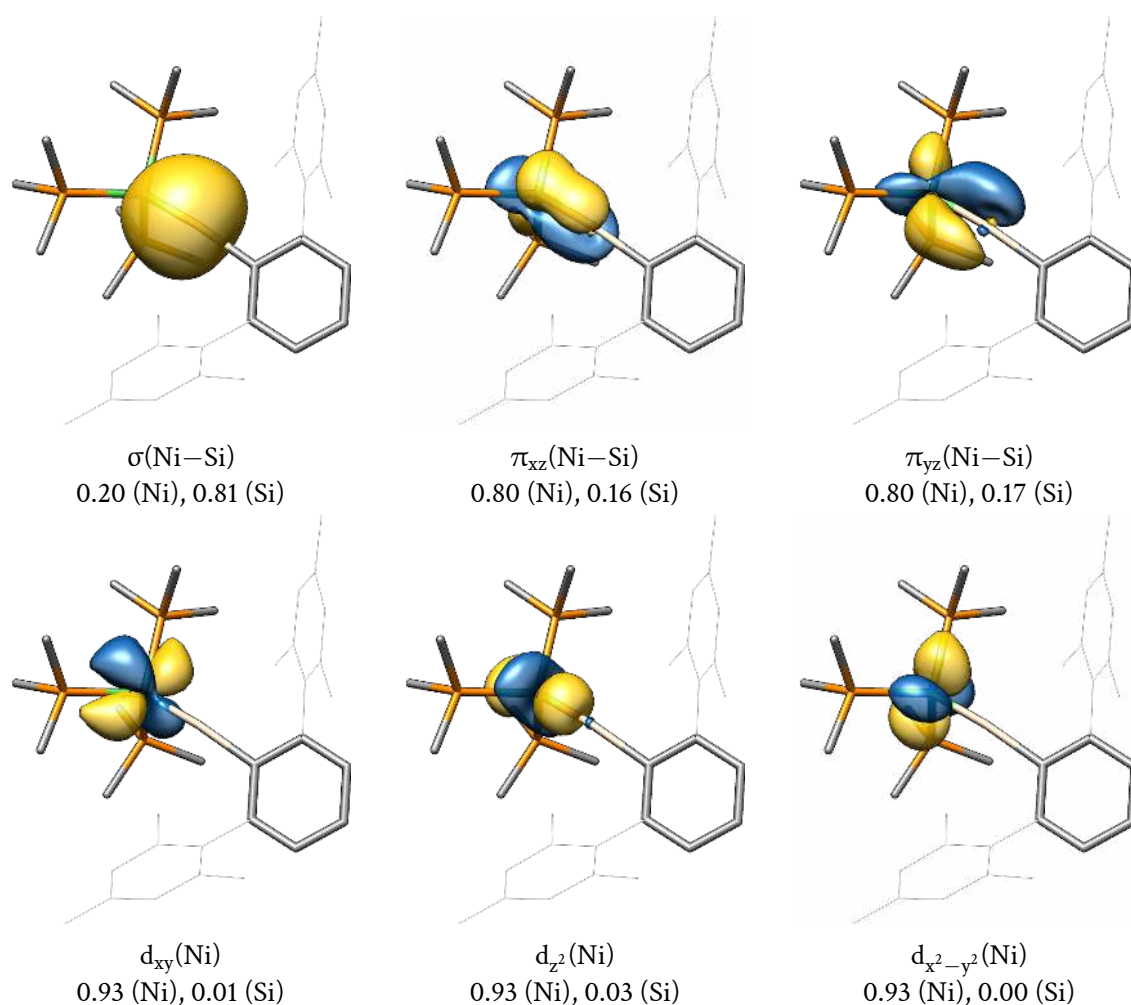


Figure 8.3: Pipek-Mezey-localized MOs of $\text{NiSiAr}^{\text{Mes}}$, their assigned orbital type and corresponding atomic Mulliken orbital populations.

From the structural and MO-analytical results, two types of bonding situation can be proposed, which are illustrated by fragment MO interaction diagrams in Scheme 8.3. On the one hand, there

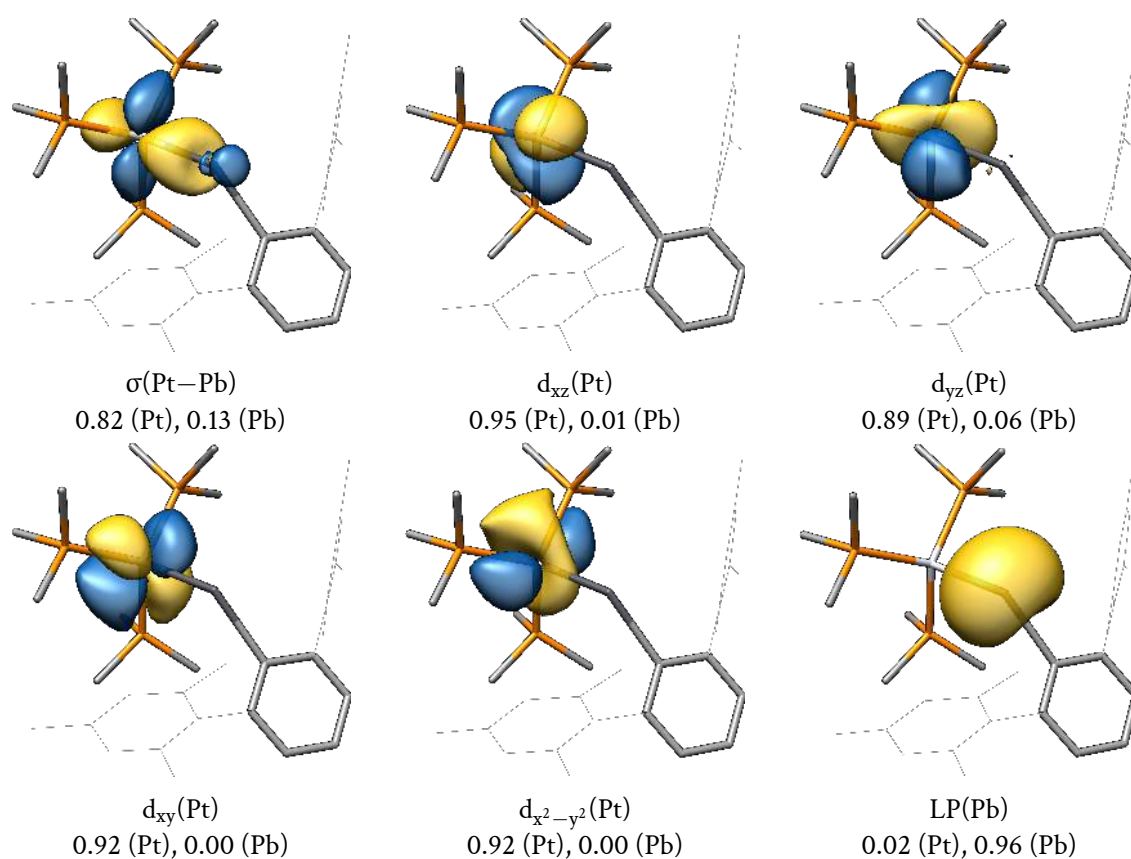
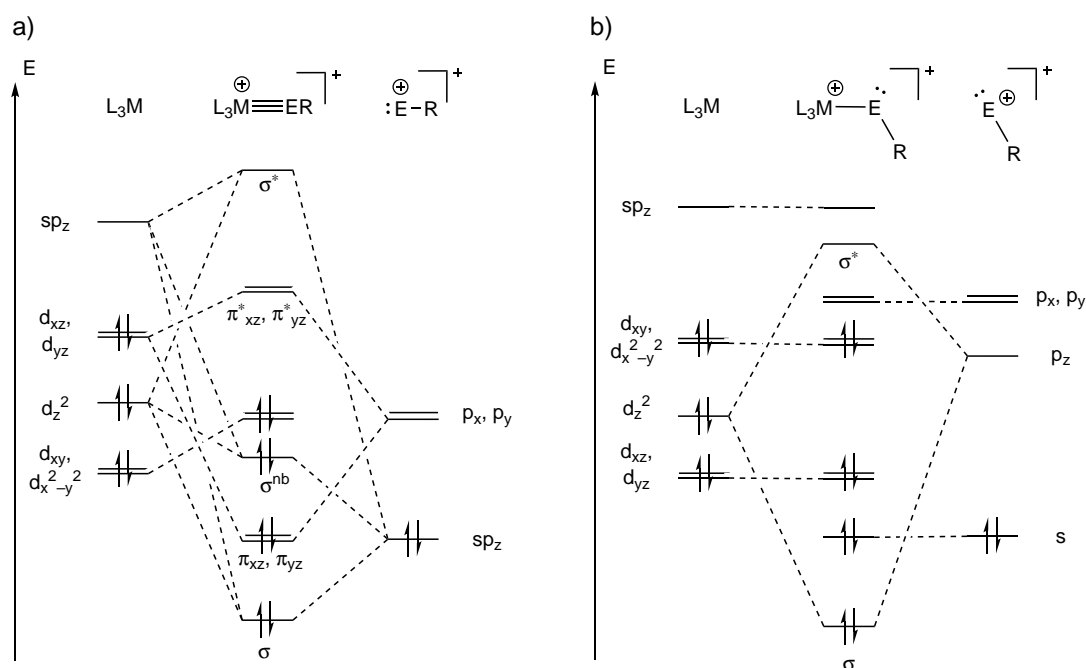


Figure 8.4: Pipek-Mezey-localized MOs of $\text{PtPbAr}^{\text{Mes}}$, their assigned orbital type and corresponding atomic Mulliken orbital populations.

are a) tetrylidyne complexes with $\text{M}\equiv\text{E}$ triple bonding that can be described by the classical Dewar-Chatt-Duncanson model. The neutral ML_3 fragment interacts with the ER^+ fragment in the singlet state, forming metal-tetrel bonds by a $\sigma(\text{E}\rightarrow\text{M})$ donation and two $\pi(\text{M}\rightarrow\text{E})$ back donations. Herein, both the empty metal sp_z and the filled d_z^2 orbitals can interact with the filled sp hybrid orbital of the tetrel, which leads to a σ -bonding, a σ^* -antibonding and a non-bonding σ^{nb} MO, where the latter can be regarded as metal-centered d_z^2 orbital. The π -bonds result from $d_{xz}(\text{M})\rightarrow p_x(\text{E})$ and $d_{yz}(\text{M})\rightarrow p_y(\text{E})$ interactions, and the remaining orbitals are responsible for metal-ligand or tetrel-substituent bonding.

On the other hand, case b) describes metallotetrylenes with only a M-E single bond by a $\sigma(\text{M}\rightarrow\text{E})$ donation, and an electron lone pair at the tetrel center of the bent M-E-C moiety, which is further stabilized by relativistic effects.

After investigating the structures, MOs and LMOs of all studied MER complexes, they can be classified according to Scheme 8.4: All carbon and silicon compounds as well as the complex $\text{NiGeAr}^{\text{Mes}}$ are considered as tetrylidyne complexes (case a), whereas the complexes $\text{PdSnAr}^{\text{Mes}}$, $\text{PdPbAr}^{\text{Mes}}$, $\text{PtSnAr}^{\text{Mes}}$ and $\text{PtPbAr}^{\text{Mes}}$ show clear metallotetrylene character (case b). The germanium system $\text{PdGeAr}^{\text{Mes}}$ and $\text{PtGeAr}^{\text{Mes}}$ as well as the nickel-tin and nickel-lead complexes $\text{NiSnAr}^{\text{Mes}}$ and $\text{NiPbAr}^{\text{Mes}}$ are borderline cases between a) and b). They show a similar σ -bonding as the tetrylidyne complexes, albeit with weakened $\pi(\text{M-E})$ bonds and more bent M-E-C1 units (142.7 to



Scheme 8.3: Qualitative MO interaction diagram depicting the bonding situations of a) the tetrylidyne complex (similar to the diagram for $[L_3M\equiv CR]$ by P. Hofmann^[371]) and b) the metallotetrylene case.

150.9°) compared to the carbon and silicon compounds (see the appendix for more information on these complexes).

The extensive analysis of the canonical and localized MOs of the compounds B-XI-Ge and B-XI-Sn suggests an electronic structure very similar to Fischer-type aminocarbene complexes and the presence of both ylidene and allenic Lewis resonance forms due to the amino substituent attached to the tetrel atom. A detailed discussion can be found in the full publication text.

NiCAr ^{Mes}	NiSiR	NiGeAr ^{Mes}	NiSnAr ^{Mes}	NiPbAr ^{Mes}
PdCAr ^{Mes}	PdSiR	PdGeAr ^{Mes}	PdSnAr ^{Mes}	PdPbAr ^{Mes}
PtCAr ^{Mes}	PtSiR	PtGeAr ^{Mes}	PtSnAr ^{Mes}	PtPbAr ^{Mes}

tetrylidyne complex
metallotetrylene

Scheme 8.4: Classification of the compounds assessed throughout this study: R = Ar^{Mes}, Tbb. The hatched complexes also exhibit characteristics of the metallotetrylene type.

8.4. Bond Dissociation Energies and Natural Population Analysis

To assess the M–E bond strength in the MER complexes, bond cleavage (*BCE*) and bond dissociation energies (*BDE*) were computed. Due to the positive charge of the complex cations, two different fragmentation schemes are reasonable: First, the splitting $[(\text{PMe}_3)_3\text{MER}]^+ \rightarrow [\text{M}(\text{PMe}_3)_3] + [\text{ER}]^+$ into two closed-shell singlet fragments¹ with large singlet-triplet excitation energies ranging from 191.4 to 214.3 $\text{kJ}\cdot\text{mol}^{-1}$ for the metal fragments and 140.8 to 174.7 $\text{kJ}\cdot\text{mol}^{-1}$ for the tetryliumylidene ions. Alternatively, the $[(\text{PMe}_3)_3\text{MER}]^+ \rightarrow [\text{M}(\text{PMe}_3)_3]^+ + [\text{ER}]$ cleavage into two open-shell doublet spin state fragments is conceivable, where the doublet state is preferred for all fragments by 120.3 to 284 $\text{kJ}\cdot\text{mol}^{-1}$ over the quartet spin state.

Table 8.2: Calculated *BCEs* and *BDEs* of the M–E bonds of the MER complexes in $\text{kJ}\cdot\text{mol}^{-1}$ at the level of theory II to give the $\text{ML}_3 + \text{ER}^+$ and $\text{ML}_3^+ + \text{ER}$ fragment combinations. *BCEs* and *BDEs* of the energetically more favourable fragmentation scheme are highlighted in bold.

	<i>BCE</i>		<i>BDE</i>	
	$\text{ML}_3 + \text{ER}^+$	$\text{ML}_3^+ + \text{ER}$	$\text{ML}_3 + \text{ER}^+$	$\text{ML}_3^+ + \text{ER}$
$\text{NiCAr}^{\text{Mes}}$	718.6	544.3	521.8	461.6
NiSiTbb	470.4	427.9	402.5	377.5
$\text{NiSiAr}^{\text{Mes}}$	491.5	421.4	392.3	368.9
$\text{NiGeAr}^{\text{Mes}}$	459.3	387.7	365.0	340.0
$\text{NiSnAr}^{\text{Mes}}$	383.9	346.0	316.9	304.5
$\text{NiPbAr}^{\text{Mes}}$	342.7	328.6	291.7	285.6
$\text{PdCAr}^{\text{Mes}}$	625.1	469.7	404.2	340.1
PdSiTbb	415.3	395.0	333.0	304.1
$\text{PdSiAr}^{\text{Mes}}$	427.4	387.9	322.5	295.3
$\text{PdGeAr}^{\text{Mes}}$	383.2	349.2	289.4	260.5
$\text{PdSnAr}^{\text{Mes}}$	321.9	319.5	253.6	237.3
$\text{PdPbAr}^{\text{Mes}}$	293.3	309.0	240.4	230.4
$\text{PtCAr}^{\text{Mes}}$	799.3	618.3	486.0	411.3
PtSiTbb	504.0	462.5	373.5	334.0
$\text{PtSiAr}^{\text{Mes}}$	520.3	450.2	362.1	324.1
$\text{PtGeAr}^{\text{Mes}}$	444.0	386.3	314.5	274.9
$\text{PtSnAr}^{\text{Mes}}$	354.6	332.6	274.1	247.2
$\text{PtPbAr}^{\text{Mes}}$	313.5	307.8	251.1	230.5

The comparison of the fragmentation schemes reveals that the bond dissociation is favoured into open-shell doublet fragments for all complexes except $\text{PdSnAr}^{\text{Mes}}$ in terms of the *BCE* and for all complexes in terms of the *BDE* (see Table 8.2). If only the more favoured fragmentation pathway is discussed, both the *BCEs* and *BDEs* follow the trend $\text{C} \gg \text{Si} > \text{Ge} > \text{Sn} \approx \text{Pb}$. Thus, the strongest

¹A triplet ground state is only observed for the structurally relaxed $[\text{CAr}^{\text{Mes}}]^+$ fragment due to an bond activation of the Mes substituent.

M–E bonds are obtained for the triply bonded carbyne complexes, and the heavier complexes with large metallotetrylene character as discussed before show weaker bonds.

Furthermore, the charge distribution of the complex cations was studied with the natural population analysis method (NPA) in the NBO7 framework using natural atomic orbitals (NAOs) and the results are summarized in Table 8.3 and Figure 8.5. Interestingly, the metal atoms Ni, Pd and Pt are almost electroneutral for E = Si and Ge (-0.03 to $+0.05$ e) or even slightly negatively charged for the heavier Sn and Pb tetrels (-0.21 to -0.09 e). Accordingly, most of the cationic charge resides on the tetrel atoms in a range between $+0.58$ (PtGeAr^{Mes}) and $+1.07$ e (NiPbAr^{Mes}), following the order $\text{Si} \approx \text{Ge} < \text{Sn} \approx \text{Pb}$. The entire ML₃ units carry total charges of $+0.46$ (NiPbAr^{Mes}) to $+0.76$ e (PtGeAr^{Mes}), whereas the heavier ER groups have on average slightly smaller charges from $+0.24$ (PtGeAr^{Mes}) to $+0.54$ e (NiPbAr^{Mes}).

In contrast, the high electronegativity of carbon leads to a completely different charge distribution in the carbyne complexes, which is reflected by its negative partial charges (-0.13 to -0.24 e) and a considerably higher group partial charge of the ML₃ unit ($+1.18$ to $+1.28$ e) than observed in the heavier congeners.

Table 8.3: Calculated NPA charges in e for the M and E atoms and the [ML₃] and [ER] units in the complex cations [L₃MER]⁺.

	M	E	[ML ₃]	[ER]
NiCAr ^{Mes}	+0.35	-0.13	+1.18	-0.18
NiSiTbb	±0.00	+0.76	+0.62	+0.38
NiSiAr ^{Mes}	±0.00	+0.78	+0.67	+0.33
NiGeAr ^{Mes}	+0.05	+0.66	+0.59	+0.41
NiSnAr ^{Mes}	-0.09	+1.05	+0.48	+0.52
NiPbAr ^{Mes}	-0.09	+1.07	+0.46	+0.54
PdCAr ^{Mes}	+0.31	-0.15	+1.18	-0.18
PdSiTbb	-0.03	+0.73	+0.66	+0.34
PdSiAr ^{Mes}	-0.03	+0.75	+0.71	+0.29
PdGeAr ^{Mes}	-0.01	+0.65	+0.71	+0.29
PdSnAr ^{Mes}	-0.15	+0.98	+0.56	+0.44
PdPbAr ^{Mes}	-0.17	+1.02	+0.53	+0.47
PtCAr ^{Mes}	+0.35	-0.24	+1.28	-0.28
PtSiTbb	-0.02	+0.65	+0.71	+0.29
PtSiAr ^{Mes}	-0.02	+0.68	+0.75	+0.25
PtGeAr ^{Mes}	±0.00	+0.58	+0.76	+0.24
PtSnAr ^{Mes}	-0.19	+0.96	+0.67	+0.33
PtPbAr ^{Mes}	-0.21	+1.00	+0.55	+0.45

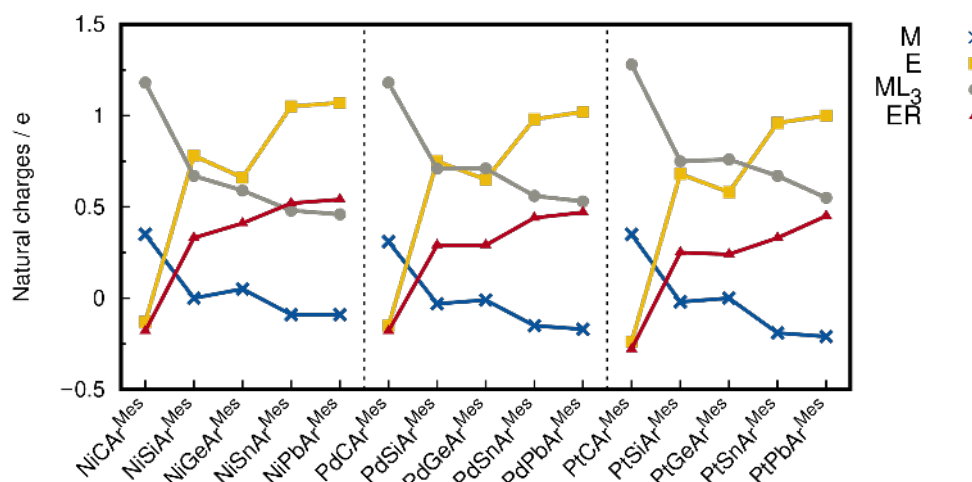


Figure 8.5: Illustration of the calculated NPA charges for the M and E atoms and the $[ML_3]$ and $[ER]$ units in the complex cations $[L_3MEAr^{Mes}]^+$. The connecting lines have no physical meaning and are only drawn to visualize the trends.

8.5. ETS-NOCV and EDA Analyses

The ETS-NOCV bond analysis represents the combination of the extended transition state (ETS)^[145] method and natural orbitals of chemical valence (NOCV)^[146,147] and was employed here to obtain a deeper understanding of the metal-tetrel bonding in the MER complexes. It was carried out on the level I-optimized structures using the ADF 2021.103 program package^[372] at the B97-D3(BJ)/TZ2P^[373] level of theory, which is comparable to the level of theory I. The overall interaction energy (ΔE_{int}) of the studied complexes is decomposed via an energy decomposition analysis (EDA) according to Equation 8.1:

$$\Delta E_{\text{int}} = \Delta E_{\text{orb}} + \Delta E_{\text{Pauli}} + \Delta E_{\text{elstat}} + \Delta E_{\text{disp}} = -BCE \quad (8.1)$$

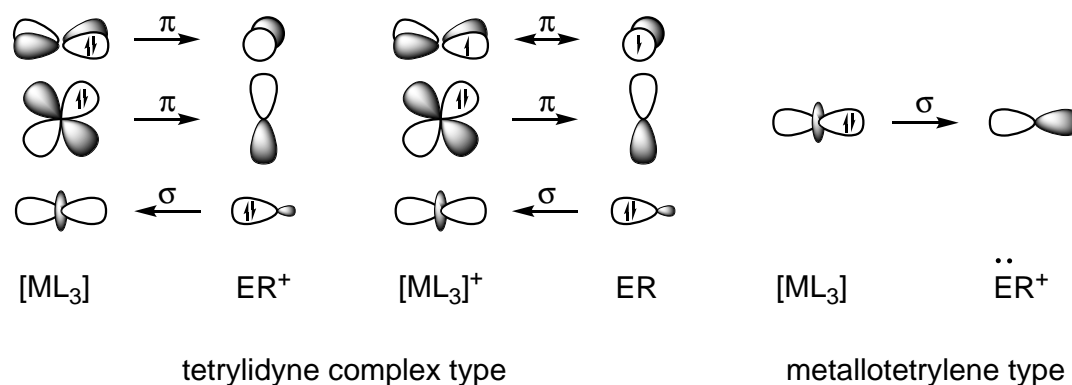
Herein, the ΔE_{orb} represents the attractive interaction between the occupied and virtual MOs of the fragments, ΔE_{Pauli} the Pauli repulsion energy between the occupied orbitals of the fragments, and ΔE_{elstat} and ΔE_{disp} their electrostatic and London dispersive interaction energies. The electronic reference state of the fragments is usually defined by their lowest $|\Delta E_{\text{orb}}|$ contribution.^[147] In contrast to the favoured doublet state M–E fragmentations by the BCE/BDE analysis discussed above, most of the electronic reference states calculated from the ETS-NOCV analysis are the low-spin singlet states, leading to a fragmentation into the ML_3 and ER^+ fragments. The exceptions are all carbyne complexes as well as $NiGeAr^{Mes}$ and $PtGeAr^{Mes}$, for which the doublet spin states are found to be their reference states. The overview about the EDA components of all MER complexes given in Equation 8.1 and their discussion is accessible in the full publication text in the appendix. Of particular interest is the decomposition of the orbital interaction energy ΔE_{orb} into its dominant NOCV contributions that allow for visual inspection. The hereby obtained deformation densities are exemplarily depicted for the complexes $NiSiTbb$, $NiGeAr^{Mes}$ and $PtPbAr^{Mes}$, and the NOCVs of the other tetrylidyne complexes and metallotetrylenes appear similar to those of

$\text{NiSiTbb}/\text{NiGeAr}^{\text{Mes}}$ and $\text{PtPbAr}^{\text{Mes}}$, respectively (c.f. Scheme 8.4).

For NiSiTbb , the two largest contributions (ca. $-200 \text{ kJ}\cdot\text{mol}^{-1}$) can be identified as π -back donations from the metal to the tetrel fragment, whereas the third contribution is considerably weaker ($-54 \text{ kJ}\cdot\text{mol}^{-1}$) and represents the σ -type $[\text{SiTbb}]^+ \rightarrow [\text{ML}_3]$ donation. The interpretation of the NOCV interactions in $\text{NiGeAr}^{\text{Mes}}$ appears more complicated due to the separation into the α - and β -spin contributions. However, in essence a similar situation as for NiSiTbb is observed, with two π -type donations with a lower strength of -179.6 and $-135.7 \text{ kJ}\cdot\text{mol}^{-1}$ than in the silylidyne complex.² The found $\sigma([\text{GeAr}^{\text{Mes}}] \rightarrow [\text{ML}_3]^+)$ interaction of $-77.4 \text{ kJ}\cdot\text{mol}^{-1}$ is slightly stronger than in NiSiTbb as the charge donation does not proceed against the charge gradient of the fragments.

In contrast, the visible π -type donations in the complex $\text{PtPbAr}^{\text{Mes}}$ are rather weak with -74.7 and $-26.8 \text{ kJ}\cdot\text{mol}^{-1}$ for $\Delta E_{\text{orb},2}$ and $\Delta E_{\text{orb},3}$, respectively, whereas a strong σ -type donation from the $[\text{Pt}(\text{PMe}_3)_3]$ to the $[\text{PbAr}^{\text{Mes}}]^+$ fragment is identified ($-180.1 \text{ kJ}\cdot\text{mol}^{-1}$), which directly reflects the earlier assigned metallotetrylene character in this complex type.

Finally, Scheme 8.5 provides an overview over the three conceivable bonding situations that were obtained by the analysis of the structure, canonical and localized MOs, bond dissociation energies and ETS-NOCVs of cationic group 10 tetrylidyne complexes studied in this work. Complementary to the description of one $\sigma(\text{E} \rightarrow \text{M})$ donation and two $\pi(\text{M} \rightarrow \text{E})$ back donations in tetrylidyne complexes, their $\text{M} \equiv \text{E}$ triple bond can also be rationalized by one π -type electron spin-pairing interaction bond, which replaces one of the π back donations. In contrast to those, the metallotetrylene type involves a cationic tetrylidyne fragment $[\text{ER}]^+$ with an electron lone pair on the tetrel atom that is bonded via a metal-centered σ bond.



Scheme 8.5: Schematic representation of the bonding situations found in the herein studied MER complexes.

²Due to the interaction of two doublet spin state fragments, only the second π -type donation $\Delta E_{\text{orb},2}$ stems exclusively from the metal. The first π -type interaction is given as both the π -donation from the singly occupied SOMO of $[\text{GeAr}^{\text{Mes}}]$ to the SOMO of $[\text{Ni}(\text{PMe}_3)_3]^+$ and from the SOMO of $[\text{Ni}(\text{PMe}_3)_3]^+$ to the SOMO of the $[\text{GeAr}^{\text{Mes}}]$ fragment.

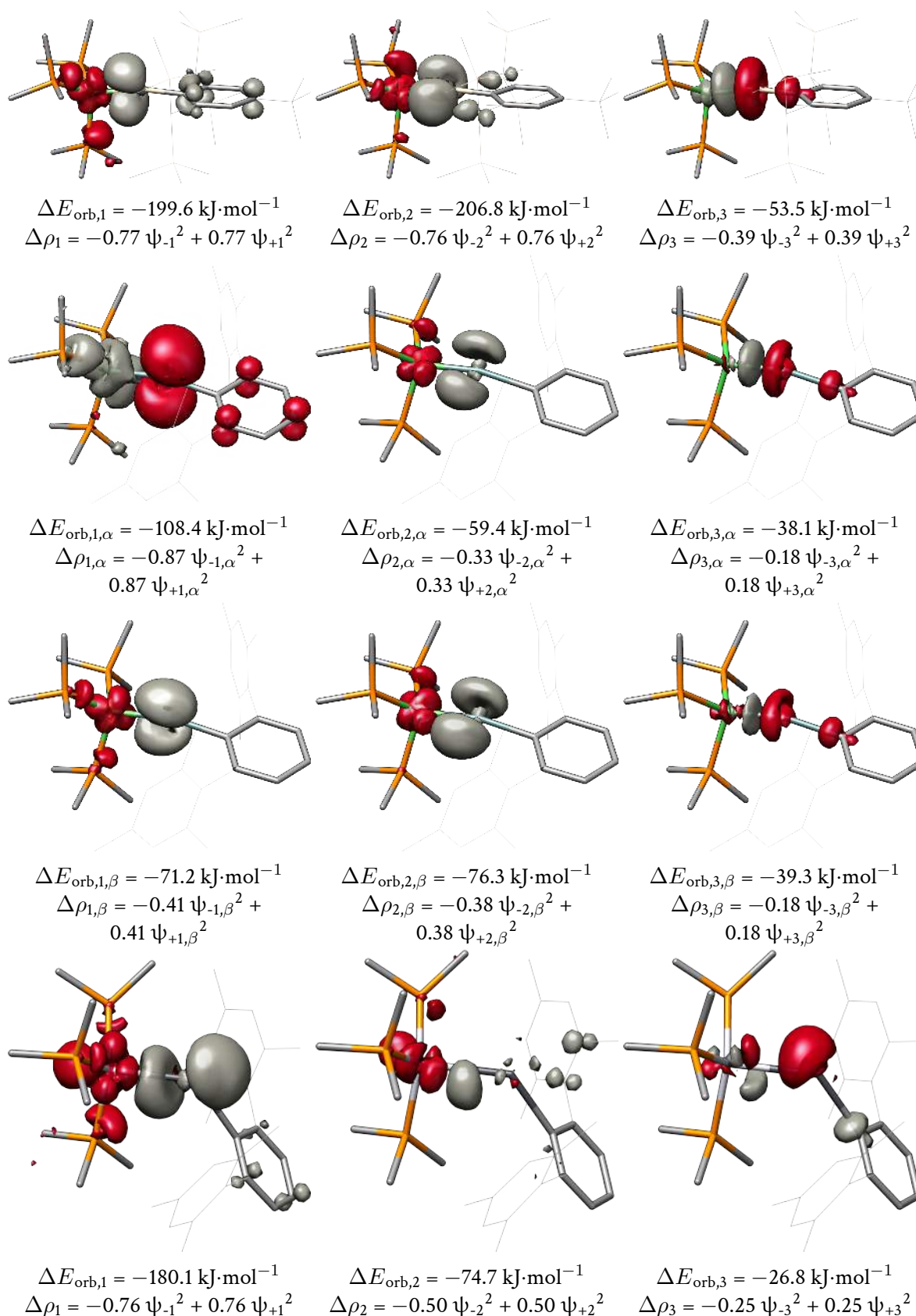


Figure 8.6: Isosurface plots (isosurface value = $0.002 \text{ e Bohr}^{-3}$ of deformation densities $\Delta\rho_n$ in $\text{e}\cdot\text{Bohr}^{-3}$ of complementary NOCVs (ψ_{-n} and ψ_{+n}) of NiSiTbb (top), NiGeAr^{Mes} (middle, split into α - and β -spin derived deformation densities) and PtPbAr^{Mes} (bottom), given with their respective eigenvalues. Regions of charge depletion ($\Delta\rho_n < 0 \text{ e Bohr}^{-3}$) are shown in red and regions of charge accumulation ($\Delta\rho_n > 0 \text{ e Bohr}^{-3}$) are shown in grey.

8.6. Metallotetrylene Isomers

During the structure optimizations of the MER complexes the surprisingly flexible M–E–C1 bond angle was found, which significantly deviates from 180° for most of the structures (c.f. Table 8.1). PES scans of the M–E–C1 bond angle revealed particularly flat hypersurfaces for E = Sn and Pb, and remarkable isomers with angles below 100°, denoted as MER-2, could be observed and identified to be minimum structures. Whereas these MER-2 isomers are unfavoured for the case a)-assigned tetrylidyne complexes by more than 45 kJ·mol⁻¹ (see the appendix for the PES scan plots), the strongly bent isomers PdSnAr^{Mes}-2, PdPbAr^{Mes}-2, PtSnAr^{Mes}-2 and PtPbAr^{Mes}-2 were found to be energetically favoured by 13 to 29 kJ·mol⁻¹.

As the most extreme example, the optimized gas phase structure of PtPbAr^{Mes}-2 is depicted in Figure 8.7 and selected structural parameters are provided in the caption. Accordingly, the decrease of the M–E–C1 angle to 94.3° is accompanied with a considerable M–E bond elongation from 267.7 pm in PtPbAr^{Mes} to 281.9 pm, and the metal adopts a distorted square-planar coordination.

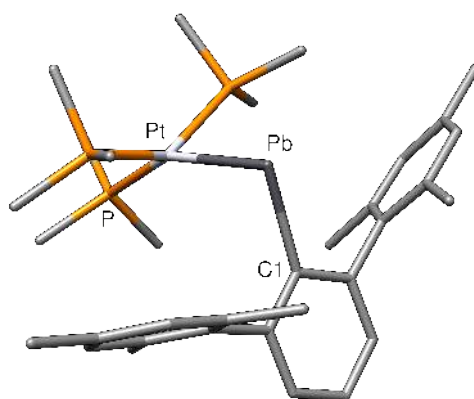


Figure 8.7: Optimized minimum gas phase structure of the even more bent isomer PtPbAr^{Mes}-2. Selected structural parameters: Pt–Pb: 281.9 pm, Pb–C1: 233.7 pm, Pt–Pb–C1: 94.3°.

The analysis of the LMOs reveals a pronounced electron lone pair at the lead atom as well as a metal-centered $\sigma(\text{Pt-Pb})$ bond with atomic Mulliken populations of 0.75 and 0.20 at the Pt and Pb atoms, respectively (Figure 8.8). The absence of any significant π -type interactions is also visible from the NOCV analysis of PtPbAr^{Mes}-2 that only reveals one $\sigma(\text{M}\rightarrow\text{E})$ donation, but with a remarkable strength of -299.1 kJ·mol⁻¹, which exceeds that of PtPbAr^{Mes} by 119 kJ·mol⁻¹. Ultimately, this leads to a net preference of the strongly bent isomer PtPbAr^{Mes}-2 by 67.2 kJ·mol⁻¹ based on ΔE_{orb} . Until now, only class a) group 10 tetrylidyne complexes were synthesized so far, with the metallotetrylene combinations remaining elusive. The strongly bent M–E–R moiety and the energetic preference of the even more bent isomers MER-2 in particular make them exciting molecules to study further by experiment and theory.

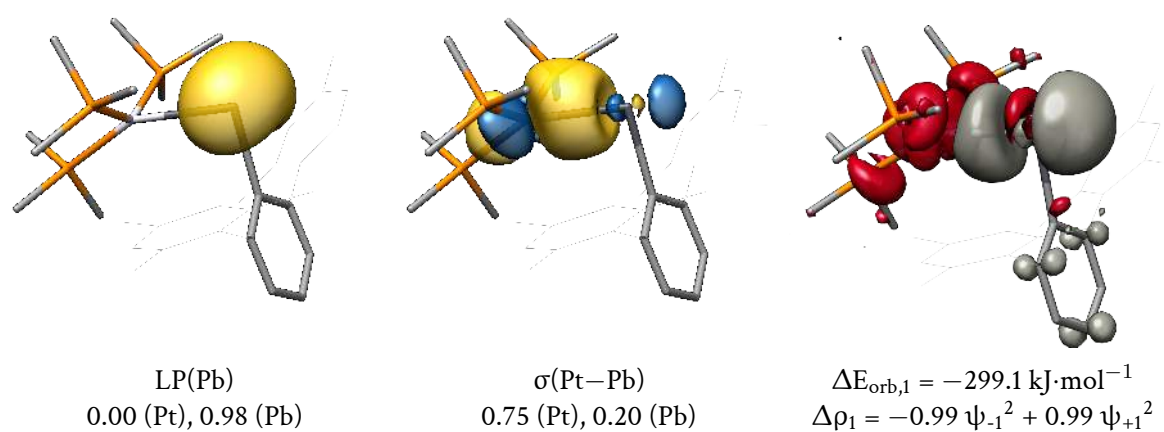


Figure 8.8: Left and middle: Pipek-Mezey LMOs of $\text{PtPbAr}^{\text{Mes-2}}$ (isosurface value $0.04 \text{ e}^{1/2} \text{ Bohr}^{-3/2}$), their attributed bond type and corresponding atomic Mulliken populations. Right: Isosurface plots (isosurface value = $0.002 \text{ e}\cdot\text{Bohr}^{-3}$ of deformation densities $\Delta\rho_n$ in $\text{e}\cdot\text{Bohr}^{-3}$ of complementary NOCVs (ψ_{-n} and ψ_{+n}), given with their respective eigenvalues. Regions of charge depletion ($\Delta\rho_n < 0 \text{ e Bohr}^{-3}$) are shown in red and regions of charge accumulation ($\Delta\rho_n > 0 \text{ e Bohr}^{-3}$) are shown in grey.

Part C.

Mass Spectrometric Studies of Group 6 Germylidyne Complexes

9. Fundamental Principles of Mass Spectrometry

Mass Spectrometry (MS) is an analytical method to generate and separate ions in the gas phase based on their mass-to-charge ratio by applying electrical and/or magnetical fields.^[374] The relative abundance of isotopologues allows for qualitative and quantitative insight of a given ion. Since 1908, the pioneering work of Nobel prize laureates J. J. Thomson^[375–377] and F. W. Aston^[378, 379] paved the way for several decades of development to further refine this valuable method. Nowadays, mass spectrometry is regarded as an indispensable tool in various scientific communities, such as chemistry, biochemistry, medicine and more.^[380, 381]

Every mass spectrometric measurement consists of three steps: the ionization of the sample (for neutral analytes) and transfer into the gas phase, the separation of the generated ions by a mass analyzer and the ion detection (Figure 9.1).

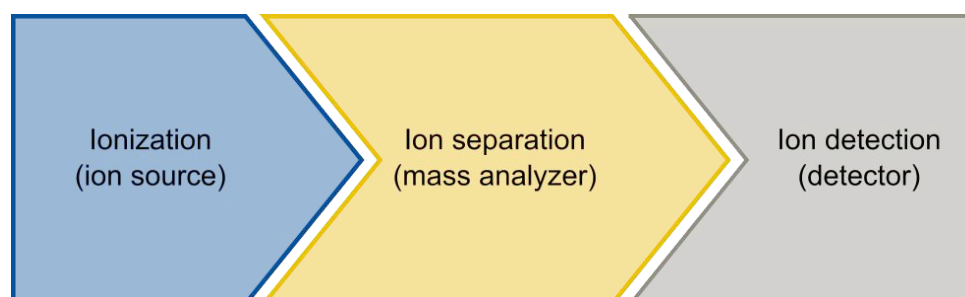


Figure 9.1: Illustration of the key steps of a mass spectrometric measurement.

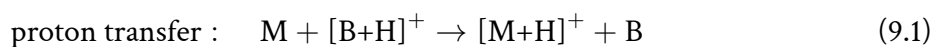
In contrast to non-destructive analytical methods like infra-red or nuclear magnetic resonance spectroscopy, for mass spectrometry the analyte is consumed during the measurement and needs to be safely injected into the mass spectrometer. Fortunately, the necessary sample amount is very low (\leq microgram range typically).^[374]

Regarding all three components of a MS measurement (Figure 9.1), the tremendous effort of scientists in the last century introduced a pronounced methodological variability. Many techniques are available on how to ionize a given sample depending on its molecular properties, what type of mass analyzer is used for the ion separation and which detector method. Two particular ionization methods, Atmospheric Pressure Chemical Ionization (APCI) and Liquid Injection Field Desorption Ionization (LIFDI), are briefly introduced in the following as they are relevant for the herein

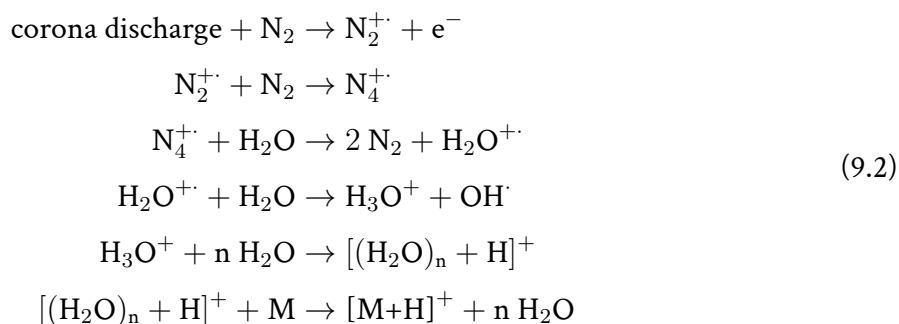
presented work. A detailed discussion of the ion separation and detection topics is omitted here, but can readily be found in standard textbooks.^[374]

Atmospheric Pressure Chemical Ionization (APCI)

The underlying method of APCI is Chemical Ionization (CI), which is a soft ionization method, i.e. the generated ions have a rather low internal energy and are thus less prone to fragment during the ionization. CI was originally developed in the year 1950 by V. L. Tal'roze *et al.*^[382] and later on established as a method by M. S. B. Munson and F. H. Field.^[383–386] Herein, ions are generated in high vacuum via contacts of neutral gaseous analyte molecules M with reagent ions $[B+H]^+$ (Equation 9.1), where the latter are formed in the first instance from a reagent gas B by autoproteination.



In the APCI modification, the analyte solution is injected at atmospheric pressure into a nebulizer gas, typically dinitrogen, to form an aerosol (Figure 9.2). After passing a heater (ca. 500 °C), the obtained vapor gets in contact with a corona discharge needle (ca. 5 kV) and leads to the protonation of the analyte M by a cascade of ion-molecule reactions involving the nebulizer gas and water/proton clusters:



Liquid Injection Field Desorption Ionization (LIFDI)

Also during the mid of the last century, in the year 1959, H. D. Beckey presented the first focusing field ionization (FI) source.^[387] Here, the volatile analyte is desorbed from surfaces in high vacuum and then ionized by an electric field (ca. $10 \text{ V} \cdot \text{nm}^{-1}$). Subsequently, the desorption and ionization step was combined in such a way that the sample is directly applied on the emitter, which accelerates the formed ions by the electric field (Figure 9.3 a).^[388, 389]



As no excess energy is transferred to the resulting analyte ion after the electron loss (Equation 9.3), field desorption (FD) mass spectra generally feature an exceptionally low amount of observed ion

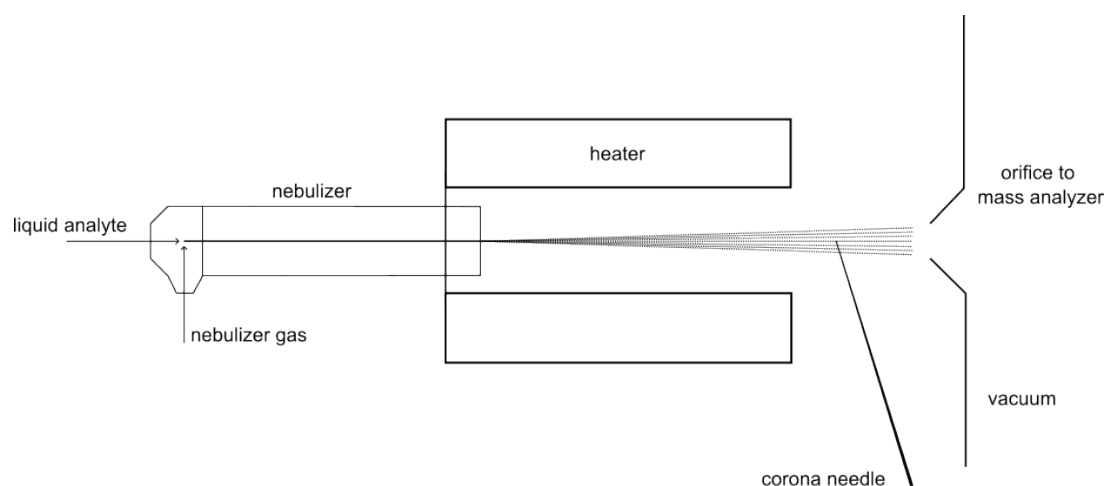


Figure 9.2: Schematical illustration of an APCI source. Adapted from reference [374].

fragmentation, and thus FD belongs to the softest ionization methods. However, FD has the disadvantage that the emitter needs to be loaded before inserting it into the ion source chamber. This disables the possibility of continuous-flow experiments, and it is also especially problematic for water- and oxygen-sensitive analytes that decompose during the sample preparation and emitter loading.

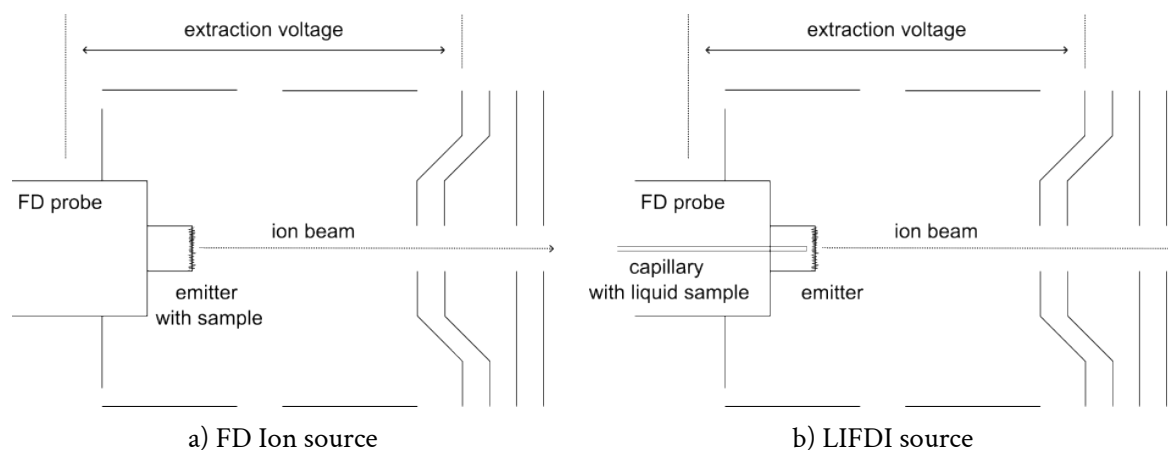


Figure 9.3: Schematical illustration of the FD and LIFDI source setups. Adapted from reference [374].

The idea of LIFDI is to transport the liquid analyte solution through a thin capillary directly onto the field emitter before the measurement is started (Figure 9.3 b).^[390] The droplets that impinge from the capillary on the emitter are then distributed by adsorption over the entire emitter surface. Due to the high vacuum within the ion source chamber, the solvent evaporates directly, and the analyte remains on the emitter ready for the measurement.

With this modification the risk of analyte decomposition is lowered significantly if the capillary is connected with an inert sample vial, achievable with Schlenk techniques. Alternatively, the LIFDI source can also be connected with a glove box apparatus. LIFDI mass spectrometry is thus a remarkable analytical method for the soft ionization of air- and moisture-sensitive compounds.^[390–393]

10. Mass Spectrometric Studies of Group 6 Germylidyne Complexes

The work presented in the this chapter was already published and is reprinted (adapted) with permission of the other author from

L. R. Maurer, M. Engeser, *Group 6 germylidyne complexes in the gas phase by LIFDI and APCI mass spectrometry*, *European Journal of Mass Spectrometry* **2023**, *29*, 44-57; DOI 10.1177/14690667221137465.

My own manuscript contributions comprise

- Measuring all complexes of this study via LIFDI and APCI mass spectrometry
- Interpretation of the experimental results
- Writing of the manuscript

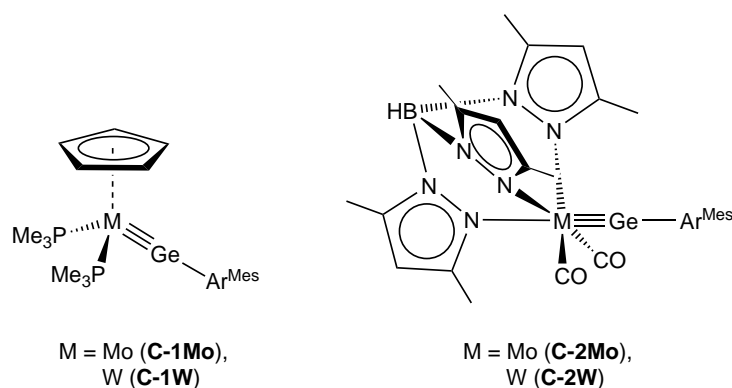
The following chapter provides an overview of the topic's main results and conclusions. The complete publication can be found in the appendix.

10.1. Introduction

The first triple bonds between a group 14 tetrel atom and a transition metal were achieved by E. O. Fischer *et al.* in the year 1973 (*Fischer-type carbyne complexes*)^[334, 335] and R. Schrock *et al.* only two years later (*Schrock-type alkylidyne complexes*)^[357] followed by a plethora of studies on these fascinating compounds.^[337, 350, 358, 394] The first heavier transition metal tetrylidyne complexes were successfully isolated since 1996 for E = Ge by P. P. Power *et al.*,^[339] and for E = Sn, Pb, and Si by the group of A. C. Filippou,^[341–344, 346] This field of chemistry has been expanded nowadays to include many more metal tetrel combinations.^[267, 362, 364, 395, 396]

Typically, these complexes are difficult to handle in solution and suffer from an extreme susceptibility towards moisture and oxygen, rendering it exceptionally challenging to explore molecular properties and reactivity in the gas phase using mass spectrometric measurements. In this regard, mass spectrometry was not employed so far for heavier tetrylidyne complexes, but only observed for analytical purposes in some cases to confirm a successful synthesis.^[149, 397–400] Here, advanced Schlenk and glove box techniques as well as inert sample injection methods are crucial to transfer the sensitive compounds from the safe vessel into the gas phase within the mass spectrometer.

As a first entry point, the four group 6 germlylidyne complexes $[\text{Cp}(\text{PMe}_3)_2\text{M}\equiv\text{GeAr}^{\text{Mes}}]$ (M = Mo (C-1Mo), W (C-1W))^[401, 402] and $[\text{Tp}'(\text{CO})_2\text{M}\equiv\text{GeAr}^{\text{Mes}}]$ (M = Mo (C-2Mo), W (C-2W)),^[267, 402] were selected ($\text{Ar}^{\text{Mes}} = 2,6\text{-dimesitylphenyl}$; $\text{Tp}' = \kappa^3\text{-}N,N',N''\text{-hydridotris}(3,5\text{-dimethylpyrazolyl})\text{-borate}$, see Scheme 10.1). By keeping the GeAr^{Mes} unit unvaried, the observation of trends caused by the metal and its coordination sphere is facilitated.



Scheme 10.1: Lewis formulae of the complexes C-1M and C-2M (M = Mo, W) studied in this work. $\text{Ar}^{\text{Mes}} = 2,6\text{-dimesitylphenyl}$.

Toluene solutions of these complexes were studied by two mass spectrometric procedures: On the one hand, the mildly ionizing LIFDI technique for inert sample injection was coupled with a MAT90 sector instrument and the samples were transferred via a fused silica capillary into the ion source. On the other hand, APCI mass spectra of C-1M and C-2M were recorded in positive mode and standard conditions on a LTQ Orbitrap XL instrument. In the latter case, also collision-induced dissociation (CID) and higher-energy collisional dissociation (HCD) experiments were carried out (see the complete instrumental details in the full publication in the appendix).

10.2. Results and Discussion

Figures 10.1 and 10.2 depict the LIFDI spectra of the complexes **C-1Mo** and **C-1W**, respectively, and reveal the successful detection of the intact molecular ions $[M]^+$ as base peaks with the expected isotope patterns and masses (**C-1Mo**: found m/z 700.2, calculated 700.2 u for $[C_{35}H_{48}GeMoP_2]^+$; **C-1W**: found m/z 786.3, calc. 786.2 u for $[C_{35}H_{48}GeW_2]^+$). Degradation products are absent in the LIFDI spectrum of the complex **C-1Mo** and the only other considerable signal is found to correspond to toluene (found m/z 92.0, calc. 92.1 u for $[C_7H_8]^+$). In contrast, the tungsten germylydine complex **C-1W** turned out to be more sensitive, and the second most intensive signal is observed to belong to the ion $[Ar^{Mes}+H]^+$ at m/z 314.3 (calc. 314.2 u for $[C_{24}H_{26}]^+$), suggesting the cleavage of the Ge–C bond.

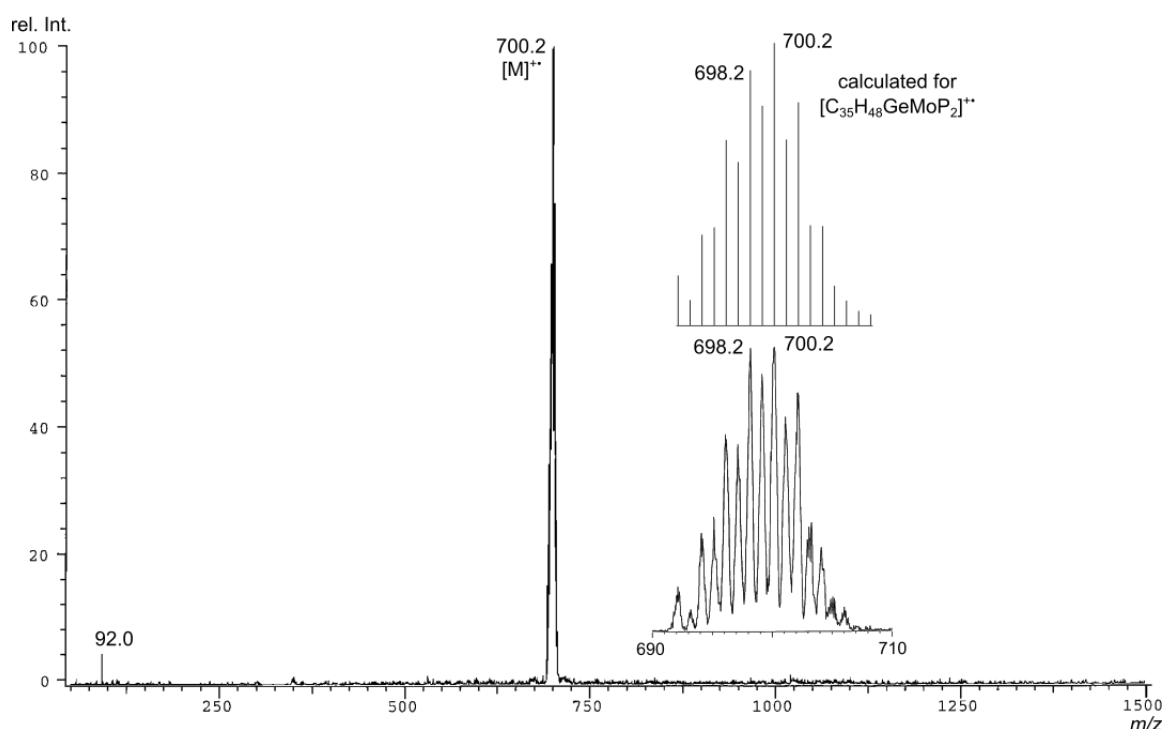


Figure 10.1: LIFDI-MAT90 spectrum of the complex **C-1Mo** as summation over 23 scans. The insert shows a zoom of the $[M]^+$ m/z region and the calculated isotope pattern for comparison.

The obtained LIFDI spectra for the complexes **C-2Mo** (Figure 10.3) and **C-2W** (Figure 10.4) appear similarly and feature the molecular ions $[M]^+$ as base peaks (**C-2Mo**: found m/z 836.2, calc. 836.2 u for $[C_{41}H_{47}BGeMoN_6O_2]^+$; **C-2W**: found m/z 922.2, calc. 922.3 u for $[C_{41}H_{47}BGeWN_6O_2]^+$). However, in contrast to the Cp-coordinated germylydine complexes, hydrogen and oxygen adducts $[M+2H+3O]^+$ at m/z 886.3 and 971.8 are present here for **C-2Mo** and **C-2W**, respectively. This can be rationalized as the $[M+H_2O+O_2]^+$ species, present despite careful sample preparation. Interestingly, the single adducts of dioxygen and water, $[M+O_2]^+$ and $[M+H_2O]^+$ are not detected. The high-resolution APCI-Orbitrap mass spectra of all four complexes are highly comparable to the LIFDI-MAT90 spectra with signals for the molecular ion $[M]^+$ as clear base peaks and low

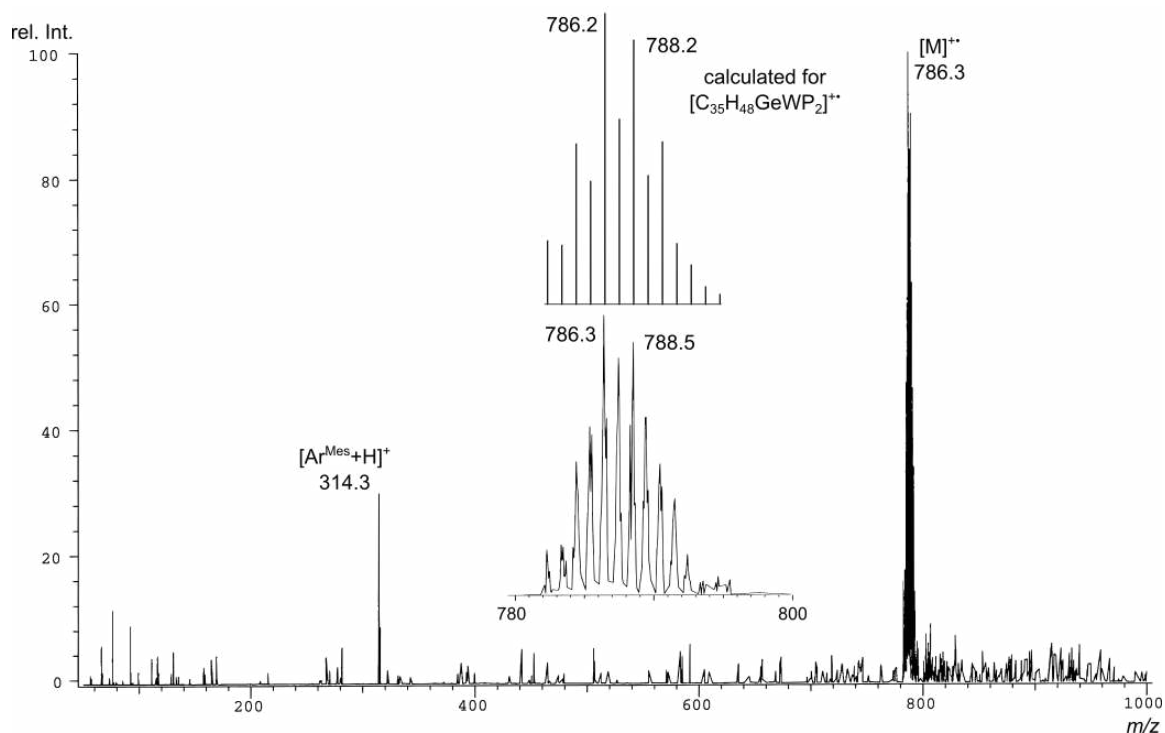


Figure 10.2: LIFDI-MAT90 spectrum of C-1W as summation over 5 scans. The insert shows a zoom of the $[M]^+$ m/z region and the calculated isotope pattern for comparison.

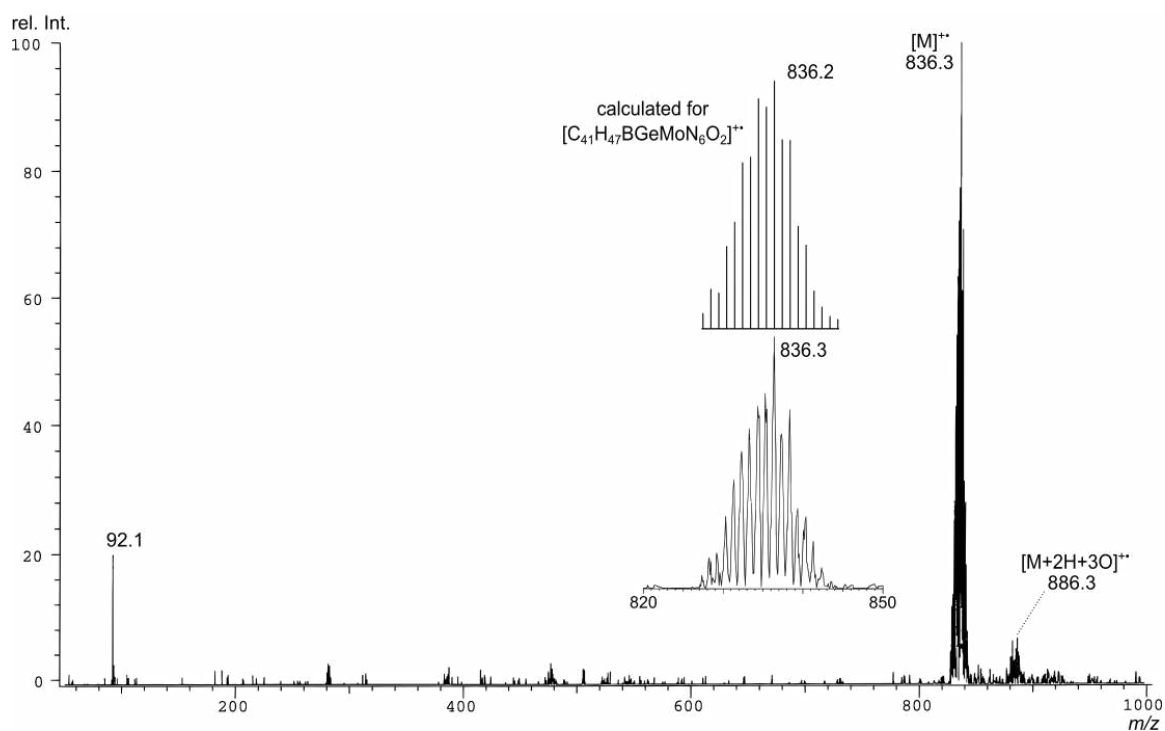


Figure 10.3: LIFDI-MAT90 spectrum of C-2Mo as summation over 17 scans. The insert shows a zoom of the $[M]^+$ m/z region and the calculated isotope pattern for comparison.

degradation of the complexes (e.g. $[Ar^{Mes}+H]^+$ and $[M+H_2O]^+$). Noteworthy, signals are observed for the germylydine fragment $[Ar^{Mes}Ge]^+$ in the APCI mass spectra of the compounds C-1Mo and C-1W (exemplarily depicted in Figure 10.5) that suggests the cleavage of the $M\equiv Ge$ triple bond

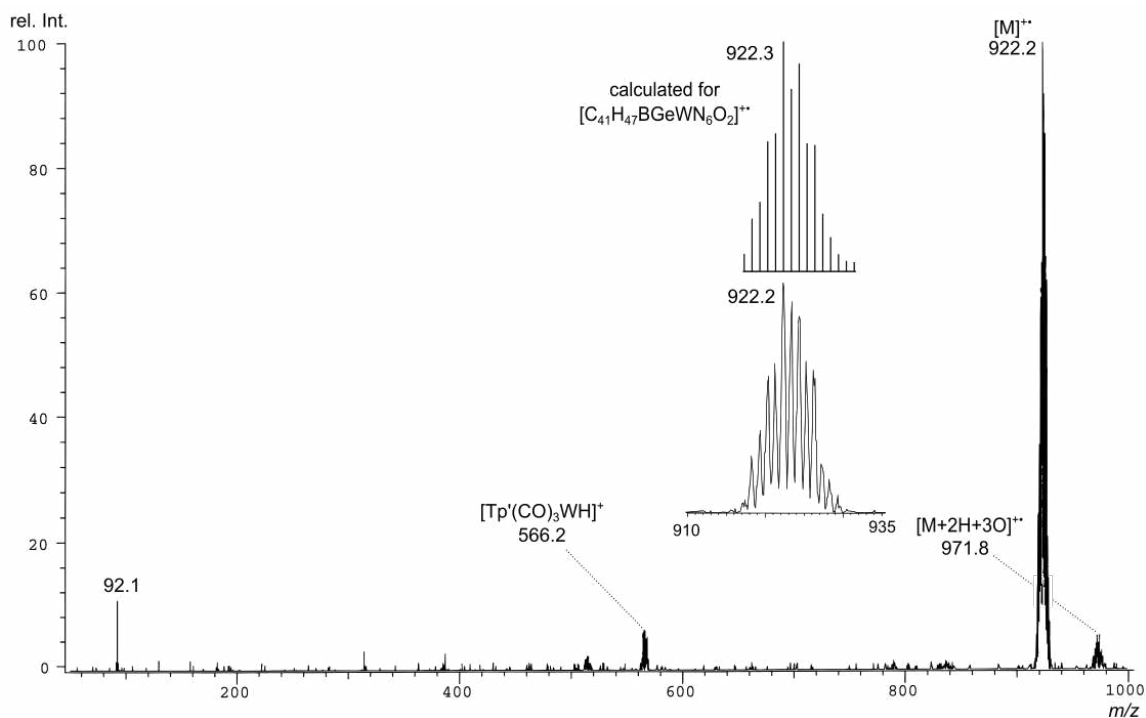


Figure 10.4: LIFDI-MAT90 spectrum of C-2W as summation over 21 scans. The insert shows a zoom of the $[M]^{++}$ m/z region and the calculated isotope pattern for comparison.

in the gas phase in the mass spectrometer (found m/z 387.114 (C-1Mo) and 387.116 (C-1W), calc. 387.117 u for $[C_{24}H_{25}Ge]^+$).

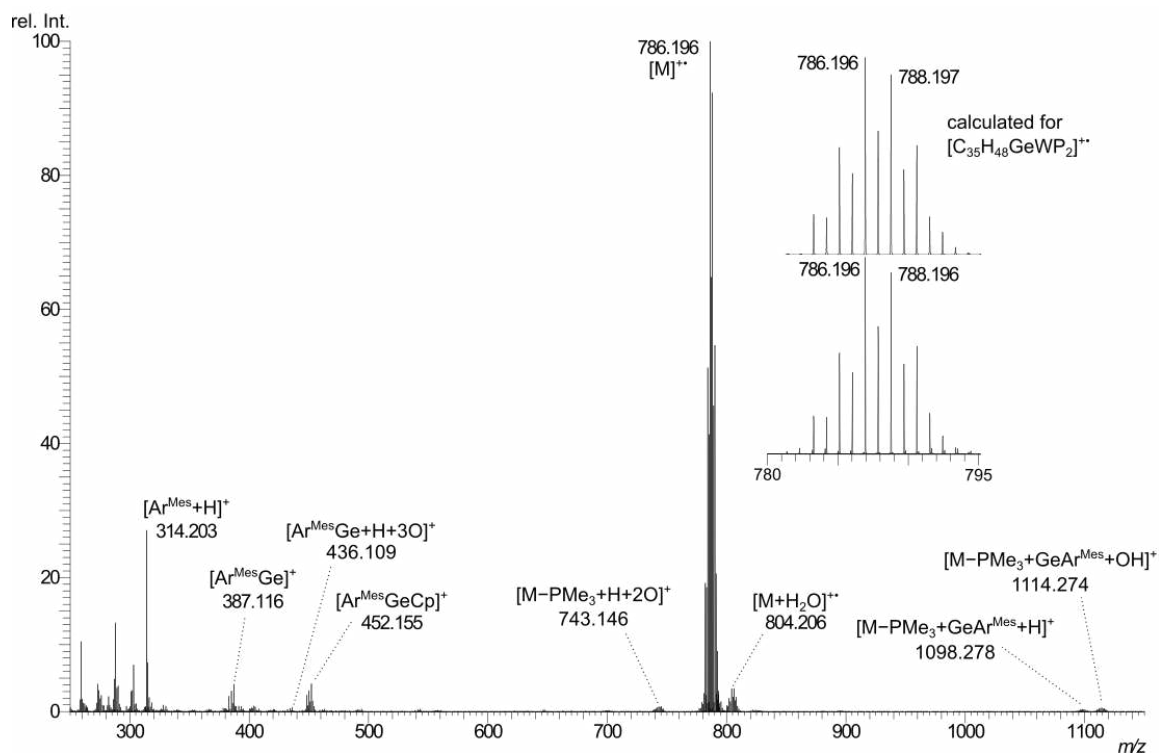


Figure 10.5: APCI-Orbitrap spectrum of C-1W. The insert shows a zoom of the $[M]^{++}$ m/z region and the calculated isotope pattern for comparison.

Of particular interest is the behaviour of the $[M]^{+}$ ions within collision-induced excitations and the influence of the ligand sphere of the transition metal atom. For **C-1Mo**, a CID energy of 15 eV leads to an almost exclusive fragmentation to the ion $[M-2PMe_3]^{+}$ at m/z 548.056 under the loss of two trimethylphosphane ligands (Figure 10.6). The further activation of this ion in a three-staged tandem MS experiment (MS^3) experiment does not lead to a further ligand cleavage off the metal centre, but instead only induces a cascade of several dihydrogen eliminations and cleavage of $CH_3\cdot$.

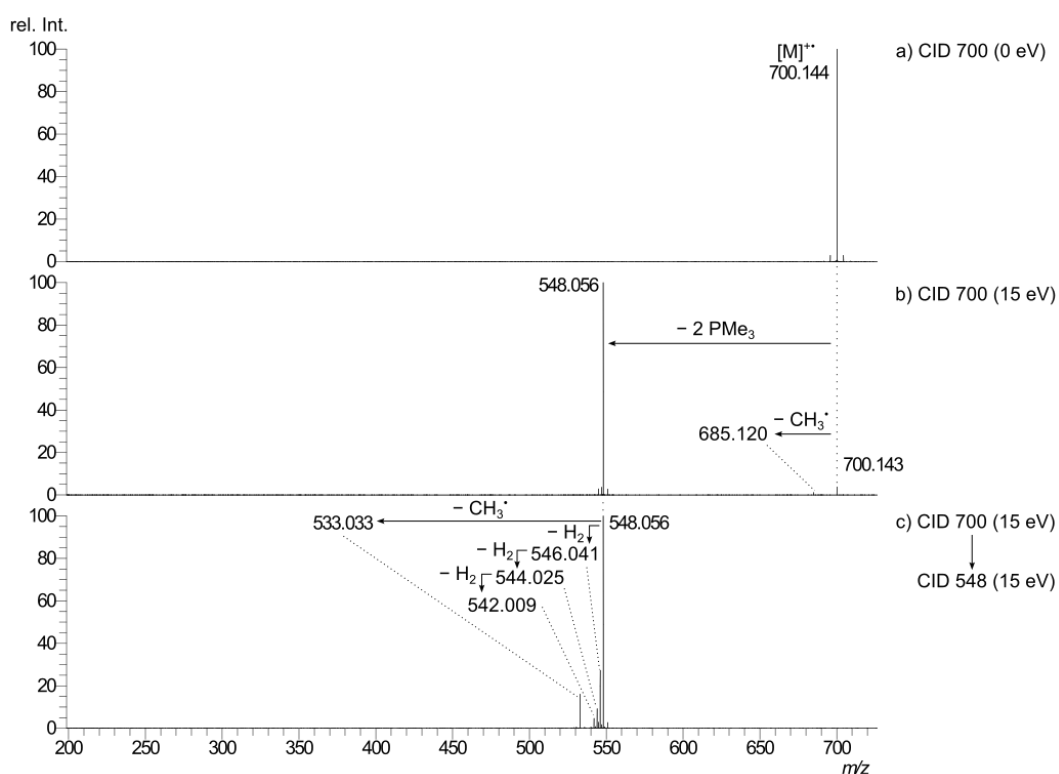


Figure 10.6: APCI-Orbitrap CID spectra for the fragmentation of **C-1Mo** with mass selection of the most abundant signal in the isotope pattern (m/z 700) at a) 0 eV and b) 15 eV, and the further activation of the m/z 548 ion at c) 15 eV in an MS^3 experiment.

In contrast, in the CID spectra of **C-1W** the most dominant fragment is found to be the elimination of a methyl radical to m/z 771.171 (Figure 10.7), which is observed to be negligible for the CID experiment of the molybdenum analogue **C-1Mo**. The MS^3 experiment of the resulting $[M-CH_3]^+$ cation reveals a complex fragmentation pattern, with cleavages of the phosphane PMe_2H to m/z 709.143, of PMe_3 and H_2 to m/z 693.112 (base peak) and of a presumable diphosphane P_2Me_4 to m/z 649.129. The latter may be followed by a methyl group elimination to m/z 634.106 ($[M-2PMe_3]^+$) with low intensity and suggests an interesting P–C bond activation of the trimethylphosphane ligands by the tungsten center in the ion $[M-CH_3]^+$, which rationalizes this more complicated fragmentation behaviour.

As carbonyl ligands are prone to dissociation in MS experiments,^[403] the CID spectra of the complexes **C-2Mo** (Figure 10.8) and **C-2W** (Figure 10.9) feature the expected carbonyl expulsions $[M-CO]^{+}$ at m/z 808.220 and 894.267, respectively. Whereas a double carbonyl loss is only

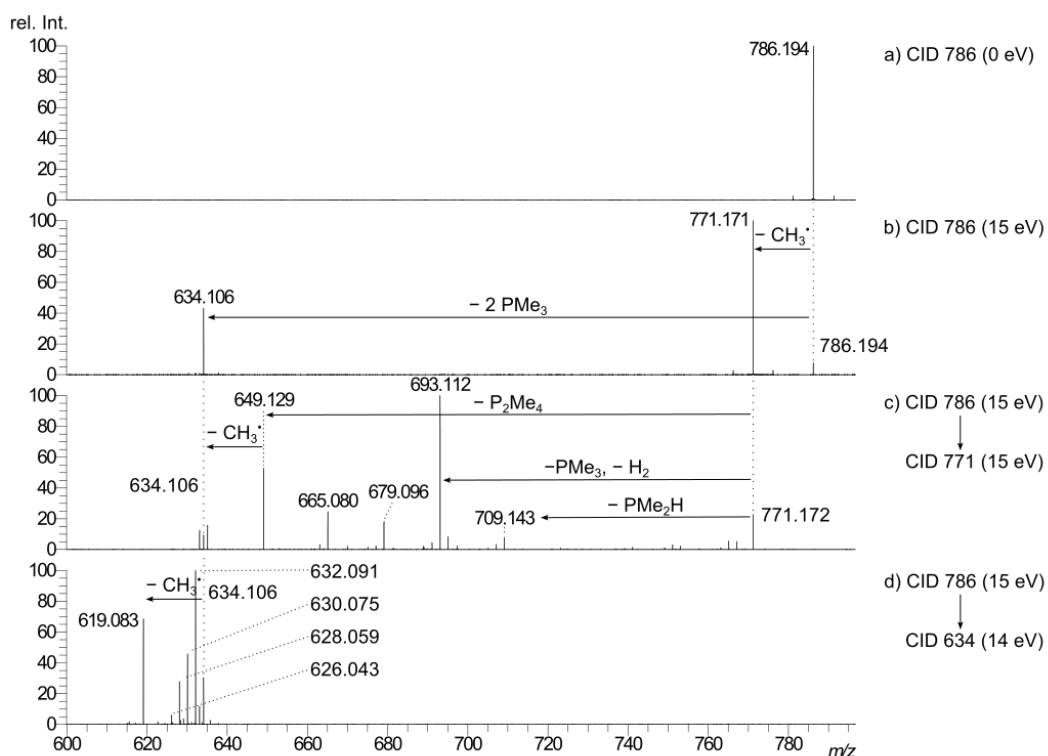


Figure 10.7: APCI-Orbitrap CID spectra for the fragmentation of **C-1W** with mass selection of the most abundant signal in the isotope pattern (m/z 786) at a) 0 eV and b) 15 eV, and the further activation of the c) m/z 771 ion at 15 eV and d) m/z 634 ion at 14 eV in MS³ experiments.

observed for the protonated molecular ion $[M+H]^+$ ion to $[M+H-2CO]^+$ at m/z 781.232 (calc. 781.232 u for $[C_{39}H_{48}BGeMoN_6]^+$) for **C-2Mo**, the mass-selected molecular ion of **C-2W** shows the sequential carbonyl loss to $[M-2CO]^+$ at m/z 886.269 (calc. 866.269 u for $[C_{39}H_{47}BGeN_6W]^+$), followed by the elimination of dihydrogen to the ion $[M-2CO-H_2]^+$ at m/z 864.254. For both complexes however, residual water in the ion trap is observed to coordinate to the free metal binding sites of the $[M-CO]^+$ ions and forms the stabilized $[M-CO+H_2O]^+$ ions at m/z 826.229 and 912.275, respectively.

As an alternative to the CID method, HCD experiments were also performed for this class of compounds for the very first time, which mostly reproduce the fragmentation pattern already observed in the CID spectra of the herein-studied germylydine complexes. The depiction of the HCD spectra and their detailed discussion can be found in the complete publication in the appendix.

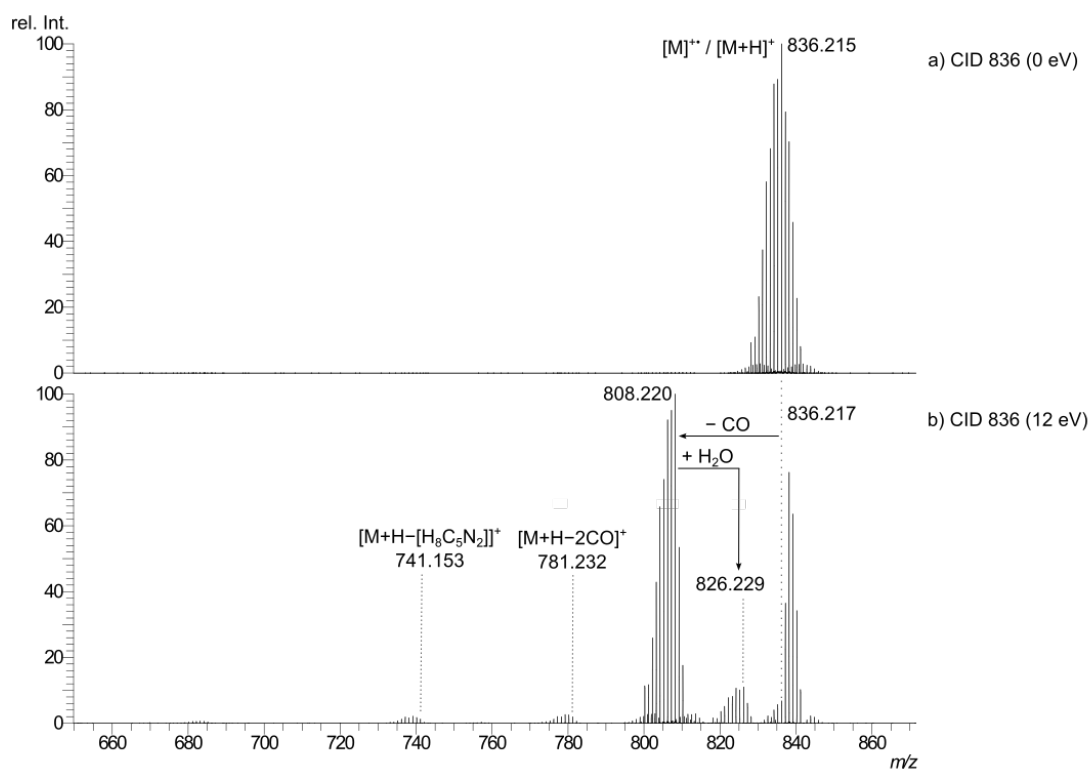


Figure 10.8: APCI-Orbitrap CID spectra for the fragmentation of complex C-2Mo with mass selection of the whole m/z 836 isotope pattern at a) 0 eV and b) 12 eV.

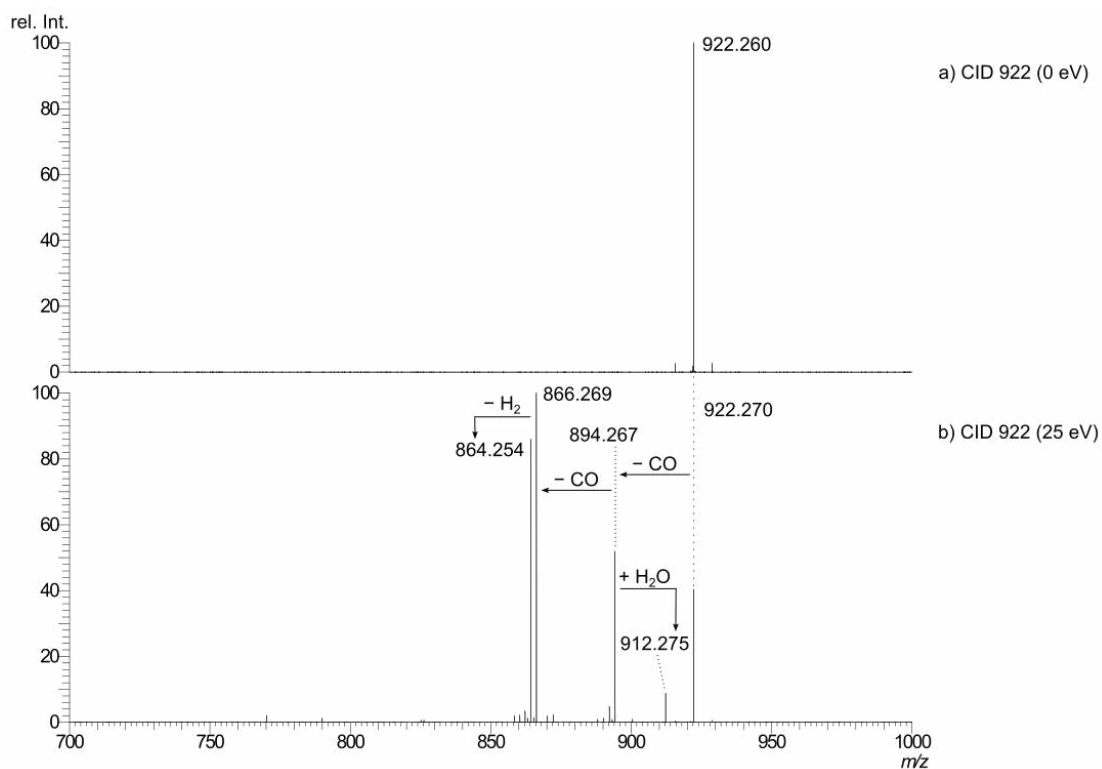


Figure 10.9: APCI-Orbitrap CID spectra for the fragmentation of complex C-2W with mass selection of the most abundant signal in the isotope pattern (m/z 922) at a) 0 eV and b) 25 eV.

Part D.

Summary and Outlook

11. Summary and Outlook

Modern computational chemistry is a versatile tool for the investigation of the electronic structure of molecules and proves to be especially valuable for chemical questions that cannot or only with great effort be answered by the experiment. It is therefore both the supporting and predictive character of this method that makes it indispensable for modern chemistry.

Of particular interest in the challenging but also rewarding research field of low-valent main group and transition metal chemistry, computational chemistry was employed in this thesis to study the electronic structure and thermodynamics of various organometallic and elementorganic compounds synthesized in our group. In this regard, their unique bonding patterns could be successfully elucidated and were put into context with available experimental and literature data.

Dispersion-corrected *meta*-GGA density functional theory combined with a triple- ζ basis set was employed as the working horse of this thesis due to its beneficial ratio between accuracy and computational cost. In some cases the results were further supported by high-level double hybrid density functional theory combined with a quadruple- ζ basis set. The obtained molecular wave function was readily analyzed by a toolbox of sophisticated methods, including intrinsic bond orbital (IBO) analysis, natural bond orbital (NBO) analysis or the extended transition state method combined with natural orbitals of chemical valence (ETS-NOCV).

As a side topic, group 6 transition metal germylydine complexes were experimentally studied by mass spectrometry in the gas phase and their behaviour towards induced dissociations could be revealed for the first time.

In the following, the main conclusions from each chapter are summarized. As (computing) time is limited, not every aspect of these fascinating molecules could be brought to light, and thus, this chapter is accompanied by recommendations on the next steps to fully understand these compounds and their reactivity.

Calculations on the first isolable iminosilylidene (SIDipp)SiCNAr^{Mes}

The free iminosilylidene SiCNH is an energetically high-lying isomer of the [H,C,N,Si] hypersurface and was not observed so far experimentally. By stabilization with an N-heterocyclic carbene, the first iminosilylidene (SIDipp)SiCNAr^{Mes} could be successfully isolated by our group after reduction of the silyliumylidene salt [(SIDipp)Si(Br)CNAr^{Mes}][B(3,5-(CF₃)₂)₄]. The aim was here to explore the electronic structures of the reaction products and rationalize the observed stereodynamics in solution.

Theoretical calculations on the latter cation revealed a strongly pyramidalized silicon atom that is connected to the SIDipp, CNAr^{Mes} and Br substituents via typical σ -type single bonds. The observed molecular orbitals support the presumed presence of an electron lone pair at silicon, and the quite localized structure is further confirmed by NBO and NRT analyses.

In contrast, the electronic key feature of the iminosilylenylidene $(\text{SIDipp})\text{SiCNAr}^{\text{Mes}}$ is its 3-center-2-electron- $\pi_{\text{oop}}(\text{C}_{\text{NHC}}-\text{Si}-\text{C}_{\text{CNR}})$ back bond as found in the HOMO (Figure 11.1 right), which is responsible for a significant shortening of the $\text{Si}-\text{C}_{\text{NHC}}$ and $\text{Si}-\text{C}_{\text{CNR}}$ bonds compared to the cationic precursor. The further computational analysis did not only afford the presumed in-plane lone pair at the silicon atom (Figure 11.1 left), but could also show the considerable charge flow from the silicon atom to both the SIDipp and isocyanide ligands with NPA charges of -0.01 and -0.39 e as result of the π back-bonding. The well-known strongly σ -donating properties of NHC ligands could be reproduced by calculating a higher bond dissociation energy of the $\text{Si}-\text{C}_{\text{NHC}}$ bond ($252.6 \text{ kJ}\cdot\text{mol}^{-1}$) compared to the $\text{Si}-\text{C}_{\text{CNR}}$ bond ($216.9 \text{ kJ}\cdot\text{mol}^{-1}$).

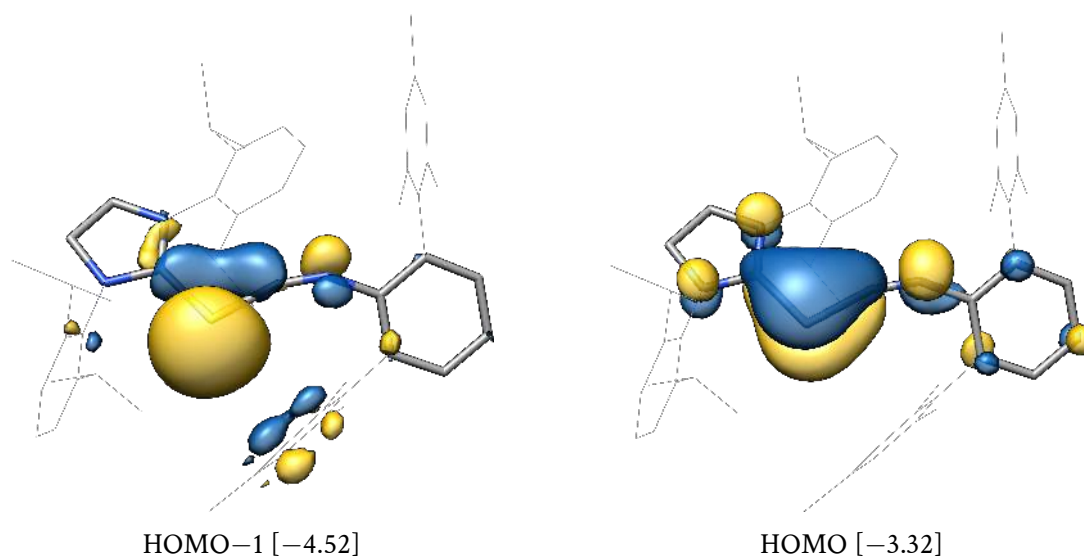


Figure 11.1: Selected canonical molecular orbitals of $(\text{SIDipp})\text{Si}(\text{CNAr}^{\text{Mes}})$ and their energy eigenvalues in eV.

The fluxional structure of the iminosilylenylidene, as evidenced by NMR spectroscopy in solution, could also be elucidated: Mechanistic calculations revealed a two-step topomerization-enantiomerization process via an NHC rotation and an energetically easily accessible $\text{C}_{\text{CNR}}-\text{N}-\text{C}_{\text{R}}$ -linear structure, that is clearly favoured over a concerted pathway. Here, energies of the calculated transition states and intermediate structures fit well to the experimental barriers derived from the NMR experiments.

Finally, the iminosilylenylidene $(\text{SIDipp})\text{SiCNAr}^{\text{Mes}}$ was successfully used as a $(\text{SIDipp})\text{Si}$ transfer reagent to afford the first NHC-stabilized chlorogermasilyne $(\text{SIDipp})\text{Si}(\text{Cl})\text{GeAr}^{\text{Mes}}$. Herein, the subsequent theoretical analyses not only confirmed the presence of an electron lone pair at the two-coordinated germanium atom (HOMO-1, see Figure 11.2), but also a 3-center-2-electron- $\pi_{\text{oop}}(\text{C}_{\text{NHC}}-\text{Si}-\text{Ge})$ bond in the HOMO, as also indicated by the short $\text{Si}-\text{C}_{\text{NHC}}$ and $\text{Si}-\text{Ge}$ bond

distances of 187.0 and 231.1 pm. Interestingly, although the NRT analysis shows a higher resonance weight for the Si=Ge doubly-bonded Lewis structure of 51 % than for the Si=C_{SIDipp} resonance motif (31 %), the calculated bond dissociation energy of the Si–SIDipp bond was found to be clearly higher.

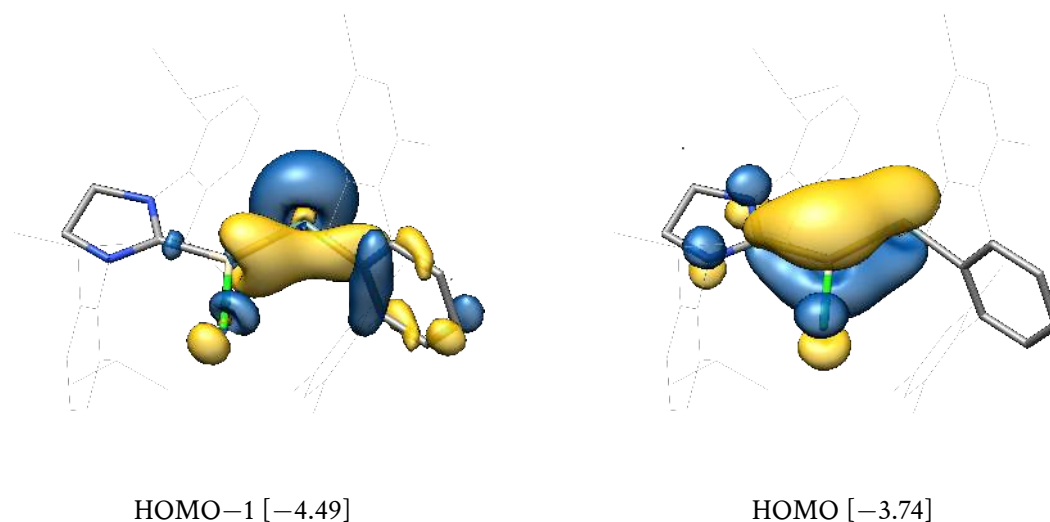


Figure 11.2: Selected canonical molecular orbitals of (SIDipp)Si(Cl)GeAr^{Mes} and their energy eigenvalues in eV.

Further studies on iminosilylenes

Additional experimental work by our group also afforded the differently substituted iminosilylenes (SIDipp)Si(CNR) with R = Me and Mes. As the synthesis of the *p*Tolyl-substituted iminosilylidene (SIDipp)Si(CN*p*Tol) only led to the formation of its *head-to-head* dimer, the unusual stability of the smaller methyl-substituted iminosilylidene attracts attention.

In this work, the spatial and electronic structure of the iminosilylenes (SIDipp)Si(CNR) was elucidated also in comparison to the experimental results, and it was shown that the influence of the isocyanide substituent is only minor. As expected, the dimerization of the iminosilylenes to their 1,2-disiletan-bisylidenes was calculated to be strongly favoured thermodynamically despite the increased sterical repulsion in the four-membered ring compounds.

As an alternative route, some iminosilylenes could also be synthesized starting from the disilicon(0) compound (SIDippSi)₂. The calculation of the thermodynamics confirmed an energetic and enthalpic preference of this reaction, which could be attributed to London dispersion forces in the case of the sterically demanding Ar^{Mes} substituent. The reaction is postulated to proceed via the 3-membered disilirane-1,2-ylidene-3-imines (SIDippSi)₂CNR, which was supported by calculating a plausible mechanistic pathway leading to this intermediate.

However, the calculations on this topic so far gave no clear indication why the methyl-substituted iminosilylidene (SIDipp)SiCNMe can be obtained as a monomer, whereas the *p*Tolyl-substituted

derivative dimerizes directly. Thus, further theoretical work should concentrate on the formation mechanism of the iminosilylenylidenes, both by substitution and from $(\text{SIDippSi})_2$.

Experimental work in our group on this topic recently led to the isolation of cyclic alkylamino carbene (CAAC)-stabilized iminosilylenylidenes $(\text{CAAC}^{\text{Me}})\text{Si}(\text{CNR})$. As also shown in this thesis, the donating and accepting properties of CAAC^{Me} ligands compared to NHCs are capable of altering the spatial and electronic structure of a given molecule. In this regard, preliminary calculations on the CAAC^{Me} -stabilized iminosilylenylidenes reveal shortened $\text{Si}-\text{CAAC}^{\text{Me}}$ and elongated $\text{Si}-\text{CNR}$ bonds, that confirm the higher π -acidity of the CAAC ligands. The analysis of their canonical MOs reveals the expected electron lone pair at the silicon atom (HOMO-1, see Figure 11.3) and the $\pi_{\text{oop}}(\text{C}_{\text{CAAC}}-\text{Si}-\text{C}_{\text{CNR}})$ bond (HOMO). Thus, the electronic structure of the CAAC^{Me} -supported iminosilylenylidenes is suggested to be similar to their NHC-stabilized analogues.

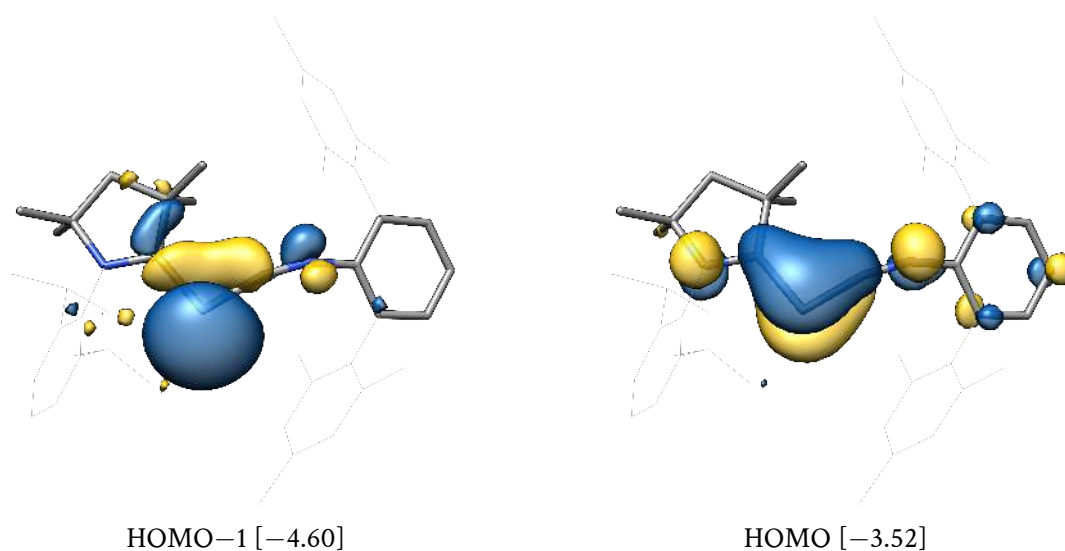


Figure 11.3: Selected canonical molecular orbitals of $(\text{CAAC}^{\text{Me}})\text{Si}(\text{CNAr}^{\text{Mes}})$ and their energy eigenvalues in eV.

Furthermore, experimental studies show that the *meta*-Xylol- and mesityl-substituted CAAC^{Me} -stabilized iminosilylenylidenes undergo dimerization, but in a *head-to-tail* fashion, contrary to the *head-to-head* dimerization observed for $(\text{SIDippSi})(\text{CN}p\text{Tol})$. A direct comparison cannot be made as the synthesis of the CAAC^{Me} -stabilized iminosilylenylidene $(\text{CAAC}^{\text{Me}})\text{Si}(\text{CN}p\text{Tol})$ was unsuccessful so far. Quantum chemical calculation indeed evidence that a dimerization of the CAAC^{Me} -substituted iminosilylenylidenes is strongly thermodynamically favoured. However, the calculated electronic and free Gibbs energies for the *head-to-head* dimerization reaction are still more negative by approximately $20 \text{ kJ}\cdot\text{mol}^{-1}$ than those for the experimentally observed *head-to-tail* isomers. It should thus also be within the scope of further theoretical work on this topic to elucidate the dimerization mechanism to explain the overall formation of the *head-to-tail* dimers for the CAAC-stabilized iminosilylenylidenes. As the HOMO of these compounds features $\pi(\text{Si}-\text{C})$ contributions, this might indicate an electronic structure similar to silenes $\text{R}_2\text{Si}=\text{CR}_2$, which are known to dimer-

ize either *head-to-head* or *head-to-tail*, depending on the polarization of the $\pi(\text{Si}-\text{C})$ bond and the substituents R.^[404, 405]

Theoretical studies on siladicarbenes and siladiimides

Carbodicarbenes, CL_2 are a relatively new compound class, which have been studied for approx. 15 years with theoretical and experimental approaches. They can be regarded to be based on the carbodiphosphorane class of compounds, which is known since the 1960s. A key feature of carbodicarbenes is the two-coordinated carbon atom, which displays *carbone* character, that is formally having a carbon atom with two free electron lone pairs. In reality, the π -type electron lone pair at the carbon atom is substantially delocalized towards the ligands and better described by a $\pi_{\text{oop}}(\text{L}-\text{C}-\text{L})$ multi-center bond.

Siladicarbenes as heavier homologues of carbodicarbenes share many structural and electronic features of carbodicarbenes and are known for more than 10 years, however, a heteroleptic siladicarbene with only NHC ligands was elusive so far.

Based on the successful isolation of such compounds, $(\text{SIDipp})\text{Si}(\text{IiPr}_2\text{Me}_2)$ and $(\text{IDipp})\text{Si}(\text{IiPr}_2\text{Me}_2)$, in our group, extensive theoretical studies on these novel molecules were presented in this work. It could be shown that their electronic structure differs from that of literature-known homoleptic NHC- and CAAC-derived siladicarbenes, but is indeed similar to that of heteroleptic mixed NHC- and CAAC-stabilized derivatives.

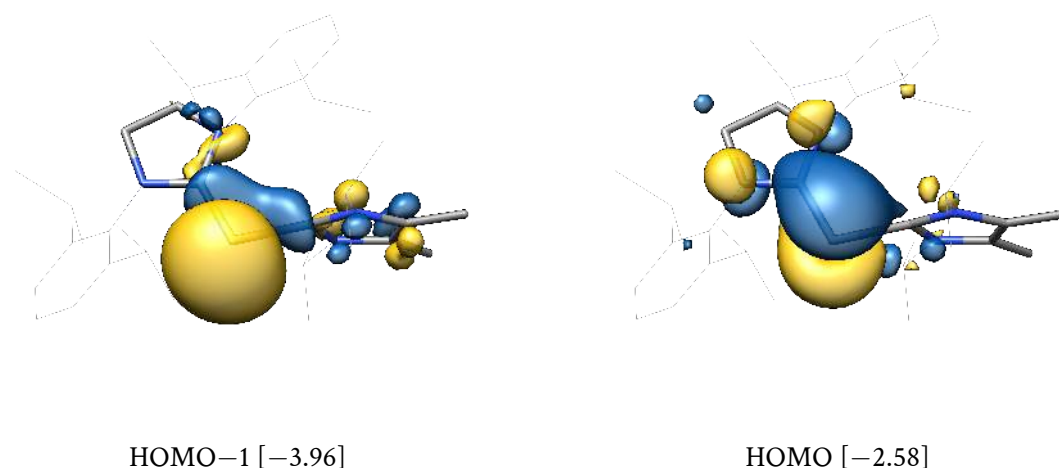


Figure 11.4: Selected canonical molecular orbitals of $(\text{SIDipp})\text{Si}(\text{IiPr}_2\text{Me}_2)$ and their energy eigenvalues in eV.

The heteroleptic environment at the silicon atom leads to an asymmetric Si-carbene bonding. The (S)IDipp ligands are lying co-planar to the filled p-type orbital at the Si atom, which enables a $\pi(\text{Si}-\text{C}_{(\text{S})\text{IDipp}})$ bond to be formed (HOMO, Figure 11.4). In contrast, the IiPr_2Me_2 carbene binds to the Si atom with a longer σ -type bond and is oriented perpendicular to the ((S)IDipp)Si plane. A second π_{ip} -type bond by the interaction between the silicon lone pair (HOMO-1) and

the IiPr_2Me_2 carbene is not pronounced.

A detailed fragment molecular orbital interaction diagram was presented to illustrate the bonding interactions between the silicon atom and the NHCs, supported by localized MO, NBO, NRT and NPA analyses.

Additionally, various conformers were calculated that display other bond situations or mimic those observed in homoleptic siladicalbenes. However, all of these were found to lie considerably higher in energy than the minimum structures. For example, the coplanar orientation of the (S)IDipp and IiPr_2Me_2 carbenes is lying more than $90 \text{ kJ}\cdot\text{mol}^{-1}$ higher in energy. The inverse conformer, where the IiPr_2Me_2 carbene is forced to form the π -type bond with the silicon atom and the (S)IDipp ligand is oriented perpendicularly, is more than $150 \text{ kJ}\cdot\text{mol}^{-1}$ higher in energy for (SIDipp)Si(IiPr_2Me_2).

The calculated first and second proton affinities of approximately 1250 and $870 \text{ kJ}\cdot\text{mol}^{-1}$ are considerably higher than those of comparable literature compounds and underline the high nucleophilicity and formal *silylone* character at the central silicon atom. This was further examined by calculating several Lewis acid (LA) adducts (SIDipp)Si(LA)(IiPr_2Me_2), where the Lewis acid coordinates to the $\pi_{\text{oop}}(\text{NHC}-\text{Si}-\text{NHC}')$ bond and leads to compounds with a trigonal-pyramidal (e.g. LA = BH_3 , CuCl) or trigonal-planar silicon atom (e.g. LA = AlMes_2Br , $[\text{CoCp}(\text{C}_2\text{H}_4)]$), depending mostly on the sterical demand of the Lewis acid.

Both siladicalbenes display a complex behaviour in solution NMR-spectroscopy, which was rationalized with the help of quantum chemical calculations to consist of three separate stereodynamic processes, involving stereo-inversions at one carbene nitrogen atom and Si– C_{NHC} bond rotations. By potential energy surface scans and transition state searches most of the experimentally estimated barriers could be confirmed.

The siladicalbene (SIDipp)Si(IiPr_2Me_2) was reacted with azides to obtain the IiPr_2Me_2 -stabilized siladiimide (IiPr_2Me_2)Si(NAr^{Mes})₂ under the loss of the SIDipp ligand. The accompanying theoretical analysis presented in this work revealed a strongly π -delocalized N–Si–N' moiety with only weak π -type delocalization into the IiPr_2Me_2 carbene. Bond dissociation energy calculations reveal a much higher cost to cleave one of the Si–N bonds ($420 \text{ kJ}\cdot\text{mol}^{-1}$) than the Si– IiPr_2Me_2 bond ($250 \text{ kJ}\cdot\text{mol}^{-1}$).

Future work focusses on the completion of the stereodynamics of the here studied siladicalbenes, as their partially flat hypersurfaces prohibited fully optimized transition states confirmed by intrinsic reaction coordinate methods.

So far, the selective cleavage of the NHC in (IiPr_2Me_2)Si(NAr^{Mes})₂ to obtain the unstabilized siladiimide Si(NAr^{Mes})₂ was not successful experimentally. Although R. West *et al.* reported on the existence of the siladiimide Si(NSiMe_3)₂ in a low-temperature matrix already in 1987,^[222] the isolation of a room-temperature stable siladiimide remains elusive. Access to the formal *head-to-tail* dimer, the 1,3-diaza-2,4-disiletidine $[\text{Si}(\text{NSiMe}_3)(\text{NAr}^{\text{TriPP}})]_2$, was achieved by H. W. Roesky *et al.* in 2011 via a different route.^[406]

Preliminary calculations on the siladiimide $\text{Si}(\text{NAr}^{\text{Mes}})_2$ yield the gas phase minimum structure depicted in Figure 11.5 with its closest contacts between the silicon atom and the periphery, which suggests some stabilization of the silicon atom by π -donation from the mesityl substituents. This can also be found in the canonical MOs, for example in the HOMO–12.

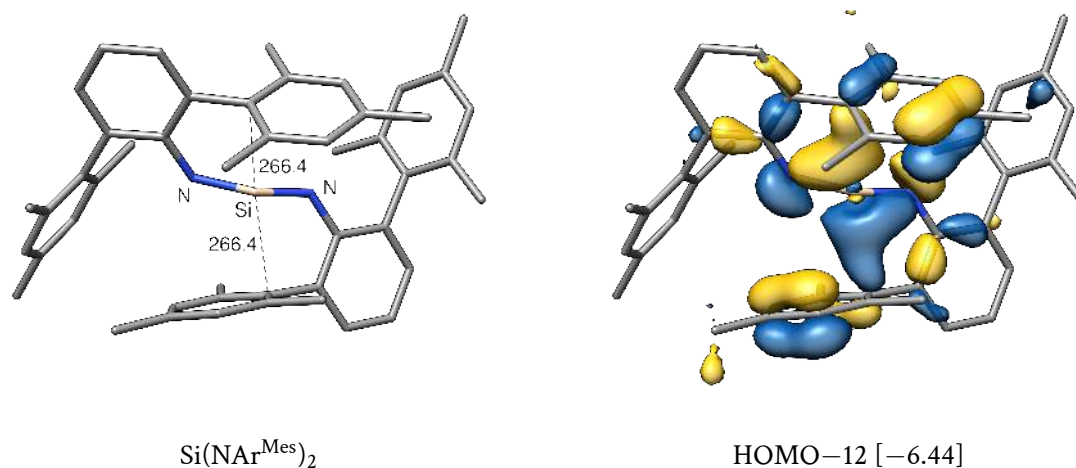


Figure 11.5: Left: minimum gas phase structure of the siladiimide $\text{Si}(\text{NAr}^{\text{Mes}})_2$ and closest contacts between the Si atom and the mesityl substituents in pm. Right: Canonical molecular orbital with the energy eigenvalue in eV.

The relatively short Si–C distances and the presence of orbital interaction between the silicon atom and the Ar^{Mes} substituent suggest that C–H or even C–C bond activations by silicon may prevent the realization of this compound in the experiment. Moreover, the dimerization energy to the *head-to-tail* dimer similar to that mentioned above by H. W. Roesky *et al.* could be calculated. The highly negative electronic dimerization energy of $-305.2 \text{ kJ}\cdot\text{mol}^{-1}$ is not countered by the decrease of entropy, still leading to a dimerization free Gibbs energy of $-157.0 \text{ kJ}\cdot\text{mol}^{-1}$.

CAAC-stabilized heavier ditetrelynes and ditetrelenylenes

Recently, CAAC-stabilized heavier ditetrelynes $(\text{CAAC}^{\text{Me}})\text{Si}(\text{Br})\text{Ge}^{\text{r}}\text{Tbb}$ and ditetrelenylenes $(\text{CAAC}^{\text{Me}})\text{ESi}(\text{Br})\text{Tbb}$ ($\text{E} = \text{Si}, \text{Ge}$) were successfully synthesized in our group. The herein presented detailed theoretical analyses of those compounds could highlight the impact of the cyclic alkyl amino ligand, especially in comparison with related NHC-supported compounds. It was shown that the high π -acidity of the CAACs leads to a considerable $\pi(\text{E}-\text{E}')$ bond delocalization into the carbene, and thus, many of the studied compounds feature π -type 3-center-2-electron bonds, as also evidenced by different quantum chemical tools like the IBO or NBO/NRT/NPA methods.

Furthermore, stereodynamic processes as observed in solution by NMR spectroscopy were examined in more detail by theory, for example for the disilavinylidene $(\text{CAAC}^{\text{Me}})\text{SiSi}(\text{Br})\text{Tbb}$, and could be confirmed or specified.

First experimental reactivity studies of these compounds were accompanied by quantum chemical calculations and presented in this thesis. This concerns the reduction product of a CAAC^{Me}-supported bromogermasilyne, obtained as potassium salt of a CAAC^{Me}-stabilized heavier acetylide ion (CAAC^{Me})Si(K)GeTbb, which was thoroughly investigated.

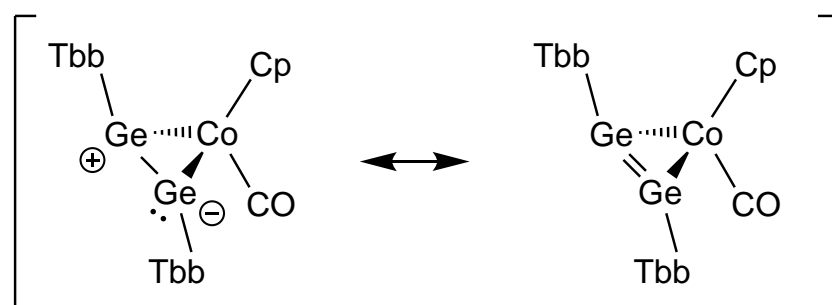
The bond situation in the bromide-abstracted cation [(CAAC^{Me})Si(Tbb)Ge]⁺ was also elucidated and afforded again a delocalization of the $\pi(\text{Si}-\text{Ge})$ bond to the carbene ligand, but also a weak arene stabilization of the naked germanium atom.

Several rearrangement reactions were discussed in this chapter and their calculated thermodynamical quantities were presented, which support the experimental results. However, detailed mechanistic studies were not successful and are subject to further investigations. Especially for the radical metathesis reaction between the disilicon(I)-dihalide [(CAAC^{Me})SiBr]₂ and the digermynes TbbGeGeTbb, only intermediates were proposed accompanied by thermodynamic considerations. The thorough investigation of its underlying mechanism lies well within the scope of density functional theory and should be addressed in order to fully understand this reaction. This in turn would also simplify its transfer to other low-valent main group systems.

Computational studies on digermynes cobalt complexes

Ditetrelynes, group 14 compounds REER with a formal E≡E triple bond, are known for almost 25 years, but their η^2 -coordination chemistry to transition metal fragments is still heavily underdeveloped so far. In this regard, several unprecedented digermynes cobalt complexes could be synthesized in our group and were studied theoretically in this work.

The carbonyl-containing complex [CoCp(CO)(TbbGeGeTbb)] features an asymmetric three-membered CoGeGe ring system with two significantly different Ge–Co bond lengths, which is also persistent for model systems where the size of the digermynes substituents is reduced. As it could be shown by a multi-dimensional potential energy surface scan, the alteration of both Ge–Co bonds lies in the low energy regime and a symmetrical structure is easily accessible within 10 kJ·mol⁻¹. The wave function analysis revealed that the complex can be described by both zwitterionic Ge⁺–Ge⁻ and Ge=Ge-type resonance structures (Figure 11.1).



Scheme 11.1: Suggested dominating resonance formulas for the digermynes cobalt complex [CoCp(CO)(TbbGeGeTbb)].

The stereodynamics of the complex [CoCp(CO)(TbbGeGeTbb)] as observed in solution by NMR spectroscopy were investigated in detail. Various reasonable stereodynamic mechanisms were calculated and the lowest-energy path was found to proceed via unusual germylene-germylidene complexes that allow for a simultaneous topomerization and enantiomerization in the complex.

Theoretical results on the carbonyl-free digermine complex [CoCp(TbbGeGeTbb)] suggest a four electron-donating digermine ligand and a 3-center-2-electron $\pi_{\text{oop}}(\text{Co}-\text{Ge}-\text{Ge})$ back-bonding. A symmetry-allowed δ -type bonding within the digermacobaltirene heterocycle was discussed, but found to be negligible due to insufficient Ge–Co orbital overlap. Nucleus-independent chemical shift (NICS) calculations were performed that indicate non-aromatic (or even weakly anti-aromatic) character for the delocalized ring system.

The reaction of the digermine cobalt complex [CoCp(CO)(TbbGeGeTbb)] with alkynes resulted in the formation of the first digermacobaltacyclopentatrienes [CoCp(TbbGe(RCCR)GeTbb)] and their electron structure was extensively discussed in this work. It could be shown that these complexes are best described by two localized Ge=Co and one C=C double bond.

First thermodynamic results on the formation of the digermacyclopentatrienes were presented in this work and support the experimental observations. However, full mechanistic pathways involving optimized and confirmed transition states could not be obtained so far, but are subject to further investigations in the future.

It is also recommended to extend the ditetrelene cobalt complexes to other tetrels apart from germanium. Initial calculations indicate that the corresponding disilyne cobalt complex [CoCp(CO)(TbbSiSiTbb)] (Figure 11.6 left) possesses a structure close to its germanium analogue with a similarly flat energy hypersurface regarding the Si–Co bonds.

In contrast, the distannyne analogue [CoCp(CO)(TbbSnSnTbb)] features a long Sn–Sn single bond with a calculated distance of 299.8 pm, which is considerably longer than the sum of the Pyykkoe single bond radii (280 pm).^[228] A derivative of this complex, [CoCp(CO)(Ar^{Dipp}Sn)₂] could be synthesized recently in our group by T. Deckstein.^[407] Its sc-XRD structure is depicted in Figure 11.6 right and features an even longer Sn–Sn separation of 312.2(1) pm, that is only surpassed by the calculated Sn–Sn distance of 330.0 pm in the gas phase. The long Sn–Sn separations indicate the loss of the tin-tin bond and instead a pronounced bistannylene character in this complex, which is supported by the shape of the HOMO–1 and HOMO (Figure 11.7).

The electronic nature of group 10 tetrylidyne complexes

In this chapter, a broad theoretical study on experimentally known and elusive group 10 tetrylidyne complex cations [M(PMe₃)₃ER]⁺ was presented (M = Ni, Pd, Pt; E = C, Si, Ge, Sn, Pb; R = Ar^{Mes}, Tbb (for Si only)). Their electronic structure was analyzed by inspection of the canonical MOs and IBOs, by the NPA method, and by the ETS-NOCV decomposition scheme.

All employed methods supported the initial indication by the analysis of the calculated gas phase

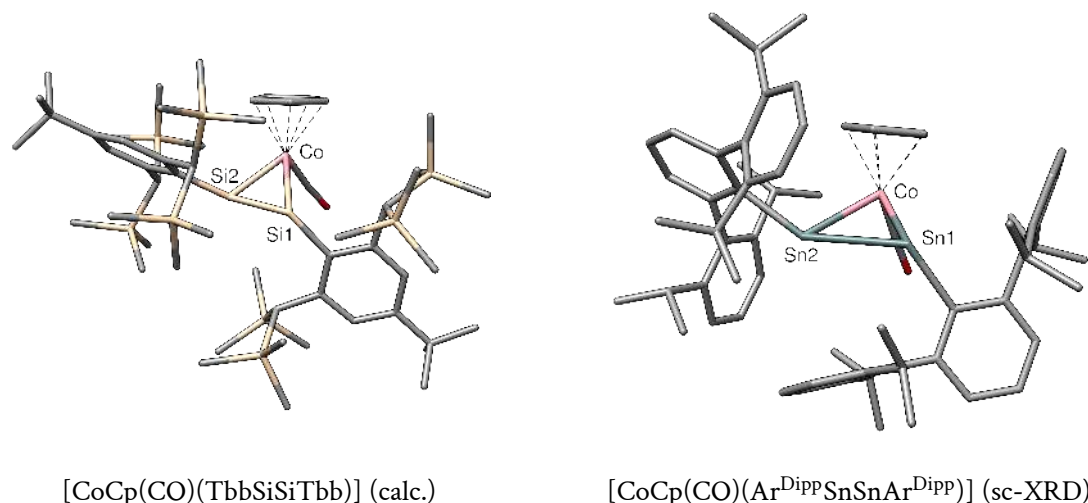


Figure 11.6: Left: calculated minimum gas phase structure of the disilyne cobalt complex $[\text{CoCp}(\text{CO})(\text{TbbSiSiTbb})]$. Si1–Si2: 221.9 pm; Si1–Co: 239.8 pm; Si2–Co: 230.6 pm. Right: sc-XRD structure of the distannyne cobalt complex $[\text{CoCp}(\text{CO})(\text{Ar}^{\text{Dipp}}\text{SnSnAr}^{\text{Dipp}})]$ synthesized by T. Deckstein.^[407] Sn1–Sn2: 312.2(1) pm; Sn1–Co: 258.5(2) pm; Sn2–Co: 256.8(2) pm.

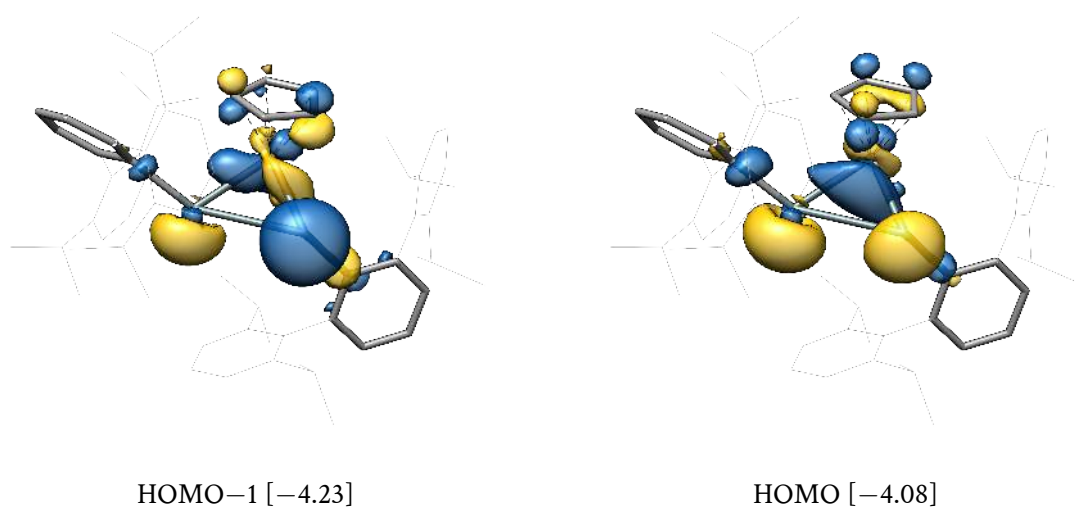


Figure 11.7: Selected canonical molecular orbitals of the distannyne cobalt complex $[\text{CoCp}(\text{CO})(\text{Ar}^{\text{Dipp}}\text{SnSnAr}^{\text{Dipp}})]$ and their energy eigenvalues in eV.

structures, that the studied complexes can be divided into two classes: tetrelidyne complexes and metallotetrelenes (for $M = \text{Pd}, \text{Pt}$ with $E = \text{Sn}, \text{Pb}$). Whereas the first resemble typical *Fischer-type* carbyne complexes with an $M\equiv E$ triple bond consisting of a $\sigma(E\rightarrow M)$ donation and two $\pi(M\rightarrow E)$ back donations, the latter comprise only a metal-centered σ -bond, a free electron lone pair on the tetrel atom and a considerably bent $M-E-R$ moiety.

The analysis of the potential energy hypersurface revealed strongly bent metallotetrylene isomers with M–E–R bond angles below 100°, which are even found to be global minimum structures for the heaviest metal–tetrel combinations. According to the preliminary theoretical results these complexes feature a distorted square-planar coordination environment at the 16 valence electron metal center and a strong $\sigma(\text{M}\rightarrow\text{E})$ bond. A more in-depth analysis of these isomers and considerations regarding their reactivity and potential experimental isolation are pending. Interestingly, a similar situation is observed for the isoelectronic group 9 complexes $[(\text{PMe}_3)_3\text{MEAr}^{\text{Mes}}]$ with M = Rh, Ir and E = Sn, Pb: Calculations by J. Rump from our group show that there also highly bent isomers with M–E–C angles < 100° exist, which are roughly isoenergetic to the less bent complexes with M–E–C angles of approximately 145°. [408].

Mass spectrometric studies of group 6 germylidyne complexes

Finally, except for quantum chemistry, this thesis also presented inert mass spectrometry of group 6 germylidyne complexes. With the advent of mass spectrometrical methods to analyze air- and moisture-sensitive compounds, especially in the field of ionization sources, the compounds $[\text{MCp}(\text{PMe}_3)_2\text{GeAr}^{\text{Mes}}]$ and $[\text{MTp}'(\text{CO})_2\text{GeAr}^{\text{Mes}}]$ with M = Mo and W could be analyzed for the very first time.

Several APCI and LIFDI mass spectra were shown that depict the successful measurements of the complexes without serious decomposition and feature the molecular ions $[\text{M}]^+$ as base peaks.

Further chemical insight was obtained by collision-induced dissociation (CID) and higher-energy collisional dissociation (HCD) experiments that evidence the fragmentation of the ligand sphere around the metal. Interestingly, this does not only involve the phosphine and carbonyl ligands which are known to be prone to dissociation in the gas phase after activation, but also the dissociation of the germylidyne fragment under cleavage of the $\text{M}\equiv\text{Ge}$ triple bond was observed.

Since the discovery of the first heavier tetrylidyne complex more than 25 years ago, many representatives of this compound class could be isolated for the heavier tetrels E = Si to Pb and the majority of transition metals. The mass spectrometric results presented in this thesis are only the first step in exploring the gas phase properties of these compounds. Therefore, future work in this regard should comprise both other transition metals (early and late) and other tetrels. For the latter, it remains to be seen if the MS sample injection and ionization is still suitable for the extremely sensitive silylidyne complexes. Ultimately, it is envisioned that after transfer in the gas phase and ionization, ion-molecule reactions in the gas phase can be conducted, for example with alkenes and alkynes. Here the comparison to the solution chemistry is obvious, where [2+2]-cycloaddition products of silylidyne complexes with alkynes could already be isolated and characterized. [151, 322–325] Mass spectrometry also offers the Infrared Multiple Photon Dissociation (IRMPD) technique, [409] which can be used to activate ions in the gas phase. By this, a cycloreversion reaction of the [2+2]-

cycloaddition products of silylidyne complexes might be reachable. Apart from the cleavage into a silylidyne complex and an alkyne, this reaction might also lead to unprecedented silynes RSiCR' .

Part E.

Appendix

(NHC)Si=C=N-R: A Two-Coordinated Si⁰-Isocyanide Compound as Si(NHC) Transfer Reagent

Surender Karwasara, Leonard R. Maurer, Benjamin Peerless, Gregor Schnakenburg, Ujjal Das,* and Alexander C. Filippou*



Cite This: *J. Am. Chem. Soc.* 2021, 143, 14780–14794



Read Online

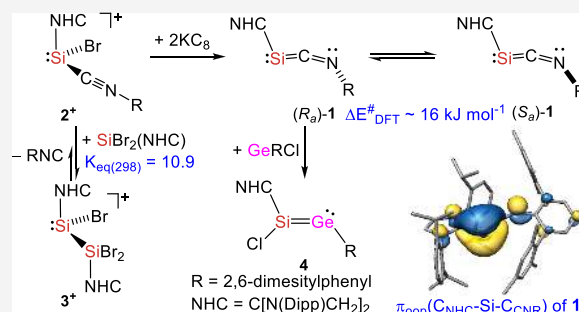
ACCESS |

Metrics & More

Article Recommendations

Supporting Information

ABSTRACT: Experimental and theoretical studies are reported of the first two-coordinated Si⁰-isocyanide compound (SIDipp)Si=C=N-Ar^{Mes} (**1**: SIDipp (NHC) = C[N(Dipp)CH₂]₂, Ar^{Mes} = 2,6-dimesitylphenyl), supported by an N-heterocyclic carbene (NHC). A Si atom economic two-step synthesis of **1** involves a 2e reduction of the isocyanide-stabilized silyliumylidene salt [SiBr(CNAr^{Mes})(SIDipp)][B(Ar^F)₄] (2[B(Ar^F)₄], Ar^F = B(C₆H₃-3,5-(CF₃)₂)₄) with KC₈. 2[B(Ar^F)₄] was obtained from SiBr₂(SIDipp) after bromide abstraction with an equimolar mixture of Na[B(Ar^F)₄] and Ar^{Mes}NC. Exact adherence to the stoichiometry is crucial in the latter reaction, since 2[B(Ar^F)₄] reacts with SiBr₂(SIDipp) via isocyanide exchange to afford the disilicon(II) salt [Si₂Br₃(SIDipp)₂][B(Ar^F)₄] (3[B(Ar^F)₄]), the reaction leading to an equilibrium that favors 3[B(Ar^F)₄] (K_{eq}(298 K) = 10.6, ΔH^o = -10.6 kJ mol⁻¹; ΔS^o = -16.0 J mol⁻¹ K⁻¹). 3[B(Ar^F)₄] was obtained selectively from the 2:1 reaction of SiBr₂(SIDipp) with Na[B(Ar^F)₄] and fully characterized. Detailed studies of **1** reveal an intriguing structure featuring a planar C_{NHC}-Si-C-N skeleton with a V-shaped geometry at the dicoordinated Si⁰ center, a slightly bent Si=C=N core, a C_{NHC}-Si-C_{CNR} 3c-2e out of plane π-bond (HOMO), and an *antitropical* conformation of the SIDipp and Ar^{Mes} substituents leading to axial chirality and the presence of two enantiomers, (*R_a*)-**1** and (*S_a*)-**1**. Compound **1** displays structural dynamics in solution, rapidly interconverting the enantiomers. The silacumulene **1** is a potent Si(SIDipp) transfer agent as demonstrated by the synthesis and full characterization of the NHC-supported germsilyne (Z)-(SIDipp)(Cl)Si=GeAr^{Mes} (**4**) from **1** and Ge(Ar^{Mes})Cl.



1. INTRODUCTION

Cyano- and isocyanosilylenes, such as Si(CN)H and Si(NC)H, are a class of very reactive Si^{II} species, which are of particular interest in the context of the rich interstellar chemistry of silicon, the seventh most abundant element cosmically.¹ Quantum chemical studies of the [H,Si,C,N] potential energy hypersurface predict the presence of six lowest lying singlet isomers and their corresponding triplets, with the singlet cyanosilylene **I** being the global minimum structure followed by the singlet isocyanosilylene **II** at slightly higher energy (Figure 1).² The six isomers can be divided into three classes: (a) the aforementioned cyano- and isocyanosilylene (**I**, **II**), (b) the 3-H-2-aza-1-silacyclopropenylidene **III** and silaisocyanocarbene **IV**, which are formally the side-on and end-on addition products of hydrogen cyanide (HCN) to a ¹Si atom, and (c) the iminosilylenylidene **V** and 2-H-2-aza-1-silacyclopropenylidene **VI**, the formal hydrogen isocyanide (HNC) addition products of ¹Si (Figure 1).

Generation and spectroscopic identification of these species are very challenging, and only the isomers **I**–**IV** could be observed so far. Thus, isomers **I** and **II** were produced upon

high-voltage discharge of a SiH₄/NCCN mixture or SiMe₃CN and studied by molecular beam Fourier-transform microwave or laser-induced fluorescence spectroscopy,^{1b,d} whereas co-condensation of thermally generated Si atoms with HCN in an argon matrix was shown by IR spectroscopy to give **IV**, which photoisomerizes upon irradiation (λ > 700 nm) to the isomers **III** and **I**.^{1a} Among the aforementioned isomers of the [H,Si,C,N] system, the elusive iminosilylenylidene **V** is particularly interesting as an N-analogue of the silaketenyldiene (SiCO)³ and, similar to **IV**, has a very small singlet–triplet gap (E_T – E_S (ΔE_{S-T}) ≈ -5 kJ mol⁻¹).^{2a}

Recent developments in the chemistry of silicon in unusually low oxidation states have illustrated that N-heterocyclic carbenes (NHCs) are particularly suitable Lewis bases for

Received: June 29, 2021

Published: September 1, 2021



ACS Publications

© 2021 American Chemical Society

14780

<https://doi.org/10.1021/jacs.1c06628>
J. Am. Chem. Soc. 2021, 143, 14780–14794

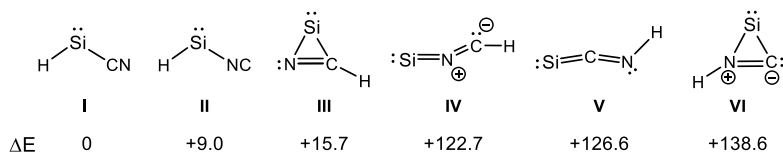


Figure 1. Six lowest lying singlet isomers I–VI of the $[H,Si,C,N]$ potential energy hypersurface ordered with increasing energy relative to the global minimum I. Relative energies are given in kJ mol^{-1} at the RHF-UCCSD(∞) + E_T + E_{cc} + E_{BD} + E_{SO} + E_{CG} + E_{ZPE} level of theory.^{2a} Formal charges are encircled in the Lewis structures of this and all other figures unless otherwise stated, and the two dots at the Si, C, and N atoms represent a lone pair of electrons.

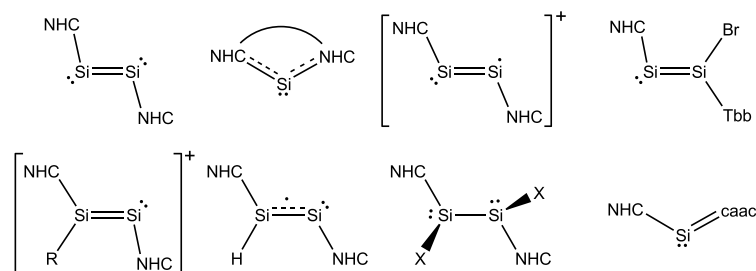


Figure 2. Examples of NHC-containing Si^0/Si^1 compounds (NHC = N-heterocyclic carbene; Tbb = $\text{C}_6\text{H}_2-2,6-[\text{CH}(\text{SiMe}_3)_2]-4\text{-}^t\text{Bu}$; R = H, Me, Et, X = Cl – I; caac = cyclic alkyl(amino)carbene). Formal charges were not included in the Lewis structures for the sake of simplicity; the two dots at the Si atoms represent a lone pair of electrons, and the one dot an unpaired electron.

the thermodynamic stabilization of highly reactive, unsaturated Si species, leading to a series of isolable closed-shell and open-shell Si^0/Si^1 compounds with intriguing electronic structures (Figure 2).⁴ On the basis of these studies, we presumed that NHCs might be also employed to stabilize iminosilylenes, leading to unprecedented Si^0 -isocyanide compounds featuring dicoordinated Si centers with a large synthetic potential.

However, isocyanides are weaker σ -donors than NHCs, as indicated by their lower proton affinities.⁵ Therefore, isocyanide compounds of low-coordinate silicon are scarce, rendering the objective quite challenging.^{6,7} In fact, only a few isocyanide-silylene adducts of the general formula $\text{R}_2\text{Si}(\text{CNR})$ (R = univalent group) have been isolated heretofore featuring pyramidal-tricoordinated silicon centers (Figure 3, top).⁶

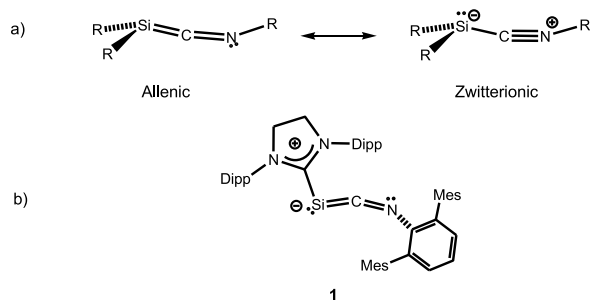


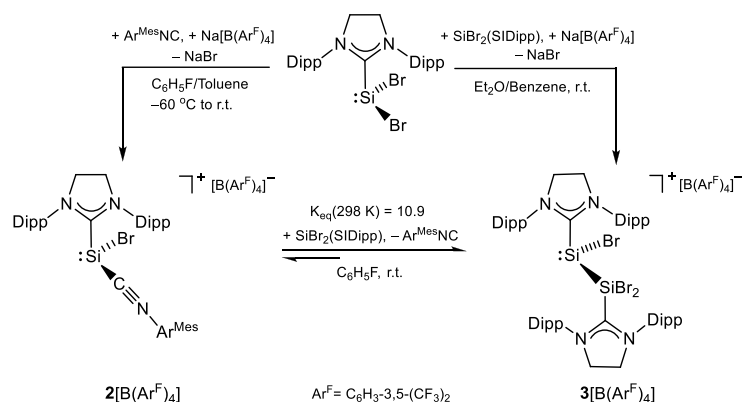
Figure 3. (a) Resonance structures of isocyanide-silylene adducts; (b) Si^0 -isocyanide compound (SIDipp)Si=C=N(Ar^{Mes}) (1) reported in this work.

Recently, also the 1-silaketiminyl lithium compounds $\text{R}_2\text{B}(\text{Li})\text{Si}=\text{C}=\text{NR}'$ (BR_2 = diamino-boryl; R' = 1-adamantyl, 2,6-diisopropylphenyl) were reported,⁷ and reductive coupling of two isocyanides was achieved at a bis(NHSi) scaffold (NHSi = N-heterocyclic silylene).⁸ Structural, spectroscopic, and quantum chemical studies indicate that the bonding in $\text{R}_2\text{Si}(\text{CNR})$ can be described by an allenic and a zwitterionic

resonance structure (Figure 3a), providing a rationale for the observed isocyanide dissociation and silylene-type reactivity of these compounds,^{6a,b,9} which differs from the addition chemistry of the $\text{Si}=\text{C}$ bonds of silylenes¹⁰ and 1-silaallenes.¹¹ These studies implied that electropositive substituents on silicon, which are known to decrease the singlet–triplet gap of silylenes,¹² should increase the contribution of the allenic form, leading to a stronger $\text{Si}-\text{C}_{\text{isocyanide}}$ bond. With this in mind we assumed that $\text{Si}(\text{NHC})$ fragments, having a triplet ground state,¹³ would bind strongly to isocyanides. We report in the following the realization of this idea with the isolation and full characterization of an NHC-stabilized iminosilylidene (Figure 3, bottom) and demonstrate the utility of this Si^0 -isocyanide compound as a $\text{Si}(\text{NHC})$ transfer reagent by its quantitative conversion to the unprecedented NHC-stabilized germasilyne (Z)-(SIDipp)(Cl)Si=GeAr^{Mes} (SIDipp = C[N-(Dipp)CH₂]₂, Dipp = 2,6-diisopropylphenyl; Ar^{Mes} = C₆H₃-2,6-Mes₂, Mes = 2,4,6-trimethylphenyl).

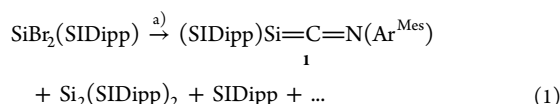
2. RESULTS AND DISCUSSION

2.1. Syntheses, Solid-State Structures, and Spectroscopic Studies of 1 and the Base-Stabilized Silyliumylidene Salts 2[B(Ar^F)₄] and 3[B(Ar^F)₄]. Earlier reactivity studies of our and other groups had shown that the Si^{II} dihalides, $\text{SiX}_2(\text{NHC})$ (X = Cl–I),¹⁴ are suitable starting materials for the synthesis of many novel dicoordinated silicon compounds containing silicon–element multiple bonds.^{4b,d,e,13,15} Most importantly, two-electron reduction of $\text{SiX}_2(\text{NHC})$ with potassium graphite (KC_8) was found in our group to afford the Si^0 compounds $\text{Si}_2(\text{NHC})_2$ in moderate yields, enabling us to explore their chemistry.^{4c,7,8} This let us presume that co-reduction of $\text{SiX}_2(\text{NHC})$ with a bulky isocyanide, which could provide the required steric protection to the generated reactive Si^0 center, might lead to a stable Si^0 isocyanide compound, and we have chosen $\text{Ar}^{\text{Mes}}\text{NC}$ (Ar^{Mes} = C₆H₃-2,6-Mes₂; Mes = mesityl) as a possible candidate to trap the $\text{Si}^0(\text{NHC})$ fragment. In fact, treatment of an equimolar

Scheme 1. Conversion of SiBr₂(SIDipp) to the Silyliumylidene Salts 2[B(Ar^F)₄] and 3[B(Ar^F)₄] and Ligand Exchange Equilibrium between 2[B(Ar^F)₄] and 3[B(Ar^F)₄]^a


^aFormal charges were not included in the Lewis structures for the sake of simplicity.

mixture of SiBr₂(SIDipp)^{14c} and Ar^{Mes}NC with 2.1 equiv of KC₈ in diethyl ether at -40 °C followed by warming to room temperature was accompanied by a rapid color change of the solution from yellow to purple, the characteristic color of the NHC-stabilized iminosilyliumylidene **1** (eq 1).



Conditions (a): +Ar^{Mes}NC, +2KC₈, -2KBr, -16C/Et₂O, -40 °C to rt.

Detailed ¹H NMR spectroscopic analysis of the diethyl ether- and benzene-soluble products revealed however the formation of a mixture of **1**, Si₂(SIDipp)₂, SIDipp, and unreacted Ar^{Mes}NC, with **1** (16%) and Si₂(SIDipp)₂ (10%) being the minor components, which prevented the isolation of **1** in an acceptable yield (SI (Supporting Information), Section 2.1.1).

Looking for a more efficient approach to **1**, we next attempted to preinstall the Ar^{Mes}NC ligand at the Si^{II} center by halide abstraction from SiX₂(NHC), forming an isocyanide-stabilized silyliumylidene salt. In fact, addition of SiBr₂(SIDipp) to a 1:1 (v/v) toluene/fluorobenzene solution containing an equimolar mixture of Na[B(Ar^F)₄] (Ar^F = C₆H₃-3,5-(CF₃)₂) and Ar^{Mes}NC at -60 °C followed by warming to ambient temperature led to an intense yellow solution and precipitation of NaBr. Analysis of the reaction mixture by IR and ¹H NMR spectroscopy revealed a quite selective conversion to the silyliumylidene salt 2[B(Ar^F)₄] (Scheme 1). No reaction of SiBr₂(SIDipp) with Ar^{Mes}NC was observed in the absence of Na[B(Ar^F)₄], and no intermediates could be observed by NMR spectroscopy at room temperature during the conversion of SiBr₂(SIDipp) into 2[B(Ar^F)₄], suggesting that the intermediate formed upon bromide abstraction from SiBr₂(SIDipp) by Na[B(Ar^F)₄] is rapidly trapped by the isocyanide to give 2[B(Ar^F)₄]. Notably, an excess of SiBr₂(SIDipp) should be avoided in this reaction, since SiBr₂(SIDipp) displaces the Ar^{Mes}NC ligand from 2[B(Ar^F)₄] yielding the disilicon(II) salt [Si₂Br₃(SIDipp)₂][B(Ar^F)₄] (3[B(Ar^F)₄]) (Scheme 1).

Compound 2[B(Ar^F)₄] is the first isocyanide-stabilized halosilyliumylidene salt to be reported.¹⁶ It was isolated after

workup as a very sensitive, intense yellow solid and was fully characterized (SI, Section 2.2). The solid-state structure of 2[B(Ar^F)₄]·(C₆H₅F) was determined by single-crystal X-ray diffraction (sc-XRD) analysis of yellow-orange crystals, which are composed of well-separated trigonal pyramidal isocyanide-stabilized silyliumylidene cations (Figure 4) and [B(Ar^F)₄]⁻

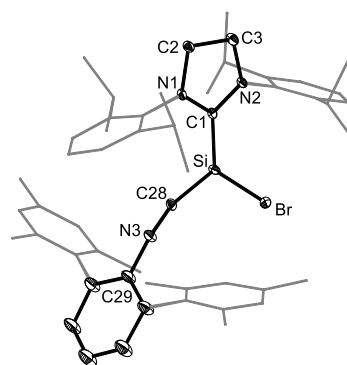


Figure 4. DIAMOND plot of the structure of the cation 2⁺ in the crystal lattice of 2[B(Ar^F)₄]; thermal ellipsoids are set at 30% probability, and hydrogen atoms were omitted. In this and all other structures the Dipp substituents of the NHC and the Mes substituents of the Ar^{Mes} group are presented in wire frame for the sake of clarity. Selected bond lengths (Å), bond angles (deg), and torsion angles (deg): Si–C1 1.977(4), Si–C28 1.952(5), Si–Br 2.261(3), C28–N3 1.150(5); Br–Si–C1 95.8(2), Br–Si–C28 90.5(2), C1–Si–C28 100.3(2), Si–C28–N3 148.8(4), C28–N3–C29 171.9(5); N2–C1–Si–C28 172.4(3), N2–C1–Si–Br 80.8(3), C1–Si–C28–N3 168.6(7).

anions. The sum of bond angles at the trigonal pyramidal coordinated Si center ($\sum \angle(\text{Si}) = 286.6^\circ$) compares well with that of SiBr₂(SIDipp) ($\sum \angle(\text{Si}) = 290^\circ$), suggesting in line with the results of the natural bond orbital (NBO) analysis the presence of a stereochemically active lone pair of electrons at silicon. The Si–C_{isocyanide} bond length of 2[B(Ar^F)₄] (1.952(5) Å) is similar to the Si–C_{NHC} bond length (1.977(4) Å) and lies in a typical range of Si–C donor–acceptor σ -bonds. Also the degree of pyramidalization (DP) of the cation of 82%¹⁷ does not indicate any significant Si–C_{isocyanide} π -bonding resulting from Si(n)→ $\pi^*(\text{C}\equiv\text{NR})$ back-donation. This is

supported by the Wiberg bond index (WBI) obtained from NBO analysis and the total bond order of the Si–C_{CNR} and Si–C_{NHC} bonds obtained from natural resonance theory (NRT-BO), indicating the presence of strong, polarized Si–C_{CNR} and Si–C_{NHC} single bonds in 2⁺ (WBI(Si–C_{CNR}) = 0.87, WBI(Si–C_{NHC}) = 0.71; NRT-BO(Si–C_{CNR}) = 1.0, NRT-BO(Si–C_{NHC}) = 1.0) (Section 2.3.1).

The C≡N bond length of 2⁺ (1.150(5) Å) is very close to that of free Ar^{Mes}NC (1.158(3) Å),¹⁸ and the C–N–C_R moiety approaches linearity (∠(C–N–C_R) = 171.9(5)°).

Further insight into the structure and dynamics of 2[B(Ar^F)₄] in solution was provided by IR and ¹H/¹³C/²⁹Si NMR spectroscopy. In fact, the IR spectrum of 2[B(Ar^F)₄] in C₆H₅F displays a characteristic ν(C≡N) band at 2143 cm⁻¹, which is significantly blue shifted from that of 1 (ν(C≡N) in solid state = 1778 cm⁻¹) and appears at even higher energy than that of free Ar^{Mes}NC (ν(C≡N) in C₆H₅F = 2119 cm⁻¹), suggesting, in combination with the structural features of 2[B(Ar^F)₄], the presence of a RN≡C→Si donor–acceptor σ-bond with weak Si(n)→π*(C≡NR) back-bonding.⁹ The ¹H and ¹³C NMR spectra of 2[B(Ar^F)₄] in D₅-chlorobenzene unequivocally indicate the presence of a configurationally stable, stereogenic Si center in the trigonal pyramidal cations and a fast rotation of the Ar^{Mes}NC and NHC ligands about the respective Si–C bonds at room temperature. The ¹³C NMR spectrum of 2[B(Ar^F)₄] displays a distinctive C_{carbene} signal at δ = 183.7, which appears at higher field than that of SiBr₂(SIDipp) (δ = 188.7 ppm in D₆-benzene)^{14c} and of 1 (δ = 210.8 ppm in D₆-benzene), and also a distinctive C_{isocyanide} signal at δ = 167.7 ppm, which is upfield shifted of that of free Ar^{Mes}NC (δ_{CN} = 169.6 ppm in D₅-chlorobenzene) and of 1 (δ_{CN} = 197.9 ppm in D₆-benzene), indicating the pronounced σ-acceptor character of the fragment [SiBr(NHC)]⁺ in 2⁺.¹⁹ 2[B(Ar^F)₄] features a similar ²⁹Si NMR chemical shift (δ_{Si} = –50.2 ppm in D₅-chlorobenzene) to that of the NHC-stabilized iodosilyliumylidene salt [Si(IME₂Pr₂)(IDipp)]I (δ_{Si} = –55.3 ppm in D₂-dichloromethane),^{14d} the high-field shift being typical for trigonal pyramidal NHC-stabilized silyliumylidenes.²⁰ Notably the ²⁹Si chemical shift of 2[B(Ar^F)₄] also compares well with those of the aryl isocyanide-diarylsilylene adducts reported by N. Tokitoh et al. (δ_{Si} = –47.9 to –57.8 ppm).^{6a}

Interestingly, compound 2[B(Ar^F)₄] undergoes an isocyanide exchange reaction with SiBr₂(SIDipp) to give the disilicon salt [Si₂Br₃(SIDipp)₂][B(Ar^F)₄] (3[B(Ar^F)₄]) (Scheme 1). Monitoring of the forward reaction (2[B(Ar^F)₄] + SiBr₂(SIDipp)) as well as the back reaction (3[B(Ar^F)₄] + Ar^{Mes}NC) by ¹H and ²⁹Si NMR spectroscopy in D₅-chlorobenzene at 298 K revealed that a ligand exchange equilibrium between 2[B(Ar^F)₄] and 3[B(Ar^F)₄] is established, which lies slightly on the site of 3[B(Ar^F)₄] (K_{eq}(298 K) = 10.6, ΔG°_{298 K} = –5.9 kJmol⁻¹) (Scheme 1). The temperature dependence of the equilibrium was also studied by variable-temperature ¹H NMR spectroscopy in the temperature range of 298–343 K, and the standard reaction enthalpy ΔH° and reaction entropy ΔS° were derived from a van't Hoff plot. The obtained values (ΔH° = –10.6 kJ mol⁻¹; ΔS° = –16.0 J mol⁻¹ K⁻¹) indicate that formation of 3[B(Ar^F)₄] is a slightly exothermic reaction that is entropically disfavored with increasing temperature (SI, Section 2.3). Notably, this equilibrium is an unprecedented example of a reversible ligand substitution at a cationic Si(II) center.¹⁶

The disilicon(II) salt 3[B(Ar^F)₄] was independently obtained upon treatment of SiBr₂(SIDipp) with Na[B(Ar^F)₄] in the molar ratio 2:1 in a diethyl ether/benzene mixture at ambient temperature and isolated after workup as an extremely air-sensitive, yellow solid in 62% yield, which was fully characterized (Scheme 1, SI (Section 2.4)). Compound 3[B(Ar^F)₄] represents the first example of an NHC-stabilized [Si₂X₃]⁺ salt to be reported.¹⁶ The crystal lattice of 3[B(Ar^F)₄]·(C₆H₅F)·0.5(C₂H₁₂) is composed of well-separated [Si₂Br₃(SIDipp)₂]⁺ cations and [B(Ar^F)₄][–] anions. The [Si₂Br₃(SIDipp)₂]⁺ cations feature a trigonal pyramidal bonded Si1 center of chirality (∑∠(Si1) = 284.2°), which is connected via a Si–Si bond to the tetrahedral coordinated Si2 center and carries according to NBO analysis a lone pair of electrons in a hybrid orbital with 77% s-character (Figure 5). The Si–Si

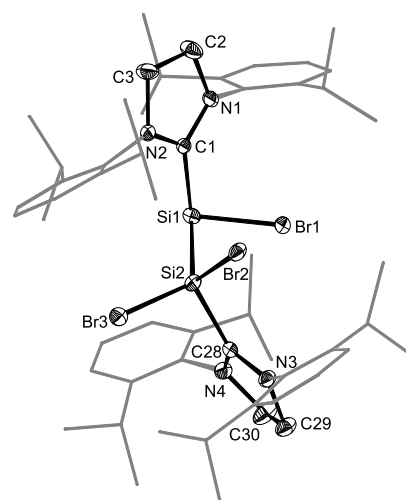


Figure 5. DIAMOND plot of the structure of the cation 3⁺ in the crystal lattice of 3[B(Ar^F)₄]; thermal ellipsoids are set at 30% probability, and hydrogen atoms were omitted. Selected bond lengths (Å), bond angles (deg), and torsion angles (deg): Si1–Si2 2.353(2), Si1–C1 1.973(5), Si2–C28 1.970(5), Si1–Br1 2.316(1), Si2–Br2 2.234(1), Si2–Br3 2.197(1); C1–Si1–Si2 100.1(2), C1–Si1–Br1 99.6(2), Br1–Si1–Si2 84.54(6), Si1–Si2–C28 106.8(2), Br2–Si2–Br3 104.79(6); C1–Si1–Si2–C28 155.7(2), Br1–Si1–Si2–Br3 175.9(1).

bond length of 2.353(2) Å fits exactly to that of α-silicon (2.352 Å)²¹ and indicates, in combination with the NBO and NRT bonding analyses, the presence of a strong single bond (WBI(Si–Si) = 0.9; NRT-BO(Si–Si) = 1.0) that is markedly polarized toward the Si2 atom (SI, Section 6.9).

The two Si–C_{NHC} bond lengths (*d*(Si1–C1) = 1.973(5) Å; *d*(Si2–C28) = 1.970(5) Å) are equal to that of 2[B(Ar^F)₄] (1.977(4) Å), which is also reflected in essentially equal Wiberg bond indices (3⁺: WBI(Si1–C_{NHC}) = 0.70, WBI(Si2–C_{NHC}) = 0.70; 2⁺: WBI(Si–C_{NHC}) = 0.71) and NRT total bond orders (3⁺: NRT-BO(Si1–C_{NHC}) = 1.1, NRT-BO(Si2–C_{NHC}) = 1.0; 2⁺: NRT(Si–C_{NHC}) = 1.0), pointing to strong Si–C_{NHC} single bonds.

The ¹H and ¹³C{¹H} NMR spectra of 3[B(Ar^F)₄] reveal, as in the case of 2[B(Ar^F)₄], that a stereomutation of the tricoordinated, stereogenic Si center by pyramidal inversion or an intermolecular process does not occur in solution at room temperature and show moreover the presence of two

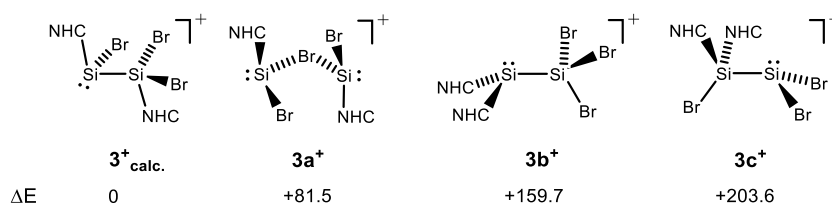
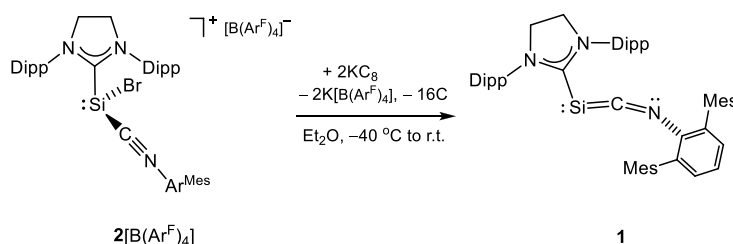


Figure 6. Conceivable regioisomers $3a^+–3c^+$ ordered with increasing energy relative to the minimum structure 3^+_{calc} . Relative energies are given in kJ mol^{-1} at the B97-D3(BJ)-ATM/def2-TZVP level of theory; NHC = SIDipp.

Scheme 2. Two-Electron Reduction of the Si^{II} Salt $2[\text{B}(\text{Ar}^{\text{F}})_4]$ to the Si^0 Isocyanide Compound 1^{a}



^aFormal charges were not included in the Lewis structures for the sake of simplicity.

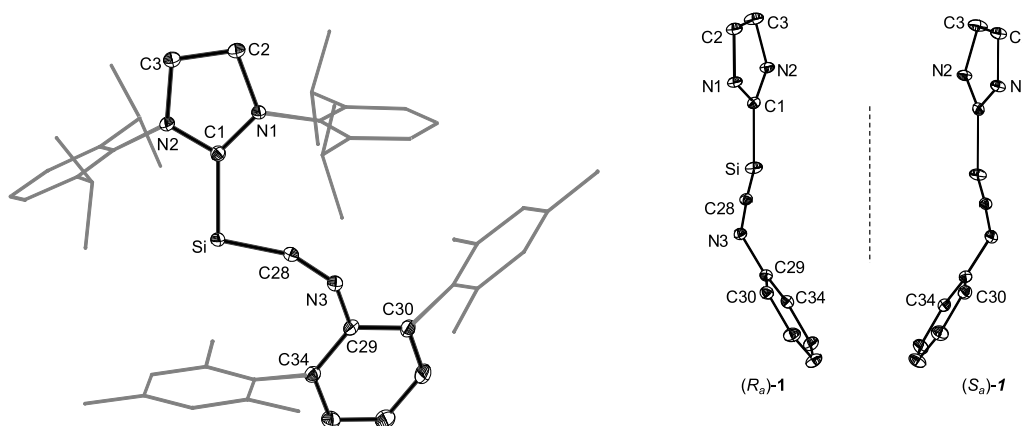


Figure 7. Left: DIAMOND plot of the structure of 1 (R_a)- 1 enantiomer); thermal ellipsoids are set at 50% probability, and hydrogen atoms were omitted. Selected bond lengths (Å) and bond and torsion angles (deg): Si–C1 1.894(1), Si–C28 1.784(1), C28–N3 1.224(1), N3–C29 1.411(1); C1–Si–C28 100.40(5), Si–C28–N3 158.81(9), C28–N3–C29 133.0(1), C1–Si–N3–C29 $-130.90(1)$, N1–C1–Si–C28 $-27.5(1)$, Si–N3–C29–C30 156.9(1). Right: View of 1 along the N3–Si chirality axis leading to the enantiomers (R_a)- 1 and (S_a)- 1 ; the Dipp and Mes groups were omitted for the sake of clarity.

constitutionally heterotopic Si sites leading consequently to a double set of signals for the NHC groups (SI, Section 2.4). Thus, the $^{29}\text{Si}\{^1\text{H}\}$ NMR spectrum of $3[\text{B}(\text{Ar}^{\text{F}})_4]$ in D_5 -chlorobenzene shows two signals at -34.7 and -32.7 ppm for the tricoordinated (Si1) and tetracoordinated (Si2) silicon atoms, respectively, and the $^{13}\text{C}\{^1\text{H}\}$ NMR spectrum displays two distinctive, low-field shifted signals for the Si1 and Si2 bonded C_{NHC} atoms at $\delta = 188.1$ and 172.3 ppm, respectively. All these data indicate that a topomerization (“degenerate isomerization”)²² leading to a site exchange of the NHC ligands in the cation 3^+ does not proceed at ambient temperature. This is in line with the results of quantum chemical studies revealing that regioisomers of 3^+ , such as $3a^+–3c^+$, which are conceivable intermediates in such a process, are local minima on the energy hypersurface, which appear however at considerably higher energy than the minimum structure 3^+ (Figure 6).

Compound $2[\text{B}(\text{Ar}^{\text{F}})_4]$ proved to be a very suitable starting material for the synthesis of the NHC-stabilized iminosilylenylidene 1 . Thus, two-electron reduction of $2[\text{B}(\text{Ar}^{\text{F}})_4]$, which was generated *in situ* from $\text{SiBr}_2(\text{SIDipp})$, $\text{Ar}^{\text{Mes}}\text{NC}$, and $\text{Na}[\text{BAr}^{\text{F}}_4]$ in diethyl ether, with KC_8 at -40 °C afforded selectively 1 containing some $\text{Ar}^{\text{Mes}}\text{NC}$ in 70% crude yield (Scheme 2). Compound 1 was isolated after crystallization from *n*-hexane as a dark purple, very air-sensitive solid in analytically pure form. It is thermally quite stable and melts upon heating to a purple liquid at $160–163$ °C with incipient decomposition releasing $\text{Ar}^{\text{Mes}}\text{NC}$ as the only identifiable product.

Compound 1 is the first neutral Si^0 -isocyanide compound to be reported and was fully characterized (SI, Section 2.1.2). The molecular structure of 1 was determined by an sc-XRD analysis of metallic shiny, green-blue crystals and features a cumulene-type, slightly bent $\text{Si}=\text{C}=\text{N}$ skeleton ($\angle(\text{Si}–\text{C}28–\text{N}3) =$

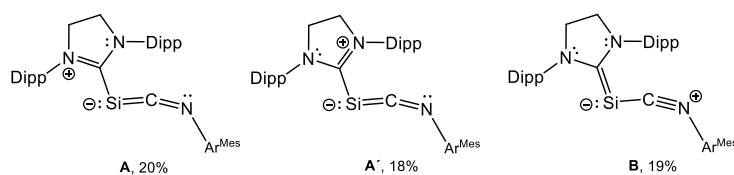


Figure 8. Main canonical forms of **1** and their weight percentage obtained from the NRT bonding analysis.

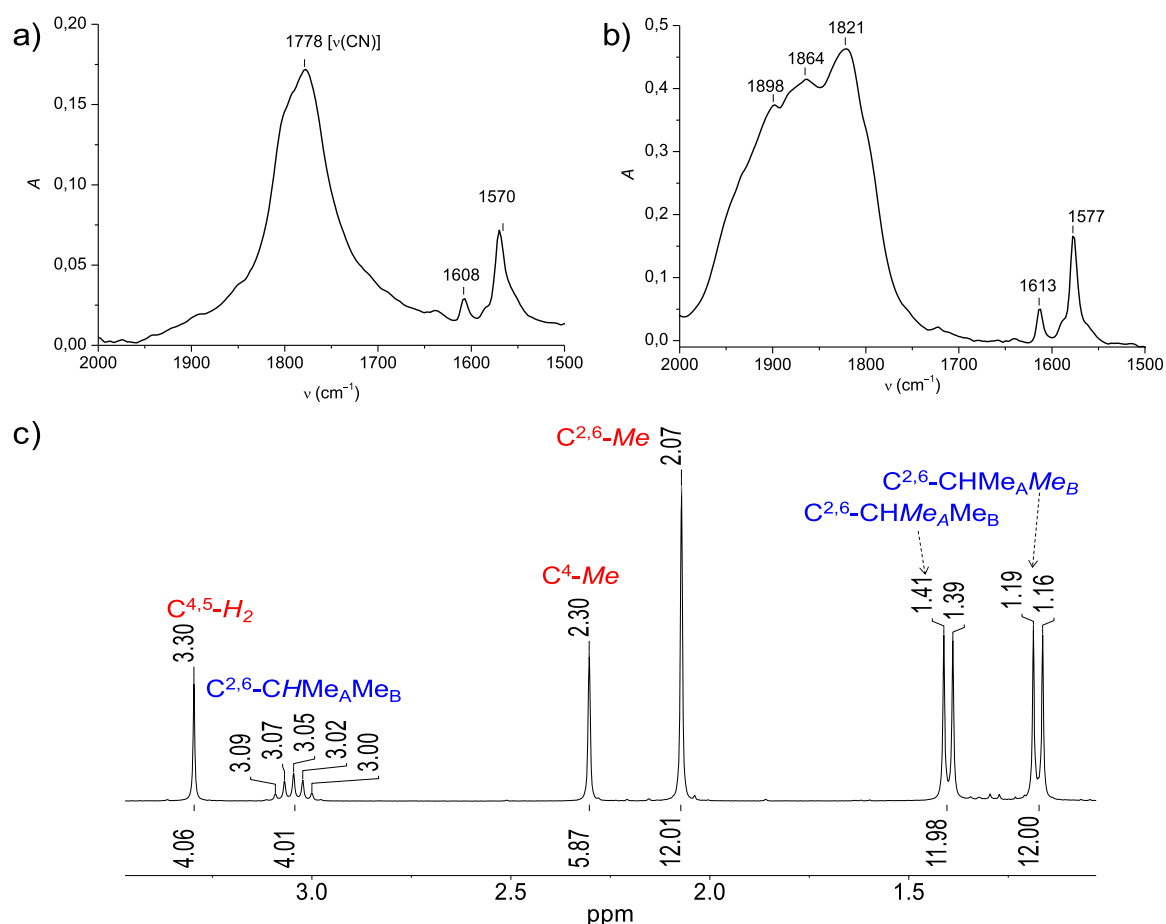


Figure 9. (a) Solid-state IR spectrum of **1** in the region 2000–1500 cm^{-1} . (b) IR spectrum of **1** in *n*-hexane solution in the region 2000–1500 cm^{-1} . (c) ^1H NMR spectrum (300.1 MHz, $\delta = 1.20\text{--}3.40$ ppm) of **1** in D_6 -benzene at 298 K showing the simple pattern of the alkyl proton signals due to fluxionality.

158.81(9) $^\circ$) with a V-shaped geometry at the dicoordinated silicon (Figure 7). The atoms C1, Si, C28, and N3 are *trans* arranged, as shown by the torsion angle C1–Si–C28–N3 of 173.8(2) $^\circ$. The bonding angle at silicon ($\angle(\text{C1–Si–C28}) = 100.40(5)^\circ$) is slightly larger than that in other NHC compounds of dicoordinated silicon, such as $\text{Si}_2(\text{IDipp})_2$ (93.37(5) $^\circ$, IDipp = C[N(Dipp)CH] $_2$),^{4a} $\text{Si}_2(\text{SIDipp})_2$ (93.07(5) $^\circ$),²³ [(IDipp)Si=SiR(IDipp)][B(Ar^F) $_4$] (95.34(6) $^\circ$ (R = H); 95.13(6) $^\circ$ (R = Me); 96.61(7) $^\circ$ (R = I)),^{4e,f} and (*Z*)-(SIDipp)Si=SiBr(Tbb) (97.6(1) $^\circ$, Tbb = C $_6$ H $_2$ -2,6-[CH(SiMe $_3$) $_2$] $_2$ -4^tBu),^{4d} suggesting the presence of a stereochemically active lone pair of electrons in a mainly *s*-type orbital, in line with the results of the quantum chemical studies (Section 2.3.1).

Salient structural parameters of **1** are (a) the conformation of the NHC and Ar^{Mes} substituents leading to axial chirality (Figure 7, right), (b) the short Si–C_{CNR} bond, the elongated C–N(Ar^{Mes}) bond, and the considerable bending of the C–N–C_R skeleton compared with that of free Ar^{Mes}NC and 2[B(Ar^F) $_4$], and (c) the shortened Si–C_{carbene} bond. In fact, the NHC and Ar^{Mes} substituents adopt an *antichiral* conformation, leading to axial chirality, with the chirality axis passing through the atoms Si and N3.²⁴ The two enantiomers, which are characterized with the stereodescriptors (*R_a*)-**1** and (*S_a*)-**1**, differ in the sign of the torsion angle C1–Si–N3–C29 ((*R_a*)-**1**: $-130.90(1)^\circ$, (*S_a*)-**1**: $+130.90(1)^\circ$) (Figure 7, right).²⁵ Notably, this spatial arrangement of the substituents in **1** is reminiscent of heteroallenes, i.e., carbodiimides,²⁶ ketenimines,²⁷ and 1-aza-3-phosphaallenes (RP=C=NR).²⁸

The Si–C_{CNR} bond of **1** (1.784(1) Å) is considerably shorter than a typical Si–C single bond (1.87–1.91 Å),²⁹ but longer than the Si=C bonds of silenes (1.69–1.76 Å),^{10a} 1-silaallenes (1.693(3)–1.704(4) Å),¹¹ and 1-silaketeniminyllithium compounds (1.725(4) and 1.730(2) Å)⁷ due to delocalization of the π electron density to the C_{NHC} atom, leading to a C_{NHC}–Si–C_{CNR} 3c-2e π_{oop} -bond in **1** (*vide infra*). Notably, the Si–C_{CNR} bond of **1** compares well with the Si–C bond lengths of the dialkylsilaketenimines [C(SiMe₃)₂CH₂]₂SiCNR ($d(\text{Si–C}) = 1.782(2)$ Å (R = 1-adamantyl), 1.794(3) Å (R = Dipp)), displaying considerable allenic character (Figure 3a).^{6b}

The C–N bond length of **1** (1.224(1) Å) lies in between the C \equiv N triple-bond length of nitrilium salts (1.115(3)–1.157(2) Å)^{19c,30} and the C=N bond lengths of imines (ca. 1.27 Å).³¹ It is considerably larger than the C \equiv N bond length of 2[B(Ar^F)₄] (1.150(5) Å) and free Ar^{Mes}NC (1.158(3) Å),¹⁸ but compares well with that of diarylcarbodiimides,^{26a} normal ketenimines ($d(\text{C–N}) = 1.20$ – 1.23 Å),²⁷ the 1-aza-3-phosphaallenes Mes*P=C=NR (1.209(4) Å, (R = Ph); 1.214(6) Å (R = *p*-chlorophenyl)),^{28a,b} and the dialkylsilaketenimines [C(SiMe₃)₂CH₂]₂SiCNR (R = 1-adamantyl: $d(\text{C–N}) = 1.210(3)$ Å; R = Dipp: $d(\text{C–N}) = 1.203(3)$ Å).^{6b} Also the angle at N ($\angle(\text{C28–N3–C29}) = 133.00(10)^\circ$) is considerably smaller than that in free Ar^{Mes}NC (178.1(3)^o)¹⁸ and 2[B(Ar^F)₄] (171.9(5)^o), but similar to that found in the 1-aza-3-phosphaallenes Mes*P=C=NR ($\angle(\text{C–N–C}) = 130.5^\circ$ (R = Ph), 128.3(4)^o (R = *p*-chlorophenyl)).^{28a,b} All structural features of **1** presented above suggest a considerable contribution of the heterocumulene canonical forms **A** and **A'** to the resonance hybrid (Figure 8). They are in line with the NBO and NRT bonding analyses yielding a much larger WBI and NRT-BO of the Si–C_{CNR} bond of **1** (WBI = 1.3, NRT-BO = 1.5) than that of 2⁺ (WBI = 0.9, NRT-BO = 1.0), but a smaller WBI and NRT-BO of the C–NAr^{Mes} bond of **1** (WBI = 1.9, NRT-BO = 2.3) than that of 2⁺ (WBI = 2.3, NRT-BO = 2.8) (*vide infra*).

Notably, the NHC plane is only slightly tilted out of the skeletal plane of **1** passing through the atoms C1, Si, C28, and N3, as shown by the angle between the two planes of 19.24(5)^o (Figure 7, right). This allows for a conjugation of the Si–C_{CNR} π_{oop} -bond (oop = out of the skeletal plane of **1**) with the C_{NHC}-centered acceptor p orbital, leading to a C_{NHC}–Si–C_{CNR} 3c-2e π_{oop} -bond and a shortening of the Si–C_{NHC} bond. In fact, the Si–C_{NHC} distance in **1** (1.894(1) Å) is not only shorter than those of the Si(II) compounds 2[B(Ar^F)₄] (1.977(4) Å) and 3[B(Ar^F)₄] (1.973(5) Å) but also shorter than those of the dicoordinated Si⁰-NHC compounds Si₂(IDipp)₂ (1.927(2) Å),^{4a} Si₂(SIDipp)₂ (1.924(2) Å),²³ and (Z)-(SIDipp)Si=SiBr(Tbb) (1.937(4) Å),^{4d} which all feature an orthogonal orientation of the NHC plane with respect to the C_{NHC}–Si–E (E = Si, P) core, preventing a π conjugation and the formation of a 3c-2e π -bond (SI, Section 5.1). The presence of Si–C_{NHC} π -bonding in **1** is confirmed by the results of the NRT analyses, revealing a considerable contribution of the canonical form **B** to the bonding in **1** (Figure 8) and a larger Si–C_{NHC} NRT total bond order in **1** (NRT–BO = 1.3) than that in Si₂(IDipp)₂ (NRT–BO = 1.0) or Si₂(SIDipp)₂ (NRT–BO = 1.0) (Section 2.3.1). Notably, the C_{NHC}–Si–C_{CNR} 3c-2e π_{oop} -bond of **1** is reminiscent of that of the siladibene Si(bNHC) (bNHC = bidentate N-heterocyclic carbene), which also features shortened Si–C_{NHC} bonds ($d(\text{Si–C}_{\text{carbene}}) = 1.864(1)$ and 1.874(1) Å).^{4b}

The most distinctive spectroscopic feature of **1** is the exceptional bathochromic shift of the CN stretching mode, which gives rise to a strong IR band in the solid state at 1778 cm⁻¹ (Figure 9a). In fact, the $\nu(\text{C}\equiv\text{N})$ absorption band of **1** is shifted by ca. 360 cm⁻¹ to lower wavenumbers with respect to that of 2[B(Ar^F)₄] ($\nu(\text{C}\equiv\text{N}) = 2143$ cm⁻¹), illustrating the profound influence of the two-electron reduction of 2⁺ on the Si–C_{CNR} bond. Notably, the $\nu(\text{C}\equiv\text{N})$ band of **1** appears also at considerably lower wavenumbers than that of the disilaketenimines [L(Br)Ga]₂Si(CNCy) ($\nu(\text{C}\equiv\text{N}) = 2093$ cm⁻¹, L = HC[C(Me)N(Dipp)]₂) and (SiMe₃)₃Si('Bu₃Si)-SiCNXy ($\nu(\text{C}\equiv\text{N}) = 1966$ cm⁻¹, Xy = 2,6-dimethylphenyl) reported recently.^{6d,e} In *n*-hexane solution, the $\nu(\text{C}\equiv\text{N})$ absorption band is broadened and shows several maxima between 1900 and 1800 cm⁻¹, suggesting extensive structural dynamics of **1** in solution (Figure 9b and Section 2.3.2).

Also the NMR spectra suggest a fluxional structure of **1** in solution. In fact, the ¹H NMR spectrum of **1** displays only two singlets for the methyl protons of the Ar^{Mes} substituent in the integral ratio of 6:12 and only two doublets for the methyl protons, one septet for the methine protons and one singlet for the methylene protons of the NHC group in the integral ratio of 12:12:4:4, respectively (Figure 9c). This is quite different from what would be expected for **1** in case of a rigid skeleton and retention of the axial chirality of **1** in solution, even if rotation of the Ar^{Mes} and NHC substituent about the respective N–C(Ar^{Mes}) and Si–C_{NHC} bonds is fast on the NMR time scale. The stereodynamic process causing the fluxionality could not be resolved by VT ¹H NMR spectroscopy of **1** in the temperature range 183–298 K in toluene-*d*₈. This observation is in line with the results of the analysis of the potential energy hypersurface (PES) at the B97-D3(BJ)-ATM/def2-TZVP level of theory (Section 2.3.2), which suggest that **1** is quite flexible, undergoing two dynamic processes with low barriers, rationalizing the simple ¹H NMR spectrum of **1** (Figure 9c). The first process involves a rotation of the Ar^{Mes} substituent about the N–C bond and proceeds via a barrier of ca. 16 kJ mol⁻¹ interconverting the enantiomers (R_a)-**1** and (S_a)-**1**. It is coupled with a linearization of the isocyanide at the N atom and skeletal flexing rendering the flanking Mes groups and their diastereotopic C²/C⁶ and C³/C⁵ positions chemically equivalent. The second process including a rotation of the NHC about the Si–C_{NHC} bond proceeds via a barrier of 41.0 kJ mol⁻¹ and leads to a site exchange of the diastereotopic N-Dipp groups.

The ¹³C NMR spectrum of **1** in D₆-benzene displays two characteristic signals for the Si-bonded C_{isocyanide} and C_{NHC} atoms at $\delta = 197.9$ and 210.8 ppm, respectively, which both appear at considerably higher frequency than those of 2[B(Ar^F)₄] ($\delta(\text{C}_{\text{CNR}}) = 167.7$ ppm; $\delta(\text{C}_{\text{NHC}}) = 183.7$ ppm). Both signals are flanked by a pair of Si satellites, yielding quite small ¹J(Si, C_{CNR}) and ¹J(Si, C_{NHC}) coupling constants of 9.5 and 27 Hz, respectively (SI, Figure S14).³² The strong deshielding of the C_{isocyanide} signal appears to be a common feature of compounds with pronounced azaallene structure.^{6e,7,27b,28a} The ²⁹Si{¹H} spectrum of **1** displays a distinctive, high-field shifted signal at $\delta = -141.8$ ppm. Interestingly, the ²⁹Si NMR chemical shift of **1** is very different from that of the siladibenes Si(bNHC) ($\delta_{\text{Si}} = -80.1$ ppm in D₆-benzene)^{4b} and Si(Pr₂Me₂)(caac^{Me}) ($\delta_{\text{Si}} = 2.04$ ppm; Pr₂Me₂ = C[N(Pr)C(Me)]₂, caac^{Me} = C[N(Dipp)-CMe₂CH₂CMe₂]),^{4h} but similar to those of the 1-silaketeniminyllithium compounds R₂B(Li)Si=C=NR' ($\delta_{\text{Si}} = -144.0$

Scheme 3. Synthesis of the NHC-Stabilized Germsilyne 4

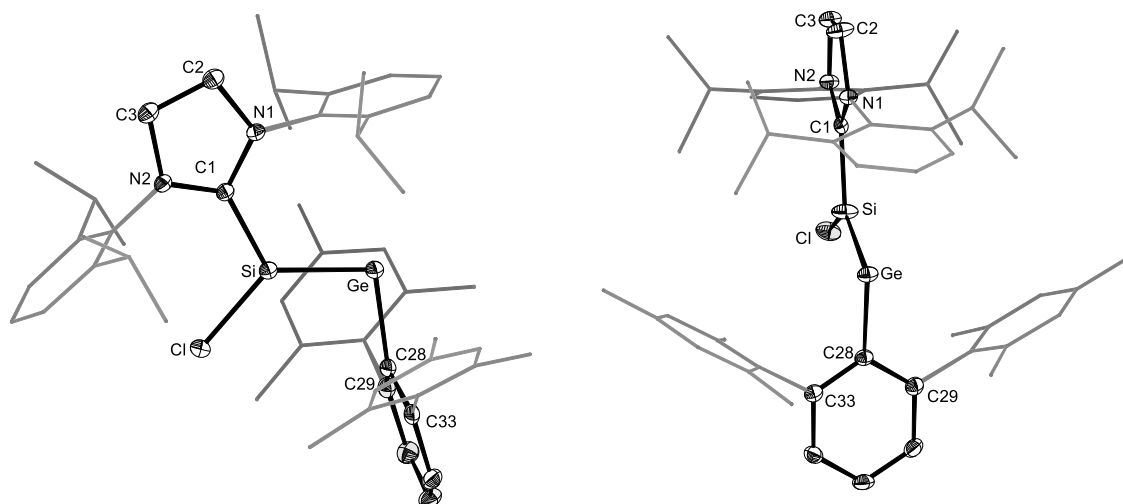
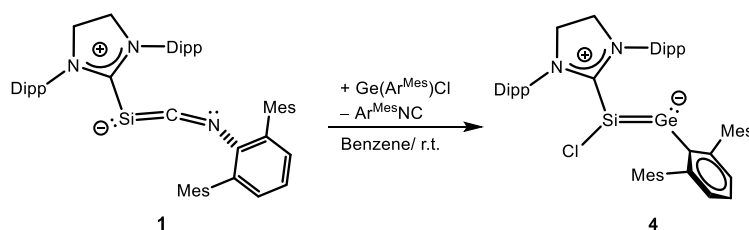


Figure 10. Top view of the planar skeleton of **4** (left) and side view of **4** along the Ge=Si bond (right); thermal ellipsoids are set at the 50% probability level, and hydrogen atoms were omitted. Bond lengths (Å), bond angles (deg), and torsion angles (deg) (the values in square brackets are of the second independent molecule found in the asymmetric unit): Si–Ge 2.2841(5) [2.2651(5)], Si–C1 1.877(2) [1.878(2)], Si–Cl 2.1027(6) [2.0921(6)], Ge–C28 2.024(2) [2.036(2)]; Ge–Si–C1 122.02(5) [122.14(5)], Ge–Si–Cl 130.81(2) [128.61(2)], C1–Si–Cl 107.11(5) [108.41(5)], Si–Ge–C28 100.87(5) [98.91(5)], Cl–Si–Ge–C28–3.25(6) [4.94(6)], C1–Si–Ge–C28–179.93(7) [173.21(8)].

($R' = 1$ -adamantyl), $\delta_{\text{Si}} = -162.4$ ($R' = \text{Dipp}$)).⁷ Notably, a comparison of the ^{29}Si NMR chemical shifts of silicon(0) NHC compounds shows that these span a range of ca. 400 ppm (SI, Section 5.1).

Compound **1** was also characterized by UV–vis–NIR spectroscopy. Its purple solutions in *n*-hexane display two intense absorption bands at $\lambda = 341$ nm ($\epsilon_{\lambda} = 1.37 \times 10^4$ L mol $^{-1}$ cm $^{-1}$) and 525 nm ($\epsilon_{\lambda} = 1.72 \times 10^4$ L mol $^{-1}$ cm $^{-1}$) as well as a weaker band at $\lambda = 670$ nm ($\epsilon_{\lambda} = 1.4 \times 10^3$ L mol $^{-1}$ cm $^{-1}$) (SI, Section 3).

Compound **1** features a HOMO at high energy ($E = -3.32$ eV at the B97-D3(BJ)-ATM/def2-TZVP level of theory) representing the $\text{C}_{\text{NHC}}\text{--Si--C}_{\text{CNR}}$ 3c-2e π_{oop} -bond (Section 2.3.1). This let us presume that **1** should easily undergo a one-electron oxidation and prompted us to study the redox properties of **1** by cyclic voltammetry. In fact, the cyclic voltammogram of **1** in fluorobenzene at room temperature reveals a quasi-reversible one-electron oxidation followed by a chemical reaction (EC process) at a half-wave potential $E_{1/2}$ of -469 mV versus the $[\text{Fe}(\eta^5\text{-C}_5\text{Me}_5)_2]^{1+/0}$ redox couple (SI, Section 4). The half-wave potential of **1** lies between those of $\text{Si}_2(\text{IDipp})_2$ ($E_{1/2}$ in 1,2-difluorobenzene = -794 mV) and $(\text{IDipp})\text{Si}=\text{PMes}^*$ ($E_{1/2}$ in 1,2-difluorobenzene = -53 mV).¹³ Notably, the difference in the oxidation potentials of **1** and $\text{Si}_2(\text{IDipp})_2$ of 325 mV reflects well the energy difference of the HOMOs of the two compounds (0.41 eV at the B97-D3(BJ)-ATM/def2-TZVP level of theory).

2.2. First Reactivity Studies of 1. Compound **1** proved to be also a powerful nucleophile enabling access to novel unsaturated silicon compounds. In fact, addition of $\text{Ge}(\text{Ar}^{\text{Mes}})\text{Cl}$ to a purple solution of **1** in toluene at ambient temperature was accompanied by an instantaneous color change to blue. Analysis of the reaction solution by ^1H NMR spectroscopy revealed the selective elimination of $\text{Ar}^{\text{Mes}}\text{NC}$ and formation of the NHC-stabilized germsilyne **4** (Scheme 3). The conversion of **1** to **4** presumably involves in the first step a Lewis base–acid adduct formation of **1** with $\text{Ge}(\text{Ar}^{\text{Mes}})\text{Cl}$, followed by chloride migration from the Ge to the Si center and elimination of $\text{Ar}^{\text{Mes}}\text{NC}$. It is an unprecedented reaction in monatomic silicon(0) chemistry, illustrating the synthetic potential of **1** as a $\text{Si}^0(\text{NHC})$ transfer reagent. In fact, several reactions of siladicalbenes (“silylones”) and related monatomic Si^0 compounds have been reported, but in none of them was a ligand elimination observed due to the rigid, chelating ligand scaffold of the silylones.³³ In this context, it is noteworthy that the reaction of **1** with $\text{Ge}(\text{Ar}^{\text{Mes}})\text{Cl}$ is reminiscent of those of the transition metal complexes $[\text{ML}_4(\text{N}_2)_2]$ ($M = \text{Mo}, \text{W}$; $L = \text{phosphane}$) with the organohalotetrylenes $\text{E}(\text{R})\text{X}$ ($\text{E} = \text{Ge} - \text{Pb}$, $\text{X} = \text{Cl-I}$, $\text{R} = \text{bulky alkyl or aryl group}$), affording the tetrylidyne complexes $\text{trans-}[\text{XL}_4\text{M}\equiv\text{ER}]$, which also involve a halide migration with concomitant elimination of a neutral 2e-donor ligand (N_2) to form a multiple bond.³⁴

Compound **4** is the first NHC-supported heteroditetrylene to be reported. It was isolated after crystallization from *n*-

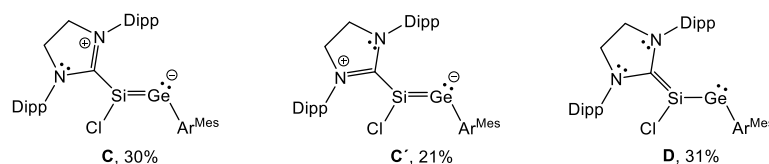


Figure 11. Main canonical forms of **4** and their weight percentage obtained from the NRT analysis.

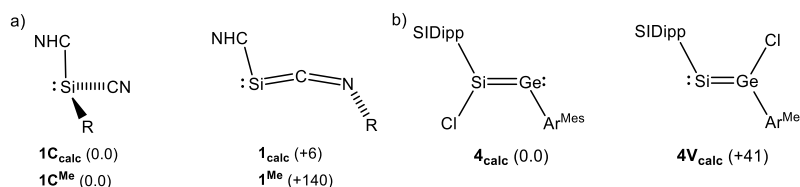


Figure 12. (a) Isomers of 1_{calc} (NHC = SIDipp, R = Ar^{Mes}) and the model system 1^{Me} (NHC = C[N(Me)CH₂]₂, R = Me). (b) Isomers of 4_{calc} . Relative energies are given in kJ mol⁻¹ in parentheses at the B97-D3(BJ)-ATM/def2-TZVP level of theory.

hexane in 44% yield as a blue, very air-sensitive crystalline solid, which turns immediately yellow upon exposure to air and decomposes upon heating at 100 °C to a black mass. Only three NHC-supported homonuclear ditetrylnes have been reported to date.³⁵ For comparison reasons several NHC-supported disilynes, Si₂(Tbb)₂(NHC) (NHC = IMe₄, IEt₂Me₂, IⁱPr₂Me₂), and digermynes, Ge₂R₂(IME₄) (R = Tbb, Si(C₆H₄-4-Me)(CH(SiMe₃)₂)₂), were also isolated and fully characterized in our group (SI, Section 5.2).

The solid-state structure of 4-0.5(n-C₆H₁₄) was determined by sc-XRD analysis of blue single crystals (Figure 10). Compound **4** features a planar core composed of the atoms Cl, Si, C1, Ge, and C28, in which a trigonal planar coordinated Si atom ($\sum(\angle\text{Si}) = 359.9^\circ$) is connected to a V-shaped dicoordinated Ge atom via a Si=Ge bond (2.275(9) Å).³⁶ Notably, the NHC five-membered ring is arranged coplanar to the core of the molecule, as evidenced by the dihedral angle φ_{NHC} of 6(2)° between the least-squares plane of the NHC ring and the plane passing through the atoms C1, Si, and Ge. Hence, compound **4** differs from all other NHC-supported ditetrylnes, in which the NHC groups are tilted out of the planar core of the molecules ($\varphi_{\text{NHC}} = 43.1(1)–86.4(2)^\circ$, SI, Section 5.2). This allows for a conjugation of the Si=Ge π -bond with the C_{NHC}-centered acceptor orbital and the formation of a 3c-2e π_{oop} -bond, leading to an elongation of the Si=Ge bond and a shortening of the Si–C_{NHC} bond in **4**. In fact, the Si=Ge bond length of **4** (2.275(9) Å) lies in the upper limit of reported Si=Ge bond lengths (2.214–2.276 Å)³⁷ and is also longer than the Si=Ge bond length (2.250(9) Å) calculated from the arithmetic mean of the average Si=Si bond length (2.200(9) Å) and Ge=Ge bond length (2.299(10) Å) of the presently known NHC-supported disilynes and digermynes, respectively (SI, Section 5.2). Similarly, the Si–C_{NHC} bond length of **4** (1.878(1) Å)³⁶ is shorter than the mean Si–C_{NHC} bond length (1.915(7) Å) of the NHC-supported disilynes. Notably, also the angle at the dicoordinated Ge atom of **4** ($\angle\text{Si–Ge–C28} = 100.87(5)^\circ$) is smaller than those found in the NHC-supported disilynes and digermynes (106.6(2)–120.35(2)°). All these structural features are in line with the NBO and NRT bonding analysis of **4** (see Section 2.3.1), suggesting a considerable contribution of the silagermyne canonical forms **C** and **C'** but also the silenylgermylene form **D** to the resonance hybrid (Figure 11).

Despite the presence of considerable π -bonding in the Si–C_{NHC} bond, rotation of the NHC about the Si–C_{NHC} bond is fast on the NMR time scale, leading to a rapid site exchange of the Dipp substituents and a single set of signals. This is in line with the quantum chemical calculations of the NHC rotational profile predicting a small barrier of only ca. 18 kJ mol⁻¹ for the NHC rotation (SI, Section 6.13). Compound **4** is distinguished by a ²⁹Si NMR signal at $\delta = 81.8$ ppm, which appears at lower field than those of (IME₄)(R)Si=SiR (R = SiⁱPr(CH(SiMe₃)₂)₂; $\delta = 28.7$ ppm,^{35a} R = Tbb; $\delta = 21.1$ ppm (SI, Section 5.2).

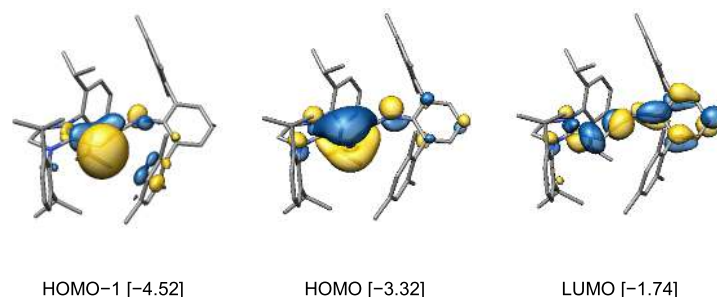
2.3. Quantum Chemical Studies. **2.3.1. Comparative Studies of the Electronic Structures of 1, 2⁺, and 4.** The electronic structures of compounds **1**, **2⁺**, and **4** were investigated by quantum chemical calculations at the B97-D3(BJ)-ATM/def2-TZVP level of theory (SI, Section 6). Geometry optimization afforded gas phase minimum structures (1_{calc} , 2^+_{calc} , and 4_{calc}) displaying bond lengths and angles in close agreement with **1**, **2⁺**, and **4**, respectively. Remarkably, 1_{calc} was not found to be the global minimum structure on the potential energy hypersurface (PES). In fact, a search for other isomers revealed that 1_{calc} is less stable by 6 kJ mol⁻¹ than the NHC-stabilized cyanosilylene $1^{\text{C}_{\text{calc}}}$ featuring a trigonal pyramidal coordinated Si atom ($\sum^\circ(\text{Si}) = 333^\circ$) and Si–C_{NHC}, Si–CN, and C–N bond lengths of 1.929, 1.863, and 1.168 Å, respectively (Figure 12a). The energy difference between the NHC-stabilized iminosilylenide and cyanosilylene isomer increases considerably to $\Delta E = +140$ kJ mol⁻¹ in the case of the model systems (SIME)Si(CN)Me ($1^{\text{C}_{\text{Me}}}$) and (SIME)Si=C=NMe (1^{Me}) featuring the sterically less demanding N-heterocyclic carbene C[N(Me)CH₂]₂ (SIME) bearing methyl substituents at the N atoms (Figure 12a). It can be rationalized with the larger repulsion between the sterically more demanding NHC and R substituents in $1^{\text{C}_{\text{calc}}}$ leading to a destabilization of $1^{\text{C}_{\text{calc}}}$ versus 1_{calc} . Notably, the same relative stability of the two isomers was found for the NHC-free species **I** and **V** (Figure 1).

Analysis of the PES of 4_{calc} afforded also another minimum structure, the NHC-stabilized gerasilylenylidene (*Z*)-(SIDipp)Si=GeCl(Ar^{Mes}) ($4^{\text{V}_{\text{calc}}}$), which appears, however, at higher energy ($\Delta E = +41$ kJ mol⁻¹) than 4_{calc} (Figure 12b). Notably, the opposite relative stability was found by DFT calculations at the B97-D3/TZVP level of theory for the related “disilicon” system, with the NHC-stabilized disilavinyl-

Table 1. Selected Results of the Natural Bond Orbital (NBO), Natural Resonance Theory (NRT), and Natural Population (NPA) Analyses of 1_{calc} , 2^+_{calc} , and 4_{calc}

NBO A–B	occ ^a	NHO (A,B) ^b hyb (pol in %)	WBI ^c A–B	NRT-BO ^d tot/cov/ion	atom/group	$q/\sum q^e$
1_{calc}						
$\sigma(\text{Si}-\text{C}_{\text{NHC}})$	1.92	$\text{sp}^{6.5}(23)$, $\text{sp}^{1.3}(77)$	1.0	1.3/0.7/0.6	Si	+0.40
$\sigma(\text{Si}-\text{C}_{\text{CNR}})$	1.96	$\text{sp}^{6.4}(24)$, $\text{sp}^{0.6}(76)$	1.3	1.5/0.9/0.6	C_{CNR}	-0.04
$\pi(\text{Si}-\text{C}_{\text{CNR}})$	1.57	p(47), p(53)			N_{CNR}	-0.45
$\sigma(\text{C}-\text{NR})$	1.99	$\text{sp}^{1.7}(35)$, $\text{sp}(65)$	1.9	2.3/1.5/0.8		
$\pi(\text{C}-\text{NR})$	1.91	p(34), p(66)				
Si(LP)	1.75	$\text{sp}^{0.4}$			CNR	-0.39
$\text{N}_{\text{CNR}}(\text{LP})$	1.55	$\text{sp}^{7.3}$			NHC	-0.01
$\text{C}_{\text{NHC}}(\text{LV})$	0.95	p				
2^+_{calc}						
$\sigma(\text{Si}-\text{C}_{\text{NHC}})$	1.92	$\text{sp}^{8.5}(23)$, $\text{sp}^{1.5}(77)$	0.7	1.0/0.5/0.5	Si	+0.69
$\sigma(\text{Si}-\text{C}_{\text{CNR}})$	1.96	$\text{sp}^{10.5}(23)$, $\text{sp}^{0.6}(77)$	0.9	1.0/0.5/0.6	C_{CNR}	+0.18
$\sigma(\text{C}-\text{NR})$	1.99	$\text{sp}^{1.6}(34)$, $\text{sp}^{0.9}(66)$	2.3	2.8/1.9/0.9	N_{CNR}	-0.33
$\pi_1(\text{C}-\text{NR})$	1.98	p(33), p(67)			Br	-0.30
$\pi_2(\text{C}-\text{NR})$	1.95	p(35), p(65)			CNR	+0.19
Si(LP)	1.76	$\text{sp}^{0.4}$			NHC	+0.42
4_{calc}						
$\sigma(\text{Si}-\text{C}_{\text{NHC}})$	1.95	$\text{sp}^{2.9}(25)$, $\text{sp}^{1.4}(75)$	1.0	1.3/0.7/0.6	Si	+0.53
$\pi(\text{Si}-\text{C}_{\text{NHC}})$	1.59	p(57), p(43)			Ge	+0.29
$\sigma(\text{Si}-\text{Ge})$	1.93	$\text{sp}^{0.8}(63)$, $\text{sp}^{9.8}(37)$	1.4	1.5/1.0/0.5	Cl	-0.40
$\sigma(\text{Si}-\text{Cl})$	1.98	$\text{sp}^{4.3}(24)$, $\text{sp}^{3.0}(76)$		1.0/0.5/0.5	NHC	+0.06
Ge(LP)	1.89	$\text{sp}^{0.2}$			Ar^{Mes}	-0.48

^aOcc = occupancy. ^bNHO = natural hybrid orbital, pol (polarization) = $(C_i)^2 \times 100\%$, where C_i = coefficient of NHO. ^cWiberg bond index. ^dTotal, covalent, and ionic NRT bond order. ^e q = NPA charge of the atom, $\sum q$ = total NPA charge of the group.

**Figure 13.** Selected Kohn–Sham molecular orbitals of 1_{calc} and their energy eigenvalues in eV; isosurface value = $0.04 \text{ e}^{1/2} \text{ bohr}^{-3/2}$.

lidene (*Z*)-(NHC)Si=Si(Br)R (NHC = C[N(C₆H₃-2,6-Me₂)CH₂]₂, R = C₆H₃-2,6-[CH(SiH₃)₂]₂) being more stable by 33 kJ mol⁻¹ than the NHC-stabilized bromodisilyne (*Z*)-(NHC)(Br)Si=SiR.^{4d}

Natural bond orbital analysis of the wave function of 1_{calc} led to a leading natural Lewis structure (NLS) with localized bond pair NBOs for the Si–C_{NHC}, Si–C_{CNR}, and C–NR σ -bonds as well as one $\pi(\text{C}-\text{NR})$ bond featuring a high Lewis occupancy above 1.90e (Table 1). Both the Si–C_{NHC} and Si–C_{CNR} σ -bonds are strongly polarized toward the carbon atoms (77% (C_{NHC}), 76% (C_{CNR})) and are formed from Si natural hybrid orbitals (NHOs) with a very high p-character (87%), whereas the $\sigma(\text{C}-\text{NR})$ and $\pi(\text{C}-\text{NR})$ bonds are polarized toward the N atom (ca. 65%). Considerable delocalization is evidenced by the low Lewis occupancy of the $\pi_{\text{oop}}(\text{Si}-\text{C}_{\text{CNR}})$ NBO with 1.57e, which is slightly polarized toward the C_{CNR} atom (53%), the presence of a lone vacant (LV) NBO of pure p-character at the C_{NHC} atom with an occupancy of 0.95e, and a second-order perturbation energy (SOPE) of 53 kJ mol⁻¹ between the donor $\pi_{\text{oop}}(\text{Si}-\text{C}_{\text{CNR}})$ NBO and the acceptor LV-NBO at the C_{NHC}

atom. This delocalization is also manifested in the corresponding natural localized molecular orbital (NLMO) showing a considerable contribution of the $\pi_{\text{oop}}(\text{Si}-\text{C}_{\text{CNR}})$ NBO (71%) and of a C_{NHC} p-NAO (24%) (NAO: natural atomic orbital). Additional delocalization is provided by the low Lewis occupancy of 1.55e of the LP (lone pair) NBO at the N_{isocyanide} atom featuring a high p-character (88%), a SOPE (LP-(N_{isocyanide}) \rightarrow $\pi^*_{\text{oop}}(\text{Si}-\text{C}_{\text{CNR}})$) of 51 kJ mol⁻¹, and a significant non-Lewis occupancy of 0.32e of the $\pi^*_{\text{oop}}(\text{Si}-\text{C}_{\text{CNR}})$ NBO pointing to a 3c-4e π -bond (hyperbond) in the Si=C=N skeleton. Finally, the leading NBO Lewis structure of 1_{calc} features an LP-NBO at the Si atom of high s-character (71%) with an electron occupancy of 1.75e, which according to second-order perturbation analysis results from electron delocalization into the $\pi^*_{\text{in}}(\text{C}-\text{NR})$ with a SOPE energy of 293 kJ mol⁻¹ contributing to a non-Lewis occupancy of the $\pi^*_{\text{in}}(\text{C}-\text{NR})$ NBO of 0.30e. The corresponding NLMO shows consequently an 87% contribution of the LP-NBO (Si) and 10% contribution of the respective N and C p-NAOs.

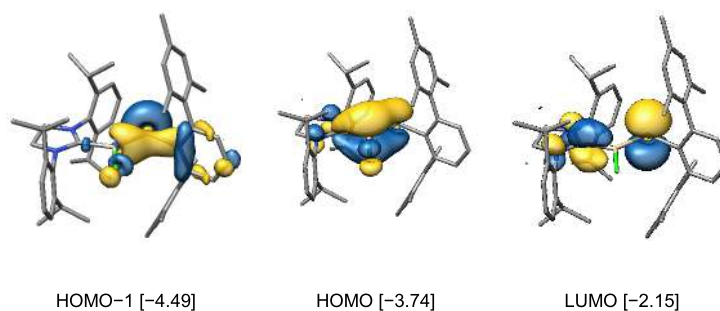


Figure 14. Selected Kohn–Sham molecular orbitals of 4_{calc} and their energy eigenvalues in eV; isosurface value = $0.04 \text{ e}^{1/2} \text{ bohr}^{-3/2}$.

All these results are reflected in the frontier orbitals of 1_{calc} with the HOMO–1 being the lone pair orbital at Si with some $\pi^*_{\text{in}}(\text{C}–\text{NR})$ contribution, the HOMO representing the $3c-2e \pi^*_{\text{oop}}(\text{C}_{\text{NHC}}–\text{Si}–\text{C}_{\text{CNR}})$ -bond with considerable $\pi^*_{\text{oop}}(\text{C}–\text{NR})$ contribution, and the LUMO being mainly the $\pi^*_{\text{oop}}(\text{Si}–\text{C}–\text{NR})$ -bond (Figure 13). This is also in line with the results of an NRT analysis of 1_{calc} giving an overall 38% weight of NLS containing a $\text{Si}=\text{C}=\text{NR}$ skeleton (cf. A and A', Figure 8) and a 19% weight of NLS containing a $\text{C}_{\text{NHC}}=\text{Si}–\text{C}\equiv\text{NR}$ skeleton (cf. B, Figure 8). Notably, natural population analysis reveals a considerable charge transfer from the Si(SIDipp) to the $\text{Ar}^{\text{Mes}}\text{NC}$ part in 1_{calc} , leading to a high negative NPA charge in the isocyanide group ($q(\text{Ar}^{\text{Mes}}\text{NC}) = -0.39$) that is mainly accumulated on the Si-bonded $\text{C}_{\text{isocyanide}}$ atom ($1_{\text{calc}}: q(\text{C}_{\text{NAr}^{\text{Mes}}}) = -0.04$; free $\text{Ar}^{\text{Mes}}\text{NC}: q(\text{C}_{\text{NAr}^{\text{Mes}}}) = +0.29$). In comparison, the SIDipp group is almost electroneutral in 1_{calc} ($q(\text{SIDipp}) = -0.01$), leading to a much higher positive NPA charge at Si ($q(\text{Si}) = +0.40$) than that found in Si(bNHC) ($q(\text{Si}) = +0.19$, $\text{bNHC} = \text{H}_2\text{C}[\text{NC}(\text{H})\text{C}(\text{H})\text{N}(\text{H})\text{C}]_2$).^{4b}

An additional insight into the chemical bonding of 1_{calc} was provided by analyzing the Si– C_{CNR} bond formation using the ETS-NOCV method (SI, Section 6.3). Notably, the total orbital interaction energy contributes 42% to the overall attractive interaction energy between the fragments (SIDipp)Si and $\text{C}_{\text{NAr}^{\text{Mes}}}$ in the singlet state and is composed of mainly two contributions, the first one involving a donation of $0.74e$ from the C-centered lone pair of the $\text{Ar}^{\text{Mes}}\text{NC}$ fragment into the vacant Si-centered σ -symmetric orbital of the Si(SIDipp) fragment ($\Delta E_{\text{orb}(1)} = -136.2 \text{ kJ mol}^{-1}$) and the second one involving a rather strong back-donation ($\Delta E_{\text{orb}(2)} = -219.5 \text{ kJ mol}^{-1}$) of $0.93e$ from the $\pi(\text{Si}–\text{C}_{\text{NHC}})$ bonding orbital into the $\pi^*_{\text{oop}}(\text{C}\equiv\text{NAr}^{\text{Mes}})$ antibonding orbital.

The NBO analysis of 2^+_{calc} yielded a leading NLS with localized bond pair NBOs for the $\sigma(\text{Si}–\text{C}_{\text{NHC}})$, $\sigma(\text{Si}–\text{C}_{\text{CNR}})$, $\sigma(\text{C}–\text{NR})$, and the two $\pi(\text{C}–\text{NR})$ bonds having a high Lewis occupancy ($>1.90e$), as well as an LP-NBO at the silicon atom with a similar Lewis occupancy ($1.75e$) and s-character (71%) to 1_{calc} (Table 1). This is in line with the results of NRT analysis pointing to a main contribution of NLS featuring a Si– C_{NHC} and Si– C_{CNR} single bond, a $\text{C}\equiv\text{NR}$ bond, and a lone pair of electrons at Si to the resonance hybrid (78% weight of the NLS, SI, Section 6.7). NPA analysis indicates, different from 1_{calc} , a considerable charge flow from the $\text{Ar}^{\text{Mes}}\text{NC}$ and the NHC groups to the electrophilic Si^{II} atom ($q(\text{Si}) = +0.69$) of 2^+_{calc} , leading to a depletion of electron density in both groups ($q(\text{Ar}^{\text{Mes}}\text{NC}) = +0.19$; $q(\text{NHC}) = +0.42$). The quite different electronic structures of 2^+_{calc} and 1_{calc} are finally evidenced in the quite different NRT bond orders of their Si– C_{CNR} and Si– C_{NHC} bonds (Table 1).

A combined NBO and NPA analysis provided also a thorough insight into the electronic structure of 4_{calc} (Table 1). The leading NBO Lewis structure features localized bond pair NBOs for the Si– C_{NHC} , Si–Ge, and Si–Cl σ -bonds and an LP-NBO at the Ge atom with high Lewis occupancies close to or above $1.90e$. Notably the Si–Ge σ -bond is polarized toward the Si atom (63%) and is formed from an $\text{sp}^{0.8}$ Si-NHO and an almost pure p-NHO (Ge). Considerable delocalization is evidenced by the low Lewis occupancy ($1.59e$) of the $\pi^*_{\text{oop}}(\text{Si}–\text{C}_{\text{NHC}})$ NBO, which is slightly polarized toward the Si atom (57%), the presence of an LV-NBO of pure p-character at the Ge atom with a non-Lewis occupancy of $0.53e$, and a SOPE ($\pi^*_{\text{oop}}(\text{Si}–\text{C}_{\text{NHC}}) \rightarrow \text{LV}(\text{Ge})$) of 32 kJ mol^{-1} . This delocalization is also shown in the corresponding NLMO, revealing a 78% contribution of the $\pi^*_{\text{oop}}(\text{Si}–\text{C}_{\text{NHC}})$ NBO and 20% contribution of the p-NAO (Ge). The NBO results are reflected in the frontier orbitals of 4_{calc} (Figure 14). The HOMO–1 contains mainly the lone pair at the Ge atom, the HOMO corresponds to the $3c-2e \pi^*_{\text{oop}}(\text{C}_{\text{NHC}}–\text{Si}–\text{Ge})$ -bond, and the LUMO corresponds to the empty p^*_{oop} orbital at the Ge atom with some antibonding $\pi^*_{\text{oop}}(\text{Si}–\text{C}_{\text{NHC}})$ contribution. The NRT analysis of 4_{calc} points, in line with the NBO analysis, to a major contribution of the NLS C and C' (total weight = 51%) and a minor contribution of the NLS D (31% weight) to the resonance hybrid, leading to a Si–Ge NRT-BO of 1.5 and a Si– C_{NHC} NRT-BO of 1.3 (Figure 11, Table 1). NPA analysis of 4_{calc} indicates a considerable charge flow from the Si(Cl)(NHC) to the GeAr^{Mes} fragment, leading to a negative NPA charge of the GeAr^{Mes} group ($q(\text{GeAr}^{\text{Mes}}) = -0.19$).

In order to explore the potential involvement of **1** in dissociative processes, the SIDipp and $\text{Ar}^{\text{Mes}}\text{NC}$ ligand dissociation energies of 1_{calc} were calculated at the B97-D3(BJ)-ATM/def2-TZVP level of theory (SI, Section 6.14). NHC dissociation from 1_{calc} requires a considerable energy of $\Delta E_{\text{el}} = 252.6 \text{ kJ mol}^{-1}$. The resulting iminosilylidene fragment $\text{SiC}_{\text{NAr}^{\text{Mes}}}$ has a triplet ground state with a $\Delta E_{\text{t}\rightarrow\text{s}}$ gap of $+48.5 \text{ kJ mol}^{-1}$ and features similar structural parameters to the parent species $^3[\text{SiCNH}]$ (SI, Figure S68).^{2a,b} The Si– C_{NHC} bond dissociation energy of 1_{calc} compares well with that of the Si^0 compound $\text{Si}_2(\text{SIDipp})_2$ ($246.3 \text{ kJ mol}^{-1}$) and lies in between those of the Si^{II} compound $\text{SiBr}_2(\text{SIDipp})$ ($189.5 \text{ kJ mol}^{-1}$) and 2^+_{calc} ($366.9 \text{ kJ mol}^{-1}$). $\text{Ar}^{\text{Mes}}\text{NC}$ dissociation from 1_{calc} requires also a considerable energy of $216.9 \text{ kJ mol}^{-1}$ and leads to the fragment $[\text{Si}(\text{SIDipp})]$ featuring like $[\text{SiC}_{\text{NAr}^{\text{Mes}}}]$ a triplet ground state with a $\Delta E_{\text{t}\rightarrow\text{s}}$ gap of $+19.4 \text{ kJ mol}^{-1}$. The Si– C_{CNR} dissociation energy of 1_{calc} is similar to that of 2^+_{calc} ($210.2 \text{ kJ mol}^{-1}$), suggesting that $\text{Ar}^{\text{Mes}}\text{NC}$ displacement reactions, such as the conversion of **1** to **4** (Scheme 3) and $2[\text{B}(\text{Ar}^{\text{F}})_4]$ to

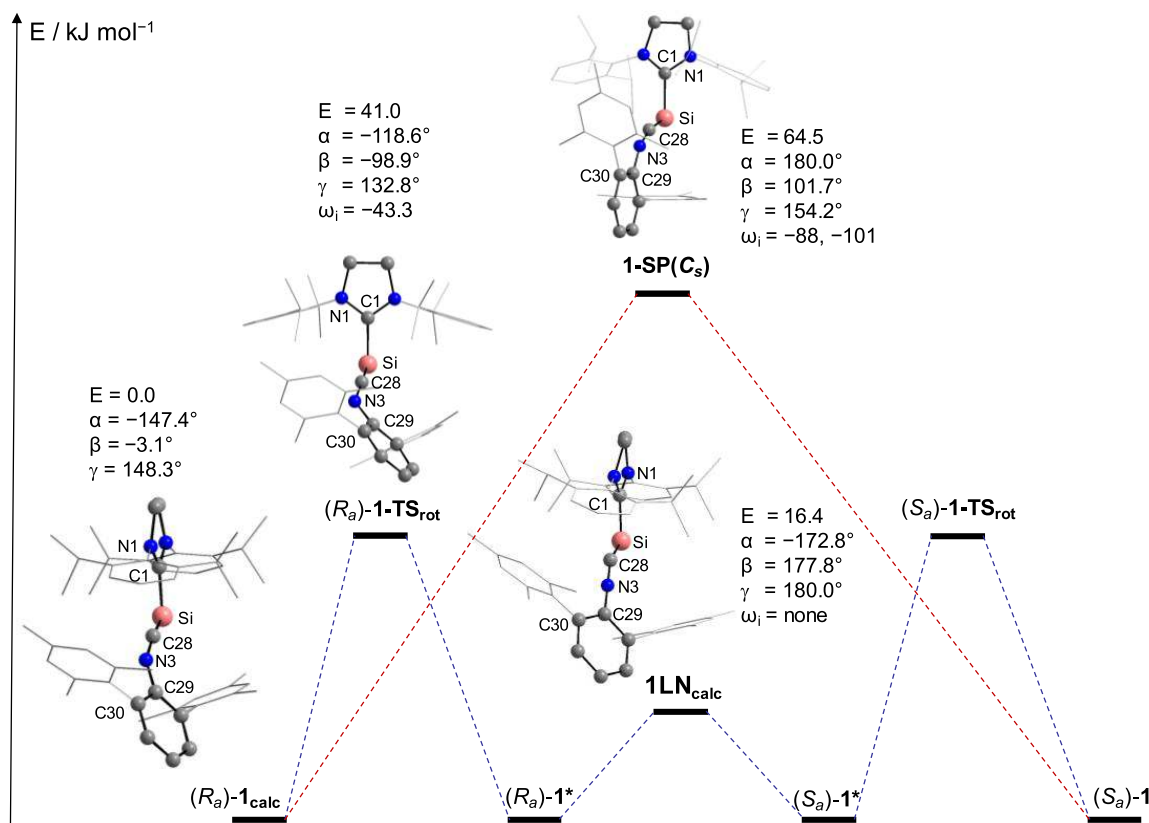


Figure 15. Proposed mechanism for the stereodynamics of 1_{calc} ; ω_i = harmonic imaginary frequencies in cm^{-1} , E = energy versus $(R_a)-1_{\text{calc}}$ in kJ mol^{-1} , α : skeletal torsion angle C1–Si–N3–C29, β : NHC torsion angle N1–C1–Si–C28, γ : angle C28–N3–C29.

$3[\text{B}(\text{Ar}^{\text{F}})_4]$ (Scheme 1), which occur rapidly even below room temperature, most probably follow associative pathways.

2.3.2. Computational Study of the Stereodynamics of 1_{calc} Several relaxed PES scans of 1_{calc} were carried out to rationalize the stereodynamics of **1** (SI, Section 6.15). A scan of the PES by varying the N1–C1–Si–C28 torsion angle (β) shows that rotation of the NHC about the Si–C_{NHC} bond proceeds via the chiral transition state $(R_a)-1\text{-TS}_{\text{rot}}$ (Figure 15) with an energy barrier of 41.0 kJ mol^{-1} to give the topomer $(R_a)-1^*$, in which the diastereotopic N-Dipp groups have exchanged their position. This diastereotopomerization process does not interconvert the enantiomers $(R_a)-1$ and $(S_a)-1$, though, and therefore does not lead to an exchange of the diastereotopic C² and C⁶ or C³ and C⁵ positions of the Dipp substituents (SI, Figure S73, green squares), which requires a C_s symmetric transition state with the symmetry plane passing through the C1–Si–C28–N3 skeletal plane.

Therefore, a second process was presumed to be operative, which was analyzed by PES scans involving a variation of the torsion angle Si–N3–C29–C30 (τ), i.e., a rotation of the Ar^{Mes} group about the N3–C29 bond. A maximum barrier of 12.7 kJ mol^{-1} was found showing that rotation of the Ar^{Mes} group about the N3–C29 bond occurs easily (SI, Figure S74, black circles). Notably, a close inspection of the structural parameters of the single-point structures at each scan step revealed only a slight twisting of the NHC out of the C1–Si–C28–N3 skeleton but not a full rotation. Furthermore, a concomitant increase of the angle γ (C28–N3–C29) toward

linearity ($\gamma = 170.9^\circ$) was observed upon decrease of the torsion angle τ from 180° to 100° (SI, Figure S74, blue triangles), as well as a change of the skeletal torsion angle C1–Si–N3–C29 (α) from -130° to -177° , indicating that the skeleton C1–Si–N3–C29 approaches an *antiperiplanar* conformation. This let us presume that enantiomerization of $(R_a)-1_{\text{calc}}$ might be connected with a linearization of the isocyanide moiety at the N atom and concomitant antiperiplanar conformation of the C1–Si–N3–C29 skeleton. In fact, a search of the PES gave an N-linear conformer 1LN_{calc} ($\alpha = -172.8^\circ$, $\beta = 3.26^\circ$, $\gamma = 180.0^\circ$) as a local minimum structure, which lies 16.4 kJ mol^{-1} higher in energy than $(R_a)-1_{\text{calc}}$ and features an almost free rotation of the Ar^{Mes} about the N3–C29 bond interconverting the enantiomers (Figure 15). Attempts to find the transition state connecting $(R_a)-1^*$ with 1LN_{calc} failed due to the flatness of the hypersurface.

Finally, a coupled (concomitant) process of NHC rotation (topomerization) and enantiomerization ($(R_a)-1 \rightleftharpoons (S_a)-1$) via a structurally constrained C_s symmetric species **1-SP** ($\alpha = 180^\circ$, $\beta = 101.7^\circ$) was found to be energetically highly unfavorable, as it is a second-order saddle point in the PES of $(R_a)-1_{\text{calc}}$ with two significant imaginary frequencies of -88 and -101 cm^{-1} and lies at 64.5 kJ mol^{-1} higher in energy relative to $(R_a)-1_{\text{calc}}$ (Figure 15). The above studies suggest that the stereodynamics of **1** proceeds stepwise via an NHC rotation and Ar^{Mes} rotation, the latter being coupled with an $(R_a)-1$ to $(S_a)-1$ interconversion (racemization) via the N-linear conformer 1LN_{calc} .

3. CONCLUSION

A systematic approach to the NHC-supported iminosilylenylidene (SIDipp)Si=C=NAr^{Mes} (**1**: SIDipp (NHC) = C[N-(Dipp)CH₂]₂, Ar^{Mes} = 2,6-dimesitylphenyl) was developed starting from SiBr₂(NHC). It involves in the key step a 2e reduction of the isocyanide-stabilized silyliumylidene salt [SiBr(CNAr^{Mes})(NHC)][B(Ar^F)₄] (2[B(Ar^F)₄], Ar^F = C₆H₃-3,5-(CF₃)₂), which was obtained from SiBr₂(NHC) upon bromide abstraction with Na[B(Ar^F)₄] in the presence of Ar^{Mes}NC. Comparative, comprehensive structural, spectroscopic, and quantum chemical studies provided a thorough insight into the unusual structure of the unprecedented silacumulene **1**, which is quite different from that of its precursor **2**⁺ and features an almost planar C_{NHC}-Si-C-N skeleton with a V-shaped geometry at the dicoordinated Si atom, a slightly bent Si=C=N core, and a C_{NHC}-Si-C_{CNR} 3c-2e out-of-plane π -bond. The *antitlinal* conformation of the NHC and Ar^{Mes} substituents leads to axial chirality and the presence of two enantiomers (*R_a*)-**1** and (*S_a*)-**1** differing in the sign of the torsion angle C_{NHC}-Si-N-C(Ar^{Mes}). Due to its flexible skeleton, compound **1** displays structural dynamics in solution interconverting rapidly the enantiomers (*R_a*)-**1** and (*S_a*)-**1**. Compound **1**, which can be strikingly viewed as a Si⁰ isocyanide compound, features a high electron density at silicon, leading to a low redox potential. Most appealing is, however, the synthetic potential of **1** as a Si⁰(NHC) transfer reagent in oxidative additions demonstrated in the present work by its selective conversion with Ge(Ar^{Mes})Cl to the NHC-supported silagermyne (Z)-(NHC)(Cl)Si=GeAr^{Mes} belonging to a novel class of Si=Ge compounds.

■ ASSOCIATED CONTENT

SI Supporting Information

The Supporting Information is available free of charge at <https://pubs.acs.org/doi/10.1021/jacs.1c06628>.

Syntheses, properties, spectroscopic and analytical data, illustrations of the IR, ¹H NMR, ¹³C{¹H} NMR, and ²⁹Si{¹H} NMR spectra of compounds **1**, 2[B(Ar^F)₄], 3[B(Ar^F)₄], and **4**, cyclic voltammetry studies and UV-vis spectra of **1**, crystallographic data and structure refinement parameters of **1-4**·0.5(*n*-C₆H₁₄), and details of the quantum chemical calculations (PDF)

Cartesian coordinates of the calculated structures (TXT)

Accession Codes

CCDC 1973825–1973826 and 2035005–2035006 contain the supplementary crystallographic data for this paper. These data can be obtained free of charge via www.ccdc.cam.ac.uk/data_request/cif, or by emailing data_request@ccdc.cam.ac.uk, or by contacting The Cambridge Crystallographic Data Centre, 12 Union Road, Cambridge CB2 1EZ, UK; fax: +44 1223 336033.

■ AUTHOR INFORMATION

Corresponding Authors

Ujjal Das – Institute of Inorganic Chemistry, University of Bonn, D-53121 Bonn, Germany; orcid.org/0000-0002-1895-5767; Email: udas@uni-bonn.de

Alexander C. Filippou – Institute of Inorganic Chemistry, University of Bonn, D-53121 Bonn, Germany; orcid.org/0000-0002-6225-8977; Email: filippou@uni-bonn.de

Authors

Surendar Karwasara – Institute of Inorganic Chemistry, University of Bonn, D-53121 Bonn, Germany

Leonard R. Maurer – Institute of Inorganic Chemistry, University of Bonn, D-53121 Bonn, Germany; orcid.org/0000-0003-2433-1130

Benjamin Peerless – Institute of Inorganic Chemistry, University of Bonn, D-53121 Bonn, Germany; orcid.org/0000-0002-5387-5842

Gregor Schnakenburg – Institute of Inorganic Chemistry, University of Bonn, D-53121 Bonn, Germany

Complete contact information is available at:

<https://pubs.acs.org/doi/10.1021/jacs.1c06628>

Notes

The authors declare no competing financial interest.

■ ACKNOWLEDGMENTS

This publication is dedicated to Professor Werner R. Thiel on the occasion of his 60th birthday. We thank the Rheinische Friedrich-Wilhelms Universität Bonn for the financial support of this work. We are very grateful to the Fonds of the Chemical Industry (FCI) for the financial support of L.R.M. with a Kekulé Fellowship. We also thank Maximilian Bogner for the cyclic voltammetry studies, Andreas Lülldorf for the UV-vis studies, and Mrs. Kühnel-Lysek, Mrs. Anna Martens, Mrs. Hannelore Spitz, Dipl.-Ing. Karin Prochnicki, and Mrs. Charlotte Rödde for their contributions to the elemental analyses, NMR measurements, and single-crystal X-ray diffraction studies.

■ REFERENCES

- (1) (a) Maier, G.; Reisenauer, H. P.; Egenolf, H.; Glatthaar, J. Reaction of Silicon Atoms with Hydrogen Cyanide: Generation and Matrix-Spectroscopic Identification of CHNSi and CNSi Isomers. *Eur. J. Org. Chem.* **1998**, *1998*, 1307. (b) Sanz, M. E.; McCarthy, M. C.; Thaddeus, P. Laboratory Detection of HSiCN and HSiNC. *Astrophys. J.* **2002**, *577*, L71. (c) McCarthy, M. C.; Gottlieb, C. A.; Thaddeus, P. Silicon molecules in space and in the laboratory. *Mol. Phys.* **2003**, *101*, 697. (d) Evans, C. J.; Dover, M. R. Spectroscopic Investigation of the Electronic $\tilde{A}^1A' - \tilde{X}^1A'$ Transition of HSiNC. *J. Phys. Chem. A* **2009**, *113*, 8533.
- (2) (a) Flores, J. R.; Pérez-Juste, I.; Carballeira, L. A theoretical study of the SiCNH isomers. *Chem. Phys.* **2005**, *313*, 1. (b) Wang, Q.; Ding, Y.; Sun, C. Potential energy surface study of [H, Si, C, N] and its ions. *Chem. Phys.* **2006**, *323*, 413. (c) Thorwith, S.; Harding, M. E. Coupled-cluster calculations of C₂H₂Si and CNHSi structural isomers. *J. Chem. Phys.* **2009**, *130*, 214303.
- (3) (a) Lembke, R. R.; Ferrante, R. F.; Weltner, W., Jr. SiCO, SiN₂, and Si(CO)₂ Molecules: Electron Spin Resonance and Optical Spectra at 4 K. *J. Am. Chem. Soc.* **1977**, *99*, 416. (b) Petraco, N. D. K.; Brown, S. T.; Yamaguchi, Y.; Schaefer, H. F., III The silaketenylidene (SiCO) molecule: Characterization of the $\tilde{X}^3\Sigma^-$ and $\tilde{A}^3\Pi$ states. *J. Chem. Phys.* **2000**, *112*, 3201.
- (4) (a) Wang, Y.; Xie, Y.; Wei, P.; King, R. B.; Schaefer, H. F., III; Schleyer, P. v. R.; Robinson, G. H. A Stable Silicon(0) Compound with a Si=Si Double Bond. *Science* **2008**, *321*, 1069. (b) Xiong, Y.; Yao, S.; Inoue, S.; Epping, J. D.; Driess, M. A Cyclic Silylone ("Siladibene") with an Electron-Rich Silicon(0) Atom. *Angew. Chem., Int. Ed.* **2013**, *52*, 7147; *Angew. Chem.* **2013**, *125*, 7287. (c) Arz, M. I.; Straßmann, M.; Meyer, A.; Schnakenburg, G.; Schiemann, O.; Filippou, A. C. One-Electron Oxidation of a Disilicon(0) Compound: An Experimental and Theoretical Study of [Si₂]⁺ Trapped by N-Heterocyclic Carbenes. *Chem. - Eur. J.* **2015**, *21*, 12509. (d) Ghana, P.; Arz, M. I.; Das, U.; Schnakenburg, G.; Filippou,

- A. C. Si=Si Double Bonds: Synthesis of an NHC-Stabilized Disilavinylidene. *Angew. Chem., Int. Ed.* **2015**, *54*, 9980; *Angew. Chem.* **2015**, *127*, 10118. (e) Arz, M. I.; Geiß, D.; Straßmann, M.; Schnakenburg, G.; Filippou, A. C. Silicon(I) chemistry: the NHC-stabilised silicon(I) halides $\text{Si}_2\text{X}_2(\text{Idipp})_2$ (X = Br, I) and the disilicon(I)-iodido cation $[\text{Si}_2(\text{I})(\text{Idipp})_2]^+$. *Chem. Sci.* **2015**, *6*, 6515. (f) Arz, M. I.; Straßmann, M.; Geiß, D.; Schnakenburg, G.; Filippou, A. C. Addition of Small Electrophiles to N-Heterocyclic-Carbene-Stabilized Disilicon(0): A Revisit of the Isolobal Concept in Low-Valent Silicon Chemistry. *J. Am. Chem. Soc.* **2016**, *138*, 4589. (g) Arz, M. I.; Schnakenburg, G.; Meyer, A.; Schiemann, O.; Filippou, A. C. The Si_2H radical supported by two N-heterocyclic carbenes. *Chem. Sci.* **2016**, *7*, 4973. (h) Li, Y.; Chan, Y.-C.; Li, Y.; Purushothaman, I.; De, S.; Parameswaran, P.; So, C.-W. Synthesis of a Bent 2-Silaallene with a Perturbed Electronic Structure from a Cyclic Alkyl(amino) Carbene-Diiodosilylene. *Inorg. Chem.* **2016**, *55*, 9091.
- (5) (a) Meot-Ner, M.; Karpas, Z.; Deakne, C. A. Ion Chemistry of Cyanides and Isocyanides. I. The Carbon Lone Pair as Proton Acceptor: Proton Affinities of Isocyanides. Alkyl Cation Affinities of N, O, and C Lone-Pair Donors. *J. Am. Chem. Soc.* **1986**, *108*, 3913. (b) Liu, M.; Yang, I.; Buckley, B.; Lee, J. K. Proton Affinities of Phosphines versus N-Heterocyclic Carbenes. *Org. Lett.* **2010**, *12*, 4764.
- (6) (a) Takeda, N.; Kajiwara, T.; Suzuki, H.; Okazaki, R.; Tokitoh, N. Synthesis and Properties of the First Stable Silylene–Isocyanide Complexes. *Chem. - Eur. J.* **2003**, *9*, 3530. (b) Abe, T.; Iwamoto, T.; Kabuto, C.; Kira, M. Synthesis, Structure, and Bonding of Stable Dialkylsilylketenimines. *J. Am. Chem. Soc.* **2006**, *128*, 4228. (c) Takeuchi, K.; Ichinohe, M.; Sekiguchi, A. A New Disilene with π -Accepting Groups from the Reaction of Disilyne $\text{RSi}\equiv\text{SiR}$ (R = $\text{Si}i\text{Pr}[\text{CH}(\text{SiMe}_3)_2]$) with Isocyanides. *J. Am. Chem. Soc.* **2012**, *134*, 2954. (d) Ganesamoorthy, C.; Schoening, J.; Wölper, C.; Song, L.; Schreiner, P. R.; Schulz, S. A silicon–carbonyl complex stable at room temperature. *Nat. Chem.* **2020**, *12*, 608. (e) Reiter, D.; Holzner, R.; Porzelt, A.; Frisch, P.; Inoue, S. Silylated silicon–carbonyl complexes as mimics of ubiquitous transition-metal carbonyls. *Nat. Chem.* **2020**, *12*, 1131.
- (7) Zhu, L.; Zhang, J.; Yang, H.; Cui, C. Synthesis of Silaketenimine Anion and Its Coupling with Isocyanide. *J. Am. Chem. Soc.* **2019**, *141*, 19600.
- (8) Wang, Y.; Kostenko, A.; Hadlington, T. J.; Luecke, M.; Yao, S.; Driess, M. Silicon-Mediated Selective Homo- and Heterocoupling of Carbon Monoxide. *J. Am. Chem. Soc.* **2019**, *141*, 626.
- (9) Mansikkamäki, A.; Power, P. P.; Tuononen, H. M. Computational Analysis of $n \rightarrow \pi^*$ Back-Bonding in Metallylene–Isocyanide Complexes $\text{R}_2\text{MCNR}'$ (M = Si, Ge, Sn; R = $t\text{Bu}$, Ph; R' = Me, $t\text{Bu}$, Ph). *Organometallics* **2013**, *32*, 6690.
- (10) For two more recent review articles on silenes see: (a) Ottosson, H.; Eklöf, A. M. Silenes: Connectors between classical alkenes and nonclassical heavy alkenes. *Coord. Chem. Rev.* **2008**, *252*, 1287. (b) Milnes, K. K.; Pavelka, L. C.; Baines, K. M. Cycloaddition of carbonyl compounds and alkynes to (di)silenes and (di)germenes: reactivity and mechanism. *Chem. Soc. Rev.* **2016**, *45*, 1019.
- (11) For reviews on heavy allenes including 1-silaallenes see: (a) Escudé, J.; Ranaivonjatovo, H.; Rigon, L. Heavy Allenes and Cumulenes $\text{E}=\text{C}=\text{E}'$ and $\text{E}=\text{C}=\text{C}=\text{E}'$ (E = P, As, Si, Ge, Sn; E' = C, N, P, As, O, S). *Chem. Rev.* **2000**, *100*, 3639. (b) Eichler, B.; West, R. Chemistry of Group 14 Heteroallenes. *Adv. Organomet. Chem.* **2000**, *46*, 1. (c) Escudé, J.; Ranaivonjatovo, H. Group 14 and 15 Heteroallenes $\text{E}=\text{C}=\text{C}$ and $\text{E}=\text{C}=\text{E}'$. *Organometallics* **2007**, *26*, 1542.
- (12) (a) Holthausen, M. C.; Koch, W.; Apeloig, Y. Theory Predicts Triplet Ground-State Organic Silylenes. *J. Am. Chem. Soc.* **1999**, *121*, 2623. (b) Sekiguchi, A.; Tanaka, T.; Ichinohe, M.; Akiyama, K.; Tero, S.-K. Bis(tri-tert-butylsilyl)silylene: Triplet Ground State Silylene. *J. Am. Chem. Soc.* **2003**, *125*, 4962. (c) Sekiguchi, A.; Tanaka, T.; Ichinohe, M.; Akiyama, K.; Gaspar, P. P. Tri-tert-butylsilylsilylenes with Alkali Metal Substituents ($t\text{Bu}_3\text{Si}$)SiM (M = Li, K): Electronically and Sterically Accessible Triplet Ground States. *J. Am. Chem. Soc.* **2008**, *130*, 426.
- (13) Geiß, D.; Arz, M. I.; Straßmann, M.; Schnakenburg, G.; Filippou, A. C. Si=P Double Bonds: Experimental and Theoretical Study of an NHC-Stabilized Phosphasilylenylidene. *Angew. Chem., Int. Ed.* **2015**, *54*, 2739; *Angew. Chem.* **2015**, *127*, 2777.
- (14) (a) Filippou, A. C.; Chernov, O.; Schnakenburg, G. $\text{SiBr}_2(\text{Idipp})$: A Stable N-Heterocyclic Carbene Adduct of Dibromosilylene. *Angew. Chem., Int. Ed.* **2009**, *48*, 5687; *Angew. Chem.* **2009**, *121*, 5797. (b) Ghadwal, R. S.; Roesky, H. W.; Merkel, S.; Henn, J.; Stalke, D. Lewis Base Stabilized Dichlorosilylene. *Angew. Chem., Int. Ed.* **2009**, *48*, 5683; *Angew. Chem.* **2009**, *121*, 5793. (c) Filippou, A. C.; Chernov, O.; Schnakenburg, G. Chromium–Silicon Multiple Bonds: The Chemistry of Terminal N-Heterocyclic-Carbene-Stabilized Halosilylidyne Ligands. *Chem. - Eur. J.* **2011**, *17*, 13574. (d) Filippou, A. C.; Lebedev, Y. N.; Chernov, O.; Straßmann, M.; Schnakenburg, G. Silicon(II) Coordination Chemistry: N-Heterocyclic Carbene Complexes of Si^{2+} and Si^+ . *Angew. Chem., Int. Ed.* **2013**, *52*, 6974; *Angew. Chem.* **2013**, *125*, 7112.
- (15) (a) Filippou, A. C.; Baars, B.; Chernov, O.; Lebedev, Y. N.; Schnakenburg, G. Silicon–Oxygen Double Bonds: A Stable Silanone with a Trigonal-Planar Coordinated Silicon Center. *Angew. Chem., Int. Ed.* **2014**, *53*, 565; *Angew. Chem.* **2014**, *126*, 576. (b) Ghana, P.; Arz, M. I.; Chakraborty, U.; Schnakenburg, G.; Filippou, A. C. Linearly Two-Coordinated Silicon: Transition Metal Complexes with the Functional Groups $\text{M}\equiv\text{Si}-\text{M}$ and $\text{M}=\text{Si}=\text{M}$. *J. Am. Chem. Soc.* **2018**, *140*, 7187.
- (16) For two review articles on cations of heavier group 14 elements in low oxidation states see: (a) Swamy, V. S. S. N.; Pal, S.; Khan, S.; Sen, S. S. Cations and dications of heavier group 14 elements in low oxidation states. *Dalton Trans.* **2015**, *44*, 12903. (b) Powley, S. L.; Inoue, S. NHC-Stabilised Silyliumylidene Ions. *Chem. Rec.* **2019**, *19*, 2179.
- (17) The degree of pyramidalization (DP, %) was calculated using the equation $\text{DP} = [(360^\circ - \sum \angle(\text{Si})) / 90^\circ] \times 100$. It amounts to 0% when the sum of angles at silicon is 360° (trigonal planar coordination of silicon) and to 100% when the sum of angles at silicon is 270° , i.e., when the three-coordinated silicon atom uses exclusively p orbitals for the bonding.
- (18) Fox, B. J.; Sun, Q. Y.; DiPasquale, A. G.; Fox, A. R.; Rheingold, A. L.; Figueroa, J. S. Solution Behavior and Structural Properties of $\text{Cu}(\text{I})$ Complexes Featuring *m*-Terphenyl Isocyanides. *Inorg. Chem.* **2008**, *47*, 9010.
- (19) Notably, addition of strong σ -acceptors, such as carbenium ions, to isocyanides leads to a considerable upfield shift of the isocyanide carbon as shown in a comparison of the ^{13}C chemical shifts of isocyanides with those of nitrilium salts (cf. δ_{CN} of $\text{MeNC} = 158.2$ ppm and δ_{CN} of $[\text{MeNCMe}]\text{SbCl}_6 = 109.6$ ppm): (a) Stephany, R. W.; de Bie, M. J. A.; Drenth, W. A ^{13}C -NMR and IR study of isocyanides and some of their complexes. *Org. Magn. Reson.* **1974**, *6*, 45. (b) Shrestha-Davadi, P. B.; Jochims, J. C. On the Synthesis of Nitrilium Salts from Nitriles and Chloroformates. *Synthesis* **1993**, *1993*, 426. (c) van Dijk, T.; Burck, S.; Rong, M. K.; Rosenthal, A. J.; Nieger, M.; Slootweg, J. C.; Lammertsma, K. Facile Synthesis of Phosphaamidines and Phosphaamidines using Nitrilium Ions as an Imine Synthone. *Angew. Chem., Int. Ed.* **2014**, *53*, 9068; *Angew. Chem.* **2014**, *126*, 9214.
- (20) (a) Agou, T.; Hayakawa, N.; Sasamori, T.; Matsuo, T.; Hashizume, D.; Tokitoh, N. Reactions of Diaryldibromodisilenes with N-Heterocyclic Carbenes: Formation of Formal Bis-NHC Adducts of Silyliumylidene Cations. *Chem. - Eur. J.* **2014**, *20*, 9246. (b) Li, Y.; Chan, Y.-C.; Leong, B.-X.; Li, Y.; Richards, E.; Purushothaman, I.; De, S.; Parameswaran, P.; So, C.-W. Trapping a Silicon(I) Radical with Carbenes: A Cationic cAAC–Silicon(I) Radical and an NHC–Parent-Silyliumylidene Cation. *Angew. Chem., Int. Ed.* **2017**, *56*, 7573; *Angew. Chem.* **2017**, *129*, 7681. (c) Frisch, P.; Inoue, S. NHC-stabilized silyl-substituted silyliumylidene ions. *Dalton Trans.* **2019**, *48*, 10403.

(21) Holleman, A. F.; Wiberg, E. *Inorganic Chemistry*; Academic Press: San Diego/London, 2001; *Lehrbuch der Anorganischen Chemie*, 101. verbesserte und stark erweiterte Auflage, deGruyter: Berlin, 2001.

(22) For the nomenclature of intramolecular exchange processes see: Binsch, G.; Eliel, E. L.; Kessler, H. Nomenclature for Intramolecular Exchange Processes. *Angew. Chem., Int. Ed. Engl.* **1971**, *10*, 570; *Angew. Chem.* **1971**, *83*, 618.

(23) Chernov, O. Novel Molecular Si(II) Precursors for Synthesis of the First Compounds with Metal-Silicon Triple Bonds. Dissertation, Universität Bonn, 2012.

(24) For the terms anticlinical conformation and chirality axis see: Moss, G. P. Basic terminology of stereochemistry (IUPAC Recommendations 1996). *Pure Appl. Chem.* **1996**, *68*, 2193.

(25) For the determination of the configuration of molecules with an axis of chirality see: (a) Eliel, E. L.; Wilen, S. H. *Stereochemistry of Organic Compounds*; Wiley: New York, 1994; Chapter 14. (b) Wang, C.; Wu, W. A Simple Method To Determine the R or S Configuration of Molecules with an Axis of Chirality. *J. Chem. Educ.* **2011**, *88*, 299.

(26) (a) Williams, A.; Ibrahim, I. T. Carbodiimide Chemistry: Recent Advances. *Chem. Rev.* **1981**, *81*, 589. (b) Damrauer, R.; Lin, H.; Damrauer, N. H. Computational Studies of Carbodiimide Rings. *J. Org. Chem.* **2014**, *79*, 3781 and references therein.

(27) (a) Runge, W. In *The Chemistry of Ketenes, Allenes, and Related Compounds*; Patai, S., Ed.; Wiley-Interscience: Chichester, England, 1980; Part 1, pp 45–98. (b) Lambrecht, J.; Gambke, B.; von Seyerl, J.; Huttner, G.; Nell, G. K.-v.; Herzberger, S.; Jochims, J. C. Stereoisomerisierungen von Keteniminen. *Chem. Ber.* **1981**, *114*, 3751. (c) Jochims, J. C.; Lambrecht, J.; Burkert, U.; Zsolnai, L.; Huttner, G. The mechanism of the stereoisomerization of N-aryl ketenimines. *Tetrahedron* **1984**, *40*, 893. (d) Wolf, R.; Wong, M. W.; Kennard, C. H. L.; Wentrup, C. A Remarkably Stable Linear Ketenimine. *J. Am. Chem. Soc.* **1995**, *117*, 6789. (e) Zhang, Z.; Bu, X.; Zhang, J.; Liu, R.; Zhou, X.; Weng, L. Insertion of Ketenimines into the Ln–C σ -Bond of Organolanthanides: A New Strategy for Synthesis of Lanthanide 1-Azaallyl Complexes. *Organometallics* **2010**, *29*, 2111.

(28) (a) Yoshifuji, M.; Niitsu, T.; Toyota, K.; Namoto, N.; Hirotsu, K.; Odagaki, Y.; Higuchi, T.; Nagase, S. X-ray structure of a sterically protected 1-aza-3-phospha-allene. *Polyhedron* **1988**, *7*, 2213. (b) Zhou, X.-G.; Zhang, L.-B.; Cai, R.-F.; Wu, Q.-J.; Weng, L.-H.; Huang, Z.-E. Synthesis, structure and reactions of 1-(p-chlorophenyl)-3-(2,4,6-tri-t-butylphenyl)-1-aza-3-phospha-allene. *J. Organomet. Chem.* **2000**, *604*, 260. (c) Liu, L.; Ruiz, D. A.; Munz, D.; Bertrand, G. A Singlet Phosphinidene Stable at Room Temperature. *Chem.* **2016**, *1*, 147.

(29) Kaftory, M.; Kapon, M.; Botoshansky, M. In *The Chemistry of Organic Silicon Compounds*; Rappoport, Z.; Apeloig, Y., Eds.; Wiley: Chichester, 1998; Vol. 2, p 181.

(30) (a) Gjøystdal, A. C.; Rømming, C. The Geometry of an N-Aryl-Alkyl nitrilium Ion. Low Temperature X-Ray Study of N-(2,6-Dimethylphenyl)-Acetonitrilium Tetrafluoroborate. *Acta Chem. Scand.* **1977**, *31b*, 56. (b) Xie, Z.; Liston, D. J.; Jelínek, T.; Mitro, V.; Bau, R.; Reed, C. A. A new weakly coordinating anion: approaching the silylium (silicenium) ion. *J. Chem. Soc., Chem. Commun.* **1993**, 384. (c) Schulz, A.; Villinger, A. Pseudohalonium Ions: $[\text{Me}_3\text{Si}-\text{X}-\text{SiMe}_3]^+$ (X=CN, OCN, SCN, and NNN). *Chem. - Eur. J.* **2010**, *16*, 7276. (d) Haiges, R.; Baxter, A. F.; Goetz, N. R.; Axhausen, J. A.; Soltner, T.; Kornath, A.; Christe, K. O. Protonation of nitriles: isolation and characterization of alkyl- and aryl nitrilium ions. *Dalton Trans.* **2016**, *45*, 8494.

(31) Allen, F. H.; Kennard, O.; Watson, D. G.; Brammer, L.; Orpen, A. G.; Taylor, R. Tables of Bond Lengths determined by X-Ray and Neutron Diffraction. Part 1. Bond Lengths in Organic Compounds. *J. Chem. Soc., Perkin Trans. 2* **1987**, S1.

(32) Blechta, V. Applications of Silicon–Carbon Coupling Constants. In *Annual Reports in NMR Spectroscopy*; Webb, G. A., Ed.; Elsevier, 2009; Vol. 67, pp 97–264.

(33) (a) Yao, S.; Xiong, Y.; Driess, M. A New Area in Main-Group Chemistry: Zerovalent Monoatomic Silicon Compounds and Their Analogues. *Acc. Chem. Res.* **2017**, *50*, 2026. (b) Wang, Y.; Karni, M.;

Yao, S.; Kaushansky, A.; Apeloig, Y.; Driess, M. Synthesis of an Isolable Bis(silylene)-Stabilized Silylone and Its Reactivity Toward Small Gaseous Molecules. *J. Am. Chem. Soc.* **2019**, *141*, 12916.

(c) Siemes, L. C.; Keuter, J.; Hepp, A.; Lips, F. Reactions of a Silicon-Based Cyclic Silylone with Chalcogens. *Inorg. Chem.* **2019**, *58*, 13142.

(34) (a) Filippou, A. C.; Portius, P.; Philippopoulos, A. I.; Rohde, H. Triple Bonding to Tin: Synthesis and Characterization of the Stannylyne Complex $\text{trans-}[\text{Cl}(\text{PMe}_3)_4\text{W}\equiv\text{Sn}-\text{C}_6\text{H}_5-2,6\text{-Mes}_2]$. *Angew. Chem., Int. Ed.* **2003**, *42*, 445; *Angew. Chem.* **2003**, *115*, 461.

(b) Filippou, A. C.; Rohde, H.; Schnakenburg, G. Triple Bond to Lead: Synthesis and Characterization of the Plumbylydyne Complex $\text{trans-}[\text{Br}(\text{PMe}_3)_4\text{Mo}\equiv\text{Pb}-\text{C}_6\text{H}_5-2,6\text{-Trip}_2]$. *Angew. Chem., Int. Ed.* **2004**, *43*, 2243; *Angew. Chem.* **2004**, *116*, 2293. (c) Filippou, A. C.; Schnakenburg, G.; Philippopoulos, A. I.; Weidemann, N. Ge_2 Trapped by Triple Bonds between Two Metal Centers: The Germlylydyne Complexes $\text{trans,trans-}[\text{Cl}(\text{depe})_2\text{M}\equiv\text{Ge}-\text{Ge}\equiv\text{M}(\text{depe})_2\text{Cl}]$ (M=Mo, W) and Bonding Analyses of the $\text{M}\equiv\text{Ge}-\text{Ge}\equiv\text{M}$ Chain. *Angew. Chem., Int. Ed.* **2005**, *44*, 5979; *Angew. Chem.* **2005**, *117*, 6133.

(35) (a) Yamaguchi, T.; Sekiguchi, A.; Driess, M. An N-Heterocyclic Carbene–Disilyne Complex and Its Reactivity toward ZnCl_2 . *J. Am. Chem. Soc.* **2010**, *132*, 14061. (b) Rit, A.; Campos, J.; Niu, H.; Aldridge, S. A stable heavier group 14 analogue of vinylidene. *Nat. Chem.* **2016**, *8*, 1022. (c) Sindlinger, C. P.; Aicher, F. S. W.; Wesemann, L. Cationic Stannylynes: In Situ Generation and NMR Spectroscopic Characterization. *Inorg. Chem.* **2017**, *56*, 548.

(36) The unweighted mean values x_u of the individual bonding parameters of the two molecules of **4** found in the asymmetric unit were used for the discussion. The corrected sample standard deviations σ (values in parentheses) were calculated using the equation $\sigma^2 = \sum(x_i - x_u)^2 / (n^2 - n)$, where x_i is the respective individual value and $n = 2$.

(37) Four classes of compounds featuring Si=Ge bonds (germasilenes, NHC-supported silagermenylenes, 1,3-digermasilaallenes, and 2-germasilaallenes) have been characterized by single-crystal X-ray diffraction and show Si=Ge bond lengths between 2.214 and 2.276 Å.

Supporting Information

6. Electronic structure calculations

Electronic structure calculations were carried out in the gas phase using the ORCA 4.1.1 program.^[S28] All calculations were performed using the DFT method B97-D3(BJ)-ATM/def2-TZVP (method-I), which consists of a GGA functional B97-D3(BJ)^[S29] in combination with the three body dispersion energy correction functional (ATM)^[S30], the triple- ζ quality basis set def2-TZVP^[S31] for all atoms and the auxiliary basis set of the type def2/J for the RI-J^[S32] approximation of the Coulomb integral (J). For numerical precision settings the DFT double integration grid *GRID3* was used for SCF iterations and *GRID5* for the final energy evaluation after complete SCF convergence.

The ORCA default Quasi-Newton optimiser, that uses the Broyden-Fletcher-Goldfarb-Shanno (BFGS) iterative algorithm, was used for the geometry optimization along with the above mentioned numerical precision criteria. The optimization was carried out in redundant internal coordinates using the initial model Hessian of Almlöf. The optimized structures were verified as stationary points on the potential energy surface (PES) by two-sided numerical differentiation of the analytical gradients to obtain harmonic frequencies after SCF convergence by the following criteria – no significant imaginary frequency (minimum), one significant imaginary frequency (first-order saddle point or transition state), two significant imaginary frequencies (second-order saddle point). The potential energy surfaces of the compounds were studied by relaxed potential energy surface scans of an angle or dihedral angle followed by constrained structure optimization and single point energy calculation (SPE) after each scan step.

Natural bond orbital (NBO) analysis in combination with the NBO based natural population analysis (NPA) and natural resonance theory analysis (NRT) were carried out by employing the method-I and by using the NBO6.0 version of the NBO program.^[S33] The NBO analysis was performed on the best Natural Lewis Structure (NLS) that was found by NBO. The following abbreviations were used for the NBO analysis: LP = Lewis 1-center valence lone pair, BD = Lewis 2c-2e bond orbital, BD* = non-Lewis 2c-2e antibond orbital, LV = non-Lewis

[S28] Neese, F. *Wiley Interdisciplinary Reviews: Computational Molecular Science* **2012**, *2*, 73.

[S29] a) Grimme, S.; Antony, J.; Ehrlich, S.; Krieg, H. *J. Chem. Phys.* **2010**, *132*, 154104. b) Grimme, S.; Ehrlich, S.; Goerigk, L. *J. Comput. Chem.* **2011**, *32*, 1456.

[S30] a) Axilrod, B. M.; Teller, E. *J. Chem. Phys.* **1943**, *11*, 299 b) Muto, Y. *Proc. Phys. Math. Soc. Jpn.* **1943**, *17*, 629.

[S31] a) Weigend, F.; Ahlrichs, R. *Phys. Chem. Chem. Phys.* **2005**, *7*, 3297. b) Weigend, F. *Phys. Chem. Chem. Phys.* **2006**, *8*, 1057.

[S32] Vahtras, O.; Almlöf, J.; Feyereisen, M. W. *Chem. Phys. Lett.* **1993**, *213*, 514.

[S33] Glendening, E. D.; Badenhoop, J. K.; Reed, A. E.; Carpenter, J. E.; Bohmann, J. A.; Morales, C. M.; Landis, C. R.; Weinhold, F. *Theoretical Chemistry Institute, University of Wisconsin, Madison* **2013**.

Supporting Information

lone vacant orbital. In cases where the NBO iteration cycles showed threshold Lewis occupancies less than 1.90e for the core bonding motifs, multi-reference NRT analyses were carried out as local NRT in order to circumvent the convergence problem arising from the too many natural Lewis structures (NLSs).

The graphical representations of the Kohn-Sham canonical molecular orbitals and calculated structures were created by using the UCSF Chimera program.^[S34]

6.1. Optimized structures of the constitutional isomer and conformers of (*R_a*)-**1**_{calc} and the model system **1**^{Me}

The molecular structure of **1** contains two independent axially chiral molecules (*R_a*)-**1** and (*S_a*)-**1** in the unit cell differing in the sign of the torsion angles C1–Si–N3–C29 ((*R_a*)-**1**: $-130.90(1)^\circ$, (*S_a*)-**1**: $+130.90(1)^\circ$) and N1–C1–Si–C28 ((*R_a*)-**1**: $-27.5(1)^\circ$, (*S_a*)-**1**: $+27.5(1)^\circ$). The cartesian coordinates of (*R_a*)-**1** were used for the structure optimization leading to the calculated structure (*R_a*)-**1**_{calc} (Figure S53, left). The frequency calculation yielded only a single imaginary frequency of -10 cm^{-1} for the rotation of a methyl group of the Ar^{Mes} substituent, and thus (*R_a*)-**1**_{calc} was considered to be a true minimum in the potential energy surface (PES). The bonding parameters of (*R_a*)-**1**_{calc} are in good agreement with those of (*R_a*)-**1** (Table S9). Notably, the angles C1–Si–N3–C29 (α), N1–C1–Si–C28 (β), and C28–N3–C29 of (*R_a*)-**1**_{calc} differ to some extent from those of (*R_a*)-**1** presumably due to the very flat PES for the torsional motions involving the torsion angles α , β and Si–N3–C29–C30, which affect also the angle C28–N3–C29 (see Section 6.15 for the stereodynamics of (*R_a*)-**1**_{calc}). Remarkably, the NHC-stabilized cyanosilylene constitutional isomer **1C**_{calc} was found to be slightly more stable than (*R_a*)-**1**_{calc} (Figure S53, right).

The structural parameters of (*R_a*)-**1**_{calc} and the model compound (IMe₄)Si=C=NMe (**1**^{Me}; IMe₄ = C[N(Me)C(Me)C(Me)]₂) differ significantly (Figure S54 and Table S11). The most notable differences are: a) the Si=C=N skeleton is almost linear in **1**^{Me}, whereas it is slightly bent in (*R_a*)-**1**_{calc}; b) the torsion angle C1–Si–N3–C29 (α) is -90° in **1**^{Me} versus -147° in (*R_a*)-**1**_{calc}; c) the Si–C_{NHC} bond length of **1**^{Me} is longer and the Si–C_{CNR} bond length shorter than the corresponding bond lengths of (*R_a*)-**1**_{calc}; d) the C28–N3–C29 angle is smaller in **1**^{Me}; and e) the torsion angle β is -41.6° in **1**^{Me}, whereas it is -3.1° in (*R_a*)-**1**_{calc}. A similar trend for the relative stability was found for the NHC-stabilized cyanosilylene (IMe₄)Si(CN)Me (**1C**^{Me}) and **1**^{Me} with a much larger energetic preference for **1C**^{Me} (Figure S54). Two conformers were found as local minima in the PES of the (*R_a*)-**1**_{calc}. The linear conformers **1LN**_{calc} and **1LC**_{calc}

[S34] Pettersen, E. F.; Goddard, T. D.; Huang, C. C.; Couch, G. S.; Greenblatt, D. M.; Meng, E. C.; Ferrin, T. E. *J. Comput. Chem.* **2004**, *25*, 1605.

Supporting Information

were obtained by constrained geometry optimizations, during which the angle C–N–C_R and Si–C28–N3 was fixed at 180.0°, respectively (*Figure S55, Table S13*).

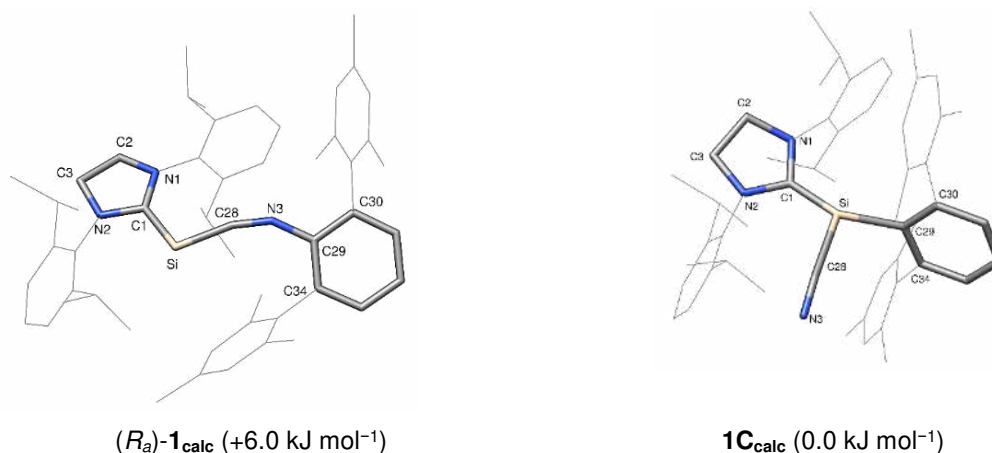


Figure S53. Optimized minimum structure of $(R_a)\text{-1}_{\text{calc}}$ (left) and the global minimum structure $\mathbf{1C}_{\text{calc}}$ (right); relative electronic energies are given in parentheses.

Table S9. Comparison of selected calculated and experimental bonding parameters (bond lengths / Å, bond and torsion angles / °) of $(R_a)\text{-1}_{\text{calc}}$ and $(R_a)\text{-1}$.

	Si–C1	Si–C28	N3–C28	N3–C29	C1–Si–C28
$(R_a)\text{-1}_{\text{calc}}$	1.875	1.803	1.213	1.373	101.5
$(R_a)\text{-1}$	1.894(2)	1.784(1)	1.224(2)	1.410(2)	100.4(1)
	Si–C28–N3	C28–N3–C29	C1–Si–C28–N3	N1–C1–Si–C28	C1–Si–N3–C29
$(R_a)\text{-1}_{\text{calc}}$	156.6	148.3	167.9	-3.1	-147.4
$(R_a)\text{-1}$	158.8(1)	133.0(1)	173.8(2)	-27.5(1)	-130.90(1)

Table S10. Selected calculated bond lengths (Å) and bond angles (°) of the constitutional isomer $\mathbf{1C}_{\text{calc}}$.

Si–C1	Si–C28	C28–N3	Si–C29
1.929	1.863	1.168	1.950
C1–Si–C28	Si–C28–N3	C1–Si–C29	$\Sigma\Delta(\text{Si})$
102.8	166.2	132.8	335.1

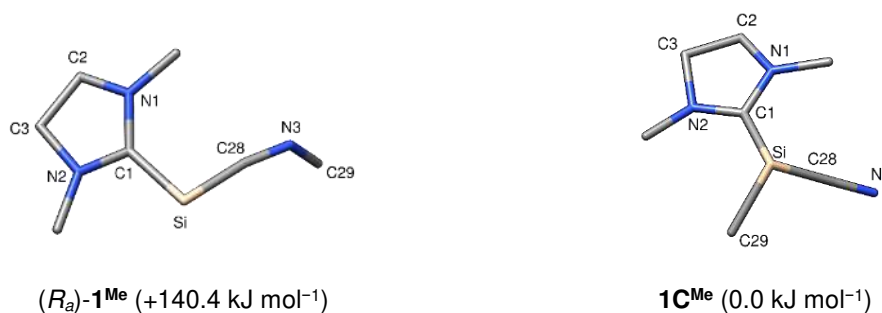


Figure S54. Optimized minimum structure of $(R_a)\text{-1}^{\text{Me}}$ (left) and its constitutional isomer $\mathbf{1C}^{\text{Me}}$ (right); relative electronic energies are given in parentheses.

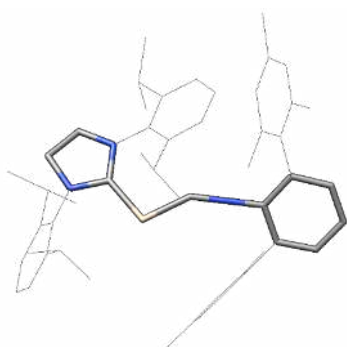
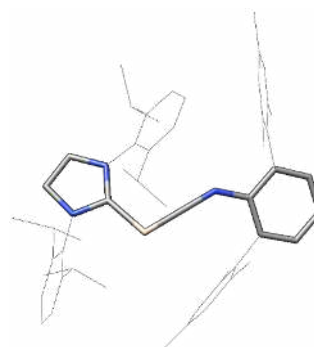
Supporting Information

Table S11. Comparison of selected calculated bonding parameters (bond lengths / Å, bond and torsion angles / °) of **1^{Me}** and (*R_a*)-**1_{calc}**.

	Si-C1	Si-C28	N3-C28	N3-C29	C1-Si-C28
1^{Me}	1.920	1.786	1.221	1.459	93.3
(<i>R_a</i>)- 1_{calc}	1.875	1.803	1.213	1.373	101.5
	Si-C28-N3	C28-N3-C29	C1-Si-C28-N3	N1-C1-Si-C28	C1-Si-N3-C29
1^{Me}	170.0	127.2	-165.9	-41.6	-94.1
(<i>R_a</i>)- 1_{calc}	156.6	148.3	167.8	-3.1	-147.4

Table S12. Selected calculated bond lengths (in Å) and bond angles (in Å) of the model compound **1C^{Me}**.

Si-C1	Si-C28	C28-N3	Si-C29
1.928	1.890	1.167	1.931
C1-Si-C28	Si-C28-N3	C1-Si-C29	Σ ₄ (Si)
95.9	174.8	107.9	302.0

**1LN_{calc}** (+16.4 kJ mol⁻¹)**1LC_{calc}** (+24.0 kJ mol⁻¹)**Figure S55.** Optimized minimum structures of the linear conformers of (*R_a*)-**1_{calc}**: (left) **1LN_{calc}** with the angle C28-N3-C29 fixed at 180.0°; (right) **1LC_{calc}** with the angle Si-C28-N3 fixed at 180.0°; relative electronic energies are given in parentheses; the same atom numbering was used as for (*R_a*)-**1_{calc}**.**Table S13.** Comparison of selected calculated bonding parameters (bond lengths / Å, bond and torsion angles / °) of **1LN_{calc}**, **1LC_{calc}**, (*R_a*)-**1_{calc}** and (*R_a*)-**1**.

	Si-C1	Si-C28	N3-C28	N3-C29	C1-Si-C28
1LN_{calc}	1.866	1.826	1.199	1.355	102.6
1LC_{calc}	1.876	1.794	1.220	1.385	104.0
(<i>R_a</i>)- 1_{calc}	1.875	1.803	1.213	1.373	101.5
(<i>R_a</i>)- 1	1.894(2)	1.784(1)	1.224(2)	1.410(2)	100.4(1)
	Si-C28-N3	C28-N3-C29	C1-Si-C28-N3	N1-C1-Si-C28	C1-Si-N3-C29
1LN_{calc}	146.7	180.0	-173.4	3.3	-172.8
1LC_{calc}	180.0	139.3	-	-8.9	-142.3
(<i>R_a</i>)- 1_{calc}	156.6	148.3	167.8	-3.1	-147.4
(<i>R_a</i>)- 1	158.8(1)	133.0(1)	173.8(2)	-27.5(1)	-130.90(1)

Supporting Information

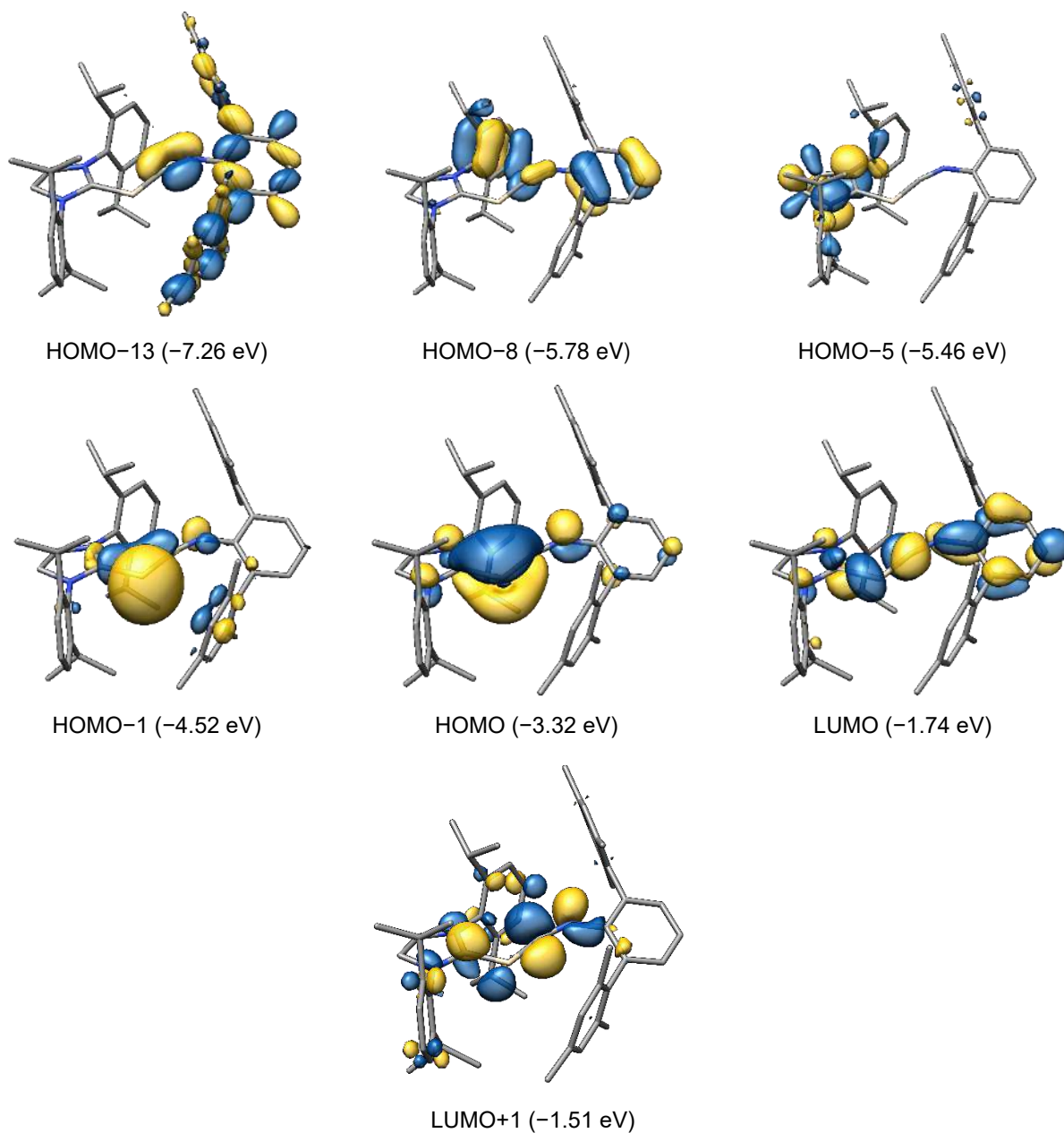
6.2. Selected Kohn-Sham orbitals of (*R_a*)-1_{calc}

Figure S56. Selected KS orbitals of (*R_a*)-1_{calc} and their orbital energies in parentheses. The isosurface value is set to $0.04 \text{ e}^{1/2} \cdot \text{Bohr}^{-3/2}$.

Supporting Information

6.3. ETS-NOCV analysis of $\mathbf{1}_{\text{calc}}$

An additional insight into the chemical bonding of $\mathbf{1}_{\text{calc}}$ to those given by NBO, NRT and NPA analyses (Chapter 6.4) was provided by analyzing the interaction between the fragment Si(SiDipp) and CNAr^{Mes} using a combination of the Extended Transition State (ETS) method with the method based on the Natural Orbitals for Chemical Valence (NOCV) as implemented in the ORCA 4.1.1 program package.^[S35] Within the ETS scheme the energy of formation of $\mathbf{1}_{\text{calc}}$ (ΔE_{int}) is analyzed starting from the fragments Si(SiDipp) and CNAr^{Mes} in their equilibrium geometry and electronic ground state. $\Delta E_{\text{int}} = -\text{BDE}$, where BDE is the Si–C_{CNR} bond dissociation energy (216.9 kJ mol⁻¹, *Table S24*).^[S36] The ETS scheme has a certain degree of arbitrariness, since the picture it provides for the Si–C_{CNR} bond depends on the choice of the fragments and their reference electronic states. We have decided to use the fragments Si(SiDipp) and CNAr^{Mes} in their singlet reference states given the considerably larger singlet to triplet gap ($\Delta E_{\text{s}\rightarrow\text{t}}$) of +296.3 kJ mol⁻¹ of $\text{Ar}^{\text{Mes}}\text{NC}$ compared with that of the Si(SiDipp) species ($\Delta E_{\text{s}\rightarrow\text{t}} = -19.4$ kJ mol⁻¹). The ETS scheme decomposes ΔE_{int} into a number of chemically meaningful components given in Equation 1. The results of the ETS energy decomposition analysis are collected in *Table S14*. Notably, the total orbital interaction ΔE_{orb} contributes 42% to the total attractive interaction energy ($\Delta E_{\text{elstat}} + \Delta E_{\text{disp}} + \Delta E_{\text{orb}} = -1222.9$ kJ mol⁻¹) between the Si(SiDipp) and CNAr^{Mes} fragments.

$$\Delta E_{\text{int}} = -\text{BDE} = \Delta E_{\text{prep}} + \Delta E_{\text{elstat}} + \Delta E_{\text{Pauli}} + \Delta E_{\text{disp}} + \Delta E_{\text{orb}} \quad (\text{Eq. 1})$$

$\Delta E_{\text{int}} = -\text{BDE}$, where BDE is the Si_{SiDipp}–C_{CNR} bond dissociation energy (*Figure S68*). ΔE_{prep} is the sum of the preparation energies of the fragments, ΔE_{elstat} is the electrostatic interaction energy, ΔE_{Pauli} is the Pauli repulsion energy, ΔE_{disp} is the dispersion interaction energy and ΔE_{orb} is the total orbital interaction energy.

The orbital interaction energy ΔE_{orb} can be further divided into different contributions, which can be expressed within the NOCV scheme in terms of few complementary pairs of NOCVs enabling to assess a compact picture of the chemical bond by visualization of the deformation density contributions. Three pairs of complementary NOCVs ($\phi_{\pm k}$, $k = 1, 2, 3$, *Figure S57*, left and middle columns) were found in the NOCV analysis with eigen values v_k significantly higher than 0.1 indicating that the remaining 202 NOCV pairs, which were required to describe the electron density of the fragments, do not participate in the Si_{SiDipp}–C_{CNR} bond formation (contribution to chemical valence $\sim (v_k)^2 < 0.01$). The $\phi_{\pm k}$ NOCVs

[S35] a) Michalak, A.; Mitoraj, M. P.; Ziegler, T. *J. Phys. Chem. A* **2008**, *112*, 1933. b) Radon, M. *Theor. Chem. Account.* **2008**, *120*, 337. c) Mitoraj, M. P.; Michalak, A.; Ziegler, T. *J. Chem. Theory Comput.* **2009**, *5*, 962.

[S36] Zhao, L.; Hermann, M.; Schwarz, W. H. E.; Frenking, G. *Nat. Rev.* **2019**, *3*, 48.

Supporting Information

Table S14. Results of the ETS-energy decomposition analysis of the Si-C_{CNR} bond in **1**_{calc} (energies in kJ mol⁻¹).

ΔE_{int}	ΔE_{prep}	$\Delta E_{\text{elstat}}^{[\text{S37}]}$	ΔE_{pauli}	ΔE_{disp}	ΔE_{orb}	BDE
-216.9	56.4	-573.2	949.6	-139.6	-510.1	216.9

$\Delta E_{\text{prep}} = \Delta E_{\text{prep}}(\text{SiSiDipp}) + \Delta E_{\text{prep}}(\text{Ar}^{\text{Mes}}\text{NC})$. $\Delta E_{\text{prep}}(\text{SiSiDipp})$ is composed of two components a) the triplet to singlet excitation energy of Si(SiDipp) of +19.4 kJ mol⁻¹ and b) its structural promotion energy (10.9 kJ mol⁻¹) to the frozen geometry found in **1**_{calc}. $\Delta E_{\text{prep}}(\text{Ar}^{\text{Mes}}\text{NC})$ is the structural promotion energy of Ar^{Mes}NC (26.1 kJ mol⁻¹) to the frozen geometry found in **1**_{calc}.

describe the Si_{SiDipp}-C_{CNR} bonding interactions and the ϕ_{-k} NOCVs display the antibonding interactions. For example, ϕ_{+1} and ϕ_{+2} describe the Si-C_{CNR} σ -bond and Si-C_{CNR} π_{oop} -bond with an eigen value v_1 of +0.93e and v_2 of +0.74e, respectively, whereas the complementary NOCVs ϕ_{-1} and ϕ_{-2} are the corresponding σ^* and π^* bonds, respectively (*Figure S57*, left and middle columns). Notably, the $\phi_{\pm 3}$ NOCV pair describes the in-plane Si_{SiDipp}-C_{CNR} π -interaction, however its contribution to the deformation density is significantly lower than those of $\phi_{\pm k}$ ($k = 1, 2$), as can be seen from its eigen value $v_{\pm 3}$ of $\pm 0.46e$. During the process of Si-C_{CNR} bond formation, the electron density flows from the antibonding NOCVs to the bonding complementary NOCVs. This is clearly visible in the contributions of the complementary NOCV pairs to the deformation density ($\Delta\rho_k$) plots showing three orbital interactions (*Figure S57*, right column) – a) $\Delta\rho_1$ involves a donation of 0.74e from the C-centered lone pair of the Ar^{Mes}NC fragment into the vacant σ -symmetric orbital at Si of the Si(SiDipp) fragment with a $\Delta E_{\text{orb}(1)}$ of -136.2 kJ mol⁻¹, b) a rather strong back-donation ($(\Delta E_{\text{orb}(2)} = -219.5 \text{ kJ mol}^{-1})$) of 0.93e from the $\pi(\text{Si-C}_{\text{NHC}})$ bonding orbital into the $\pi^*_{\text{oop}}(\text{C}\equiv\text{NR})$ anti-bonding orbital of the Ar^{Mes}NC fragment and c) a weaker back-donation ($\Delta E_{\text{orb}(3)} = -171.7 \text{ kJ mol}^{-1}$) with a transfer of only 0.46e from the lonepair orbital at Si into the $\pi^*_{\text{ip}}(\text{C}\equiv\text{NR})$ orbital. Notably, $\Delta E_{\text{orb}(2)}$ was found to contribute mostly (42%) to the total ΔE_{orb} . The calculated Nalewajski-Mrozek bond order (V) of the Si-C_{CNR} bond using the equation $V = 0.5 \sum (\phi_k)^2$ was found to be 1.6^[S35a] comparing well with the Si-C_{CNR} NRT-BO of 1.5 (Chapter 6.4).

[S37] This value was calculated on the B97-D3(BJ)/def2-TZVP level of theory using the Turbomole V7.1 program package. Turbomole V7.1: a) Ahlrichs, R.; Bär, M.; Häser, M.; Horn, H.; Kölmel, C. *Chem. Phys. Lett.* **1989**, *162*, 165. b) TURBOMOLE Version 7.0, a development of University of Karlsruhe and Forschungszentrum GmbH Karlsruhe, **1989–2007**; TURBOMOLE GmbH, since **2007**. c) Furche, F.; Ahlrichs, R.; Hättig, C.; Klopper, W.; Sierka, M.; Weigend, F. *WIREs Comput. Mol. Sci.* **2014**, *4*, 91.

Supporting Information

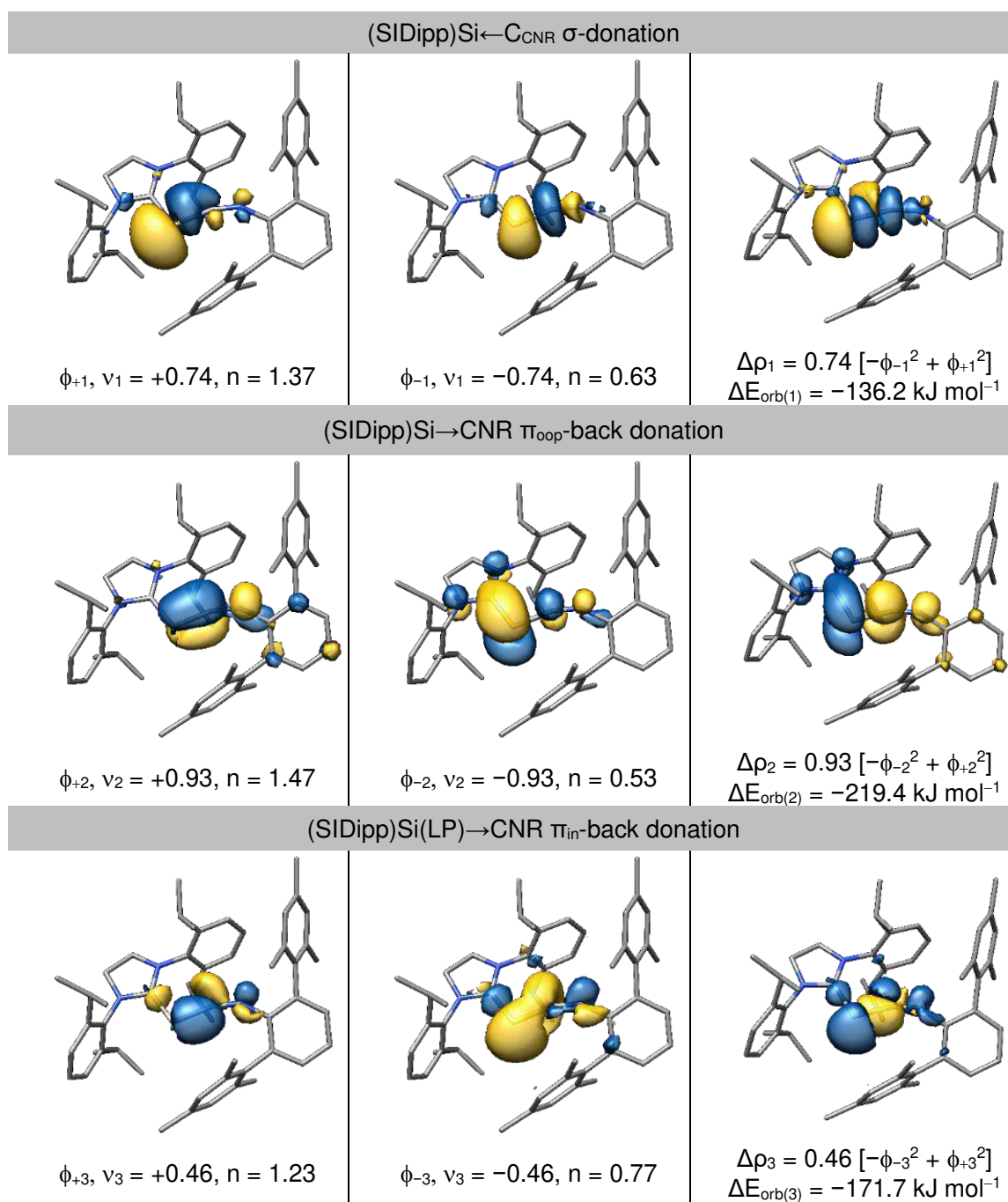


Figure S57. *left and middle columns:* three complementary pairs of NOCVs of $\mathbf{1}_{\text{calc}}$ describing the Si-C_{CNR} bond formation. *right column:* deformation density plots showing the contribution of the NOCV pairs ($\phi_{\pm k}$, $k = 1, 2, 3$); v_k = eigen value, n = electron occupancy of the natural orbital in $\mathbf{1}_{\text{calc}}$,^{[S35b)] $\Delta\rho$ = deformation density (differential density), charge flow: blue → yellow; isosurface value = 0.002 e^{1/2}·Bohr^{-3/2}.}

Supporting Information

6.4. Results of the NBO, NRT and NPA analyses of (*R_a*)-1_{calc}**Table S15.** Selected NBOs, WBI, NRT-BO and NPA charges of (*R_a*)-1_{calc}.

NBO A-B	Occ. ^a	NHO (A,B) ^b , hyb (pol in %)	WBI ^c A-B	NRT-BO ^d tot/cov/ion	atom/ group	q/Σq ^e
σ(Si-C _{NHC})	1.92	sp ^{6.5} (23), sp ^{1.3} (77)	1.0	1.3/0.7/0.6	Si	+0.40
σ(Si-C _{CNR})	1.96	sp ^{6.4} (24), sp ^{0.6} (76)	1.3	1.5/0.9/0.6	C _{CNR}	-0.04
π(Si-C _{CNR})	1.57	p(47), p(53)			N _{CNR}	-0.45
σ(C-NR)	1.99	sp ^{1.7} (35), sp(65)	1.9	2.3/1.5/0.8		
π(C-NR)	1.91	p(34), p(66)				
Si(LP)	1.75	sp ^{0.4}			CNR	-0.39
N _{CNR} (LP)	1.55	sp ^{7.3}			NHC	-0.01
C _{NHC} (LV)	0.95	p				

^a: Occ.= occupancy; ^b: NHO = Natural Hybrid Orbital, pol. (polarization) = (C_i)²·100%, where C_i = coefficient of NHO; ^c: Wiberg bond index; ^d: total, covalent and ionic NRT bond order; ^e: q = NPA charge of the atom, Σq = total NPA charge of the group.

Table S16. Second order perturbation theory analysis of the Fock matrix in NBO basis of (*R_a*)-1_{calc} for selected donor and acceptor NBOs.

Donor NBO	Acceptor NBO	Non-Lewis occ.	E ⁽²⁾ (kJ mol ⁻¹)
π(Si-C _{CNR})	LV(C _{NHC})	0.95	53
LP(Si)	π*(C-NR)	0.30	292
LP(N1 _{NHC})	LV(C _{NHC})	0.95	106
LP(N2 _{NHC})	LV(C _{NHC})	0.95	110
LP(N _{CNR})	π*(Si-C _{CNR})	0.32	51

Natural Lewis Structures (NLSs) of (*R_a*)-1_{calc}

A local NRT analysis including the N_{NHC}, C_{NHC}, Si=C=N skeleton atoms and the ring carbon atoms of the central Ar^{Mes} phenyl ring yielded 105 NLSs with contributions ranging from 9.56 – 0.10% covering 98% of the resonance hybrid. Inspection of these NLSs according to the core bonding motif (marked blue in *Figure S58*) yielded five main NLSs **1A-E**. The core bonding motif of **1A-E** was found in 30, 19, 15, 8 and 10 NLSs, respectively.

Supporting Information

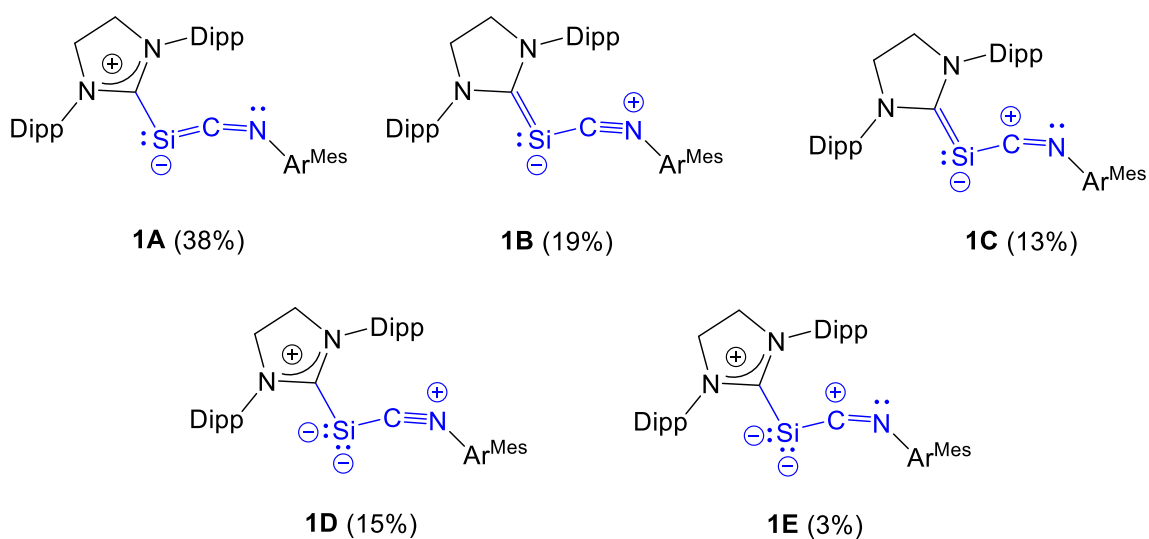


Figure S58. Natural Lewis Structures (NLSs) of (R_a) - 1_{calc} and their NRT weight % in the resonance hybrid.

6.5. Comparison of selected calculated and experimental bonding parameters of 2^+_{calc} and 2^+

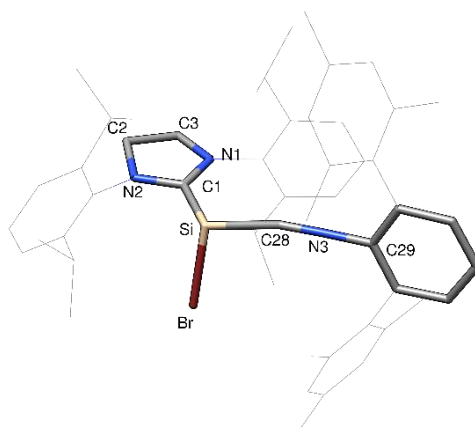


Figure S59. Optimized minimum structure of 2^+_{calc} .

Table S17. Comparison of selected calculated and experimental structural parameters (bond lengths / Å, angles / °) of 2^+_{calc} and 2^+ .

	Si–C1	Si–Br	Si–C28	N–C28
2^+_{calc}	1.976	2.316	1.935	1.171
2^+	1.977(4)	2.262(2)	1.952(5)	1.149(6)
	N3–C29	C1–Si–Br	C1–Si–C28	Si–C28–N3
2^+_{calc}	1.374	96.8	100.1	149.7
2^+	1.401(6)	95.8(2)	100.4(2)	148.7(4)
	C28–N3–C29	N1–C1–Si–C28	$\Sigma_4(\text{Si})$	
2^+_{calc}	178.4	–8.2	291.9	
2^+	171.8(4)	–25.3(4)	286.7	

Supporting Information

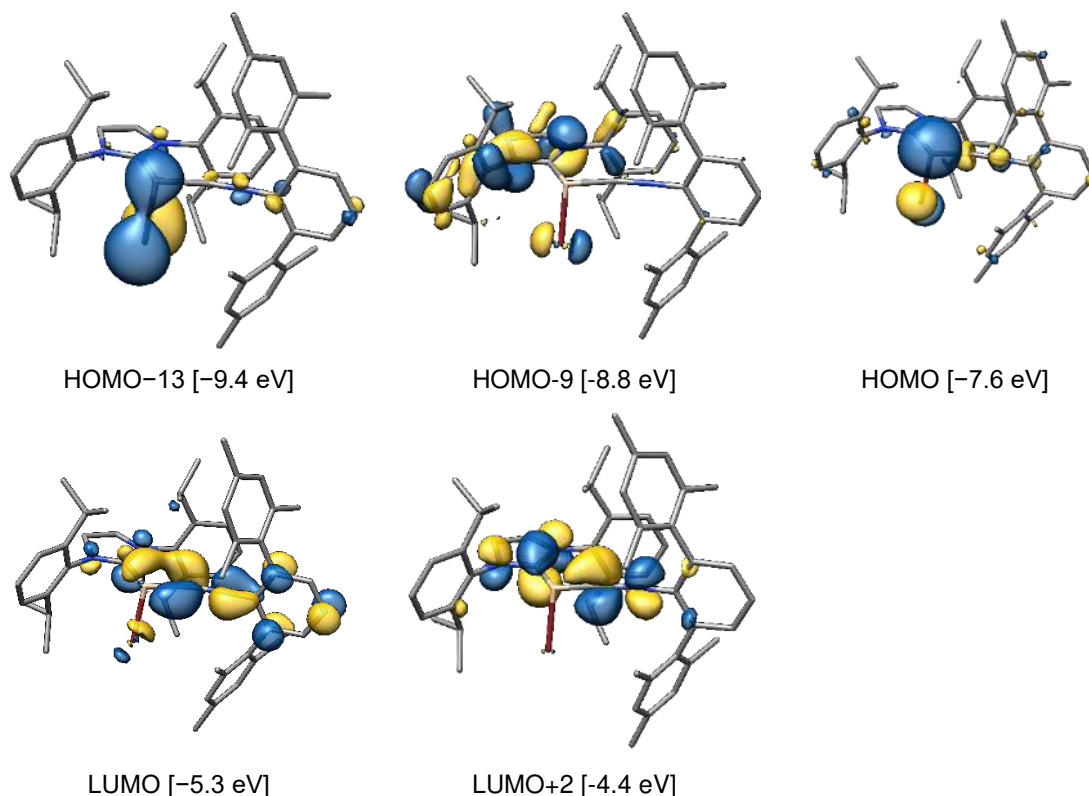
6.6. Selected Kohn-Sham orbitals of 2^+_{calc} 

Figure S60. Selected KS orbitals of 2^+_{calc} and their orbital energies in parentheses. The isosurface value is set to $0.04 \text{ e}^{1/2} \cdot \text{Bohr}^{-3/2}$.

6.7. Results of NBO, NPA and NRT analysis of 2^+_{calc}

Table S18. Selected NBOs, WBI, NRT-BO and NPA charges of 2^+_{calc} .

NBO A-B	Occ. ^a	NHO (A,B) ^b , hyb (pol in %)	WBI ^c A-B	NRT-BO ^d tot/cov/ion	atom/ group	$q/\sum q^e$
$\sigma(\text{Si}-\text{C}_{\text{NHC}})$	1.92	$\text{sp}^{8.5}(23)$, $\text{sp}^{1.5}(77)$	0.7	1.0/0.5/0.5	Si	+0.69
$\sigma(\text{Si}-\text{C}_{\text{CNR}})$	1.96	$\text{sp}^{10.5}(23)$, $\text{sp}^{0.6}(77)$	0.9	1.0/0.5/0.6	C_{CNR}	+0.18
$\sigma(\text{C}-\text{NR})$	1.99	$\text{sp}^{1.6}(34)$, $\text{sp}^{0.9}(66)$	2.3	2.8/1.9/0.9	N_{CNR}	-0.33
$\pi_1(\text{C}-\text{NR})$	1.98	$p(33)$, $p(67)$			Br	-0.30
$\pi_2(\text{C}-\text{NR})$	1.95	$p(35)$, $p(65)$			CNR	+0.19
Si(LP)	1.76	$\text{sp}^{0.4}$			NHC	+0.42

^a: Occ.= occupancy; ^b: NHO = Natural Hybrid Orbital, pol. (polarization) = $(C_i)^2 \cdot 100\%$, where C_i = coefficient of NHO; ^c: Wiberg bond index; ^d: total, covalent and ionic NRT bond order; ^e: q = NPA charge of the atom, $\sum q$ = total NPA charge of the group.

Supporting Information

Natural Lewis Structures (NLSs) of 2^+_{calc}

A local NRT analysis involving the N_{NHC} , C_{NHC} , Br, Si-C \equiv N skeleton atoms and the six ring carbon atoms of the central Ar^{Mes} phenyl ring yielded 83 NLSs with contributions ranging from 6.90 – 0.10%, covering 98% of the resonance hybrid. Inspection of these NLSs according to the core bonding motif (marked blue in *Figure S61*) yielded three main NLS for the core of 2^+_{calc} representing 95% of the resonance hybrid. The core bonding motif of 2^+_{A} , 2^+_{B} , 2^+_{C} and 2^+_{D} was found in 45, 19, 6 and 5 NLSs, respectively.

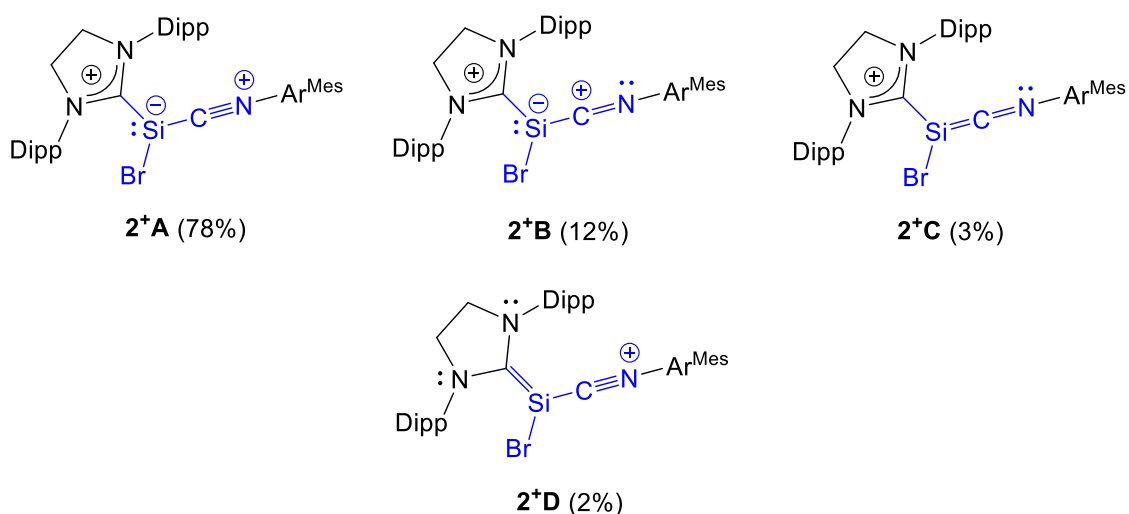


Figure S61. Natural Lewis Structures (NLSs) of 2^+_{calc} and their NRT weight % in the resonance hybrid.

Supporting Information

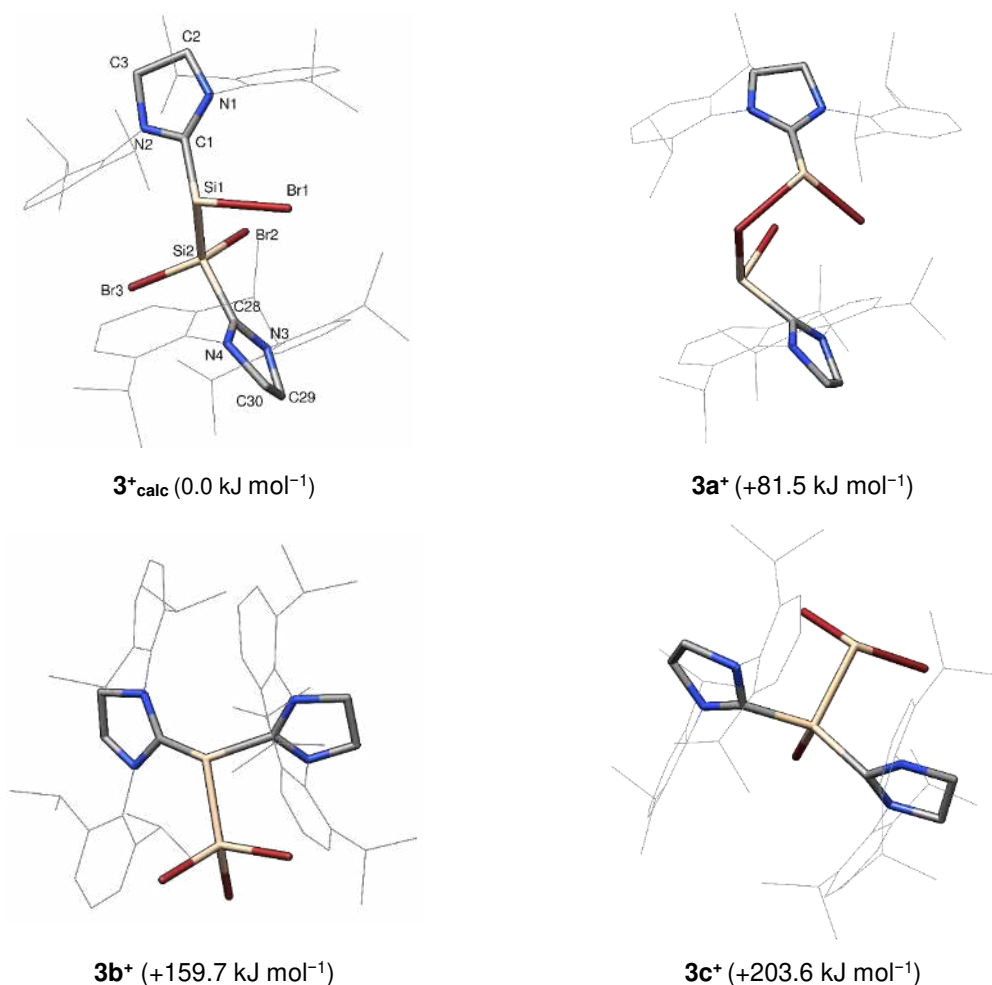
6.8. Optimized structures of 3^+_{calc} and its constitutional isomers $3a^+$, $3b^+$ and $3c^+$ 

Figure S62. Optimized minimum structures of 3^+_{calc} and its constitutional isomers ($3a^+$, $3b^+$, $3c^+$); relative pure electronic energies are given in parentheses.

Table S19. Comparison of the selected calculated and experimental structural parameters (bond lengths / Å, angles / °) of 3^+_{calc} and 3^+ .

	C1–Si1	C28–Si2	Si1–Si2	Si1–Br1
3^+_{calc}	1.981	1.985	2.370	2.391
3^+	1.973(5)	1.970(5)	2.353(2)	2.316(1)
	Si2–Br2	Si2–Br3	C1–Si1–Si2–C28	$\Sigma_4(\text{Si1})$
3^+_{calc}	2.262	2.250	163.0	286.4
3^+	2.234(1)	2.197(1)	155.7(2)	284.2

Supporting Information

6.9. Results of NBO, NPA and NRT analysis of 3^{+}_{calc} **Table S20.** Selected NBOs, WBI, NRT-BO and NPA charges of 3^{+}_{calc} .

NBO A–B	Occ. ^a	NHO (pol.) ^b A, B [%]	WBI ^c A–B	NRT-BO ^d tot/cov/ion	atom/ group	q/ $\sum q^e$
$\sigma(\text{Si1}-\text{C1})$	1.93	$\text{sp}^{9.8}(21)$, $\text{sp}^{1.4}(79)$	0.7	1.1/0.7/0.4	Si1	+0.51
$\sigma(\text{Si1}-\text{Si2})$	1.90	$\text{p}(35)$, $\text{sp}^{1.2}(65)$	0.9	1.0/0.3/0.7	Si2	+0.70
$\sigma(\text{Si1}-\text{Br1})$	1.94	$\text{p}(22)$, $\text{sp}^{4.0}(78)$	0.7	1.0/0.6/0.4	C1-NHC	+0.27
$\sigma(\text{Si2}-\text{C28})$	1.93	$\text{sp}^{4.1}(26)$, $\text{sp}^{1.6}(74)$	0.7	1.0/0.5/0.5	C28-NHC	+0.43
$\sigma(\text{Si2}-\text{Br2})$	1.97	$\text{sp}^{4.4}(30)$, $\text{sp}^{5.0}(70)$	0.9	1.0/0.4/0.6	SiBr	+0.40
$\sigma(\text{Si2}-\text{Br3})$	1.96	$\text{sp}^{4.7}(30)$, $\text{sp}^{4.6}(70)$	0.9	1.0/0.4/0.5	SiBr ₂	+0.60
Si1(LP)	1.82	$\text{sp}^{0.3}$				

^a: Occ.= occupancy; ^b: NHO = Natural Hybrid Orbital, pol. (polarization) = $(C_i)^2 \cdot 100\%$, where C_i = coefficient of NHO; ^c: Wiberg bond index; ^d: total, covalent and ionic NRT bond order; ^e: q = NPA charge of the atom, $\sum q$ = total NPA charge of the group.

Natural Lewis Structures (NLSs) of 3^{+}_{calc}

A local NRT analysis was done using all N-heterocyclic ring atoms and the Si_2Br_3 core atoms.

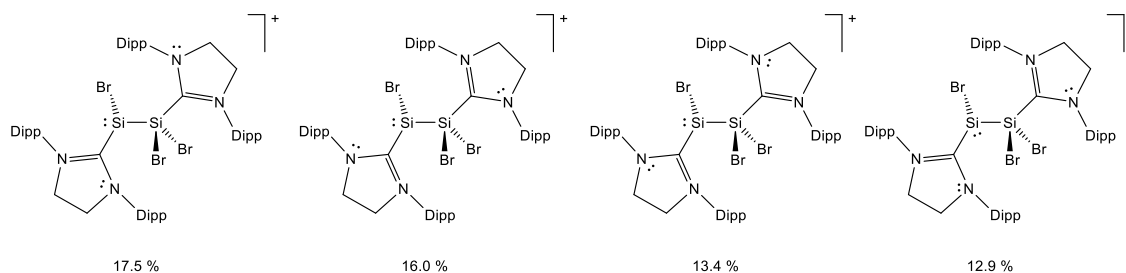


Figure S63. Natural Lewis Structures (NLSs) of 3^{+}_{calc} and their NRT weight % in the resonance hybrid; formal charges were omitted for the sake of clarity.

Supporting Information

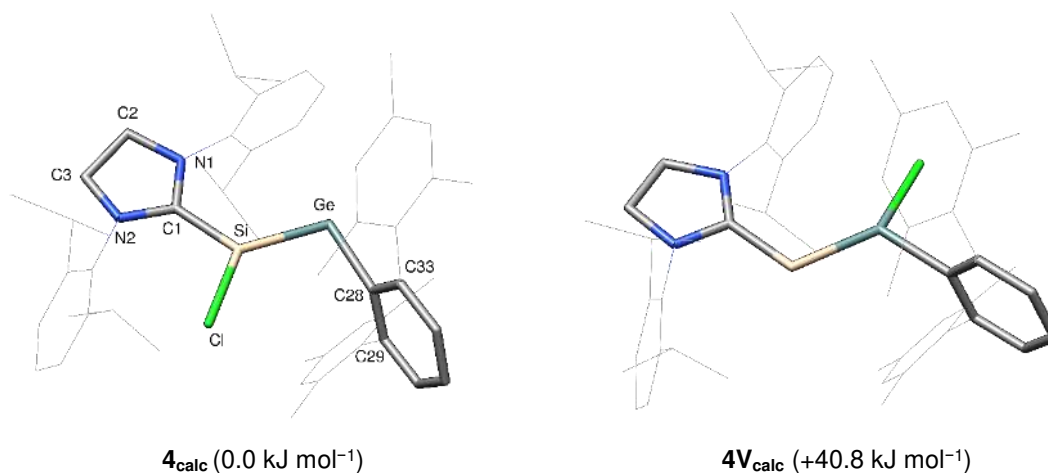
6.10. Optimized structure of 4_{calc} and its constitutional isomer $4V_{\text{calc}}$ 

Figure S64. Optimized minimum structure of 4_{calc} and its constitutional isomer $4V_{\text{calc}}$; relative pure electronic energies are given in parentheses.

Table S21. Comparison of selected calculated and experimental structural parameters (bond lengths / Å, angles / °) of 4_{calc} and $4V_{\text{calc}}$.

	Si–C1	Si–Ge	Ge–Cl	Ge–C28	C1–Si–Cl
4_{calc}	1.870	2.311	2.120	2.046	108.5
4^{a}	1.877(2), 1.878(2)	2.284(1), 2.265(1)	2.103(1), 2.091(1)	2.024(2), 2.036(2)	107.1(1), 108.4(1)
$4V_{\text{calc}}$	1.910	2.275	2.242	2.003	–
	Si–Ge–Cl	C1–Si–Ge	Si–Ge–C28	C1–Si–Ge–C28	
4_{calc}	–	121.2	97.6	–176.1	
4^{a}	–	122.0(1), 122.1(1)	100.9(1), 98.9(1)	–179.9(1), 173.2(1)	
$4V_{\text{calc}}$	144.5	110.5	113.5	–178.2	

a) The structural parameters of the two independent molecules of **4** are given.

Supporting Information

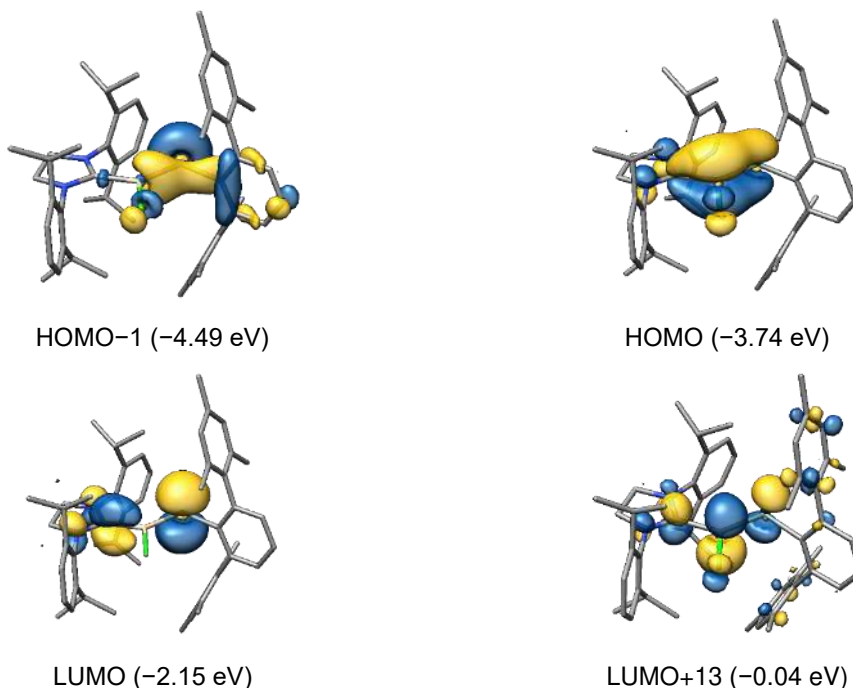
6.11. Selected Kohn-Sham orbitals of 4_{calc} 

Figure S65. Selected KS orbitals of 4_{calc} and their orbital energies in parentheses. The isosurface value is set to $0.04 \text{ e}^{1/2} \cdot \text{Bohr}^{-3/2}$.

6.12. Results of NBO, NPA and NRT analysis of 4_{calc}

Table S22. Selected NBOs, WBI, NRT-BO and NPA charges of 4_{calc} .

NBO A-B	Occ. ^a	NHO (A,B) ^b , hyb (pol in %)	WBI ^c A-B	NRT-BO ^d tot/cov/ion	atom/ group	$q/\sum q^e$
$\sigma(\text{Si}-\text{C}_{\text{NHC}})$	1.95	$\text{sp}^{2.9}(25)$, $\text{sp}^{1.4}(75)$	1.0	1.3/0.7/0.6	Si	+0.53
$\pi(\text{Si}-\text{C}_{\text{NHC}})$	1.59	$p(57)$, $p(43)$			Ge	+0.29
$\sigma(\text{Si}-\text{Ge})$	1.93	$\text{sp}^{0.8}(63)$, $\text{sp}^{9.8}(37)$	1.4	1.5/1.0/0.5	Cl	-0.40
$\sigma(\text{Si}-\text{Cl})$	1.98	$\text{sp}^{4.3}(24)$, $\text{sp}^{3.0}(76)$		1.0/0.5/0.5	NHC	+0.06
Ge(LP)	1.89	$\text{sp}^{0.2}$			Ar ^{Mes}	-0.48

^a: Occ.= occupancy; ^b: NHO = Natural Hybrid Orbital, pol. (polarization) = $(C_i)^2 \cdot 100\%$, where C_i = coefficient of NHO; ^c: Wiberg bond index; ^d: total, covalent and ionic NRT bond order; ^e: q = NPA charge of the atom, $\sum q$ = total NPA charge of the group.

Table S23. Second order perturbation theory analysis of the Fock matrix in NBO basis of 4_{calc} for the selected important donor and acceptor NBOs.

Donor NBO	Acceptor NBO	Non-Lewis occ.	$E^{(2)}$ (kJ mol ⁻¹)
$\pi(\text{Si}-\text{C}_{\text{NHC}})$	LV(Ge)	0.53	32
LP(N1 _{NHC})	$\pi^*(\text{Si}-\text{C}_{\text{NHC}})$	0.48	47
LP(N2 _{NHC})	$\pi^*(\text{Si}-\text{C}_{\text{NHC}})$	0.48	46

Supporting Information

Natural Lewis Structures (NLSs) of 4_{calc}

A local NRT analysis of 4_{calc} including the atoms N_{NHC} , C_{NHC} , Si, Ge Cl and the ring carbon atoms of the central Ar^{Mes} phenyl ring yielded 54 NLSs with contributions ranging from 12.1% – 0.1% covering 94% of the resonance hybrid. Inspection of these NLSs according to the core bonding motif (marked blue in *Figure S66*) yielded three NLS **4A-C**. The core bonding motif of **1A-E** was found in 17, 20 and 21 NLSs, respectively.

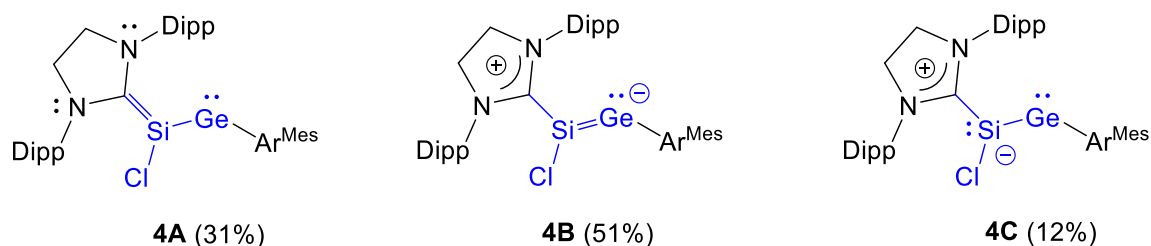


Figure S66. Natural Lewis Structures (NLSs) of 4_{calc} and their NRT weight % in the resonance hybrid.

6.13. Relaxed potential energy surface scan for the NHC-rotation in 4_{calc}

A PES scan of 4_{calc} was carried out varying the N2-C1-Si-Ge torsion angle from 10° to 180° in steps of 10° . A maximum value of 18 kJ mol^{-1} was obtained for the barrier to NHC-rotation at a N2-C1-Si-Ge torsion angle of 90° . A transition state optimization was not performed.

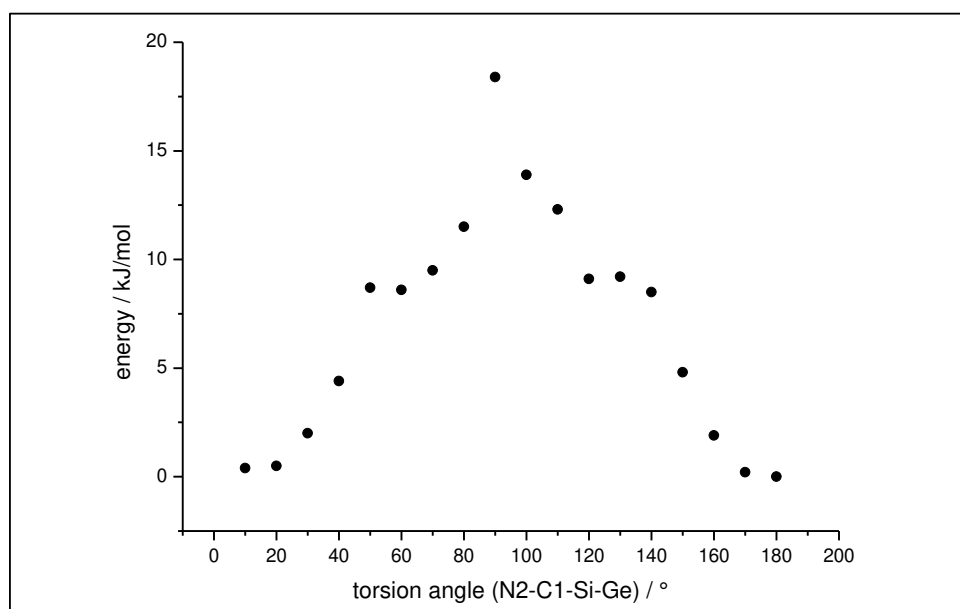


Figure S67. Plot of the energy versus the torsion angle N2-C1-Si-Ge obtained from a relaxed PES scan of 4_{calc} in scan steps of 10° .

Supporting Information

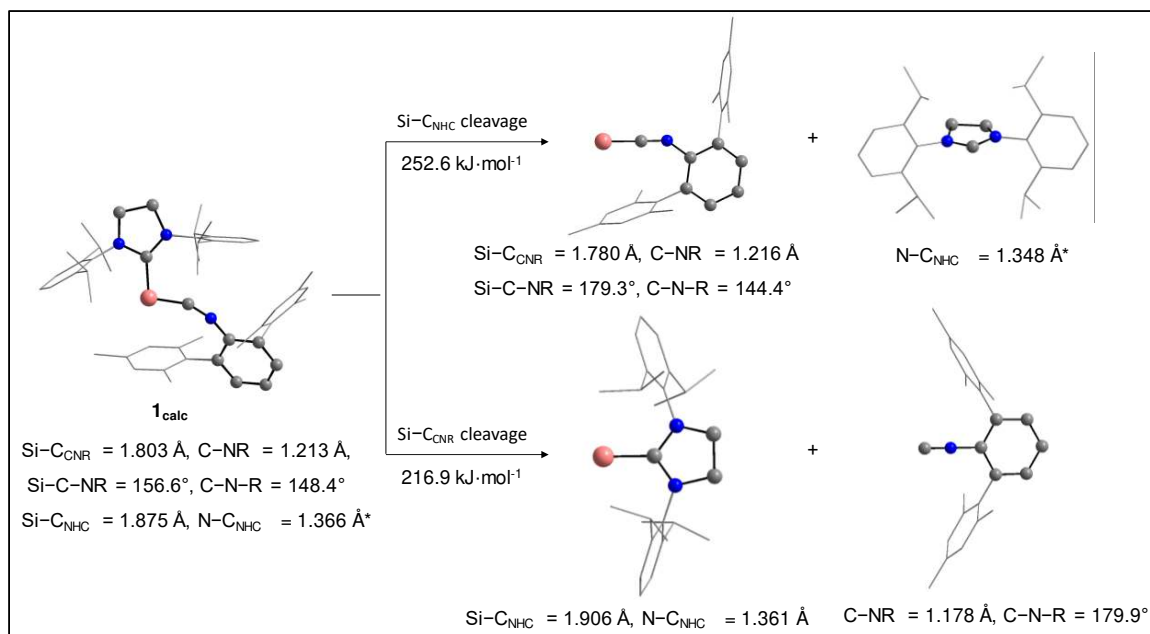
6.14. Bond dissociation energy (BDE) calculations of 1_{calc} , 2^+_{calc} and related Si(II) and Si(0) NHC compounds

Figure S68. Bond dissociation processes in 1_{calc} and comparison of selected calculated bonding parameters of the fragments; the bond lengths marked with an asterisk (*) are the average values of the two N-C_{NHC} bonds.

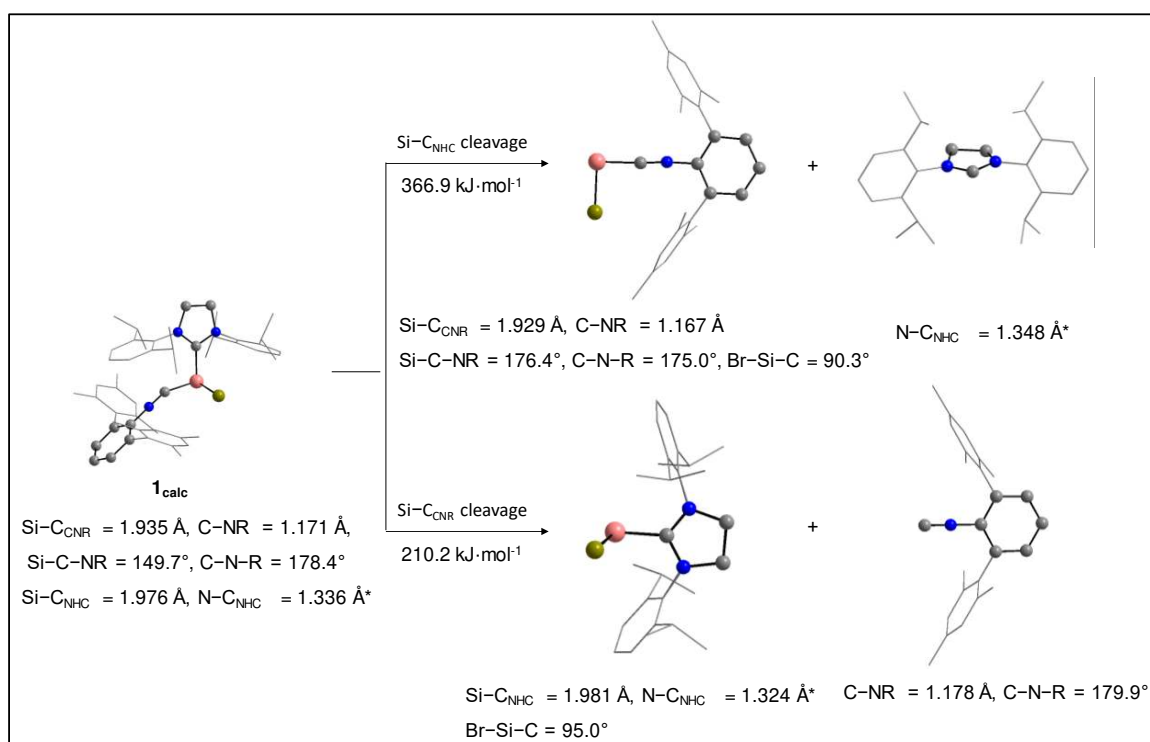


Figure S69. Bond dissociation processes in 2^+_{calc} and comparison of selected calculated bonding parameters of the fragments; the bond lengths marked with an asterisk (*) are the average values of the two N-C_{NHC} bonds.

Supporting Information

Table S24. Calculated ligand dissociation energies (ΔE_{el}) of $\mathbf{1}_{calc}$, $\mathbf{2}^+_{calc}$ and related silicon compounds into the respective fragments in their electronic ground states at the B97-D3(BJ)-ATM/def2-TZVP level of theory.

Si-C _{NHC} Dissociation			ΔE_{el} (kJ mol ⁻¹)
Si(SiDipp)(CNAr ^{Mes}) ($\mathbf{1}_{calc}$)	→	³ [SiCNAr ^{Mes}] ^a + ¹ [SiDipp]	252.6
Si ₂ (SiDipp) ₂	→	¹ [Si ₂ (SiDipp)] + ¹ [SiDipp]	246.3
Si ₂ (IDipp) ₂	→	¹ [Si ₂ (IDipp)] + ¹ [IDipp]	252.1
SiBr ₂ (SiDipp)	→	¹ [SiBr ₂] + ¹ [SiDipp]	189.5
SiBr ₂ (IDipp)	→	¹ [SiBr ₂] + ¹ [IDipp]	195.5
[SiBr(CNAr ^{Mes})(SiDipp)] ⁺ ($\mathbf{2}^+_{calc}$)	→	¹ [SiBr(CNAr ^{Mes}) ⁺] + ¹ [SiDipp]	366.9
Si-C _{CNR} Dissociation			ΔE_{el} (kJ mol ⁻¹)
Si(SiDipp)(CNAr ^{Mes}) ($\mathbf{1}_{calc}$)	→	³ [Si(SiDipp)] ^b + ¹ [CNAr ^{Mes}]	216.9
[SiBr(CNAr ^{Mes})(SiDipp)] ⁺ ($\mathbf{2}^+_{calc}$)	→	¹ [SiBr(SiDipp)] ⁺ + ¹ [CNAr ^{Mes}]	210.2

a) $\Delta E_{t \rightarrow s} = +48.5$ kJ mol⁻¹; b) $\Delta E_{t \rightarrow s} = +19.4$ kJ mol⁻¹.

The calculated NHC bond dissociation energies of Si₂(IDipp)₂ and SiBr₂(IDipp) at the B97-D3(BJ)-ATM/def2-TZVP level of theory are considerably higher than those previously obtained at the B3LYP/6-311+G**(Si,C_{NHC},N_{NHC})/6-31G*(C,H) and B3LYP/TZVPP(Si,Br,C_{NHC})/6-31G*(C,H) levels of theory respectively.^[S38] The difference can be traced back to the very repulsive nature of the B3LYP functional lacking dispersive effects.^[39]

6.15. Computational study of the stereodynamics of $\mathbf{1}_{calc}$

Compound **1** crystallizes in a achiral space group and contains in its unit cell a pair of the enantiomers (*R_a*)-**1** and (*S_a*)-**1** differing in the sign of the torsion angles C1–Si–N3–C29 (α) and N1–C1–Si–C28 (β) (Figure S70, Figure S71). The ¹H NMR spectrum of **1** in solution shows, however, one singlet for the C^{2,6}-positioned methyl groups of the mesityl substituents, one singlet for the C^{4,5}-H₂ protons of the N-heterocyclic ring of SiDipp and a single set of signals for the Dipp substituents and their C²/C⁶ and C³/C⁵-bonded groups (Figure S10 and Figure S11). This observation is not compatible with the axial chirality of **1** and the stereochemical arrangement of the NHC and Ar^{Mes} groups, which let us assume, that a rapid racemization of **1** ((*R_a*)-**1** ⇌ (*S_a*)-**1**) occurs in solution as well as a rotation of the NHC about the Si–C1 bond and a rotation of the Ar^{Mes} group about the N3–C29 bond.

In order to rationalize the stereodynamics of **1** (Figure S72) various scans of the potential energy hypersurface were carried out (Figure S73 - Figure S74). At first the energy profile for

[S38] a) Arz, M. I.; Straßmann, M.; Meyer, A.; Schnakenburg, G.; Schiemann, O.; Filippou, A. C. *Chem. Eur. J.* **2015**, *21*, 12509. b) Filippou, A. C.; Chernov, O.; Schnakenburg, G. *Angew. Chem., Int. Ed.* **2009**, *48*, 5687; *Angew. Chem.* **2009**, *121*, 5797.

[S39] Filippou, A. C.; Das, U.; Rump, J.; Kumar, S.; Baus, L.; personal communication.

Supporting Information

the rotation of the NHC around the Si–C1 bond was studied by varying the torsion angle β from (-3.1°) to (-173°) (Figure S73). A maximum barrier of 45.8 kJ mol^{-1} was obtained at a β angle of -103° (Figure S73, black circles). Notably, during the NHC rotation the skeletal torsion angle α (C1–Si–N3–C29) varied from -147.7° to -117.9° (Figure S73, green squares), but did not change the sign indicating that the NHC rotation involves a chiral path leading from $(R_a)\text{-1}_{\text{calc}}$ to its topomer $(R_a)\text{-1}^*_{\text{calc}}$, in which the diastereotopic N-Dipp substituents have exchanged their position. The transition state $(R_a)\text{-1-TS}_{\text{rot}}$ for the diastereotopomerisation was obtained by transition state optimization after calculating the exact Hessian matrix of the structure obtained as the energetic maximum of the PES scan of the torsion angle β , and lies 41 kJ mol^{-1} higher in energy than $(R_a)\text{-1}_{\text{calc}}$. It displays one imaginary frequency of -43 cm^{-1} involving the out of the skeletal plane (C1–Si–C28–N3) twisting mode of the N-heterocyclic ring and features an α angle of -118.6° , a β angle of -98.9° and an angle at the isocyanide atom C28–N3–C29 (γ) of 132.8° (Figure S72). The process described above, though, does not interconvert the enantiomers $(R_a)\text{-1}$ and $(S_a)\text{-1}$, and therefore does not lead to an exchange of the diastereotopic C² and C⁶ or C³ and C⁵ positions of the Dipp substituents, which would require a C_s symmetric transition state or intermediate with the symmetry plane passing through the C1–Si–C28–N3 skeleton. Therefore, a second process was presumed to be operative, which was analysed by PES scans involving a variation of the torsion angle Si–N3–C29–C30 (τ), i.e. a rotation of the Ar^{Mes} group about the N3–C29 bond starting from a value of 180° close to that found for $(R_a)\text{-1}_{\text{calc}}$ (-176°) (Figure S74). A maximum barrier of $+12.7 \text{ kJ mol}^{-1}$ was found at a torsion angle of 60° showing that rotation of the Ar^{Mes} group about the N3–C29 bond occurs easily (Figure S74, black circles). Notably, a close inspection of the structural parameters of the single-point structures at each scan step revealed only a slight twisting of the NHC out of the C1–Si–C28–N3 skeleton (the β angle varied from -10.5° to $+21.7^\circ$) but not a full rotation. Furthermore, a concomitant increase of the angle γ (C28–N3–C29) towards linearity ($\gamma = 170.9^\circ$) was observed upon decrease of the torsion angle τ from 180° to 100° (Figure S74), as well as a change of the skeletal torsion angle α from -130° to -177° indicating that the skeleton C1–Si–N3–C29 approaches an antiperiplanar conformation. This let us presume that enantiomerization of $(R_a)\text{-1}_{\text{calc}}$ might be connected with a linearization of the isocyanide moiety at the N-atom and a concomitant antiperiplanar conformation of the C1–Si–N3–C29 skeleton. In fact, a search of the PES gave a N-linear conformer $\mathbf{1LN}_{\text{calc}}$ ($\alpha = -172.8^\circ$, $\beta = 3.26^\circ$, $\gamma = 180.0^\circ$) as a local minimum structure, which lies $+16.4 \text{ kJ mol}^{-1}$ higher in energy than $(R_a)\text{-1}_{\text{calc}}$ (Figure S72) and features an almost barrierless rotation of the Ar^{Mes} about the N3–C29 bond interconverting the enantiomers. Attempts to find the transition state connecting $(R_a)\text{-1}^*$ with $\mathbf{1LN}_{\text{calc}}$ failed due to the flatness of the hypersurface.

Supporting Information

Finally, a coupled (concomitant) process of NHC rotation (topomerization) and enantiomerization ($(R_a)\text{-1} \rightleftharpoons (S_a)\text{-1}$) via a structurally constrained C_s symmetric species **1-SP** ($\alpha = 180^\circ$, $\beta = 101.7^\circ$) was found to be energetically highly unfavorable as it is a second-order saddle point in the PES of $(R_a)\text{-1}_{\text{calc}}$ with two significant imaginary frequencies of -101 and -88 cm^{-1} and lies at $+64.5 \text{ kJ mol}^{-1}$ higher in energy relative to $(R_a)\text{-1}_{\text{calc}}$ **1** (Figure S72). The above studies suggest that the stereodynamics of **1** proceeds stepwise via a NHC rotation and Ar^{Mes} rotation the latter being coupled with an $(R_a)\text{-1}$ to $(S_a)\text{-1}$ interconversion (racemization) via the N-linear conformer **1LN**_{calc} (Figure S72).

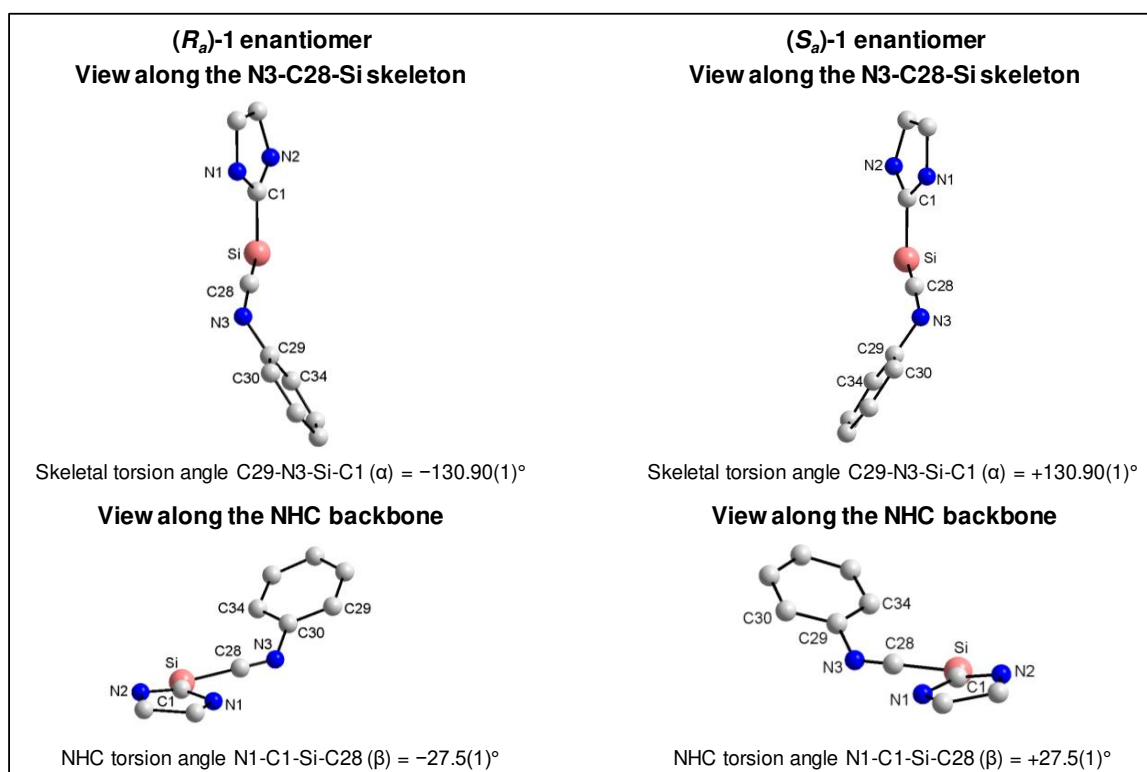


Figure S70. DIAMOND plots of the enantiomers $(S_a)\text{-1}$ and $(R_a)\text{-1}$ with their torsion angles α and β ; the Dipp and Mes substituents are omitted for the sake of clarity.

Supporting Information

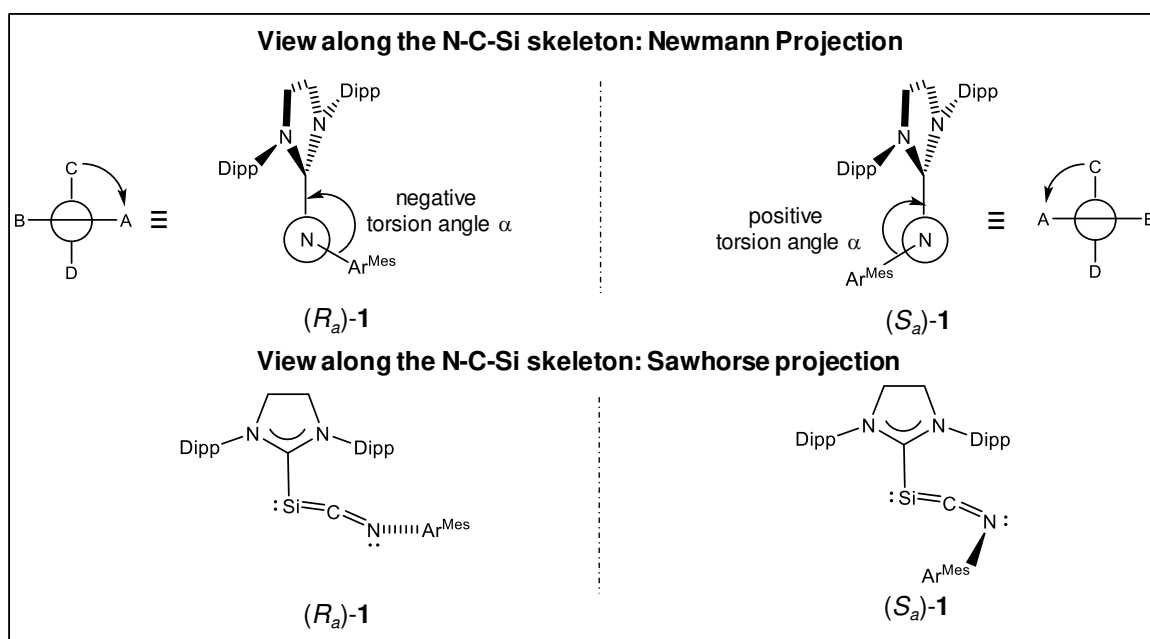


Figure S71. R_a and S_a configuration of the axially chiral **1**, in which the chirality axis passes through the N and Si atoms of the Si=C=N skeleton and its relation to the skeletal torsion angle α . For each pair of substituents (A-B and C-D), the higher ranking substituents were chosen using the Cahn-Ingold-Prelog sequence rule (A > B, C > D), with A being the Ar^{Mes}, B the lone pair at the N atom, C the C_{NHC} atom and D the lone pair at the Si atom. The arrow from the substituent with the higher priority on the line with a circle to the one with higher priority on the solid line determines the configuration (R_a : clockwise, S_a : anti-clockwise).

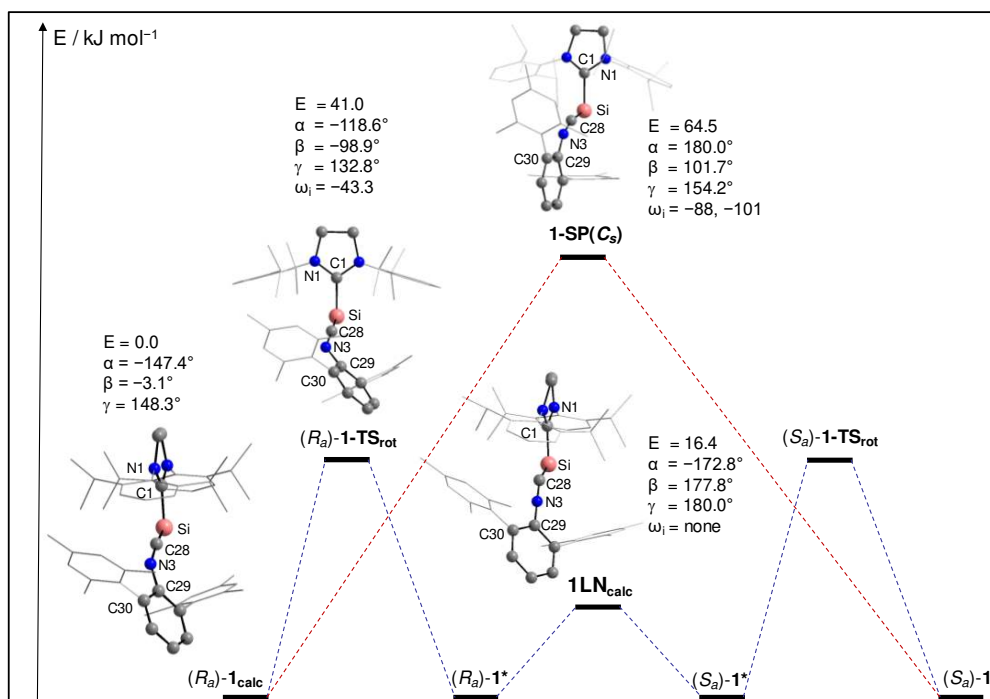


Figure S72. Proposed mechanism for the enantioimerization of **1**_{calc}; ω_i = harmonic imaginary frequencies in cm^{-1} , E = energy in kJ mol^{-1} versus (R_a)-**1**_{calc}, α : skeletal torsion angle C1-Si-N3-C29, β : NHC torsion angle N1-C1-Si-C28, γ : angle C28-N3-C29.

Supporting Information

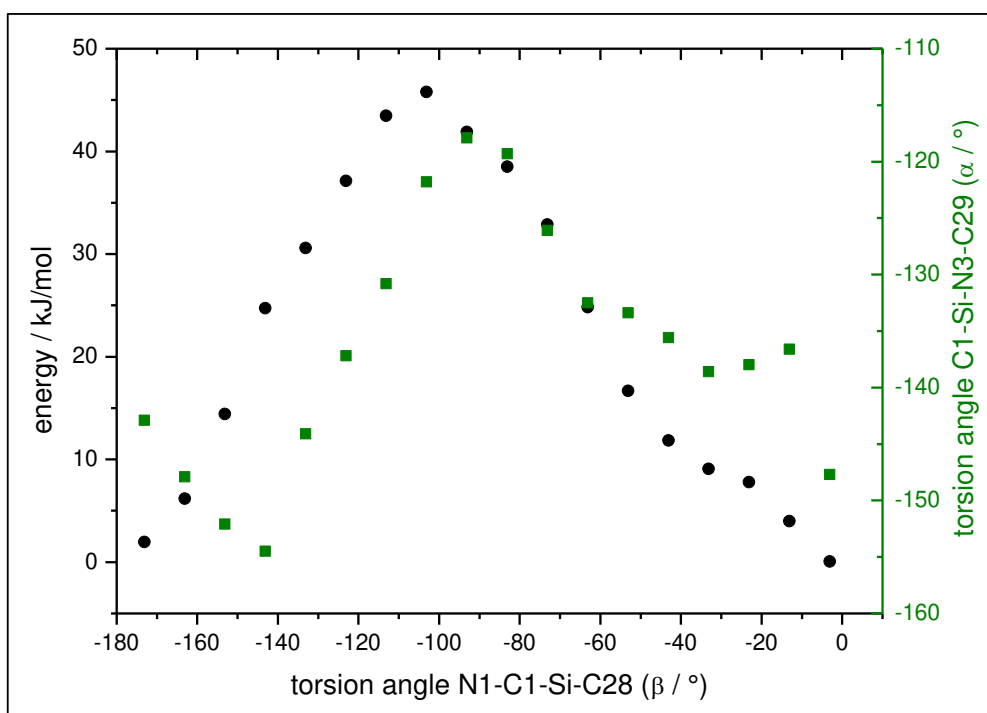


Figure S73. Plot of the energy (black circles) and the torsion angle C1-Si-N3-C29 (α) (green squares) versus the torsion angle N1-C1-Si-C28 (β) obtained from the relaxed PES scan of (R_a) -1_{calc} in scan steps of 10°.

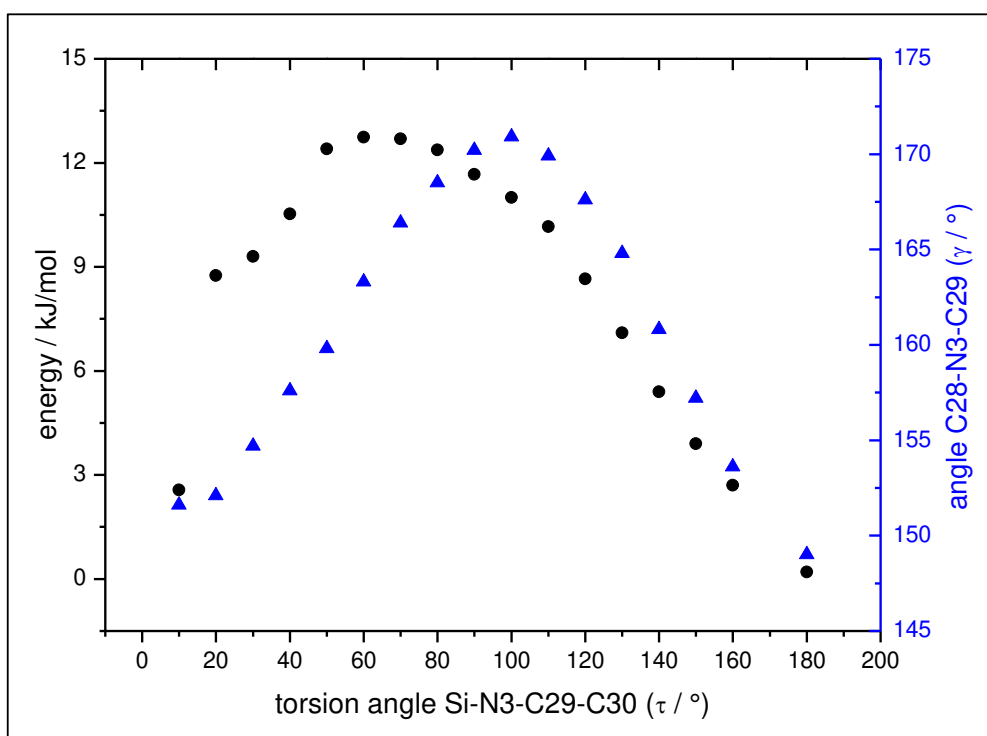


Figure S74. Plot of the energy (black circles) and the angle C28-N3-C29 (γ) (blue triangles) versus the Si-N3-C29-C30 (τ) torsion angle obtained from the relaxed PES scan of (R_a) -1_{calc} in scan steps of 10°.

Further Studies on Iminosilylenidenes

Isocyanide structures

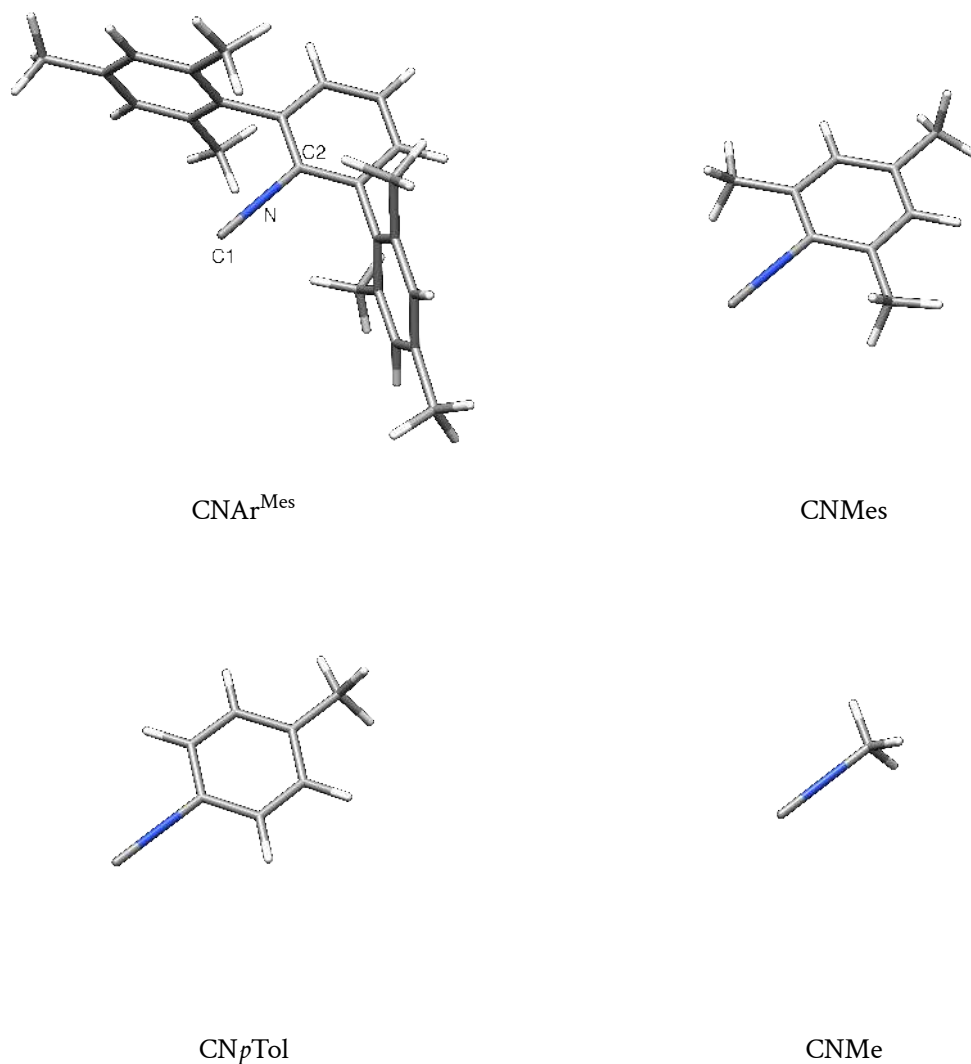
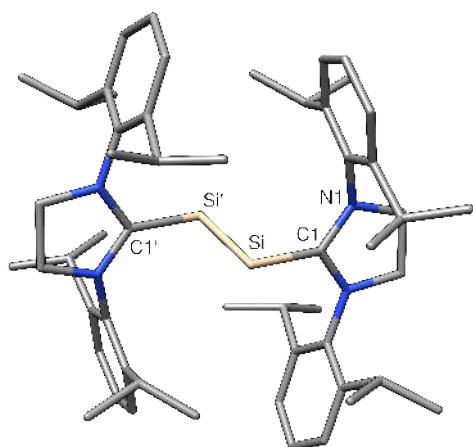


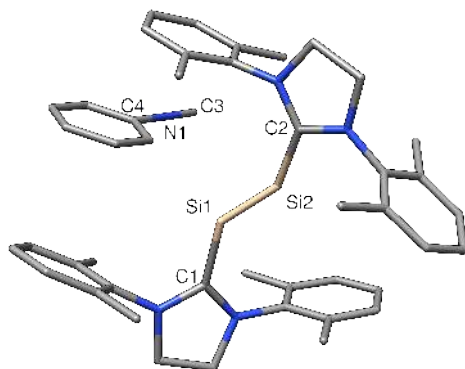
Figure 11.8: Level of theory I-optimized gas phase structures of the isocyanides CNR with $\text{R} = \text{Ar}^{\text{Mes}}, \text{Mes}, ^p\text{Tol}$ and Me. See Table 11.1 for the structural parameters.

Table 11.1: Selected structural parameters of the calculated isocyanides CNR. Bond lengths and angles are given in pm and degrees, respectively.

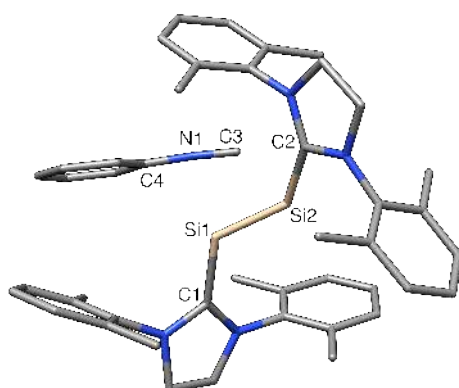
	C1-N	N-C _R	C1-N-C _R
CNAr^{Mes}	117.8	138.2	179.7
CNMe	117.9	138.3	179.9
CN^pTol	117.9	138.2	179.8
CNMe	117.4	142.0	180.0

(SIDippSi)₂

Si–C1	192.1
Si–Si'	224.6
C1–Si–Si2	95.1
C'–Si–Si'–C1'	–180.0
N1–C1–Si–Si'	94.1

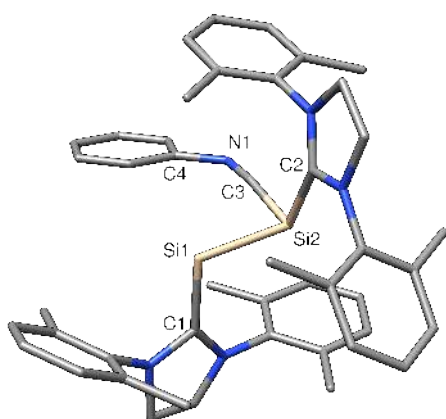
{((SIX)Si)₂+CNPh}

Si1–C1	193.3	C1–Si1–Si2	100.4
Si2–C2	191.8	C2–Si2–Si1	95.6
Si1–Si2	225.1	C3–N1–C4	177.8
Si1···C3	676.9	C1–Si1–Si2–C2	–170.9
Si2···C3	552.6		
C3–N1	117.8		
N1–C4	138.5		

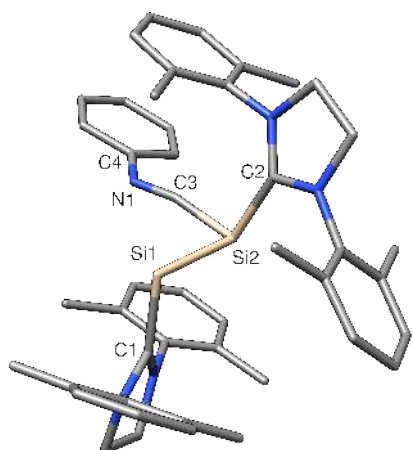
A-7X-TS1 ($\nu_{TS} = 77i \text{ cm}^{-1}$)

Si1–C1	192.4	C1–Si1–Si2	100.3
Si2–C2	192.0	C2–Si2–Si1	95.6
Si1–Si2	230.2	C3–N1–C4	159.1
Si1···C3	363.4	C1–Si1–Si2–C2	–164.7
Si2···C3	251.4		
C3–N1	119.1		
N1–C4	137.3		

A-7X-Int

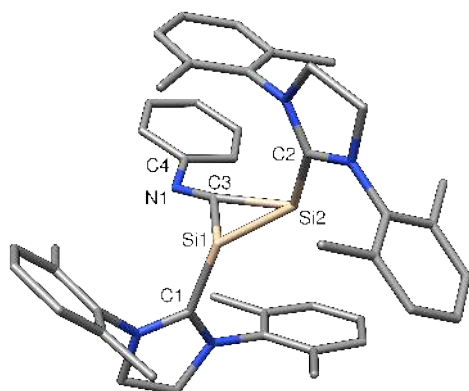


Si1–C1	188.5	C1–Si1–Si2	102.2
Si2–C2	190.2	C2–Si2–Si1	103.2
Si1–Si2	238.0	C3–N1–C4	136.5
Si1···C3	291.3	C1–Si1–Si2–C2	–153.8
Si2–C3	180.8	$\Sigma\angle(\text{Si2})$	290.8
C3–N1	122.1		
N1–C4	138.7		

A-7X-TS2 ($\nu_{\text{TS}} = 40i \text{ cm}^{-1}$)

Si1–C1	188.1	C1–Si1–Si2	100.2
Si2–C2	191.1	C2–Si2–Si1	103.6
Si1–Si2	237.7	C3–N1–C4	130.9
Si1···C3	283.5	C1–Si1–Si2–C2	–154.0
Si2–C3	179.7	$\Sigma\angle(\text{Si2})$	288.6
C3–N1	122.6		
N1–C4	139.2		

A-7X



Si1–C1	194.1	C1–Si1–Si2	106.9
Si2–C2	191.4	C2–Si2–Si1	82.9
Si1–Si2	246.6	C3–N1–C4	123.1
Si1–C3	191.4	C1–Si1–Si2–C2	–170.6
Si2–C3	192.1	$\Sigma\angle(\text{Si1})$	252.2
C3–N1	128.8	$\Sigma\angle(\text{Si2})$	230.9
N1–C4	140.1	$\Sigma\angle(\text{C3})$	355.6

Siladibene and Siladiimide Compounds

NHC Structures

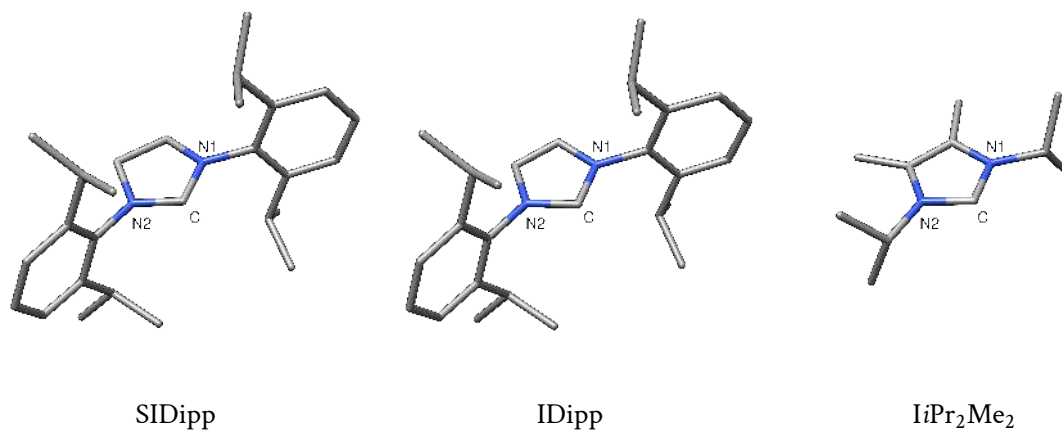


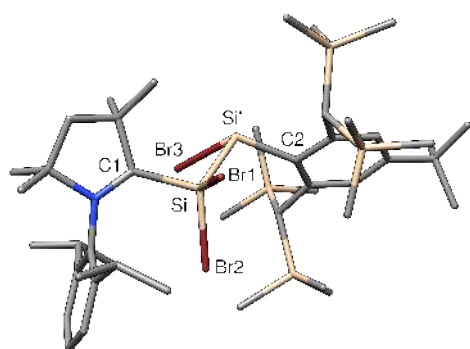
Figure 11.9: Level of theory I-optimized gas phase structures of N-heterocyclic carbenes. See Table 11.2 for their structural parameters.

Table 11.2: Selected structural parameters of the calculated free NHCs SIDipp, IDipp and IiPr₂Me₂ in their singlet ground state. Bond lengths and angles are given in pm and degrees, respectively.

	C–N1	C–N2	N–C–N	$\Sigma\angle(N1)$	$\Sigma\angle(N2)$
SIDipp	134.7	134.8	105.7	359.4	359.3
IDipp	137.4	137.4	101.2	360.0	360.0
IiPr ₂ Me ₂	136.8	136.8	102.7	359.9	360.0

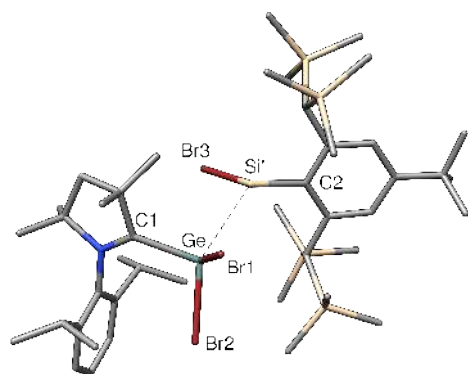
CAAC-stab. Heavier Ditetrelynes and Ditetrelenylenes

(CAAC^{Me})Si(Br)₂Si(Br)Tbb (A-16Si')



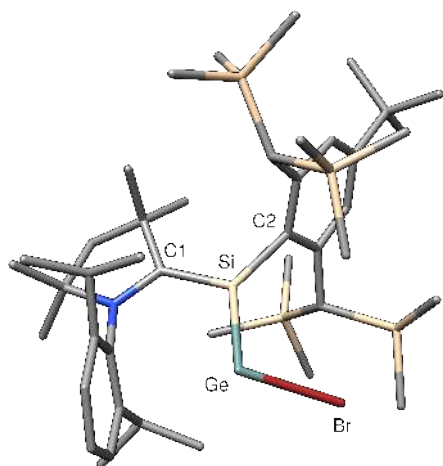
Si–C1	198.3	C1–Si–Si'	112.8
Si–Si'	241.4	$\Sigma\angle(Si')$	301.8
Si–Br1	233.2		
Si–Br2	229.0		
Si'–Br3	247.2		
Si'–C2	194.8		

(CAAC^{Me})Ge(Br)₂Si(Br)Tbb (A-16Ge')



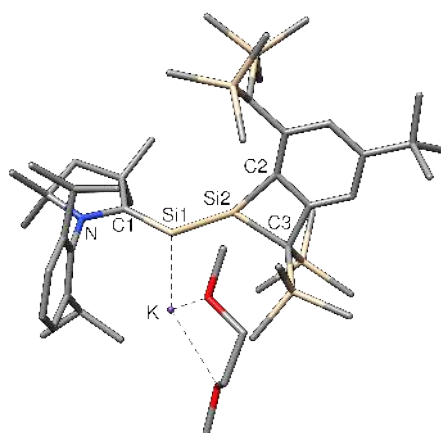
Ge—C1	215.6	C1—Ge···Si'	103.9
Ge···Si'	298.4	Σ∠(Ge)	303.8
Ge—Br1	244.2		
Ge—Br2	246.7		
Si'—Br3	238.2		
Si'—C2	190.5		

(CAAC^{Me})Si(Tbb)GeBr (A-21)



Si—C1	183.0	C1—Si—Ge	114.8
Si—Ge	241.1	Si—Ge—Br	101.1
Si—C2	190.7	C1—Si—Ge—Br	152.1
Ge—Br	246.2	Σ∠(Si)	360.0

(CAAC^{Me})Si(Br)₂Si(Br)Tbb (A-23)



Si1—C1	182.3	C1—Si1—Si2	107.8
Si1—Si2	234.7	N—C1—Si1—Si2	175.0
Si1—K	325.3		
Si2—H	150.3		
Si2—C2	188.7		
Si2—C3	201.1		

Digermyne Cobalt Complexes

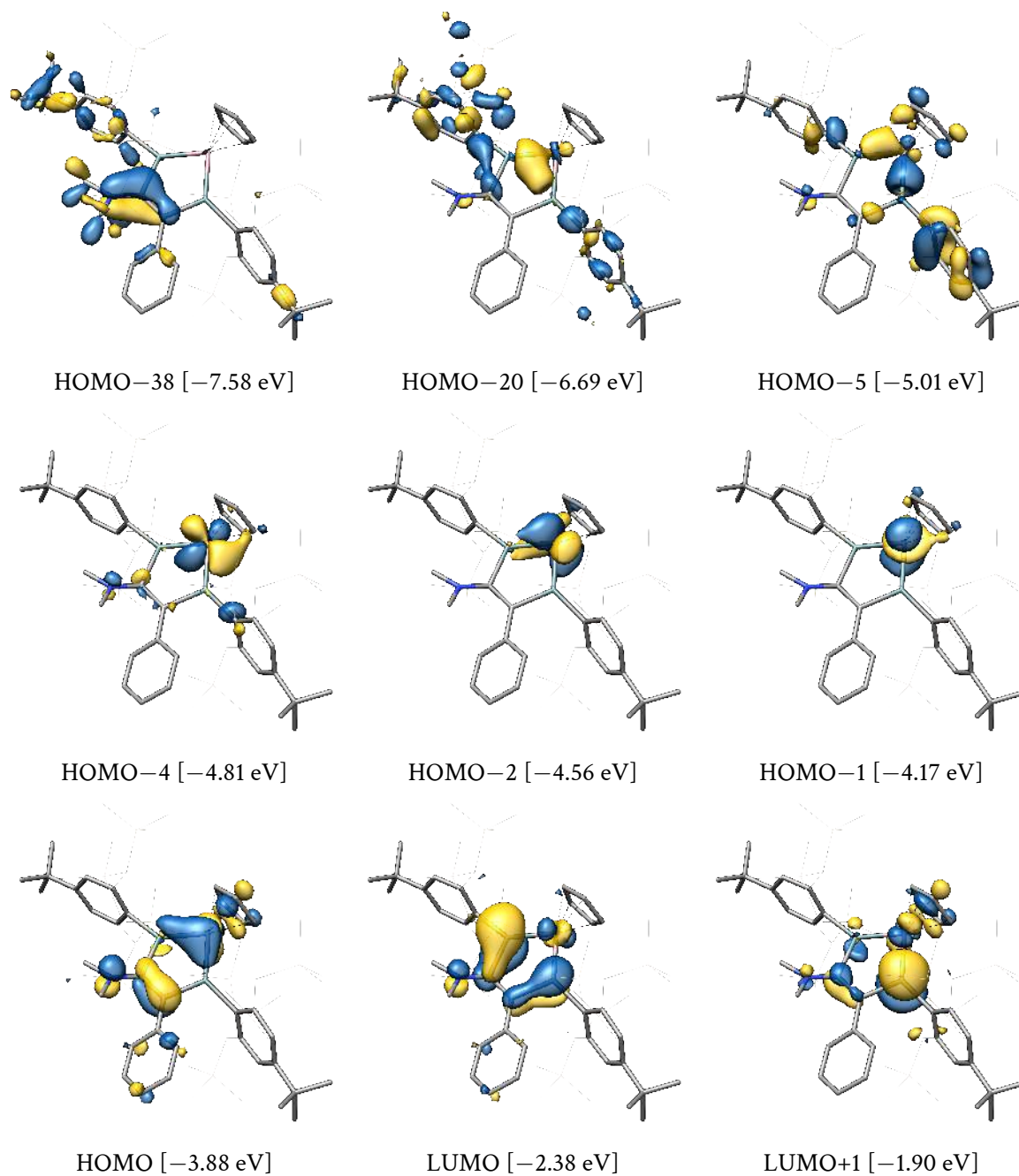


Figure 11.10: Selected canonical molecular orbitals of the complex B-7 and their energy eigenvalues.

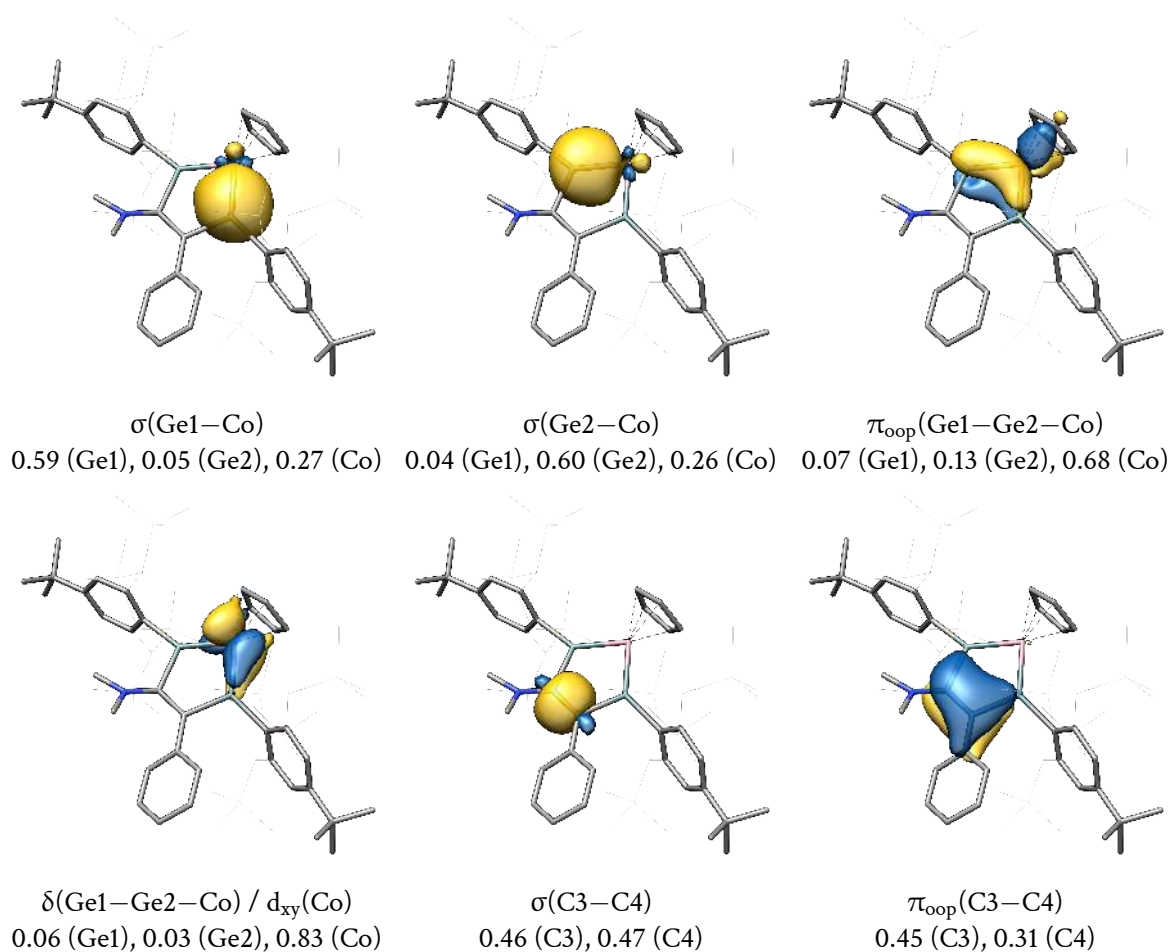
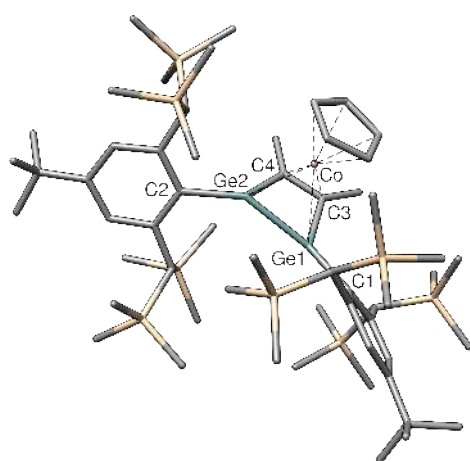


Figure 11.11: Selected intrinsic bond orbitals (IBOs) of the complex B-7 and their atomic Löwdin orbital populations.

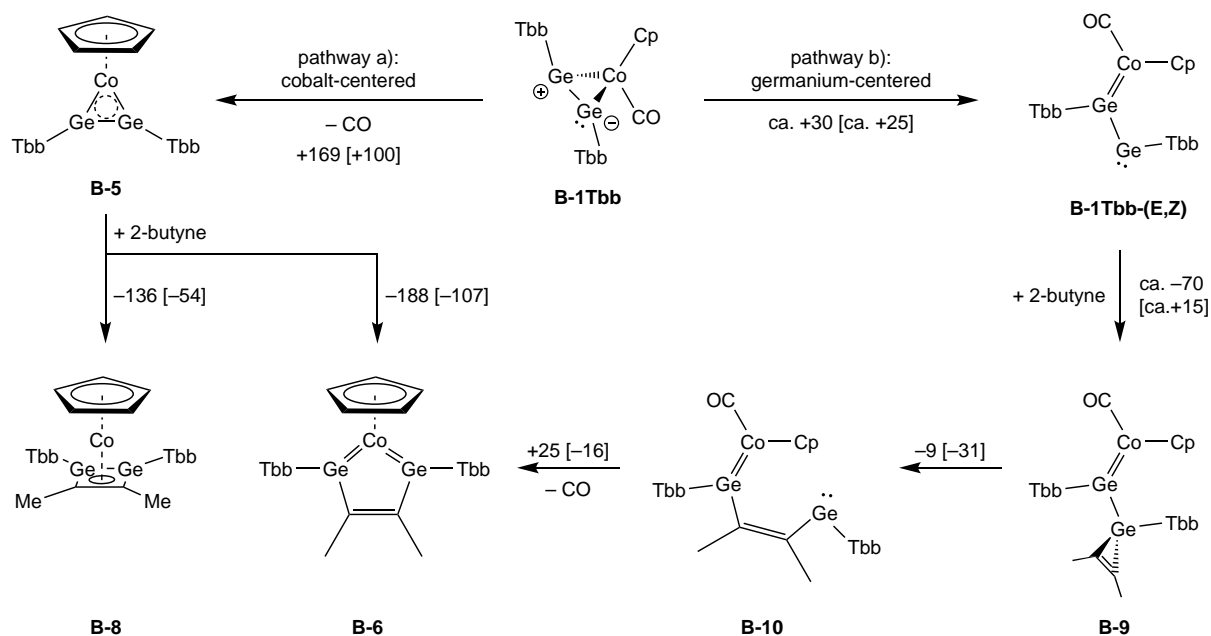
[CoCp(η^4 -(TbbGeC(Me)C(Me)GeTbb))] (B-8)



Ge1-Co	252.7	C3-Co	202.8
Ge2-Co	231.8	C4-Co	204.7
Ge1-Ge2	243.3	C1-Ge1-Ge2	149.4
Ge1-C1	199.9	C1-Ge1-C3	130.3
Ge2-C2	197.7	C1-Ge1-Ge2-C2	-72.2
Ge1-C3	197.0	$\Sigma\angle(\text{Ge1})$	354.4
Ge2-C4	195.1	$\Sigma\angle(\text{Ge2})$	346.7
C3-C4	142.0		

$\Sigma\angle(\text{Ge1,Ge2})$ are without the cobalt atom

More information on the postulated mechanisms to B-6

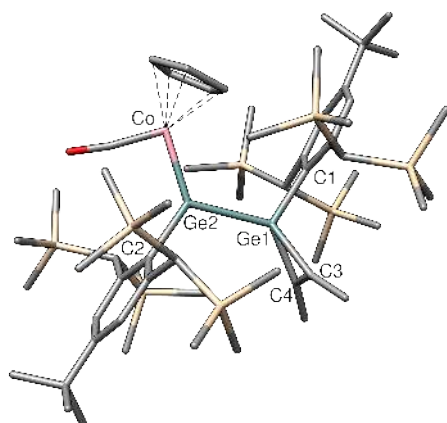


Scheme 11.2: Conceivable mechanisms for the reaction of the digermayne cobalt complex B-1Tbb to the digermacobaltacyclopentatriene B-6. The numbers without and within square brackets give the reaction electronic and free Gibbs energies, respectively. See Table 11.3 for more thermochemical quantities.

Table 11.3: Calculated thermochemical values at 298.15 K and 1 atm of the reaction pathways proposed in Scheme 11.2. Energies and enthalpies are given in $\text{kJ}\cdot\text{mol}^{-1}$, the entropy in $\text{J}\cdot\text{K}^{-1}\cdot\text{mol}^{-1}$.

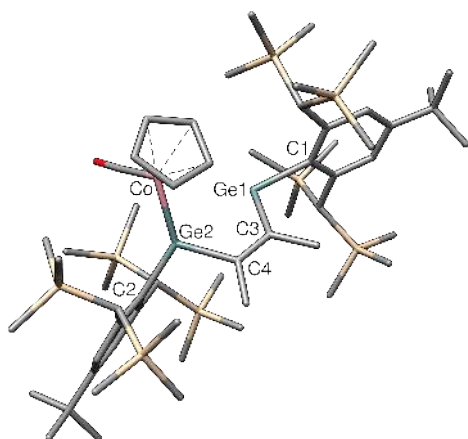
pathway a)	ΔE	ΔU	ΔH	ΔS	ΔG
B-1Tbb \rightarrow B-5 + CO	169.4	157.6	160.1	201.7	100.0
B-5 + 2-butyne \rightarrow B-6	-188.2	-177.4	-179.9	-245.1	-106.8
B-5 + 2-butyne \rightarrow B-8	-136.2	-121.9	-124.4	-235.7	-54.1
pathway b)					
B-1Tbb \rightarrow B-1Tbb-(E,Z)	≈ 30	≈ 25	≈ 25	≈ 10	≈ 25
B-1Tbb-(E,Z) + 2-butyne \rightarrow B-9	≈ -70	≈ -50	≈ -50	≈ -220	≈ 15
B-9 \rightarrow B-10	-9.2	-16.2	-16.2	49.0	-30.8
B-10 \rightarrow B-6 + CO	24.5	15.7	18.2	116.1	-16.4

[CoCp(CO)(Ge(Tbb)Ge(C2Me2)Tbb)] (B-9)



Ge1–Ge2	254.0	C3–C4	132.5
Ge2–Co	223.2	Ge1–Ge2–Co	120.4
Ge1–C1	199.3	C1–Ge1–Ge2	109.8
Ge1–C3	196.8	C1–Ge1–Ge2–C2	175.1
Ge1–C4	196.4	$\Sigma\angle(\text{Ge2})$	360.0
Ge2–C2	201.3		

[CoCp(CO)(Ge(Tbb)C(Me)C(Me)GeTbb)] (B-10)



Ge1···Ge2	337.4	C1–Ge1–C3	99.4
Ge1–C1	206.3	Ge1–C3–C4–Ge2	–19.1
Ge1–C3	203.6	$\Sigma\angle(\text{Ge2})$	357.6
Ge2–Co	222.0		
Ge2–C2	200.4		
Ge2–C4	199.7		
C3–C4	136.2		



Article

The Electronic Nature of Cationic Group 10 Ylidyne Complexes

Leonard R. Maurer [†], Jens Rump [†] and Alexander C. Filippou ^{*}

Institute of Inorganic Chemistry, University of Bonn, D-53121 Bonn, Germany; l.maurer@uni-bonn.de (L.R.M.); jens.rump@uni-bonn.de (J.R.)

* Correspondence: filippou@uni-bonn.de

† These authors contributed equally to this work.

Abstract: We report a broad theoretical study on $[(\text{PMe}_3)_3\text{MER}]^+$ complexes, with $M = \text{Ni, Pd, Pt}$, $E = \text{C, Si, Ge, Sn, Pb}$, and $R = \text{Ar}^{\text{Mes}}, \text{Tbb}$, ($\text{Ar}^{\text{Mes}} = 2,6\text{-dimesitylphenyl}$; $\text{Tbb} = \text{C}_6\text{H}_2\text{-}2,6\text{-}[\text{CH}(\text{SiMe}_3)_2]_2\text{-}4\text{-tBu}$). A few years ago, our group succeeded in obtaining heavier homologues of cationic group 10 carbyne complexes via halide abstraction of the tetrylidene complexes $[(\text{PMe}_3)_3\text{M}=\text{E}(\text{X})\text{R}]$ ($\text{X} = \text{Cl, Br}$) using a halide scavenger. The electronic structure and the M–E bonds of the $[(\text{PMe}_3)_3\text{MER}]^+$ complexes were analyzed utilizing quantum-chemical tools, such as the Pipek–Mezey orbital localization method, the energy decomposition analysis (EDA), and the extended-transition state method with natural orbitals of chemical valence (ETS-NOCV). The carbyne, silylyidyne complexes, and the germylydyne complex $[(\text{PMe}_3)_3\text{NiGeAr}^{\text{Mes}}]^+$ are suggested to be tetrylydyne complexes featuring donor–acceptor metal tetrel triple bonds, which are composed of two strong $\pi(\text{M}\rightarrow\text{E})$ and one weaker $\sigma(\text{E}\rightarrow\text{M})$ interaction. In comparison, the complexes with $M = \text{Pd, Pt}$; $E = \text{Sn, Pb}$; and $R = \text{Ar}^{\text{Mes}}$ are best described as metallotetrylenes and exhibit considerable M–E–C bending, a strong $\sigma(\text{M}\rightarrow\text{E})$ bond, weakened M–E π -components, and lone pair density at the tetrel atoms. Furthermore, bond cleavage energy (BCE) and bond dissociation energy (BDE) reveal preferred splitting into $[\text{M}(\text{PMe}_3)_3]^+$ and $[\text{ER}]$ fragments for most complex cations in the range of $293.3\text{--}618.3\text{ kJ}\cdot\text{mol}^{-1}$ and $230.4\text{--}461.6\text{ kJ}\cdot\text{mol}^{-1}$, respectively. Finally, an extensive study of the potential energy hypersurface varying the M–E–C angle indicates the presence of isomers with M–E–C bond angles of around 95° . Interestingly, these isomers are energetically favored for $M = \text{Pd, Pt}$; $E = \text{Sn, Pb}$; and $R = \text{Ar}^{\text{Mes}}$ over the less-bent structures by $13\text{--}29\text{ kJ}\cdot\text{mol}^{-1}$.

Keywords: group 10 metal; tetrylydyne complexes; multiple bonds; DFT



Citation: Maurer, L.R.; Rump, J.; Filippou, A.C. The Electronic Nature of Cationic Group 10 Ylidyne Complexes. *Inorganics* **2023**, *11*, 129. <https://doi.org/10.3390/inorganics11030129>

Academic Editor: Markus Bursch

Received: 16 February 2023

Revised: 13 March 2023

Accepted: 15 March 2023

Published: 18 March 2023



Copyright: © 2023 by the authors. Licensee MDPI, Basel, Switzerland. This article is an open access article distributed under the terms and conditions of the Creative Commons Attribution (CC BY) license (<https://creativecommons.org/licenses/by/4.0/>).

1. Introduction

Complexes of the general formula $L_n\text{M}\equiv\text{E}-\text{R}$ ($M = \text{d-block element}$, $E = \text{Si-Pb}$, $R = \text{singly bonded substituent}$, and $L_n = \text{ligand sphere}$), featuring a triple bond between a transition metal and the tetrels Si–Pb, are an intriguing class of compounds [1,2]. As heavier homologues of the Fischer-type carbyne complexes [3–7], these compounds, which are called tetrylydyne complexes, have a synthetic potential in organoelement and organometallic chemistry. Following the first reports of germylydyne complexes by P. P. Power et al. [8,9], numerous group 6 germylydyne complexes [10–14] as well as first representatives featuring metal–tin triple bonds [15,16] and metal–lead triple bonds [17–19] were obtained by our group using an efficient N_2 or PMe_3 elimination reaction of d^6 metal complexes with organotetrel(II)halides. Later on, the first group 6 silylydyne complexes were prepared from tailor-made 18 VE carbonyl metalates with NHC-stabilized silicon(II)halides [20,21], 1,2-dihalodisilenes [22,23], and base-supported silyliumylidene ions [24], or from the reactions of chloro/hydrosilylidene complexes with Lewis acids [25–28]. The isolation of these compounds is demanding and requires a fine stereoelectronic tuning of the metal fragment (ML_n) as well as a steric protection of the electrophilic tetrel center by a bulky substituent R, circumventing head-to-tail dimerization [29] or intra- and intermolecular σ -bond activation by the $\text{M}\equiv\text{E}-\text{R}$ functionality.

Previous quantum chemical analyses suggest that tetrylidyne complexes of the heavier group 14 elements have a similar electronic structure to that of Fischer-type carbyne complexes [6,10,16–18,30–34]. The M=E bonds are quite polar and composed of a σ bond, which is slightly less polarized toward the tetrel atom E than in Fischer-type carbyne complexes, and two π bonds, which are considerably more polarized to the metal center M than in their carbon analogues. This leads to partially positively charged ER ligands in the heavier tetrylidyne complexes, whereas the CR ligands in the related Fischer-type carbyne complexes bear a negative partial charge. The M=E–R bonding can be well described using the Dewar–Chatt–Duncanson model [35,36], comprising an $ER^+ \rightarrow ML_n^-$ σ donation and two $ML_n^- \rightarrow ER^+$ π back donations (Figure 1a). Alternatively, the M=E–R bonding in tetrylidyne complexes can be described by the interaction of the neutral, open-shell fragments (ML_n) and ER in their doublet electronic state (Figure 1b). In comparison, the related Schrock-type alkylidyne complexes [37,38] feature M=C bonds with two rather nonpolar π components. The M=C bonding in these compounds can be best described by electron pairing between the neutral open-shell fragments ML_n and ER in their quartet electronic state (Figure 1c) [30].

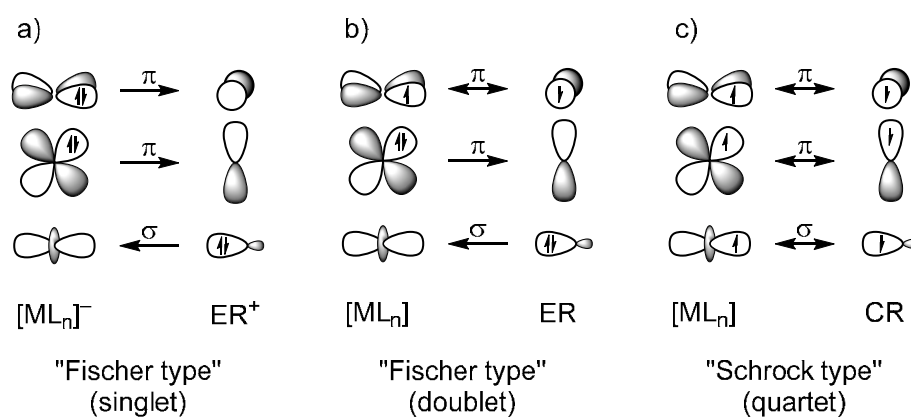
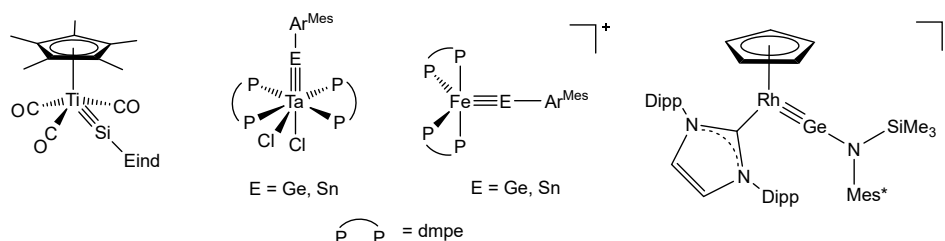


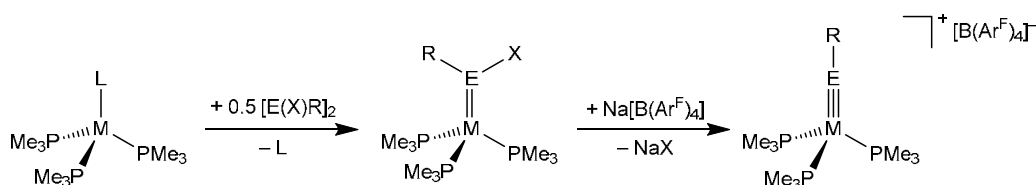
Figure 1. Schematic representation of the dominant orbital interactions in the heavier group 14 tetrylidyne complexes and Fischer-type carbyne complexes using charged, closed-shell fragments (a) or neutral fragments in the doublet state (b); dominant orbital interactions in the Schrock-type alkylidyne complexes using neutral, open-shell fragments in the quartet state (c).

While earlier experimental work focused on group 6 metal tetrylidyne complexes [8–20,39–42], more recent studies have shown that group 4 (Ti) [43], group 5 (Nb, Ta) [22,44], group 7 (Mn, Re) [45–47], group 8 (Fe, Os) [26,48], and group 9 metals (Co, Rh) [49,50] can also be incorporated into triple bonding with the heavier tetrels Si–Pb, significantly expanding this promising field of chemistry (Scheme 1).



Scheme 1. Examples for heavier tetrylidyne complexes of group 4, 5, 8, and 9 metals obtained by our group. Eind = 1,1,3,3,5,5,7,7-octaethyl-*s*-hydrindacene-4-yl, Ar^{Mes} = 2,6-dimesitylphenyl, dmpe = 1,2-bis(dimethylphosphino)ethane, Dipp = 2,6-di-*iso*-propylphenyl, and Mes^* = 2,4,6-*tert*-butylphenyl.

In this context, access to compounds where even the carbon analogues are very rare is particularly appealing. Illustrative examples are the tetrylidyne complexes of the group 10 metals. In fact, after the first report of a cationic nickel aminocarbonyl complex, $[(\text{CO})_2(\text{PPh}_3)\text{Ni}=\text{CN}^i\text{Pr}_2][\text{BCl}_4]$, by E. O. Fischer et al. ca. 40 years ago [51], no other group 10 carbonyl complexes have been isolated to date. Some years ago, a two-step approach to the first group 10 tetrylidyne complexes was developed by our group (Scheme 2) [52]. The first step involves a thermal ligand substitution reaction of $[\text{M}(\text{PMe}_3)_3\text{L}]$ ($\text{M} = \text{Ni}, \text{Pt}$; $\text{L} = \text{PMe}_3, \text{GaCp}^*, \text{Cp}^* = \text{C}_5(\text{CH}_3)_5$) with organotetrel(II)halides leading to the ylidyne complexes $[(\text{PMe}_3)_3\text{M}=\text{E}(\text{X})\text{R}]$, which, in the second step, are transformed into the targeted tetrylidyne complexes after halide abstraction with $\text{Na}[\text{B}(\text{Ar}^F)_4]$ (Scheme 2). Thereby, the nickel silylidyne, germlylidyne, and stannylidyne complex cations $[(\text{PMe}_3)_3\text{Ni}=\text{ER}]^+$ ($\text{E} = \text{Si}, \text{R} = \text{Tbb}$ (**NiSiTbb_{exp}**); $\text{E} = \text{Ge}, \text{R} = \text{Ar}^{\text{Mes}}$ (**NiGeAr^{Mes}_{exp}**); $\text{E} = \text{Sn}, \text{R} = \text{Ar}^{\text{Mes}}$ (**NiSnAr^{Mes}_{exp}**)) and the platinum silylidyne and germlylidyne complex cations $[(\text{PMe}_3)_3\text{Pt}=\text{ER}]^+$ ($\text{E} = \text{Si}, \text{R} = \text{Tbb}$ (**PtSiTbb_{exp}**); $\text{E} = \text{Ge}, \text{R} = \text{Ar}^{\text{Mes}}$ (**PtGeAr^{Mes}_{exp}**)) were isolated as red-brown (**NiSiTbb_{exp}**), violet-brown (**NiGeAr^{Mes}_{exp}** and **NiSnAr^{Mes}_{exp}**), and orange (**PtSiTbb_{exp}**) borate salts and fully characterized (Scheme 2). More recently, the analogous triphenylphosphane nickel complex salts $[(\text{PPh}_3)_3\text{Ni}=\text{EN}(\text{Si}^i\text{Pr}_3)(\text{Dipp})][\text{B}(\text{Ar}^F)_4]$ were also prepared by T. J. Hadlington et al. using the same approach [53].



Scheme 2. Two-step synthesis of the group 10 metal tetrylidyne complexes $[(\text{PMe}_3)_3\text{M}=\text{ER}][\text{B}(\text{Ar}^F)_4]$ developed by our group ($\text{M} = \text{Ni}, \text{Pt}$; $\text{L} = \text{PMe}_3, \text{Ga}(\text{C}_5(\text{CH}_3)_5)$; $\text{E} = \text{Si}, \text{Ge}, \text{Sn}$; $\text{X} = \text{Cl}, \text{Br}$; $\text{R} = \text{Tbb}, \text{Ar}^{\text{Mes}}, \text{Ar}^F = \text{C}_6\text{H}_3\text{-3,5}-(\text{CF}_3)_2$).

We present here an extensive theoretical study of the whole series of the tetrylidyne complex cations $[(\text{PMe}_3)_3\text{MER}]^+$ (**MER**: $\text{M} = \text{Ni}, \text{Pd}, \text{Pt}$; $\text{E} = \text{C}, \text{Si}, \text{Ge}, \text{Sn}, \text{Pb}$; $\text{R} = \text{Ar}^{\text{Mes}}, \text{Tbb}$ (Si)), employing a comprehensive quantum chemical toolset that includes the Pipek–Mezey orbital localization and the extended-transition state method with natural orbitals of chemical valence (ETS–NOCV), among others. This study shows that most complexes have considerable M–E triple bond characteristics and a similar electronic structure to that of Fischer-type carbonyl complexes (Figure 1a,b). Remarkably, with increasing atomic number of M and E an increasing bending of the M–E–R unit, an elongation of the M–E bond and a continuous change in the electronic structure from a metal tetrylidyne complex to a metallotetrylene are predicted in theory. This leads in the case of combinations of Pd/Pt–Sn/Pb to complexes featuring increased electron lone pair density at the tetrel atom and a $\sigma(\text{M} \rightarrow \text{E})$ bond, which therefore can be also viewed as base-stabilized tetryliumylidene cations, in which the 16 VE ML_3 fragments act as a Lewis base. Moreover, the potential energy hypersurface of all complexes $\text{E} = \text{Si}, \text{Ge}, \text{Sn}, \text{Pb}$ except **NiSiR** suggests the presence of isomers, which feature narrow M–E–C bond angles of around 95° and distorted square-planar coordinated metal centers.

2. Results and Discussion

2.1. Structural Results

We decided to use the five experimentally available tetrylidyne complex cations **NiSiTbb_{exp}**, **NiGeAr^{Mes}_{exp}**, **NiSnAr^{Mes}_{exp}**, **PtSiTbb_{exp}**, and **PtGeAr^{Mes}_{exp}** from our group as anchor points of this study and completed the homologous series $[(\text{PMe}_3)_3\text{MER}]^+$ ($\text{M} = \text{Ni}, \text{Pd}, \text{Pt}$; $\text{E} = \text{C}, \text{Si}, \text{Ge}, \text{Sn}, \text{Pb}$) by including the 10 hitherto experimentally missing complex cations, resulting in overall 15 metal–tetrel combinations. The substituent was chosen to be Ar^{Mes} . In case of $\text{E} = \text{Si}$, the complex cations **MSiTbb** were also studied

in order to compare them with the experimentally known systems $[(\text{PMe}_3)_3\text{Ni}=\text{SiTbb}]^+$ (**NiSiTbb**_{exp}) and $[(\text{PMe}_3)_3\text{Pt}=\text{SiTbb}]^+$ (**PtSiTbb**_{exp}). For comparison reasons, we also studied the amino derivatives $[(\text{PPh}_3)_3\text{Ni}=\text{EN}(\text{Si}^i\text{Pr}_3)(\text{Dipp})]^+$ (E = Ge (**B-Ge**), E = Sn (**B-Sn**)). The structures of all complexes were optimized at the B97-D3 (BJ)-ATM/def2-TZVP level of theory, abbreviated in the following as level I (see also the Materials and Methods section for the full computational details) and confirmed as minima by successive numerical or analytical frequency calculations. A collection of selected bonding parameters is given in Table 1, which indicates several trends, which are discussed in the following.

Table 1. Selected calculated bonding parameters of the group 10 tetrelidyne complex cations $[(\text{PMe}_3)_3\text{MER}]^+$ (**MER**: M = Ni, Pd, Pt; E = C, Si, Ge, Sn, Pb; R = Ar^{Mes}, Tbb (Si)) at the B97-D3 (BJ)-ATM/def2-TZVP level of theory (0 K, gas phase). Experimental bonding parameters of **MER**_{exp} were obtained from sc-XRD data at 100–123 K [52]. For **NiGeAr**^{Mes}_{exp} and **PtGeAr**^{Mes}_{exp}, the bonding parameters of the two independent complex cations found in the unit cell are listed. The experimental bonding parameters of **B-E**_{exp} were taken from ref. [53]. Bond lengths and angles are given in picometers and degrees, respectively.

Compound	M–E	E–C1	M–E–C1
NiCAr ^{Mes}	169.1	141.3	168.4
NiSiTbb	204.5	184.0	167.2
NiSiTbb _{exp}	203.11(7)	183.8(2)	172.40(8)
NiSiAr ^{Mes}	204.2	186.6	163.8
NiGeAr ^{Mes}	213.3	197.1	165.3
NiGeAr ^{Mes} _{exp}	210.40(6)	194.6(4)	164.9(1)
NiSnAr ^{Mes}	210.20(6)	195.0(4)	166.5(1)
NiSnAr ^{Mes} _{exp}	235.1	219.4	150.9
NiPbAr ^{Mes}	228.08(9)	214.0(5)	165.1(2)
PdCAr ^{Mes}	244.9	229.7	142.7
PdSiTbb	244.9	229.7	142.7
PdCAr ^{Mes}	182.0	140.9	168.4
PdSiTbb	215.1	184.0	163.1
PdSiAr ^{Mes}	216.1	187.6	150.7
PdGeAr ^{Mes}	227.9	199.5	144.9
PdSnAr ^{Mes}	251.6	222.9	134.4
PdPbAr ^{Mes}	263.1	232.4	129.6
PtCAr ^{Mes}	179.9	141.2	175.1
PtSiTbb	215.8	183.8	168.1
PtSiTbb _{exp}	213.43(7)	184.2(3)	173.83(9)
PtSiAr ^{Mes}	215.7	186.3	166.1
PtGeAr ^{Mes}	228.4	198.9	149.7
PtGeAr ^{Mes} _{exp}	222.42(7)	194.7(7)	161.8(2)
PtSnAr ^{Mes}	222.69(8)	195.2(7)	163.3(2)
PtSnAr ^{Mes}	255.1	223.9	132.1
PtPbAr ^{Mes}	267.7	233.1	127.3
compound	Ni–E	E–N	Ni–E–N
B-Ge	218.3	186.4	173.4
B-Ge _{exp}	215.9(1)	185.3(2)	175.9(1)
B-Sn	239.6	209.1	167.8
B-Sn _{exp}	235.5(1)	206.6(6)	173.6(2)

(a) The calculated M–E bond lengths are in all cases slightly longer than those obtained with single-crystal X-ray diffraction (sc-XRD) analyses. The difference Δ between the calculated and experimental values ranges from 1.4 to 7.0 pm and continuously increases with increasing atomic number of the tetrel (e.g., M = Ni: $\Delta = 1.4$ pm (E = Si); $\Delta = 3.0$ pm (E = Ge, using the mean value of the Ni–Ge bond lengths of the two complex cations found in the asymmetric unit of the crystal lattice); $\Delta = 7.0$ pm (E = Sn)) and with increasing atomic number of the metal (e.g., E = Ge: $\Delta = 3.0$ pm (M = Ni); $\Delta = 5.8$ pm (M = Pt)).

The experimental M=E bond lengths are the shortest reported to date. For example, the Ni=Si bond of **NiSiTbb_{exp}** (203.11(7) pm) is shorter than the Ni=Si bond of [(PMe₃)₃Ni=Si(Br)Tbb] (210.2(2) pm) and of [(η⁶-toluene)Ni=Si(C(SiMe₃)₂CH₂)₂] (209.4(1) pm), the latter one being the shortest Ni=Si bond reported to date [54,55]. Similarly, the Pt=Si bond of **PtSiTbb_{exp}** (213.43(7) pm) is shorter than the Pt=Si bond of [(PMe₃)₃Pt=Si(Br)Tbb] (219.96(9) pm) and other reported Pt=Si bonds [56]. Furthermore, the Ni=Ge bond of **NiGeAr^{Mes}_{exp}** (210.30(6) pm) is shorter than that of **B-Ge_{exp}** (215.9(1) pm) and shorter than the Ni=Ge bond of [(PMe₃)₃Ni=Ge(Cl)Ar^{Mes}] (216.10(4) pm), the latter bond being the shortest Ni=Ge bond reported to date [52]. Finally, the Ni=Sn bond of **NiSnAr^{Mes}_{exp}** (228.08(9) pm) is shorter than that of **B-Sn_{exp}** (235.5(1) pm) and shorter than the Ni=Sn bond of [(PMe₃)₃Ni=Sn(Cl)Ar^{Mes}] (234.48(9) pm), the latter bond being the shortest Ni=Sn bond reported to date [57]. All these bonding parameters provide structural evidence for the presence of M=E triple bonds in these complexes.

At this point, we want to emphasize that the comparison between experimental solid-state structures obtained by single-crystal X-ray diffraction at 100–123 K versus theoretical single-molecule gas-phase calculations at 0 K is likely to exhibit certain deviations. However, we checked the reliability of our calculated structures at the level of theory **I** with those obtained at the TPSS [58] -D3(BJ)-ATM/def2-TZVP and PW6B95 [59] -D3(BJ)-ATM/def2-TZVP levels of theory and found no considerable differences (see Supplementary Materials). This is somewhat expected as the influence of the density functional approximation (DFA) on the structure is generally considered to be low in contrast to that of the employed basis set [60–63]. Furthermore, with the large differences found between the experimental and calculated M–E–C1 bond angles of **NiSnAr^{Mes}** and **PtGeAr^{Mes}**, we assessed the curvature of the potential energy hypersurface (PES) with PES scans, varying the M–E–C1 angle. Surprisingly, altering the angle by ±20° costs only 5.7 kJ·mol⁻¹ (**NiSnAr^{Mes}**) and 6.3 kJ·mol⁻¹ (**PtGeAr^{Mes}**), indicating a very flat PES (see Section 2.5) with high flexibility regarding the M–E–C1 bond angle.

We also examined the relativistic influence on our compounds by all-electron calculations, explicitly treating relativistic effects with the zero-order regular approximation (ZORA) method [64]. The structure optimization of **PtPbAr^{Mes}** at the ZORA-**I** level of theory using the SARC-ZORA-TZVP basis set for platinum and lead resulted in a structure very similar to the one obtained at the level of theory **I**, which uses effective core potentials (ECPs) for the heavier atoms (see the SI). This is in line with previous reports that testify to an at least comparable performance of ECPs to explicit relativistic treatment with ZORA or Douglas–Kroll–Hess (DKH) techniques [65–67].

(b) The calculated E–C1 bond lengths of the silyliidyne complexes **MSiTbb** compare very well to the experimental ones, but for E = Ge, Sn, the E–C1 bond lengths of the calculated structures are larger. Here, too, the deviation ranging from 2.3 to 5.4 pm continuously increases with increasing atomic number of the tetrel (e.g., M = Ni: Δ = 2.3 pm (E = Ge); Δ = 5.4 pm (E = Sn)) and the metal center (e.g., E = Ge: Δ = 2.3 pm (M = Ni); Δ = 3.9 pm (M = Pt)).

(c) Notably, the calculated M–E bond lengths for E = Si, Ge fit well to those obtained using Pyykkö's covalent triple bond radii [68], for example, for **NiSiAr^{Mes}** (204.2 pm found vs. 203 pm expected), **PtSiAr^{Mes}** (215.7 pm found vs. 212 pm expected), or **NiGeAr^{Mes}** (213.3 pm found vs. 215 pm expected). However, for E = Sn, Pb, the calculated M–E bond lengths are considerably larger than those suggested by Pyykkö, especially for the compounds **PdSnAr^{Mes}** (251.6 pm found vs. 244 pm expected), **PdPbAr^{Mes}** (263.1 pm found vs. 249 pm expected), **PtSnAr^{Mes}** (255.1 pm found vs. 242 pm expected), and **PtPbAr^{Mes}** (267.7 pm found vs. 247 pm expected), which rather appear in the region between metal–tetrel single- and double-bond lengths according to Pyykkö. Of course, conclusions from the latter comparison have to be cautiously made, as Pyykkö's triple bond radii were obtained by adding up atomic radii that were derived from a limited benchmark set. It should be also considered that the calculated M–E bond lengths significantly depend on the M–E–C1 bond angle (vide infra). For example, a constrained structure optimization

with the M–E–C1 bond angle of $\text{PdSnAr}^{\text{Mes}}$, $\text{PdPbAr}^{\text{Mes}}$, $\text{PtSnAr}^{\text{Mes}}$, and $\text{PtPbAr}^{\text{Mes}}$ set to 180° yields structures with M–E bond lengths of 245.5 pm, 254.9 pm, 245.5 pm, and 257.1 pm, respectively. These bond lengths are much closer to those predicted using the triple bond radii of Pyykkö.

(d) The E–C1 bond lengths increase within group 14 as expected and stay roughly the same for E = Si when the metal atom is exchanged between Ni, Pd, and Pt. This is not the case for the compounds with E = Ge, Sn, Pb and M = Pd, Pt, for which slightly longer tetrel–carbon bonds are obtained (ca. 3–4 pm longer). This lengthening can be explained in terms of Bent's rule [69] with the decreased s character of the hybrid orbital of E used for the E–C1 bond reflecting the reluctance for hybridization of the heavier main group elements [70–72].

(e) The M–E–C1 bond angles show a high degree of variability with values ranging from 168.4° ($\text{NiCAr}^{\text{Mes}}$, $\text{PdCAr}^{\text{Mes}}$) down to 127.3° ($\text{PtPbAr}^{\text{Mes}}$). The calculated M–E–C1 values of the silylidyne complexes (R = Tbb) only slightly vary with the metal (NiSiTbb : 167.2° , PdSiTbb : 163.1° , and PtSiTbb : 168.1°), being ca. 6° smaller than the experimental values ($\text{NiSiTbb}_{\text{exp}}$: $172.40(8)^\circ$, $\text{PtSiTbb}_{\text{exp}}$: $173.83(9)^\circ$) and fall in the range of typical experimental M–E–C angles of heavier tetrylidyne complexes ($156\text{--}179^\circ$ [1,73]). This is also the case for $\text{NiGeAr}^{\text{Mes}}$ (165.3°), but for M = Pd, Pt and E = Ge, Sn, Pb, the calculated M–E–C1 bond angles (e.g., $\text{NiSnAr}^{\text{Mes}}$: 150.9° , $\text{NiPbAr}^{\text{Mes}}$: 142.7° , $\text{PtGeAr}^{\text{Mes}}$: 149.7° , $\text{PtSnAr}^{\text{Mes}}$: 132.1° , and $\text{PtPbAr}^{\text{Mes}}$: 127.3°) are considerably smaller as graphically shown in Figure 2. The M–E–C1 angles generally decrease in the order C > Si > Ge > Sn > Pb, the decrease being more pronounced for palladium and platinum than for nickel. The only exception to this trend is $\text{NiSiAr}^{\text{Mes}}$ with a Ni–Si–C1 angle of 163.8° , which is smaller than the Ni–Ge–C1 angle of $\text{NiGeAr}^{\text{Mes}}$ (165.3°).

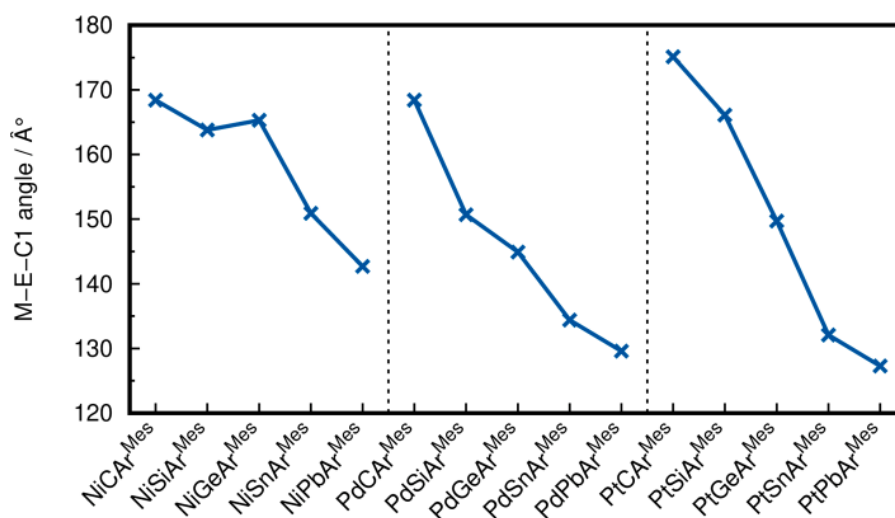


Figure 2. M–E–C1 angle of the minimum structures plotted for every system. The connecting lines have no physical meaning and are only drawn to visualize the trends.

Based on these trends derived from the structures in combination with the analysis of the molecular orbitals (vide infra), the calculations suggest two different complex classes, namely tetrylidyne complexes with an approximately linear M–E–C1 linkage and a M=E triple bond and compounds with a considerably bent M–E–C1 moiety and an increased lone pair density at the tetrel center, which are reminiscent of metallotetrylenes. This classification is given in Scheme 3, with all carbon and silicon systems as well as $\text{NiGeAr}^{\text{Mes}}$ belonging to the first class, whereas the systems $\text{PdSnAr}^{\text{Mes}}$, $\text{PdPbAr}^{\text{Mes}}$, $\text{PtSnAr}^{\text{Mes}}$, and $\text{PtPbAr}^{\text{Mes}}$ belong to the second class of compounds. While $\text{NiSnAr}^{\text{Mes}}$, $\text{NiPbAr}^{\text{Mes}}$, $\text{PdGeAr}^{\text{Mes}}$, and $\text{PtGeAr}^{\text{Mes}}$ also feature considerably bent M–E–C1 units,

these complexes exhibit electronic structures close to those of the tetrylidyne complexes and therefore lie in between the two complex classes.

NiCAr ^{Mes}	NiSiR	NiGeAr ^{Mes}	NiSnAr ^{Mes}	NiPbAr ^{Mes}
PdCAr ^{Mes}	PdSiR	PdGeAr ^{Mes}	PdSnAr ^{Mes}	PdPbAr ^{Mes}
PtCAr ^{Mes}	PtSiR	PtGeAr ^{Mes}	PtSnAr ^{Mes}	PtPbAr ^{Mes}

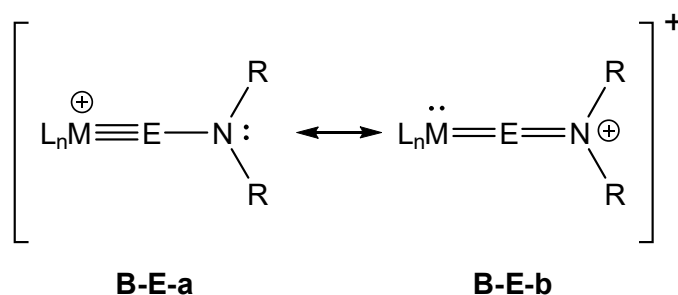
tetrylidyne complex
metallotetrelene

Scheme 3. Classification of the compounds assessed throughout this study: R = Ar^{Mes}, Tbb. The hatched complexes also exhibit characteristics of the metallotetrelene type.

As mentioned in the Introduction, we also investigated the geometric and electronic structure of the cationic complexes [L₃Ni≡EN(SiⁱPr₃)(Dipp)]⁺ of T. J. Hadlington et al. We performed gas-phase structure optimizations starting from the solid-state structures of **B-Ge_{exp}** and **B-Sn_{exp}** available from ref. [53] at the level of theory I to be consistent with our other results. The structural parameters for both **B-E_{exp}** and **B-E** are listed in Table 1, and a comparison with the calculated structures of ref. [53] can be found in the Supplementary Materials.

The calculated Ni–E and E–N bond lengths of the gas-phase structures are again 1.1–4.1 pm longer than those of the solid-state structures, and the calculated Ni–E–N angles 2.5° (**B-Ge**) and 5.9° (**B-Sn**) are smaller than the experimental ones. Compared with our systems, **B-Ge** and **B-Sn** feature longer Ni–E bond lengths (218.3 pm in **B-Ge** vs. 213.3 pm in NiGeAr^{Mes}; 239.6 pm in **B-Sn** vs. 235.1 pm in NiSnAr^{Mes}). The same holds for the solid-state structures. Another salient difference is the larger Ni–E–N angles of the complexes of T. J. Hadlington et al., with values of 173.4° and 167.8° for **B-Ge** and **B-Sn**, respectively, compared with the Ni–E–C1 bond angles of NiGeAr^{Mes} (165.3°) and NiSnAr^{Mes} (150.9°). A possible explanation is the increased repulsion between the sterically more demanding Ni(PPh₃)₃ fragment and the tetrylidyne ligand in **B-Ge** and **B-Sn**, which is reduced by an elongation of the Ni–E bond and a widening of the Ni–E–N bond angle.

Alternatively, an electronic effect might be present originating from a (N→E) π donation, which in terms of the Lewis formalism is represented by the allenic form **B-E-b** (Scheme 4). To clarify which is the dominant effect causing the Ni≡E bond elongation and the widening of the Ni–E–N bond angle in **B-Ge** and **B-Sn**, the corresponding PMe₃-containing complex cation [(PMe₃)₃Ni≡GeN(SiⁱPr₃)(Dipp)]⁺ (**B-Ge-PMe₃**) was structurally optimized at the theoretical level I. The obtained Ni–Ge bond length of 214.2 pm is close to that found for NiGeAr^{Mes} (213.3 pm), and the Ni–Ge–N angle of **B-Ge-PMe₃** (163.7°) compares well with the Ni–Ge–C1 bond angle of NiGeAr^{Mes} (165.3°), suggesting that the longer bond length and larger Ni–Ge–N bond angle in **B-Ge** result from the increased steric repulsion between the sterically demanding PPh₃ ligands and the tetrel-bonded amino substituent. A closer look at the MOs of **B-Ge** and **B-Sn** suggests a certain extent of (N→E) π donation, but this is apparently much smaller than in Fischer-type aminocarbonyne [6,7,74–78] complexes and does not influence the M≡E bond lengths.



Scheme 4. Lewis representation of the M=E-bond in **B-Ge** and **B-Sn** using the tetrylidyne resonance form **B-E-a** and the allenic resonance form **B-E-b**; the encircled charges in the resonance form are formal charges.

2.2. Molecular Orbital Analysis

As one of the most direct results of an electronic structure calculation, we analyzed the canonical (Kohn–Sham) molecular orbitals (MOs) in the beginning. The MOs of the compounds $\text{NiSiAr}^{\text{Mes}}$ (Figure 3) and $\text{PtPbAr}^{\text{Mes}}$ (Figure 4) were selected as representatives for the discussion; the selected MOs of the other systems can be found in the SI.

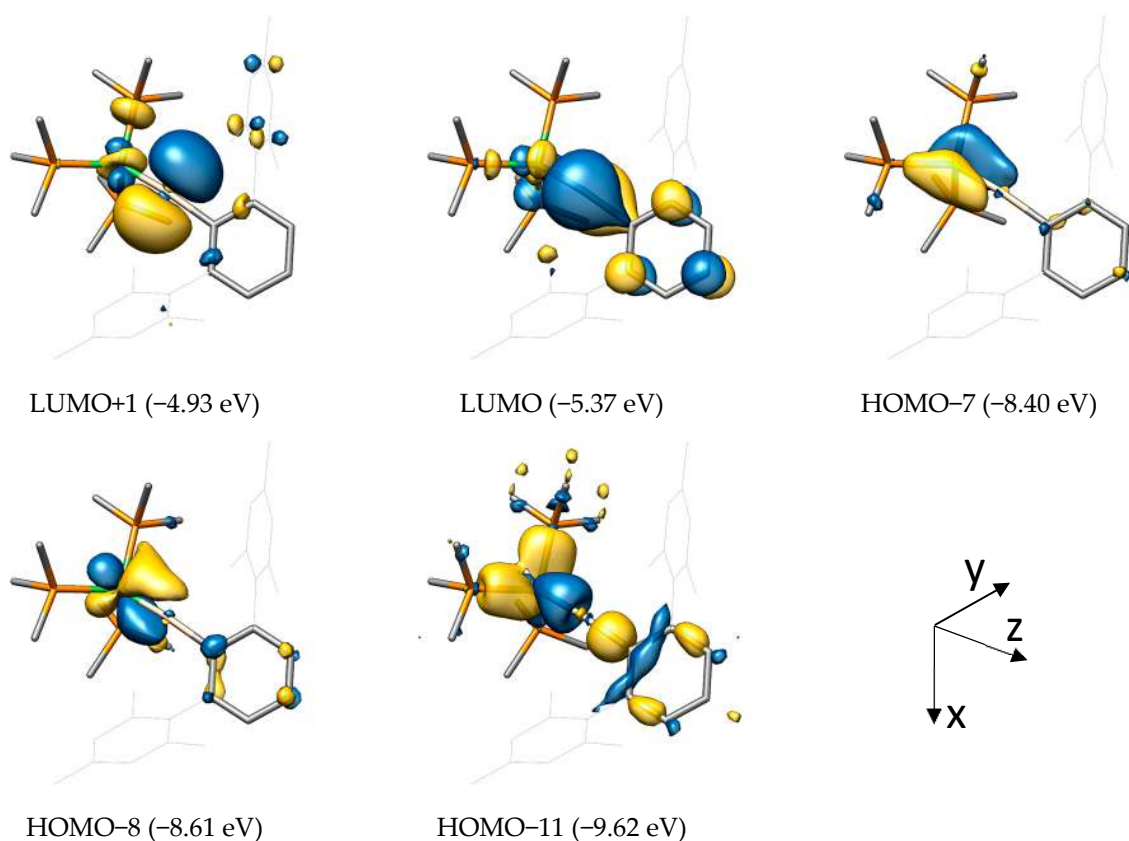


Figure 3. Selected molecular orbitals and their respective orbital energies of $\text{NiSiAr}^{\text{Mes}}$. Hydrogen atoms are omitted for clarity; the isosurface value was set to $0.04 \text{ e}^{1/2} \text{ Bohr}^{-3/2}$.

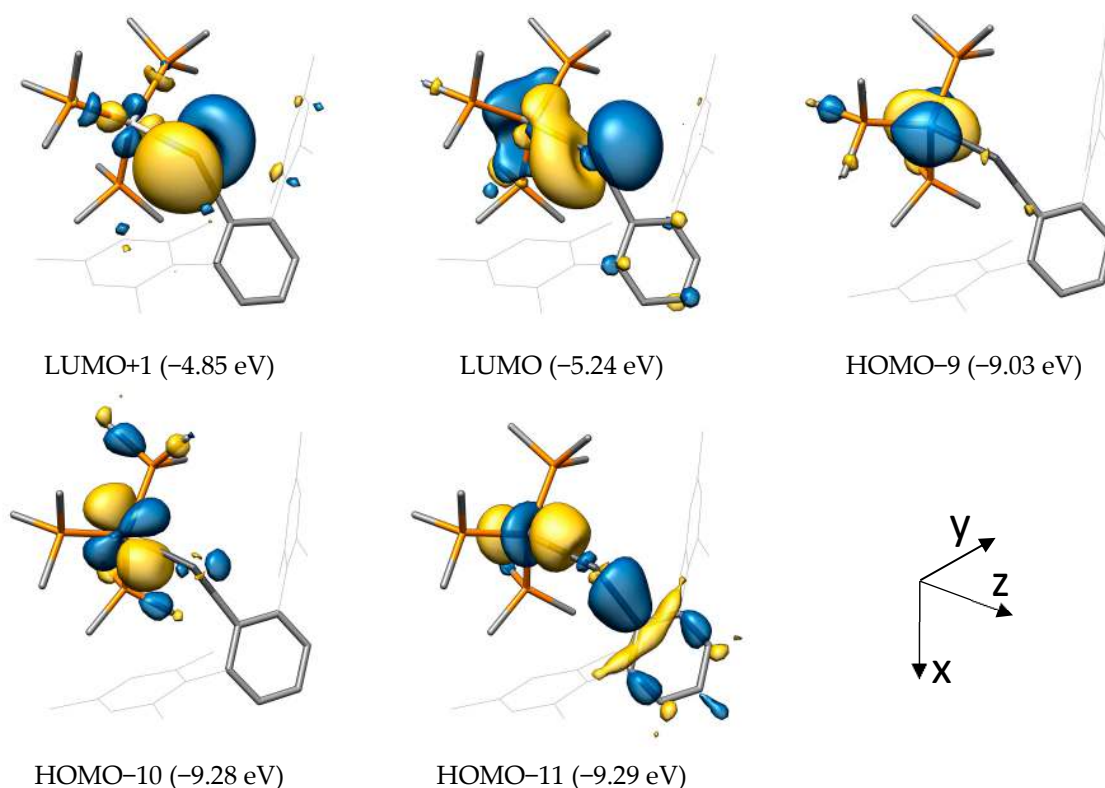


Figure 4. Selected molecular orbitals and their respective orbital energies of $\text{PtPbAr}^{\text{Mes}}$. Hydrogen atoms are omitted for clarity; the isosurface value was set to $0.04 \text{ e}^{1/2} \text{ Bohr}^{-3/2}$.

Although heavily delocalized, the low-lying HOMO-11 (highest occupied molecular orbital (HOMO)) in $\text{NiSiAr}^{\text{Mes}}$ corresponds to the $\sigma(\text{M}-\text{E})$ bond with $\sigma(\text{E}-\text{C})$ bond character. The metal-centered HOMO-8 and HOMO-7 represent the $\pi_{xz}(\text{M}-\text{E})$ and $\pi_{yz}(\text{M}-\text{E})$ bonds, respectively, with their antibonding, tetrel-centered counterparts being the lowest unoccupied molecular orbital (LUMO) and LUMO+1.

For $\text{PtPbAr}^{\text{Mes}}$, the $\sigma(\text{M}-\text{E})$ bond is represented by HOMO-11, where the participation of the metal d_z^2 is evident. In contrast to $\text{NiSiAr}^{\text{Mes}}$, no clear π bonds are found between the metal and tetrel, but rather metal-centered d_{xz} (HOMO-10) and d_{yz} (HOMO-9) orbitals without significant orbital contribution from the lead atom. Correspondingly, the antibonding $\pi^*(\text{M}-\text{E})$ orbitals have a high contribution from the empty tetrel- p_x (LUMO, distorted due to $\text{M}-\text{E}-\text{C}$ bending) and tetrel- p_y (LUMO+1) orbital, and only a small metal d -orbital participation.

As the canonical MOs are challenging to interpret due to their delocalized nature, we applied the Pipek–Mezey localization scheme to generate localized Pipek–Mezey MOs (LMOs) by a unitary transformation, not altering the physical meaningfulness of the orbitals [79]. Again, the LMOs are shown for $\text{NiSiAr}^{\text{Mes}}$ (Figure 5) and $\text{PtPbAr}^{\text{Mes}}$ (Figure 6), being the anticipated extremes in terms of the bonding situation.

As already expected from the canonical MOs, localized $\sigma(\text{M}-\text{E})$, $\pi_{xz}(\text{M}-\text{E})$, and $\pi_{yz}(\text{M}-\text{E})$ bonds are found for $\text{NiSiAr}^{\text{Mes}}$, resulting in a triply bonded $\text{M}-\text{E}$ moiety. The corresponding Mulliken populations further show that the σ bond is strongly polarized toward the silicon atom (0.20 for Ni, 0.81 for Si), whereas both π bonds are polarized toward the metal atom (π_{xz} : 0.80 for Ni and 0.16 for Si; π_{yz} : 0.80 for Ni and 0.17 for Si). This bonding situation is reminiscent of that in Fischer-type carbyne complexes discussed in the Introduction. Furthermore, the $\text{Ni}(0) 3d^{10}$ system demands the presence of three more

metal-centered orbitals, which can be identified within the LMO framework as d_{xy} , d_z^2 , and $d_{x^2-y^2}$, all with negligibly low contributions of the silicon atom (<0.04).

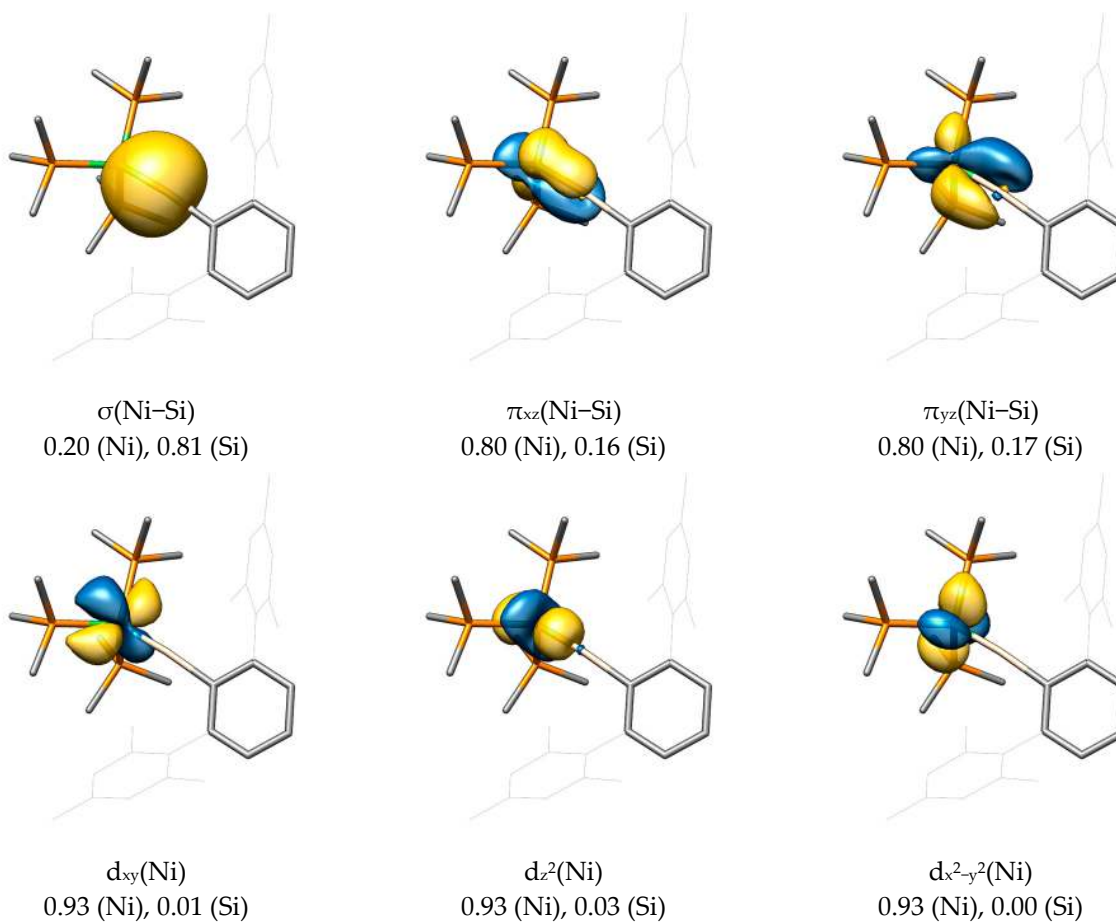


Figure 5. Pipek–Mezey-localized molecular orbitals of $\text{NiSiAr}^{\text{Mes}}$, their assigned orbital type, and corresponding Mulliken populations. Hydrogen atoms are omitted for clarity, and the isosurface value was set to $0.04 e^{1/2} \text{ Bohr}^{-3/2}$. The same coordinate system is applied as seen in Figure 3.

For the sake of completeness, the LMOs for the $\sigma(\text{Si-C1})$ and $\sigma(\text{Ni-P})$ bonds were also found and feature the expected orbital polarization toward carbon and phosphorus, respectively, based on electronegativity. It should be mentioned that the central phenyl ring of the Tbb and Ar^{Mes} substituents is also capable of delocalizing its aromatic π electrons over the formally empty p_x orbital of the tetrel. Such a π stabilization would, to some extent, compete with the d_{xz} back-donation of the metal atom, thus lowering the bond order between metal and tetrel. This effect, however, is assumed to be small due to the inferior π -donor ability of the phenyl substituent compared with that of the amino (NR_2) or alkoxy (OR) substituents (vide supra) and due to a decreasing p-orbital overlap between the tetrel and the phenyl group in the series $\text{C} > \text{Si} > \text{Ge} > \text{Sn} > \text{Pb}$. The Mulliken population for this $\pi(\text{E-C})$ LMO decreases—regardless of the metal—from 0.11 (Si) to rather insignificant values of 0.06 (Ge), 0.03 (Sn), and 0.02 (Pb). This conclusion was also drawn in a study by K. K. Pandey et al. in 2011 on cationic tetrylidyne complexes of molybdenum and tungsten bearing a mesityl substituent [73].

For the main LMOs of $\text{PtPbAr}^{\text{Mes}}$, a $\sigma(\text{Pt-Pb})$ LMO was found, which—in contrast to $\text{NiSiAr}^{\text{Mes}}$ —is not polarized toward the tetrel but toward the metal center (0.82 for Pt and 0.13 for Pb). The involved metal orbital is also different and can be rationalized as a $d_{x^2-z^2}$

orbital (in terms of symmetry the same as the d_z^2 orbital). This orbital is filled, as stated above, due to the presence of a d^{10} metal system, so it seems clear that this M–E interaction comes from the overlap of a filled metal orbital with an empty p orbital at the tetrel atom.

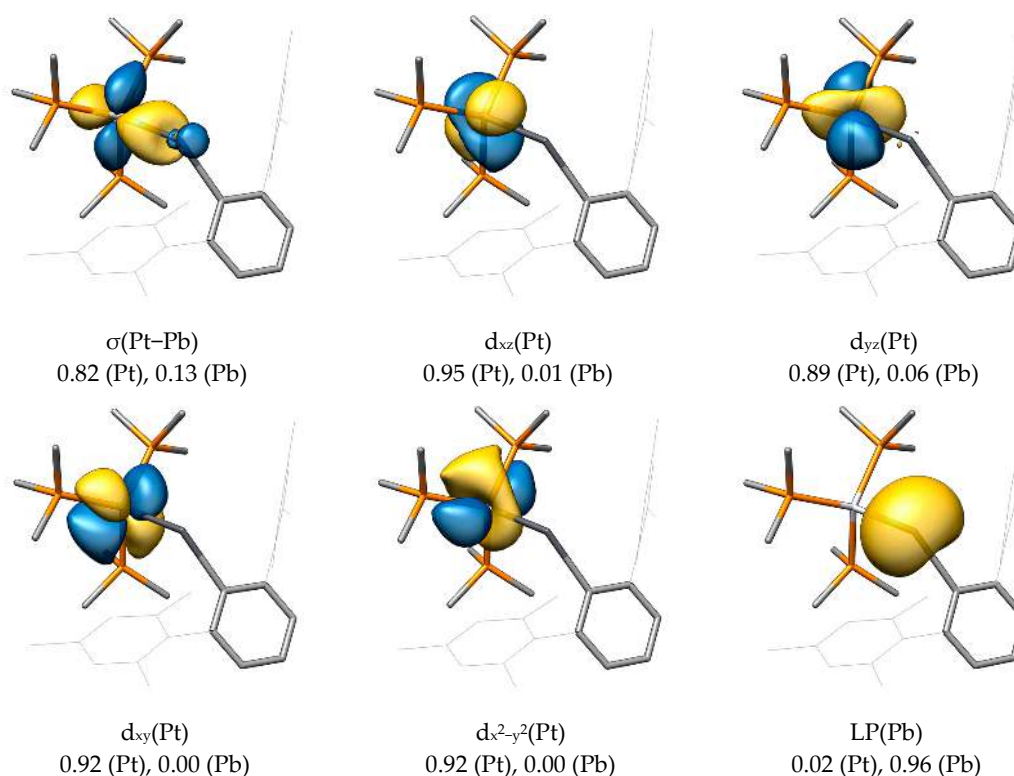
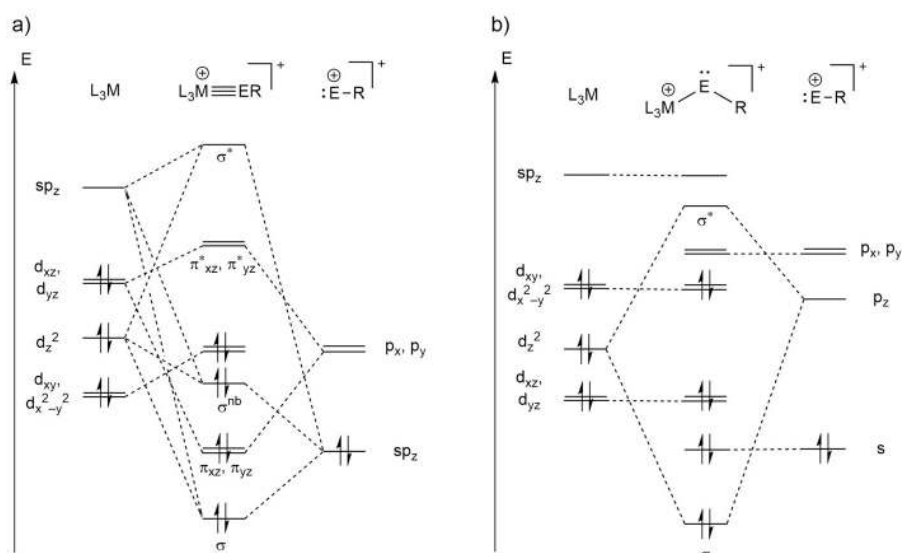


Figure 6. Pipek–Mezey-localized molecular orbitals of $\text{PtPbAr}^{\text{Mes}}$, their assigned orbital type, and corresponding Mulliken populations. Hydrogen atoms are omitted for clarity; the isosurface value was set to $0.04 e^{1/2} \text{ Bohr}^{-3/2}$. The same coordinate system was applied as shown in Figure 3.

No $\pi(\text{M-E})$ LMOs were found for $\text{PtPbAr}^{\text{Mes}}$, although the d_{xz} and d_{yz} orbitals on Pt show the correct orientation. The hereby resulting metallotetrylene picture is confirmed by the presence of an electron lone pair (LP) at Pb without significant contribution of the platinum atom, as shown by the Mulliken population (0.02 for Pt and 0.96 for Pb).

Ultimately, this leads to the formulation of two types of bonding situations, which are qualitatively presented in Scheme 5. Case a involves tetrylidyne complexes for which the $\text{M}\equiv\text{E}$ bonding can be described by a $\sigma(\text{E}\rightarrow\text{M})$ donation and two $\pi(\text{M}\rightarrow\text{E})$ back donations between a neutral ML_3 and an ER^+ fragment in the singlet state. As both the empty metal sp_z (according to a Löwdin population analysis of the LUMO of $\text{Ni}(\text{PMe}_3)_3$) and the filled d_z^2 orbital have the appropriate symmetry to interact with the filled sp hybrid orbital of the tetrel, three MOs result: a σ -bonding and a σ^* -antibonding orbital as well as a nonbonding σ^{nb} MO that can be approximately considered as a metal-centered d_z^2 orbital, as confirmed by the LMOs above (Figure 5). The degenerate π_{xz} and π_{yz} bonds result from the interaction of the filled, almost degenerate metal- d_{xz} and $-d_{yz}$ orbitals (the d_{xz} and d_{yz} orbitals are degenerate only in the case of a C_{3v} -symmetric ML_3 fragment) with the empty, approximately degenerate tetrel- p_x and $-p_y$ orbitals. The degeneracy of the p_x and p_y orbitals is lifted in case of a π -donor substituent at the tetrel atom, such as an amino or alkoxy group, leading to a $\pi_{\text{oop}}(\text{E-N})$ or $\pi_{\text{oop}}(\text{E-O})$ MO as well as a $\pi^*_{\text{oop}}(\text{M-E})$ MO with $\pi^*(\text{E-N})$ or $\pi^*(\text{E-O})$ contribution. The remaining orbitals on the metal atom are used for

bonding to the phosphane ligands, whereas the second sp hybrid orbital on the tetrel is responsible for the bond to the substituent R.



Scheme 5. Qualitative MO interaction diagram depicting the bonding situations of (a) the tetrylidyne complex (similar to the diagram for $L_3M \equiv CR$ of P. Hofmann [80]) and (b) the metallotetrylene case.

The other case (b), found especially for **PtPbAr^{Mes}**, is the metallotetrylene type, with one $\sigma(M \rightarrow E)$ donation constituting the M–E single bond, and an electron lone pair at the tetrel center, causing a considerably bent M–E–C moiety. Here, the sp hybridization on the tetrel is not favored anymore, and the electron lone pair resides in an s orbital, further stabilized by relativistic effects that is not participating in bonding to the metal atom. The empty tetrel- p_z acceptor orbital interacts with the filled metal d_z^2 orbital but is also partially involved in bonding to the substituent R (see HOMO–11 in Figure 4).

After investigating the Mos and LMOs of all compounds in this study, the classification of Scheme 3 was obtained: All carbon and silicon compounds and the **NiGeAr^{Mes}** complex can be described as tetrylidyne complexes (case a), whereas **PdSnAr^{Mes}**, **PdPbAr^{Mes}**, **PtSnAr^{Mes}**, and **PtPbAr^{Mes}** are best described as metallotetrylenes (case b). The germanium systems **PdGeAr^{Mes}** and **PtGeAr^{Mes}** as well as **NiSnAr^{Mes}** and **NiPbAr^{Mes}** lie between cases a and b and show a similar σ bonding to the tetrylidyne complexes, which is why we consider them more like tetrylidyne complexes, albeit with weakened $\pi(M-E)$ bonds, compared with the silicon compounds.

We also studied the canonical Mos of compound **B-Ge** and found three Mos resulting from the interaction of the $d_{xz}(Ni)$, $p_x(Ge)$, and $p_x(N)$ orbitals (Figure 7), which are the π_{xz} , π^{nb}_{xz} , and π^*_{xz} orbitals. The bonding π_{xz} orbital is the low-lying HOMO–27, which shows mostly $\pi(Ge-N)$ bonding with a very small $d_{xz}(M)$ orbital contribution. The nonbonding combination π^{nb}_{xz} with one nodal plane is HOMO–3. It shows no contribution from the germanium atom but only from the metal and nitrogen atoms. Finally, LUMO+1 comprises the antibonding combination π^*_{xz} with a large contribution of the p_x orbital at the tetrel atom. As can be seen in HOMO–27, some $\pi_{xz}(M-E)$ bonding interaction is present but is diminished by the presence of the nitrogen atom, leading to a $\pi(E-N)$ interaction.

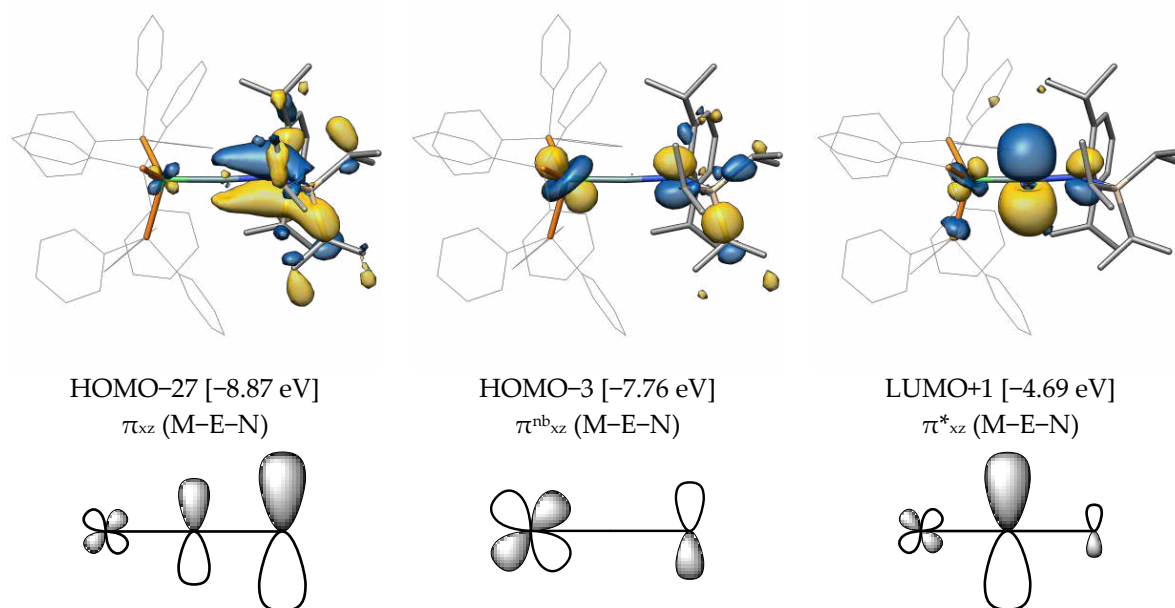


Figure 7. Selected canonical MOs of **B-Ge**, their respective orbital energies, and the type of bond they represent. Hydrogen atoms are omitted for clarity; the isosurface value was set to $0.04 \text{ e}^{1/2} \text{ Bohr}^{-3/2}$. The same coordinate system was applied as shown in Figure 3.

The MOs mentioned above were not discussed in the publication of T. J. Hadlington et al. The MO description was limited to HOMO, HOMO-1, and HOMO-2, which were presented by the authors as two π - and one M-E σ -bonding orbital. However, by employing a more modest isosurface value of $0.04 \text{ e}^{1/2} \cdot \text{Bohr}^{-3/2}$ and comparing it with similar orbitals in our compounds, we suggest that these orbitals correspond to the metal-centered $d_{x^2-y^2}$, d_{xy} , and σ^{nb} orbitals, respectively (more details on this can be found in the SI).

The aromatic groups of the triphenylphosphane ligands in **B-Ge** further amplify the delocalized character of the canonical frontier MOs, making them harder to interpret. This is why we also carried out a Pipek–Mezey orbital localization for **B-Ge**, and selected LMOs (localized molecular orbitals) are presented in Figure 8. It can be seen that apart from the $\sigma(\text{Ni-Ge})$ and $\sigma(\text{Ge-N})$ bonds, three π -type orbitals emerge from the orbital localization ($\pi_{yz}(\text{Ni-Ge})$, $\pi_{xz}(\text{Ni-Ge})$, and $\pi_{xz}(\text{Ge-N})$). Whereas π_{yz} LMO corresponds to a (Ni-Ge) π bond, the presence of two xz -oriented π -type LMOs (one $\pi(\text{Ni-Ge})$ and one $\pi(\text{Ge-N})$ LMO) suggests the presence of both the ylidyne and allenic Lewis resonance forms in compound **B-Ge**, as discussed in Scheme 4. Furthermore, the Mulliken populations of these LMOs clearly suggest the typical Fischer-type characteristic of these complexes, with high tetrel contributions for the σ bond (0.73, E→M donation) and low ones for the two π bond orbitals (0.18, 0.12, M→E back-donation).

Together with the very similar results obtained for the tin analogue **B-Sn** (see the SI), the canonical and localized molecular orbital analysis suggests a similar bonding situation as in Fischer-type aminocarbyne complexes. However, the $\pi(\text{E-N})$ interaction in **B-Ge** and **B-Sn** is expected to be weaker than in the Fischer aminocarbyne complexes as evidenced by the small contribution of the tetrel atom in the π_{xz} LMOs.

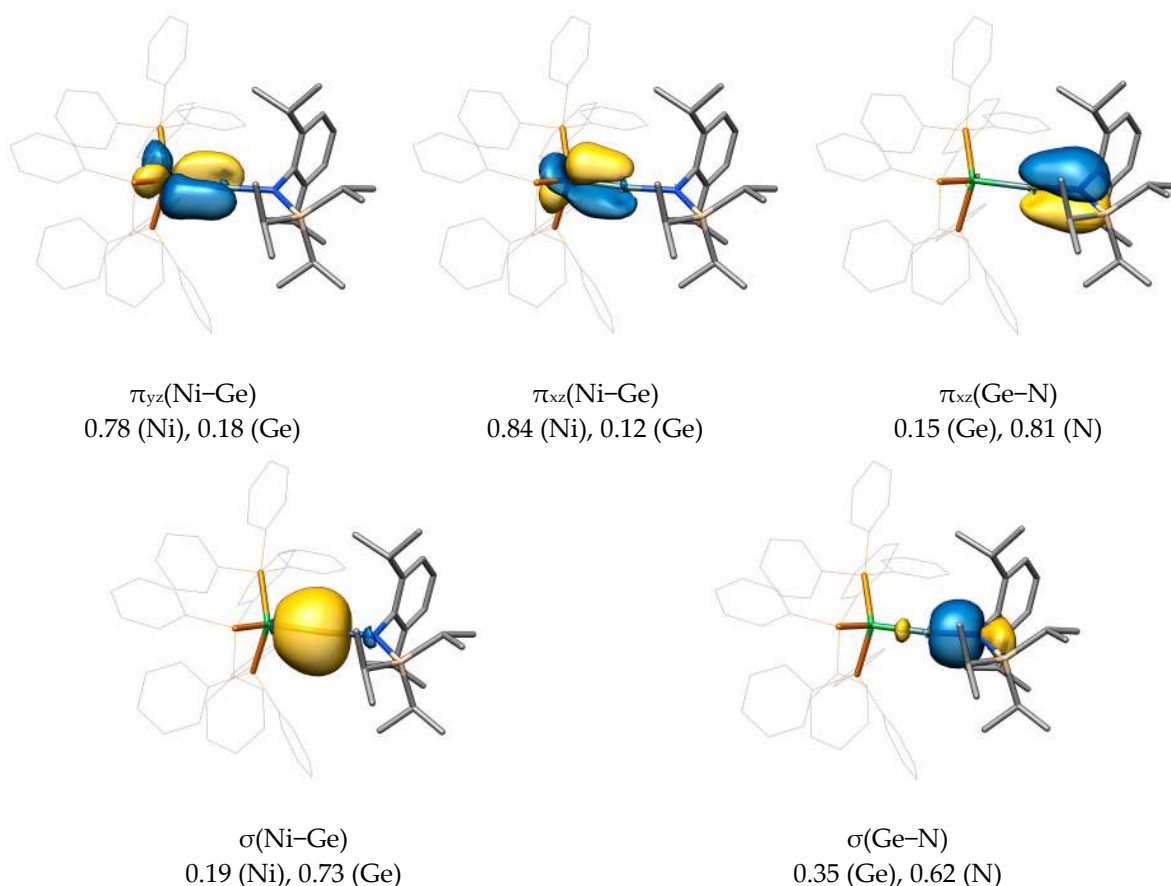


Figure 8. Selected Pipek–Mezey-localized molecular orbitals of **B-Ge**, their attributed bond type, and corresponding Mulliken populations. Hydrogen atoms are omitted for clarity; the isosurface value was set to $0.04 e^{1/2} \text{ Bohr}^{-3/2}$. The same coordinate system was applied as shown in Figure 3.

2.3. Bond Dissociation Energies and Natural Population Analysis

Bond dissociation energies provide insights into the strength of bonds and create a basis for the discussion of the correlation between bond strengths and bond orders. Herein, we differentiate between the bond cleavage energy (*BCE*), which describes the cleavage of a molecule without structural relaxation of the fragments in which the total spin of the fragments must be equal to the spin of the unfragmented molecule, and the bond dissociation energy (*BDE*), in which the structural relaxation of the fragments is taken into consideration. Both energies are purely electronic. *BDEs* that were corrected by the zero-point vibrational energies (*ZPVEs*) as well as the respective inner energies ΔU , enthalpies ΔH° , entropies ΔS° , and Gibbs free energies ΔG° at standard ambient conditions 298.15 K and 1 atm are given in the SI together with their definitions.

The first step in obtaining the lowest possible *BCEs* and *BDEs* is determining the charges and spin states of the fragments. For gas-phase calculations, a cleavage into oppositely charged fragments is heavily disfavored due to strong coulombic attraction between the fragments. As a result of the cationic nature of the compounds presented herein, there are two reasonable schemes for the fragmentation of the *M–E* bond:

- i $[(\text{PMe}_3)_3\text{ME-R}]^+ \rightarrow [\text{M}(\text{PMe}_3)_3] + [\text{E-R}]^+$: An investigation of the electronic states of the fragments $[\text{ML}_3]$ and $[\text{E-R}]^+$ revealed that all fragments have a singlet ground state, with the only exception being the structurally relaxed $[\text{C-Ar}^{\text{Mes}}]^+$ fragment, which is stabilized in the triplet state after activation of the Mes substituent (see

the calculated structure file). The singlet–triplet excitation energies range from 191.4 kJ·mol⁻¹ ([Ni(PMe₃)₃]) to 214.3 kJ·mol⁻¹ ([Pd(PMe₃)₃]) for the metal fragments and from 140.8 kJ·mol⁻¹ ([Si–Tbb]⁺) to 174.7 kJ·mol⁻¹ ([Sn–Ar^{Mes}]⁺) for the tetryliumylidene ions.

- ii [(PMe₃)₃ME–R]⁺ → [M(PMe₃)₃]⁺ + [E–R]: This fragmentation scheme involves an interaction of two open-shell fragments either in their doublet or quartet states. The doublet state is preferred by all fragments with doublet–quartet excitation energies ranging from 232.5 kJ·mol⁻¹ ([Ni(PMe₃)₃]⁺) to 284.0 kJ·mol⁻¹ ([Pd(PMe₃)₃]⁺) for the metal fragments and from 120.3 kJ·mol⁻¹ ([C–Ar^{Mes}]) to 218.7 kJ·mol⁻¹ ([Pb–Ar^{Mes}]) for the tetrylidyne fragments (see the SI for details).

The following trends in the *BCEs* and *BDEs* given in Table 2 and Figure 9 were found:

- Concerning the *BCEs*, the fragmentation into the [ML₃]⁺ and [ER] fragments is favored for all compounds by 2.4 kJ·mol⁻¹ (**PdSnAr^{Mes}**) to 181.0 kJ·mol⁻¹ (**PtCAR^{Mes}**), except for **PdPbAr^{Mes}**, for which the cleavage into the [ML₃] and [ER]⁺ fragments is favored by 15.7 kJ·mol⁻¹.
- The *BDEs* are lower for the dissociation into the [ML₃]⁺ and [ER] fragments in all cases, and the energetic differences between the two fragmentation schemes are lower than for the *BCEs* in most cases, ranging from 6.1 kJ·mol⁻¹ (**NiPbAr^{Mes}**) to 74.7 kJ·mol⁻¹ (**PtCAR^{Mes}**).
- When comparing the energetic differences ΔBCE and ΔBDE between the two fragmentation schemes in dependence on the transition metal, the observed trend is Ni \approx Pt > Pd for the $\Delta BCEs$ and Pt > Pd > Ni for the $\Delta BDEs$ ($\Delta BCE = BCE(i) - BCE(ii)$ and $\Delta BDE = BDE(i) - BDE(ii)$, where i and ii denote the fragmentation schemes).
- The energetic difference between the two fragmentation schemes (ΔBCE and ΔBDE) follows the order C >> Si > Ge > Sn > Pb regarding the tetrel for both the ΔBCE and ΔBDE . The substituent effect (Ar^{Mes} vs. Tbb) in the silylidyne complexes on the *BCEs* and *BDEs* is minute. However, because the *BCEs* of **MSiTbb** are slightly lower for the fragmentation into the ML₃ + ER⁺ fragments than those of **MSiAr^{Mes}** but slightly higher for the fragmentation into the ML₃⁺ + ER fragments, the $\Delta BCEs$ of the **MSiTbb** complexes are lower than the $\Delta BCEs$ of the **MSiAr^{Mes}** and **MGeAr^{Mes}** complexes. For ΔBDE , the difference between Si and Ge is negligible.

For the remaining trends, only the values in Table 2 given in bold are discussed in the following:

- The *BCEs*, if ordered by transition metal, follow the order Pt > Ni > Pd for E = C and Si and the order Ni > Pt > Pd for E = Ge, Sn and Pb. In comparison, the *BDEs*, if ordered by the transition metal, follow the order Ni > Pt > Pd for all tetrels. The reason for this difference is a significantly higher structural relaxation energy of the Pt(PMe₃)₃ fragment (avg. 104.4 kJ·mol⁻¹) followed by the Pd(PMe₃)₃ (avg. 63.9 kJ·mol⁻¹) and Ni(PMe₃)₃ fragments (avg. 54.8 kJ·mol⁻¹), which lowers the *BDEs* of the **PtER** complexes more than the *BDEs* of the **PdER** and **NiER** complexes in comparison with the respective *BCEs*.
- If ordered by tetrel, the *BCEs* and *BDEs* follow the trend C >> Si > Ge > Sn \approx Pb. This means that the M–E bonds of the carbyne complexes are, as expected, the strongest. However, the heavier ylidene complexes exhibit considerable *BCEs* and *BDEs*. These are lower than those of the carbyne complexes, with the difference, though, being considerably smaller than those of the ditetrylidyne complexes. For example, the experimental dissociation enthalpy ΔH° of acetylene of 964.8 ± 2.9 kJ·mol⁻¹ [81] ($\Delta H^\circ_{\text{calc}}(\text{HCCCH}) = 953.0 \text{ kJ}\cdot\text{mol}^{-1}$ at the level of theory I and 970.2 kJ·mol⁻¹ at the level of theory II) is ca. 13 times larger than that of the distannyne Ar^{Dipp}SnSnAr^{Dipp} ($\Delta H_{\text{exp}} = 72.0 \pm 7.1 \text{ kJ}\cdot\text{mol}^{-1}$) [82]. Similarly, a calculation of the gas-phase dissociation enthalpy $\Delta H^\circ_{\text{calc}}$ of Ar^{Dipp}SnSnAr^{Dipp} at the level of theory I leads to a value of 160.7 kJ·mol⁻¹, which is still only a small fraction of that of the analogous acetylene derivative Ar^{Dipp}C≡CAr^{Dipp} ($\Delta H^\circ_{\text{calc}} = 721.7 \text{ kJ}\cdot\text{mol}^{-1}$). In comparison, the *BDE* of **NiSnAr^{Mes}** is still 63 % and 66 % of the *BDE* of **NiCAR^{Mes}** on

- the level theory I and II, respectively, illustrating the considerable bond strength of the $M\equiv E$ triple bonds. An important implication of this comparison is that $C\equiv C$ bonds are stronger than $M\equiv C$ bonds, whereas the opposite is true for the heavier group 14 elements Si–Pb (i.e., the *BDEs* of the $E-E$ bonds in E_2R_2 are smaller than those of the $M\equiv E$ bonds).
- (g) The choice of tetrel generally has a larger influence on the *BCEs* and *BDEs* than the choice of the transition metal. For example, the *BCEs* of $NiGeAr^{Mes}$, $PdGeAr^{Mes}$, and $PtGeAr^{Mes}$ are within $40\text{ kJ}\cdot\text{mol}^{-1}$ of each other, whereas the *BDEs* of $NiSiAr^{Mes}$ and $NiPbAr^{Mes}$ differ by $83.3\text{ kJ}\cdot\text{mol}^{-1}$.

Table 2. Calculated *BCEs* and *BDEs* in $\text{kJ}\cdot\text{mol}^{-1}$ at theory level II of the $M-E$ bonds of the $[L_3MER]^+$ complexes to give the $ML_3 + ER^+$ and $ML_3^+ + ER$ fragment combinations ($M = Ni-Pt$; $L = PMe_3$; $E = C-Pb$; $R = Ar^{Mes}, Tbb$ (Si)). *BCEs* and *BDEs* of the energetically favorable fragmentation scheme are highlighted in bold.

Compound	<i>BCE</i>		<i>BDE</i>	
	$ML_3 + ER^+$	$ML_3^+ + ER$	$ML_3 + ER^+$	$ML_3^+ + ER$
$NiCAr^{Mes}$	718.6	544.3	521.8	461.6
$NiSiTbb$	470.4	427.9	402.5	377.5
$NiSiAr^{Mes}$	491.5	421.4	392.3	368.9
$NiGeAr^{Mes}$	459.3	387.7	365.0	340.0
$NiSnAr^{Mes}$	383.9	346.0	316.9	304.5
$NiPbAr^{Mes}$	342.7	328.6	291.7	285.6
$PdCAr^{Mes}$	625.1	469.7	404.2	340.1
$PdSiTbb$	415.3	395.0	333.0	304.1
$PdSiAr^{Mes}$	427.4	387.9	322.5	295.3
$PdGeAr^{Mes}$	383.2	349.2	289.4	260.5
$PdSnAr^{Mes}$	321.9	319.5	253.6	237.3
$PdPbAr^{Mes}$	293.3	309.0	240.4	230.4
$PtCAr^{Mes}$	799.3	618.3	486.0	411.3
$PtSiTbb$	504.0	462.5	373.5	334.0
$PtSiAr^{Mes}$	520.3	450.2	362.1	324.1
$PtGeAr^{Mes}$	444.0	386.3	314.5	274.9
$PtSnAr^{Mes}$	354.6	332.6	274.1	247.2
$PtPbAr^{Mes}$	313.5	307.8	251.1	230.5

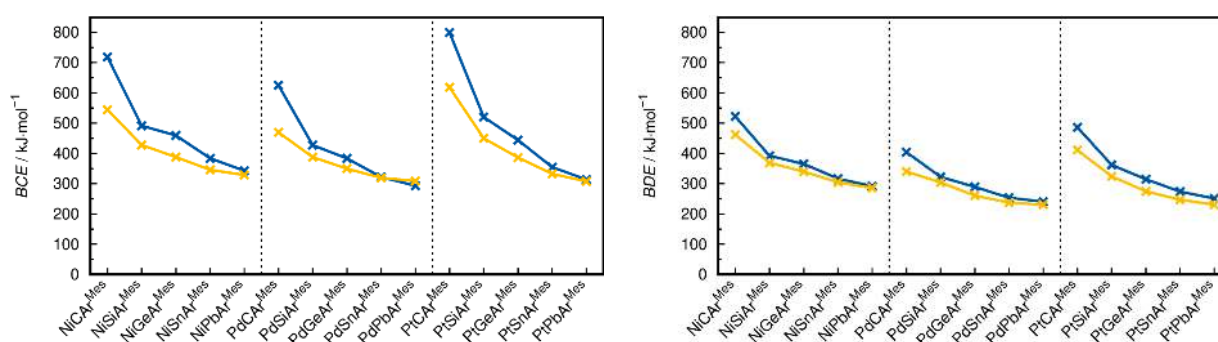


Figure 9. Plots of the *BCEs* (left) and *BDEs* (right) of the $[L_3MER]^+$ complexes ($M = Ni-Pt$; $L = PMe_3$; $E = C-Pb$; $R = Ar^{Mes}, Tbb$ (Si)). Energies corresponding to the cleavage into $ML_3 + ER^+$ fragments are marked in blue; energies corresponding to the cleavage into $ML_3^+ + ER$ fragments are marked in yellow. The connecting lines have no physical meaning and are only drawn to visualize the trends.

As the charge distribution in the group 10 ylydyne complex cations is an important consideration for the comprehension of these compounds, atomic charges were calculated at the level of theory I from a natural population analysis (NPA) in the natural bond orbital (NBO) framework using natural atomic orbitals (NAOs). The results are given in Table 3

and Figure 10. The metal atoms Ni, Pd, and Pt are either almost electroneutral for E = Si and Ge, with charges in the range of -0.03 e (**PdSiR**) to $+0.05$ e (**NiGeAr^{Mes}**), or slightly negatively charged for E = Sn, Pb, with charges from -0.21 e (**PtPbAr^{Mes}**) to -0.09 e (**NiSnAr^{Mes}**, **NiPbAr^{Mes}**). A significant positive charge of $+0.58$ e (**PtGeAr^{Mes}**) to $+1.07$ e (**NiPbAr^{Mes}**) is carried by the tetrel atoms Si, Ge, Sn, and Pb, where the positive charges of the Si and Ge atoms are smaller than those of the Sn and Pb atoms. The entire ML₃ units carry total charges of $+0.46$ e (**NiPbAr^{Mes}**) to $+0.76$ e (**PtGeAr^{Mes}**), and the ER unit charges range for E = Si–Pb from $+0.24$ e (**PtGeAr^{Mes}**) to $+0.54$ e (**NiPbAr^{Mes}**). Overall, the silylidyne and germylidyne complexes behave very similarly but slightly differ from the charge distribution in the stannylidyne and plumblyidyne complexes. The dependence of the NPA charges on the tetrel atom is also much higher than on the metal atom.

Table 3. Calculated charges in e for the M and E atoms and the ML₃ and ER units in the complex cations [L₃MER]⁺ obtained from natural population analysis (NPA) on the theory I level.

Compound	M	E	ML ₃	ER
NiCAr ^{Mes}	+0.35	−0.13	+1.18	−0.18
NiSiTbb	±0.00	+0.76	+0.62	+0.38
NiSiAr ^{Mes}	±0.00	+0.78	+0.67	+0.33
NiGeAr ^{Mes}	+0.05	+0.66	+0.59	+0.41
NiSnAr ^{Mes}	−0.09	+1.05	+0.48	+0.52
NiPbAr ^{Mes}	−0.09	+1.07	+0.46	+0.54
PdCAr ^{Mes}	+0.31	−0.15	+1.18	−0.18
PdSiTbb	−0.03	+0.73	+0.66	+0.34
PdSiAr ^{Mes}	−0.03	+0.75	+0.71	+0.29
PdGeAr ^{Mes}	−0.01	+0.65	+0.71	+0.29
PdSnAr ^{Mes}	−0.15	+0.98	+0.56	+0.44
PdPbAr ^{Mes}	−0.17	+1.02	+0.53	+0.47
PtCAr ^{Mes}	+0.35	−0.24	+1.28	−0.28
PtSiTbb	−0.02	+0.65	+0.71	+0.29
PtSiAr ^{Mes}	−0.02	+0.68	+0.75	+0.25
PtGeAr ^{Mes}	±0.00	+0.58	+0.76	+0.24
PtSnAr ^{Mes}	−0.19	+0.96	+0.67	+0.33
PtPbAr ^{Mes}	−0.21	+1.00	+0.55	+0.45

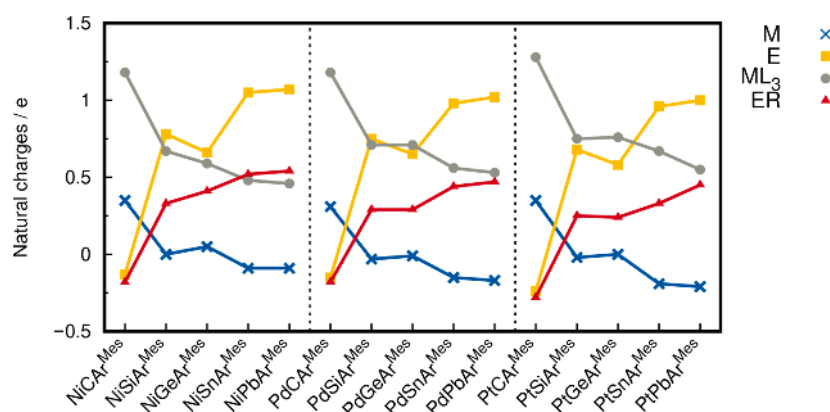


Figure 10. Calculated charges in e for the M atoms (x, blue), the E atoms (■, yellow), the ML₃ units (●, grey), and the ER (▲, red) units in the complex cations [L₃MER]⁺ derived from natural population analysis (NPA) at the level I theory. The connecting lines have no physical meaning and are only drawn to visualize the trends.

These charges are comparable to the NPA charges for the complexes **B-Ge** and **B-Sn**, where the Ni atoms carry only small charges (**B-Ge**: $+0.05$ e, **B-Sn**: -0.19 e), and the tetrel

atoms carry high positive charges of +1.01 e (**B-Ge**) and +1.42 e (**B-Sn**) [53]. The charges on the Ge and Sn atoms of **B-Ge** and **B-Sn** are higher than the charges in the Ar^{Mes}-containing complexes due to the more electronegative amino substituent.

The group 10 ylidene complexes with the heavier tetrel atoms have a quite different charge distribution from the group 10 carbyne complexes. This can be attributed to the special position of carbon among the group 14 elements in the periodic table reflected in its much higher electronegativity than that of its heavier congeners. This results in negative partial charges on the carbon atoms in the carbyne complexes, whereas the heavier tetrel atoms carry positive partial charges. Additionally, a clear shift in electron density from the ML₃ to the ER unit is observed, leading to negatively charged ER ligands in the carbyne complexes, whereas the heavier tetrelidyne ligands ER (E = Si–Pb) are positively charged. For the same reason, the metal center carries a positive partial charge in the carbyne complexes but is electroneutral or slightly negatively charged in the heavier tetrelidyne complexes, and the ML₃ unit carries a much larger positive partial charge in the carbyne complexes than in the heavier group 14 analogues.

2.4. ETS-NOCV and EDA

A very useful tool in the analysis of the chemical bond is the combination of the extended-transition state (ETS) [83] method and natural orbitals of chemical valence (NOCV) [84,85]. The ETS-NOCV analysis was carried out on the level I optimized structures using the ADF program package, as described in Section 3. Within the ETS-NOCV scheme, an energy decomposition analysis (EDA) is used to decompose the interaction energy (ΔE_{int}) of the complexes [L₃M≡E–R]⁺ into chemically meaningful components (Equation (1)):

$$\Delta E_{\text{int}} = \Delta E_{\text{orb}} + \Delta E_{\text{Pauli}} + \Delta E_{\text{elstat}} + \Delta E_{\text{disp}} = -BCE \quad (1)$$

The orbital interaction energy ΔE_{orb} represents the attractive interactions between the occupied molecular orbitals and the virtual orbitals of the two fragments. The Pauli repulsion energy ΔE_{Pauli} results from the destabilizing interaction between the occupied orbitals of the fragments. The third term, ΔE_{elstat} , is the electrostatic interaction energy between the fragments as they are combined in the final molecule with the densities kept frozen, and the dispersion interaction energy ΔE_{disp} describes the long-ranged dispersive interactions of the fragments.

Because the choice of the electronic reference states of the fragments has a significant influence on all of the energy components and their sum, there is a certain degree of arbitrariness involved in the ETS scheme. The best way to determine the most appropriate electronic reference state of the interacting fragments is dependent on ΔE_{orb} [85]. It is assumed that the combination of electronic reference states for which $|\Delta E_{\text{orb}}|$ becomes minimal most closely represents the electronic states of the fragments that are formed upon fragmentation. Another argument is that $|\Delta E_{\text{orb}}|$ could otherwise be arbitrarily increased by the choice of arbitrary electronic states.

Interestingly, the electronic reference states for most fragments are the low-spin singlet states (Table 4), which means the compounds are fragmented into L₃M and ER⁺. This contrasts the preference for the cleavage into the L₃M⁺ and ER fragments according to the BCEs. The electronic reference state of the fragments in case of the carbyne complexes and NiGeAr^{Mes} and PtGeAr^{Mes} are the L₃M⁺ and ER fragments in their doublet states, in line with the preferred fragmentation scheme according to the BCEs.

Table 4. Orbital interaction energies ΔE_{orb} in $\text{kJ}\cdot\text{mol}^{-1}$ between the ML_3 and ER^+ fragments in their electronic singlet (s) states and the fragments ML_3^+ and ER in their electronic doublet (d) states. Values calculated on the B97-D3 (BJ)/TZ2P//I level of theory. The preferred fragment combination is given in bold.

Compound	ΔE_{orb}	
	ML_3 (s) + ER^+ (s)	ML_3^+ (d) + ER (d)
NiCAR^{Mes}	−848.6	−645.3
NiSiTbb	−498.1	−522.8
NiSiAr^{Mes}	−521.9	−486.2
NiGeAr^{Mes}	−461.1	−443.5
NiSnAr^{Mes}	−372.7	−377.6
NiPbAr^{Mes}	−331.9	−370.1
PdCAR^{Mes}	−828.7	−671.7
PdSiTbb	−472.0	−493.8
PdSiAr^{Mes}	−496.5	−494.5
PdGeAr^{Mes}	−426.8	−428.1
PdSnAr^{Mes}	−334.8	−366.9
PdPbAr^{Mes}	−291.1	−345.8
PtCAR^{Mes}	−1072.2	−903.3
PtSiTbb	−585.8	−635.1
PtSiAr^{Mes}	−606.9	−573.8
PtGeAr^{Mes}	−510.8	−499.1
PtSnAr^{Mes}	−380.4	−401.8
PtPbAr^{Mes}	−319.6	−362.4

The carbyne complexes prefer fragmentation into L_3M^+ and ER rather than fragmentation into L_3M and ER^+ due to the higher electronegativity of the carbon atom compared with its heavier homologs. Because ΔE_{orb} directly depends on the charge transfer between and within the fragments, the fragments in which the atomic charges are closest to the respective atomic charges of the unfragmented molecule are favored. In case of the carbyne complexes, the natural charges of the carbon atoms in the CAR^{Mes} fragments are +0.23 e (**NiCAR^{Mes}**), +0.28 e (**PdCAR^{Mes}**), and +0.27 e (**PtCAR^{Mes}**); in the $[\text{CAR}^{\text{Mes}}]^+$ fragment, they are +0.53 e, independent of the metal. The charges of the carbyne carbon atoms in the carbyne complexes are −0.13 e (**NiCAR^{Mes}**), −0.15 e (**PdCAR^{Mes}**), and −0.24 e (**PtCAR^{Mes}**), which are more similar to the respective charges of the CAR^{Mes} fragments than to those of the $[\text{CAR}^{\text{Mes}}]^+$ fragments.

The ETS-NOCVs were also carried out using the triplet electronic reference states of the ML_3 and ER^+ fragments and the quartet electronic reference states of the ML_3^+ and ER fragments, but these resulted in much higher orbital interaction energies than the low-spin calculations.

The notable results are that $|\Delta E_{\text{orb}}|$ is highest for the carbyne complexes ranging from $-645.3 \text{ kJ}\cdot\text{mol}^{-1}$ (**NiCAR^{Mes}**) to $-903.3 \text{ kJ}\cdot\text{mol}^{-1}$ (**PtCAR^{Mes}**), followed by the silylidyne and germylidyne complexes with a ΔE_{orb} of $-426.8 \text{ kJ}\cdot\text{mol}^{-1}$ (**PdGeAr^{Mes}**) to $-585.8 \text{ kJ}\cdot\text{mol}^{-1}$ (**PtSiTbb**), and the Sn and Pb compounds with a ΔE_{orb} of $-291.1 \text{ kJ}\cdot\text{mol}^{-1}$ (**PdPbAr^{Mes}**) to $-380.4 \text{ kJ}\cdot\text{mol}^{-1}$ (**PtSnAr^{Mes}**).

The same trends were observed for ΔE_{Pauli} and $|\Delta E_{\text{elstat}}|$ (see the SI). The dispersion interaction energy is almost identical for all complexes. The total interaction energy corresponds to the BCE, with slightly different values due to the different levels of theory (see Section 2.3).

Interestingly, the **NiSnAr^{Mes}** and **NiPbAr^{Mes}** complexes show no appreciable differences in the orbital interaction energies from their metallotetrylene counterparts (**PdSnAr^{Mes}**, **PdPbAr^{Mes}**, **PtSnAr^{Mes}**, and **PtPbAr^{Mes}**).

The orbital interaction energy can be further split into contributions of individual NOCVs, which allows for a detailed delineation of the bonding situation. Because the NOCVs are related to the fragment MOs, the fragment MOs involved in the bonding can be inferred by inspection of the NOCVs.

For the sake of simplicity, we only discuss the deformation densities of **NiSiTbb**, **NiGeAr^{Mes}** and **PtPbAr^{Mes}**. All compounds marked as tetrylidyne complexes in Scheme 3 exhibit similar NOCVs to either **NiSiTbb** or **NiGeAr^{Mes}**, and all compounds marked as metallotetrylenes are similar to **PtPbAr^{Mes}**. More details can be found the SI.

As shown in the top row of Figure 11, the three largest contributions to the orbital interaction energy of **NiSiTbb** are two π -symmetric and one σ -symmetric interaction. The first interaction ($\Delta E_{\text{orb},1} = -199.6 \text{ kJ}\cdot\text{mol}^{-1}$) is identified as the π -back donation from the HOMO-1 of $\text{Ni}(\text{PMe}_3)_3$ to the LUMO+1 of SiTbb^+ . This interaction is marginally weaker than the second π -back donation ($\Delta E_{\text{orb},2} = -206.8 \text{ kJ}\cdot\text{mol}^{-1}$) from the HOMO of $\text{Ni}(\text{PMe}_3)_3$ to the LUMO of SiTbb^+ . This slight difference is due to the competition of the first π donation with the π interaction of the empty p_x orbital on the Si atom with the phenyl ring of the substituent R (vide supra). The last interaction is the σ donation ($\Delta E_{\text{orb},3} = -53.5 \text{ kJ}\cdot\text{mol}^{-1}$) from the HOMO-10 of SiTbb^+ to the LUMO of $\text{Ni}(\text{PMe}_3)_3$. Remarkably, there is a substantial difference in the contribution to the bond strength between the π - and σ -type interactions, in which the σ -donation is weaker by a factor of roughly four compared with each of the π -back donations.

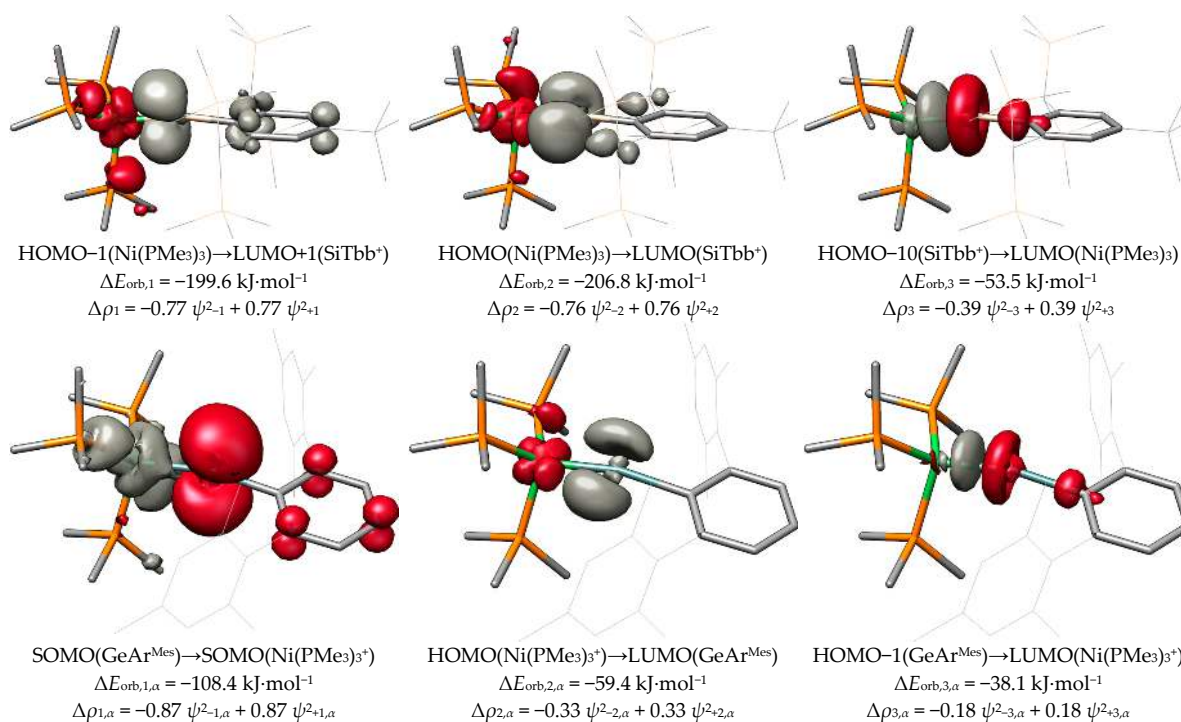


Figure 11. Cont.

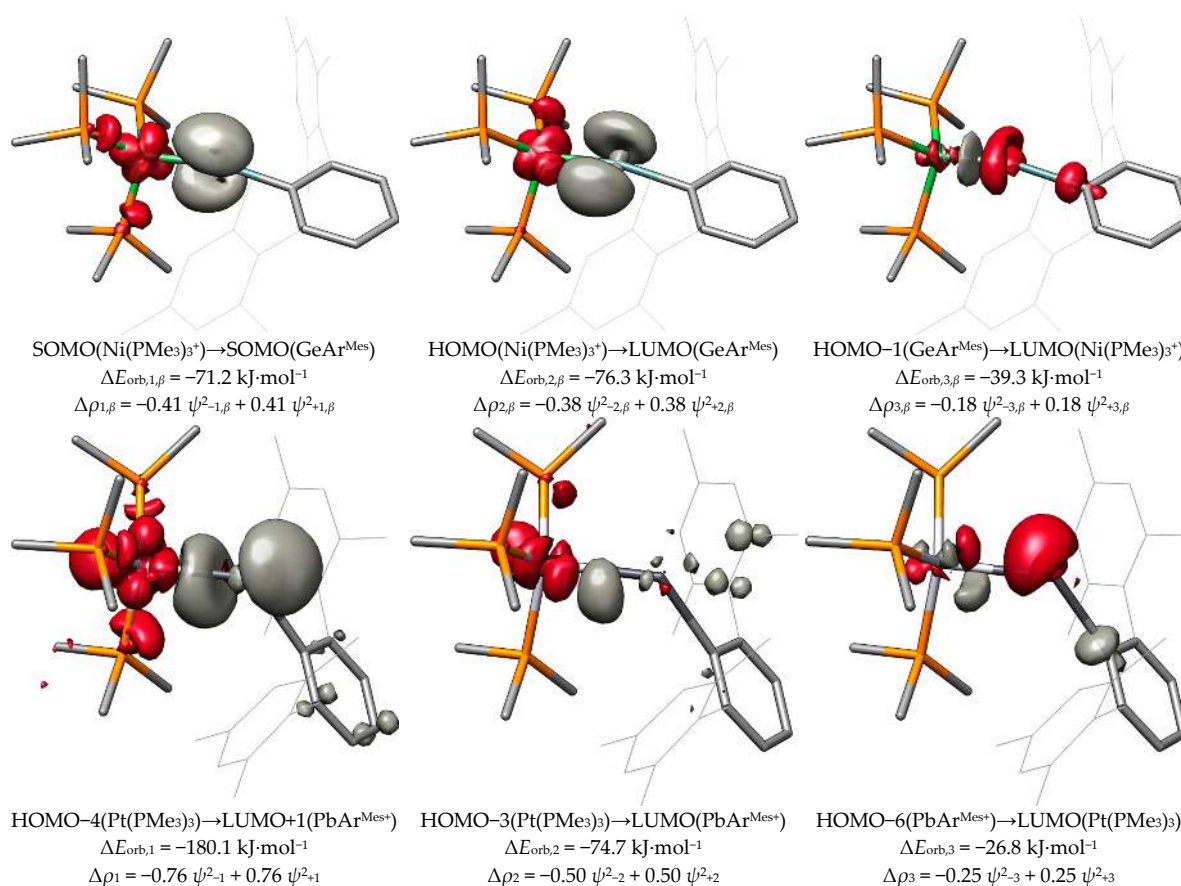


Figure 11. Isosurface plots (isosurface value = 0.002 e Bohr⁻³) of deformation densities ($\Delta\rho_n$) in e Bohr⁻³ of complementary NOCVs (ψ_{-n} and ψ_{+n}) of NiSiTbb (top), NiGeAr^{Mes} (middle, split into α - and β -spin derived deformation densities), and PtPbAr^{Mes} (bottom), given with their respective eigenvalues (ν_{-n} and ν_{+n}). Regions of charge depletion ($\Delta\rho_n < 0$ e Bohr⁻³) are shown in red, and regions of charge accumulation ($\Delta\rho_n > 0$ e Bohr⁻³) are shown in grey. Canonical fragment MOs are given in order to relate the respective NOCV interactions to the fragment orbital interactions. The canonical fragment MOs are not directly related to the NOCVs and were obtained through visual comparison of the NOCVs with the fragment MOs. Level of theory: B97-D3 (BJ)/TZ2P//I. The same coordinate system was applied as shown in Figure 3.

Because the interaction of the fragments in NiGeAr^{Mes} takes place between the two open-shell doublet fragments GeAr^{Mes} and Ni(PMe₃)₃⁺, the orbital interaction energies are further split into the α - and β -spin contributions. The first interaction is a π donation ($\Delta E_{\text{orb},1,\alpha} = -108.4 \text{ kJ}\cdot\text{mol}^{-1}$) from the singly occupied MO (SOMO) of GeAr^{Mes} to the SOMO of Ni(PMe₃)₃⁺, which is completed by the π -back donation ($\Delta E_{\text{orb},1,\beta} = -71.2 \text{ kJ}\cdot\text{mol}^{-1}$) from the SOMO of Ni(PMe₃)₃⁺ to the SOMO of GeAr^{Mes}. Expectedly, the π donation is significantly stronger than the π -back donation and is accompanied by a larger charge transfer of 0.87 e vs. 0.41 e due to the cationic nature of the Ni(PMe₃)₃⁺ fragment. The sum $\Delta E_{\text{orb},1,\alpha} + \Delta E_{\text{orb},1,\beta}$ gives the total orbital interaction energy $\Delta E_{\text{orb},1}$ of $-179.6 \text{ kJ}\cdot\text{mol}^{-1}$, which is slightly weaker than the first π interaction in NiSiTbb. The second interaction in NiGeAr^{Mes} is also composed of an α - and β -spin component; both components involve, in this case, a charge transfer in the same direction from the metal to the tetrel (M→E π -back donation). The total interaction energy $\Delta E_{\text{orb},2}$ of $-135.7 \text{ kJ}\cdot\text{mol}^{-1}$ is albeit weaker than that

in **NiSiTbb**. This is also the case for the third interaction, which is the σ donation ($\Delta E_{\text{orb},3} = -77.4 \text{ kJ}\cdot\text{mol}^{-1}$) from the HOMO-1 of GeAr^{Mes} to the LUMO of $\text{Ni}(\text{PMe}_3)_3^+$. This σ interaction is slightly stronger than that in **NiSiTbb**, which can be explained by the direction of the charge flow from the neutral fragment GeAr^{Mes} to the cationic fragment $\text{Ni}(\text{PMe}_3)_3^+$ in **NiGeAr^{Mes}**, whereas, in **NiSiTbb**, the charge flow from SiTbb^+ to $\text{Ni}(\text{PMe}_3)_3$ via the σ donation occurs against the charge gradient.

Lastly, the three strongest contributions of the metallotetrylene-like compound **PtPbAr^{Mes}** feature one strong σ -back donation ($\Delta E_{\text{orb},1} = -180.1 \text{ kJ}\cdot\text{mol}^{-1}$) from the HOMO-4 of $\text{Pt}(\text{PMe}_3)_3$ to the LUMO+1 of $[\text{PbAr}^{\text{Mes}}]^+$. Notably, the acceptor orbital of this interaction is the p_z orbital of the tetrel atom. The direction of the σ donation of the tetrylene-like compounds is opposite to that of the ylidyne complexes. The second interaction can be identified as a weak π -back donation ($\Delta E_{\text{orb},2} = -74.7 \text{ kJ}\cdot\text{mol}^{-1}$) from the HOMO-3 of $\text{Pt}(\text{PMe}_3)_3$ to the LUMO of $[\text{PbAr}^{\text{Mes}}]^+$. This interaction is significantly weaker than in the compounds **NiSnAr^{Mes}** ($\Delta E_{\text{orb},2} = -136.3 \text{ kJ}\cdot\text{mol}^{-1}$) and **NiPbAr^{Mes}** ($\Delta E_{\text{orb},2} = -113.7 \text{ kJ}\cdot\text{mol}^{-1}$). The third interaction still indicates a weak π donation ($\Delta E_{\text{orb},3} = -26.8 \text{ kJ}\cdot\text{mol}^{-1}$) from the HOMO-6 of $\text{PbAr}^{\text{Mes}+}$ to the LUMO of $\text{Pt}(\text{PMe}_3)_3$. However, there is a significant amount of intrafragment charge-redistribution present, which is why this interaction plays a negligible role in the bonding between the Pt and Pb atoms.

In Figure 12, we present the three bonding situations that describe the cationic group 10 tetrylidyne complexes discussed herein. Additionally, the tetrylidyne complexes with one σ -donating and two π -back interactions can be formulated with one π -type electron spin-pairing interaction bond replacing one of the π -back interactions. Although the formal charge of the latter type is located at the transition metal atom, no notable difference between the two types is observed regarding the charge distribution of the compounds including the heavier group 14 elements. The metallotetrylene type entails a cationic ER^+ fragment, which receives electron density from the metal fragment ML_3 via a σ bond and features notably smaller $\text{M}-\text{E}-\text{R}$ angles (vide infra).

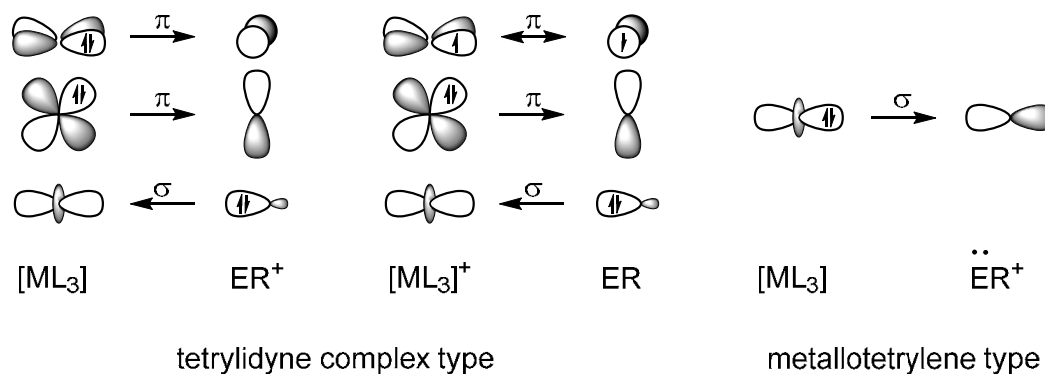


Figure 12. Schematic representation of the bonding situation found in the herein studied $[\text{L}_3\text{MER}]^+$ complexes ($\text{L} = \text{PMe}_3$).

2.5. Metallotetrylene Isomers by PES Scans

When we optimized the structures of our complexes, we were surprised by the variability in the $\text{M}-\text{E}-\text{C}1$ bond angle, which significantly deviates from 180° for most structures (Table 1). To energetically address this variability, we carried out PES scans of the $\text{M}-\text{E}-\text{C}1$ angle from 180° to 90° in steps of 10° for all heavier tetrylidyne complexes (Figure 13). As can be seen, the steepness of the PES decreases in the order $\text{Si} > \text{Ge} > \text{Sn} > \text{Pb}$; more importantly, isomers with much smaller $\text{M}-\text{E}-\text{C}1$ angles of around 95° were found for most systems, abbreviated in the following as **MER-2**, which were confirmed to be minima on the PES. These isomers are energetically not favored

for most compounds as the energy difference between the isomers with the smaller and larger M–E–C angle shows (e.g., **PdSiTbb-2**: +47.1 kJ·mol⁻¹; **NiGeAr^{Mes}-2**: +83.5 kJ·mol⁻¹; **NiSnAr^{Mes}-2**: +55.3 kJ·mol⁻¹, at the level of theory II; see the SI). However, the more bent isomers, **PdSnAr^{Mes}-2**, **PdPbAr^{Mes}-2**, **PtSnAr^{Mes}-2**, and **PtPbAr^{Mes}-2**, were found to be energetically favored by 13–29 kJ·mol⁻¹. In the following, the isomer **PtPbAr^{Mes}-2** is representatively discussed, and key properties of the other MER-2 isomers are included in the SI.

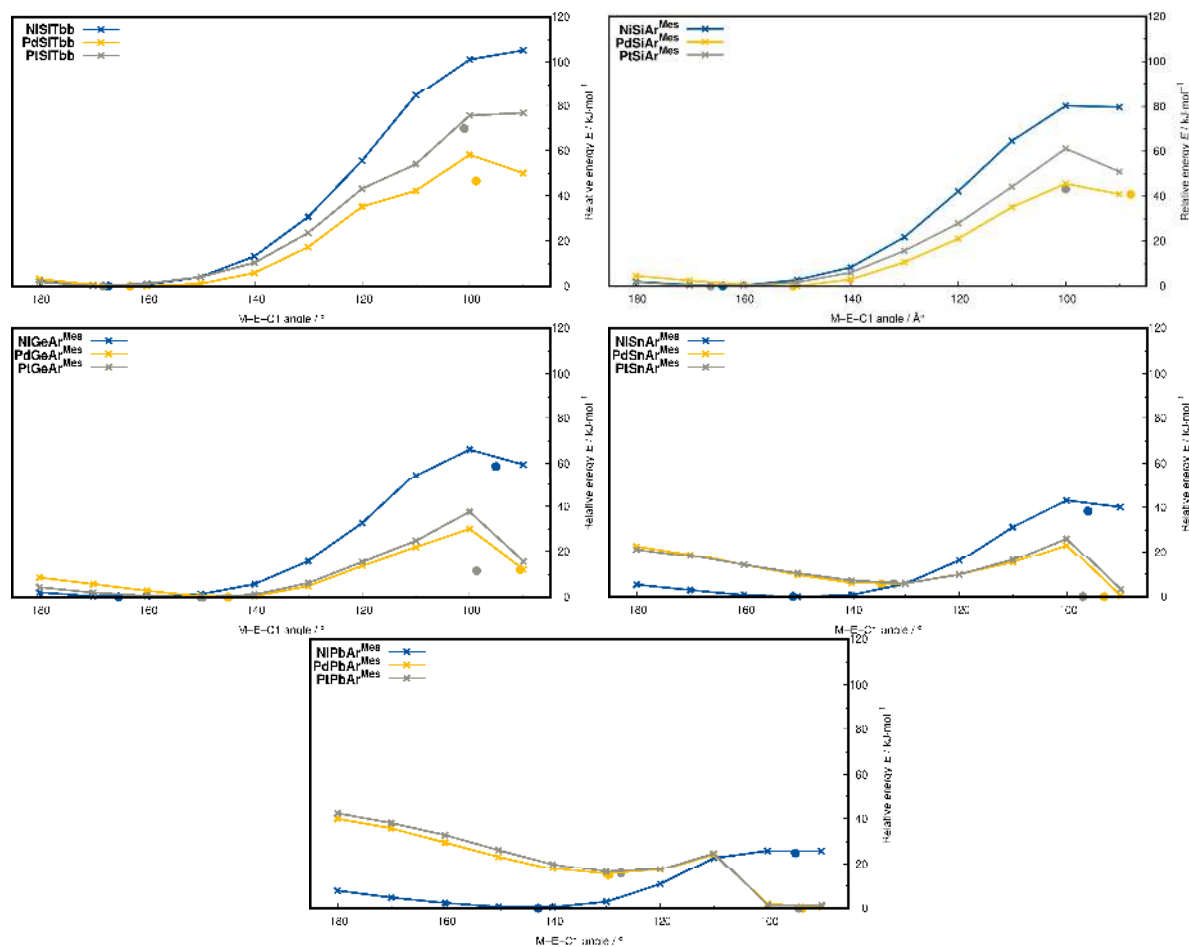


Figure 13. PES scans (theory level I) of the M–E–C bond angle for E = Si (**top left** (R = Tbb); **top right** R = Ar^{Mes}), E = Ge (**middle left**), E = Sn (**middle right**), and E = Pb (**bottom**). The connecting lines have no physical meaning and are given only to visualize the trends. The thicker dots represent confirmed minimum structures for the respective compound. No minimum structure could be obtained for the isomers of **NiSiTbb** and **NiSiAr^{Mes}**.

A comparison of the structural parameters of **PtPbAr^{Mes}-2** (Figure 14) and **PtPbAr^{Mes}** (Table 5) shows a further elongation of the M–E bond from 267.7 to 281.9 pm when decreasing the M–E–C angle to 94.3°, whereas the E–C1 bond length stays nearly the same (233.7 pm). Notably, the metal adopts a distorted square-planar coordination in **PtPbAr^{Mes}-2** (see the SI) [86].

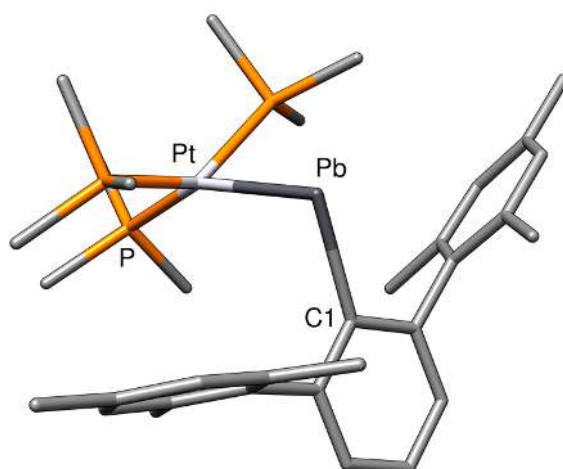


Figure 14. Minimum gas-phase structure of $\text{PtPbAr}^{\text{Mes-2}}$. Hydrogen atoms are omitted for clarity.

Table 5. Key properties of isomers $\text{PtPbAr}^{\text{Mes}}$ and $\text{PtPbAr}^{\text{Mes-2}}$. Electronic energies, bond lengths, and angles are given in $\text{kJ}\cdot\text{mol}^{-1}$, pm, and deg, respectively.

Compound	ΔE_{rel}	M–E	E–C1	M–E–C1
$\text{PtPbAr}^{\text{Mes}}$	+28.5	267.7	233.1	127.3
$\text{PtPbAr}^{\text{Mes-2}}$	0.0	281.9	233.7	94.3

Expectedly, the analysis of the LMOs of $\text{PtPbAr}^{\text{Mes-2}}$ (Figure 15) shows an electron lone pair at Pb, a $\sigma(\text{Pt}–\text{Pb})$ bond that is highly polarized toward Pt (0.75 at Pt, 0.20 at Pb), and a $\sigma(\text{Pb}–\text{C})$ bond that is highly polarized toward the carbon atom (0.81 at C1, 0.28 at Pb).

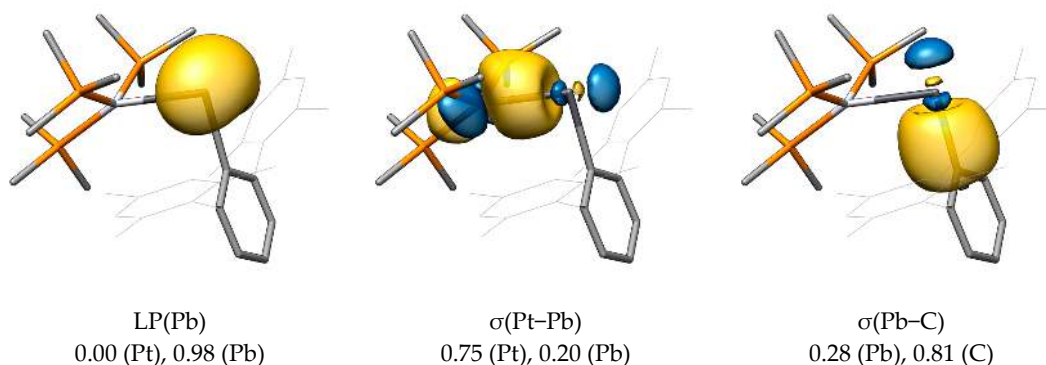


Figure 15. Pipek–Mezey-localized molecular orbitals of $\text{PtPbAr}^{\text{Mes-2}}$, their attributed bond type, and corresponding Mulliken populations. Hydrogen atoms are omitted for clarity; the isosurface value was set to $0.04 e^{1/2} \text{Bohr}^{-3/2}$.

The first deformation density of $\text{PtPbAr}^{\text{Mes-2}}$ given in Figure 16 indicates that the $\sigma(\text{Pt}–\text{Pb})$ bond is best described as a donation from the Pt atom to the Pb atom. Notably, the orbital interaction energy $\Delta E_{\text{orb},1}$ of $299.0 \text{ kJ}\cdot\text{mol}^{-1}$ is larger in $\text{PtPbAr}^{\text{Mes-2}}$ than the corresponding orbital interaction energy in $\text{PtPbAr}^{\text{Mes}}$, as shown in Table 6. The remaining orbital interactions of $\text{PtPbAr}^{\text{Mes-2}}$ are weaker than those of $\text{PtPbAr}^{\text{Mes}}$. However, the much higher $\Delta E_{\text{orb},1}$ of $\text{PtPbAr}^{\text{Mes-2}}$ compared with that of $\text{PtPbAr}^{\text{Mes}}$ ultimately leads to a net preference of the strongly bent isomer of $67.2 \text{ kJ}\cdot\text{mol}^{-1}$ based on ΔE_{orb} .

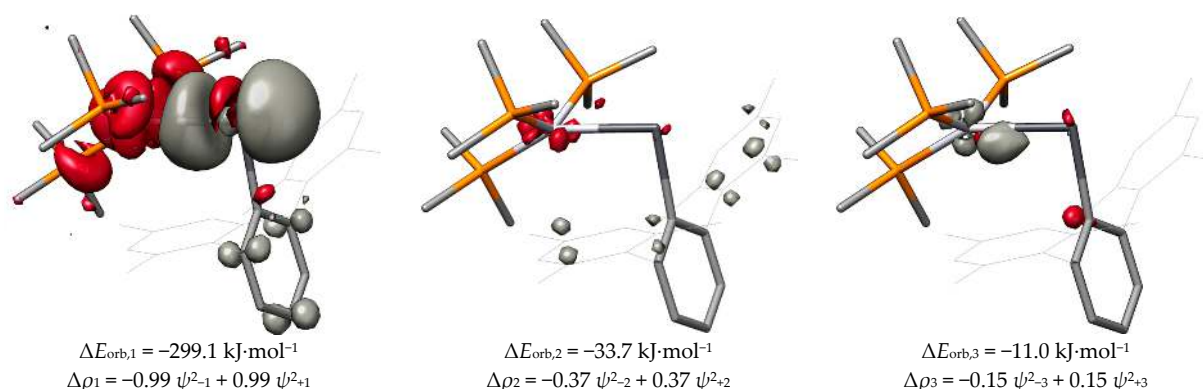


Figure 16. Isosurface plots (isosurface value = 0.002 e Bohr⁻³) of deformation densities ($\Delta\rho_n$) in e Bohr⁻³ of complementary NOCVs (ψ_{-n} and ψ_{+n}) of **PtPbAr^{Mes}-2** given with the respective eigenvalues (v_{-n} and v_{+n}). Regions of charge depletion ($\Delta\rho_n < 0$ e Bohr⁻³) are shown in red, and regions of charge accumulation ($\Delta\rho_n > 0$ e Bohr⁻³) are shown in grey. Level of theory: B97-D3 (BJ)/TZ2P//I.

Table 6. Orbital interaction energies ΔE_{orb} in kJ·mol⁻¹ between the fragments ML₃ and ER⁺ in their electronic singlet states of the isomers of **PtPbAr^{Mes}**. Values calculated at the B97-D3 (BJ)/TZ2P//I level of theory.

Compound	$\Delta E_{\text{orb},1}$	$\Delta E_{\text{orb},2}$	$\Delta E_{\text{orb},3}$	ΔE_{orb}
PtPbAr^{Mes}	-180.1	-74.7	-26.8	-319.6
PtPbAr^{Mes}-2	-299.1	-33.7	-11.0	-386.8

3. Materials and Methods

All calculations except for the ETS-NOCV calculations were carried out using the ORCA 5.0.3 program package [87]. The B97-D3 (BJ)-ATM/def2-TZVP (I) level of theory was employed for the structure optimizations, consisting of the density functional approximation (DFA) B97-D3 (BJ) with Grimme's D3 correction for the London dispersion interactions including the Becke–Johnson damping [88,89] of the additional three-body contribution of Axilrod, Teller and Muto (ATM) [90,91], and of Ahlrichs'-type triple- ζ basis set def2-TZVP [92].

To obtain high-level electronic energies, single-point energy calculations were performed in addition to the calculated structures using the PWPB95-D3(BJ)-ATM/def2-QZVPP (II) level of theory, consisting of the double-hybrid DFA PWPB95 [93] with the D3(BJ)-ATM dispersion treatment and the quadruple- ζ basis set def2-QZVPP [92]. Thermochemical quantities at the level of theory II were obtained by adding the thermodynamic corrections obtained at the level of theory I to the electronic energies obtained at the level of theory II.

For both levels of theory I and II, Stuttgart/Dresden effective core potentials (ECPs) were employed for Pd [65], Sn [66], Pt [93], and Pb [66] as well as defGrid2 numerical integration settings.

The Coulomb part of the DFAs of the levels of theory I and II was approximated with the RI-J method [94], employing the def2/J auxiliary basis sets. For the DFA PWPB95, the calculation of the exchange and MP2 correlation parts was further accelerated using the RI-JK method [95], with the matching def2/JK basis set [96], and the RI method, with the def2-QZVPP/C auxiliary basis set [97].

NPA charges were calculated with the NBO 7.0 program package [98] using the structures and wave functions obtained at the level of theory I.

The ETS-NOCV calculations were carried out using the ADF 2021.103 program package [99,100] at the B97-D3 (BJ)/TZ2P [101] level of theory, which is comparable to the level

of theory I. The ETS-NOCV calculations were carried out using the *NumericalQuality good* setting along with default settings for all other options.

Cube files of canonical and localized molecular orbitals were generated with the MultiWFN 3.6 program [102] from the wave function obtained on theory level I and visualized with UCSF Chimera version 1.13.1 [103].

4. Conclusions

A systematic theoretical study on the cationic group 10 metal complexes $[(PMe_3)_3MER]^+$ (**MER**) with $M = Ni, Pd, Pt$; $E = C, Si, Ge, Sn, Pb$; and $R = Ar^{Mes}, Tbb$ ($E = Si$), was presented. We employed several quantum chemical tools to assess the electronic structure of these complexes on the basis of compounds that were previously experimentally accessed by our group. This involved (a) a detailed inspection of the bonding parameters of the optimized structures, (b) an investigation of the canonical and Pipek–Mezey-localized MOs, (c) a comparison of the NPA charges and the M–E bond cleavage and bond dissociation energies, and (d) a calculation of the ETS-NOCV interactions. Two classes (**a** and **b**) of compounds could be identified: The first class **a** is tetrylidyne complexes, featuring Fischer-type carbyne complexes with a roughly linear M–E–R linkage and a short M≡E bond, which is composed of a $\sigma(E \rightarrow M)$ donor bond and two $\pi(M \rightarrow E)$ back bonds. The class **b** complexes display a considerably bent M–E–R linkage and longer M–E bonds, which are best described as $\sigma(M \rightarrow E)$ donor bonds with weak $\pi(M-E)$ components. Complexes of class **b** feature an increased lone pair density at the tetrel center, like metallotetrylenes. All carbon and silicon compounds belong to class **a**, whereas the complexes for $E = Sn, Pb$ and $M = Pd, Pt$ belong to class **b**. The interjacent germanium compounds as well as **NiSnAr^{Mes}** and **NiPbAr^{Mes}** show properties of both classes, but the tetrylidyne characteristic is strongly.

We also more closely examined the recently reported cationic group 10 metal complexes $[(PPh_3)_3NiEN(Si^iPr_3)(Dipp)]^+$ with $E = Ge$ (**B-Ge**) and Sn (**B-Sn**). These compounds feature the same electronic structure as the class **a** compounds. A certain extent of $\pi(N \rightarrow E)$ donation is indicated in these compounds, which is, however, much smaller than in Fischer-type aminocarbyne complexes and does not influence the M≡E bond lengths.

Finally, an extensive study of the potential energy hypersurface varying the M–E–C angles revealed metallotetrylene isomers with M–E–C bond angles of around 95° . Interestingly, these isomers are energetically favored for $M = Pd, Pt$ and $E = Sn, Pb$ over their less bent isomers by $13\text{--}29 \text{ kJ}\cdot\text{mol}^{-1}$.

Supplementary Materials: The supporting information is available at: <https://www.mdpi.com/article/10.3390/inorganics11030129/s1> and contains structural parameters of the **MER**, **MER-2**, and **B-E** complexes; comparisons of computational methods; selected canonical and localized molecular orbitals of the **MER** and **B-E** complexes; spin–spin excitation energies of the ML_3 and ER fragments, thermodynamically corrected dissociation energies of the **MER** complexes; and ETS-NOCVs of the **MER** complexes.

Author Contributions: The data reported herein were produced and presented in equal parts by L.R.M. and J.R. The results presented herein were obtained, analyzed, and discussed through close collaboration of L.R.M., J.R. and A.C.F. All authors have read and agreed to the published version of the manuscript.

Funding: This research received no external funding.

Data Availability Statement: Not applicable.

Acknowledgments: We thank the Rheinische Friedrich-Wilhelms Universität Bonn for the financial support of this work. We are very grateful to Ioannis Papazoglou for the synthesis and characterization of the discussed group 10 tetrylidyne complexes. We also highly acknowledge the scientific exchange with Gregor Schnakenburg.

Conflicts of Interest: The authors declare no conflict of interest.

References and Notes

- Hashimoto, H.; Tobita, H. Recent Advances in the Chemistry of Transition Metal–Silicon/Germanium Triple-Bonded Complexes. *Coord. Chem. Rev.* **2018**, *355*, 362–379. [\[CrossRef\]](#)
- Saini, S.; Agarwal, A.; Bose, S.K. Transition Metal Chemistry of Heavier Group 14 Congener Triple-Bonded Complexes: Syntheses and Reactivity. *Dalton Trans.* **2020**, *49*, 17055–17075. [\[CrossRef\]](#)
- Fischer, E.O.; Kreis, G.; Kreiter, C.G.; Müller, J.; Huttner, G.; Lorenz, H. *trans*-Halogeno[alkyl(aryl)carbyne]tetracarbonyl Complexes of Chromium, Molybdenum, and Tungsten—A New Class of Compounds Having a Transition Metal–Carbon Triple Bond. *Angew. Chem. Int. Ed. Engl.* **1973**, *12*, 564–565. [\[CrossRef\]](#)
- Fischer, E.O. Auf dem Weg zu Carben- und Carbin-Komplexen (Nobel-Vortrag). *Angew. Chem.* **1974**, *86*, 651–663. [\[CrossRef\]](#)
- Kim, H.P.; Angelici, R.J. Transition Metal Complexes with Terminal Carbyne Ligands. In *Advances in Organometallic Chemistry*; Elsevier: Amsterdam, The Netherlands, 1987; Volume 27, pp. 51–111. ISBN 978-0-12-031127-9.
- Fischer, H.; Hofmann, P.; Kreissl, F.R.; Schrock, R.R.; Schubert, U.; Weiss, K. *Carbyne Complexes*; Wiley-VCH: Weinheim, Germany, 1988.
- Mayr, A.; Hoffmeister, H. Recent Advances in the Chemistry of Metal–Carbon Triple Bonds. In *Advances in Organometallic Chemistry*; Elsevier: Amsterdam, The Netherlands, 1991; Volume 32, pp. 227–324. ISBN 978-0-12-031132-3.
- Simons, R.S.; Power, P.P. $(\eta^5\text{-C}_5\text{H}_5)(\text{CO})_2\text{MoGeC}_6\text{H}_3\text{-2,6-Mes}_2$: A Transition-Metal Germylyne Complex. *J. Am. Chem. Soc.* **1996**, *118*, 11966–11967. [\[CrossRef\]](#)
- Pu, L.; Twamley, B.; Haubrich, S.T.; Olmstead, M.M.; Mork, B.V.; Simons, R.S.; Power, P.P. Triple Bonding to Germanium: Characterization of the Transition Metal Germylynes $(\eta^5\text{-C}_5\text{H}_5)(\text{CO})_2\text{M}\equiv\text{Ge-C}_6\text{H}_3\text{-2,6-Mes}_2$ (M = Mo, W; Mes = C₆H₂-2,4,6-Me₃) and $(\eta^5\text{-C}_5\text{H}_5)(\text{CO})_2\text{M}\equiv\text{Ge-C}_6\text{H}_3\text{-2,6-Trip}_2$ (M = Cr, Mo, W; Trip = C₆H₂-2,4,6-i-Pr₃) and the Related Single Bonded Metallogermylenes $(\eta^5\text{-C}_5\text{H}_5)(\text{CO})_3\text{M-Ge-C}_6\text{H}_3\text{-2,6-Trip}_2$ (M = Cr, W). *J. Am. Chem. Soc.* **2000**, *122*, 650–656. [\[CrossRef\]](#)
- Filippou, A.C.; Philippopoulos, A.I.; Portius, P.; Neumann, D.U. Synthesis and Structure of the Germylyne Complexes *trans*-[X(dppe)₂W=Ge(η^1 -Cp*)] (X = Cl, Br, I) and Comparison of the W=E Bonds (E = C, Ge) by Density Functional Calculations. *Angew. Chem. Int. Ed.* **2000**, *39*, 2778–2781. [\[CrossRef\]](#)
- Filippou, A.C.; Portius, P.; Philippopoulos, A.I. Molybdenum and Tungsten Germylyne Complexes of the General Formula *trans*-[X(dppe)₂M=Ge(η^1 -Cp*)] (X = Cl, Br, I; dppe = Ph₂PCH₂CH₂PPh₂; Cp* = C₅Me₅): Syntheses, Molecular Structures, and Bonding Features of the Germylyne Ligand. *Organometallics* **2002**, *21*, 653–661. [\[CrossRef\]](#)
- Filippou, A.C.; Philippopoulos, A.I.; Portius, P.; Schnakenburg, G. Halide Substitution Reactions of the Germylydyne Complexes *trans*-[X(dppe)₂W=Ge(η^1 -Cp*)] (X = Cl, I; dppe = Ph₂PCH₂CH₂PPh₂; Cp* = C₅Me₅). *Organometallics* **2004**, *23*, 4503–4512. [\[CrossRef\]](#)
- Filippou, A.C.; Schnakenburg, G.; Philippopoulos, A.I.; Weidemann, N. Ge₂ Trapped by Triple Bonds between Two Metal Centers: The Germylydyne Complexes *trans,trans*-[Cl(depe)₂M=Ge–Ge=M(depe)₂Cl] (M = Mo, W) and Bonding Analyses of the M=Ge–Ge=M Chain. *Angew. Chem. Int. Ed.* **2005**, *44*, 5979–5985. [\[CrossRef\]](#)
- Filippou, A.C.; Weidemann, N.; Philippopoulos, A.I.; Schnakenburg, G. Activation of Aryl Germanium(II) Chlorides by [Mo(PMe₃)₆] and [W(η^2 -CH₂PMe₂)H(PMe₃)₄]: A New Route to Metal–Germanium Triple Bonds. *Angew. Chem. Int. Ed.* **2006**, *45*, 5987–5991. [\[CrossRef\]](#)
- Filippou, A.C.; Portius, P.; Philippopoulos, A.I.; Rohde, H. Triple Bonding to Tin: Synthesis and Characterization of the Stannylyne Complex *trans*-[Cl(PMe₃)₄W=Sn–C₆H₃-2,6-Mes₂]. *Angew. Chem. Int. Ed.* **2003**, *42*, 445–447. [\[CrossRef\]](#) [\[PubMed\]](#)
- Filippou, A.C.; Philippopoulos, A.I.; Schnakenburg, G. Triple Bonding to Tin: Synthesis and Characterization of the Square-Pyramidal Stannylyne Complex Cation [(dppe)₂W=Sn–C₆H₃-2,6-Mes₂]⁺ (dppe = Ph₂PCH₂CH₂PPh₂, Mes = C₆H₂-2,4,6-Me₃). *Organometallics* **2003**, *22*, 3339–3341. [\[CrossRef\]](#)
- Filippou, A.C.; Weidemann, N.; Schnakenburg, G.; Rohde, H.; Philippopoulos, A.I. Tungsten–Lead Triple Bonds: Syntheses, Structures, and Coordination Chemistry of the Plumbylydyne Complexes *trans*-[X(PMe₃)₄W=Pb(2,6-Trip₂C₆H₃)]. *Angew. Chem. Int. Ed.* **2004**, *43*, 6512–6516. [\[CrossRef\]](#) [\[PubMed\]](#)
- Filippou, A.C.; Rohde, H.; Schnakenburg, G. Triple Bond to Lead: Synthesis and Characterization of the Plumbylydyne Complex *trans*-[Br(PMe₃)₄Mo=Pb–C₆H₃-2,6-Trip₂]. *Angew. Chem. Int. Ed.* **2004**, *43*, 2243–2247. [\[CrossRef\]](#)
- Filippou, A.C.; Weidemann, N.; Schnakenburg, G. Tungsten-Mediated Activation of a Pb^{II}-N Bond: A New Route to Tungsten–Lead Triple Bonds. *Angew. Chem. Int. Ed.* **2008**, *47*, 5799–5802. [\[CrossRef\]](#)
- Filippou, A.C.; Chernov, O.; Stumpf, K.W.; Schnakenburg, G. Metal–Silicon Triple Bonds: The Molybdenum Silylydyne Complex [Cp(CO)₂Mo=Si-R]. *Angew. Chem. Int. Ed.* **2010**, *49*, 3296–3300. [\[CrossRef\]](#)
- Filippou, A.C.; Baars, B.; Chernov, O.; Lebedev, Y.N.; Schnakenburg, G. Silicon–Oxygen Double Bonds: A Stable Silanone with a Trigonal-Planar Coordinated Silicon Center. *Angew. Chem. Int. Ed.* **2014**, *53*, 565–570. [\[CrossRef\]](#) [\[PubMed\]](#)
- Filippou, A.C.; Hoffmann, D.; Schnakenburg, G. Triple Bonds of Niobium with Silicon, Germanium and Tin: The Tetrylydyne Complexes [(κ^3 -tmps)(CO)₂Nb=E-R] (E = Si, Ge, Sn; tmps = MeSi(CH₂PMe₂)₃; R = aryl). *Chem. Sci.* **2017**, *8*, 6290–6299. [\[CrossRef\]](#) [\[PubMed\]](#)
- Ghana, P.; Arz, M.I.; Chakraborty, U.; Schnakenburg, G.; Filippou, A.C. Linearly Two-Coordinated Silicon: Transition Metal Complexes with the Functional Groups M=Si–M and M=Si=M. *J. Am. Chem. Soc.* **2018**, *140*, 7187–7198. [\[CrossRef\]](#)

24. Ghana, P.; Arz, M.I.; Schnakenburg, G.; Straßmann, M.; Filippou, A.C. Metal–Silicon Triple Bonds: Access to $[\text{Si}(\eta^5\text{-C}_5\text{Me}_5)]^+$ from $\text{SiX}_2(\text{NHC})$ and Its Conversion to the Silylidyne Complex $[\text{Tp}^{\text{Me}}(\text{CO})_2\text{MoSi}(\eta^3\text{-C}_5\text{Me}_5)]$ ($\text{Tp}^{\text{Me}} = \kappa^3\text{-N,N',N''-hydridotris(3,5-dimethyl-1-pyrazolyl)borate}$). *Organometallics* **2018**, *37*, 772–780. [[CrossRef](#)]
25. Mork, B.V.; Tilley, T.D. Multiple Bonding Between Silicon and Molybdenum: A Transition-Metal Complex with Considerable Silylyne Character. *Angew. Chem. Int. Ed.* **2003**, *42*, 357–360. [[CrossRef](#)] [[PubMed](#)]
26. Hayes, P.G.; Xu, Z.; Beddie, C.; Keith, J.M.; Hall, M.B.; Tilley, T.D. The Osmium–Silicon Triple Bond: Synthesis, Characterization, and Reactivity of an Osmium Silylyne Complex. *J. Am. Chem. Soc.* **2013**, *135*, 11780–11783. [[CrossRef](#)]
27. Fukuda, T.; Yoshimoto, T.; Hashimoto, H.; Tobita, H. Synthesis of a Tungsten–Silylyne Complex via Stepwise Proton and Hydride Abstraction from a Hydrido Hydrosilylene Complex. *Organometallics* **2016**, *35*, 921–924. [[CrossRef](#)]
28. Yoshimoto, T.; Hashimoto, H.; Hayakawa, N.; Matsuo, T.; Tobita, H. A Silylyne Tungsten Complex Having an Eind Group on Silicon: Its Dimer–Monomer Equilibrium and Cycloaddition Reactions with Carbodiimide and Diaryl Ketones. *Organometallics* **2016**, *35*, 3444–3447. [[CrossRef](#)]
29. Dübek, G.; Hanusch, F.; Munz, D.; Inoue, S. An Air-Stable Heterobimetallic Si_2M_2 Tetrahedral Cluster. *Angew. Chem. Int. Ed.* **2020**, *59*, 5823–5829. [[CrossRef](#)]
30. Vyboishchikov, S.F.; Frenking, G. Structure and Bonding of Low-Valent (Fischer-Type) and High-Valent (Schrock-Type) Transition Metal Carbyne Complexes. *Chem.—Eur. J.* **1998**, *4*, 1439–1448.
31. Lein, M.; Szabó, A.; Kovács, A.; Frenking, G. Energy Decomposition Analysis of the Chemical Bond in Main Group and Transition Metal Compounds. *Faraday Discuss.* **2003**, *124*, 365–378. [[CrossRef](#)]
32. Pandey, K.K.; Lein, M.; Frenking, G. Metal Germylyne Complexes $[\text{M}\equiv\text{Ge}-\text{R}]$ and Metallogermylenes $[\text{M}-\text{Ge}-\text{R}]$: DFT Analysis of the Systems $[(\text{Cp})(\text{CO})_n\text{M}\equiv\text{GeMe}]$ ($\text{M} = \text{Cr}, \text{Mo}, \text{W}, \text{Fe}^{2+}$, $n = 2$; $\text{M} = \text{Fe}$, $n = 1$) and $[(\text{Cp})(\text{CO})_n\text{M}-\text{GeMe}]$ ($\text{M} = \text{Cr}, \text{Mo}, \text{W}$, $n = 3$; $\text{M} = \text{Fe}$, $n = 2$). *J. Am. Chem. Soc.* **2003**, *125*, 1660–1668. [[CrossRef](#)]
33. Pandey, K.K.; Lledós, A. Linear $\text{M}\equiv\text{E}-\text{Me}$ Versus Bent $\text{M}-\text{E}-\text{Me}$: Bonding Analysis in Heavier Metal–Ylidyne Complexes $[(\text{Cp})(\text{CO})_2\text{M}\equiv\text{EMe}]$ and Metallo–Ylidenes $[(\text{Cp})(\text{CO})_3\text{M}-\text{EMe}]$ ($\text{M} = \text{Cr}, \text{Mo}, \text{W}$; $\text{E} = \text{Si}, \text{Ge}, \text{Sn}, \text{Pb}$). *Inorg. Chem.* **2009**, *48*, 2748–2759. [[CrossRef](#)]
34. Pandey, K.K.; Patidar, P. Insights into the Nature of $\text{M}\equiv\text{E}$ Bonds in $[(\text{PMe}_3)_4\text{M}\equiv\text{E}(\text{Mes})]^+$ ($\text{M} = \text{Mo}, \text{W}$) and $[(\text{PMe}_3)_5\text{W}\equiv\text{E}(\text{Mes})]^+$: A Dispersion-Corrected DFT Study. *RSC Adv.* **2014**, *4*, 13034. [[CrossRef](#)]
35. Dewar, M.J.S. A Review of the π -Complex Theory. *Bull. Soc. Chim. Fr.* **1951**, *18*, C71–C79.
36. Chatt, J.; Duncanson, L.A. 586. Olefin Co-Ordination Compounds. Part III. Infra-Red Spectra and Structure: Attempted Preparation of Acetylene Complexes. *J. Chem. Soc. (Resumed)* **1953**, 2939–2947. [[CrossRef](#)]
37. Guggenberger, L.J.; Schrock, R.R. A Tantalum Carbyne Complex. *J. Am. Chem. Soc.* **1975**, *97*, 2935. [[CrossRef](#)]
38. Schrock, R.R. Multiple Metal–Carbon Bonds for Catalytic Metathesis Reactions (Nobel Lecture). *Angew. Chem. Int. Ed.* **2006**, *45*, 3748–3759. [[CrossRef](#)] [[PubMed](#)]
39. Filippou, A.C.; Barandov, A.; Schnakenburg, G.; Lewall, B.; van Gastel, M.; Marchanka, A. Open-Shell Complexes Containing Metal–Germanium Triple Bonds. *Angew. Chem. Int. Ed.* **2012**, *51*, 789–793. [[CrossRef](#)]
40. Filippou, A.C.; Stumpf, K.W.; Chernov, O.; Schnakenburg, G. Metal Activation of a Germylenoid, a New Approach to Metal–Germanium Triple Bonds: Synthesis and Reactions of the Germylidyne Complexes $[\text{Cp}(\text{CO})_2\text{M}\equiv\text{Ge}-\text{C}(\text{SiMe}_3)_3]$ ($\text{M} = \text{Mo}, \text{W}$). *Organometallics* **2012**, *31*, 748–755. [[CrossRef](#)]
41. Hicks, J.; Hadlington, T.J.; Schenk, C.; Li, J.; Jones, C. Utilizing Steric Bulk to Stabilize Molybdenum Aminogermylyne and Aminogermylene Complexes. *Organometallics* **2013**, *32*, 323–329. [[CrossRef](#)]
42. Fukuda, T.; Hashimoto, H.; Tobita, H. Reactions of a Tungsten–Germylyne Complex with Alcohols and Arylaldehydes. *Chem. Commun.* **2013**, *49*, 4232–4234. [[CrossRef](#)]
43. Wienkenhöver, N. 1,2-Dibromodisilenes: A Rich Source for Titanium Silylidyne Complexes, Acyclic Silylenes and Disilyne Dianions. Dissertation (Dr. rer. nat.), University of Bonn, Bonn, Germany, 2017.
44. Arizpe, L. Synthesis and Characterization of Complexes Featuring Tantalum–Germanium Multiple Bonds. Dissertation (Dr. rer. nat.), University of Bonn, Bonn, Germany, 2019.
45. Filippou, A.C.; Chakraborty, U.; Schnakenburg, G. Rhenium–Germanium Triple Bonds: Syntheses and Reactions of the Germylidyne Complexes $\text{mer-}[X_2(\text{PMe}_3)_3\text{Re}\equiv\text{Ge}-\text{R}]$ ($\text{X} = \text{Cl}, \text{I}, \text{H}$; $\text{R} = m\text{-terphenyl}$). *Chem.—Eur. J.* **2013**, *19*, 5676–5686. [[CrossRef](#)]
46. Chakraborty, U. Multiple Bonds between Group 7 Transition Metals and Heavier Tetrel Elements (Ge–Pb). Dissertation (Dr. rer. nat.), University of Bonn, Bonn, Germany, 2013.
47. Filippou, A.C.; Ghana, P.; Chakraborty, U.; Schnakenburg, G. Manganese–Tin Triple Bonds: A New Synthetic Route to the Manganese Stannylidyne Complex Cation $\text{trans-}[\text{H}(\text{dmpe})_2\text{Mn}\equiv\text{Sn}(\text{C}_6\text{H}_3\text{-2,6-Mes}_2)]^+$ ($\text{dmpe} = \text{Me}_2\text{PCH}_2\text{CH}_2\text{PMe}_2$, $\text{Mes} = 2,4,6\text{-trimethylphenyl}$). *J. Am. Chem. Soc.* **2013**, *135*, 11525–11528. [[CrossRef](#)] [[PubMed](#)]
48. Blom, B. Reactivity of Ylenes at Late Transition Metal Centers. Dissertation (Dr. rer. nat.), University of Bonn, Bonn, Germany, 2011.
49. Lebedev, Y.N. Multiple Bonding of Low-Valent Silicon and Germanium to Group 6 and 9 Metals. Dissertation (Dr. rer. nat.), University of Bonn, Bonn, Germany, 2014.
50. Widemann, M.; Eichele, K.; Schubert, H.; Sindlinger, C.P.; Klenner, S.; Pöttgen, R.; Wesemann, L. Synthesis and Hydrogenation of Heavy Homologues of Rhodium Carbynes: $[(\text{Me}_3\text{P})_2(\text{Ph}_3\text{P})\text{Rh}\equiv\text{E}-\text{Ar}^*]$ ($\text{E} = \text{Sn}, \text{Pb}$). *Angew. Chem. Int. Ed.* **2021**, *60*, 5882–5889. [[CrossRef](#)]

51. Fischer, E.O.; Schneider, J.R. Übergangsmetallcarbin-komplexe. *J. Organomet. Chem.* **1985**, *295*, c29–c34. [[CrossRef](#)]
52. Papazoglou, I. Unprecedented Tetrylidyne Complexes of Group 6 and 10 Metals. Dissertation (Dr. rer. nat.), University of Bonn, Bonn, Germany, 2016.
53. Keil, P.M.; Hadlington, T.J. Accessing Cationic Tetrylene-Nickel(0) Systems Featuring Donor–Acceptor E–Ni Triple Bonds (E = Ge, Sn). *Chem. Commun.* **2022**, *58*, 3011–3014. [[CrossRef](#)] [[PubMed](#)]
54. Watanabe, C.; Inagawa, Y.; Iwamoto, T.; Kira, M. Synthesis and Structures of (Dialkylsilylene)Bis(Phosphine)-Nickel, Palladium, and Platinum Complexes and (η^6 -Arene)(Dialkylsilylene)Nickel Complexes. *Dalton Trans.* **2010**, *39*, 9414. [[CrossRef](#)]
55. A CSD survey (11.08.2022) gave 6 compounds with Ni=Si double bond lengths ranging from 209.4(1) pm to 222.41(5) pm with a median and mean value of 215.1 pm and 216.4 pm, respectively
56. A CSD survey (11.08.2022) gave 5 compounds with Pt=Si double bond lengths ranging from 220.8(2) pm to 227.0(2) pm with a median and mean value of 221.2 pm and 223.1 pm, respectively
57. A CSD survey (11.08.2022) gave 1 compound with a Ni=Sn double bond length of 238.7(2) pm
58. Tao, J.M.; Perdew, J.P.; Staroverov, V.N.; Scuseria, G.E. Climbing the Density Functional Ladder: Nonempirical Meta-Generalized Gradient Approximation Designed for Molecules and Solids. *Phys. Rev. Lett.* **2003**, *91*, 146401. [[CrossRef](#)]
59. Zhao, Y.; Truhlar, D.G. Design of Density Functionals That Are Broadly Accurate for Thermochemistry, Thermochemical Kinetics, and Nonbonded Interactions. *J. Phys. Chem.* **2005**, *109*, 5656–5667. [[CrossRef](#)]
60. Bühl, M.; Kabrede, H. Geometries of Transition-Metal Complexes from Density-Functional Theory. *J. Chem. Theory Comput.* **2006**, *2*, 1282–1290. [[CrossRef](#)]
61. Waller, M.P.; Braun, H.; Hojdis, N.; Bühl, M. Geometries of Second-Row Transition-Metal Complexes from Density-Functional Theory. *J. Chem. Theory Comput.* **2007**, *3*, 2234–2242. [[CrossRef](#)] [[PubMed](#)]
62. Bühl, M.; Reimann, C.; Pantazis, D.A.; Bredow, T.; Neese, F. Geometries of Third-Row Transition-Metal Complexes from Density-Functional Theory. *J. Chem. Theory Comput.* **2008**, *4*, 1449–1459. [[CrossRef](#)]
63. Maurer, L.R.; Bursch, M.; Grimme, S.; Hansen, A. Assessing Density Functional Theory for Chemically Relevant Open-Shell Transition Metal Reactions. *J. Chem. Theory Comput.* **2021**, *17*, 6134–6151. [[CrossRef](#)] [[PubMed](#)]
64. van Wüllen, C. Molecular Density Functional Calculations in the Regular Relativistic Approximation: Method, Application to Coinage Metal Diatomics, Hydrides, Fluorides and Chlorides, and Comparison with First-Order Relativistic Calculations. *J. Chem. Phys.* **1998**, *109*, 392–399. [[CrossRef](#)]
65. Andrae, D.; Häußermann, U.; Dolg, M.; Stoll, H.; Preuß, H. Energy-Adjusted *Ab-Initio* Pseudopotentials for the Second and Third Row Transition Elements. *Theor. Chim. Acta* **1990**, *77*, 123–141. [[CrossRef](#)]
66. Metz, B.; Stoll, H.; Dolg, M. Small-Core Multiconfiguration-Dirac–Hartree–Fock-Adjusted Pseudopotentials for Post-d Main Group Elements: Application to PbH and PbO. *J. Chem. Phys.* **2000**, *113*, 2563–2569. [[CrossRef](#)]
67. Hong, G.; Dolg, M.; Li, L. A Comparison of Scalar-Relativistic ZORA and DKH Density Functional Schemes: Monohydrides, Monooxides and Monofluorides of La, Lu, Ac and Lr. *Chem. Phys. Lett.* **2001**, *334*, 396–402. [[CrossRef](#)]
68. Pyykkö, P. Additive Covalent Radii for Single-, Double-, and Triple-Bonded Molecules and Tetrahedrally Bonded Crystals: A Summary. *J. Phys. Chem. A* **2015**, *119*, 2326–2337. [[CrossRef](#)] [[PubMed](#)]
69. Bent, H.A. An Appraisal of Valence-Bond Structures and Hybridization in Compounds of the First-Row Elements. *Chem. Rev.* **1961**, *61*, 275–311. [[CrossRef](#)]
70. Power, P.P. An Update on Multiple Bonding between Heavier Main Group Elements: The Importance of Pauli Repulsion, Charge-Shift Character, and London Dispersion Force Effects. *Organometallics* **2020**, *39*, 4127–4138. [[CrossRef](#)]
71. Kutzelnigg, W. Chemical Bonding in Higher Main Group Elements. *Angew. Chem. Int. Ed. Engl.* **1984**, *23*, 272–295. [[CrossRef](#)]
72. Desclaux, J.P. Relativistic Dirac-Fock Expectation Values for Atoms with $Z = 1$ to $Z = 120$. *At. Data Nucl. Data Tables* **1973**, *12*, 311–406. [[CrossRef](#)]
73. Pandey, K.K.; Patidar, P.; Power, P.P. Structure and Bonding Energy Analysis of Cationic Metal–Ylyne Complexes of Molybdenum and Tungsten, $[(\text{MeCN})(\text{PMe}_3)_4\text{M}=\text{EMes}]^+$ (M = Mo, W; E = Si, Ge, Sn, Pb): A Theoretical Study. *Inorg. Chem.* **2011**, *50*, 7080–7089. [[CrossRef](#)]
74. Schubert, U.; Fischer, E.O.; Wittmann, D. Structure of $[(\text{CO})_5\text{CrNet}_2]\text{BF}_4$, a Key Organometallic Compound; Reaction to Give the Carbene Complex $(\text{CO})_5\text{CrC}(\text{AsPh}_2)\text{NEt}_2$. *Angew. Chem. Int. Ed. Engl.* **1980**, *19*, 643–644. [[CrossRef](#)]
75. Kostic, N.; Fenske, R. Molecular Orbital Calculations on Carbyne Complexes $\text{CpMn}(\text{CO})_2\text{CR}^+$ and $(\text{CO})_5\text{CrCNet}_2^+$. Frontier-Controlled Nucleophilic Addition to Metal–Carbon Triple Bond. *J. Am. Chem. Soc.* **1981**, *103*, 4677–4685. [[CrossRef](#)]
76. Filippou, A.C.; Grünleitner, W.; Fischer, E.O.; Imhof, W.; Huttner, G. Übergangsmetall-Carbin-Komplexe: XCIX. Synthese und Röntgenstruktur von $(\eta^5\text{-C}_5\text{Me}_5)(\text{CO})_2\text{Mo}=\text{CNet}_2$, dem ersten niedervalenten Diethylaminocarbin-Komplex von Molybdän mit einem Pentamethylcyclopentadienyl-Liganden. *J. Organomet. Chem.* **1991**, *413*, 165–179. [[CrossRef](#)]
77. Filippou, A.C.; Portius, P.; Jankowski, C. Aminomethylene Complexes of Molybdenum(IV) and Tungsten(IV) Bearing 1,2-Dithiolato Ligands. *J. Organomet. Chem.* **2001**, *617–618*, 656–670. [[CrossRef](#)]
78. Biancalana, L.; Marchetti, F. Aminocarbyne Ligands in Organometallic Chemistry. *Coord. Chem. Rev.* **2021**, *449*, 214203. [[CrossRef](#)]
79. Pipek, J.; Mezey, P.G. A Fast Intrinsic Localization Procedure Applicable for *ab initio* and Semiempirical Linear Combination of Atomic Orbital Wave Functions. *J. Chem. Phys.* **1989**, *90*, 4916–4926. [[CrossRef](#)]
80. Weiss, K. Catalytic Reactions of Carbyne Complexes. In *Carbyne Complexes*; VCH Verlagsgesellschaft: Weinheim, Germany; VCH Publishers: New York, NY, USA, 1988; p. 205.

81. Ervin, K.M.; Gronert, S.; Barlow, S.E.; Gilles, M.K.; Harrison, A.G.; Bierbaum, V.M.; DePuy, C.H.; Lineberger, W.C.; Ellison, G.B. Bond Strengths of Ethylene and Acetylene. *J. Am. Chem. Soc.* **1990**, *112*, 5750–5759. [[CrossRef](#)]
82. Lai, T.Y.; Tao, L.; Britt, R.D.; Power, P.P. Reversible Sn–Sn Triple Bond Dissociation in a Distannylene: Support for Charge-Shift Bonding Character. *J. Am. Chem. Soc.* **2019**, *141*, 12527–12530. [[CrossRef](#)]
83. Ziegler, T.; Rauk, A. On the Calculation of Bonding Energies by the Hartree Fock Slater Method: I. The Transition State Method. *Theor. Chim. Acta* **1977**, *46*, 1–10. [[CrossRef](#)]
84. Michalak, A.; Mitoraj, M.; Ziegler, T. Bond Orbitals from Chemical Valence Theory. *J. Phys. Chem. A* **2008**, *112*, 1933–1939. [[CrossRef](#)]
85. Mitoraj, M.P.; Michalak, A.; Ziegler, T. A Combined Charge and Energy Decomposition Scheme for Bond Analysis. *J. Chem. Theory Comput.* **2009**, *5*, 962–975. [[CrossRef](#)] [[PubMed](#)]
86. Okuniewski, A.; Rosiak, D.; Chojnacki, J.; Becker, B. Coordination Polymers and Molecular Structures among Complexes of Mercury(II) Halides with Selected 1-Benzoylthioureas. *Polyhedron* **2015**, *90*, 47–57. [[CrossRef](#)]
87. Neese, F. Software Update: The ORCA Program System—Version 5.0. *WIREs Comput. Mol. Sci.* **2022**, *12*, e1606. [[CrossRef](#)]
88. Grimme, S.; Antony, J.; Ehrlich, S.; Krieg, H. A Consistent and Accurate Ab Initio Parametrization of Density Functional Dispersion Correction (DFT-D) for the 94 Elements H–Pu. *J. Chem. Phys.* **2010**, *132*, 154104. [[CrossRef](#)] [[PubMed](#)]
89. Grimme, S.; Ehrlich, S.; Goerigk, L. Effect of the Damping Function in Dispersion Corrected Density Functional Theory. *J. Comput. Chem.* **2011**, *32*, 1456–1465. [[CrossRef](#)] [[PubMed](#)]
90. Axilrod, B.M.; Teller, E. Interaction of the van Der Waals Type Between Three Atoms. *J. Chem. Phys.* **1943**, *11*, 299–300. [[CrossRef](#)]
91. Muto, Y. Force between Nonpolar Molecules. *Proc. Phys. Math. Soc. Jpn.* **1943**, *17*, 629–631.
92. Weigend, F.; Ahlrichs, R. Balanced Basis Sets of Split Valence, Triple Zeta Valence and Quadruple Zeta Valence Quality for H to Rn: Design and Assessment of Accuracy. *Phys. Chem. Chem. Phys.* **2005**, *7*, 3297–3305. [[CrossRef](#)]
93. Goerigk, L.; Grimme, S. Efficient and Accurate Double-Hybrid-Meta-GGA Density Functionals—Evaluation with the Extended GMTKN30 Database for General Main Group Thermochemistry, Kinetics, and Noncovalent Interactions. *J. Chem. Theory Comput.* **2011**, *7*, 291–309. [[CrossRef](#)]
94. Vahtras, O.; Almlöf, J.; Feyereisen, M.W. Integral Approximations for LCAO-SCF Calculations. *Chem. Phys. Lett.* **1993**, *213*, 514–518. [[CrossRef](#)]
95. Weigend, F.; Kattannek, M.; Ahlrichs, R. Approximated Electron Repulsion Integrals: Cholesky Decomposition versus Resolution of the Identity Methods. *J. Chem. Phys.* **2009**, *130*, 164106. [[CrossRef](#)]
96. Weigend, F. Hartree–Fock Exchange Fitting Basis Sets for H to Rn. *J. Comput. Chem.* **2008**, *29*, 167–175. [[CrossRef](#)]
97. Hellweg, A.; Hättig, C.; Höfener, S.; Klopper, W. Optimized Accurate Auxiliary Basis Sets for RI-MP2 and RI-CC2 Calculations for the Atoms Rb to Rn. *Theor. Chem. Acc.* **2007**, *117*, 587–597. [[CrossRef](#)]
98. Glendening, E.D.; Badenhoop, J.K.; Reed, A.E.; Carpenter, J.E.; Bohmann, J.A.; Morales, C.M.; Karafiloglou, P.; Landis, C.R.; Weinhold, F. *NBO 7.0*; 2018.
99. te Velde, G.; Bickelhaupt, F.M.; Baerends, E.J.; Fonseca Guerra, C.; van Gisbergen, S.J.A.; Snijders, J.G.; Ziegler, T. Chemistry with ADF. *J. Comput. Chem.* **2001**, *22*, 931–967. [[CrossRef](#)]
100. Baerends, E.J.; Ziegler, T.; Atkins, A.J.; Autschbach, J.; Baseggio, O.; Bashford, D.; Bérces, A.; Bickelhaupt, F.M.; Bo, C.; Boerrigter, P.M.; et al. *ADF*; 2021.
101. Van Lenthe, E.; Baerends, E.J. Optimized Slater-Type Basis Sets for the Elements 1–118. *J. Comput. Chem.* **2003**, *24*, 1142–1156. [[CrossRef](#)] [[PubMed](#)]
102. Lu, T.; Chen, F. Multiwfn: A Multifunctional Wavefunction Analyzer. *J. Comput. Chem.* **2012**, *33*, 580–592. [[CrossRef](#)]
103. Pettersen, E.F.; Goddard, T.D.; Huang, C.C.; Couch, G.S.; Greenblatt, D.M.; Meng, E.C.; Ferrin, T.E. UCSF Chimera—A Visualization System for Exploratory Research and Analysis. *J. Comput. Chem.* **2004**, *25*, 1605–1612. [[CrossRef](#)]

Disclaimer/Publisher’s Note: The statements, opinions and data contained in all publications are solely those of the individual author(s) and contributor(s) and not of MDPI and/or the editor(s). MDPI and/or the editor(s) disclaim responsibility for any injury to people or property resulting from any ideas, methods, instructions or products referred to in the content.

Supporting Information

The Electronic Nature of Cationic Group 10 Ylidyne Complexes

Leonard R. Maurer^{1,3,†}, Jens Rump^{2,3,†} and Alexander C. Filippou^{3,*}

¹ E-Mail: l.maurer@uni-bonn.de

² E-Mail: jens.rump@uni-bonn.de

³ Institute of Inorganic Chemistry, University of Bonn, D-53121 Bonn, Germany

* Correspondence: filippou@uni-bonn.de

† Contributed equally to this work and are joint first authors

Table of Contents

1) Structural parameters of tetrylidyne complexes $[M\equiv E-R]^+$ and their metallotetrylene isomers $[M-\ddot{E}-R]^+$	2
2) Influence of other levels of theory on the structures of NiSiTbb , NiSnAr^{Mes} and PtGeAr^{Mes}	4
3) Comparison of methods for treating relativistic effects.....	4
4) Calculated and experimental data of compounds B-Ge and B-Sn	5
5) Selected canonical MOs of compounds MER	6
6) Selected Pipek-Mezey localized MOs of compounds MER	23
7) Selected canonical and localized MOs of compounds B-Ge and B-Sn	31
8) Spin-spin excitation energies for the fragments of compounds MER	32
9) <i>BCEs</i> and <i>BDEs</i> of MSiAr^{Mes}	33
10) Thermodynamically corrected <i>BDEs</i>	33
11) EDA components of the interaction energy of MER	35
12) ETS-NOCV deformation densities of compounds MER	36
13) Metallotetrylene isomers MER-2 as found by PES scans	47

1) Structural parameters of tetrylidyne complexes $[M \equiv E-R]^+$ and their metallotetrylene isomers $[M-E-R]^+$

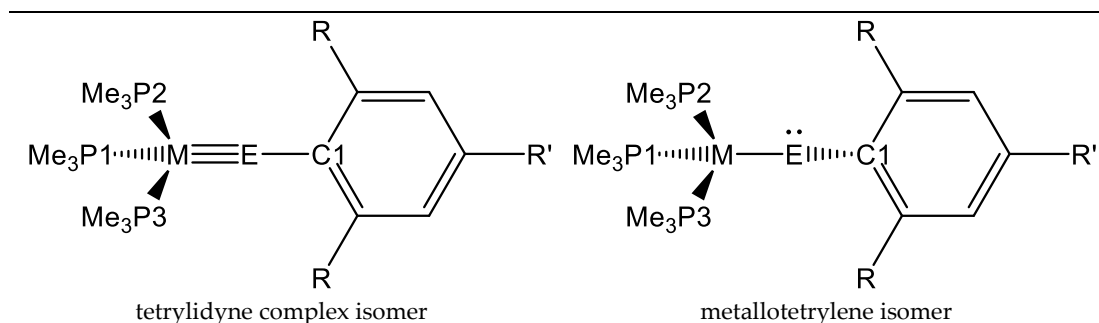


Figure S1. Lewis representations for the numbering of the tetrylidyne complexes and metallotetrylene isomers.

The geometry index τ_4 is used to distinguish whether the geometry of the coordination centre M is planar or tetrahedral. The formula is:

$$\tau_4 = \frac{\beta - \alpha}{360^\circ - \vartheta} + \frac{180^\circ - \beta}{180^\circ - \vartheta}$$

where $\beta > \alpha$ are the two greatest valence angles of the coordination centre; $\vartheta = \cos^{-1}(-1/3) \approx 109.5^\circ$ is a tetrahedral angle.[1] When τ_4 is close to 0 the structure is similar to square planar, while if τ_4 is close to 1 then the structure is similar to tetrahedral.

Table S1. Selected bond parameters of level of theory **I** optimized gas-phase structures (calc.) and structures obtained experimentally by single crystal X-ray diffraction (exp.) of group 10 tetrylidyne complexes. Bond lengths and angles are given in pm and deg, respectively.

compound	M-E	E-C1	M-E-C1	M-P1	M-P2	M-P3	τ_4
NiCAr^{Mes} (calc.)	169.1	141.3	168.4	221.9	224.5	226.4	0.80
NiSiTbb_{exp} (exp.)	203.11(7)	183.8(2)	172.40(8)	218.96(8)	220.04(7)	220.54(8)	0.93
NiSiTbb (calc.)	204.5	184.0	167.2	219.8	221.7	221.9	0.92
NiSiAr^{Mes} (calc.)	204.2	186.6	163.8	219.0	221.9	222.4	0.90
NiGeAr^{Mes_{exp}} (exp.)	210.40(6)	194.6(4)	164.9(2)	216.1(1)	220.3(1)	220.1(1)	0.91
NiGeAr^{Mes} (calc.)	210.20(6)	195.0(4)	166.5(1)	218.1(1)	218.7(2)	220.4(1)	0.91
NiGeAr^{Mes} (calc.)	213.3	197.1	165.3	219.4	221.7	222.0	0.91
NiSnAr^{Mes_{exp}} (exp.)	228.08(9)	214.0(5)	165.1(2)	233.9(4) ^a	220.8(3) ^a	212.7(4) ^a	0.90
NiSnAr^{Mes} (calc.)	235.1	219.4	150.9	217.5	221.4	222.3	0.92
NiPbAr^{Mes} (calc.)	244.9	229.7	142.7	216.7	221.1	222.0	0.92
PdCAr^{Mes} (calc.)	182.0	140.9	168.4	235.2	237.7	239.8	0.77
PdSiTbb (calc.)	215.1	184.0	163.1	234.3	237.7	238.0	0.89
PdSiAr^{Mes} (calc.)	216.1	187.6	150.7	232.0	238.0	239.3	0.86
PdGeAr^{Mes} (calc.)	227.9	199.5	144.9	231.2	237.42	238.6	0.87
PdSnAr^{Mes} (calc.)	251.6	222.9	134.4	230.5	236.8	238.8	0.87
PdPbAr^{Mes} (calc.)	263.1	232.4	129.6	230.2	236.3	238.6	0.83
PtCAr^{Mes} (calc.)	179.9	141.2	175.1	235.4	236.3	237.8	0.79
PtSiTbb_{exp} (exp.)	213.43(7)	184.2(3)	173.83(9)	231.81(8)	232.65(7)	232.81(8)	0.93
PtSiTbb (calc.)	215.8	183.8	168.1	232.3	234.8	234.7	0.90
PtSiAr^{Mes} (calc.)	215.7	186.3	166.1	231.4	234.6	235.4	0.88
PtGeAr^{Mes_{exp}} (exp.)	222.42(7)	194.7(7)	161.8(2)	226.8(2)	232.3(2)	231.4(2)	0.89
PtGeAr^{Mes} (calc.)	222.69(8)	195.2(7)	163.3(2)	228.8(2)	230.3(3)	232.2(2)	0.88
PtGeAr^{Mes} (calc.)	228.4	198.9	149.7	229.0	234.0	235.6	0.88
PtSnAr^{Mes} (calc.)	255.1	223.9	132.1	228.6	234.0	235.8	0.83
PtPbAr^{Mes} (calc.)	267.7	233.1	127.3	228.7	233.4	235.4	0.79

^a: Due to structural disorder of the PMe₃ ligands the Ni-P bond lengths of **NiSnAr^{Mes_{exp}}** vary in a wide range and are inaccurate.

Table S2. Selected bond parameters of level of theory I optimized gas-phase (calc.) structures of group 10 metallotetrylenes. Bond lengths and angles are given in pm and deg, respectively.

compound	M-E	E-C1	M-E-C1	M-P1	M-P2	M-P3	τ_4
NiCAr ^{Mes} -2 (calc.)	180.6	145.0	99.7	232.3	225.0	223.8	0.51
NiSiTbb-2 (calc.)	–	–	–	–	–	–	–
NiSiAr ^{Mes} -2 (calc.)	–	–	–	–	–	–	–
NiGeAr ^{Mes} -2 (calc.)	235.9	204.0	95.1	229.5	221.0	220.7	0.51
NiSnAr ^{Mes} -2 (calc.)	256.3	224.3	96.0	226.8	219.2	219.5	0.54
NiPbAr ^{Mes} -2 (calc.)	264.2	234.3	94.8	225.5	218.8	219.0	0.54
PdCAr ^{Mes} -2 (calc.)	194.7	144.4	103.8	248.0	239.3	237.6	0.44
PdSiTbb-2 (calc.)	235.1	189.7	98.8	253.9	236.7	235.0	0.50
PdSiAr ^{Mes} -2 (calc.)	232.4	191.0	87.9	248.6	237.0	235.9	0.61
PdGeAr ^{Mes} -2 (calc.)	246.4	202.7	90.6	247.9	236.9	236.8	0.50
PdSnAr ^{Mes} -2 (calc.)	270.3	223.6	93.1	246.7	234.6	234.9	0.44
PdPbAr ^{Mes} -2 (calc.)	277.4	232.7	93.6	244.0	233.3	233.8	0.43
PtCAr ^{Mes} -2 (calc.)	196.4	145.1	108.9	245.2	234.7	233.4	0.43
PtSiTbb-2 (calc.)	239.0	191.0	101.0	250.0	230.6	232.2	0.49
PtSiAr ^{Mes} -2 (calc.)	238.1	192.5	100.0	249.0	232.2	232.0	0.42
PtGeAr ^{Mes} -2 (calc.)	250.7	204.0	98.7	245.0	231.8	231.7	0.41
PtSnAr ^{Mes} -2 (calc.)	274.3	225.4	96.9	243.1	231.4	231.4	0.42
PtPbAr ^{Mes} -2 (calc.)	281.9	233.7	94.3	241.3	230.6	230.8	0.43

2) Influence of other levels of theory on the structures of NiSiTbb, NiSnAr^{Mes} and PtGeAr^{Mes}

Table S3. Selected bond parameters of the optimized gas-phase structures of NiSiTbb, NiSnAr^{Mes} and PtGeAr^{Mes}. Bond lengths and angles are given in pm and deg, respectively. The minimum nature of the TPSS- and PW6B95-optimized structures was not confirmed by successive numerical frequency calculations.

compound	level of theory	M-E	E-C	M-E-C1
NiSiTbb	B97-D3(BJ)-ATM/def2-TZVP	204.5	184.0	167.2
	TPSS-D3(BJ)-ATM/def2-TZVP	204.0	183.6	167.7
	PW6B95-D3(BJ)-ATM/def2-TZVP	201.2	182.6	165.2
NiSnAr ^{Mes}	B97-D3(BJ)-ATM/def2-TZVP	235.1	219.4	150.9
	TPSS-D3(BJ)-ATM/def2-TZVP	232.4	217.4	149.3
	PW6B95-D3(BJ)-ATM/def2-TZVP	231.3	217.1	149.8
PtGeAr ^{Mes}	B97-D3(BJ)-ATM/def2-TZVP	228.4	198.9	149.7
	TPSS-D3(BJ)-ATM/def2-TZVP	226.7	197.2	151.3
	PW6B95-D3(BJ)-ATM/def2-TZVP	225.4	196.2	150.2

3) Comparison of methods for treating relativistic effects

The compound that is influenced most by relativistic effects is presumed to be **PtPbAr^{Mes}** with two elements of the sixth period. As can be seen in Table S4 the differences in the structural parameters obtained by using ECPs and the ZORA method are small. It is expected that the more accurate ZORA method would improve the results, but this is outmatched here by the great cost/benefit ratio of the ECPs.

Table S4. Comparison of the structure of **PtPbAr^{Mes}** with electronic core potentials (ECP) or explicit relativistic treatment by the Zero Order Regular Approximation (ZERO) method. Bond lengths and angles are given in pm and deg, respectively.

PtPbAr^{Mes}	Pt-Pb	Pb-C1	Pt-P1	Pt-P2	Pt-P3	Pt-Pb-C1
ECP	267.7	233.1	235.4	228.7	233.4	127.3
ZORA	266.4	233.1	233.7	227.5	232.0	128.3

4) Calculated and experimental data of compounds **B-Ge** and **B-Sn**

Table S5. Comparison of selected structural parameters of theoretically and experimentally obtained structures of compounds **B-Ge** and **B-Sn**. The values for **B-E'** and **B-E_{exp}** were taken from ref. [2]. **B-Ge-PMe₃** refers to [(PMe₃)₃Ni=GeN(SiⁱPr₃)(Dipp)]⁺. Bond lengths and angles are given in pm and deg, respectively.

compound	level of theory	M-E	E-N	M-E-N
B-Ge-PMe₃	B97-D3(BJ)-ATM/def2-TZVP	214.2	184.9	163.7
B-Ge	B97-D3(BJ)-ATM/def2-TZVP	218.3	186.4	173.4
B-Ge'	ω B97XD/def2-SVP (Ni,Ge: def2-TZVPP)	212.7	181.0	174.3
B-Ge_{exp}		215.9(1)	185.3(2)	175.9
B-Sn	B97-D3(BJ)-ATM/def2-TZVP	239.6	209.1	167.8
B-Sn'	ω B97XD/def2-SVP (Ni,Sn: def2-TZVPP)	232.8	202.6	169.3
B-Sn_{exp}		235.5(1)	206.6(6)	173.7

5) Selected canonical MOs of compounds MER

In all following figures the isosurface value is set to $0.04 \text{ e}^{1/2} \text{ Bohr}^{-3/2}$ and hydrogen atoms are omitted for clarity. Due to the Tbb and Ar^{Mes} substituents enhancing the delocalized nature of the MOs, the same sets of orbitals could not be depicted for each compound equally. This, in contrast, is much more straightforward for the Pipek-Mezey localized MOs (*vide infra*).

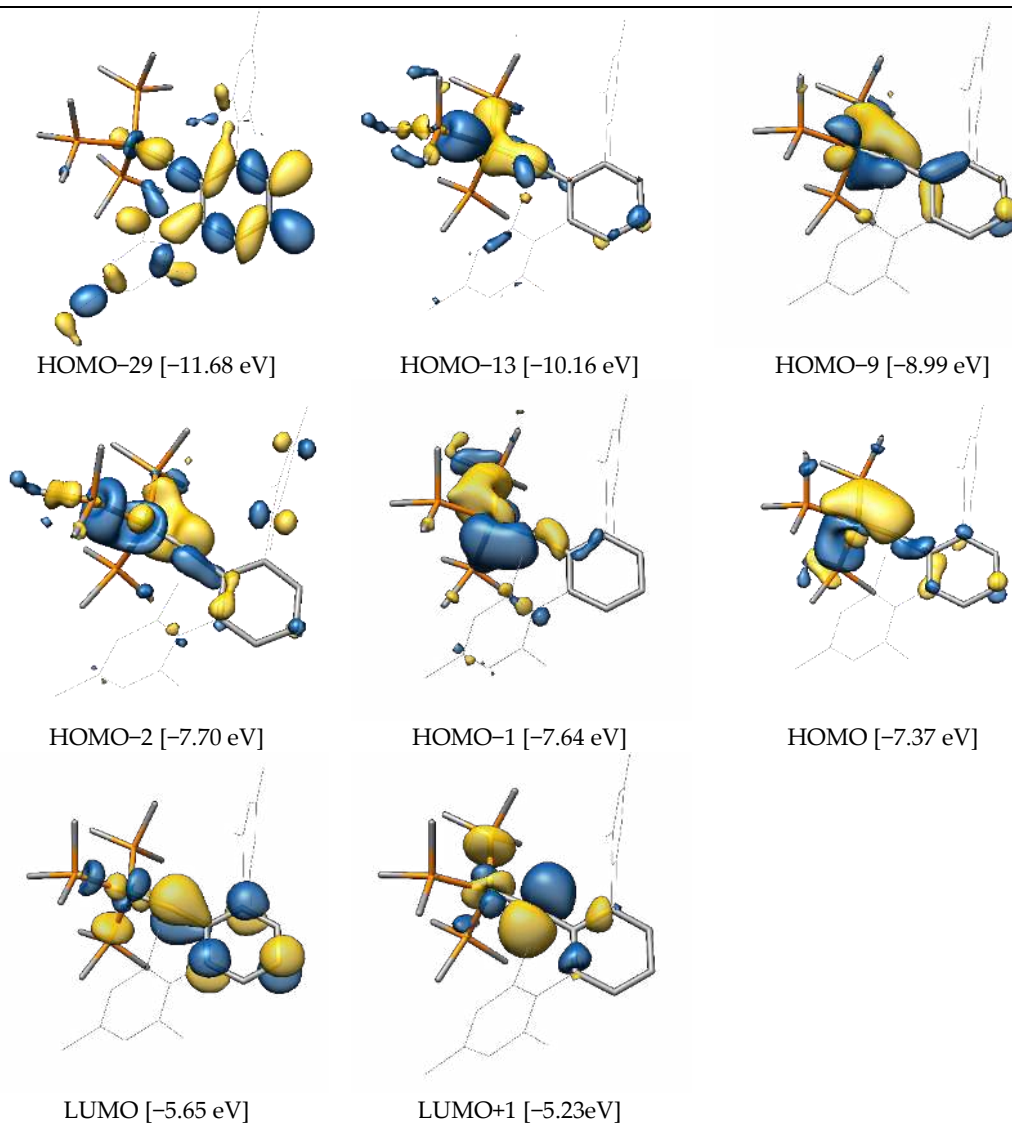
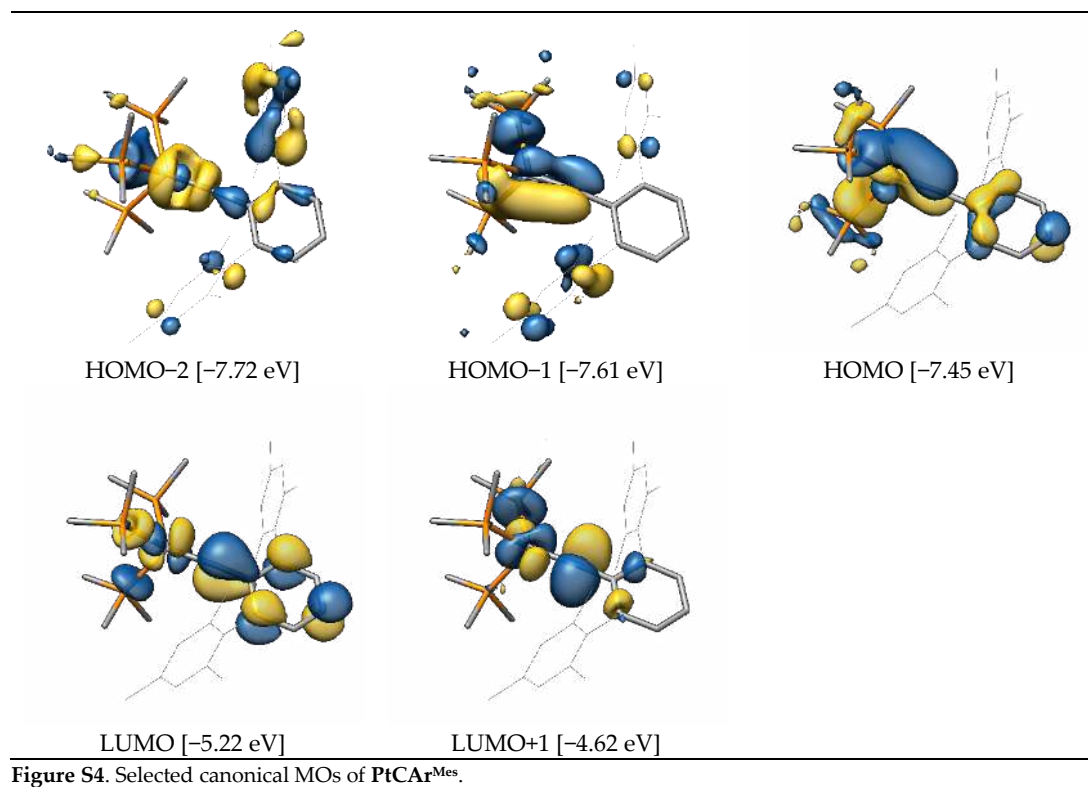
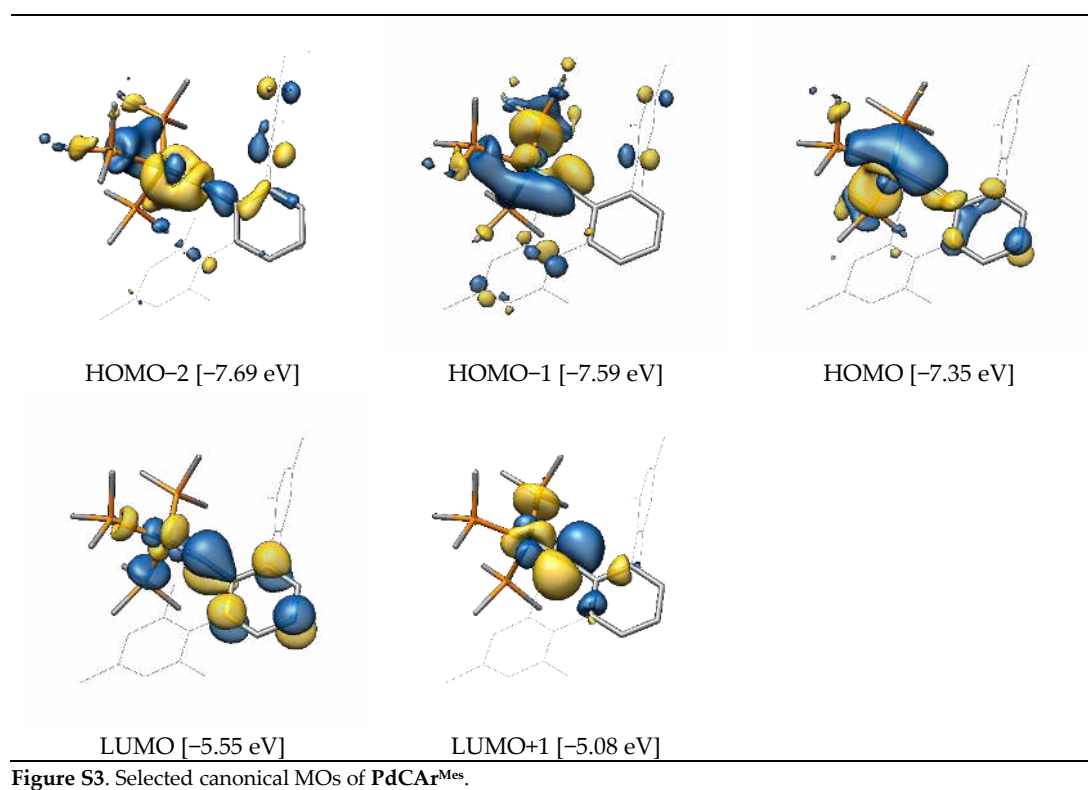


Figure S2. Selected canonical MOs of NiCAr^{Mes}.



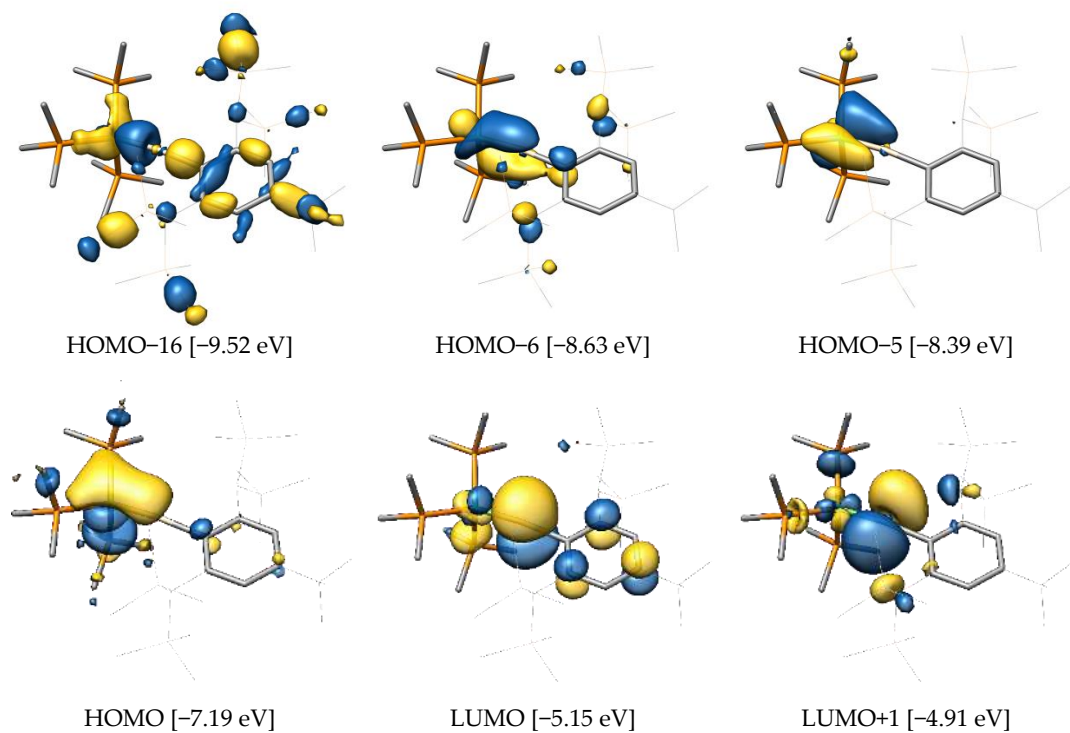


Figure S5. Selected canonical MOs of NiSiTbb.

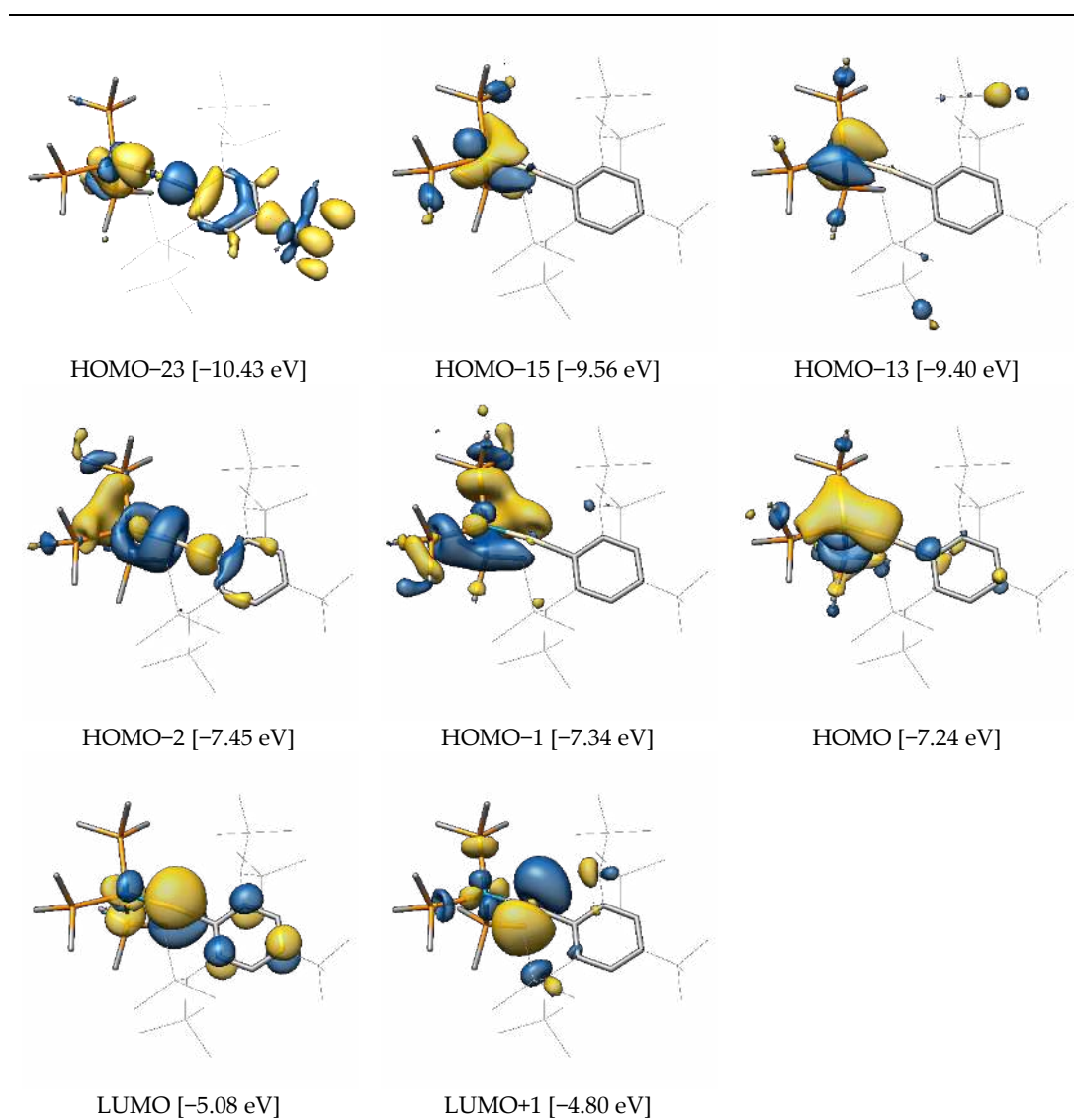


Figure S6. Selected canonical MOs of PdSiTbb.

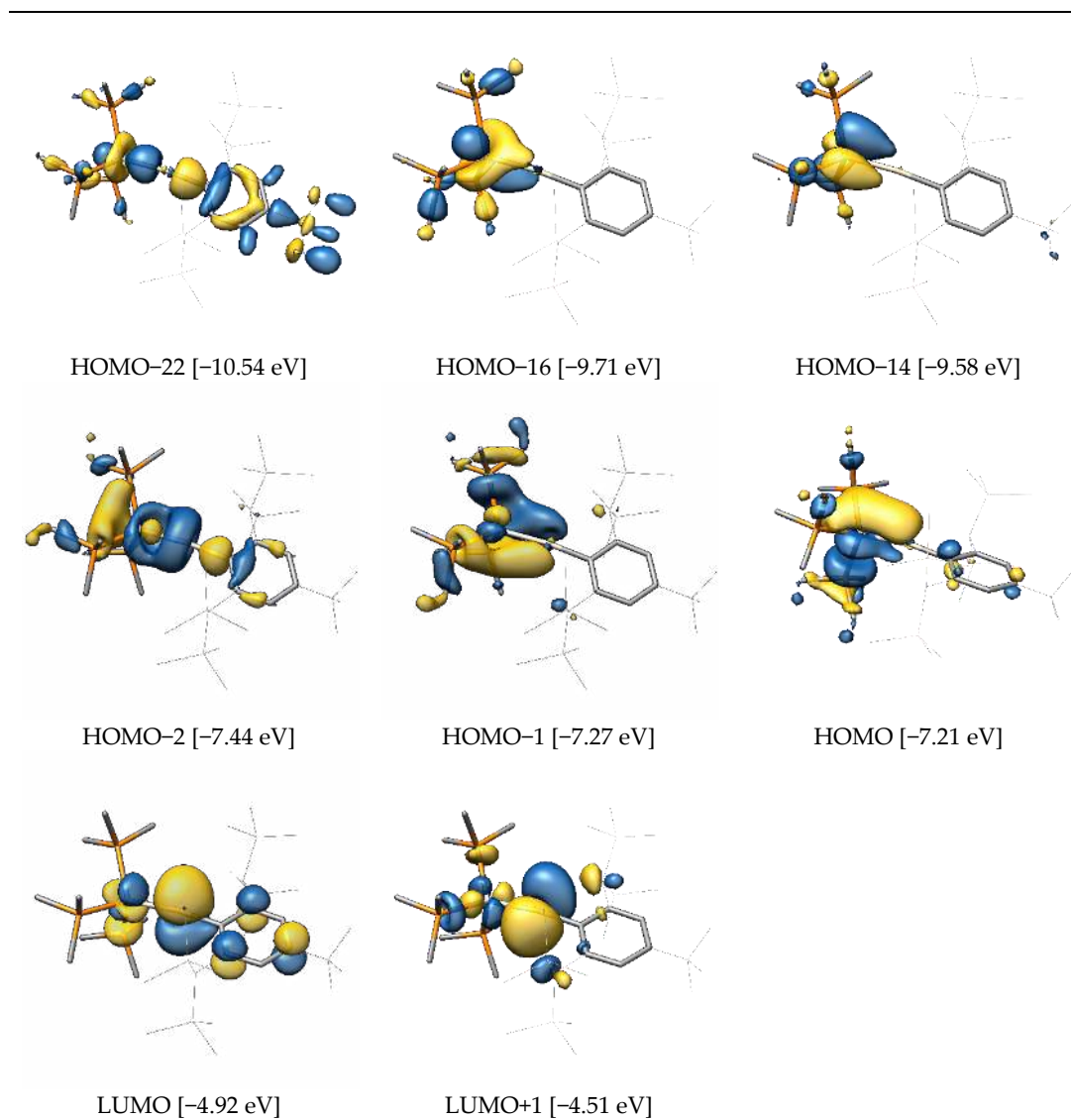


Figure S7. Selected canonical MOs of **PtSiTbb**. The HOMO is depicted in a slightly different perspective for better visibility of the orbital lobes.

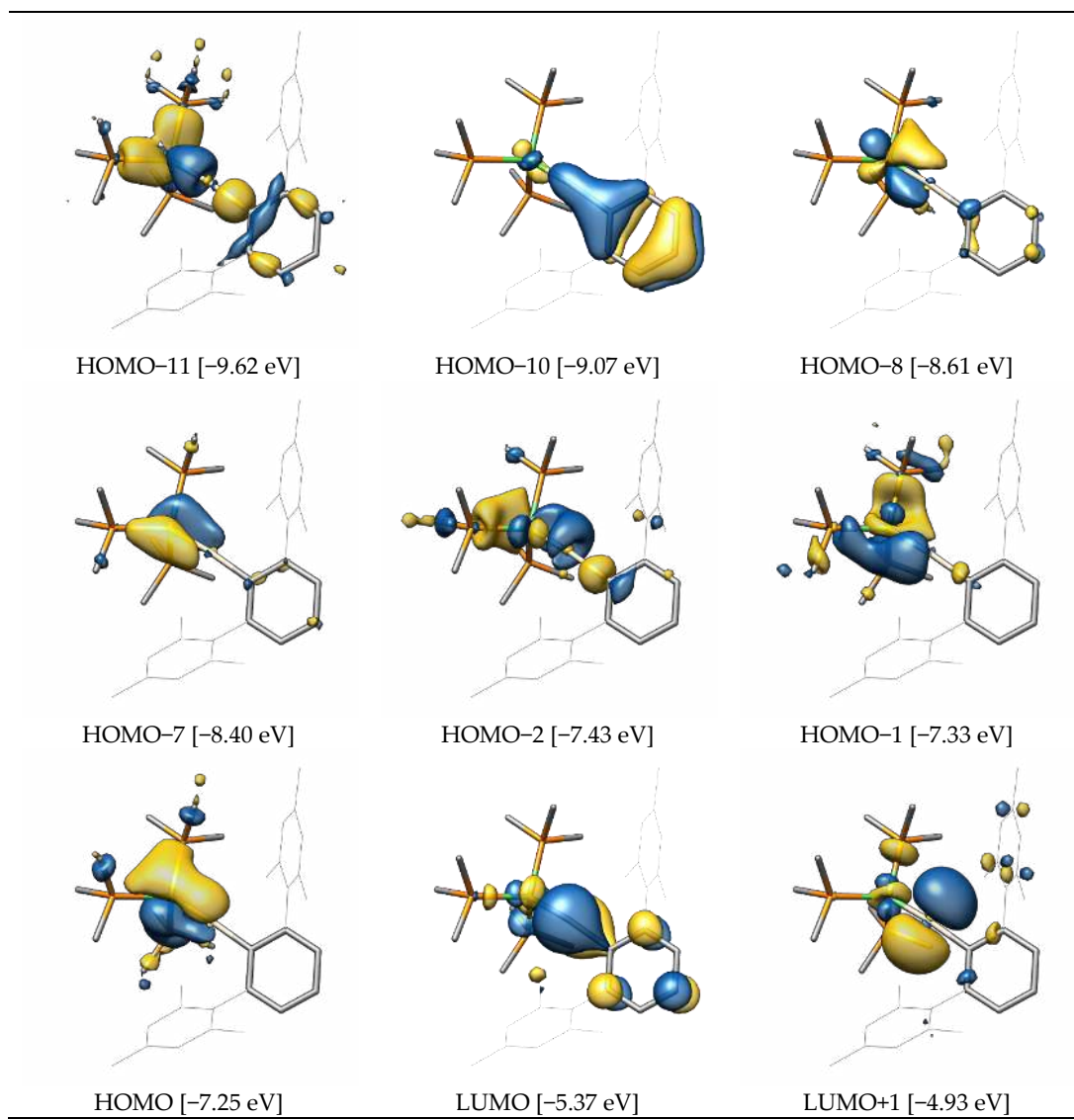


Figure S8. Selected canonical MOs of NiSiAr^{Mes}.

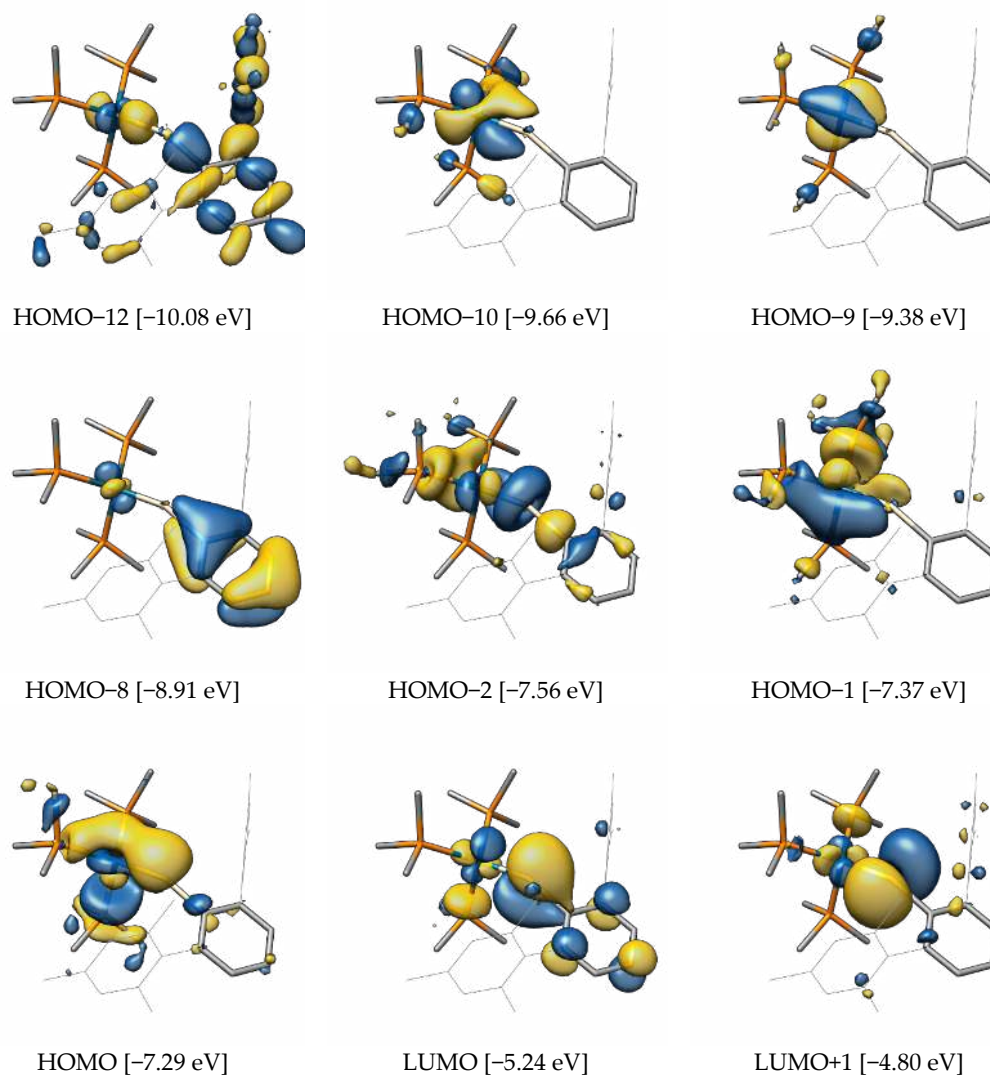


Figure S9. Selected canonical MOs of PdSiAr^{Mes}.

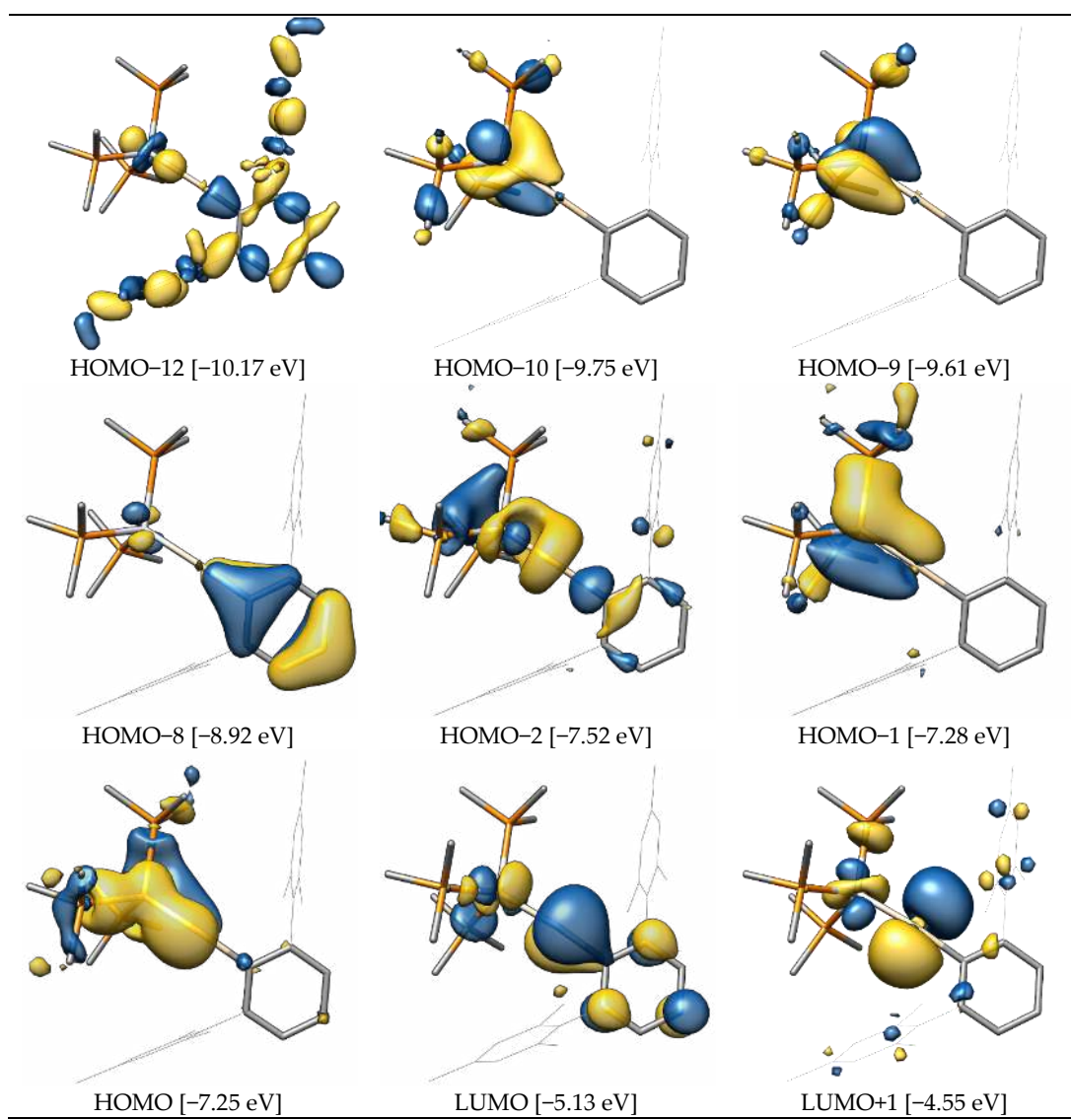


Figure S10. Selected canonical MOs of PtSiAr^{Mes}.

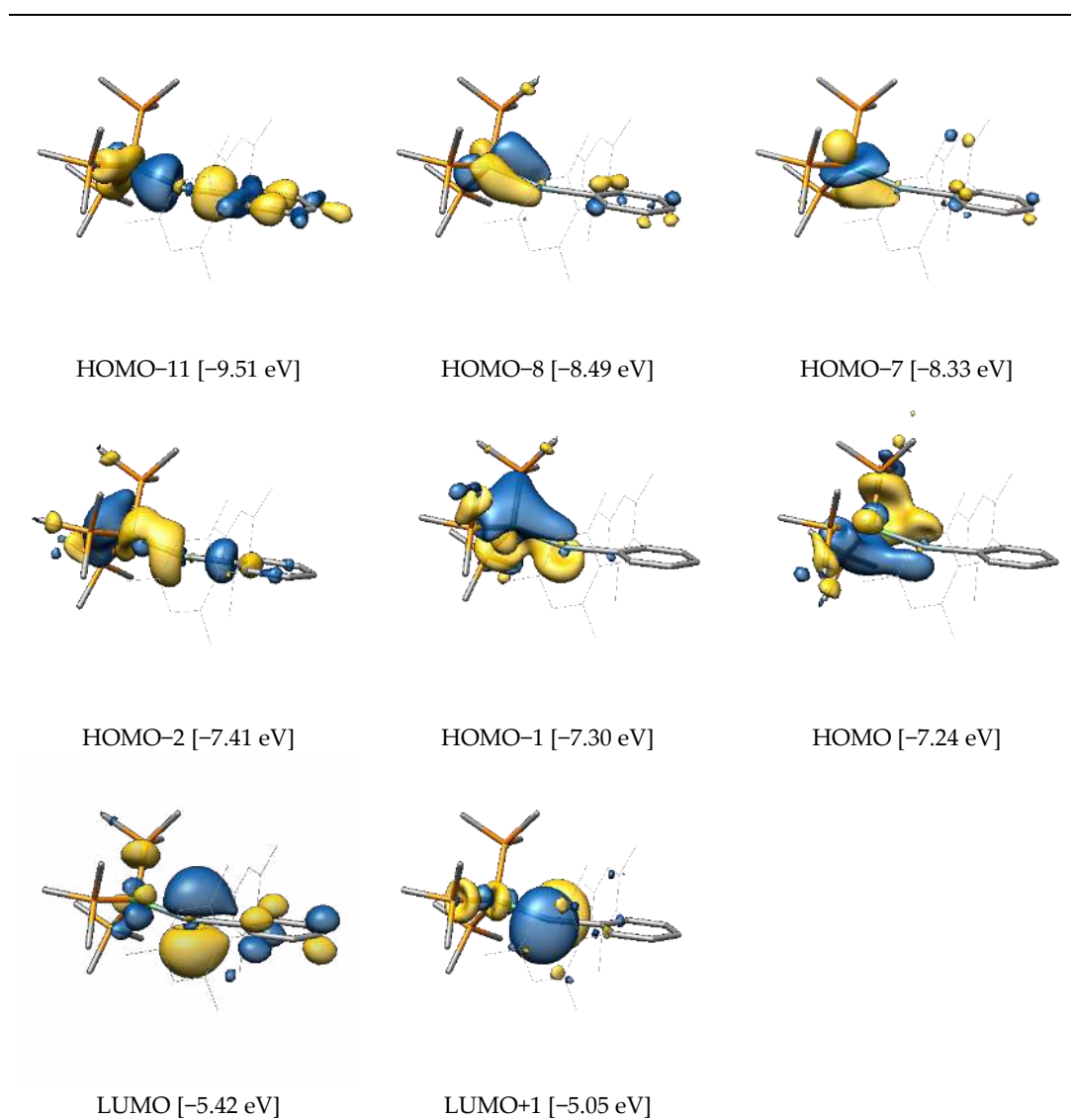


Figure S11. Selected canonical MOs of $\text{NiGeAr}^{\text{Me}_s}$. Although difficult to see, the non-bonding $\pi(\text{M-E})$ -type character in the HOMO is also present in the HOMO-1 and should not be mistaken for the $\pi(\text{M-E})$ bond.

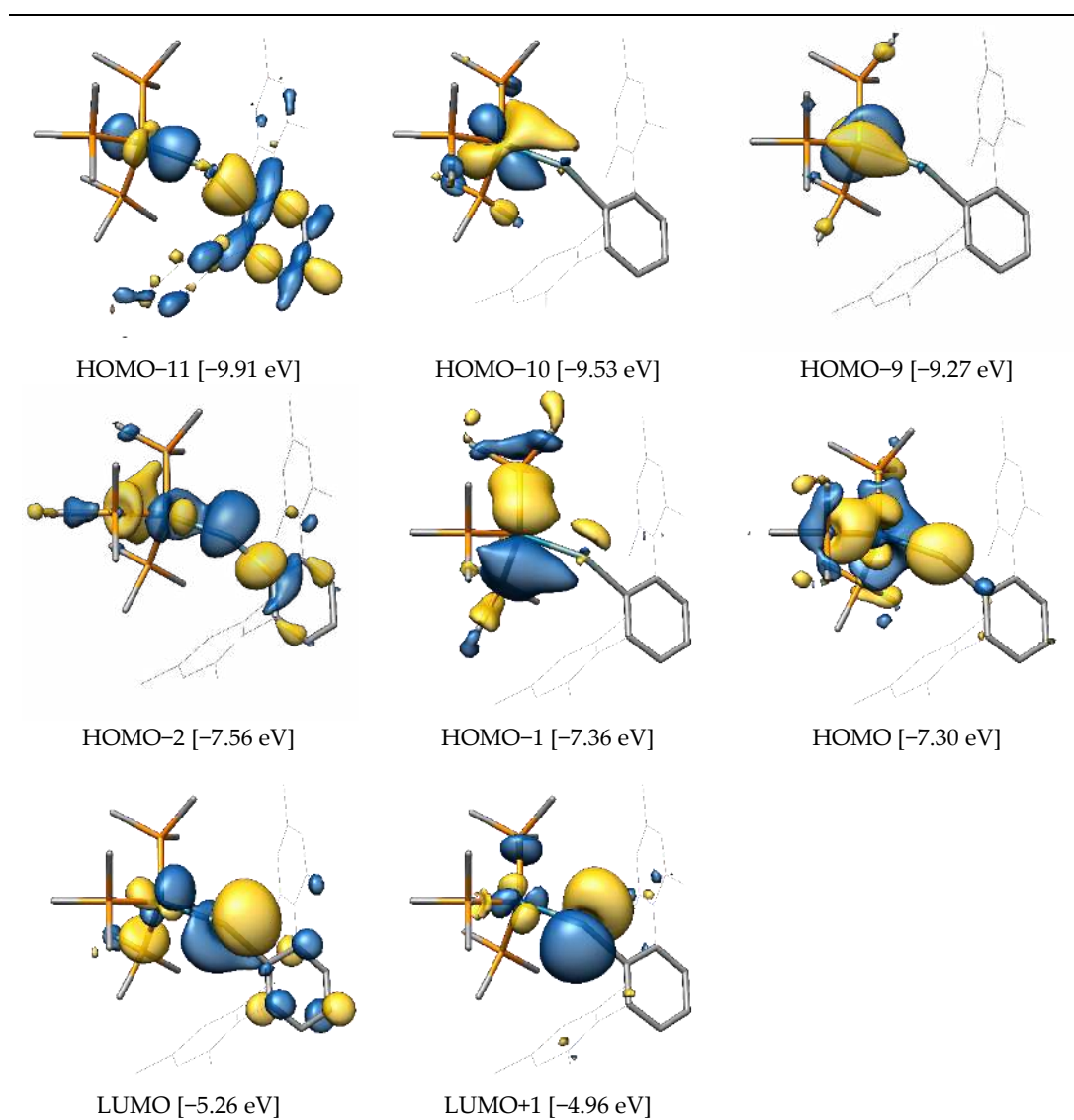


Figure S12. Selected canonical MOs of PdGeAr^{Mes}.

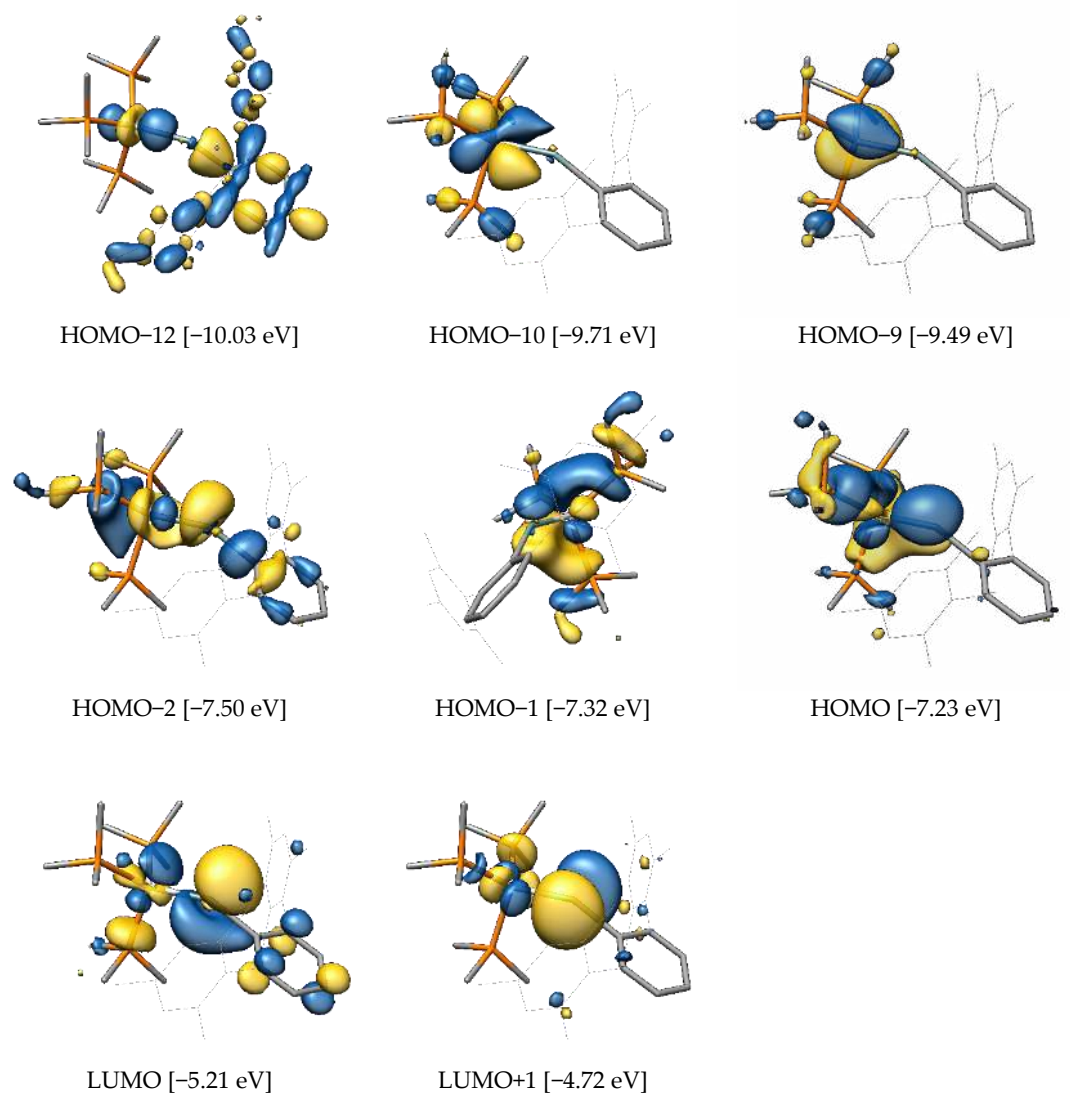


Figure S13. Selected canonical MOs of $\text{PtGeAr}^{\text{Mes}}$. The HOMO-1 is depicted in a different perspective for better visibility of the orbital lobes.

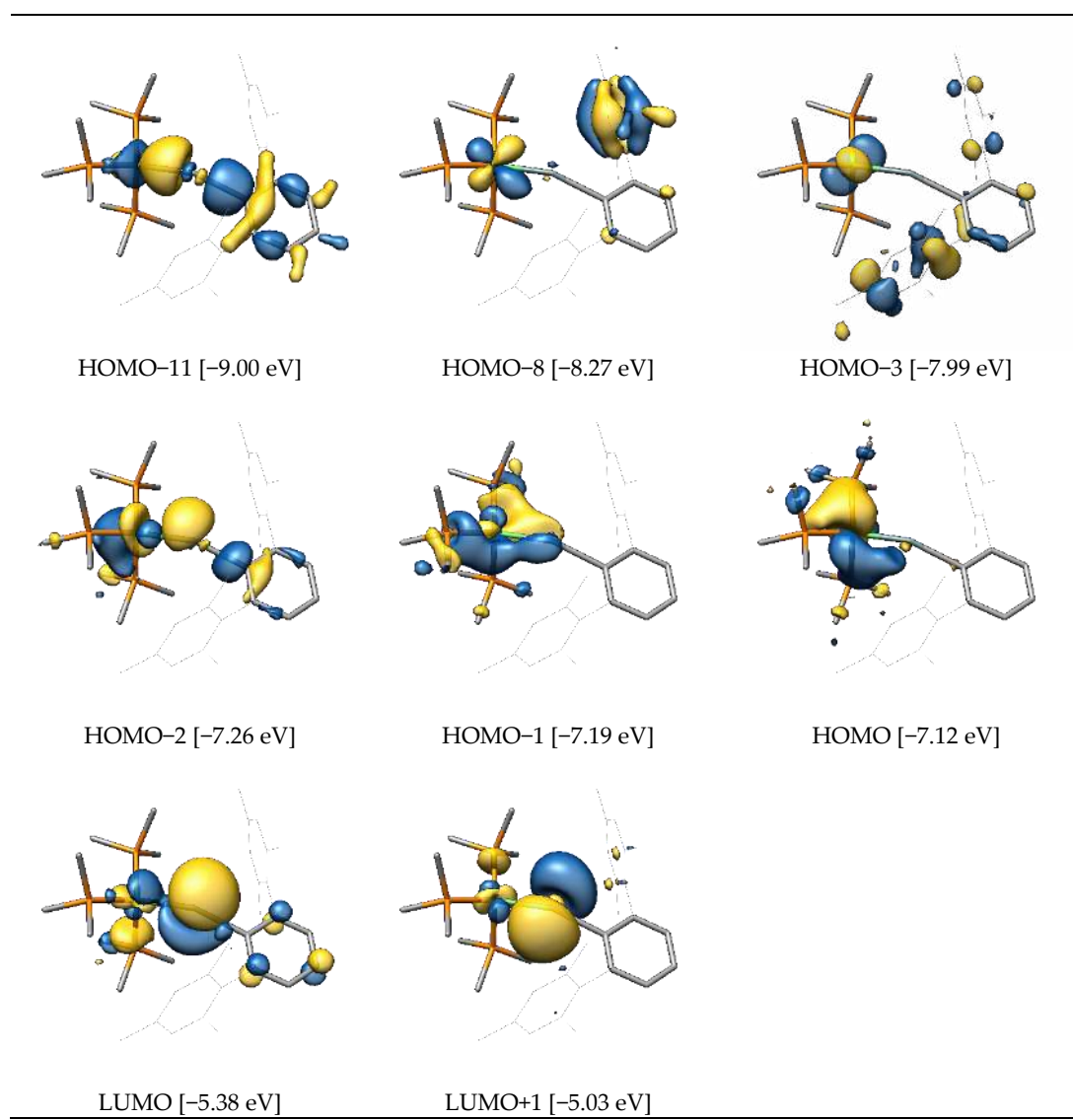


Figure S14. Selected canonical MOs of NiSnAr^{Mes}.

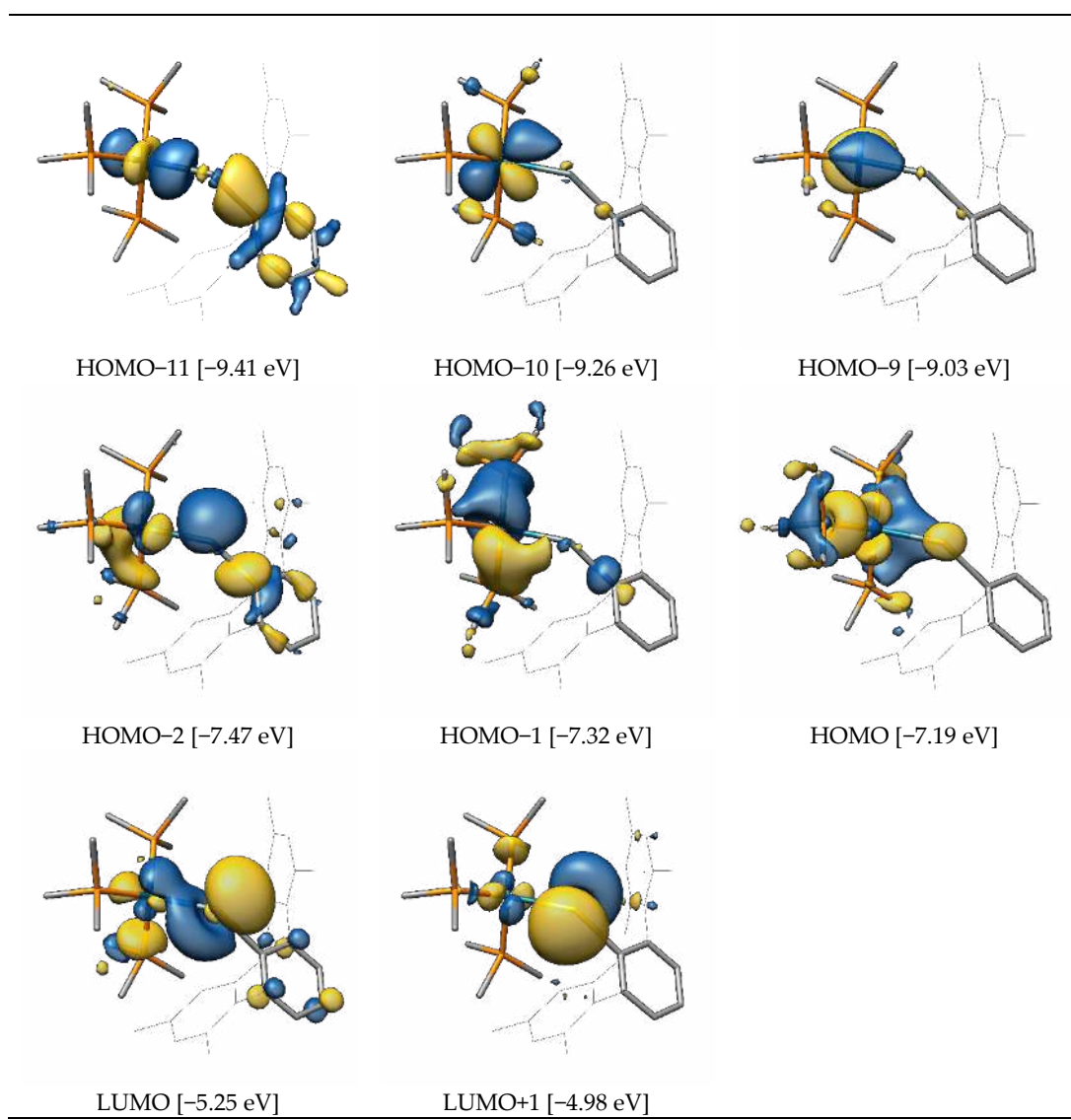


Figure S15. Selected canonical MOs of PdSnAr^{Mes}.

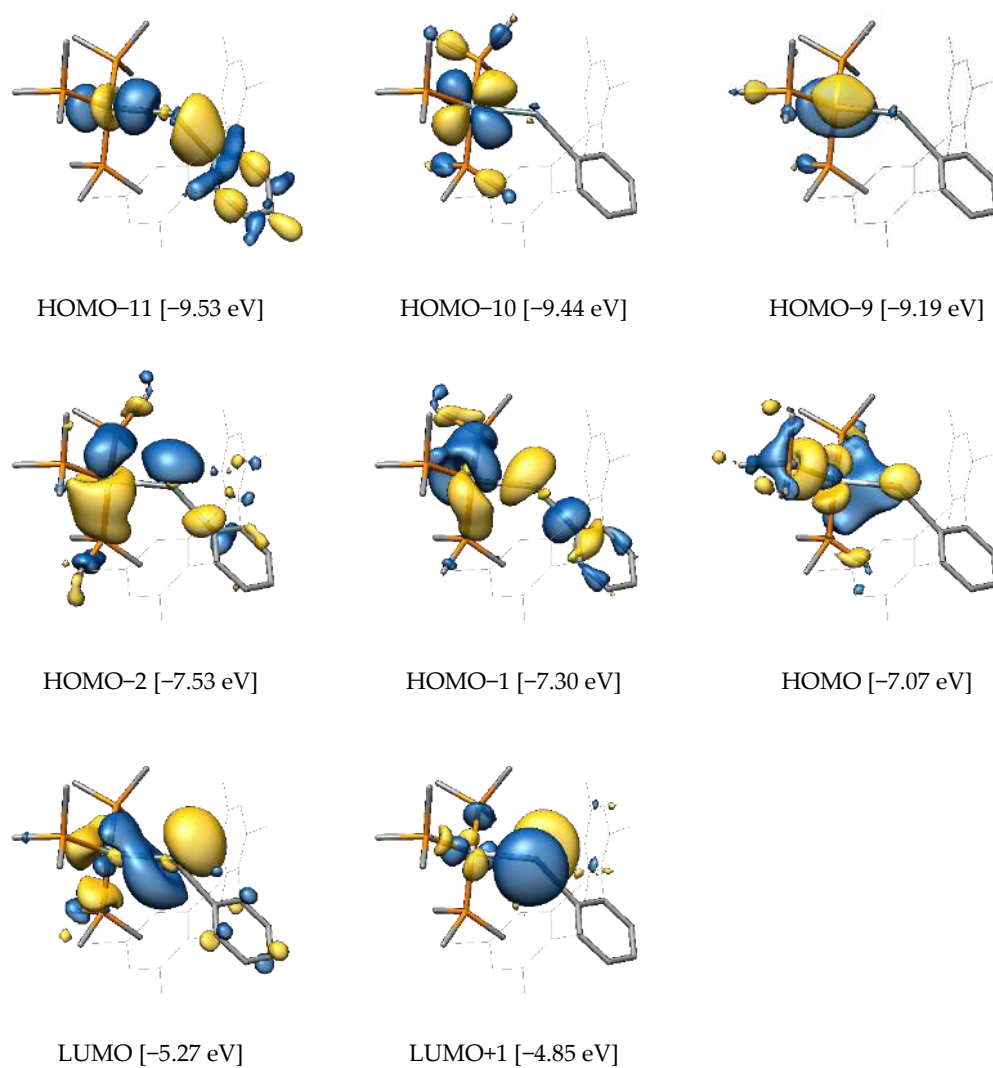


Figure S16. Selected canonical MOs of $\text{PtSnAr}^{\text{Mes}}$.

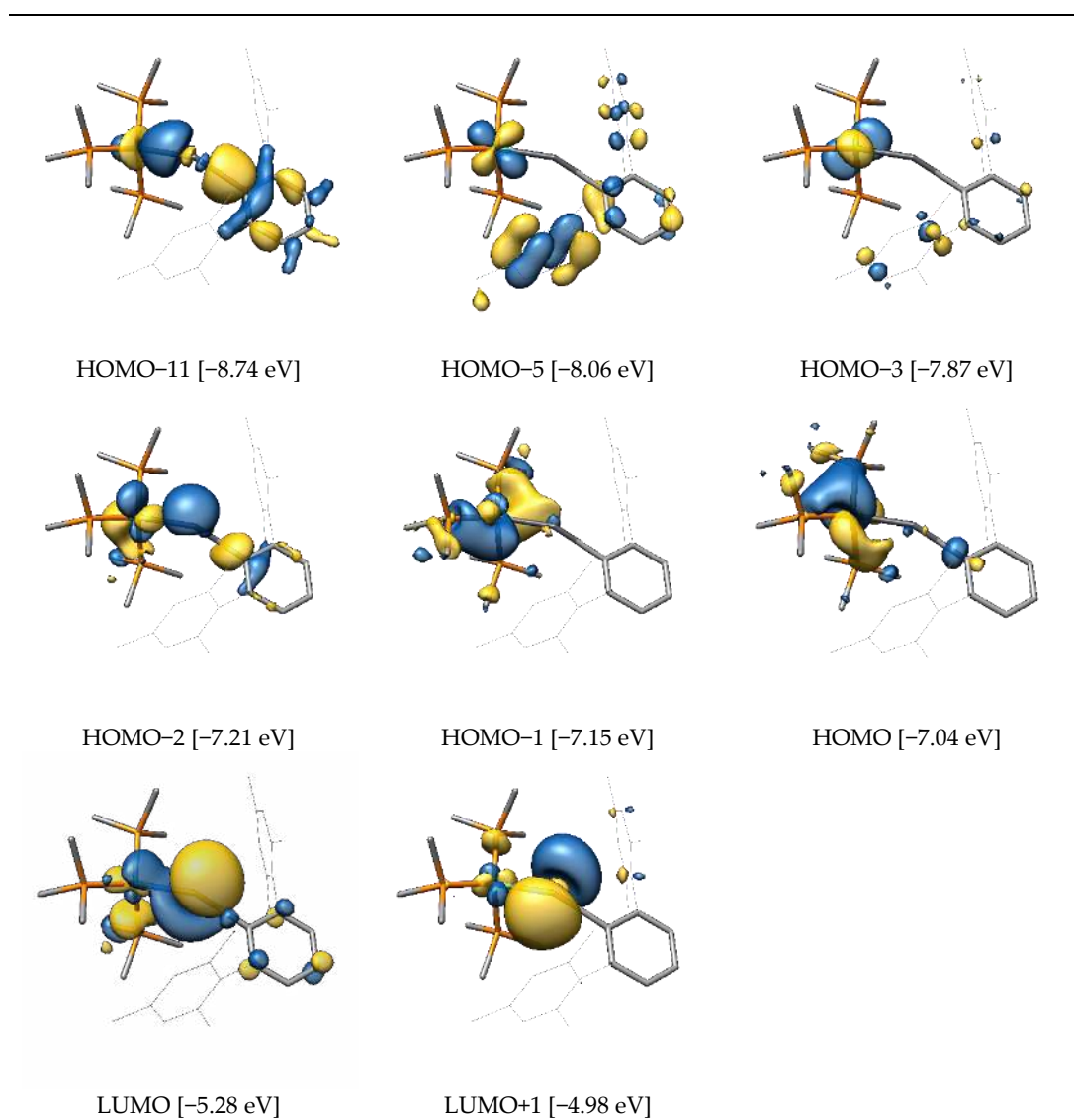


Figure S17. Selected canonical MOs of NiPbAr^{Mes}.

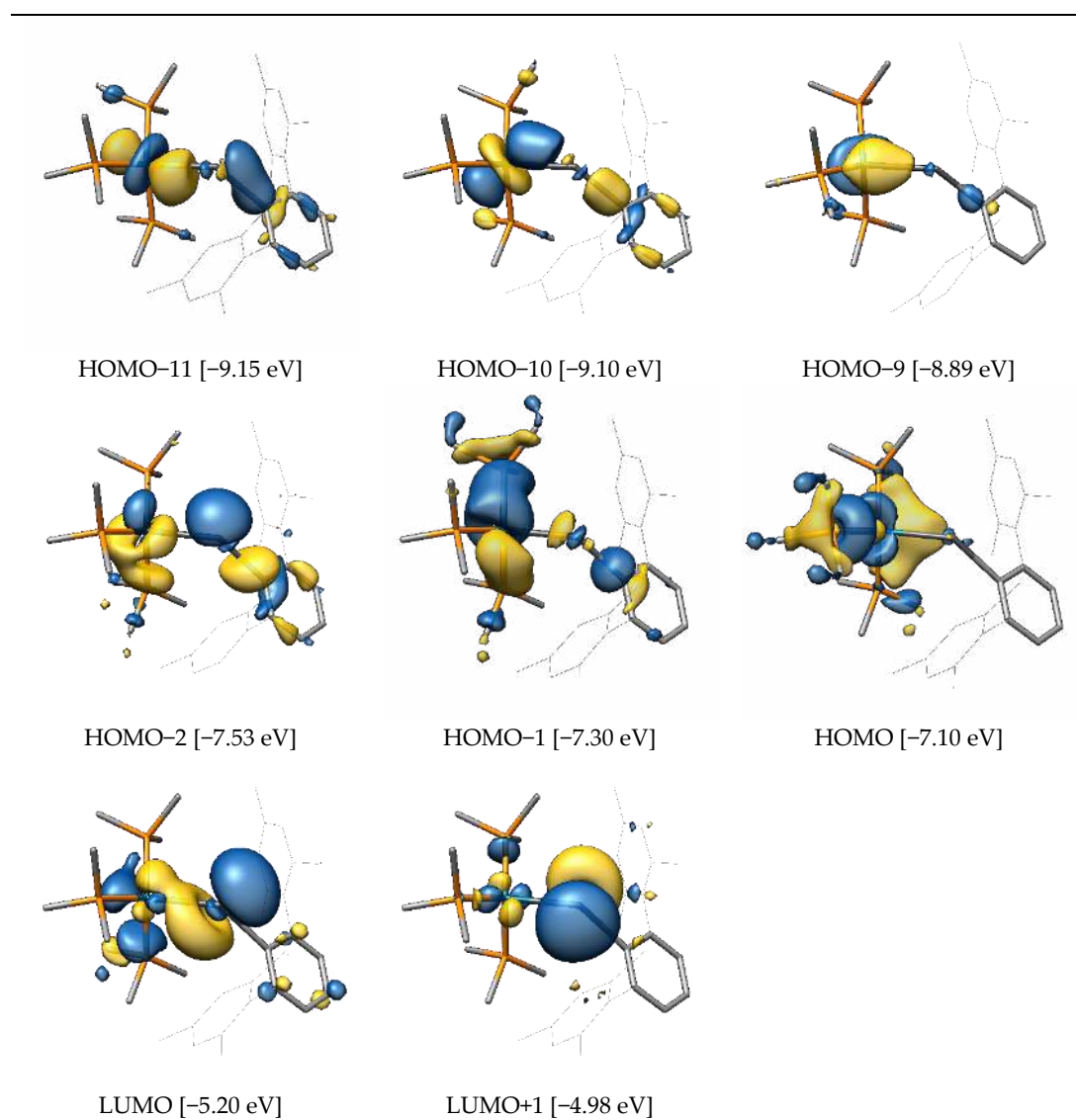


Figure S18. Selected canonical MOs of PdPbAr^{Mes}.

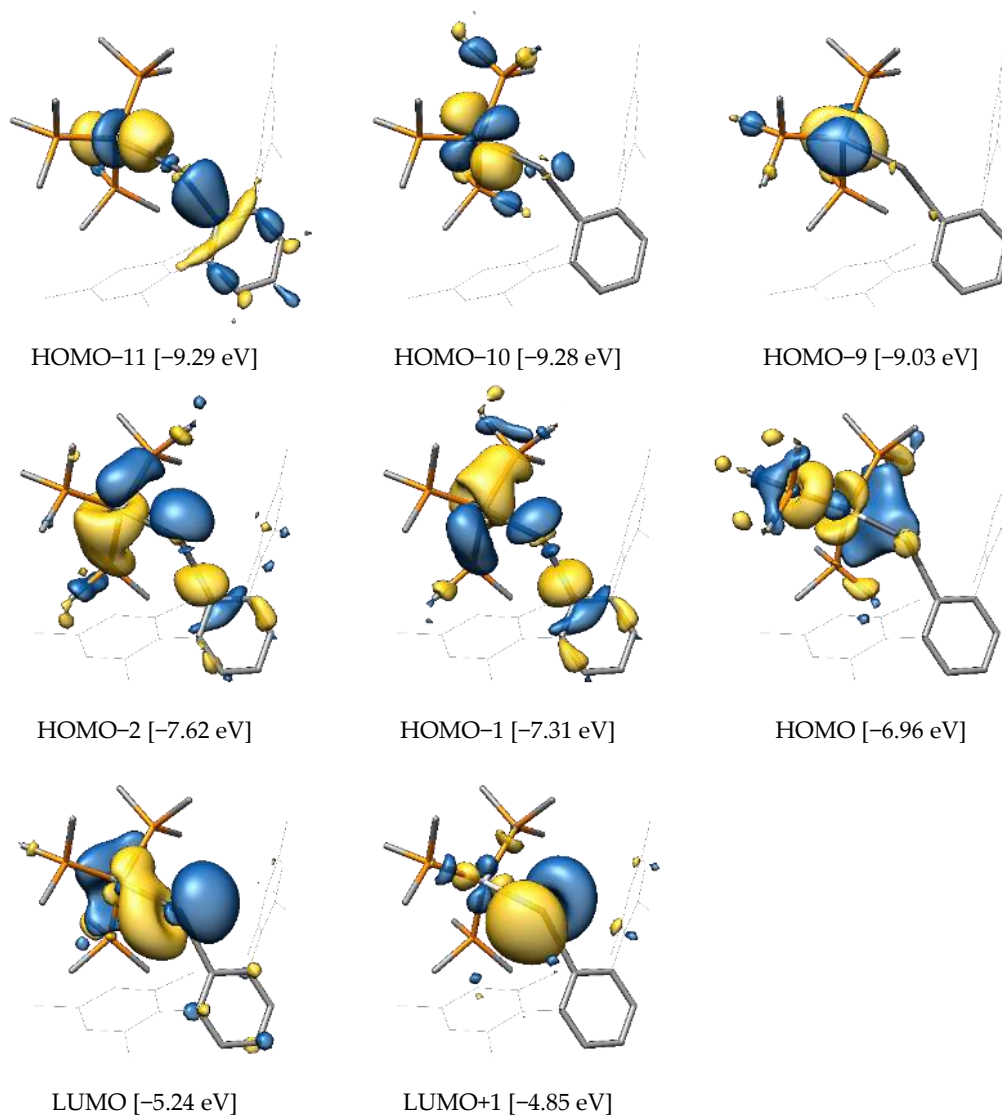


Figure S19. Selected canonical MOs of $\text{PtPbAr}^{\text{Mes}}$.

6) Selected Pipek-Mezey localized MOs of compounds **MER**

In all following figures the isosurface value is set to $0.04 e^{1/2} \text{ Bohr}^{-3/2}$ and hydrogen atoms are omitted for clarity. For each localized MO, the attributed bond type and corresponding atomic Mulliken populations are also given.

The $\sigma(\text{M-P})$, $\sigma(\text{E-C})$ and $\pi(\text{E-C})$ as well as the three lone pair type orbitals $d_1(\text{M})$, $d_2(\text{M})$ and $d_3(\text{M})$ at the metal atom not used for π -bonding are plotted exemplary only for **NiSiTbb** and **PtPbAr^{Mes}** as they look very similar for all compounds, with only the participation of the E atom decreasing in the $\pi(\text{E-C})$ type LMO according to the Mulliken populations.

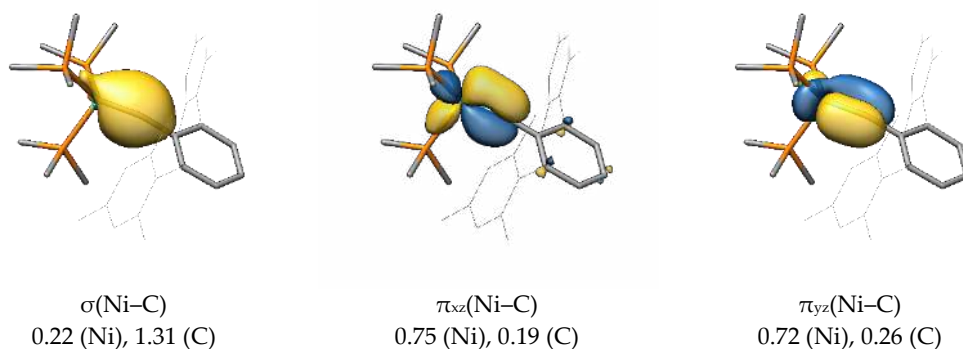


Figure S20. Selected Pipek-Mezey MOs of compound **NiCAr^{Mes}**.

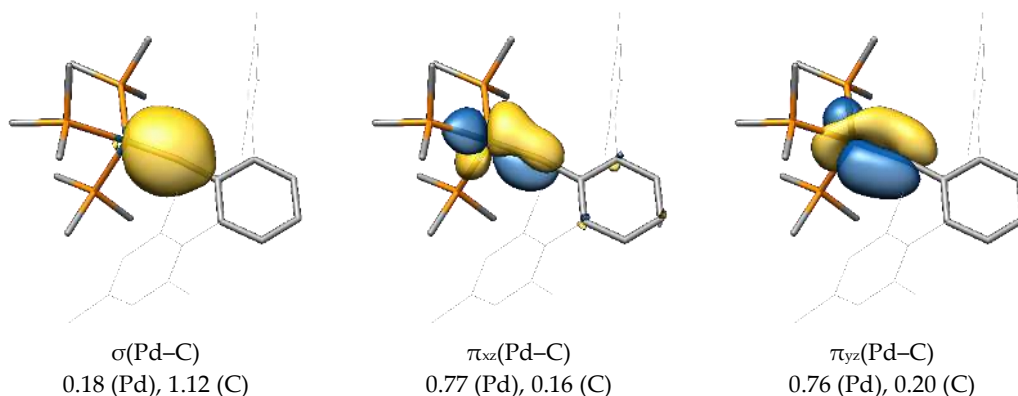


Figure S21. Selected Pipek-Mezey MOs of compound **PdCAr^{Mes}**.

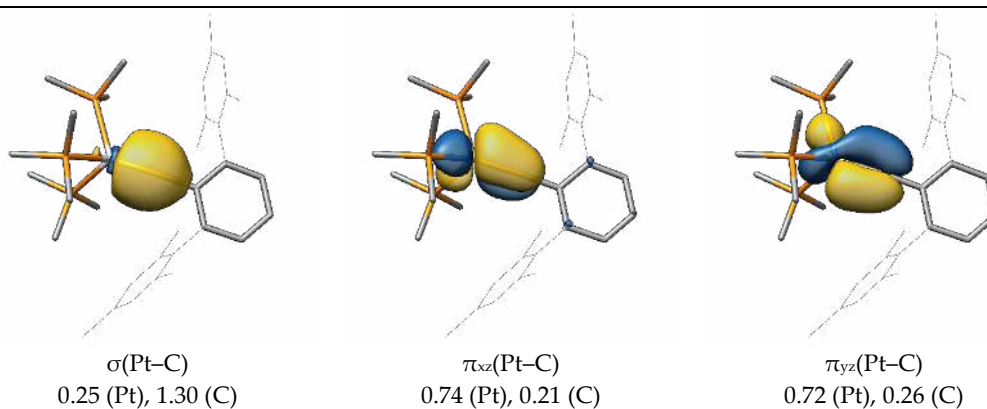


Figure S22. Selected Pipek-Mezey MOs of compound **PtCAr^{Mes}**.

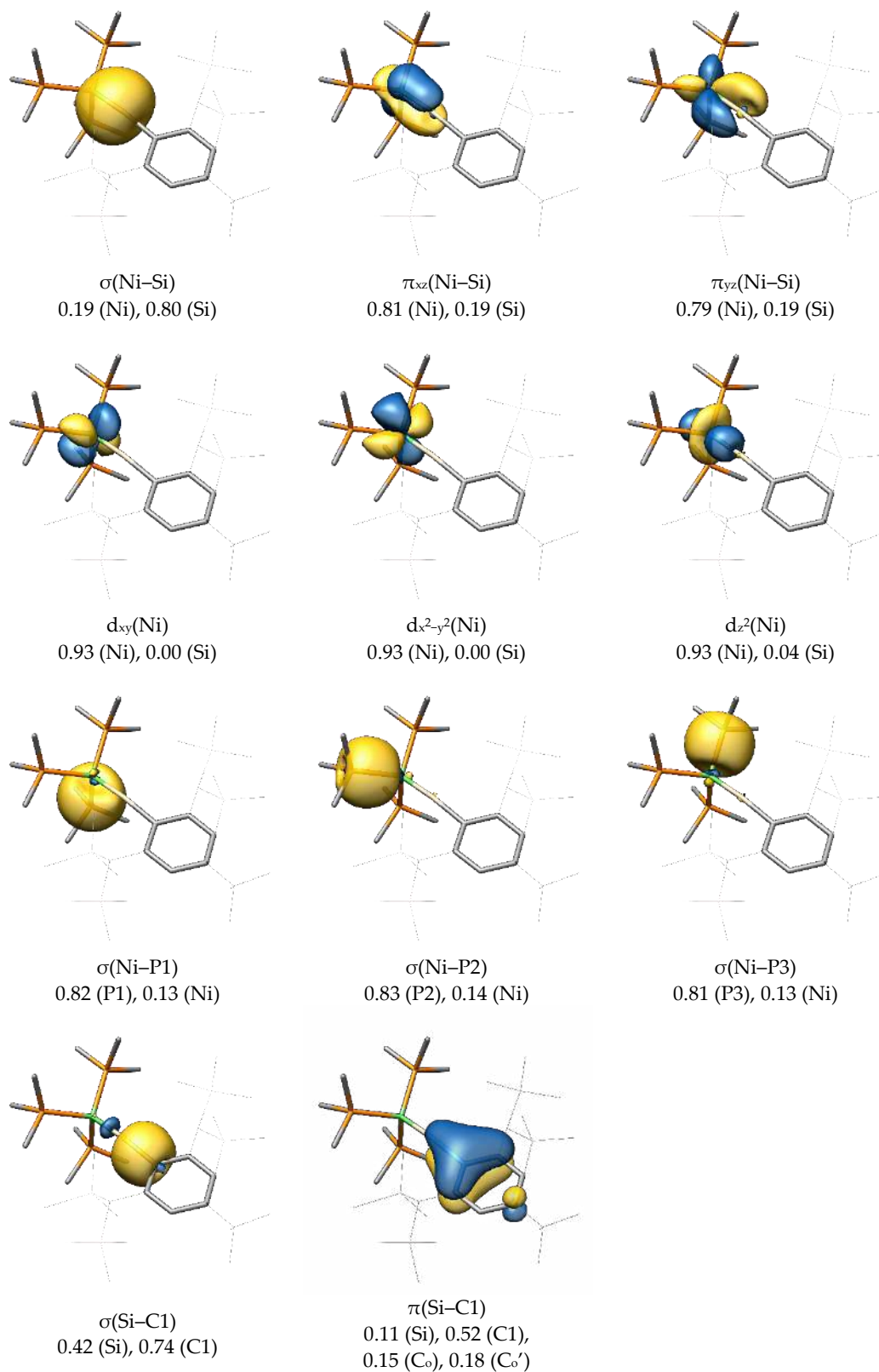


Figure S23. Selected Pipek-Mezey MOs of compound NiSiTbb. C_o = ortho carbon atoms of the phenyl substituent.

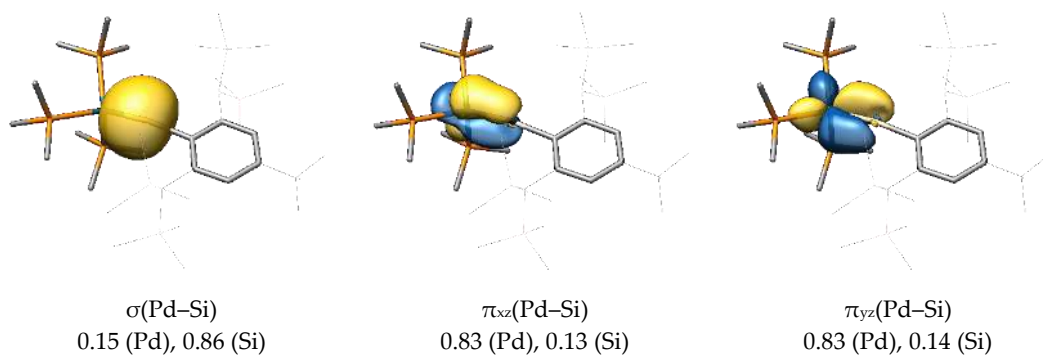


Figure S24. Selected Pipek-Mezey MOs of compound **PdSiTbb**.

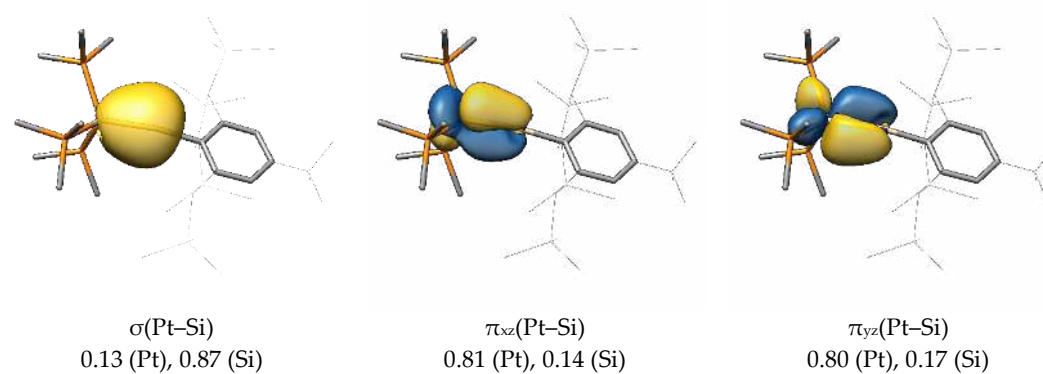


Figure S25. Selected Pipek-Mezey MOs of compound **PtSiTbb**.

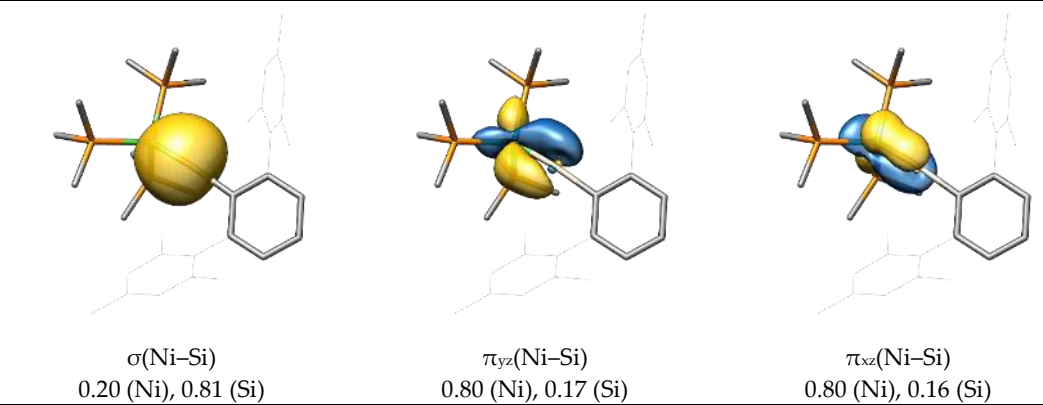


Figure S26. Selected Pipek-Mezey MOs of compound **NiSiAr^{Mes}**.

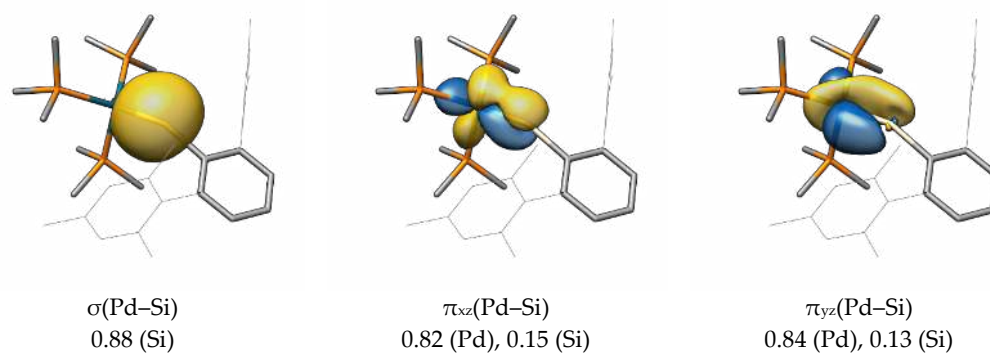


Figure S27. Selected Pipek-Mezey MOs of compound $\text{PdSiAr}^{\text{Mes}}$.

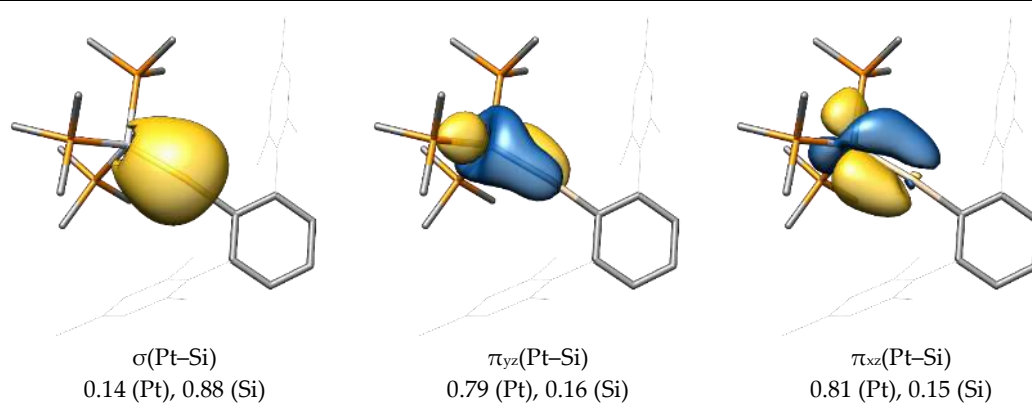


Figure S28. Selected Pipek-Mezey MOs of compound $\text{PtSiAr}^{\text{Mes}}$.

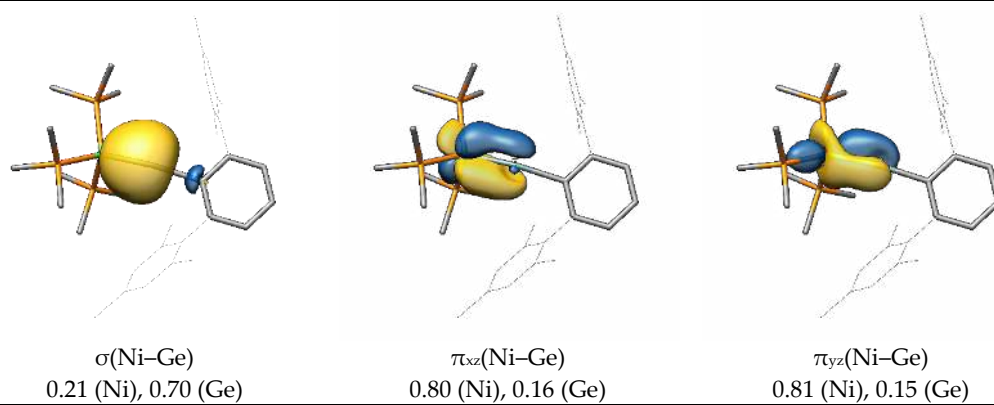


Figure S29. Selected Pipek-Mezey MOs of compound $\text{NiGeAr}^{\text{Mes}}$.

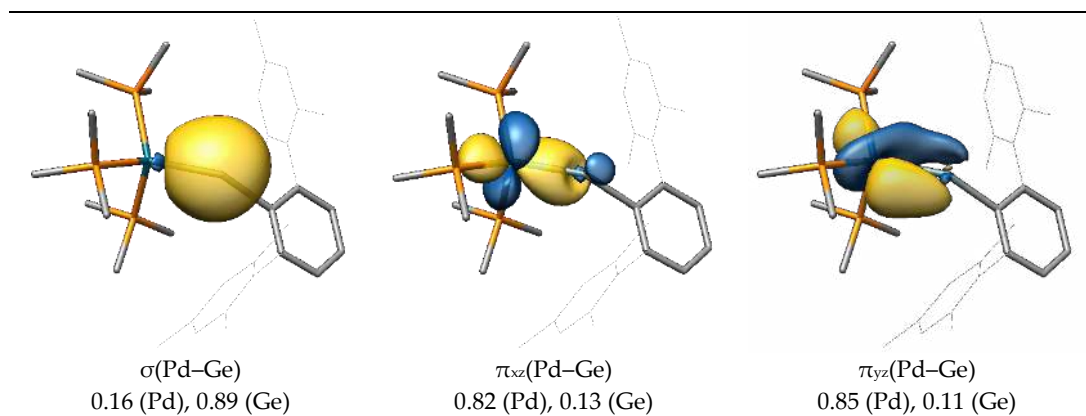


Figure S30. Selected Pipek-Mezey MOs of compound $\text{PdGeAr}^{\text{Mes}}$. Due to the M-E-C bending, the $\pi_{xz}(\text{Pd-Ge})$ orbital appears distorted.

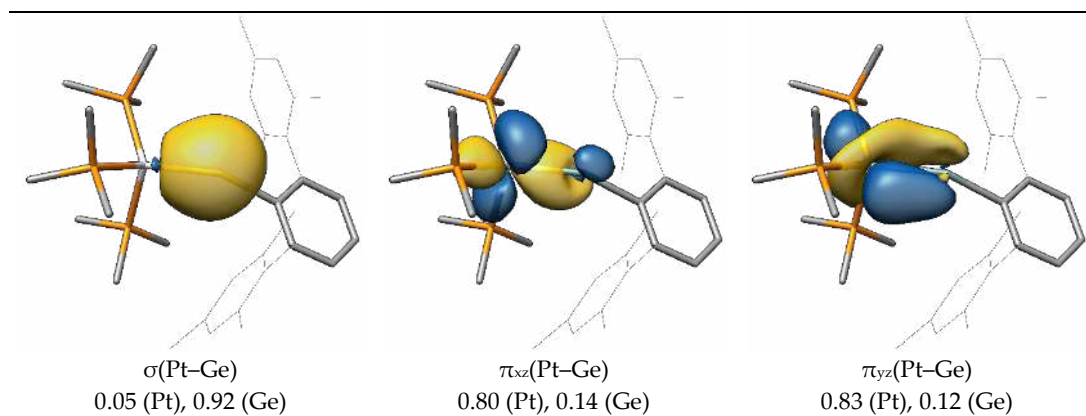


Figure S31. Selected Pipek-Mezey MOs of compound $\text{PtGeAr}^{\text{Mes}}$.

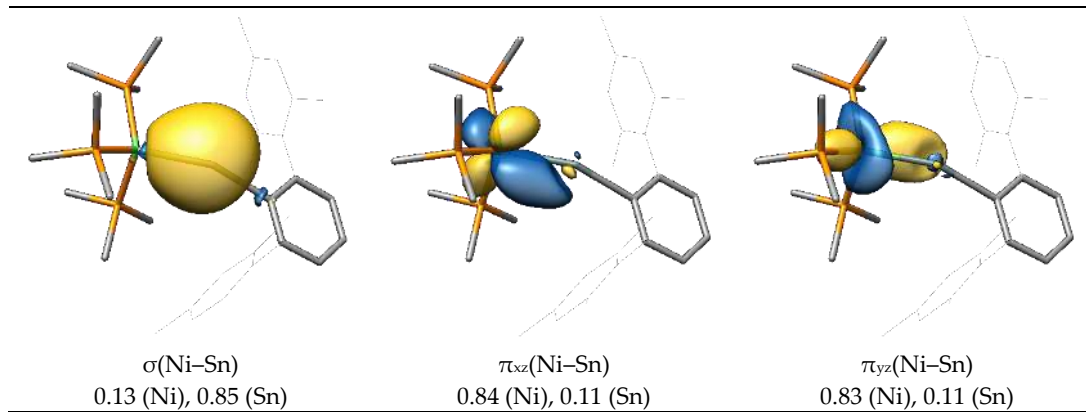


Figure S32. Selected Pipek-Mezey MOs of compound $\text{NiSnAr}^{\text{Mes}}$.

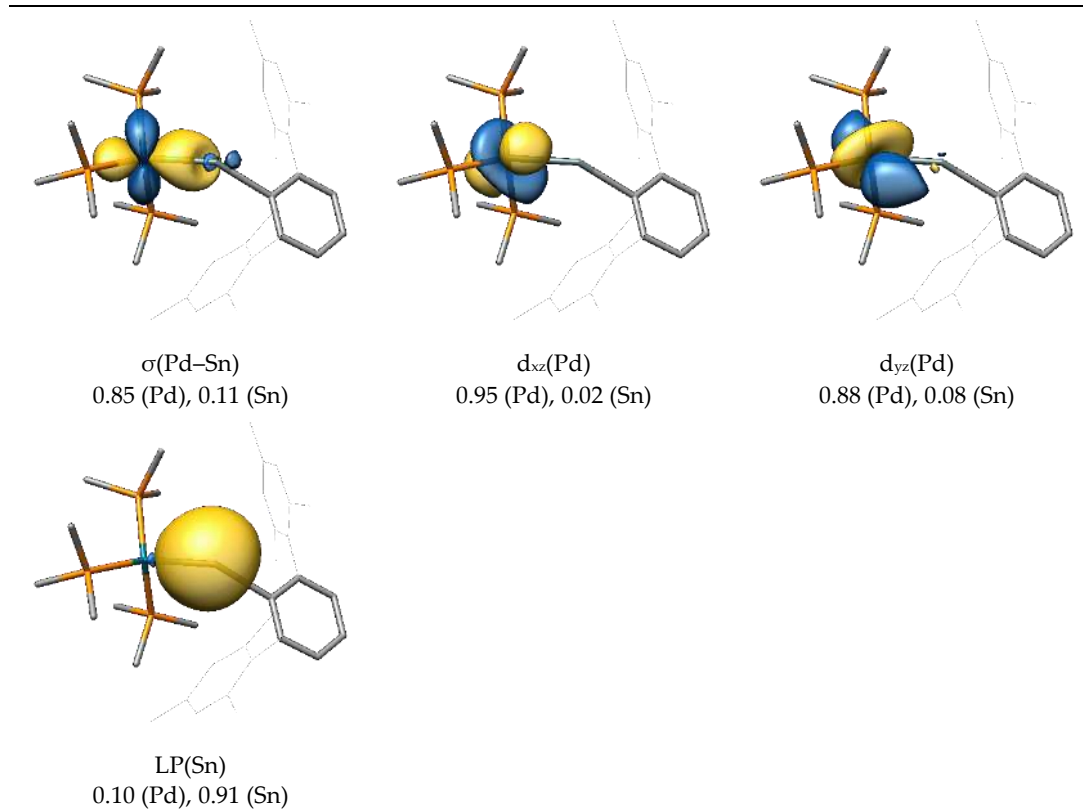


Figure S33. Selected Pipek-Mezey MOs of compound $\text{PdSnAr}^{\text{Mes}}$.

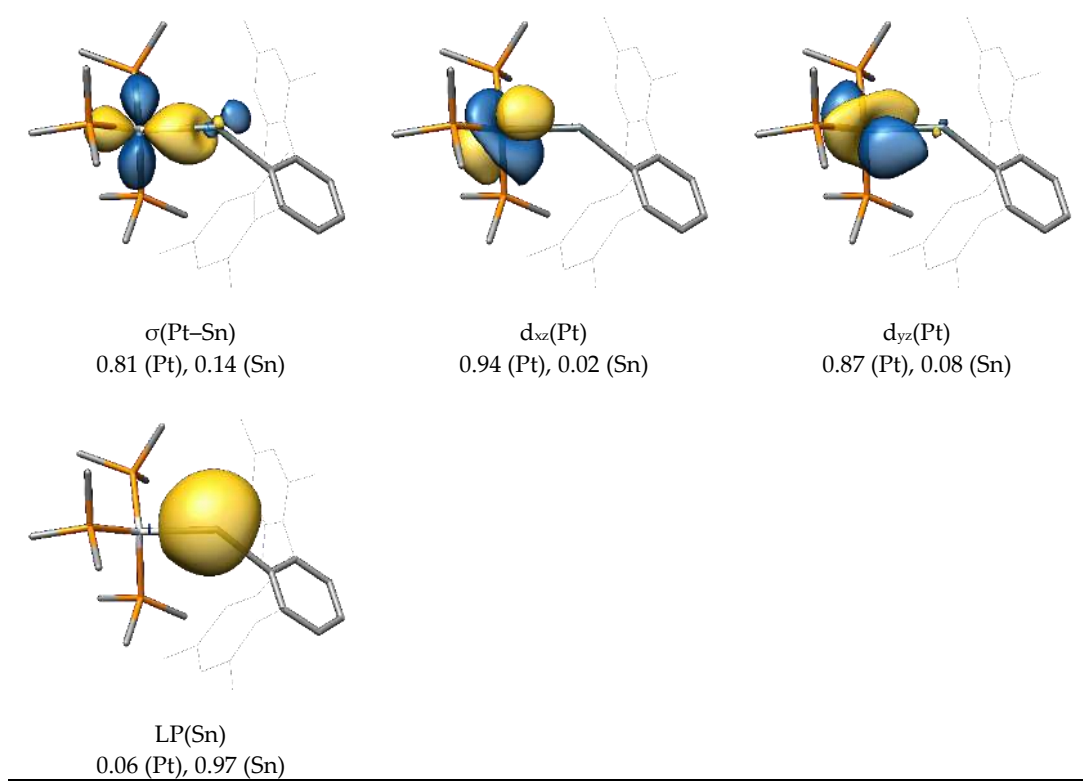


Figure S34. Selected Pipek-Mezey MOs of compound $\text{PtSnAr}^{\text{Mes}}$.

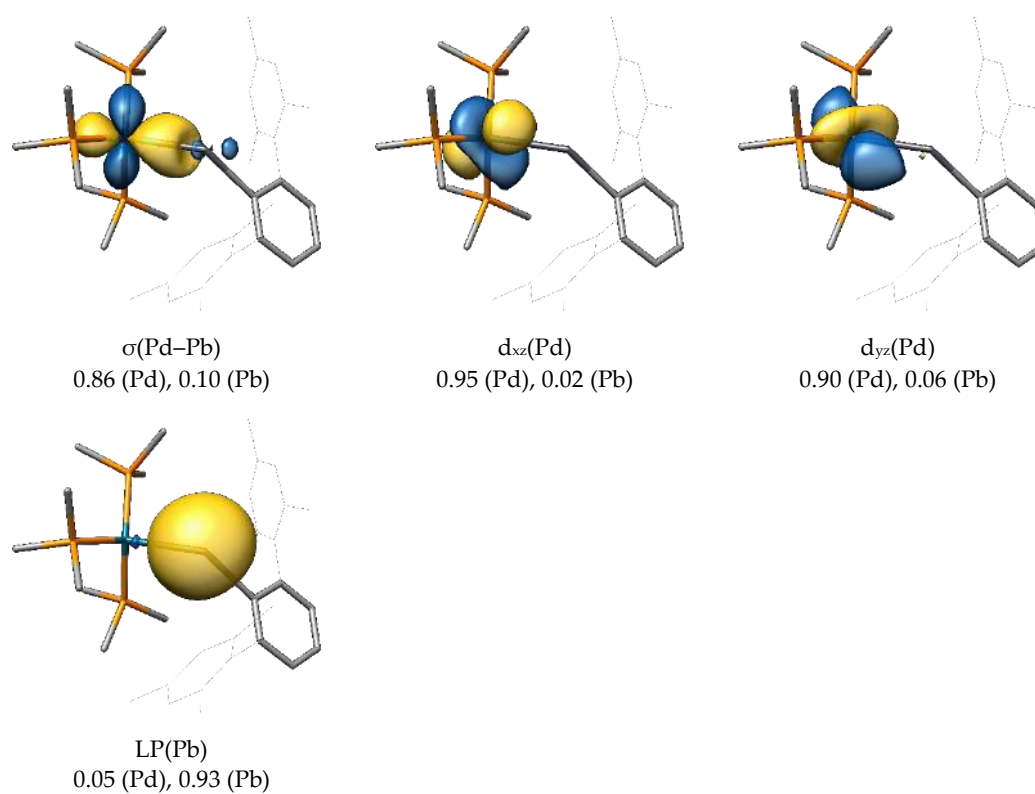
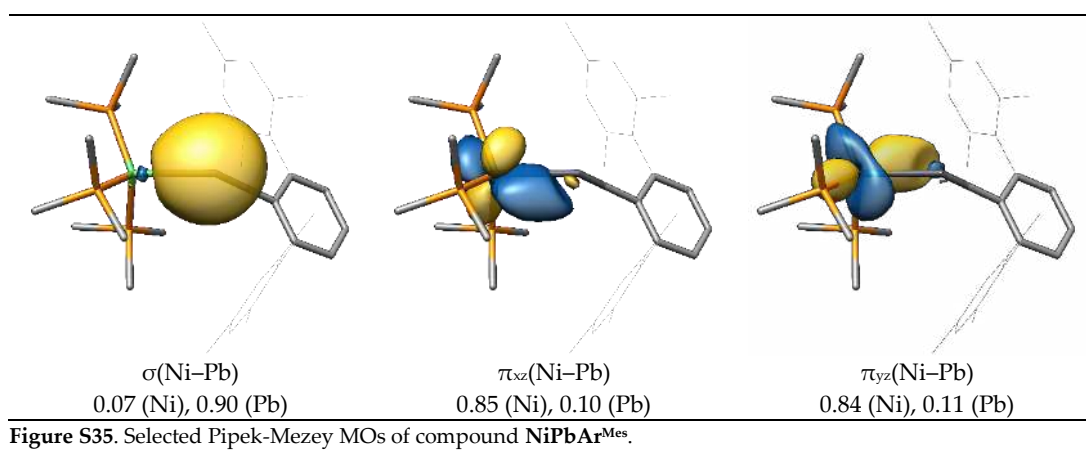


Figure S36. Selected Pipek-Mezey MOs of compound $\text{PdPbAr}^{\text{Mes}}$.

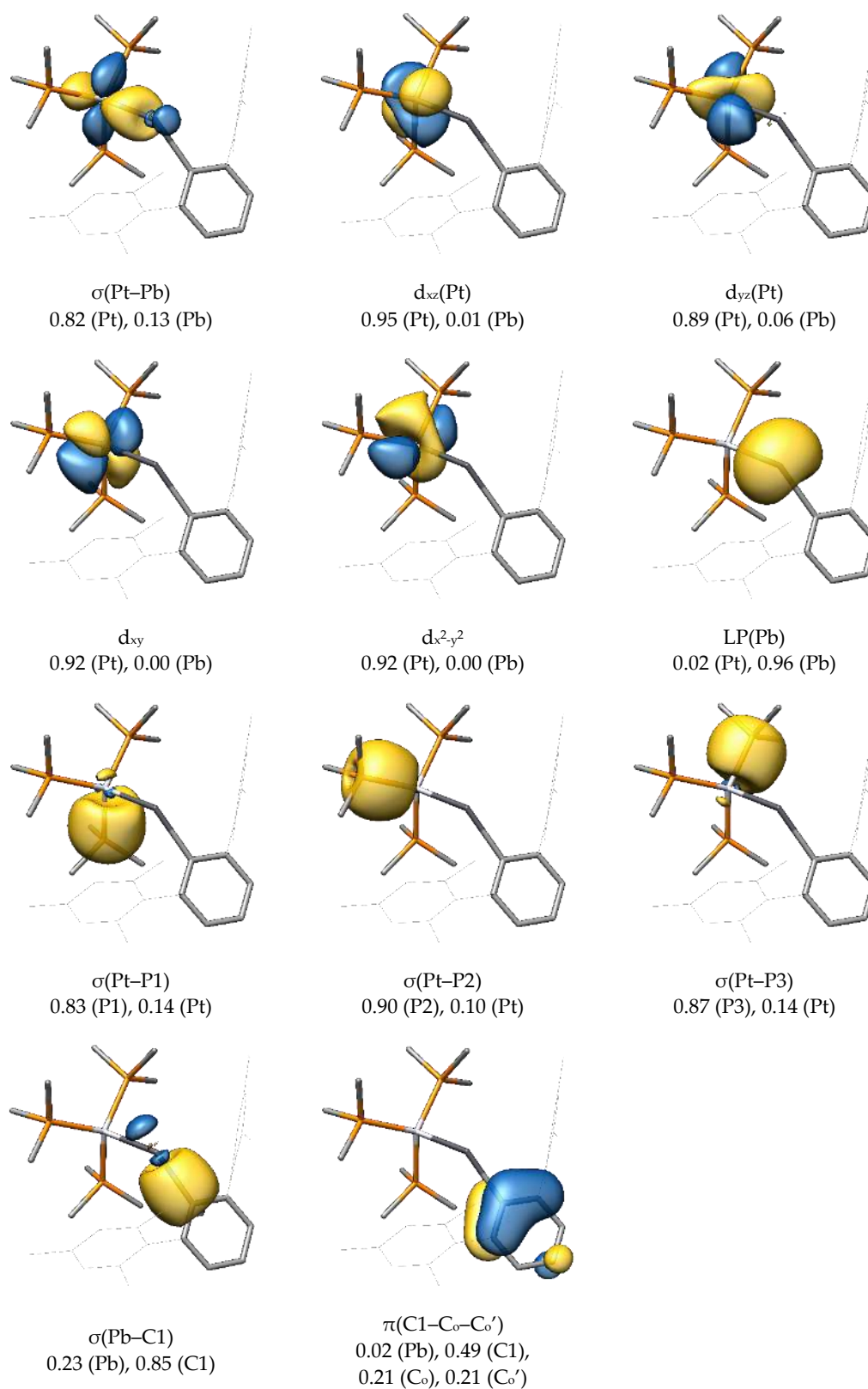


Figure S37. Selected Pipek-Mezey MOs of compound $\text{PtPbAr}^{\text{Mes}}$.

7) Selected canonical and localized MOs of compounds **B-Ge** and **B-Sn**

In the main text, some canonical orbitals of **B-Ge** are already presented (**Figure 7**) and show the bonding (π_{xz}), non-bonding ($\pi^{nb_{xz}}$) and antibonding ($\pi^{*_{xz}}$) combinations of the filled metal d_{xz} , empty tetrel p_x and filled nitrogen p_x orbitals. We searched for the same combinations in the MOs of **B-Sn**, but we were only able to find convincing representations of the $\pi^{nb_{xz}}$ and $\pi^{*_{xz}}$ orbitals (**Figure S38**), with the π_{xz} combination presumably lying very low in energy and further obscured by the enhanced delocalization caused by the PPh_3 ligands.

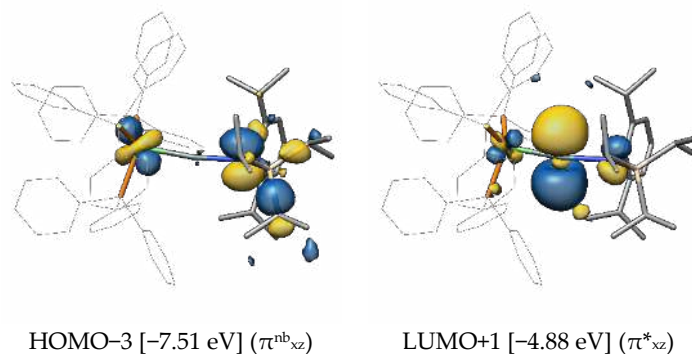


Figure S38. Selected canonical orbitals of **B-Sn**, their respective orbital energies and the type of bond they represent. Hydrogen atoms are omitted for clarity, the isosurface value is set to $0.04 \text{ e}^{1/2} \text{ Bohr}^{-3/2}$. It was not possible to find a convincing orbital combination of the π_{xz} (all-in-phase) bond, although it is assumed to be present by symmetry considerations of the HOMO-3 and LUMO+1.

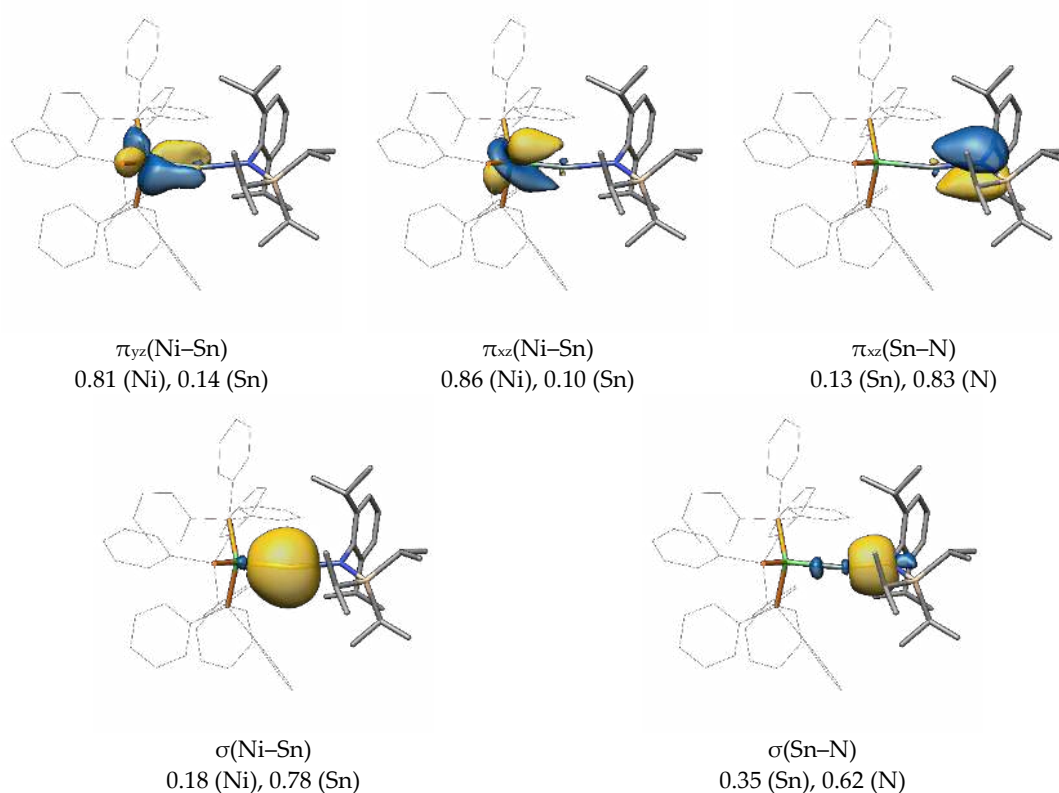


Figure S39. Selected Pipek-Mezey localized molecular orbitals of **B-Sn**, their attributed bond type and corresponding Mulliken populations. Hydrogen atoms are omitted for clarity, the isosurface value is set to $0.04 \text{ e}^{1/2} \text{ Bohr}^{-3/2}$.

However, as for **B-Ge**, the Pipek-Mezey localized MOs reveal the presence of competing $\pi_{xz}(\text{Ni-Sn})$ and $\pi_{xz}(\text{Sn-N})$ bonds (**Figure S39**). Based on the associated Mulliken Populations, the LMOs of **B-Sn** can clearly confirm the picture of a tetrylidyne complex with one $\sigma(\text{Sn}\rightarrow\text{M})$ and two $\pi(\text{M}\rightarrow\text{Sn})$ dative bonds, whose $\text{M}\equiv\text{E}$ bond order is slightly decreased by the competitive $\pi(\text{N}\rightarrow\text{Sn})$ donation.

As mentioned in the main text, we think that the $\pi_{xz}(\text{M-E})$ and $\pi_{yz}(\text{M-E})$ interactions in the canonical HOMO and HOMO-1 are non-bonding interactions. With the same isosurface value as for our own complexes in this study ($0.04 \text{ e}^{1/2} \text{ Bohr}^{-3/2}$), the HOMO-1 of **B-Ge** is mostly metal-centred (**Figure S40 a**), but when the isosurface value is decreased to $0.02 \text{ e}^{1/2} \text{ Bohr}^{-3/2}$, it shows a considerable orbital lobe on the germanium atom, which can be easily misunderstood as bonding interaction. However, by closer inspection of the lobes and comparison with our own complexes (see **Figure S40 c** and also section 5 of the SI), only half of the metal d-orbital can positively interact with the tetrel p-orbital, whereas the other half has a negative interaction being anti-bonding. In total, this leads to a cancellation of both interactions, being non-bonding in total.

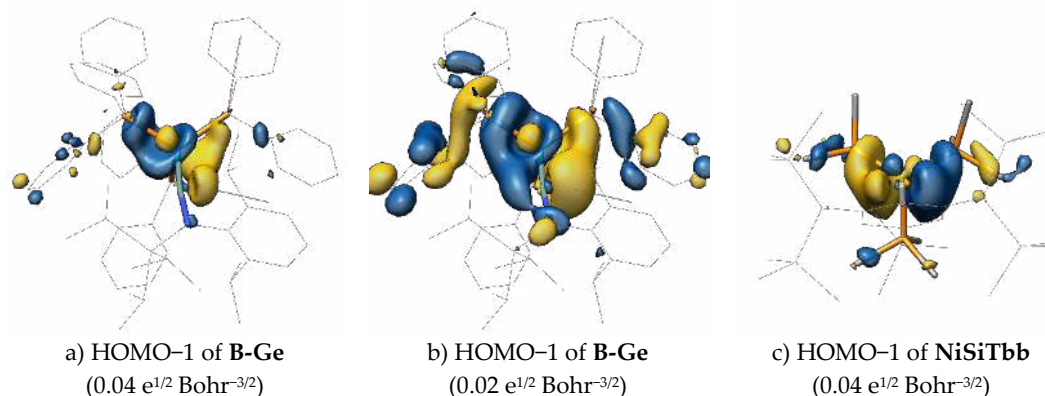


Figure S40. Canonical HOMO-1 of **B-Ge** (a,b) and **NiSiTbb** (c) for comparison with different isosurface values in brackets. The view for a) and b) is slightly above the Ge-Ni bond axis, while for c) it is along the Si-Ni bond axis to highlight the non-bonding nature of this MO. Hydrogen atoms are omitted for clarity.

8) Spin-spin excitation energies for the fragments of compounds **MER**

Table S6. Electronic singlet-triplet $\Delta E_{\text{el}}(\text{s}\rightarrow\text{t})$ and doublet-quartet $\Delta E_{\text{el}}(\text{d}\rightarrow\text{q})$ excitation energies for the structurally relaxed fragments of **MER** in $\text{kJ}\cdot\text{mol}^{-1}$.

fragment	Level of theory I		Level of theory II	
	$\Delta E_{\text{el}}(\text{s}\rightarrow\text{t})$	$\Delta E_{\text{el}}(\text{d}\rightarrow\text{q})$	$\Delta E_{\text{el}}(\text{s}\rightarrow\text{t})$	$\Delta E_{\text{el}}(\text{d}\rightarrow\text{q})$
$[\text{Ni}(\text{PMe}_3)_3]^{0/+}$	191.4	232.5	209.3	241.8
$[\text{Pd}(\text{PMe}_3)_3]^{0/+}$	214.3	284.0	218.4	297.7
$[\text{Pt}(\text{PMe}_3)_3]^{0/+}$	195.3	260.5	198.9	269.0
$\text{CArMes}^{+/0}$	-31.6	120.3	-33.2	137.6
$\text{SiTbb}^{+/0}$	140.8	175.6	170.1	200.8
$\text{SiAr}^{\text{Mes}/0}$	158.9	191.9	191.1	216.8
$\text{GeAr}^{\text{Mes}/0}$	164.8	209.2	-a)	230.0
$\text{SnAr}^{\text{Mes}/0}$	174.7	212.1	-a)	228.1
$\text{PbAr}^{\text{Mes}/0}$	173.2	218.7	197.7	233.8

a) No SCF convergence could be achieved for the triplet state.

9) BCEs and BDEs of MSiAr^{Mes}**Table S7.** Calculated BCEs and BDEs in kJ·mol⁻¹ on the level of theory **II** of the M–E bonds of the [L₃MER]⁺ complexes leading to the ML₃ + ER⁺ and ML₃⁺ + ER fragment combinations. BCEs and BDEs of the energetically favourable fragmentation scheme are highlighted bold.

compound	BCE		BDE	
	ML ₃ + ER ⁺	ML ₃ ⁺ + ER	ML ₃ + ER ⁺	ML ₃ ⁺ + ER
NiSiAr ^{Mes}	491.5	421.4	392.3	368.9
PdSiAr ^{Mes}	427.4	387.9	322.5	295.3
PtSiAr ^{Mes}	520.3	450.2	362.1	324.1

10) Thermodynamically corrected BDEs

The given thermodynamic parameters are defined as follows:

- a. E_{el} – The electronic energy is defined as the sum of the components of the single point energy, resulting from the application of the Hamiltonian H to the N -electron wavefunction Ψ . This consists of the kinetic energy T , attraction between the nuclei and electrons E_{ne} , the electron-electron repulsion E_{ee} , the nuclear repulsion E_{nn} and other correcting terms like Grimme's correction for London dispersion forces E_{disp} and its three-body correction E_{ATM} :

$$H\Psi = E_{el}\Psi = (T + E_{ne} + E_{ee} + E_{nn} + E_{disp} + E_{ATM})\Psi.$$

- b. BCE – The bond cleavage energy is defined as the difference of the electronic energies E_{el} of two structurally unrelaxed fragments (A and B) and the unfragmented compound (AB). Herein the total spin of the two fragments must be equal to the spin of the molecule AB:

$$BCE = E_{el}(A) + E_{el}(B) - E_{el}(AB).$$

- c. ΔE_{relax} – The structural relaxation energy is the energy difference between the electronic energies of the structurally unrelaxed (X) and relaxed fragment (X*):

$$\Delta E_{relax}(X) = E_{el}(X) - E_{el}(X^*).$$

- d. BDE – The bond dissociation energy is the difference between the BCE and structural relaxation energies of the fragments:

$$BDE = BCE - \Delta E_{relax}(A) - \Delta E_{relax}(B).$$

- e. $U(0\text{ K})$ – The inner energy at 0 K is the sum of the electronic energy and the zero point vibrational energy E_{ZPVE} :

$$U(0\text{ K}) = E_{el} + E_{ZPVE}.$$

- f. U° – The inner energy at standard ambient conditions ($T = 298.15\text{ K}$, $p = 100.000\text{ kPa}$) additionally takes the temperature dependent vibrational (E_{vib}), rotational (E_{rot}) and translational (E_{trans}) terms into account:

$$U^\circ = E_{el} + E_{ZPVE} + E_{vib} + E_{rot} + E_{trans}.$$

g. H° – The enthalpy at standard ambient conditions is then given as:

$$H^\circ = U^\circ + k_B T.$$

h. S° – The entropy is made up of electronic (S_{el}), vibrational (S_{vib}), rotational (S_{rot}) and translational (S_{trans}) contributions:

$$S^\circ = S_{el} + S_{vib} + S_{rot} + S_{trans}.$$

i. G° – The Gibbs free energy is given as:

$$G = H - TS.$$

Table S8. Energies in $\text{kJ}\cdot\text{mol}^{-1}$ for the dissociation of the M–E bonds of the $[\text{L}_3\text{MER}]^+$ complexes into the $\text{ML}_3 + \text{ER}^+$ fragments obtained on the level of theory II. Entropies are given in $\text{J}\cdot\text{mol}^{-1}\cdot\text{K}^{-1}$. Thermodynamic corrections to the electronic energies are calculated on the level of theory I.

compound	BCE	$\Delta E_{\text{relax}}(\text{ML}_3)$	$\Delta E_{\text{relax}}(\text{ER}^+)$	BDE	$\Delta U(0\text{ K})$	ΔU°	ΔH°	ΔS°	ΔG°
NiCArMes	718.6	104.0	92.8	521.8	507.5	504.3	506.8	238.5	435.7
NiSiTbb	470.4	52.7	15.2	402.5	383.3	383.1	385.5	263.3	307.0
NiSiArMes	491.5	54.7	44.5	392.3	381.6	381.0	383.4	246.5	310.0
NiGeArMes	459.3	52.7	41.6	365.0	354.1	351.2	353.7	229.6	285.2
NiSnArMes	383.9	36.7	30.4	316.9	306.4	303.4	305.8	233.6	236.2
NiPbArMes	342.7	27.9	23.0	291.7	281.7	278.4	280.9	235.6	210.7
PdCArMes	625.1	133.6	87.3	404.2	391.9	386.0	388.5	221.2	322.6
PdSiTbb	415.3	69.1	13.2	333.0	316.9	315.4	317.9	255.5	241.7
PdSiArMes	427.4	65.4	39.5	322.5	312.6	309.6	312.1	234.9	242.1
PdGeArMes	383.2	54.3	39.5	289.4	278.8	276.5	278.9	244.4	206.1
PdSnArMes	321.9	34.6	33.7	253.6	242.7	240.4	242.9	247.1	169.2
PdPbArMes	293.3	26.3	26.6	240.4	229.8	227.2	229.6	243.7	157.0
PtCArMes	799.3	224.3	89.0	486.0	471.9	466.5	468.9	225.6	401.7
PtSiTbb	504.0	116.9	13.5	373.5	357.1	355.3	357.8	251.4	282.8
PtSiArMes	520.3	117.6	40.6	362.1	351.9	348.7	351.2	224.8	284.2
PtGeArMes	444.0	89.6	39.8	314.5	303.0	301.0	303.5	248.0	229.5
PtSnArMes	354.6	44.0	36.5	274.1	263.5	260.9	263.4	242.7	191.0
PtPbArMes	313.5	33.9	28.5	251.1	238.7	237.1	239.6	256.1	163.2

Table S9. Energies in $\text{kJ}\cdot\text{mol}^{-1}$ for the dissociation of the M–E bonds of the $[\text{L}_3\text{MER}]^+$ complexes into the $\text{ML}_3^+ + \text{ER}$ fragments obtained on the level of theory **II**. Entropies are given in $\text{J}\cdot\text{mol}^{-1}\cdot\text{K}^{-1}$. Thermodynamic corrections to the electronic energies are calculated on level of theory **I**.

compound	<i>BCE</i>	$\Delta E_{\text{relax}}(\text{ML}_3^+)$	$\Delta E_{\text{relax}}(\text{ER})$	<i>BDE</i>	$\Delta U(0\text{ K})$	ΔU°	ΔH°	ΔS°	ΔG°
NiCAr^{Mes}	544.3	69.7	12.9	461.6	442.1	443.9	446.3	283.5	361.8
NiSiTbb	427.9	42.8	7.5	377.5	364.2	363.7	366.2	269.1	286.0
NiSiAr^{Mes}	421.4	42.0	10.4	368.9	359.2	360.0	362.5	269.2	282.2
NiGeAr^{Mes}	387.7	40.4	7.3	340.0	330.0	328.7	331.1	255.6	254.9
NiSnAr^{Mes}	346.0	33.7	7.9	304.5	295.7	294.1	296.6	256.2	220.1
NiPbAr^{Mes}	328.6	32.0	11.0	285.6	279.0	276.0	278.4	246.5	204.9
PdCAr^{Mes}	469.7	122.0	7.5	340.1	323.8	321.7	324.2	251.4	249.2
PdSiTbb	395.0	84.1	6.8	304.1	295.0	292.2	294.7	246.5	221.2
PdSiAr^{Mes}	387.9	79.7	12.9	295.3	287.4	284.8	287.2	242.9	214.8
PdGeAr^{Mes}	349.2	73.5	15.2	260.5	251.9	250.1	252.5	255.7	176.3
PdSnAr^{Mes}	319.5	64.0	18.1	237.3	229.3	227.3	229.8	255.0	153.8
PdPbAr^{Mes}	309.0	59.3	19.3	230.4	224.3	220.8	223.3	239.8	151.8
PtCAr^{Mes}	618.3	200.3	6.8	411.3	393.2	391.6	394.1	259.0	316.9
PtSiTbb	462.5	123.8	4.7	334.0	324.6	321.6	324.1	245.7	250.8
PtSiAr^{Mes}	450.2	119.4	6.6	324.1	316.1	313.4	315.9	236.0	245.5
PtGeAr^{Mes}	386.3	99.9	11.5	274.9	265.5	264.1	266.5	262.5	188.3
PtSnAr^{Mes}	332.6	66.0	19.4	247.2	239.4	237.3	239.7	253.8	164.1
PtPbAr^{Mes}	307.8	57.4	19.9	230.5	222.6	220.2	222.7	255.4	146.5

11) EDA components of the interaction energy of MER

Table S10. Detailed results of the EDA of the MER compounds. Energies are given in $\text{kJ}\cdot\text{mol}^{-1}$.

compound	ΔE_{orb}	ΔE_{Pauli}	ΔE_{elstat}	ΔE_{disp}	ΔE_{int}
NiCAr^{Mes}	-645.3	1076.6	-820.6	-138.3	-527.5
NiSiTbb	-498.1	699.7	-528.8	-131.0	-458.2
NiSiAr^{Mes}	-486.2	815.4	-591.5	-131.4	-393.6
NiGeAr^{Mes}	-443.5	683.7	-482.6	-120.8	-363.3
NiSnAr^{Mes}	-372.7	521.9	-399.7	-117.7	-368.2
NiPbAr^{Mes}	-331.9	495.9	-368.8	-126.1	-330.9
PdCAr^{Mes}	-671.7	1244.0	-915.6	-126.1	-469.7
PdSiTbb	-472.0	857.3	-674.5	-116.3	-405.5
PdSiAr^{Mes}	-494.5	999.6	-755.8	-127.0	-377.7
PdGeAr^{Mes}	-426.8	688.9	-515.6	-125.1	-378.5
PdSnAr^{Mes}	-334.8	566.5	-430.7	-124.4	-312.5
PdPbAr^{Mes}	-291.1	499.0	-371.0	-130.4	-293.5
PtCAr^{Mes}	-903.3	1674.8	-1247.3	-132.1	-607.8
PtSiTbb	-585.8	1077.6	-863.1	-118.9	-490.3
PtSiAr^{Mes}	-573.8	1192.5	-929.4	-124.8	-435.5
PtGeAr^{Mes}	-499.1	1009.9	-762.2	-124.6	-376.0
PtSnAr^{Mes}	-380.4	668.3	-507.0	-132.5	-351.6
PtPbAr^{Mes}	-319.6	559.1	-417.7	-136.7	-314.9

12) ETS-NOCV deformation densities of compounds **MER**

Isosurface plots (isosurface value = 0.002 e Bohr⁻³) of deformation densities ($\Delta\rho_n$) in e Bohr⁻³ of complementary NOCVs (ψ_{-n} and ψ_{+n}), split into α - and β -spin derived deformation densities when required, given with their respective eigenvalues (v_{-n} and v_{+n}). Regions of charge depletion ($\Delta\rho_n < 0$ e Bohr⁻³) are shown in red and regions of charge accumulation ($\Delta\rho_n > 0$ e Bohr⁻³) in grey. Level of theory: B97-D3(BJ)/TZ2P//I.

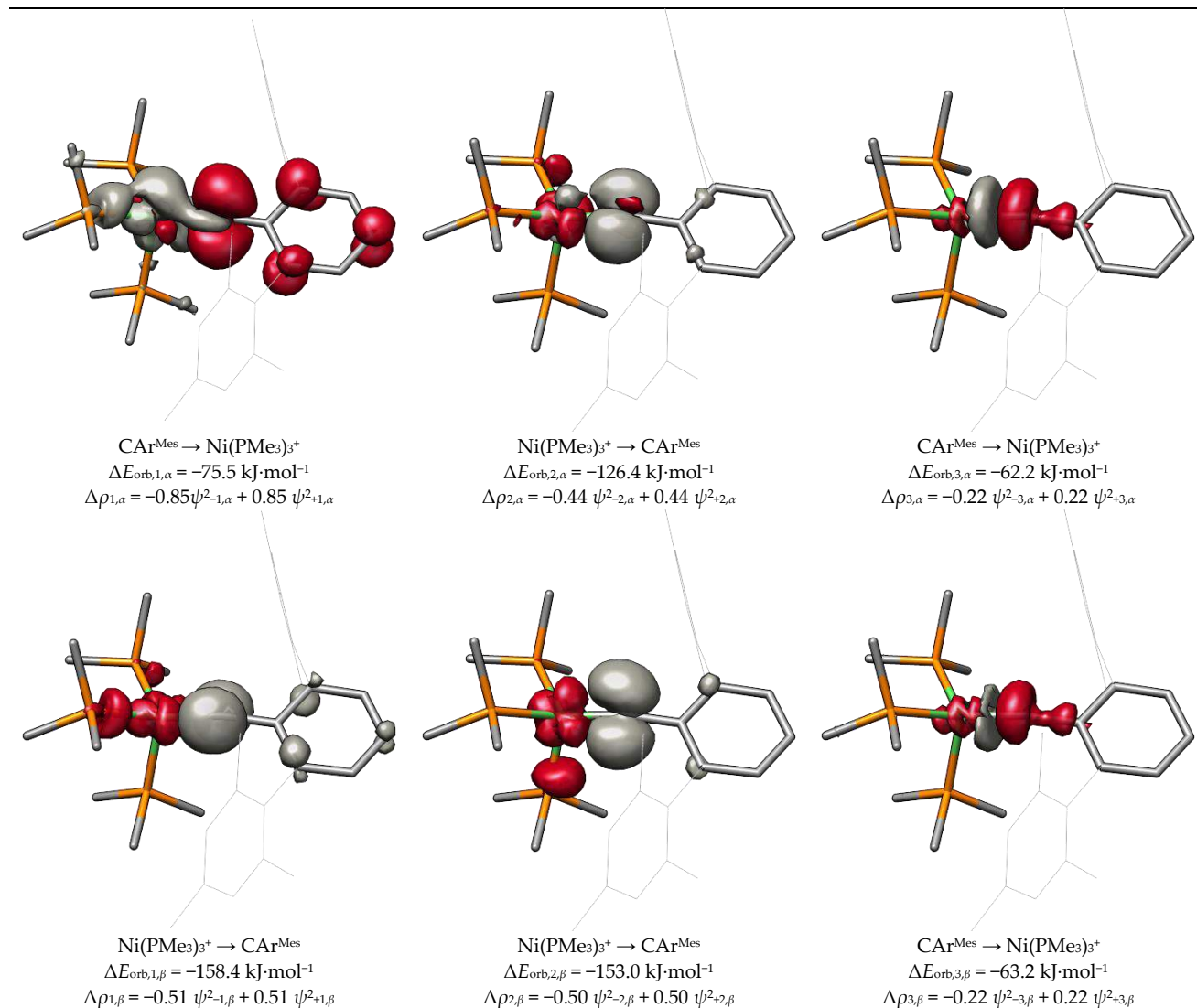


Figure S41. Deformation densities of $\text{NiCar}^{\text{Mes}}$.

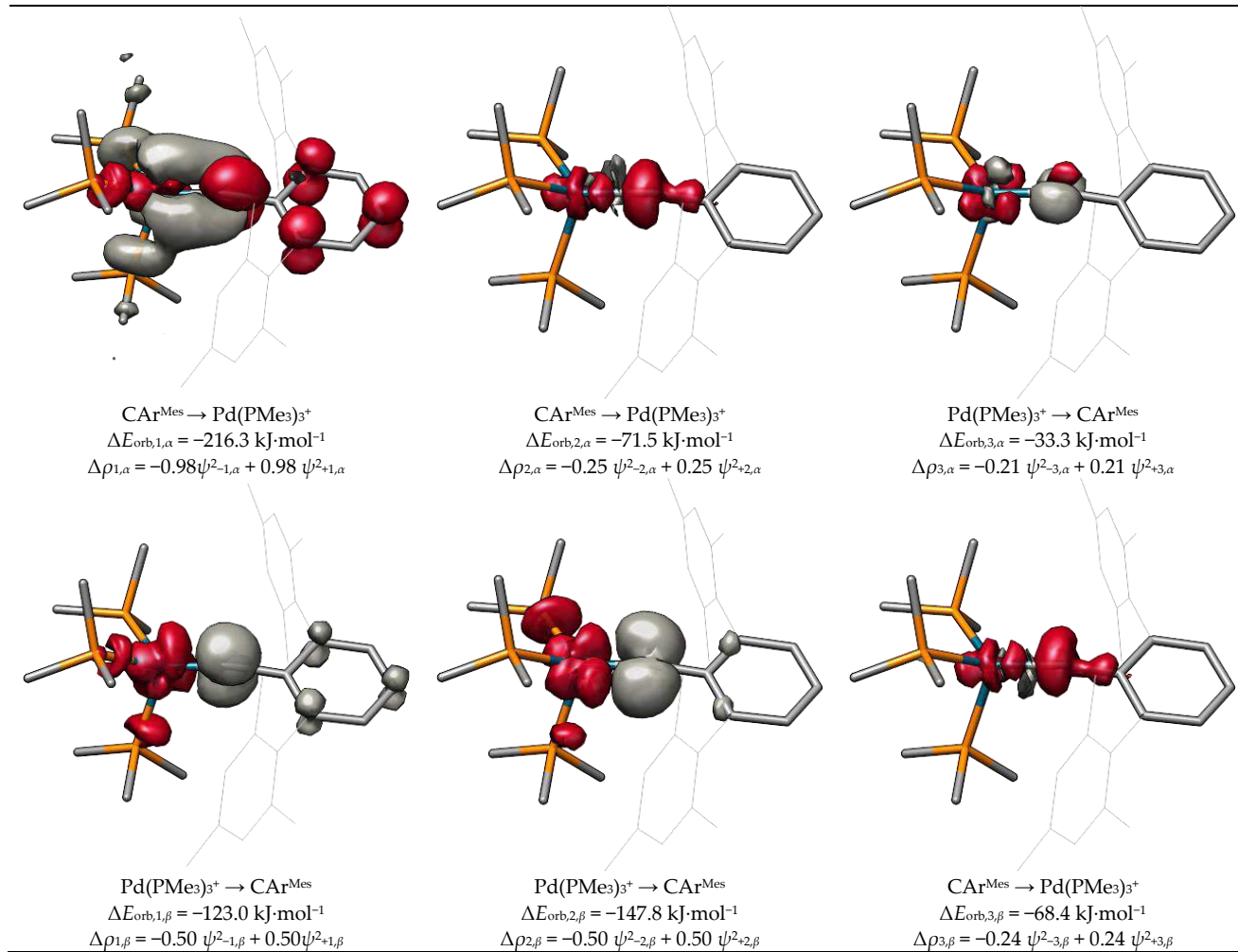


Figure S42. Deformation densities of PdCAr^{Mes}.

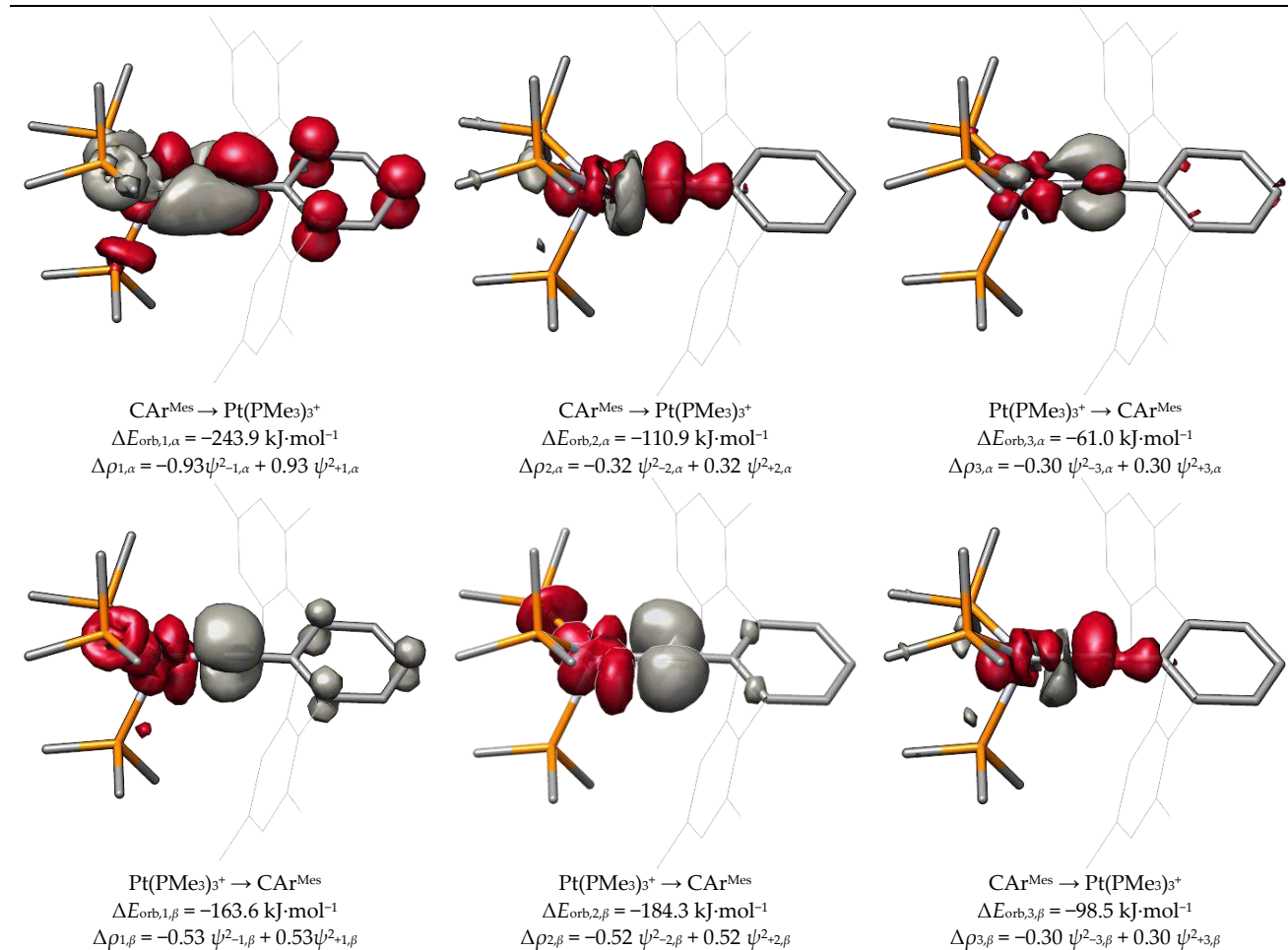


Figure S43. Deformation densities of $\text{PtCar}^{\text{Mes}}$.

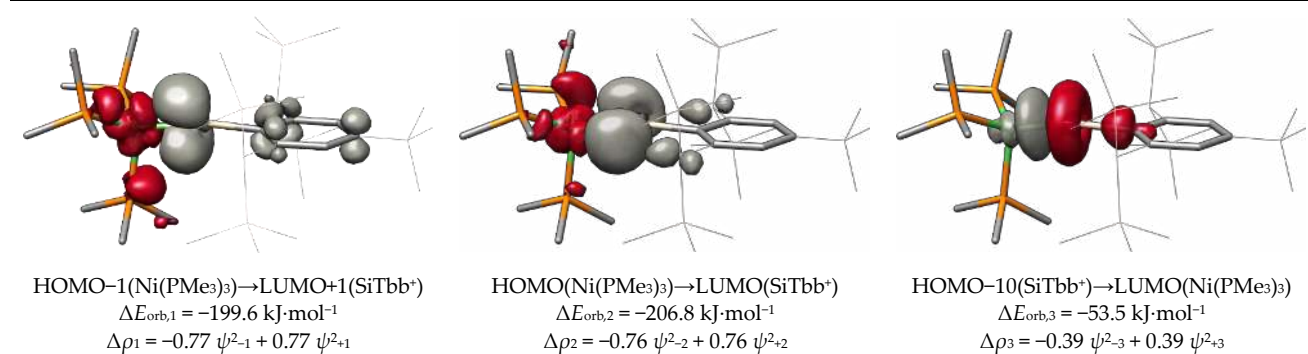


Figure S44. Deformation densities of NiSiTbb .

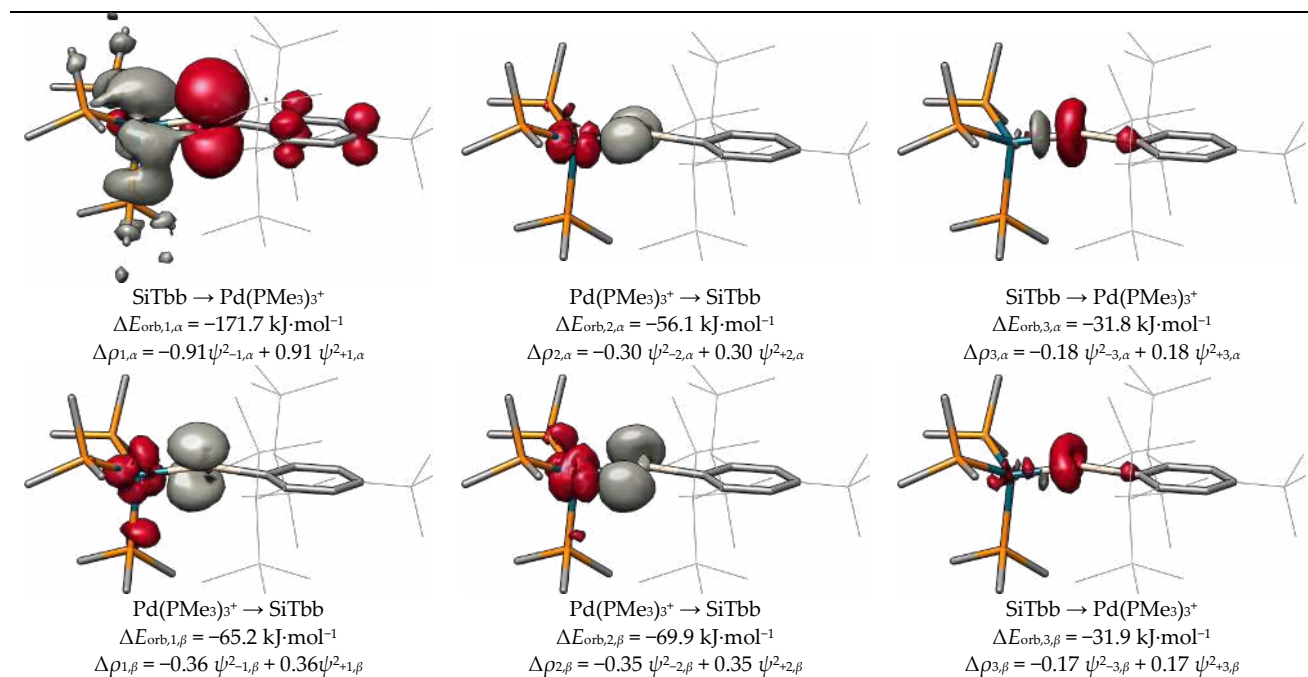


Figure S45. Deformation densities of PdSiTbb.

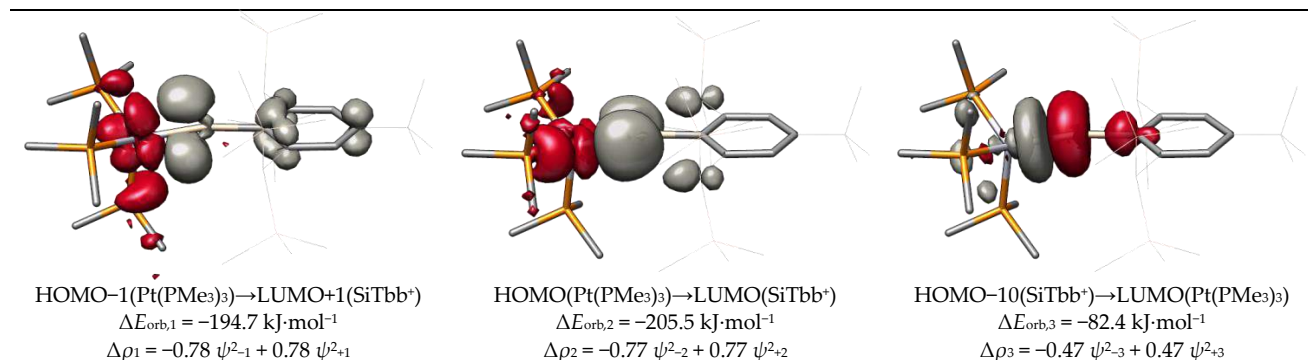
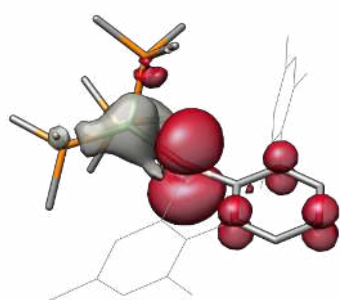
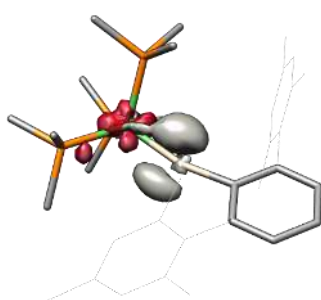


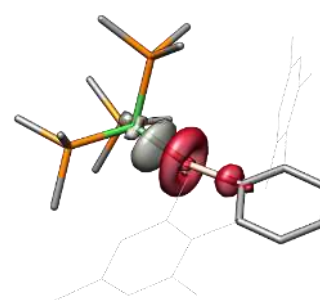
Figure S46. Deformation densities of PtSiTbb.



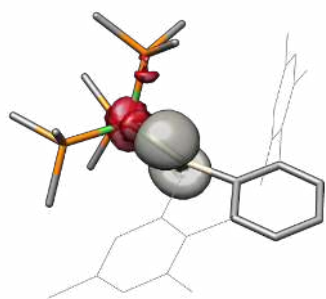
SOMO(SiAr^{Mes})→SOMO(Ni(PMe₃)₃⁺)
 $\Delta E_{\text{orb},1,\alpha} = -140.1 \text{ kJ}\cdot\text{mol}^{-1}$
 $\Delta\rho_{1,\alpha} = -0.90 \psi^{2-1,\alpha} + 0.90 \psi^{2+1,\alpha}$



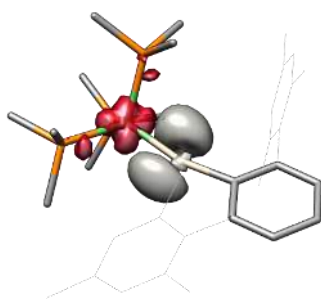
HOMO-3(Ni(PMe₃)₃⁺)→LUMO(SiAr^{Mes})
 $\Delta E_{\text{orb},2,\alpha} = -55.1 \text{ kJ}\cdot\text{mol}^{-1}$
 $\Delta\rho_{2,\alpha} = -0.29 \psi^{2-2,\alpha} + 0.29 \psi^{2+2,\alpha}$



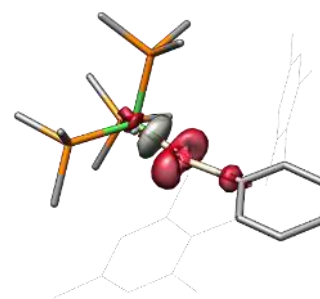
HOMO(SiAr^{Mes})→LUMO(Ni(PMe₃)₃⁺)
 $\Delta E_{\text{orb},3,\alpha} = -37.4 \text{ kJ}\cdot\text{mol}^{-1}$
 $\Delta\rho_{3,\alpha} = -0.19 \psi^{2-3,\alpha} + 0.19 \psi^{2+3,\alpha}$



SOMO(Ni(PMe₃)₃⁺)→SOMO(SiAr^{Mes})
 $\Delta E_{\text{orb},1,\beta} = -82.7 \text{ kJ}\cdot\text{mol}^{-1}$
 $\Delta\rho_{1,\beta} = -0.41 \psi^{2-1,\beta} + 0.41 \psi^{2+1,\beta}$



HOMO-3(Ni(PMe₃)₃⁺)→LUMO(SiAr^{Mes})
 $\Delta E_{\text{orb},2,\beta} = -84.7 \text{ kJ}\cdot\text{mol}^{-1}$
 $\Delta\rho_{2,\beta} = -0.37 \psi^{2-2,\beta} + 0.37 \psi^{2+2,\beta}$



HOMO(SiAr^{Mes})→LUMO(Ni(PMe₃)₃⁺)
 $\Delta E_{\text{orb},3,\beta} = -36.5 \text{ kJ}\cdot\text{mol}^{-1}$
 $\Delta\rho_{3,\beta} = -0.18 \psi^{2-3,\beta} + 0.18 \psi^{2+3,\beta}$

Figure S47. Deformation densities of NiSiAr^{Mes}.

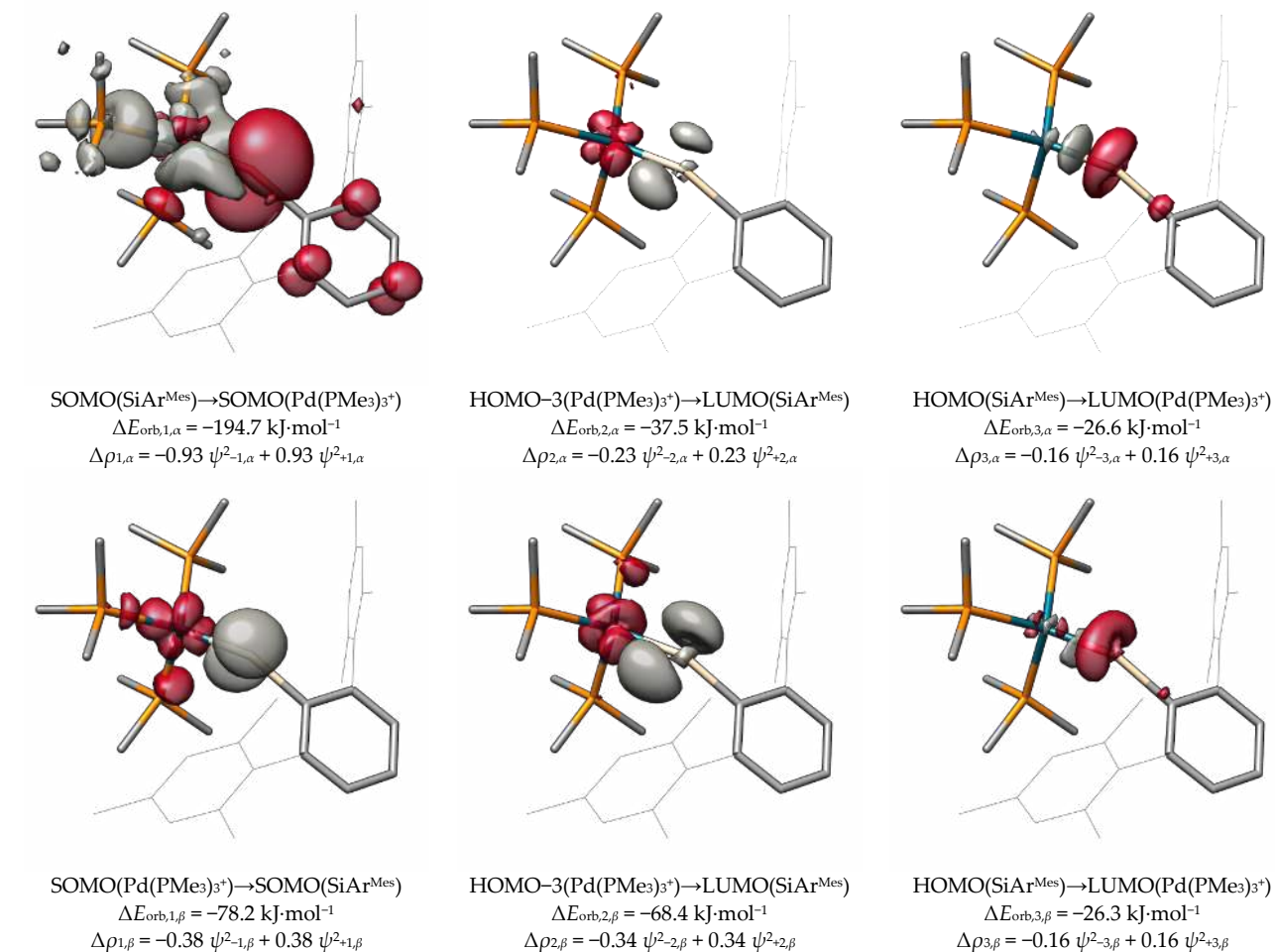


Figure S48. Deformation densities of PdSiAr^{Mes}.

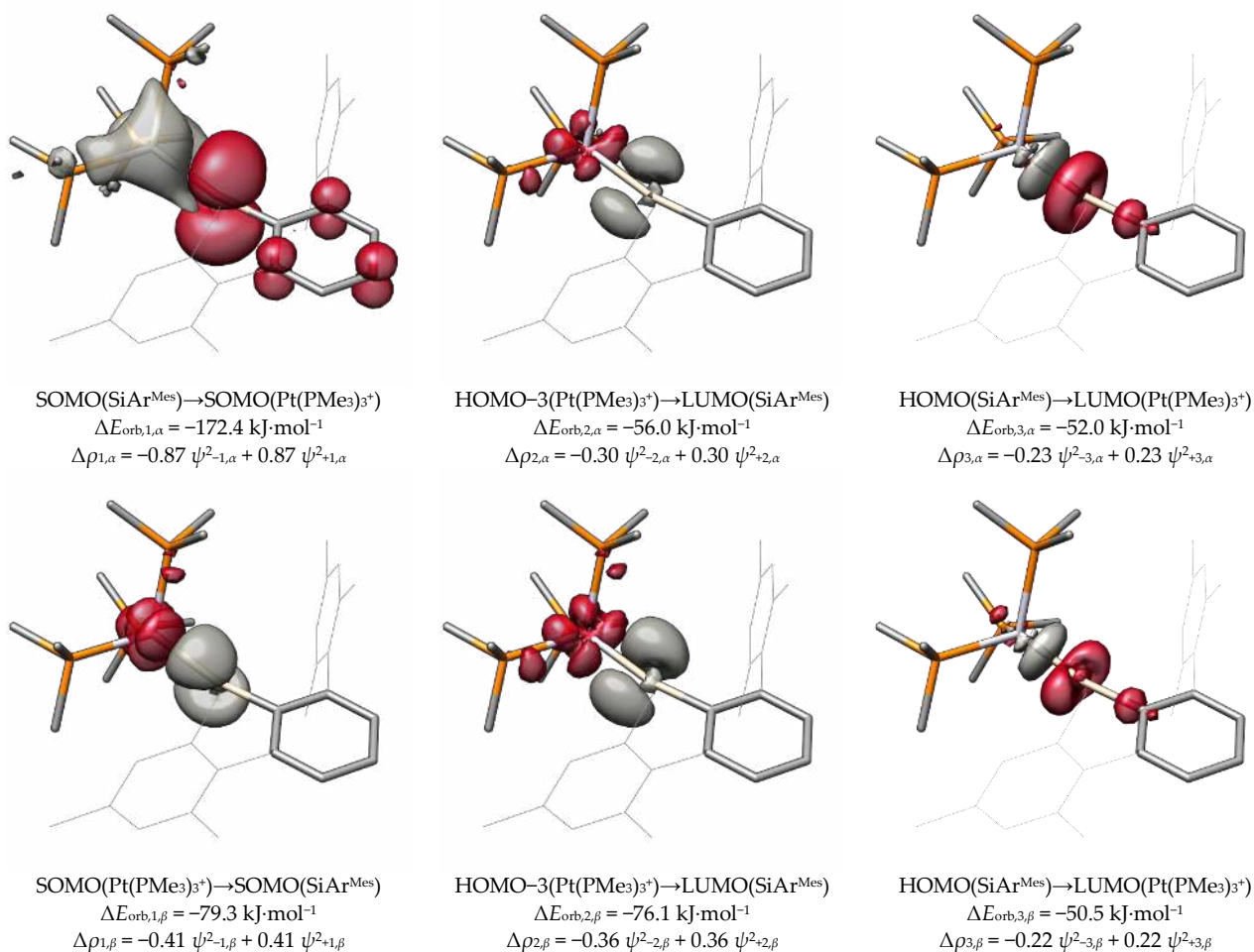
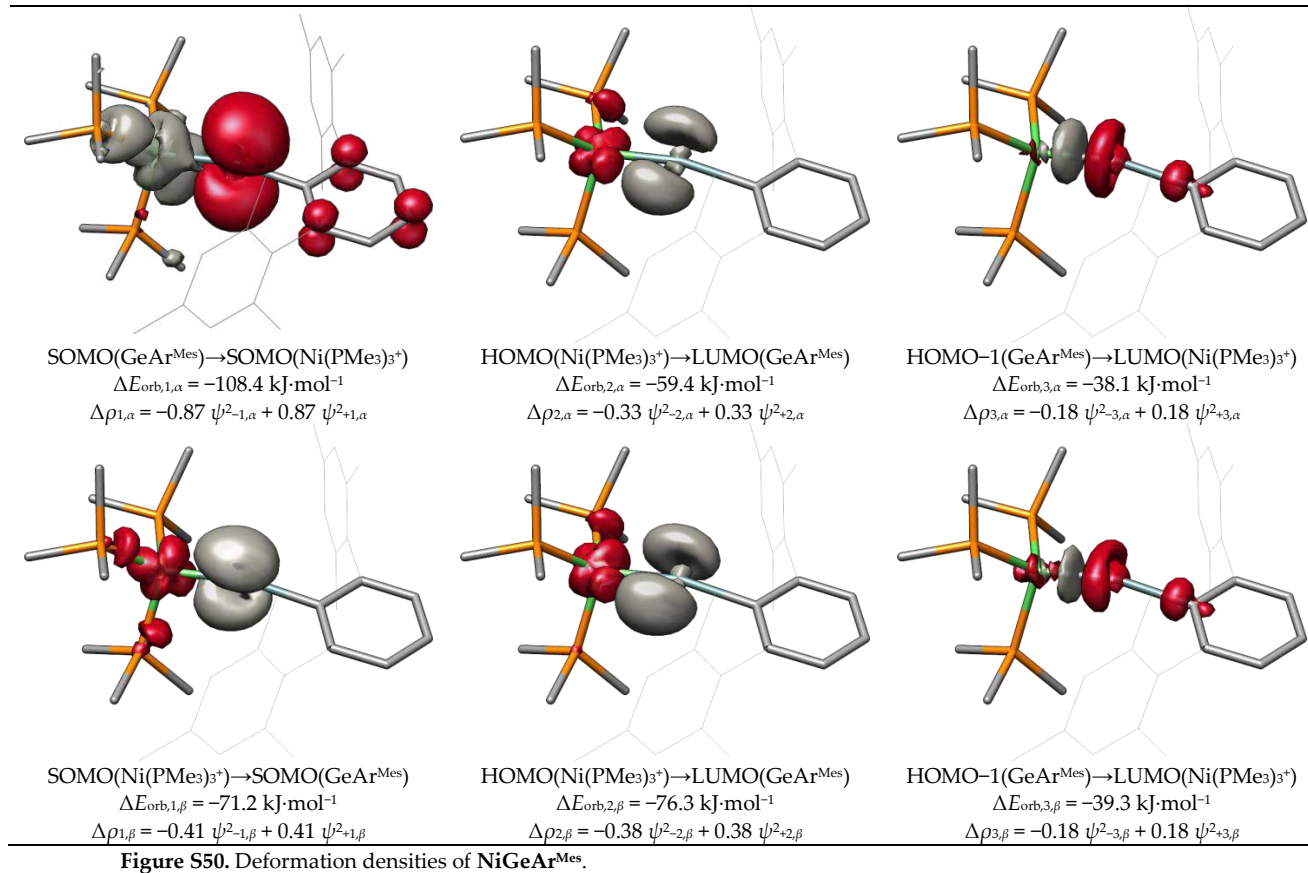
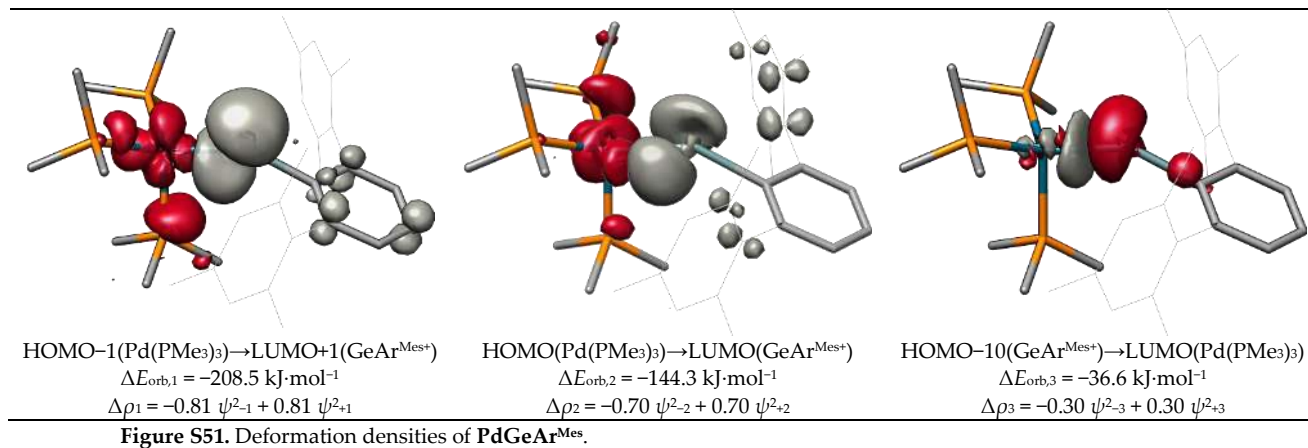
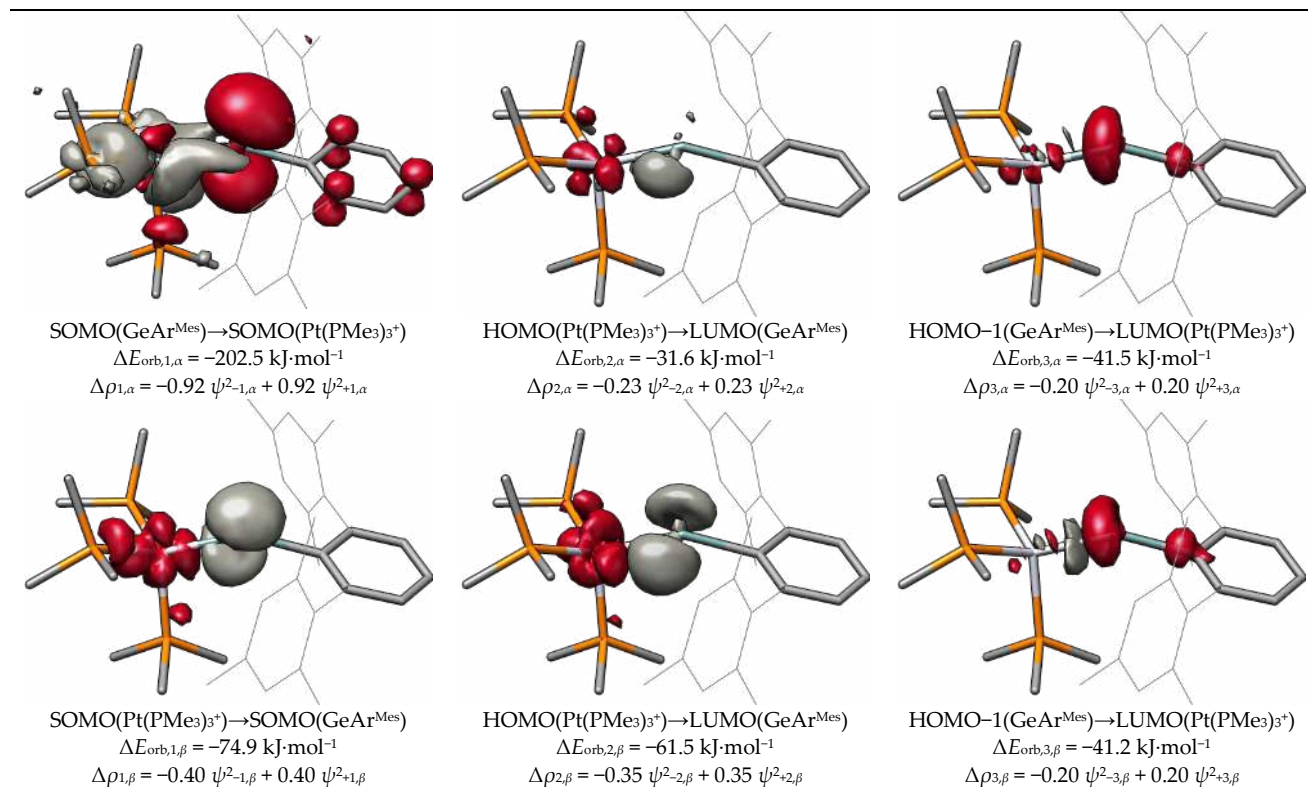
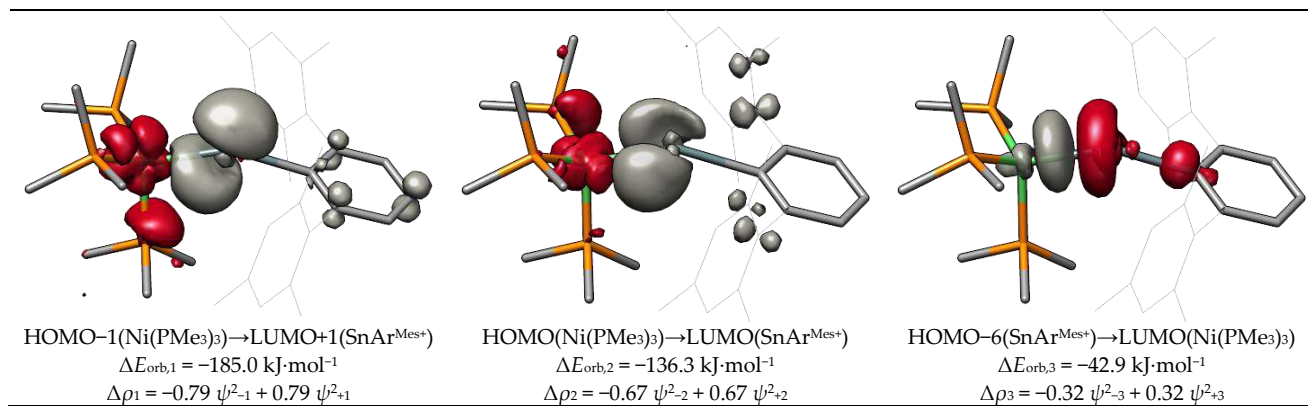
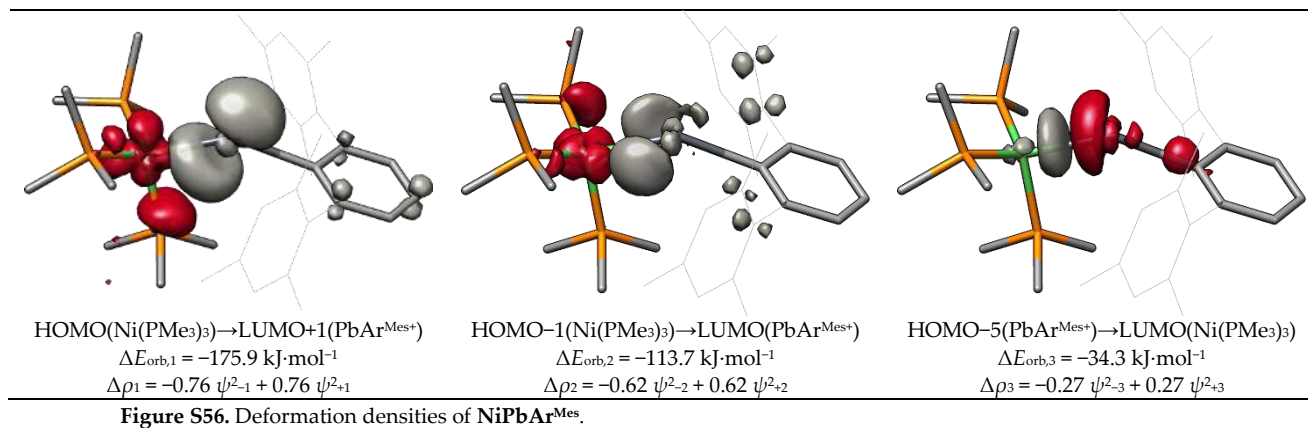
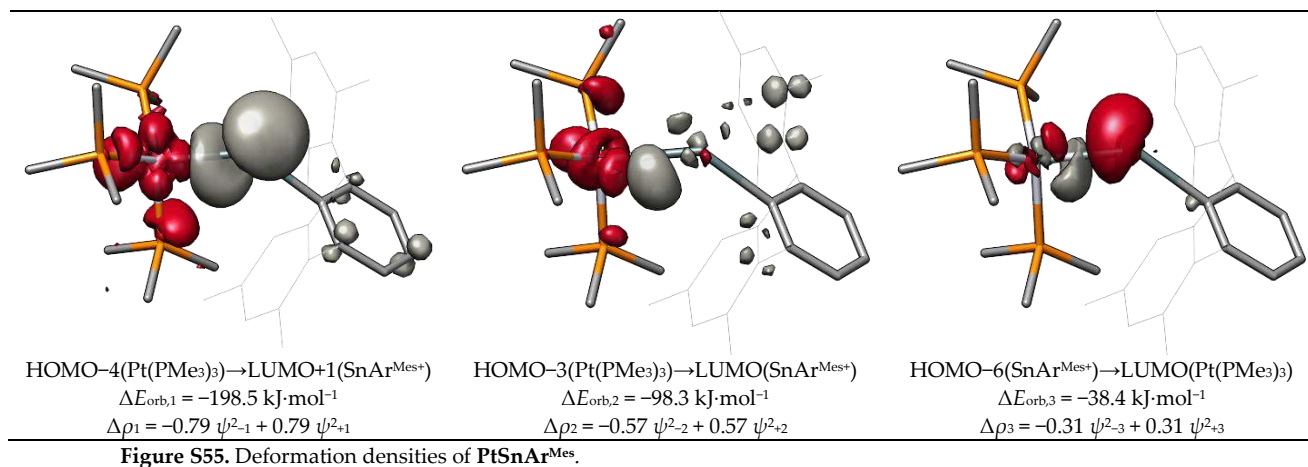
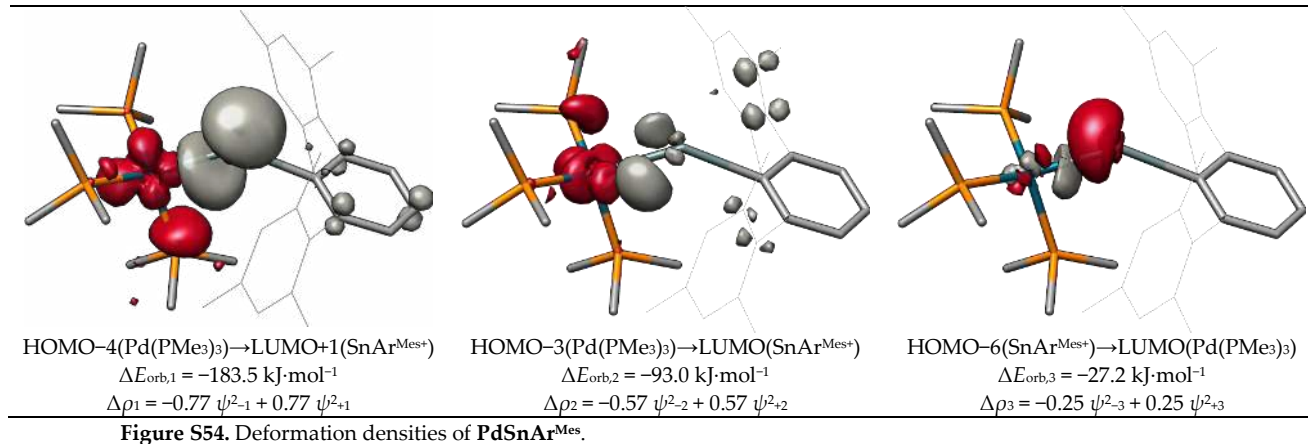
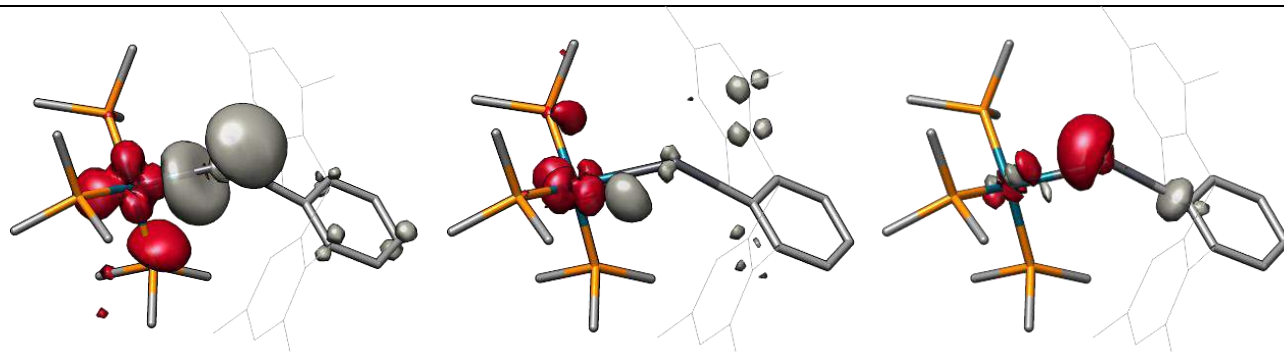


Figure S49. Deformation densities of PtSiAr^{Mes}.

Figure S50. Deformation densities of NiGeAr^{Mes}.Figure S51. Deformation densities of PdGeAr^{Mes}.

Figure S52. Deformation densities of PtGeAr^{Mes}.Figure S53. Deformation densities of NiSnAr^{Mes}.





HOMO-4(Pd(PMe₃)₃)→LUMO+1(PbAr^{Mes+})

$$\Delta E_{\text{orb},1} = -170.4 \text{ kJ}\cdot\text{mol}^{-1}$$

$$\Delta\rho_1 = -0.74 \psi^{2-1} + 0.74 \psi^{2+1}$$

HOMO-3(Pd(PMe₃)₃)→LUMO(PbAr^{Mes+})

$$\Delta E_{\text{orb},2} = -71.2 \text{ kJ}\cdot\text{mol}^{-1}$$

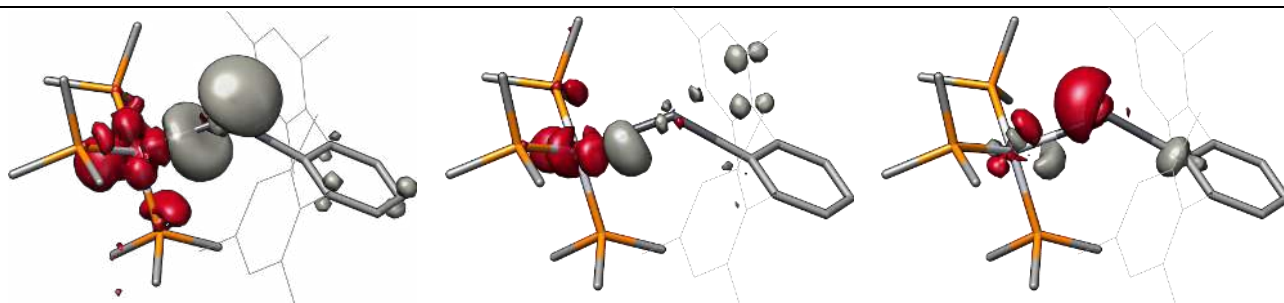
$$\Delta\rho_2 = -0.50 \psi^{2-2} + 0.50 \psi^{2+2}$$

HOMO-6(PbAr^{Mes+})→LUMO(Pd(PMe₃)₃)

$$\Delta E_{\text{orb},3} = -20.8 \text{ kJ}\cdot\text{mol}^{-1}$$

$$\Delta\rho_3 = -0.21 \psi^{2-3} + 0.21 \psi^{2+3}$$

Figure S57. Deformation densities of PdPbAr^{Mes}.



HOMO-4(Pt(PMe₃)₃)→LUMO+1(PbAr^{Mes+})

$$\Delta E_{\text{orb},1} = -180.1 \text{ kJ}\cdot\text{mol}^{-1}$$

$$\Delta\rho_1 = -0.76 \psi^{2-1} + 0.76 \psi^{2+1}$$

HOMO-3(Pt(PMe₃)₃)→LUMO(PbAr^{Mes+})

$$\Delta E_{\text{orb},2} = -74.7 \text{ kJ}\cdot\text{mol}^{-1}$$

$$\Delta\rho_2 = -0.50 \psi^{2-2} + 0.50 \psi^{2+2}$$

HOMO-6(PbAr^{Mes+})→LUMO(Pt(PMe₃)₃)

$$\Delta E_{\text{orb},3} = -26.8 \text{ kJ}\cdot\text{mol}^{-1}$$

$$\Delta\rho_3 = -0.25 \psi^{2-3} + 0.25 \psi^{2+3}$$

Figure S58. Deformation densities of PtPbAr^{Mes}.

13) Metallotetraylene isomers **MER-2** as found by PES scans**Table S11.** Key properties of metallotetraylene isomers **MER-2** derived from the **MER** complexes. ΔE_{rel} is the energy difference at level of theory II ($E(\text{MER-2}) - E(\text{MER})$). No **MER-2** isomer could be obtained for **NiSiTbb** and **NiSiAr^{Mes}**.

compound	ΔE_{rel}	MER			MER-2		
		M-E	E-C1	M-E-C1	M-E	E-C1	M-E-C1
NiSiTbb	/	204.5	184.0	167.2	/	/	/
NiSiAr^{Mes}	/	204.2	185.6	167.4	/	/	/
NiGeAr^{Mes}	83.5	213.3	197.1	165.3	235.9	204.0	95.1
NiSnAr^{Mes}	55.3	235.1	219.4	150.9	256.3	224.3	96.0
NiPbAr^{Mes}	36.4	244.9	229.7	142.7	264.2	234.3	94.8
PdSiTbb	47.1	215.1	184.0	163.1	235.1	189.7	98.8
PdSiAr^{Mes}	28.7	216.1	187.6	150.7	232.4	191.0	87.9
PdGeAr^{Mes}	1.5	227.9	199.5	144.9	246.4	202.7	90.6
PdSnAr^{Mes}	-17.6	251.6	222.9	134.4	270.3	223.6	93.1
PdPbAr^{Mes}	-25.3	263.1	232.4	129.6	277.4	232.7	93.6
PtSiTbb	78.4	215.8	183.8	168.1	239.0	191.0	101.0
PtSiAr^{Mes}	41.8	215.7	183.6	166.1	238.1	192.5	100.0
PtGeAr^{Mes}	7.4	228.4	198.9	149.7	250.7	204.0	98.7
PtSnAr^{Mes}	-13.7	255.1	223.9	132.1	274.3	225.4	96.9
PtPbAr^{Mes}	-28.5	267.7	233.1	127.3	281.9	233.7	94.3

14) References

- Okuniewski, A.; Rosiak, D.; Chojnacki, J.; Becker, B. Coordination Polymers and Molecular Structures among Complexes of Mercury(II) Halides with Selected 1-Benzoylthioureas. *Polyhedron* **2015**, *90*, 47–57, doi:10.1016/j.poly.2015.01.035.
- Keil, P.M.; Hadlington, T.J. Accessing Cationic Tetraylene-Nickel(0) Systems Featuring Donor-Acceptor E-Ni Triple Bonds (E = Ge, Sn). *Chem. Commun.* **2022**, 3011, doi:10.1039/D2CC00422D.



Original research paper

Group 6 germylidyne complexes in the gas phase by LIFDI and APCI mass spectrometry

European Journal of Mass Spectrometry
2023, Vol. 29(1) 44–57
© The Author(s) 2022
Article reuse guidelines:
sagepub.com/journals-permissions
DOI: 10.1177/14690667221137465
journals.sagepub.com/home/ems

Leonard R. Maurer and Marianne Engeser

Abstract

Although showing fascinating chemical properties and reactivity in solution, heavier tetrelidyne complexes with $M\equiv E$ triple bonds have not been studied in the gas phase before due to their high sensitivity towards air and moisture. We selected four group 6 germylidyne complexes, $[\text{Cp}(\text{PMe}_3)_2\text{M}\equiv\text{GeAr}^{\text{Mes}}]$ ($M = \text{Mo}$ (**1-Mo**), W (**1-W**), $\text{Ar}^{\text{Mes}} = 2,6\text{-dimesitylphenyl}$) and $[\text{Tp}'(\text{CO})_2\text{M}\equiv\text{GeAr}^{\text{Mes}}]$ ($M = \text{Mo}$ (**2-Mo**), W (**2-W**), $\text{Tp}' = \kappa^3\text{-}N,N',N''\text{-hydridotris}(3,5\text{-dimethylpyrazolyl})\text{ borate}$), for a mass-spectrometric study. Liquid Injection Field Desorption Ionization (LIFDI) proved to be a well-suited technique to ionize these sensitive compounds as the spectra show the molecular ions as radical cations and only minor traces of fragmentation or degradation products. In addition, Atmospheric Pressure Chemical Ionization (APCI) connected to a high-resolving tandem mass spectrometer allowed us to study the gas-phase fragmentation behaviour of these compounds. The fragmentation patterns not only comprise the expected losses of phosphane or carbonyl ligands, respectively, but also indicate C–H bond activation by the electron-deficient metal centre. An enhanced reactivity of the tungsten species is visible in a preferred methyl abstraction in the phosphane complex **1-W** compared to **1-Mo**. Although degradation in solution before ionization obviously can destroy the $M\equiv\text{Ge}$ triple bond, the cleavage of the $M\equiv\text{Ge}$ bond upon gas-phase activation is not observed for the Mo species and only as a minor pathway for the W compounds, highlighting the high bonding energy between metal and tetrel.

Keywords

germylidyne complex, metal germanium triple bond, LIFDI, APCI, mass spectrometry, collision-induced dissociation

Date received: 15 September 2022; accepted: 18 October 2022

Introduction

The first triple bonds between a transition metal and a group 14 tetrel atom were reported in the year 1973 with the carbyne complexes $[\text{X}(\text{CO})_4\text{M}\equiv\text{C-R}]$ ($\text{X} = \text{Cr, Mo, W}$; $\text{R} = \text{CH}_3, \text{Ph}$) by Nobel prize winning Fischer et al.^{1,2} Only two years later, Schrock managed to obtain an alkylidyne complex $[(\text{CH}_3)_3\text{CCH}_2)_3\text{Ta}\equiv\text{CC}(\text{CH}_3)_3]\bullet\text{Li}(\text{dmp})^3$ that comprises a slightly different electronic structure than Fischer's carbyne complexes.^{4,5} Simultaneously to the derivatization, structure elucidation and reactivity studies of Fischer-type carbyne complexes,⁶ Schrock developed the rich metathesis chemistry of alkylidyne complexes, which was also awarded with a Nobel prize later on.⁷ More than two decades later, in 1996, the group of Power successfully isolated the first heavier homologue of a carbyne complex, the germylidyne complex $[\text{Cp}(\text{CO})_2\text{Mo}\equiv\text{GeAr}^{\text{Mes}}]$ with a molybdenum germanium triple bond ($\text{Cp} = \eta^5\text{-C}_5\text{H}_5$, $\text{Ar}^{\text{Mes}} = 2,6\text{-dimesitylphenyl}$).⁸ This was then followed by the first representatives of tin,⁹ lead¹⁰ and finally silicon¹¹ by Filippou et al. In the past 20 years, this topic gained a lot of interest and a plethora of new tetrelidyne complexes could be synthesized for various metal tetrel combinations.^{12–16}

As the synthesis of these compounds is a challenge on its own, broad reactivity studies are scarce and confined to

solution chemistry.¹² Mass spectrometry as a tool to explore properties and reactivity in the gas phase is, to the best of our knowledge, completely absent for heavier tetrelidyne complexes and only observed for analytical purposes in some cases to confirm the successful synthesis.^{17–21} One of the reasons for this is the extreme susceptibility of heavier tetrelidyne complexes towards moisture and oxygen (with silicon usually the most sensitive due to its high oxophilicity), which impedes the sample introduction into the MS instrument.²²

As other analytical methods like IR or NMR greatly benefitted from advances in Schlenk and glove box techniques and became routinely applicable to sensitive samples, also mass spectrometry can rely on those methods to improve the handling of challenging compounds. Regarding the sample application, it is possible to install a glove box around the ionization source or inject the sample directly from a Schlenk tube.^{23,24} On the other hand, the ionization method can be chosen to minimize the influence of air, as done with the Liquid

Corresponding author:

Marianne Engeser, Kekulé-Institut für Organische Chemie und Biochemie, Rheinische Friedrich-Wilhelms-Universität Bonn, Bonn, Germany.
Email: marianne.engeser@uni-bonn.de

Injection Field Desorption Ionization (LIFDI) technique.²⁵ By keeping the FD emitter in a high vacuum environment and loading it via a thin capillary connected to a vial with the inertly prepared sample, the risk for the decomposition of the compound is lowered significantly.

As a first entry point into the mass spectrometric study of heavier tetrylidyne complexes, we selected four group 6 gemylydine complexes, $[\text{Cp}(\text{PMe}_3)_2\text{M}\equiv\text{GeAr}^{\text{Mes}}]$ ($\text{M} = \text{Mo}$ (**1-Mo**), W (**1-W**))^{26,27} and $[\text{Tp}'(\text{CO})_2\text{M}\equiv\text{GeAr}^{\text{Mes}}]$ ($\text{M} = \text{Mo}$ (**2-Mo**), W (**2-W**)),^{13,27} $\text{Tp}' = \kappa^3\text{-}N,N',N''\text{-hydrido-tris(3,5-dimethylpyrazolyl)borate}$, see Scheme 1). The bulky scorpionate ligand Tp' , as introduced by Trofimenko in 1966,²⁸ protects the reactive $\text{M}\equiv\text{E}$ moiety more effectively than the Cp ligand, whereas in both **1-M** and **2-M**, further kinetic stabilization is achieved by the large Ar^{Mes} substituent at the germanium atom, thus decreasing the sensitivity against moisture and oxygen. By keeping the GeAr^{Mes} unit unvaried, we facilitate the observation of trends caused by the metal and its coordination sphere.

Motivated by the unexplored gas-phase chemistry of heavier tetrylidyne complexes, we hereby present a mass spectrometric study on the four molybdenum and tungsten gemylydine complexes **1-Mo**, **1-W**, **2-Mo** and **2-W**. Application of the LIFDI technique for inert sample injection combined with its mild ionization enables us to observe intact molecular ions. By employing Atmospheric Pressure Chemical Ionization (APCI) connected to a high-resolving tandem mass spectrometer, we further explore the fragmentation behaviour of those complexes for the very first time.

Experimental details

LIFDI mass spectra were recorded in positive mode on a Thermo Finnigan MAT90 reverse geometry double focusing sector instrument equipped with a Linden CMS LIFDI source. The samples were transferred via a fused silica capillary (50 μm inner diameter) into the ion source from a small three-chamber glass vial (sample solution in one chamber, toluene in the other two for pre-, intermediate- and post-flushing, ca. 0.3 mL per chamber), which was capped by a rubber septum. Before each measurement, the LIFDI capillary and source was conditioned with pure toluene. Approximately 30 drops of the sample were applied to the emitter for each measurement. In each case, the LIFDI heating protocol was manually adjusted for optimal signal intensities.

The MAT90 instrument was operated in LProf scan mode (exponential magnet scan profile data) with a scan rate of 3 s per decade, an inter scan time of 0.2 s and a mass range of 50–1000 (**1-W**, **2-Mo**, **2-W**) and 50–1500 (**1-Mo**). The spectra are obtained as a summation over multiple scans without further background correction.

APCI mass spectra were recorded in positive mode on a Thermo Fisher Scientific LTQ Orbitrap XL instrument equipped with an APCI source. The samples were transferred via polyetheretherketone (PEEK) tubing using a syringe pump at a flow rate of 5 $\mu\text{L}\cdot\text{min}^{-1}$ from 250 μL Hamilton Gastight™ syringes. The spectra are obtained

as a sum over multiple scans for a better signal-to-noise ratio. Standard APCI source conditions were used; however, the tube lens voltage was set to 0 V for minimal fragmentation of the molecular ions.

Collision-induced dissociation (CID) and higher-energy C-trap dissociation (HCD) experiments were performed in the helium-filled ion traps of the Orbitrap XL instrument, whereas the ion detection was carried out in the orbitrap analyser. Fragmentation energies were individually optimized for each compound.

For both ionization methods, toluene solutions of the sample in concentrations of approximately 2 $\text{mmol}\cdot\text{L}^{-1}$ were used. Toluene was dried by a MBraun SPS-800 solvent purification system and stored inside the glove box in 500 mL SCHOTT DURAN® laboratory glass bottles. The sample preparation was performed in each case in the glove box to strictly exclude air and moisture. The three-chamber vials and the syringes were stored in drying ovens at 88 °C.

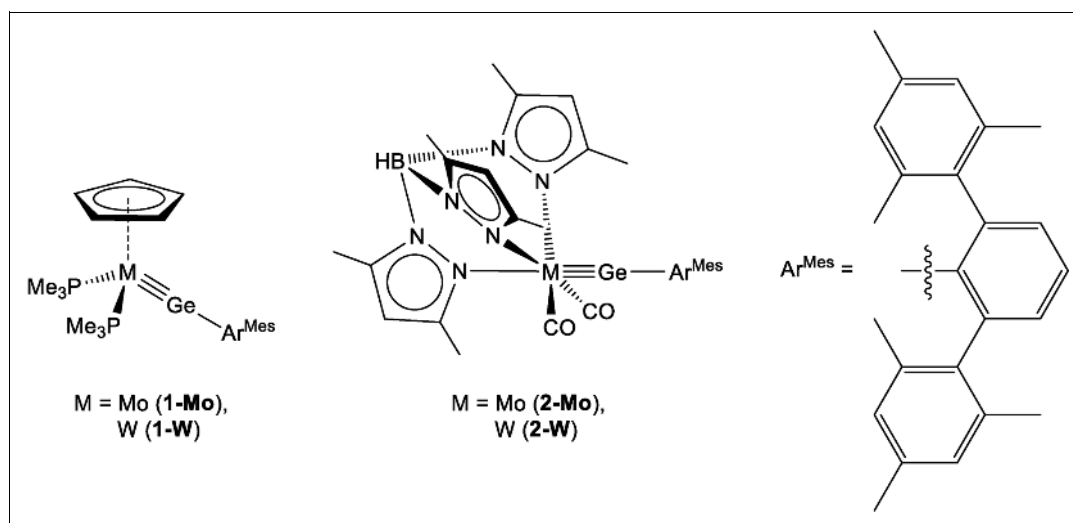
Results and discussion

LIFDI spectra

The LIFDI spectrum of **1-Mo** (Figure 1) reveals the successful detection of the intact molecular ion $[\text{M}]^{+\bullet}$ as base peak with the expected isotope pattern and mass (found m/z 700.2, calculated 700.2 u for $[\text{C}_{35}\text{H}_{48}\text{GeMoP}_2]^{+\bullet}$). The only other considerable signal in this spectrum appears to be at m/z 92.0, which corresponds to the used solvent toluene (calc. 92.1 u for $[\text{C}_7\text{H}_8]^{+\bullet}$). Degradation products are absent, as well as fragments, which illustrates the mild ionization of LIFDI.

In contrast, the tungsten gemylydine complex **1-W** turned out to be more sensitive towards degradation, as multiple measurements led to unsatisfying MS spectra. Interestingly, most degradation products appear at early LIFDI heating currents and we were able to identify a small range, where the $[\text{M}]^{+\bullet}$ is observed as base peak and the amount of decomposition peaks is small, resulting in the spectrum of Figure 2 (see Figure S1 in the Supporting Information for the corresponding spectrum averaged over the full measurement). The low signal-to-noise ratio caused by the little number of scans exacerbates the interpretation, however, the $[\text{M}]^{+\bullet}$ ion is still obtained as base peak at m/z 786.3 (calc. 786.2 u for $[\text{C}_{35}\text{H}_{48}\text{GeWP}_2]^{+\bullet}$) with matching isotope pattern. The ion $[\text{Ar}^{\text{Mes}} + \text{H}]^+$ is also visible at m/z 314.3 (calc. 314.2 u for $[\text{C}_{24}\text{H}_{26}]^+$), showing the cleavage of the Ge–C bond.

Similarly, LIFDI spectra could be obtained for compounds **2-Mo** (Figure 3) and **2-W** (Figure 4). They also feature the molecular ions $[\text{M}]^{+\bullet}$ as base peaks (**2-Mo**: found m/z 836.2, calc. 836.2 u for $[\text{C}_{41}\text{H}_{47}\text{BGeMoN}_6\text{O}_2]^{+\bullet}$; **2-W**: found m/z 922.2, calc. 922.3 u for $[\text{C}_{41}\text{H}_{47}\text{BGeWN}_6\text{O}_2]^{+\bullet}$). However, in contrast to the gemylydine complexes **1-Mo** and **1-W**, the LIFDI spectra of **2-Mo** and **2-W** additionally show the hydrogen and oxygen adducts, $[\text{M} + 2\text{H} + 3\text{O}]^{+\bullet}$ at m/z 886.3 and m/z 971.8, respectively. These could be rationalized as species



Scheme 1. Lewis formulae of complexes **1-M** and **2-M** used throughout this study.

$[\text{M} + \text{H}_2\text{O} + \text{O}_2]^{\bullet+}$, present despite careful sample preparation. Interestingly, only the adducts $[\text{M} + 2\text{H} + 3\text{O}]^{\bullet+}$ are observed in both cases, whereas the single adducts $[\text{M} + \text{O}_2]^{\bullet+}$ and $[\text{M} + \text{H}_2\text{O}]^{\bullet+}$ could not be detected. Finally, another significant signal in the LIFDI spectrum of **2-W** appears at m/z 566.2, which could be confirmed as $[\text{Tp}'(\text{CO})_3\text{WH}]^+$ with the help of high-resolving APCI Orbitrap mass spectrometry (*vide infra*).

APCI spectra and fragmentation

With the LIFDI spectra successfully showing that ionization of germylydyne complexes is possible without considerable degradation, we sought to confirm these results by employing high-resolution mass spectrometry with an Orbitrap XL instrument equipped with an APCI source.

Figures 5 and 6 show the APCI spectra of compounds **1-Mo** and **1-W**, respectively. In both cases, after flushing the capillary for a couple of minutes with the sample, the molecular ion $[\text{M}]^{\bullet+}$ is obtained once again as a base peak at m/z 700.147 (**1-Mo**, calc. 700.151 u for $[\text{C}_{35}\text{H}_{48}\text{GeMoP}_2]^{\bullet+}$) and m/z 786.196 (**1-W**, calc. 786.196 u for $[\text{C}_{35}\text{H}_{48}\text{GeWP}_2]^{\bullet+}$) with the expected isotope pattern. No further signals with intensities above 30% are present. Prominent in both spectra is the ion $[\text{Ar}^{\text{Mes}} + \text{H}]^+$ at m/z 314.202 (**1-Mo**) and 314.203 (**1-W**) that was already found in the LIFDI spectrum of **1-W** (Figure 2). Signals of air and moisture degradation products, such as $[\text{M} - \text{PMe}_3 + \text{H} + 2\text{O}]^+$ at m/z 657.101 (**1-Mo**) and 743.146 (**1-W**) or the simple water adduct $[\text{M} + \text{H}_2\text{O}]^{\bullet+}$ at m/z 718.157 (**1-Mo**) and 804.206 (**1-W**), are of low intensity (<5%), thus demonstrating the successful sample injection. Interestingly, one degradation ion could be identified as $[\text{M} - \text{PMe}_3 + \text{GeAr}^{\text{Mes}} + \text{OH}]^+$ at m/z 1026.224 (**1-Mo**, calc. 1026.228 u for $[\text{C}_{56}\text{H}_{65}\text{Ge}_2\text{MoOP}]^+$) and 1114.274 (**1-W**, calc. 1114.274 u for $[\text{C}_{56}\text{H}_{65}\text{Ge}_2\text{WOP}]^+$) that can be seen as

hydroxy-adduct of a cationic bisgermylydyne complex, a class of compounds with two germylydyne units coordinated to a metal centre that could already be isolated in the condensed phase for group 6 metals by C. Lindlahr ($\text{M} = \text{Mo}$; $\text{E} = \text{Sn}$)²⁶ and I. Papazoglou ($\text{M} = \text{Mo}$, W ; $\text{E} = \text{Ge}$)²⁹ in the Filippou group. In the spectrum of **1-W**, there is also a signal for the presumptive bisgermylydyne complex hydrogen adduct $[\text{M} - \text{PMe}_3 + \text{GeAr}^{\text{Mes}} + \text{H}]^+$ at m/z 1098.278 (calc. 1098.279 u for $[\text{C}_{56}\text{H}_{65}\text{Ge}_2\text{WP}]^+$), which is absent for **1-Mo**.

When the APCI tube lens voltage is set to 0 V, in general fragmentation is scarce, the only considerable signals being the germylydyne fragment $[\text{Ar}^{\text{Mes}}\text{Ge}]^+$ at m/z 387.114 (**1-Mo**, calc. 387.117 u for $[\text{C}_{24}\text{H}_{25}\text{Ge}]^+$) and 387.116 (**1-W**) or its degradation adducts $[\text{Ar}^{\text{Mes}}\text{GeCp}]^+$ (found at m/z 452.153 (**1-Mo**) and 452.155 (**1-W**), calc. 452.156 u for $[\text{C}_{29}\text{H}_{30}\text{Ge}]^+$), and $[\text{Ar}^{\text{Mes}}\text{Ge} + \text{H} + 3\text{O}]^+$ (found at m/z 436.106 (**1-Mo**) and 436.109 (**1-W**) calc. 436.109 u for $[\text{C}_{24}\text{H}_{26}\text{GeO}_3]^+$).

The molecular ions $[\text{M}]^{\bullet+}$ were further examined by CID experiments. For **1-Mo**, a CID energy of 15 eV resulted in almost exclusive fragmentation to the ion $[\text{M} - 2\text{PMe}_3]^{\bullet+}$ at m/z 548.056 under loss of two trimethylphosphane ligands, beneath a negligible cleavage of CH_3^{\bullet} to m/z 685.120 (Figure 7).

Collisional activation of the mass-selected m/z 548.056 $[\text{M} - 2\text{PMe}_3]^{\bullet+}$ ion in a MS^3 experiment does not lead to cleavage of further ligands off the metal centre, neither the Cp ligand nor the germylydyne unit GeAr^{Mes} , but only induces a cascade of several dihydrogen eliminations and cleavage of CH_3^{\bullet} . This fragmentation behaviour is reproduced by HCD experiments (Figure 8), showing again almost exclusively the initial cleavage of the two phosphane ligands. Notably, a signal with very small intensity at m/z 623.092 is present only in the spectrum with the full pattern mass-selected at 30 eV that could be misinterpreted as single phosphane cleavage, but it

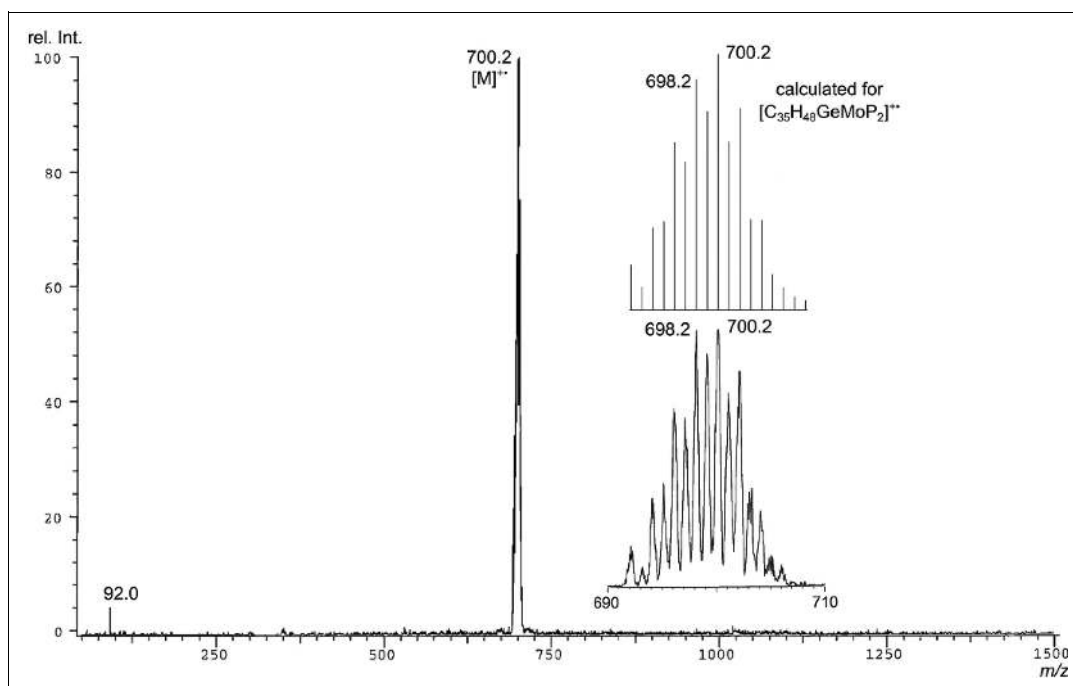


Figure 1. LIFDI-MAT90 spectrum of **1-Mo** (summation over 23 scans). The insert shows a zoom of the $[M]^{++}$ m/z region and the calculated isotope pattern for comparison.

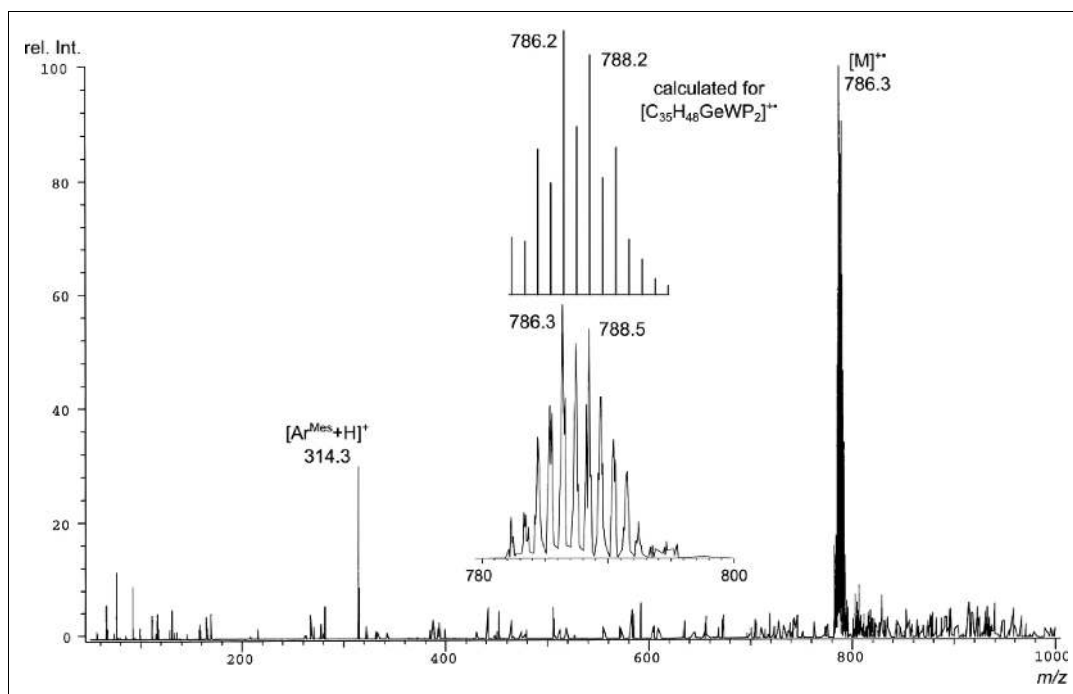


Figure 2. LIFDI-MAT90 spectrum of **1-W** (summation over 5 scans). The insert shows a zoom of the $[M]^{++}$ m/z region and the calculated isotope pattern for comparison.

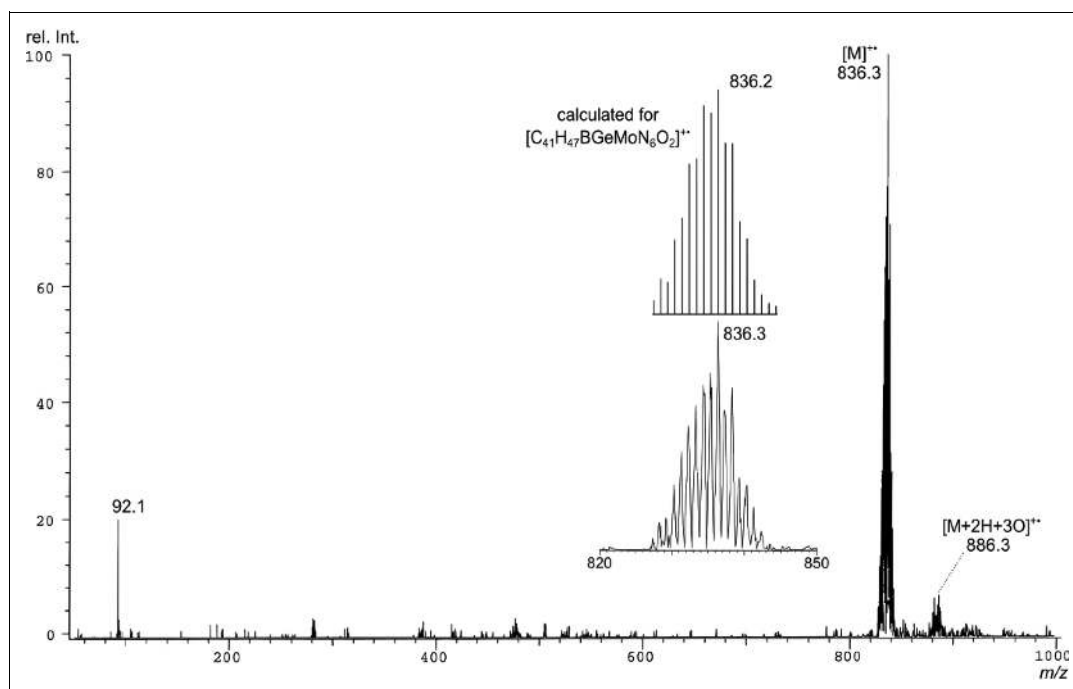


Figure 3. LIFDI-MAT90 spectrum of **2-Mo** (summation over 17 scans). The insert shows a zoom of the $[M]^{++}$ m/z region and the calculated isotope pattern for comparison.

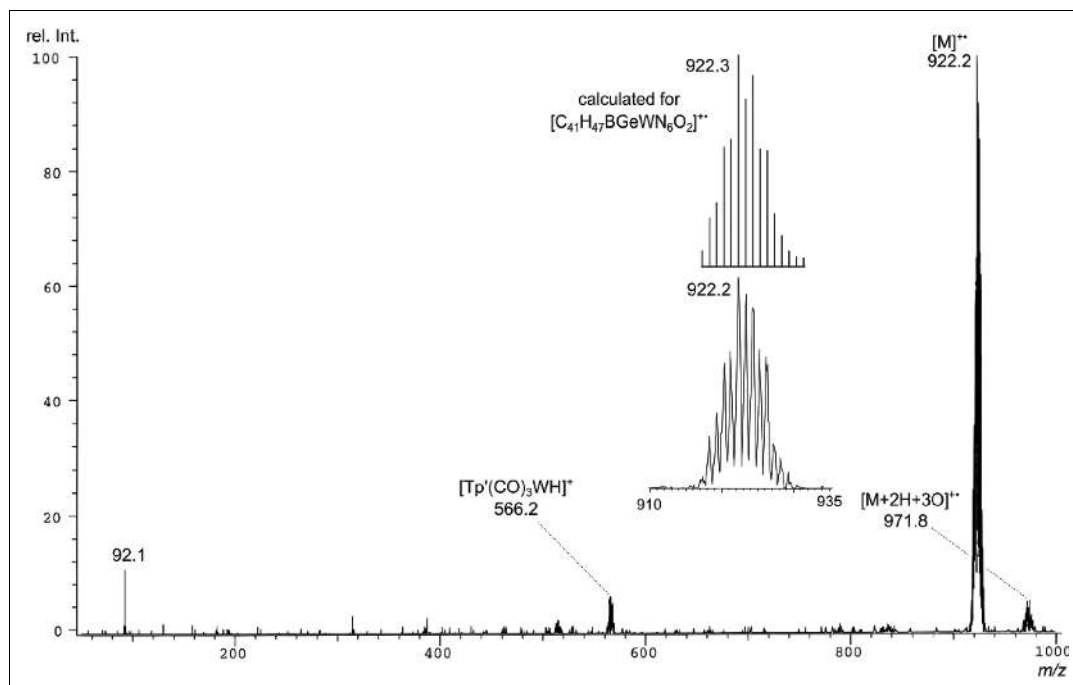


Figure 4. LIFDI-MAT90 spectrum of **2-W** (summation over 21 scans). The insert shows a zoom of the $[M]^{++}$ m/z region and the calculated isotope pattern for comparison.

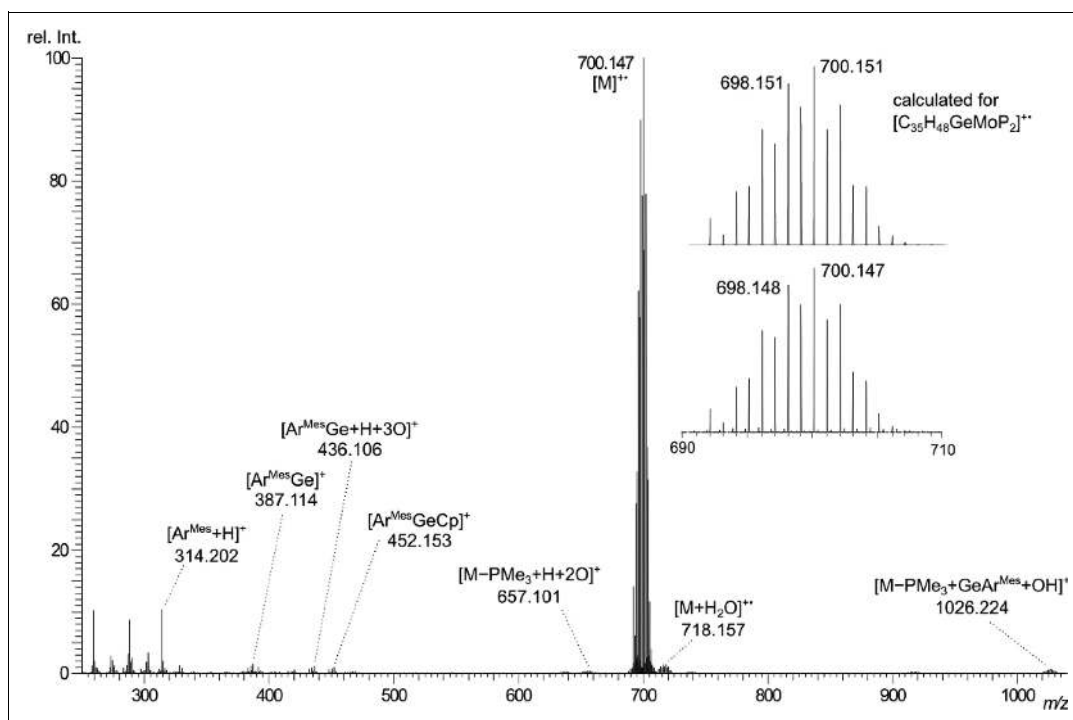


Figure 5. APCI-Orbitrap spectrum of **1-Mo**. The insert shows a zoom of the $[M]^{+}$ m/z region and the calculated isotope pattern for comparison.

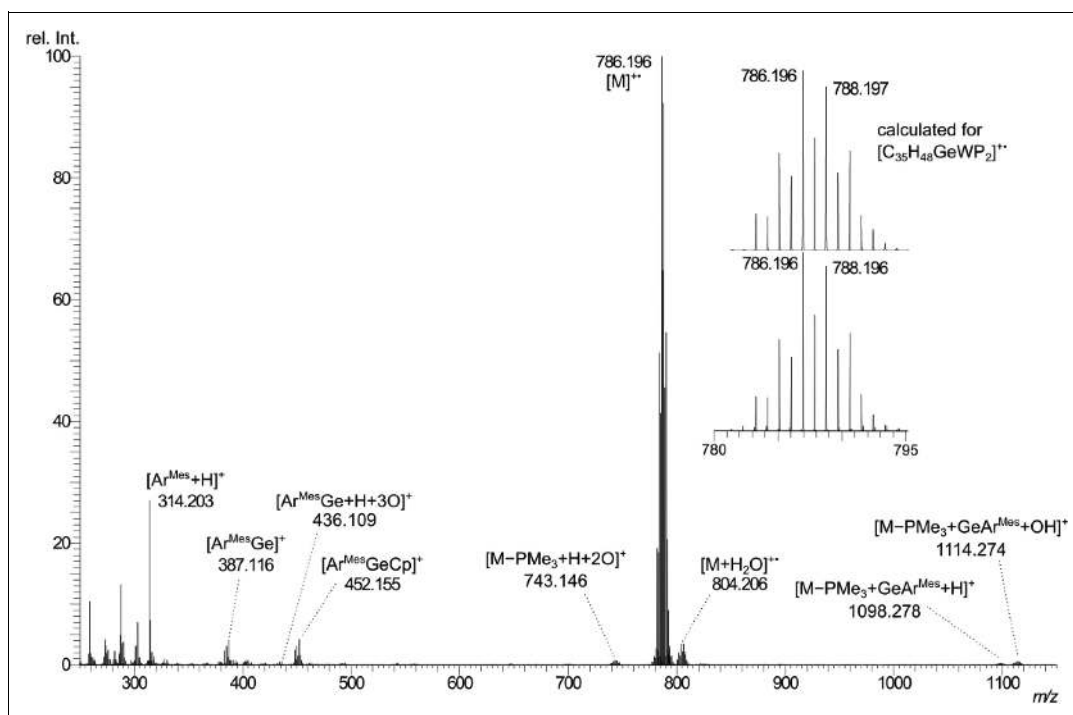


Figure 6. APCI-Orbitrap spectrum of **1-W**. The insert shows a zoom of the $[M]^{+}$ m/z region and the calculated isotope pattern for comparison.

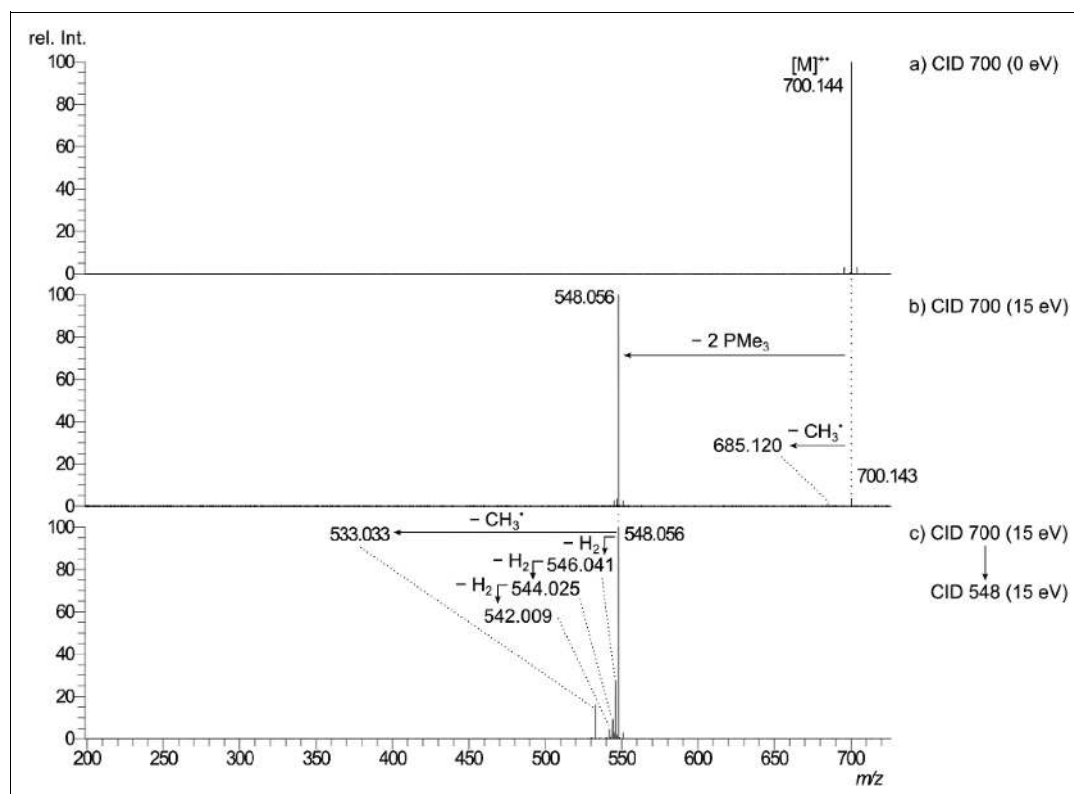


Figure 7. APCI-Orbitrap CID spectra for the fragmentation of **1-Mo** with mass selection of the most abundant signal in the isotope pattern (m/z 700) with 0 eV (a) and 15 eV (b), and the further activation of the m/z 548 ion at 15 eV (c) in a MS^3 experiment.

comprises neither the correct mass (calc. 624.107 u for $[C_{32}H_{30}GeMoP]^+$) nor the correct isotope pattern.

In contrast, the most dominant fragmentation in the CID spectra of **1-W** at 15 eV represents the elimination of a methyl radical to m/z 771.171 beside the less favoured cleavage of two PMe_3 ligands to m/z 634.106 (Figure 9). Further activation of the $[M-CH_3]^+$ cation in a MS^3 experiment reveals a complex fragmentation pattern, comprising cleavage of PMe_2H to m/z 709.143, of PMe_3 and H_2 to m/z 693.112 (base peak) and, most interestingly, cleavage of a presumable diphosphane P_2Me_4 to the fragment ion at m/z 649.129, which may be followed by a methyl group elimination to m/z 634.106 ($[M-2PMe_3]^+$), which itself shows only low intensity. This suggests that P-C bond activation of the PMe_3 substituents by the tungsten centre occurs in $[M-CH_3]^+$, which gives rise to a more complicated fragmentation behaviour. Finally, MS^3 activation of the ion $[M-2PMe_3]^+$ at m/z 634.106 reveals a very similar behaviour as of $[M-2PMe_3]^+$ of **1-Mo**, only leading to several H_2 eliminations and cleavage of another methyl group to m/z 619.083.

The HCD spectra of **1-W** mostly underline the results of the respective CID spectra (Figure 10); however, they additionally exhibit signals with very low intensities for $[Ar^{Mes}Ge]^+$ and $[CpW(PMe_3)_2-H]^+$ at m/z 387.115 and 400.069, respectively, which are formed by cleavage of the $W\equiv Ge$ triple bond.

Similarly to the cyclopentadienyl-bisphosphane germylidyne complexes **1-M**, APCI spectra of **2-Mo** (Figure 11) and **2-W** (Figure 12) could be recorded successfully without considerable degradation signals visible. The molecular ions $[M]^+$ appear as base peaks at m/z 836.216 (**2-Mo**, calc. 836.214 u for $[C_{41}H_{47}BN_6O_2GeMo]^+$) and 922.262 (**2-W**, calc. 922.259 u for $[C_{41}H_{47}BN_6O_2GeW]^+$) with some underlying $[M+H]^+$ intensity that is responsible for a slight mismatch between the found and calculated isotope patterns (more pronounced for **2-Mo**). Both spectra feature $[Ar^{Mes}+H]^+$ signals at m/z 314.203 and 314.204, respectively, as seen before in the APCI spectra of **1-Mo** and **1-W**. Furthermore, Figure 11 shows ions resulted from the cleavage of the $Mo\equiv Ge$ triple bond with and without degradation, such as $[Ar^{Mes}Ge+H+2O]^+$ at m/z 420.114 (calc. 420.114 u for $[C_{24}H_{26}GeO_2]^+$), $[Tp'(CO)_2Mo]^+$ at m/z 451.095 (calc. 451.095 u for $[C_{17}H_{22}BMoN_6O_2]^+$) or $[Tp'(CO)_3Mo]^+$ at m/z 479.090 (calc. 479.090 u for $[C_{18}H_{22}BMoN_6O_3]^+$). The $[M+2H+3O]^+$ type adducts as found in the corresponding LIFDI spectra are not observed, only the ion $[M+3H+3O]^+$ could be identified for **2-Mo** with very low intensity at m/z 887.219 (calc. 887.222 u for $[C_{41}H_{50}BGeMoN_6O_5]^+$) that could be rationalized as water-oxygen adduct of the protonated complex, $[M+H+H_2O+O_2]^+$. As the respective CID spectra of **2-M** show, carbonyl dissociation to $[M-CO]^+$ is feasible

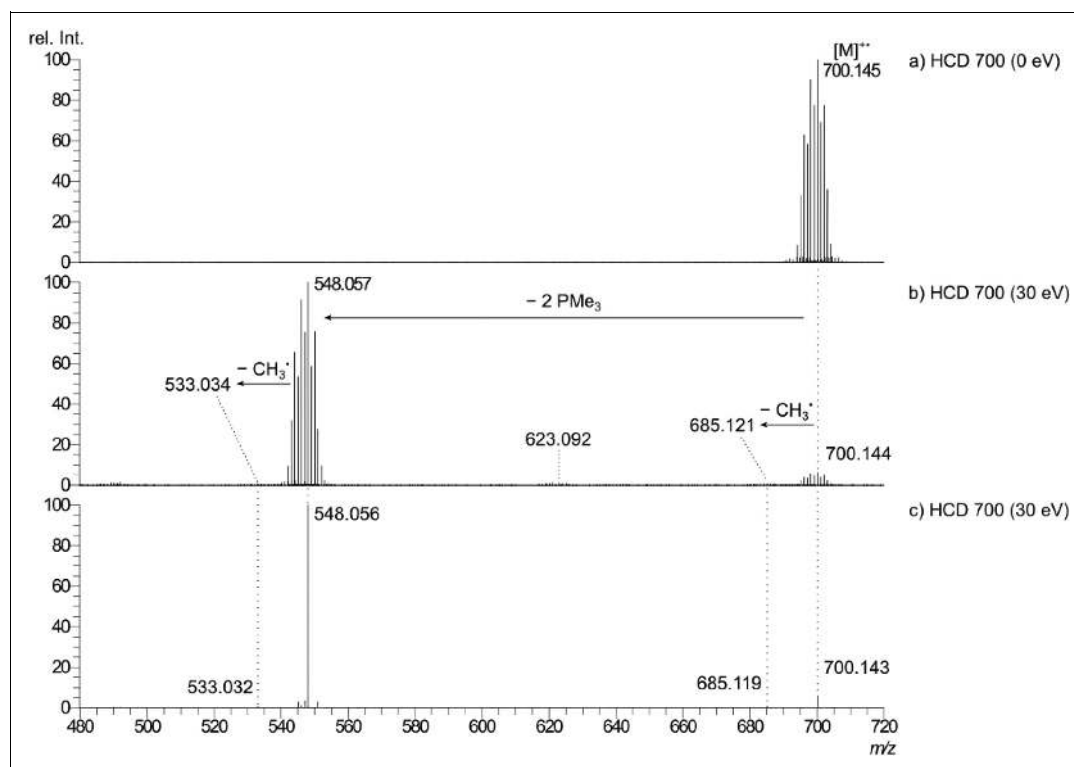


Figure 8. APCI-Orbitrap HCD spectra for the fragmentation of **1-Mo**. The whole isotope pattern was mass-selected for (a) and (b) and only the signal at m/z 700 for (c).

(*vide infra*) and can already be detected in the full spectrum at m/z 808.214 (calc. 808.219 u for $[\text{C}_{40}\text{H}_{47}\text{BGeMoN}_6\text{O}]^+$).

The APCI spectrum of **2-W** is obtained with even less considerable signals beside the $[\text{M}]^{+\bullet}$ peak. Apart from the above-mentioned $[\text{Ar}^{\text{Mes}} + \text{H}]^+$ signal, the ion $[\text{Tp}'(\text{CO})_3\text{W} + \text{H}]^+$ could be identified at m/z 566.145 (calc. 566.143 u for $[\text{C}_{18}\text{H}_{23}\text{BN}_6\text{O}_3\text{W}]^+$) with small underlying amounts of the ion $[\text{Tp}'(\text{CO})_3\text{W}]^+$, which supposedly originated from the $[\text{M} + \text{H}]^+$ and $[\text{M}]^{+\bullet}$ molecular ions, respectively.

The CID spectrum of the molecular ion of **2-Mo** at m/z 836 mainly shows carbonyl ligand dissociations (Figure 13). With a CID activation energy of 12 eV, the first CO dissociation to m/z 808.220 ($[\text{M} - \text{CO}]^+$) is most prominent, whereas the second carbonyl dissociation is only observed for the co-excited $[\text{M} + \text{H}]^+$ ion to $[\text{M} + \text{H} - 2\text{CO}]^+$ at m/z 781.232 (calc. 781.232 u for $[\text{C}_{39}\text{H}_{48}\text{BGeMoN}_6\text{O}]^+$). Due to residual water in the ion trap, which tends to coordinate to free metal binding sites, a $[\text{M} - \text{CO} + \text{H}_2\text{O}]^+$ water adduct of the singly decarbonylated germylidene complex is formed as well at m/z 826.229. Finally, the spectrum shows the fragment $[\text{M} + \text{H} - [\text{H}_8\text{C}_5\text{N}_2]]^+$ at m/z 741.153 with low intensity, which can be rationalized by cleavage of a pyrazole unit $[\text{H}_8\text{C}_5\text{N}_2]$ off the Tp' ligand again from the protonated molecular ion $[\text{M} + \text{H}]^{+\bullet}$ (calc. 741.153 u for

$[\text{C}_{36}\text{H}_{40}\text{BGeMoN}_4\text{O}_2]^+$). This fragment is reproduced in the HCD spectrum at 12 eV with the whole mass pattern isolated (Figure 14(b)), as well as an additional water adduct of this ion at m/z 759.163 along with the other ions $[\text{M} - \text{CO}]^{+\bullet}$ and $[\text{M} - \text{CO} + \text{H}_2\text{O}]^{+\bullet}$ already found by the CID experiments. However, in contrast to the fragment $[\text{M} + \text{H} - 2\text{CO}]^+$ seen in the CID spectra, here the $[\text{M} - 2\text{CO} - \text{H}_2]^{+\bullet}$ ion at m/z 778.206 (calc. 778.209 u for $[\text{C}_{39}\text{H}_{45}\text{BGeMoN}_6]^+$) superimposes the $[\text{M} + \text{H} - 2\text{CO}]^+$ signal with slightly higher intensity. Interestingly, when only the signal at m/z 836 is mass-selected, the dihydrogen cleavage is not observed and the fragment $[\text{M} - 2\text{CO}]^{+\bullet}$ at m/z 780.232 is obtained. Also, the cleavage of the pyrazole ring from the Tp' ligand is now found at m/z 740.153 for $[\text{M} - [\text{H}_8\text{C}_5\text{N}_2]]^{+\bullet}$ together with its water adduct at m/z 758.163.

Analogously, the CID spectrum in Figure 15 of the mass-selected molecular ion of **2-W** at m/z 922 shows the sequential carbonyl loss to m/z 894.267 and 886.269 (calc. 894.264 u and 866.269 u for $[\text{C}_{40}\text{H}_{47}\text{BGeN}_6\text{OW}]^+$ and $[\text{C}_{39}\text{H}_{47}\text{BGeN}_6\text{W}]^+$, respectively), with a water adduct $[\text{M} - \text{CO} + \text{H}_2\text{O}]^{+\bullet}$ of the first at m/z 912.275 and a subsequent dihydrogen loss $[\text{M} - 2\text{CO} - \text{H}_2]^{+\bullet}$ at m/z 864.254 for the latter. In contrast, the recorded HCD spectra of **2-W** (Figure 16) appear to be more complex with matching fragmentations between that with the whole isotope pattern mass-selected and that with only

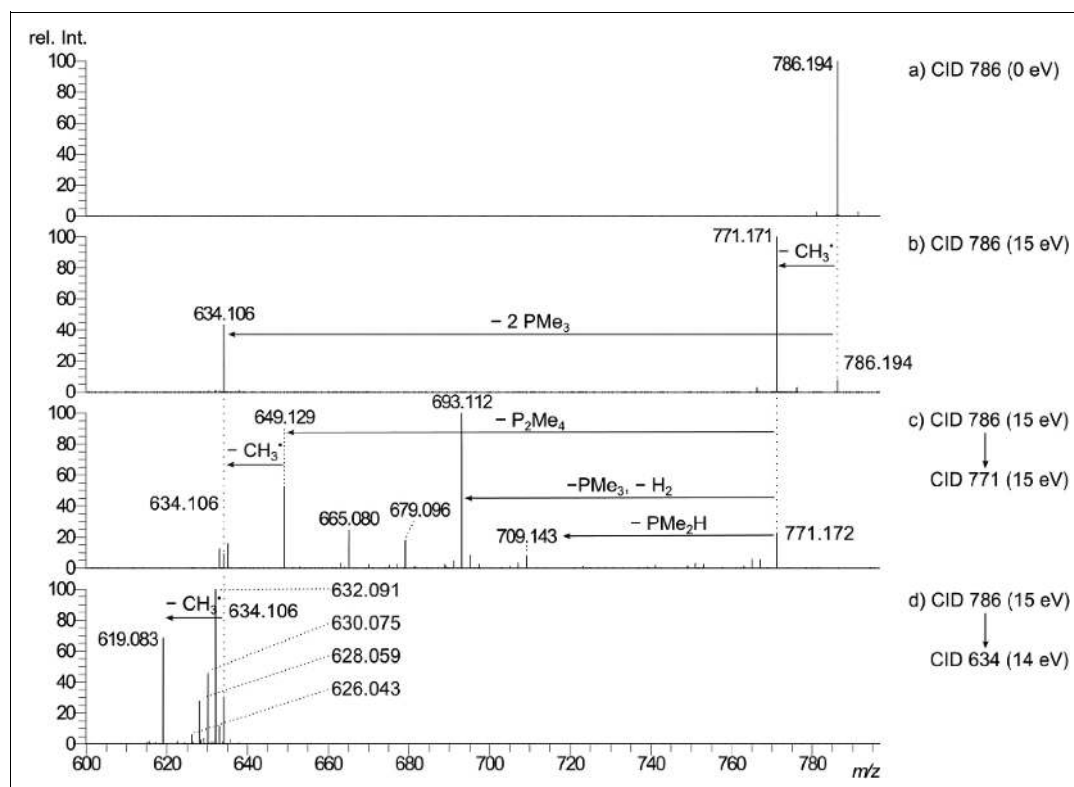


Figure 9. APCI-Orbitrap CID spectra for the fragmentation of **1-W** with mass selection of the most abundant signal in the isotope pattern (m/z 786) with 0 eV (a) and 15 eV (b), and the further activation of the mass-selected fragment ions m/z 771 at 15 eV (c) and m/z 634 at 14 eV (d) in MS^3 experiments.

the most abundant signal at m/z 922. Except for the carbonyl expulsions, a cleavage of $[CH_3CN]$ at m/z 825.243 from the decarbonylated fragment $[M-2CO]^{+\bullet}$ is observed (calc. 825.243 u for $[C_{37}H_{44}BGeN_5W]^+$), which is plausible for pyrazole rings like the Tp' ligand comprises.^{30,31} Another fragmentation based on the $[M-2CO]^{+\bullet}$ is the loss of a pyrazole ring at m/z 770.204 (calc. 770.200 u for $[C_{34}H_{39}BGeN_4W]^+$) as seen before from the (protonated) molecular ions of the Mo species.

A very interesting feature of Figure 16 is the presence of the $[Tp'WH]^+$ fragment at m/z 482.159 (and its water adduct $[Tp'WH+H_2O]^+$ at m/z 500.169), caused by $W\equiv Ge$ triple bond cleavage after excitation of the molecular ion $[M]^+$. As these signals are also present in the HCD spectrum with mass selection of only m/z 922, we think they are unlikely to originate from the $[M+H]^+$ parent ion as the amount of $[M+H]^+$ present is found quite low in **2-W** in contrast to **2-Mo** (cf. the isotope pattern zoom of Figures 11 and 12.). Instead, it is possible that, upon $W\equiv Ge$ bond breaking, one of the flanking methyl groups of the Ar^{Mes} substituent is activated by the metal centre in the reactive $[M]^{+\bullet}$ ion. Abstraction of one proton from there leads to the observed ion and the neutral $[GeAr^{Mes}-H]$ fragment, which probably undergoes consecutive rearrangements to stabilize the electronically unsaturated germanium atom.

Conclusion

A novel mass-spectrometric study of group 6 germylidyne complexes, namely $[Cp(PMe_3)_2M\equiv GeAr^{Mes}]$ and $[Tp'(CO)_2M\equiv GeAr^{Mes}]$ ($M = Mo, W$) was performed despite the high sensitivity of these compounds towards air and moisture. Both the LIFDI and APCI ionization methods in combination with advanced Schlenk and glovebox technique enabled us to record mass spectra without considerable amounts of degradation, comprising the molecular ions $[M]^+$ as base peaks in all cases. Furthermore, CID and HCD experiments were performed for this class of compounds for the very first time. The fragmentation patterns not only comprise the expected losses of phosphane and carbonyl ligands but also indicate C-H bond activation by the electron-deficient metal centre. Although degradation in solution before ionization can obviously destroy the $M\equiv Ge$ triple bond, its cleavage is not observed upon gas-phase activation for the Mo species and only as a minor pathway for the W compounds, pointing towards the high bonding energy between metal and tetrel. The higher reactivity of the tungsten germylidyne complexes is also visible in the preferred methyl abstraction in the phosphane complex **1-W** compared to **1-Mo**. With this first step being successful, we aim to study the gas-phase behaviour of other

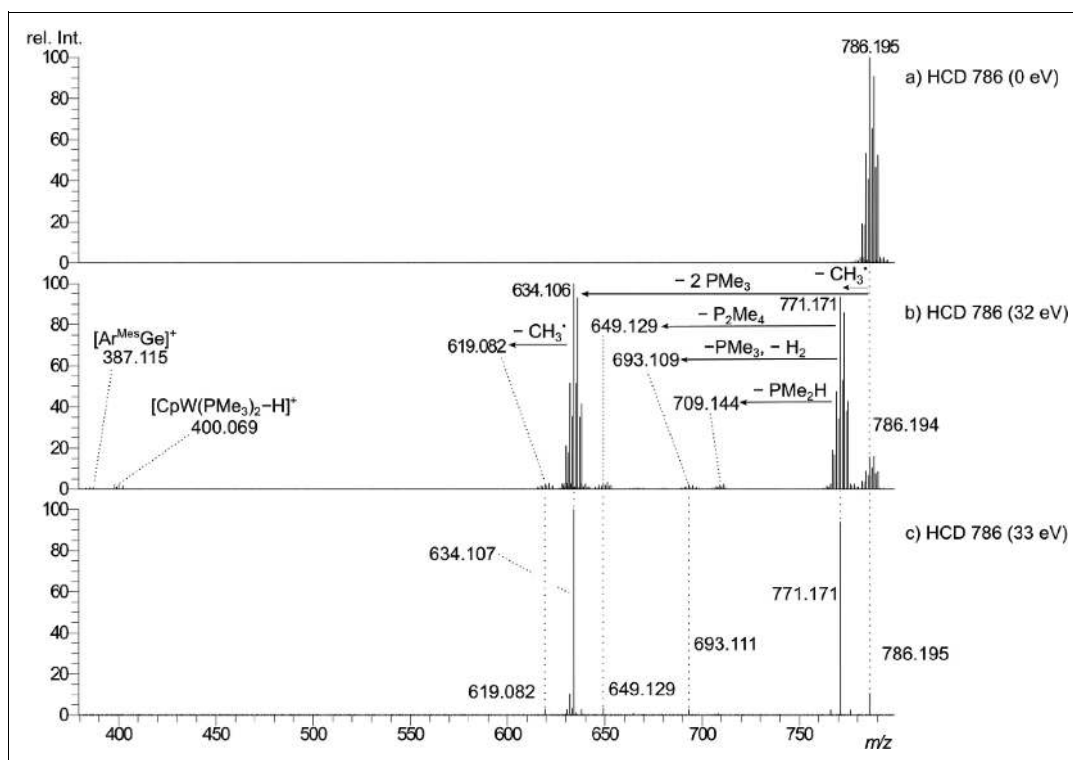


Figure 10. APCI-Orbitrap HCD spectra for the fragmentation of **1-W**. The whole isotope pattern was mass-selected for (a) and (b) and only the signal at m/z 786 for (c).

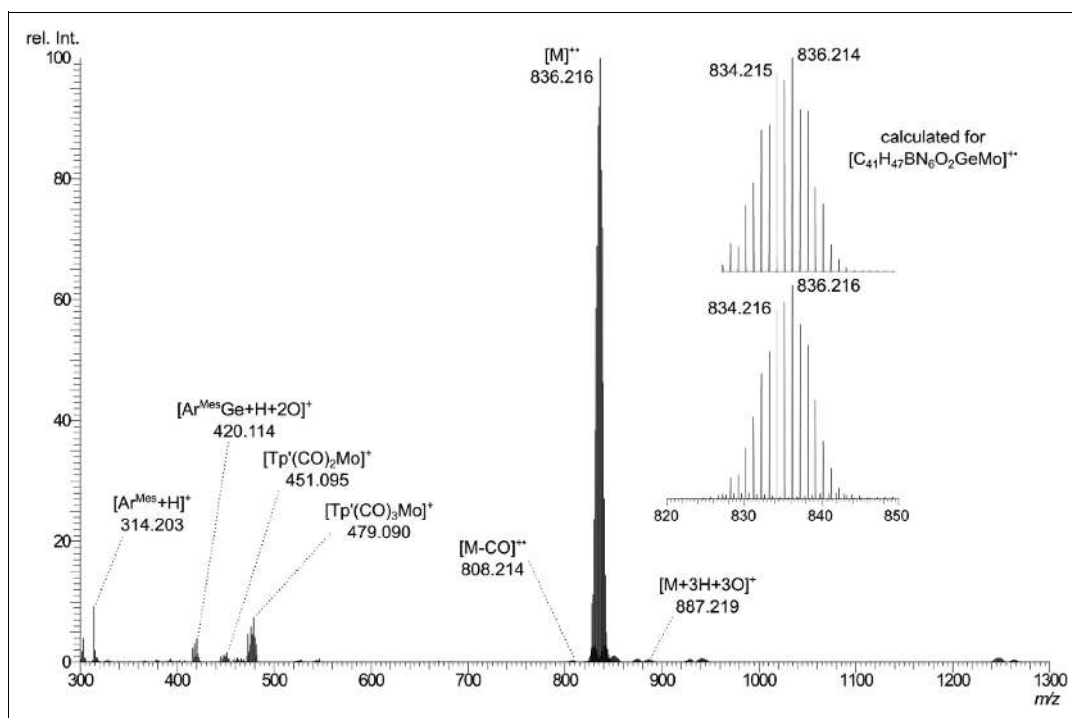


Figure 11. APCI-Orbitrap spectrum of **2-Mo**. The insert shows a zoom of the $[M]^{++}$ m/z region and the calculated isotope pattern for comparison.

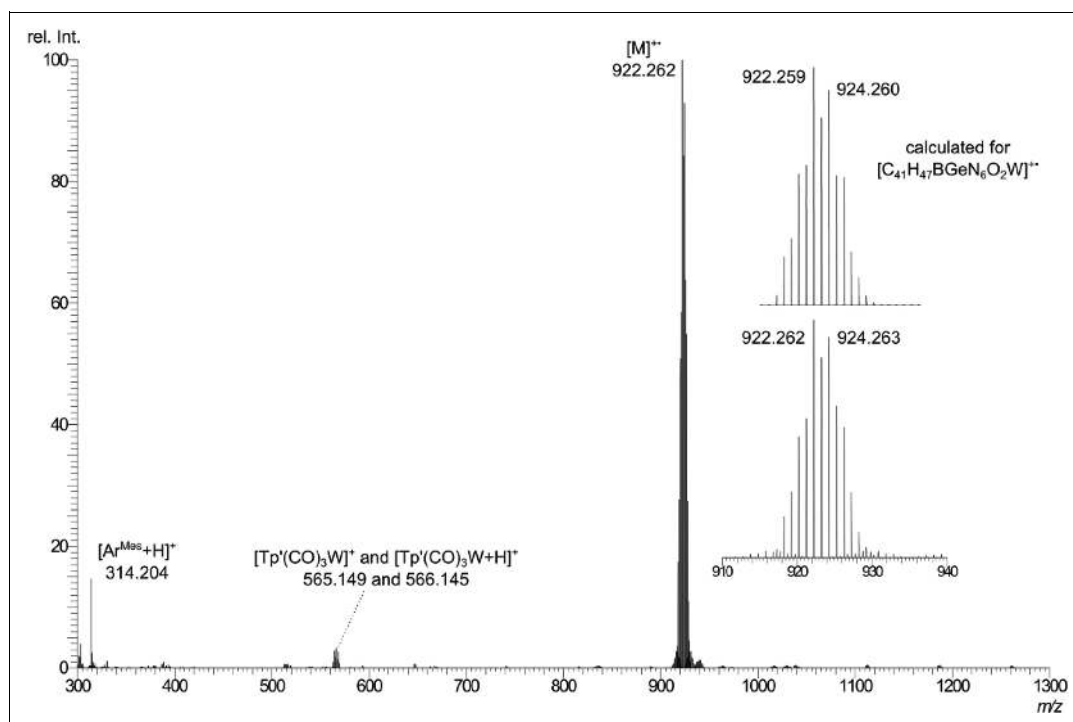


Figure 12. APCI-Orbitrap spectrum of **2-W**. The insert shows a zoom of the $[M]^{2+}$ m/z region and the calculated isotope pattern for comparison.

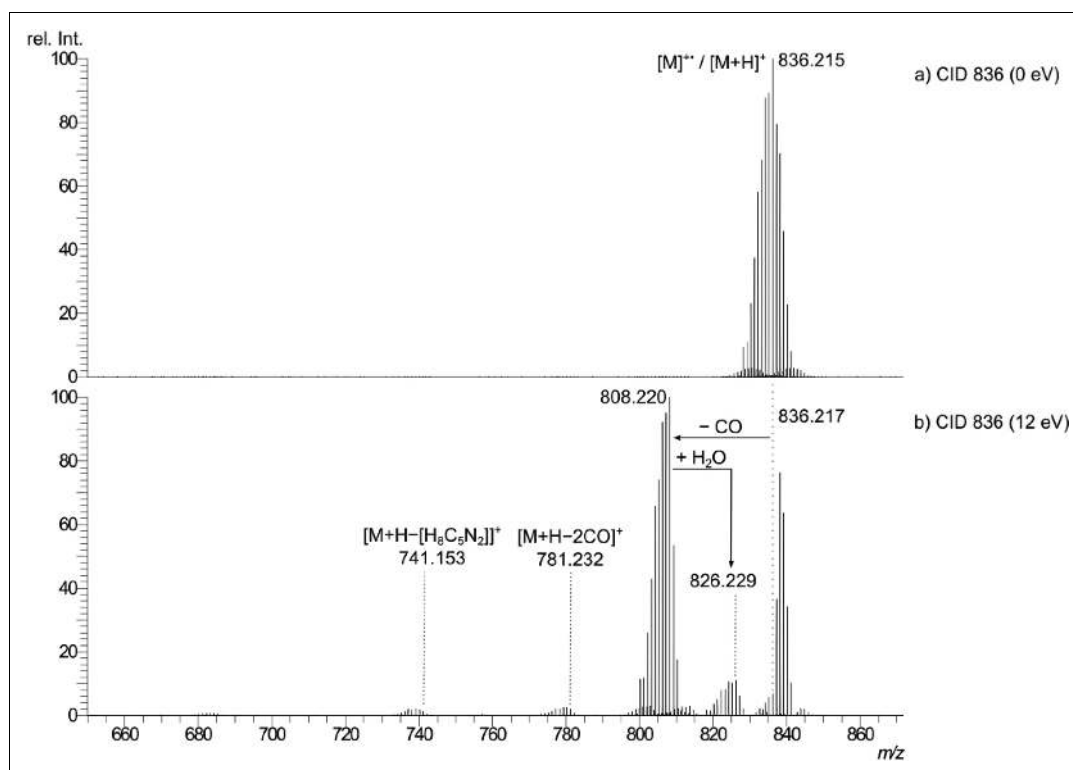


Figure 13. APCI-Orbitrap CID spectra for the fragmentation of **2-Mo** with mass selection of whole m/z 836 isotope pattern with 0 eV (a) and 12 eV (b).

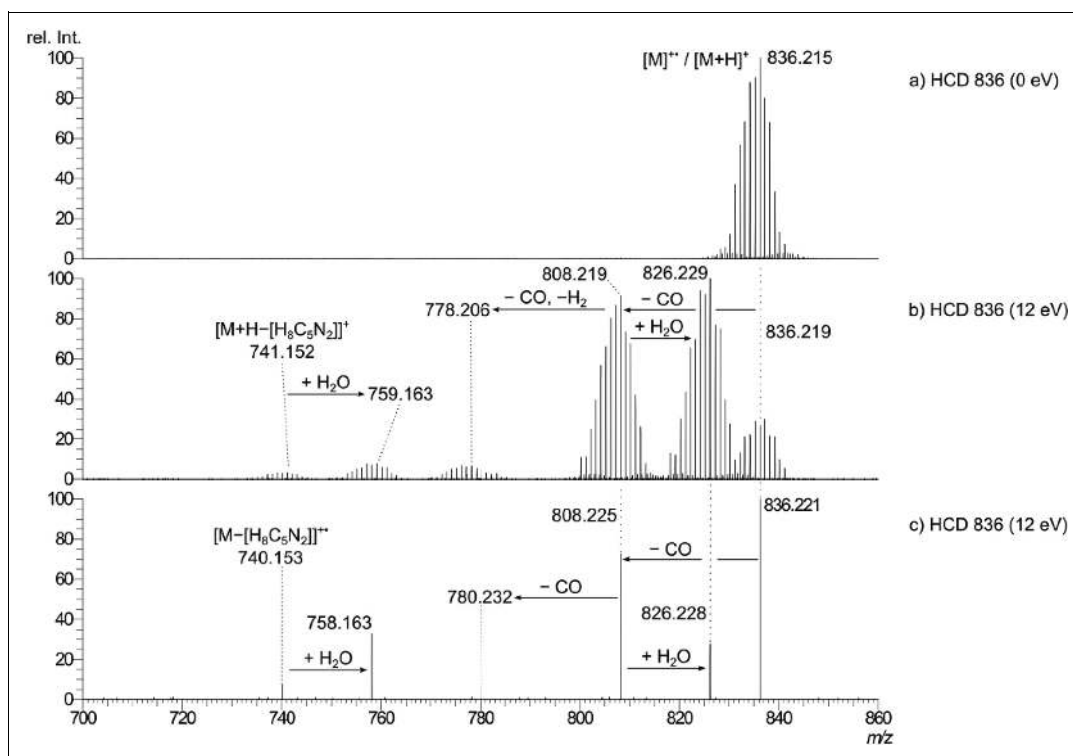


Figure 14. APCI-Orbitrap HCD spectra for the fragmentation of **2-Mo**. The whole isotope pattern was mass-selected for (a) and (b) and only the signal at m/z 836 for (c).

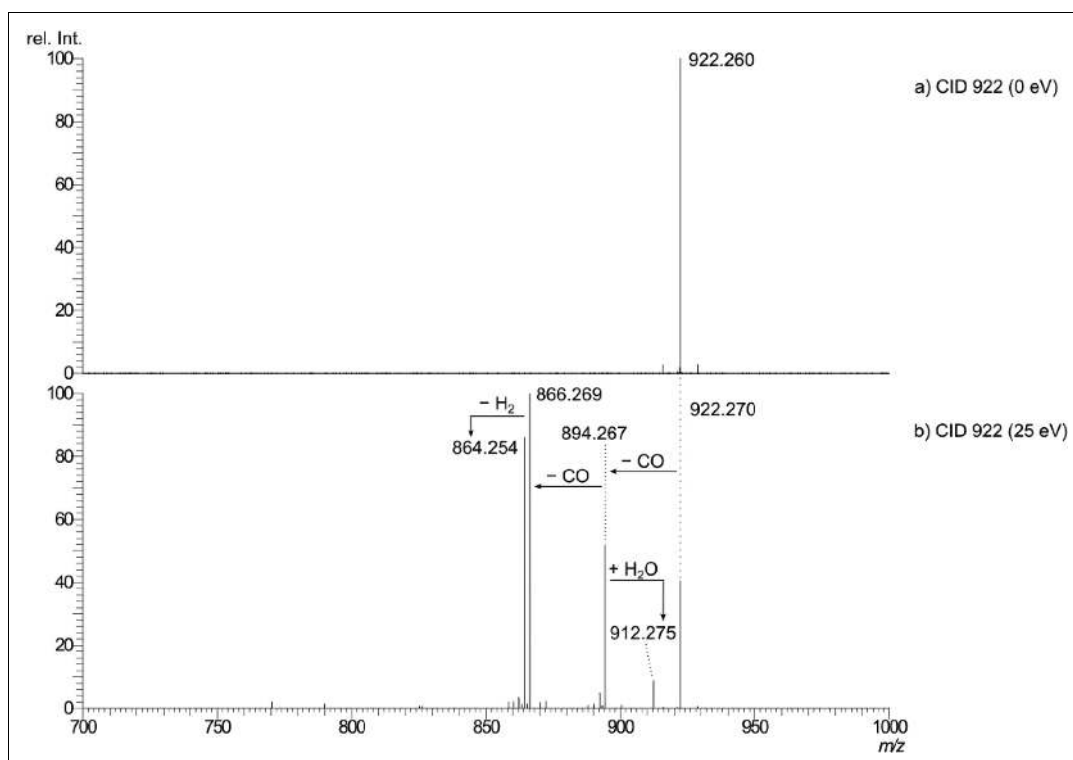


Figure 15. APCI-Orbitrap CID spectra for the fragmentation of **2-W** with mass selection of the most abundant signal in the isotope pattern (m/z 922) with 0 eV (a) and 25 eV (b).

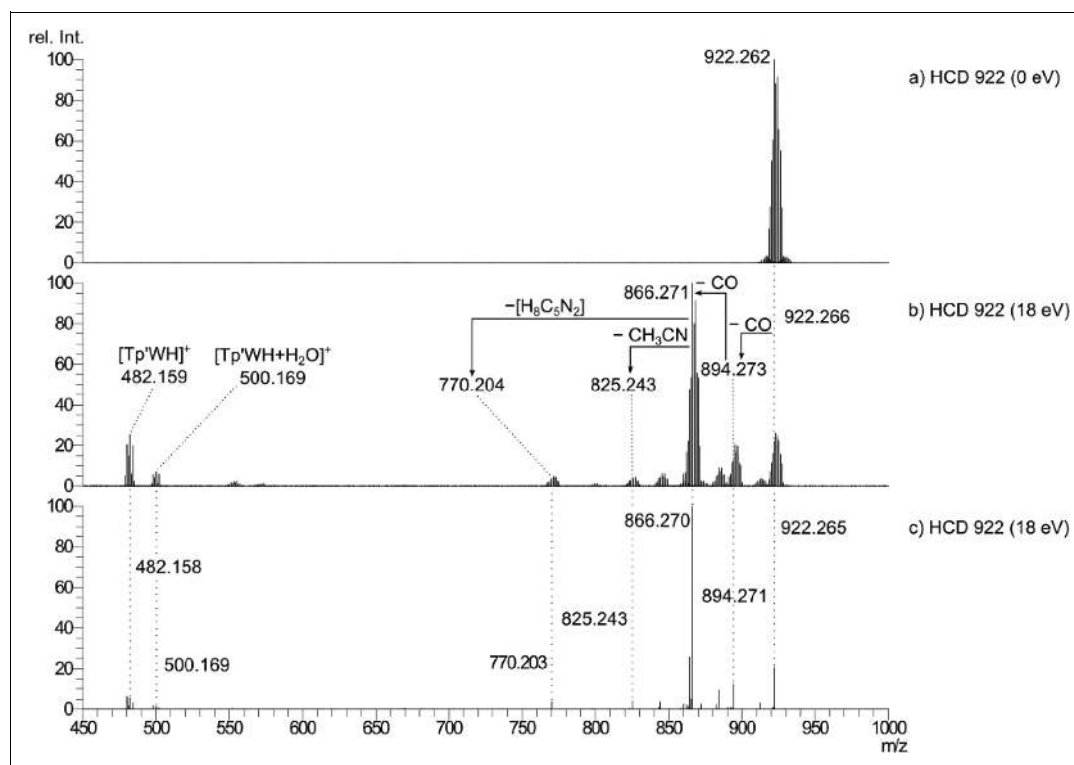


Figure 16. APCI-Orbitrap HCD spectra for the fragmentation of **2-W**. The whole isotope pattern was mass-selected for (a) and (b) and only the signal at m/z 922 for (c).

tetrelidyne complexes, including those with different metal and tetrel atoms.

Acknowledgements

The authors thank the Rheinische-Friedrich-Wilhelms-Universität Bonn and the Institute of Inorganic Chemistry for the financial support of this work. L.R.M. thanks the Fonds of the Chemical Industry for the financial support with a Kekulé Fellowship. The authors are very grateful to Prof. A.C. Filippou and his group for the intellectual input and for the lab expertise. The authors also thank the group of Prof. A.C. Filippou and particularly Dr C. Lindlahr and Dr P. Ghana for providing compounds **1-M** and **2-M**.



Declaration of conflicting interests

The author(s) declared no potential conflicts of interest with respect to the research, authorship, and/or publication of this article.

Funding

The author(s) disclosed receipt of the following financial support for the research, authorship, and/or publication of this article: This work was supported by the Fond der Chemischen Industrie (Kekulé-Fellowship for LRM).

ORCID iDs

Leonard R. Maurer  <https://orcid.org/0000-0003-2433-1130>
 Marianne Engeser  <https://orcid.org/0000-0001-6987-4126>

Supplemental material

Supplemental material for this article is available online. The LIFDI-MAT90 spectrum of **1-W** averaged over the full measurement is available in the Supporting Information.

References

1. Fischer EO, Kreis G, Kreiter CG, et al. *trans*-Halogeno [alkyl(aryl)carbyne]tetracarbonyl complexes of chromium, molybdenum, and Tungsten – A new class of compounds having a transition metal-carbon triple bond. *Angewandte Chemie International Edition in English* 1973; 12: 564–565.
2. E. O. Fischer also gives an overview on carbene and carbyne complexes during his own Nobel lecture: Fischer, EO., Nobel Lecture, December 11, 1973 (<https://www.nobelprize.org/uploads/2018/06/fischer-lecture.pdf>), see also Fischer EO. Auf dem Weg zu Carben- und Carbin-Komplexen (Nobel-Vortrag). *Angewandte Chemie* 1974; 86: 651.
3. Guggenberger LJ and Schrock RR. Tantalum carbyne complex. *Journal of the American Chemical Society* 1975; 97: 2935–2935.
4. Taylor TE and Hall MB. Theoretical comparison between nucleophilic and electrophilic transition metal carbenes using generalized molecular orbital and configuration interaction methods. *Journal of the American Chemical Society* 1984; 106: 1576–1584.
5. Vyboishchikov SF and Frenking G. Structure and bonding of low-valent (Fischer-type) and high-valent (Schrock-type) transition metal carbyne complexes. *Chemistry—A European Journal* 1998; 4: 1439–1448.

6. Fischer H, Hofmann P, Kreissl FR, et al. *Carbyne Complexes*. Weinheim: Wiley-VCH, 1988.
7. Schrock, R. R., Nobel Lecture, December 8, 2005 (<https://www.nobelprize.org/uploads/2018/06/schrock-lecture.pdf>); see also Schrock RR. Multiple metal-carbon bonds for catalytic metathesis reactions (nobel lecture). *Angewandte Chemie* 2006; 118: 3832; *Angew Chem Int Ed* 2006; 45: 3748.
8. Simons RS and Power PP. ($\eta^5\text{-C}_5\text{H}_5$)(CO)₂MoGeC₆H₃-2,6-Mes₂: a transition-metal germylyne Complex. *Journal of the American Chemical Society* 1996; 118: 11966–11967.
9. Filippou AC, Portius P, Philippopoulos AI, et al. Triple bonding to tin: synthesis and characterization of the stannylyne Complex *trans*-[Cl(PMe₃)₄W≡Sn–C₆H₃-2,6-Mes₂]. *Angewandte Chemie International Edition* 2003; 42: 445–447.
10. Filippou AC, Rohde H and Schnakenburg G. Triple bond to lead: synthesis and characterization of the plumbylydyne Complex *trans*-[Br(PMe₃)₄Mo≡Pb–C₆H₃-2,6-Trip₂]. *Angewandte Chemie International Edition* 2004; 43: 2243–2247.
11. Filippou AC, Chernov O, Stumpf KW, et al. Metal-Silicon triple bonds: the molybdenum silylydyne Complex [Cp(CO)₂Mo≡Si-R]. *Angewandte Chemie International Edition* 2010; 49: 3296–3300.
12. Hashimoto H and Tobita H. Recent advances in the chemistry of transition metal–silicon/germanium triple-bonded complexes. *Coord Chem Rev* 2018; 355: 362–379.
13. Ghana P. *Synthesis, Characterization and Reactivity of Ylidyne and μ -Ylido Complexes Supported by Scorpionato Ligands*. PhD Thesis, Rheinische Friedrich-Wilhelms-Universität Bonn, Springer Verlag (ISBN 978-3-030-02625-7), 2017.
14. Queen JD, Phung AC, Caputo CA, et al. Metathetical exchange between metal–metal triple bonds. *Journal of the American Chemical Society* 2020; 142: 2233–2237.
15. Ghana P, Rump J, Schnakenburg G, et al. Planar tetracoordinated silicon (ptSi): room-temperature stable compounds containing anti-van't Hoff/Le bel silicon. *Journal of the American Chemical Society* 2021; 143: 420–432.
16. Saini S, Agarwal A and Bose SK. Transition metal chemistry of heavier group 14 congener triple-bonded complexes: syntheses and reactivity. *Dalton Transactions* 2020; 49: 17055–17075.
17. Filippou AC, Schnakenburg G, Philippopoulos AI, et al. Ge₂ trapped by triple bonds between two metal centers: the germylydyne complexes *trans,trans*-[Cl(depe)₂M≡Ge–Ge≡M(depe)₂Cl] (M=Mo, W) and bonding analyses of the M≡Ge–Ge≡M chain. *Angewandte Chemie International Edition* 2005; 44: 5979–5985.
18. Hashimoto H, Fukuda T, Tobita H, et al. Formation of a germylyne Complex: dehydrogenation of a hydrido (hydrogermylene)tungsten Complex with mesityl isocyanate. *Angewandte Chemie International Edition* 2012; 51: 2930–2933.
19. Hicks J, Hadlington TJ, Schenk C, et al. Utilizing steric bulk to stabilize molybdenum aminogermlyne and aminogermlyne complexes. *Organometallics* 2013; 32: 323–329.
20. Yoshimoto T, Hashimoto H, Hayakawa N, et al. A silylyne tungsten Complex having an eind group on silicon: its dimer–monomer equilibrium and cycloaddition reactions with carbodiimide and diaryl ketones. *Organometallics* 2016; 35: 3444–3447.
21. Dhungana TP, Hashimoto H, Ray M, et al. Synthesis of a molybdenum hydrido(hydrogermylene) complex and its conversion to a germylyne complex: another route through dehydrogenation with nitriles. *Organometallics* 2020; 39: 4350–4361.
22. Joshi A, Killeen C, Thiessen T, et al. Handling considerations for the mass spectrometry of reactive organometallic compounds. *Journal of Mass Spectrometry* 2022; 57: Epub ahead of print March 2022: e4807. DOI: 10.1002/jms.4807.
23. Vikse KL, Woods MP and McIndoe JS. Pressurized sample infusion for the continuous analysis of air- and moisture-sensitive reactions using electrospray ionization mass spectrometry. *Organometallics* 2010; 29: 6615–6618.
24. Penafiel J, Hesketh AV, Granot O, et al. Electron ionization mass spectrometric analysis of air- and moisture-sensitive organometallic compounds. *Dalton Transactions* 2016; 45: 15552–15556.
25. Linden HB. Liquid injection field desorption ionization: a new tool for soft ionization of samples including air-sensitive catalysts and non-polar hydrocarbons. *European Journal of Mass Spectrometry* 2004; 10: 459–468.
26. Lindlahr C. *Neuartige Tetrelaylidinkomplexe der Gruppe 6 mit Trialkylphosphanliganden*. Dissertation, University of Bonn, 2014.
27. Ghana P, Arz MI, Chakraborty U, et al. Linearly two-coordinated silicon: transition metal complexes with the functional groups M≡Si–M and M=Si=M. *Journal of the American Chemical Society* 2018; 140: 7187–7198.
28. Trofimenko S. Boron-Pyrazole chemistry. *Journal of the American Chemical Society* 1966; 88: 1842–1844.
29. Papazoglou I. *Unprecedented tetrelidyne complexes of Group 6 and 10 metals*. Dissertation, University of Bonn, 2016.
30. van Thuijl J, Klebe KJ and van Houte JJ. The mass spectra of some pyrazole compounds. *Organic Mass Spectrometry* 1970; 3: 1549–1559.
31. Nishiwaki T. Electron-impact induced fragmentations of pyrazoles. *Journal of the Chemical Society B* 1967; 885–888.

Supporting Information

Group 6 Germylidyne Complexes in the Gas Phase by LIFDI
and APCI Mass Spectrometry

Leonard R. Maurer, Marianne Engeser*

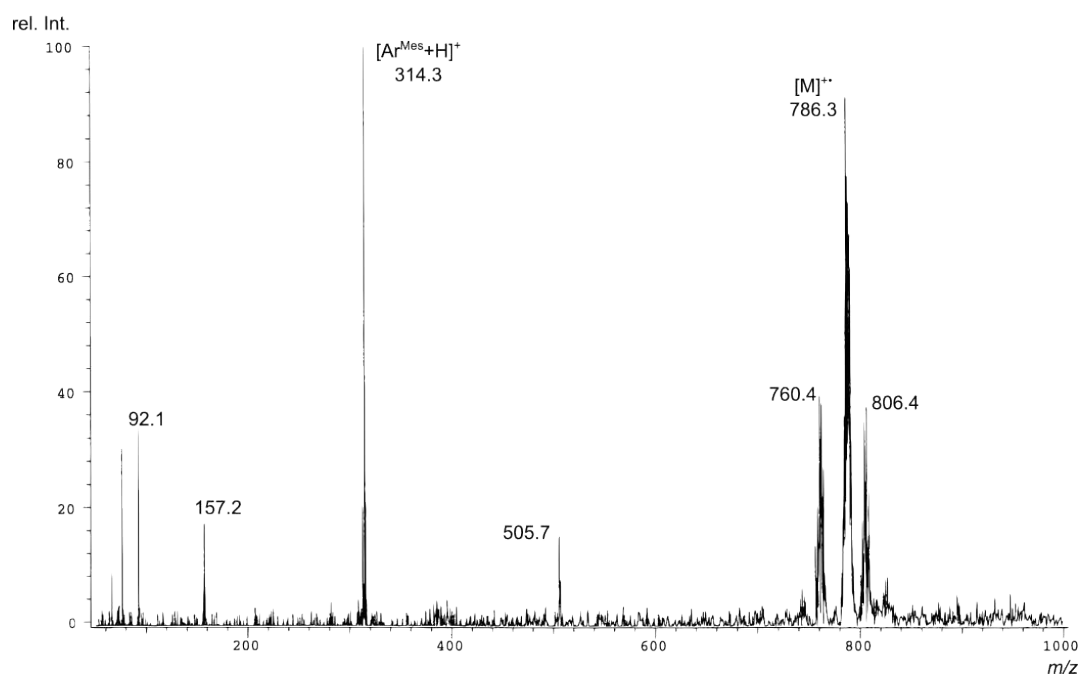


Figure S1. LIFDI-MAT90 spectrum of **1-W** (summation over the full measurement, 54 scans).

List of Abbreviations

1-ad	1-adamantyl
4-dmap	4-dimethylaminopyridine
APCI	atmospheric pressure chemical ionization
Ar ^{Dipp}	2,6-(2,6-(iPr) ₂ -C ₆ H ₃) ₂ -C ₆ H ₃
Ar ^{Mes}	2,6-(2,4,6-(CH ₃) ₃ -C ₆ H ₂) ₂ -C ₆ H ₃
Ar ^{Tripp}	2,6-(2,4,6-(iPr) ₃ -C ₆ H ₂) ₂ -C ₆ H ₃
ATM	Axilrod-Teller-Muto three-body correction
BCE	bond cleavage energy
BDE	bond dissociation energy
BDG	free Gibbs bond dissociation energy
BJ	Becke-Johnson type damping
BSIE	basis set incompleteness error
BSSE	basis set superposition error
CAAC	cyclic alkylaminocarbene
CAAC ^{Me}	C[N(2,6-(iPr) ₂ -C ₆ H ₃)C(CH ₃) ₂ CH ₂ C(CH ₃) ₂]
CC	coupled cluster
CCSD(T)	coupled cluster method with single, double and perturbative triple excitations
CDASi	cyclic dialkylsilylene
CI	configurational interaction
CID	collision induced dissociation
CN	coordination number
Cp	cyclopentadienyl, C ₅ H ₅
Dipp	diisopropylphenyl, 2,6-(iPr) ₂ -C ₆ H ₃
DFA	density functional approximation
DFT	density functional theory
DLPNO-CCSD(T)	domain-based local pair natural orbital CCSD(T)
dme	dimethoxyethane
EDA	energy decomposition analysis
ETS-NOCV	extended transition state method combined with natural orbitals of chemical valence
FMO	fragment molecular orbital
(<i>meta</i> -)GGA	(<i>meta</i> -) generalized gradient approximation
GTO	Gaussian-type orbital
HCD	higher-energy collisional dissociation
HF	Hartree-Fock
HOFMO	highest occupied fragment molecular orbital
HOMO	highest occupied molecular orbital
IAO	intrinsic atomic orbital

IBO	intrinsic bond orbital
IDipp	$C[N(2,6-(iPr)_2-C_6H_3)CH]_2$
IMe ₄	$C[N(CH_3)C(CH_3)]_2$
IiPr ₂ Me ₂	$C[N(iPr)C(CH_3)]_2$
KS-DFT	Kohn-Sham density functional theory
LCAO	linear combination of atomic orbitals
LIFDI	liquid injection field desorption ionization
LMO	localized molecular orbital
LP	electron lone pair
L(S)DA	local (spin) density approximation
LUFMO	lowest unoccupied fragment molecular orbital
LUMO	lowest unoccupied molecular orbital
LV	lone valence
Mes	mesityl, 2,4,6-(CH ₃) ₃ -C ₆ H ₂
MO	molecular orbital
MP2	second-order Møller-Plesset theory
NBO	natural bond orbital
NHC	N-heterocyclic carbene
NHO	natural hybrid orbital
NLS	natural Lewis structure
NMB	natural minimal basis
NO	natural orbital
NPA	natural population analysis
NRT	natural resonance theory
<i>p</i> Tol	<i>para</i> -tolyl
QRRHO	quasi rigid rotor harmonic oscillator
RB	Rydberg basis
sc-XRD	single-crystal X-Ray diffraction
SCF	self consistent field
SD	Slater determinant
SIDipp	$C[N(2,6-(iPr)_2-C_6H_3)CH_2]_2$
SIX	$C[N(2,6-(CH_3)_2)-C_6H_3)CH_2]_2$
SRE	structural relaxation energy
STO	Slater-type orbital
Tbb	2,6-(CH(SiMe ₃) ₂) ₂ -4- <i>t</i> Bu-C ₆ H ₂
TD-DFT	time-dependent density functional theory
thf	tetrahydrofuran
TMS	trimethylsilyl
TP'	κ^3 - <i>N,N,N'</i> -hydridotris(3,5-dimethylpyrazolyl)borate

Tripp	triisopropylphenyl, 2,4,6-(<i>i</i> Pr) ₃ -C ₆ H ₂
VT-NMR	variable temperature nuclear magnetic resonance
WBI	Wiberg bond index
WFT	wave function theory

List of Scientific Contributions

Publications

- M. L. McCrea-Hendrick, M. Bursch, K. L. Gullett, L. R. Maurer, J. C. Fettinger, S. Grimme, P. P. Power. Counterintuitive Interligand Angles in the Diaryls $E\{C_6H_3-2,6-(C_6H_2-2,4,6-iPr_3)_2\}_2$ (E = Ge, Sn, or Pb) and Related Species: The Role of London Dispersion Forces. *Organometallics* **2018**, *37*, 2075-2085. doi: 10.1021/acs.organomet.8b00225
- J. D. Queen, M. Bursch, J. Seibert, L. R. Maurer, B. D. Ellis, J. C. Fettinger, S. Grimme, P. P. Power. Isolation and Computational Studies of a Series of Terphenyl Substituted Diplumbynes with Ligand Dependent Lead–Lead Multiple-Bonding Character. *J. Am. Chem. Soc.* **2019**, *141*, 14370-14383. doi: 10.1021/jacs.9b07072
- L. R. Maurer, M. Bursch, S. Grimme, A. Hansen, Assessing Density Functional Theory for Chemically Relevant Open-Shell Transition Metal Reactions. *J. Chem. Theory Comput.*, **2021**, *17*, 6134–6151. doi: 10.1021/acs.jctc.1c00659
- S. Karwasara, L. R. Maurer, B. Peerless, G. Schnakenburg, U. Das, A. C. Filippou. (NHC)Si=C=N–R: A Two-Coordinated Si⁰-Isocyanide Compound as Si(NHC) Transfer Reagent. *J. Am. Chem. Soc.* **2021**, *143*, 36, 14780–14794. doi: 10.1021/jacs.1c06628
- L. R. Maurer, M. Engeser. Group 6 germylidyne complexes in the gas phase by LIFDI and APCI mass spectrometry. *Eur. J. Mass Spectrom.* **2023**, *29*, 1, 44-57. doi: 10.1177/14690667221137465
- L. R. Maurer, J. Rump, A. C. Filippou. The Electronic Nature of Cationic Group 10 Ylidyne Complexes. *Inorganics*, **2023**, *11*, 3, 129. doi: 10.3390/inorganics11030129
- S. Kumar, L. R. Maurer, G. Schnakenburg, U. Das, A. C. Filippou. NHC-Supported 2-Sila and 2-Germavinylidenes: Synthesis, Dynamics, First Reactivity and Theoretical Studies. *Angew. Chem. Int. Ed.*, **2024**, e202400227.

Presentations

- Lecture: Tetrylidyne Complexes in the Gas Phase: Synergy of Mass Spectrometry and Computational Chemistry. *BIGS Chemistry Summer School 2019*, Bonn, Germany.
- Poster: L. R. Maurer, A. Hansen, M. Bursch, S. Grimme*. The ROST79 data set: A Comprehensive Thermochemical Benchmark of Realistic Open-Shell Single-Reference Transition Metal Complexes. *Molecular Quantum Mechanics 2019*, Heidelberg, Germany.
- Poster: L. R. Maurer, M. Engeser*, A. C. Filippou*. Group 6 Germylidyne Complexes in the Gas Phase by LIFDI and APCI Mass Spectrometry. *BIGS Chemistry Summer School 2022*, Bonn, Germany.

- Poster: P. Palui, F. Gstrein, L. R. Maurer, U. Das, G. Schnakenburg, A. C. Filippou*. Si=Ge Double Bonds: Synthesis and Reactivity of a caac^{Me}-supported Germasilyne. *21st Conference on Inorganic Chemistry 2022*, Marburg, Germany.
- Poster: A. C. Filippou*, G. Schnakenburg, U. Das, O. Chernov, B. Baars, P. Ghana, L. R. Maurer, J. Rump. Five Crests of the Silicon Valley. *TRA Matter "Come and Get Together" Networking Symposium 2022*, Bonn, Germany.
- Poster: L. R. Maurer, S. Kumar, A. C. Filippou*. Two Heteoleptic Siladicarbenes and their Electronic Structure. *10th European Silicon Days 2023*, Montpellier, France.
- Lecture: About Silenylienes & Metalloplumbynes: Unusual low-valent Tetrel Compounds from a Theoretical Perspective. *Inorganic Chemistry Colloquium 2023*, Bonn, Germany.

Bibliography

- [1] F. Jensen, *Introduction to Computational Chemistry*, John Wiley & Sons, Inc., 3rd ed., 2017.
- [2] A. Szabo, N. Ostlund, *Modern Quantum Chemistry: Introduction to Advanced Electronic Structure Theory*, Dover Publications, 1996.
- [3] E. Schrödinger, *Annalen der Physik* 1926, 384, 361–376.
- [4] M. Born, R. Oppenheimer, *Annalen der Physik* 1927, 389, 457–484.
- [5] W. Pauli, *Z. Physik* 1925, 31, 765–783.
- [6] J. C. Slater, *Phys. Rev.* 1929, 34, 1293–1322.
- [7] L. Pauling, *Chem. Rev.* 1928, 5, 173–213.
- [8] J. E. Lennard-Jones, *Trans. Faraday Soc.* 1929, 25, 668.
- [9] C. C. J. Roothaan, *Rev. Mod. Phys.* 1951, 23, 69–89.
- [10] G. G. Hall, *Proc. R. Soc. Lond. A* 1951, 205, 541–552.
- [11] J. G. Hill, *Int. J. of Quantum Chem.* 2013, 113, 21–34.
- [12] F. Jensen, *WIREs Comput. Mol. Sci.* 2013, 3, 273–295.
- [13] W. J. Hehre, R. F. Stewart, J. A. Pople, *J. Chem. Phys.* 1969, 51, 2657–2664.
- [14] R. F. Stewart, *J. Chem. Phys.* 1969, 50, 2485–2495.
- [15] W. J. Hehre, R. Ditchfield, R. F. Stewart, J. A. Pople, *J. Chem. Phys.* 1970, 52, 2769–2773.
- [16] R. Ditchfield, W. J. Hehre, J. A. Pople, *J. Chem. Phys.* 1971, 54, 724–728.
- [17] W. J. Hehre, R. Ditchfield, J. A. Pople, *J. Chem. Phys.* 1972, 56, 2257–2261.
- [18] J. S. Binkley, J. A. Pople, W. J. Hehre, *J. Am. Chem. Soc.* 1980, 102, 939–947.
- [19] M. S. Gordon, J. S. Binkley, J. A. Pople, W. J. Pietro, W. J. Hehre, *J. Am. Chem. Soc.* 1982, 104, 2797–2803.
- [20] R. Krishnan, J. S. Binkley, R. Seeger, J. A. Pople, *J. Chem. Phys.* 1980, 72, 650–654.

- [21] T. H. Dunning, *J. Chem. Phys.* **1989**, *90*, 1007–1023.
- [22] A. Schäfer, H. Horn, R. Ahlrichs, *J. Chem. Phys.* **1992**, *97*, 2571–2577.
- [23] A. Schäfer, C. Huber, R. Ahlrichs, *J. Chem. Phys.* **1994**, *100*, 5829–5835.
- [24] F. Weigend, F. Furche, R. Ahlrichs, *J. Chem. Phys.* **2003**, *119*, 12753–12762.
- [25] F. Weigend, R. Ahlrichs, *Phys. Chem. Chem. Phys.* **2005**, *7*, 3297.
- [26] F. B. Van Duijneveldt, J. G. C. M. Van Duijneveldt-van De Rijdt, J. H. Van Lenthe, *Chem. Rev.* **1994**, *94*, 1873–1885.
- [27] G. Frenking, I. Antes, M. Böhme, S. Dapprich, A. W. Ehlers, V. Jonas, A. Neuhaus, M. Otto, R. Stegmann, A. Veldkamp, S. F. Vyboishchikov in *Reviews in Computational Chemistry, Vol. 8* (Eds.: K. B. Lipkowitz, D. B. Boyd), Wiley, 1st ed., **1996**, pp. 63–144.
- [28] T. R. Cundari, M. T. Benson, M. L. Lutz, S. O. Sommerer in *Reviews in Computational Chemistry, Vol. 8* (Eds.: K. B. Lipkowitz, D. B. Boyd), Wiley, 1st ed., **1996**, pp. 145–202.
- [29] M. Dolg, X. Cao, *Chem. Rev.* **2012**, *112*, 403–480.
- [30] D. Andrae, U. Häußermann, M. Dolg, H. Stoll, H. Preuß, *Theoret. Chim. Acta* **1990**, *77*, 123–141.
- [31] I. Shavitt in *Methods of Electronic Structure Theory* (Ed.: H. F. Schaefer), Springer US, Boston, MA, **1977**, pp. 189–275.
- [32] C. David Sherrill, H. F. Schaefer in *Advances in Quantum Chemistry, Vol. 34*, Elsevier, **1999**, pp. 143–269.
- [33] D. Cremer, *WIREs Comput. Mol. Sci.* **2013**, *3*, 482–503.
- [34] F. Coester, H. Kümmel, *Nuclear Physics* **1960**, *17*, 477–485.
- [35] R. J. Bartlett, M. Musiał, *Rev. Mod. Phys.* **2007**, *79*, 291–352.
- [36] K. Raghavachari, G. W. Trucks, J. A. Pople, M. Head-Gordon, *Chem. Phys. Lett.* **1989**, *157*, 479–483.
- [37] T. D. Crawford, H. F. Schaefer in *Reviews in Computational Chemistry, Vol. 14* (Eds.: K. B. Lipkowitz, D. B. Boyd), Wiley, 1st ed., **2000**, pp. 33–136.
- [38] R. J. Bartlett in *Theory and Applications of Computational Chemistry*, Elsevier, **2005**, pp. 1191–1221.
- [39] K. A. Peterson, D. Feller, D. A. Dixon, *Theor. Chem. Acc.* **2012**, *131*, 1079.

-
- [40] Z. Fang, M. Vasiliu, K. A. Peterson, D. A. Dixon, *J. Chem. Theory Comput.* **2017**, *13*, 1057–1066.
- [41] C. Riplinger, B. Sandhoefer, A. Hansen, F. Neese, *J. Chem. Phys.* **2013**, *139*, 134101.
- [42] Chr. Møller, M. S. Plesset, *Phys. Rev.* **1934**, *46*, 618–622.
- [43] D. Cremer, *WIREs Comput. Mol. Sci.* **2011**, *1*, 509–530.
- [44] P. Hohenberg, W. Kohn, *Phys. Rev.* **1964**, *136*, B864–B871.
- [45] R. O. Jones, *Rev. Mod. Phys.* **2015**, *87*, 897–923.
- [46] M. G. Medvedev, I. S. Bushmarinov, J. Sun, J. P. Perdew, K. A. Lyssenko, *Science* **2017**, *355*, 49–52.
- [47] L. H. Thomas, *Math. Proc. Camb. Phil. Soc.* **1927**, *23*, 542–548.
- [48] E. Fermi, *Rend. Accad. Naz. Lincei* **1927**, *6*, 602–607.
- [49] E. Fermi, *Z. Physik* **1928**, *48*, 73–79.
- [50] F. Bloch, *Z. Physik* **1929**, *57*, 545–555.
- [51] P. A. M. Dirac, *Math. Proc. Cambridge Philos. Soc.* **1930**, *26*, 376.
- [52] W. Kohn, L. J. Sham, *Phys. Rev.* **1965**, *140*, A1133–A1138.
- [53] S. F. Sousa, P. A. Fernandes, M. J. Ramos, *J. Phys. Chem. A* **2007**, *111*, 10439–10452.
- [54] L. Goerigk, A. Hansen, C. Bauer, S. Ehrlich, A. Najibi, S. Grimme, *Phys. Chem. Chem. Phys.* **2017**, *19*, 32184–32215.
- [55] J. P. Perdew, K. Schmidt, *AIP Conference Proceedings*, Antwerp (Belgium), **2001**, pp. 1–20.
- [56] M. Bursch, PhD thesis, Rheinische Friedrich-Wilhelms-Universität Bonn, Bonn, **2021**.
- [57] M. Bursch, J.-M. Mewes, A. Hansen, S. Grimme, *Angew. Chem.* **2022**, *134*, e202205735.
- [58] A. D. Becke, *J. Chem. Phys.* **1998**, *109*, 2092–2098.
- [59] J. M. Tao, J. P. Perdew, V. N. Staroverov, Scuseria, G. E., *Phys. Rev. Lett.* **2003**, *91*, 146401.
- [60] J. Harris, *Phys. Rev. A* **1984**, *29*, 1648–1659.
- [61] A. D. Becke, *J. Chem. Phys.* **1993**, *98*, 1372–1377.
- [62] T. Tsuneda, K. Hirao, *WIREs Comput. Mol. Sci.* **2014**, *4*, 375–390.

- [63] L. Goerigk, S. Grimme, *WIREs Comput. Mol. Sci.* **2014**, *4*, 576–600.
- [64] R. Eisenschitz, F. London, *Z. Physik* **1930**, *60*, 491–527.
- [65] F. London, *Z. Physik* **1930**, *63*, 245–279.
- [66] S. Grimme, A. Hansen, J. G. Brandenburg, C. Bannwarth, *Chem. Rev.* **2016**, *116*, 5105–5154.
- [67] O. A. Vydrov, T. V. Voorhis, *J. Chem. Phys.* **2010**, *133*, 244103.
- [68] S. Grimme, *J. Comput. Chem.* **2004**, *25*, 1463–1473.
- [69] S. Grimme, *J. Comput. Chem.* **2006**, *27*, 1787–1799.
- [70] S. Grimme, J. Antony, S. Ehrlich, H. Krieg, *J. Chem. Phys.* **2010**, *132*, 154104.
- [71] E. Caldeweyher, C. Bannwarth, S. Grimme, *J. Chem. Phys.* **2017**, *147*, 034112.
- [72] S. Grimme, S. Ehrlich, L. Goerigk, *J. Comput. Chem.* **2011**, *32*, 1456–1465.
- [73] B. M. Axilrod, E. Teller, *J. Chem. Phys.* **1943**, *11*, 299–300.
- [74] Y. Muto, *Proc. Phys. Math. Soc. Jpn.* **1943**, *17*, 629.
- [75] M. Bursch, E. Caldeweyher, A. Hansen, H. Neugebauer, S. Ehlert, S. Grimme, *Acc. Chem. Res.* **2019**, *52*, 258–266.
- [76] J. E. Lennard-Jones, J. A. Pople, *Proc. R. Soc. Lond. A* **1950**, *202*, 166–180.
- [77] C. Edmiston, K. Ruedenberg, *Rev. Mod. Phys.* **1963**, *35*, 457–464.
- [78] P. Pinski, C. Riplinger, E. F. Valeev, F. Neese, *J. Chem. Phys.* **2015**, *143*, 034108.
- [79] V. Fock, *Z. Physik* **1930**, *61*, 126–148.
- [80] C. Edmiston, K. Ruedenberg, *J. Chem. Phys.* **1965**, *43*, S97–S116.
- [81] W. Von Niessen, *J. Chem. Phys.* **1972**, *56*, 4290–4297.
- [82] J. M. Foster, S. F. Boys, *Rev. Mod. Phys.* **1960**, *32*, 300–302.
- [83] J. Pipek, P. G. Mezey, *J. Chem. Phys.* **1989**, *90*, 4916–4926.
- [84] R. S. Mulliken, *J. Chem. Phys.* **1955**, *23*, 1833–1840.
- [85] R. S. Mulliken, *J. Chem. Phys.* **1955**, *23*, 1841–1846.
- [86] A. E. Reed, R. B. Weinstock, F. Weinhold, *J. Chem. Phys.* **1985**, *83*, 735–746.

-
- [87] C. Fonseca Guerra, J.-W. Handgraaf, E. J. Baerends, F. M. Bickelhaupt, *J. Comput. Chem.* **2004**, *25*, 189–210.
- [88] S. Dubillard, J.-B. Rota, T. Saue, K. Faegri, *J. Chem. Phys.* **2006**, *124*, 154307.
- [89] I.-M. Høyvik, B. Jansik, P. Jørgensen, *J. Comput. Chem.* **2013**, *34*, 1456–1462.
- [90] S. Lehtola, H. Jónsson, *J. Chem. Theory Comput.* **2014**, *10*, 642–649.
- [91] B. Rousseau, A. Peeters, C. Van Alsenoy, *Journal of Molecular Structure: THEOCHEM* **2001**, *538*, 235–238.
- [92] F. L. Hirshfeld, *Theoret. Chim. Acta* **1977**, *44*, 129–138.
- [93] K. Fægri, T. Saue, *J. Chem. Phys.* **2001**, *115*, 2456–2464.
- [94] G. Knizia, *J. Chem. Theory Comput.* **2013**, *9*, 4834–4843.
- [95] J. P. Foster, F. Weinhold, *J. Am. Chem. Soc.* **1980**, *102*, 7211–7218.
- [96] A. E. Reed, F. Weinhold, *J. Chem. Phys.* **1985**, *83*, 1736–1740.
- [97] F. Weinhold, C. Landis, E. Glendening, *International Reviews in Physical Chemistry* **2016**, *35*, 399–440.
- [98] P.-O. Löwdin, *Phys. Rev.* **1955**, *97*, 1474–1489.
- [99] E. D. Glendening, F. Weinhold, *J. Comput. Chem.* **1998**, *19*, 593–609.
- [100] E. D. Glendening, F. Weinhold, *J. Comput. Chem.* **1998**, *19*, 610–627.
- [101] E. D. Glendening, J. K. Badenhop, F. Weinhold, *J. Comput. Chem.* **1998**, *19*, 628–646.
- [102] L. Pauling, G. W. Wheland, *J. Chem. Phys.* **1933**, *1*, 362–374.
- [103] Y. Wang, *J. Comput. Chem.* **2021**, *42*, 412–417.
- [104] F. Weinhold, E. D. Glendening, *J. Comput. Chem.* **2021**, *42*, 1338–1340.
- [105] Y. Wang, *J. Comput. Chem.* **2021**, *42*, 1341–1343.
- [106] M. Bursch, T. Gasevic, J. B. Stückrath, S. Grimme, *Inorg. Chem.* **2021**, *60*, 272–285.
- [107] L. Goerigk, S. Grimme, *J. Chem. Theory Comput.* **2011**, *7*, 291–309.
- [108] S. Dohm, A. Hansen, M. Steinmetz, S. Grimme, M. P. Checinski, *J. Chem. Theory Comput.* **2018**, *14*, 2596–2608.
- [109] L. R. Maurer, M. Bursch, S. Grimme, A. Hansen, *J. Chem. Theory Comput.* **2021**, *17*, 6134–6151.

- [110] B. Metz, H. Stoll, M. Dolg, *J. Chem. Phys.* **2000**, *113*, 2563–2569.
- [111] O. Vahtras, J. Almlöf, M. W. Feyereisen, *Chem. Phys. Lett.* **1993**, *213*, 514–518.
- [112] F. Weigend, *Phys. Chem. Chem. Phys.* **2006**, *8*, 1057.
- [113] F. Weigend, M. Kattannek, R. Ahlrichs, *J. Chem. Phys.* **2009**, *130*, 164106.
- [114] F. Weigend, *J. Comput. Chem.* **2008**, *29*, 167–175.
- [115] A. Hellweg, C. Hättig, S. Höfener, W. Klopper, *Theor. Chem. Acc.* **2007**, *117*, 587–597.
- [116] M. D. Hanwell, D. E. Curtis, D. C. Lonie, T. Vandermeersch, E. Zurek, G. R. Hutchison, *J. Cheminf.* **2012**, *4*, 17.
- [117] R. Dennington, T. A. Keith, J. M. Millam, *GaussView*, Semichem Inc. Shawnee Mission KS, **1998**.
- [118] S. Grimme, *Chem. Eur. J.* **2012**, *18*, 9955–9964.
- [119] E. D. Glendening, J. K. Badenhoop, A. E. Reed, J. E. Carpenter, J. A. Bohmann, C. M. Morales, C. R. Landis, F. Weinhold, *NBO 6.0*, Theoretical Chemistry Institute, University of Wisconsin, **2013**.
- [120] E. D. Glendening, J. K. Badenhoop, A. E. Reed, J. E. Carpenter, J. A. Bohmann, C. M. Morales, P. Karafiloglou, C. R. Landis, F. Weinhold, *NBO 7.0*, Theoretical Chemistry Institute, University of Wisconsin, **2018**.
- [121] T. Lu, F. Chen, *J. Comput. Chem.* **2012**, *33*, 580–592.
- [122] E. F. Pettersen, T. D. Goddard, C. C. Huang, G. S. Couch, D. M. Greenblatt, E. C. Meng, T. E. Ferrin, *J. Comput. Chem.* **2004**, *25*, 1605–1612.
- [123] P. M. Zimmerman, *J. Chem. Phys.* **2013**, *138*, 184102.
- [124] V. Ásgeirsson, B. O. Birgisson, R. Bjornsson, U. Becker, F. Neese, C. Riplinger, H. Jónsson, *J. Chem. Theory Comput.* **2021**, *17*, 4929–4945.
- [125] J. Flores, I. Pérez-Juste, L. Carballeira, *Chemical Physics* **2005**, *313*, 1–15.
- [126] M. E. Sanz, M. C. McCarthy, P. Thaddeus, *The Astrophysical Journal* **2002**, *577*, L71–L74.
- [127] C. J. Evans, M. R. Dover, *J. Phys. Chem. A* **2009**, *113*, 8533–8539.
- [128] G. Maier, H. P. Reisenauer, H. Egenolf, J. Glatthaar, *Eur. J. Org. Chem.* **1998**, *1998*, 1307–1311.
- [129] N. Takeda, T. Kajiwara, H. Suzuki, R. Okazaki, N. Tokitoh, *Chem. Eur. J.* **2003**, *9*, 3530–3543.

- [130] T. Abe, T. Iwamoto, C. Kabuto, M. Kira, *J. Am. Chem. Soc.* **2006**, *128*, 4228–4229.
- [131] K. Takeuchi, M. Ichinohe, A. Sekiguchi, *J. Am. Chem. Soc.* **2012**, *134*, 2954–2957.
- [132] C. Ganesamoorthy, J. Schoening, C. Wölper, L. Song, P. R. Schreiner, S. Schulz, *Nat. Chem.* **2020**, *12*, 608–614.
- [133] D. Reiter, R. Holzner, A. Porzelt, P. Frisch, S. Inoue, *Nat. Chem.* **2020**, *12*, 1131–1135.
- [134] L. Zhu, J. Zhang, H. Yang, C. Cui, *J. Am. Chem. Soc.* **2019**, *141*, 19600–19604.
- [135] B. Eichler, R. West in *Advances in Organometallic Chemistry*, Vol. 46, Elsevier, **2000**, pp. 1–46.
- [136] H. Ottosson, A. M. Eklöf, *Coord. Chem. Rev.* **2008**, *252*, 1287–1314.
- [137] K. K. Milnes, L. C. Pavelka, K. M. Baines, *Chem. Soc. Rev.* **2016**, *45*, 1019–1035.
- [138] A. C. Filippou, O. Chernov, G. Schnakenburg, *Angew. Chem.* **2009**, *121*, 5797–5800.
- [139] A. F. Holleman, N. Wiberg, *Grundlagen und Hauptgruppenelemente*, De Gruyter, 103rd ed., **2016**.
- [140] M. Kaftory, M. Kapon, M. Botoshansky in *PATAI'S Chemistry of Functional Groups*, Vol. 2 (Eds.: Z. Rappoport, Y. Apeloig), Wiley, 1st ed., **1998**, pp. 181–265.
- [141] B. J. Fox, Q. Y. Sun, A. G. DiPasquale, A. R. Fox, A. L. Rheingold, J. S. Figueroa, *Inorg. Chem.* **2008**, *47*, 9010–9020.
- [142] S. Yao, Y. Xiong, M. Driess, *Acc. Chem. Res.* **2017**, *50*, 2026–2037.
- [143] L. Zhao, M. Hermann, N. Holzmann, G. Frenking, *Coord. Chem. Rev.* **2017**, *344*, 163–204.
- [144] P. K. Majhi, T. Sasamori, *Chem. Eur. J.* **2018**, *24*, 9441–9455.
- [145] T. Ziegler, A. Rauk, *Theoret. Chim. Acta* **1977**, *46*, 1–10.
- [146] A. Michalak, M. Mitoraj, T. Ziegler, *J. Phys. Chem. A* **2008**, *112*, 1933–1939.
- [147] M. P. Mitoraj, A. Michalak, T. Ziegler, *J. Chem. Theory Comput.* **2009**, *5*, 962–975.
- [148] M. J. Frisch, G. W. Trucks, H. B. Schlegel, G. E. Scuseria, M. A. Robb, J. R. Cheeseman, J. A. M. Jr, T. Vreven, K. N. Kudin, J. C. Burant, J. M. Millam, S. S. Iyengar, J. Tomasi, V. Barone, B. Mennucci, M. Cossi, G. Scalmani, N. Rega, G. A. Petersson, H. Nakatsuji, M. Hada, M. Ehara, K. Toyota, R. Fukuda, J. Hasegawa, M. Ishida, T. Nakajima, Y. Honda, O. Kitao, H. Nakai, M. Klene, X. Li, J. E. Knox, H. P. Hratchian, J. B. Cross, C. Adamo, J. Jaramillo, R. Gomperts, R. E. Stratmann, O. Yazyev, A. J. Austin, R. Cammi, C. Pomelli, J. W. Ochterski, P. Y. Ayala, K. Morokuma, G. A. Voth, P. Salvador, J. J. Dannenberg, V. G.

- Zakrzewski, S. Dapprich, A. D. Daniels, M. C. Strain, O. Farkas, D. K. Malick, A. D. Rabuck, K. Raghavachari, J. B. Foresman, J. V. Ortiz, Q. Cui, A. G. Baboul, S. Clifford, J. Cioslowski, B. B. Stefanov, G. Liu, A. Liashenko, P. Piskorz, I. Komaromi, R. L. Martin, D. J. Fox, T. Keith, M. A. Al-Laham, C. Y. Peng, A. Nanayakkara, M. Challacombe, P. M. W. Gill, B. Johnson, W. Chen, M. W. Wong, C. Gonzalez, J. A. Pople, *Gaussian03 Revision B.02*, 2003.
- [149] A. C. Filippou, G. Schnakenburg, A. I. Philippopoulos, N. Weidemann, *Angew. Chem. Int. Ed.* **2005**, *44*, 5979–5985.
- [150] S. Kumar, *Dissertation in Preparation*, Rheinische Friedrich-Wilhelms-Universität Bonn, Bonn, 2024.
- [151] O. Chernov, PhD thesis, Rheinische Friedrich-Wilhelms-Universität Bonn, 2012.
- [152] H. A. Bent, *Chem. Rev.* **1961**, *61*, 275–311.
- [153] M. Weidenbruch, B. Brand-Roth, S. Pohl, W. Saak, *Polyhedron* **1991**, *10*, 1147–1152.
- [154] A. V. Marenich, C. J. Cramer, D. G. Truhlar, *J. Phys. Chem. B* **2009**, *113*, 6378–6396.
- [155] F. Ramirez, N. B. Desai, B. Hansen, N. McKelvie, *J. Am. Chem. Soc.* **1961**, *83*, 3539–3540.
- [156] H. Schmidbaur, *Nachr. Chem. Tech. Lab.* **1979**, *27*, 620–622.
- [157] H. Schmidbaur, O. Gasser, *Angew. Chem. Int. Ed. Engl.* **1976**, *15*, 502–503.
- [158] H. Schmidbaur, P. Nusstein, *Organometallics* **1985**, *4*, 344–346.
- [159] H. Schmidbaur, P. Nußstein, *Chem. Ber.* **1987**, *120*, 1281–1285.
- [160] R. Tonner, F. Öxler, B. Neumüller, W. Petz, G. Frenking, *Angew. Chem. Int. Ed.* **2006**, *45*, 8038–8042.
- [161] R. Tonner, G. Heydenrych, G. Frenking, *ChemPhysChem* **2008**, *9*, 1474–1481.
- [162] R. Tonner, G. Frenking, *Chem. Eur. J.* **2008**, *14*, 3260–3272.
- [163] R. Tonner, G. Frenking, *Chem. Eur. J.* **2008**, *14*, 3273–3289.
- [164] G. Frenking, R. Tonner, *Pure Appl. Chem.* **2009**, *81*, 597–614.
- [165] C. Esterhuysen, G. Frenking, *Chem. Eur. J.* **2011**, *17*, 9944–9956.
- [166] N. Takagi, R. Tonner, G. Frenking, *Chem. Eur. J.* **2012**, *18*, 1772–1780.
- [167] R. Tonner, G. Frenking, *Angew. Chem. Int. Ed.* **2007**, *46*, 8695–8698.

-
- [168] A. Fürstner, M. Alcarazo, R. Goddard, C. W. Lehmann, *Angew. Chem. Int. Ed.* **2008**, *47*, 3210–3214.
- [169] C. A. Dyker, V. Lavallo, B. Donnadiou, G. Bertrand, *Angew. Chem. Int. Ed.* **2008**, *47*, 3206–3209.
- [170] A. Sidiropoulos, C. Jones, A. Stasch, S. Klein, G. Frenking, *Angew. Chem. Int. Ed.* **2009**, *48*, 9701–9704.
- [171] D. S. Patel, P. V. Bharatam, *J. Org. Chem.* **2011**, *76*, 2558–2567.
- [172] C. A. Dyker, G. Bertrand, *Nat. Chem.* **2009**, *1*, 265–266.
- [173] M. Melaimi, P. Parameswaran, B. Donnadiou, G. Frenking, G. Bertrand, *Angew. Chem. Int. Ed.* **2009**, *48*, 4792–4795.
- [174] D. A. Ruiz, M. Melaimi, G. Bertrand, *Chem. Asian J.* **2013**, *8*, 2940–2942.
- [175] M. Alcarazo, C. W. Lehmann, A. Anoop, W. Thiel, A. Fürstner, *Nat. Chem.* **2009**, *1*, 295–301.
- [176] H. Schmidbaur, A. Schier, *Angew. Chem. Int. Ed.* **2013**, *52*, 176–186.
- [177] T. Morosaki, T. Suzuki, T. Fujii, *Organometallics* **2016**, *35*, 2715–2721.
- [178] M. Christl, B. Engels, *Angew. Chem. Int. Ed.* **2009**, *48*, 1538–1539.
- [179] V. Lavallo, C. A. Dyker, B. Donnadiou, G. Bertrand, *Angew. Chem. Int. Ed.* **2009**, *48*, 1540–1542.
- [180] M. M. Hänninen, A. Peuronen, H. M. Tuononen, *Chem. Eur. J.* **2009**, *15*, 7287–7291.
- [181] I. Fernández, C. A. Dyker, A. DeHope, B. Donnadiou, G. Frenking, G. Bertrand, *J. Am. Chem. Soc.* **2009**, *131*, 11875–11881.
- [182] N. Takagi, T. Shimizu, G. Frenking, *Chem. Eur. J.* **2009**, *15*, 3448–3456.
- [183] N. Takagi, T. Shimizu, G. Frenking, *Chem. Eur. J.* **2009**, *15*, 8593–8604.
- [184] N. Takagi, G. Frenking, *Theor. Chem. Acc.* **2011**, *129*, 615–623.
- [185] N. Wiberg, H.-W. Lerner, S.-K. Vasisht, S. Wagner, K. Karaghiosoff, H. Nöth, W. Ponikwar, *Eur. J. Inorg. Chem.* **1999**, *1999*, 1211–1218.
- [186] S. Ishida, T. Iwamoto, C. Kabuto, M. Kira, *Nature* **2003**, *421*, 725–727.
- [187] M. Kira, S. Ishida, T. Iwamoto, C. Kabuto, *J. Am. Chem. Soc.* **1999**, *121*, 9722–9723.

- [188] M. Kosa, M. Karni, Y. Apeloig, *J. Am. Chem. Soc.* **2004**, *126*, 10544–10545.
- [189] T. Iwamoto, T. Abe, C. Kabuto, M. Kira, *Chem. Commun.* **2005**, 5190.
- [190] T. Iwamoto, H. Masuda, C. Kabuto, M. Kira, *Organometallics* **2005**, *24*, 197–199.
- [191] M. Kosa, M. Karni, Y. Apeloig, *J. Chem. Theory Comput.* **2006**, *2*, 956–964.
- [192] T. Veszprémi, K. Petrov, C. T. Nguyen, *Organometallics* **2006**, *25*, 1480–1484.
- [193] T. Iwamoto, T. Abe, S. Ishida, C. Kabuto, M. Kira, *J. Organomet. Chem.* **2007**, *692*, 263–270.
- [194] M. Kira, T. Iwamoto, S. Ishida, H. Masuda, T. Abe, C. Kabuto, *J. Am. Chem. Soc.* **2009**, *131*, 17135–17144.
- [195] M. Kira, *Chem. Commun.* **2010**, *46*, 2893.
- [196] H. Tanaka, S. Inoue, M. Ichinohe, M. Driess, A. Sekiguchi, *Organometallics* **2011**, *30*, 3475–3478.
- [197] K. C. Mondal, H. W. Roesky, M. C. Schwarzer, G. Frenking, B. Niepötter, H. Wolf, R. Herbst-Irmer, D. Stalke, *Angew. Chem. Int. Ed.* **2013**, *52*, 2963–2967.
- [198] B. Niepötter, R. Herbst-Irmer, D. Kratzert, P. P. Samuel, K. C. Mondal, H. W. Roesky, P. Jerabek, G. Frenking, D. Stalke, *Angew. Chem. Int. Ed.* **2014**, *53*, 2766–2770.
- [199] Y. Wang, Y. Xie, P. Wei, R. B. King, H. F. Schaefer, P. Von R. Schleyer, G. H. Robinson, *Science* **2008**, *321*, 1069–1071.
- [200] Y. Xiong, S. Yao, S. Inoue, J. D. Epping, M. Driess, *Angew. Chem. Int. Ed.* **2013**, *52*, 7147–7150.
- [201] S. Sarmah, A. K. Guha, A. K. Phukan, A. Kumar, S. R. Gadre, *Dalton Trans.* **2013**, *42*, 13200.
- [202] Y. Li, Y.-C. Chan, Y. Li, I. Purushothaman, S. De, P. Parameswaran, C.-W. So, *Inorg. Chem.* **2016**, *55*, 9091–9098.
- [203] M. Wu, Y. He, L. Zhang, R. Wei, D. Wang, J. Liu, L. Leo Liu, G. Tan, *Eur. J. Inorg. Chem.* **2022**, *2022*, e202200413.
- [204] L. C. Siemes, J. Keuter, A. Hepp, F. Lips, *Inorg. Chem.* **2019**, *58*, 13142–13149.
- [205] Y. Wang, M. Karni, S. Yao, A. Kaushansky, Y. Apeloig, M. Driess, *J. Am. Chem. Soc.* **2019**, *141*, 12916–12927.
- [206] S. Yao, A. Kostenko, Y. Xiong, A. Ruzicka, M. Driess, *J. Am. Chem. Soc.* **2020**, *142*, 12608–12612.
- [207] T. Koike, T. Nukazawa, T. Iwamoto, *J. Am. Chem. Soc.* **2021**, *143*, 14332–14341.

- [208] T. Sugahara, T. Sasamori, N. Tokitoh, *Angew. Chem. Int. Ed.* **2017**, *56*, 9920–9923.
- [209] Y. Li, K. C. Mondal, H. W. Roesky, H. Zhu, P. Stollberg, R. Herbst-Irmer, D. Stalke, D. M. Andrada, *J. Am. Chem. Soc.* **2013**, *135*, 12422–12428.
- [210] Y. Xiong, S. Yao, G. Tan, S. Inoue, M. Driess, *J. Am. Chem. Soc.* **2013**, *135*, 5004–5007.
- [211] B. Su, R. Ganguly, Y. Li, R. Kinjo, *Angew. Chem.* **2014**, *126*, 13322–13325.
- [212] Y. Wang, M. Karni, S. Yao, Y. Apeloig, M. Driess, *J. Am. Chem. Soc.* **2019**, *141*, 1655–1664.
- [213] J. Xu, C. Dai, S. Yao, J. Zhu, M. Driess, *Angew. Chem. Int. Ed.* **2022**, *61*, e202114073.
- [214] J. Xu, S. Pan, S. Yao, G. Frenking, M. Driess, *Angew. Chem. Int. Ed.* **2022**, *61*, e202209442.
- [215] A. C. Filippou, Y. N. Lebedev, O. Chernov, M. Straßmann, G. Schnakenburg, *Angew. Chem.* **2013**, *125*, 7112–7116.
- [216] V. Lavallo, Y. Canac, B. Donnadiu, W. W. Schoeller, G. Bertrand, *Angew. Chem. Int. Ed.* **2006**, *45*, 3488–3491.
- [217] G. D. Frey, V. Lavallo, B. Donnadiu, W. W. Schoeller, G. Bertrand, *Science* **2007**, *316*, 439–441.
- [218] M. Soleilhavoup, G. Bertrand, *Acc. Chem. Res.* **2015**, *48*, 256–266.
- [219] I. V. Alabugin, S. Bresch, M. Manoharan, *J. Phys. Chem. A* **2014**, *118*, 3663–3677.
- [220] V. Jonas, G. Frenking, M. T. Reetz, *J. Am. Chem. Soc.* **1994**, *116*, 8741–8753.
- [221] C. Thomson, C. Glidewell, *J. Comput. Chem.* **1983**, *4*, 1–8.
- [222] S. S. Zigler, K. M. Welsh, R. West, J. Michl, *J. Am. Chem. Soc.* **1987**, *109*, 4392–4393.
- [223] M. S. Gordon, M. W. Schmidt, S. Koseki, *Inorg. Chem.* **1989**, *28*, 2161–2163.
- [224] G. Maier, H. P. Reisenauer, J. Glatthaar, R. Zetzmann, *Chem. Asian J.* **2006**, *1*, 195–202.
- [225] D. J. Grant, A. J. Arduengo, D. A. Dixon, *J. Phys. Chem. A* **2009**, *113*, 750–755.
- [226] R. Damrauer, *Polyhedron* **2015**, *97*, 13–19.
- [227] C. Seow, W.-L. Yim, Y. Li, R. Ganguly, C.-W. So, *Inorg. Chem.* **2016**, *55*, 4–6.
- [228] P. Pyykkö, *J. Phys. Chem. A* **2015**, *119*, 2326–2337.
- [229] J. Goubeau, *Angew. Chem.* **1957**, *69*, 77–82.
- [230] P. Jutzi, *Angew. Chem. Int. Ed. Engl.* **1975**, *14*, 232–245.

- [231] P. P. Power, *Chem. Rev.* **1999**, *99*, 3463–3504.
- [232] P. P. Power, *Organometallics* **2020**, *39*, 4127–4138.
- [233] P. J. Davidson, M. F. Lappert, *J. Chem. Soc. Chem. Commun.* **1973**, 317a.
- [234] D. E. Goldberg, D. H. Harris, M. F. Lappert, K. M. Thomas, *J. Chem. Soc. Chem. Commun.* **1976**, 261.
- [235] A. G. Brook, F. Abdesaken, B. Gutekunst, G. Gutekunst, R. K. Kallury, *J. Chem. Soc. Chem. Commun.* **1981**, 191.
- [236] R. West, M. J. Fink, J. Michl, *Science* **1981**, *214*, 1343–1344.
- [237] R. West, *Angew. Chem. Int. Ed. Engl.* **1987**, *26*, 1201–1211.
- [238] R. C. Fischer, P. P. Power, *Chem. Rev.* **2010**, *110*, 3877–3923.
- [239] J. D. Cotton, P. J. Davison, D. E. Goldberg, M. F. Lappert, K. M. Thomas, *J. Chem. Soc. Chem. Commun.* **1974**, 893.
- [240] N. Wiberg, W. Niedermayer, G. Fischer, H. Nöth, M. Suter, *Eur. J. Inorg. Chem.* **2002**, *2002*, 1066–1070.
- [241] N. Wiberg, S. K. Vasisht, G. Fischer, P. Mayer, *Z. anorg. allg. Chem.* **2004**, *630*, 1823–1828.
- [242] A. Sekiguchi, R. Kinjo, M. Ichinohe, *Science* **2004**, *305*, 1755–1757.
- [243] M. Stender, A. D. Phillips, R. J. Wright, P. P. Power, *Angew. Chem. Int. Ed.* **2002**, *41*, 1785–1787.
- [244] A. D. Phillips, R. J. Wright, M. M. Olmstead, P. P. Power, *J. Am. Chem. Soc.* **2002**, *124*, 5930–5931.
- [245] L. Pu, B. Twamley, P. P. Power, *J. Am. Chem. Soc.* **2000**, *122*, 3524–3525.
- [246] P. P. Power, *Organometallics* **2007**, *26*, 4362–4372.
- [247] F. Hanusch, L. Groll, S. Inoue, *Chem. Sci.* **2021**, *12*, 2001–2015.
- [248] M. Karni, Y. Apeloig, *Silicon Chem.* **2002**, *1*, 59–65.
- [249] D. Gau, T. Kato, N. Saffon-Merceron, A. De Cózar, F. P. Cossío, A. Baceiredo, *Angew. Chem. Int. Ed.* **2010**, *49*, 6585–6588.
- [250] S. Takahashi, R. Nougúé, T. Troadec, A. Baceiredo, N. Saffon-Merceron, V. Branchadell, T. Kato, *Inorg. Chem.* **2023**, *62*, 6488–6498.

- [251] A. Singh, *Dissertation in Preparation*, Rheinische Friedrich-Wilhelms-Universität Bonn, Bonn, 2024.
- [252] D. Hoffmann, PhD thesis, Rheinische Friedrich-Wilhelms-Universität Bonn, Bonn, 2021.
- [253] M. M. Gallo, T. P. Hamilton, H. F. Schaefer, *J. Am. Chem. Soc.* **1990**, *112*, 8714–8719.
- [254] H. Lee, J. H. Baraban, R. W. Field, J. F. Stanton, *J. Phys. Chem. A* **2013**, *117*, 11679–11683.
- [255] B. T. Colegrove, H. F. Schaefer, *J. Am. Chem. Soc.* **1991**, *113*, 1557–1561.
- [256] B. S. Thies, R. S. Grev, H. F. Schaefer, *Chem. Phys. Lett.* **1987**, *140*, 355–361.
- [257] K. Kobayashi, S. Nagase, *Organometallics* **1997**, *16*, 2489–2491.
- [258] M. Lein, A. Krapp, G. Frenking, *J. Am. Chem. Soc.* **2005**, *127*, 6290–6299.
- [259] H. Lischka, H. J. Koehler, *J. Am. Chem. Soc.* **1983**, *105*, 6646–6649.
- [260] J. S. Binkley, *J. Am. Chem. Soc.* **1984**, *106*, 603–609.
- [261] A. J. Boone, D. H. Magers, J. Leszczynski, *Int. J. Quant. Chem.* **1998**, *70*, 925–932.
- [262] S. Nagase, K. Kobayashi, N. Takagi, *J. Organomet. Chem.* **2000**, *611*, 264–271.
- [263] A. Jana, V. Huch, D. Scheschkewitz, *Angew. Chem. Int. Ed.* **2013**, *52*, 12179–12182.
- [264] A. Jana, M. Majumdar, V. Huch, M. Zimmer, D. Scheschkewitz, *Dalton Trans.* **2014**, *43*, 5175–5181.
- [265] A. Rit, J. Campos, H. Niu, S. Aldridge, *Nat. Chem.* **2016**, *8*, 1022–1026.
- [266] P. Ghana, M. I. Arz, U. Das, G. Schnakenburg, A. C. Filippou, *Angew. Chem.* **2015**, *127*, 10118–10123.
- [267] P. Ghana, PhD thesis, Springer International Publishing, Bonn, 2019.
- [268] S. Schwarzwald, PhD thesis, Rheinische Friedrich-Wilhelms-Universität Bonn, 2023.
- [269] R. Kobayashi, S. Ishida, T. Iwamoto, *Organometallics* **2021**, *40*, 843–847.
- [270] K. M. Krebs, D. Hanselmann, H. Schubert, K. Wurst, M. Scheele, L. Wesemann, *J. Am. Chem. Soc.* **2019**, *141*, 3424–3429.
- [271] C. Wilhelm, D. Raiser, H. Schubert, C. P. Sindlinger, L. Wesemann, *Inorg. Chem.* **2021**, *60*, 9268–9272.
- [272] V. Lavallo, Y. Canac, C. Präsang, B. Donnadiou, G. Bertrand, *Angew. Chem. Int. Ed.* **2005**, *44*, 5705–5709.

- [273] R. Jazzar, M. Soleilhavoup, G. Bertrand, *Chem. Rev.* **2020**, *120*, 4141–4168.
- [274] D. Martin, M. Soleilhavoup, G. Bertrand, *Chem. Sci.* **2011**, *2*, 389–399.
- [275] M. Melaimi, R. Jazzar, M. Soleilhavoup, G. Bertrand, *Angew. Chem. Int. Ed.* **2017**, *56*, 10046–10068.
- [276] F. Gstrein, PhD thesis, Rheinische Friedrich-Wilhelms-Universität Bonn, Bonn, **2023**.
- [277] M. I. Arz, D. Geiß, M. Straßmann, G. Schnakenburg, A. C. Filippou, *Chem. Sci.* **2015**, *6*, 6515–6524.
- [278] K. C. Mondal, H. W. Roesky, B. Dittrich, N. Holzmann, M. Hermann, G. Frenking, A. Meents, *J. Am. Chem. Soc.* **2013**, *135*, 15990–15993.
- [279] C. Mohapatra, S. Kundu, A. N. Paesch, R. Herbst-Irmer, D. Stalke, D. M. Andrada, G. Frenking, H. W. Roesky, *J. Am. Chem. Soc.* **2016**, *138*, 10429–10432.
- [280] S. Kundu, P. P. Samuel, A. Luebben, D. M. Andrada, G. Frenking, B. Dittrich, H. W. Roesky, *Dalton Trans.* **2017**, *46*, 7947–7952.
- [281] Y. Liu, H. Keil, Z. Yang, R. Herbst-Irmer, H. W. Roesky, D. Stalke, *Eur. J. Inorg. Chem.* **2020**, *2020*, 2273–2278.
- [282] R. Fleischer, *Bachelor Thesis, University of Bonn*, **2020**.
- [283] J.-D. Guo, T. Sasamori, *Chem. Asian J.* **2018**, *13*, 3800–3817.
- [284] M. L. McCrea-Hendrick, C. A. Caputo, J. Linnera, P. Vasko, C. M. Weinstein, J. C. Fettinger, H. M. Tuononen, P. P. Power, *Organometallics* **2016**, *35*, 2759–2767.
- [285] M. Härterich, B. Ritschel, M. Arrowsmith, J. Böhnke, I. Krummenacher, A. K. Phukan, H. Braunschweig, *J. Am. Chem. Soc.* **2021**, *143*, 18339–18345.
- [286] P. Palui, *Dissertation in Preparation*, Rheinische Friedrich-Wilhelms-Universität Bonn, Bonn, **2024**.
- [287] T. Yang, B. B. Dangi, R. I. Kaiser, K.-H. Chao, B.-J. Sun, A. H. H. Chang, T. L. Nguyen, J. F. Stanton, *Angew. Chem. Int. Ed.* **2017**, *56*, 1264–1268.
- [288] M. Ayoubi-Chianeh, M. Z. Kassaei, *J. Phys. Org. Chem.* **2019**, *32*, e3988.
- [289] A. Hopkinson, M. Lien, L. Csizmadia, *Chem. Phys. Lett.* **1983**, *95*, 232–234.
- [290] B. T. Luke, J. A. Pople, M. B. Krogh-Jespersen, Y. Apeloig, M. Karni, J. Chandrasekhar, P. V. R. Schleyer, *J. Am. Chem. Soc.* **1986**, *108*, 270–284.

- [291] R. K. Hilliard, R. S. Grev, *J. Chem. Phys.* **1997**, *107*, 8823–8828.
- [292] Y. Kutin, J. Reitz, P. W. Antoni, A. Savitsky, D. A. Pantazis, M. Kasanmascheff, M. M. Hansmann, *J. Am. Chem. Soc.* **2021**, *143*, 21410–21415.
- [293] R. Stegmann, G. Frenking, *Organometallics* **1995**, *14*, 5308–5315.
- [294] Y. Kuramoto, N. Sawai, Y. Fujiwara, M. Sumimoto, Y. Nakao, H. Sato, S. Sakaki, *Organometallics* **2005**, *24*, 3655–3663.
- [295] X. Wang, Y. Peng, M. M. Olmstead, H. Hope, P. P. Power, *J. Am. Chem. Soc.* **2010**, *132*, 13150–13151.
- [296] T. Yamaguchi, A. Sekiguchi, M. Driess, *J. Am. Chem. Soc.* **2010**, *132*, 14061–14063.
- [297] S. Ishida, R. Sugawara, Y. Misawa, T. Iwamoto, *Angew. Chem. Int. Ed.* **2013**, *52*, 12869–12873.
- [298] M. L. McCrea-Hendrick, C. A. Caputo, J. Linnerra, P. Vasko, C. M. Weinstein, J. C. Fettinger, H. M. Tuononen, P. P. Power, *Organometallics* **2016**, *35*, 2759–2767.
- [299] K. P. C. Vollhardt, *Acc. Chem. Res.* **1977**, *10*, 1–8.
- [300] K. P. C. Vollhardt, *Angew. Chem. Int. Ed. Engl.* **1984**, *23*, 539–556.
- [301] P. L. Pauson, S. Ventre, M. Amatore, C. Aubert, M. Petit in *Encyclopedia of Reagents for Organic Synthesis* (Ed.: John Wiley & Sons, Ltd), John Wiley & Sons, Ltd, Chichester, UK, **2013**, p. rd078.pub2.
- [302] I. U. Khand, G. R. Knox, P. L. Pauson, W. E. Watts, *J. Chem. Soc. Perkin Trans. 1* **1973**, 975.
- [303] I. U. Khand, G. R. Knox, P. L. Pauson, W. E. Watts, M. I. Foreman, *J. Chem. Soc. Perkin Trans. 1* **1973**, 977.
- [304] *The Pauson-Khand Reaction: Scope, Variations and Applications*, (Ed.: R. Rios Torres), Wiley, 1st ed., **2012**.
- [305] A. Krebs, J. Wilke in *Wittig Chemistry, Vol. 109*, Springer-Verlag, Berlin/Heidelberg, **1983**, pp. 189–233.
- [306] C. Benisch, J. Chávez, R. Gleiter, B. Nuber, H. Irngartinger, T. Oeser, H. Pritzkow, F. Rominger, *Eur. J. Inorg. Chem.* **1998**, *1998*, 629–632.
- [307] V. Y. Lee, A. Sekiguchi, *Organometallic Compounds of Low-Coordinate Si, Ge, Sn and Pb: From Phantom Species to Stable Compounds*, Wiley, 1st ed., **2010**.
- [308] T. Sasamori, T. Sugahara, T. Agou, J.-D. Guo, S. Nagase, R. Streubel, N. Tokitoh, *Organometallics* **2015**, *34*, 2106–2109.

- [309] C. Elschenbroich, *Organometallchemie*, Vieweg+Teubner Verlag, Wiesbaden, 6th ed., 2008.
- [310] P. K. Baker, K. R. Flower, M. E. Harman, M. B. Hursthouse, *J. Chem. Soc. Dalton Trans.* 1990, 3169–3173.
- [311] J. J. Kowalczyk, A. M. Arif, J. A. Gladysz, *Organometallics* 1991, 10, 1079–1088.
- [312] P. K. Baker, K. R. Flower, M. G. B. Drew, *Organometallics* 1993, 12, 276–282.
- [313] Z. Chen, C. S. Wannere, C. Corminboeuf, R. Puchta, P. V. R. Schleyer, *Chem. Rev.* 2005, 105, 3842–3888.
- [314] P. V. R. Schleyer, C. Maerker, A. Dransfeld, H. Jiao, N. J. R. Van Eikema Hommes, *J. Am. Chem. Soc.* 1996, 118, 6317–6318.
- [315] H. Fallah-Bagher-Shaidaei, C. S. Wannere, C. Corminboeuf, R. Puchta, P. V. R. Schleyer, *Org. Lett.* 2006, 8, 863–866.
- [316] A. Stanger, *J. Org. Chem.* 2006, 71, 883–893.
- [317] P. Seal, S. Chakrabarti, *J. Phys. Chem. A* 2007, 111, 9988–9994.
- [318] A. Stanger, *Eur. J. Org. Chem.* 2020, 2020, 3120–3127.
- [319] E. Kleinpeter, S. Klod, A. Koch, *Journal of Molecular Structure: THEOCHEM* 2007, 811, 45–60.
- [320] A. Stanger, *J. Phys. Chem. A* 2019, 123, 3922–3927.
- [321] F. London, *J. Phys. Radium* 1937, 8, 397–409.
- [322] P. G. Hayes, Z. Xu, C. Beddie, J. M. Keith, M. B. Hall, T. D. Tilley, *J. Am. Chem. Soc.* 2013, 135, 11780–11783.
- [323] B. Baars, PhD thesis, Rheinische Friedrich-Wilhelms-Universität Bonn, Mensch und Buch Verlag (ISBN 978-3863878641), 2017.
- [324] T. Yoshimoto, H. Hashimoto, M. Ray, N. Hayakawa, T. Matsuo, J. Chakrabarti, H. Tobita, *Chem. Lett.* 2020, 49, 311–314.
- [325] H. Hashimoto, K. Watanabe, T. Yoshimoto, N. Hayakawa, T. Matsuo, H. Tobita, *Chem. Eur. J.* 2023, e202302470.
- [326] R. F. W. Bader, *Chem. Rev.* 1991, 91, 893–928.
- [327] F. Biegler-König, J. Schönbohm, D. Bayles, *AIM2000*, 2001.
- [328] A. Krebs, J. Berndt, *Tetrahedron Lett.* 1983, 24, 4083–4086.

- [329] M. Egorov, S. Kolesnikov, Yu.T. Struchkov, M.Yu. Antipin, S. Sereda, O. Nefedov, *J. Organomet. Chem.* **1985**, *290*, c27–c30.
- [330] A. Sekiguchi, R. Izumi, S. Ihara, M. Ichinohe, V. Y. Lee, *Angew. Chem. Int. Ed.* **2002**, *41*, 1598–1600.
- [331] M. Walewska, J. Baumgartner, C. Marschner, L. Albers, T. Müller, *Chem. Eur. J.* **2016**, *22*, 18512–18521.
- [332] J. Böserle, G. Zhigulin, P. Štěpnička, F. Horký, M. Erben, R. Jambor, A. Růžicka, S. Ketkov, L. Dostál, *Dalton Trans.* **2017**, *46*, 12339–12353.
- [333] T. Y. Lai, K. L. Gullett, C.-Y. Chen, J. C. Fettinger, P. P. Power, *Organometallics* **2019**, *38*, 1421–1424.
- [334] E. O. Fischer, G. Kreis, C. G. Kreiter, J. Müller, G. Huttner, H. Lorenz, *Angew. Chem. Int. Ed. Engl.* **1973**, *12*, 564–565.
- [335] E. O. Fischer, *Angew. Chem.* **1974**, *86*, 651–663.
- [336] H. P. Kim, R. J. Angelici in *Advances in Organometallic Chemistry*, Vol. 27, Elsevier, **1987**, pp. 51–111.
- [337] Fischer, H.; Hofmann, P.; Kreissl, F.R.; Schrock, R.R.; Schubert, U.; Weiss, K., *Carbyne Complexes*, Wiley-VCH, Weinheim, **1988**.
- [338] A. Mayr, H. Hoffmeister in *Adv. Organometal. Chem.*, Vol. 32, Elsevier, **1991**, pp. 227–324.
- [339] R. S. Simons, P. P. Power, *J. Am. Chem. Soc.* **1996**, *118*, 11966–11967.
- [340] L. Pu, B. Twamley, S. T. Haubrich, M. M. Olmstead, B. V. Mork, R. S. Simons, P. P. Power, *J. Am. Chem. Soc.* **2000**, *122*, 650–656.
- [341] A. C. Filippou, P. Portius, A. I. Philippopoulos, H. Rohde, *Angew. Chem. Int. Ed.* **2003**, *42*, 445–447.
- [342] A. C. Filippou, A. I. Philippopoulos, G. Schnakenburg, *Organometallics* **2003**, *22*, 3339–3341.
- [343] A. C. Filippou, H. Rohde, G. Schnakenburg, *Angew. Chem. Int. Ed.* **2004**, *43*, 2243–2247.
- [344] A. C. Filippou, N. Weidemann, G. Schnakenburg, H. Rohde, A. I. Philippopoulos, *Angew. Chem. Int. Ed.* **2004**, *43*, 6512–6516.
- [345] A. C. Filippou, N. Weidemann, G. Schnakenburg, *Angew. Chem. Int. Ed.* **2008**, *47*, 5799–5802.

- [346] A. C. Filippou, O. Chernov, K. W. Stumpf, G. Schnakenburg, *Angew. Chem. Int. Ed.* **2010**, *49*, 3296–3300.
- [347] G. Dübek, F. Hanusch, D. Munz, S. Inoue, *Angew. Chem. Int. Ed.* **2020**, *59*, 5823–5829.
- [348] G. Schnakenburg, PhD thesis, University of Bonn, **2009**.
- [349] A. C. Filippou, A. I. Philippopoulos, P. Portius, D. U. Neumann, *Angew. Chem. Int. Ed.* **2000**, *39*, 2778–2781.
- [350] S. F. Vyboishchikov, G. Frenking, *Chem. Eur. J.* **1998**, *4*, 1439–1448.
- [351] M. Lein, A. Szabó, A. Kovács, G. Frenking, *Faraday Discuss.* **2003**, *124*, 365–378.
- [352] K. K. Pandey, M. Lein, G. Frenking, *J. Am. Chem. Soc.* **2003**, *125*, 1660–1668.
- [353] K. K. Pandey, A. Lledós, *Inorg. Chem.* **2009**, *48*, 2748–2759.
- [354] K. K. Pandey, P. Patidar, *RSC Adv.* **2014**, *4*, 13034.
- [355] M. J. S. Dewar, *Bull. Soc. Chim. Fr.* **1951**, C71–C79.
- [356] J. Chatt, L. A. Duncanson, *J. Chem. Soc.* **1953**, 2939.
- [357] L. J. Guggenberger, R. R. Schrock, *J. Am. Chem. Soc.* **1975**, *97*, 2935–2935.
- [358] R. R. Schrock, *Angew. Chem. Int. Ed.* **2006**, *45*, 3748–3759.
- [359] B. Blom, PhD thesis, University of Bonn, **2011**.
- [360] Y. N. Lebedev, PhD thesis, University of Bonn, **2014**.
- [361] N. Wienkenhöver, PhD thesis, University of Bonn, **2017**.
- [362] H. Hashimoto, H. Tobita, *Coord. Chem. Rev.* **2018**, *355*, 362–379.
- [363] L. Arizpe, PhD thesis, University of Bonn, **2019**.
- [364] S. Saini, A. Agarwal, S. K. Bose, *Dalton Trans.* **2020**, *49*, 17055–17075.
- [365] M. Widemann, K. Eichele, H. Schubert, C. P. Sindlinger, S. Klenner, R. Pöttgen, L. Wesemann, *Angew. Chem. Int. Ed.* **2021**, *60*, 5882–5889.
- [366] M. Auer, K. Zwettler, K. Eichele, H. Schubert, C. P. Sindlinger, L. Wesemann, *Angew. Chem. Int. Ed.* **2023**, *62*, e202305951.
- [367] E. O. Fischer, J. R. Schneider, *J. Organomet. Chem.* **1985**, *295*, c29–c34.
- [368] I. Papazoglou, PhD thesis, University of Bonn, **2016**.

-
- [369] P. M. Keil, T. J. Hadlington, *Chem. Commun.* **2022**, 10.1039.D2CC00422D.
- [370] K. K. Pandey, P. Patidar, P. P. Power, *Inorg. Chem.* **2011**, *50*, 7080–7089.
- [371] P. Hofmann in *Carbyne Complexes*, VCH Verlagsgesellschaft, Weinheim; VCH Publishers, New York, 1st ed., **1988**, p. 76.
- [372] G. te Velde, F. M. Bickelhaupt, E. J. Baerends, C. Fonseca Guerra, S. J. A. van Gisbergen, J. G. Snijders, T. Ziegler, *J. Comput. Chem.* **2001**, *22*, 931–967.
- [373] E. Van Lenthe, E. J. Baerends, *J. Comput. Chem.* **2003**, *24*, 1142–1156.
- [374] J. H. Gross, *Mass Spectrometry*, Springer International Publishing, Cham, **2017**.
- [375] J. Thomson, *The London Edinburgh and Dublin Philosophical Magazine and Journal of Science* **1908**, *16*, 657–691.
- [376] J. Thomson, *The London Edinburgh and Dublin Philosophical Magazine and Journal of Science* **1911**, *21*, 225–249.
- [377] J. Thomson, *The London Edinburgh and Dublin Philosophical Magazine and Journal of Science* **1912**, *24*, 209–253.
- [378] F. W. Aston, *Nature* **1919**, *104*, 393–393.
- [379] F. W. Aston, *Mass Spectra and Isotopes*, **1922**.
- [380] J. R. Yates III, *Nat. Methods* **2011**, *8*, 633–637.
- [381] A. Doerr, J. Finkelstein, I. Jarchum, C. Goodman, B. Dekker, *Nat. Methods* **2015**, *12*, 3–3.
- [382] V. L. Tal'roze, A. K. Ljubimova, *J. Mass Spectrom.* **1998**, *33*, 502–504.
- [383] M. S. B. Munson, F. H. Field, *J. Am. Chem. Soc.* **1965**, *87*, 3294–3299.
- [384] M. S. B. Munson, *J. Am. Chem. Soc.* **1965**, *87*, 2332–2336.
- [385] M. S. B. Munson, F. H. Field, *J. Am. Chem. Soc.* **1966**, *88*, 2621–2630.
- [386] B. Munson, *Int. J. Mass Spectrom.* **2000**, *200*, 243–251.
- [387] H. D. Beckey, *Z. Naturforsch. A* **1959**, *14*, 712–721.
- [388] H. Beckey, *J. Mass Spectrom. and Ion Physics* **1969**, *2*, 500–502.
- [389] H. Beckey, A. Heindrichs, H. Winkler, *J. Mass Spectrom. and Ion Physics* **1970**, *3*, A9–A11.
- [390] H. B. Linden, *Eur. J. Mass Spectrom.* **2004**, *10*, 459–468.

- [391] J. H. Gross, N. Nieth, H. B. Linden, U. Blumbach, F. J. Richter, M. E. Tauchert, R. Tompers, P. Hofmann, *Anal. Bioanal. Chem.* **2006**, *386*, 52–58.
- [392] W. H. Monillas, G. P. A. Yap, K. H. Theopold, *Angew. Chem. Int. Ed.* **2007**, *46*, 6692–6694.
- [393] D. Biskup, G. Schnakenburg, R. T. Boéré, A. Espinosa Ferao, R. K. Streubel, *Nat. Commun.* **2023**, *14*, 6456.
- [394] T. E. Taylor, M. B. Hall, *J. Am. Chem. Soc.* **1984**, *106*, 1576–1584.
- [395] J. D. Queen, A. C. Phung, C. A. Caputo, J. C. Fettinger, P. P. Power, *J. Am. Chem. Soc.* **2020**, *142*, 2233–2237.
- [396] P. Ghana, J. Rump, G. Schnakenburg, M. I. Arz, A. C. Filippou, *J. Am. Chem. Soc.* **2021**, *143*, 420–432.
- [397] H. Hashimoto, T. Fukuda, H. Tobita, M. Ray, S. Sakaki, *Angew. Chem. Int. Ed.* **2012**, *51*, 2930–2933.
- [398] J. Hicks, T. J. Hadlington, C. Schenk, J. Li, C. Jones, *Organometallics* **2013**, *32*, 323–329.
- [399] T. Yoshimoto, H. Hashimoto, N. Hayakawa, T. Matsuo, H. Tobita, *Organometallics* **2016**, *35*, 3444–3447.
- [400] T. P. Dhungana, H. Hashimoto, M. Ray, H. Tobita, *Organometallics* **2020**, *39*, 4350–4361.
- [401] C. Lindlahr, PhD thesis, University of Bonn, 2014.
- [402] P. Ghana, M. I. Arz, U. Chakraborty, G. Schnakenburg, A. C. Filippou, *J. Am. Chem. Soc.* **2018**, *140*, 7187–7198.
- [403] W. Henderson, B. K. Nickleson, L. J. McCaffrey, *Polyhedron* **1998**, *17*, 4291–4313.
- [404] E. T. Seidl, R. S. Grev, H. F. Schaefer, *J. Am. Chem. Soc.* **1992**, *114*, 3643–3650.
- [405] D. Hoffmann, T. Gross, R. Kempe, H. Oehme, *Journal of Organometallic Chemistry* **2000**, *598*, 395–402.
- [406] R. S. Ghadwal, H. W. Roesky, K. Pröpper, B. Dittrich, S. Klein, G. Frenking, *Angew. Chem. Int. Ed.* **2011**, *50*, 5374–5378.
- [407] T. Deckstein, *Dissertation in Preparation*, Rheinische Friedrich-Wilhelms-Universität Bonn, Bonn, 2024.
- [408] J. Rump, *Dissertation in Preparation*, Rheinische Friedrich-Wilhelms-Universität Bonn, Bonn, 2024.
- [409] R. L. Woodin, D. S. Bomse, J. L. Beauchamp, *J. Am. Chem. Soc.* **1978**, *100*, 3248–3250.